

Characterisation of a mouse model of Protocadherin 19

A thesis submitted to Cardiff University in accordance
with the requirements for the degree of Doctor of
Philosophy in the discipline of Neurosciences

Natalia Galindo Riera

Supervisor: Isabel Martínez Garay



September 2019

Declaration

This work has not been submitted in substance for any other degree or award at this or any other university or place of learning, nor is being submitted concurrently in candidature for any degree or another award.

Signed..... Date

STATEMENT 1

This thesis is being submitted in partial fulfillment of the requirements for the degree of Ph.D.

Signed..... Date

STATEMENT 2

This thesis is the result of my own independent work/investigation, except where otherwise stated, and the thesis has not been edited by a third party beyond what is permitted by Cardiff University's Policy on the Use of Third Party Editors by Research Degree Students. Other sources are acknowledged by explicit references. The views expressed are my own.

Signed..... Date

STATEMENT 3:

I hereby give consent for my thesis, if accepted, to be available online in the University's Open Access repository and for inter-library loan, and for the title and summary to be made available to outside organisations.

Signed..... Date

Acknowledgements

Many thanks to Doctor Isabel Martínez Garay for her kind supervision and patience over the duration of my PhD. Thank you for the opportunity to work in this amazing project and helping me in taking these first steps into my career. I would also like to thank Professor Yves Barde and Doctor Stéphane for their explanations and input in the project. Special thanks to Professor Meng Li, whose enthusiastic assessment of the project was very encouraging. Also, thanks to all member of my lab for the incredible support and effort to create a positive and smooth environment. To Dr. Xinsheng Nan for the happiness and expertise provided; to Dr. Cristina Llinares Benadero and Dr. Katharina Saeuberli for their earnest help and ideas; and to Ph.D. students Spyros Merkouris, Dr. Laura Cassels, Dr. Sven Bachmann and PhD students Sylvia Newbold, Monika Sledziowska, Sarah Ateaque and Erin Wosnitzka for daily lab life help and for their energy in providing a calm and warm environment. Very special thanks to my colleagues and friends, Dr. Hayley Dingsdale, Dr. Ellen Cross, Dr. Jessica Griffiths and Dr. Shireene Kalbassi for all the help and support and for providing an environment in the office that makes you feel at home. To PhD student Yipkin for listening to my rantings and exerting a role as a driver when I stayed late at the lab. Many thanks to my summer student Niahm, for her help in the RORB and SATB2 cortical analysis. My thanks also go to the Wellcome Trust and the Welsh Government's Sêr Cymru program, who funded this project. Last but not least, I would like to thank my parents, Carlos Galindo Pastor and Maria Riera Montero, for their invaluable and unconditional support, and my extended family and friends, for their comprehension and positive mindset during the completion of my thesis.

Several people also contributed to the completion of this thesis.

I would like to thank Dr. Isabel Martinez-Garay for conducting the *in utero* electroporations used to study the migration in Chapter 4.

Many thanks to Dr Xinsheng Nan for providing the HEK293T cell line used for the shRNA effectiveness test of Chapter 4.

Special thanks to my summer student Niahm, for her contribution in the RORB and SATB2 cortical analysis of Chapter 5.

Thanks also go to Dr. Jessica Griffiths, for the optimisation of the BGAL and PCDH19 antibodies used in Chapter 3.

Finally, I would like to also thank Dr Stéphane Badouin for providing me with the necessary equipment to perform the open field, elevated plus maze and social interaction behavioural tests, as well as Professor Riccardo Brambilla, who kindly allowed me to use the equipment needed for the 24-hour activity test conducted in Chapter 6.

Abstract

The protocadherin 19 (*PCDH19*) gene is encoded on the X-chromosome and its mutation causes Early Infantile Epileptic Encephalopathy 9 (EIEE9). This disorder is characterised by epilepsy in infancy or early childhood, often accompanied by cognitive impairment and behavioural disturbances of diverse severity in heterozygous females. Mosaicism of *PCDH19* positive and negative cells is believed to underpin the symptoms through a mechanism of cellular interference, leading to disruption in cell-cell communication, synapse formation and hyperexcitability of neurons. However, the expression and function of the gene in mammals are still poorly understood. The aim of this thesis was to characterise a *Pcdh19*-knock-out (KO) mouse model, focusing on cortical migration and lamination, and on animal behaviour. An analysis of the neuronal types expressing *Pcdh19* in the postnatal cortex was also undertaken.

By combining RNA *in situ* hybridisation and immunohistochemistry, *Pcdh19* was found to be expressed by a wide variety of excitatory and inhibitory neuronal types, although expression was strongest in layers II/III and Va. *In utero* electroporation experiments in mutant animals revealed subtle differences in the migration of *Pcdh19*-KO neurons but no significant changes in *Pcdh19* heterozygous (HET) females. Accordingly, analysis of cortical markers by immunostaining revealed only very minor differences in the number or distribution of marker-positive cells between *Pcdh19*-WT and mutant animals. The results of the behavioural analysis suggested a higher sensitivity of *Pcdh19*-HET females to new environments and demonstrated an effect of housing on the behaviour of WT animals.

Together, this study highlights the heterogeneity of *Pcdh19* expressing cells and discards major roles of this protein in cortical lamination and migration. However, the behavioural changes point to alterations in circuit formation or function. These results provide an initial path to gain insight into the pathophysiology of EIEE9.

Abbreviations

μg	Microgram (s)
μL	Microlitre (s)
μm	Micrometer (s)
10x	Low power objective, 10x magnification
5HT3aR	Ionotropic serotonin receptor 5HT3a
Amp	Ampicillin
ANOVA	Analysis of variance
AP	Alkaline phosphatase
AS Probe	Antisense probe
ASD	Autism spectrum disorder
AUC	Area under the curve
BCA	Bicinchoninic acid
BCIP/NBT	5-bromo-4-chloro-3-indolyl-phosphate/nitro blue tetrazolium
Bis-Tris	Bisamino-trismethan
BSA	Bovine serum albumin
BSNP	Burst spiking non-pyramidal cells
CA	<i>Cornu ammonis</i>
CB	Calbindin

Cb	Cerebellum
CBA	Chicken beta actin promoter
Cdh2	Cadherin 2
cDNA	Coding deoxyribonucleic acid
CGE	Caudal ganglionic eminence
CISH	Colorimetric <i>in situ</i> hybridization
CM	Conserved motifs
cm²	Square centimetre (s)
CMV promoter	Cytomegalovirus promoter
CNS	Central nervous system
CR	Calretinin
CTIP2	Chicken ovalbumin upstream promoter transcription factor interacting protein 2
<i>CTNND1</i>	catenin delta-1
CTX	Cortex
CUX1	Cut like homeobox 1
DAPI	4',6-diamidino-2-phenylindol dihydrochloride
DCX	Doublecortin
DG	Dentate gyrus
DIG	Digoxigenin

DMEM	Dulbecco's Modified Eagle Medium
DMSO	Dimethyl sulfoxide
DNA	Deoxyribonucleic acid
dNTP	Deoxynucleotide triphosphate
dsDNA	Double-stranded DNA
DTT	Dithiothreitol
dUTP	2'-deoxyuridine 5'-triphosphate
E0.5	Embryonic day 0.5 post coitum
EC	Extracellular cadherin domains
EDTA	Ethylenediaminetetraacetic acid
EGFP	Enhanced green fluorescent protein
EIEE9	Early infantile epileptic encephalopathy 9
EPM	Elevated plus maze
EPS	Expanded polystyrene
ERα	Oestrogen receptor alpha
EtOH	Ethanol
FBS	foetal bovine serum
FISH	Fluorescent <i>in situ</i> hybridization
FS	Fast-spiking
GABA	Gamma aminobutyric acid

GAD65/67	Glutamic acid decarboxylase 65 and 67
GAPDH	Glyceraldehyde 3-phosphate dehydrogenase
h	Hours
HA-tag	Human influenza hemagglutinin tag
HEBS	HEPES saline buffer
HEK293T	Human embryonic kidney cells experiment 293 transformed with large T antigen
HET	Heterozygous
HPC	Hippocampus
HRP	Horseradish peroxidase
IHC	Immunohistochemistry
IP	Intermediate progenitor
IRES	Internal ribosomal entry site
IS	Irregular spiking
ISH	<i>In situ</i> hybridization
IUE	<i>In utero</i> electroporation
Kan	Kanamycin sulphate
KCl	Potassium chloride
kDa	Kilodalton (s)
KH₂PO₄	Potassium phosphate monobasic

KO	Knock-out
L	Litre (s)
LDS	Lithium dodecyl sulphate
LHX2	LIM homeobox 2
M	Molar
MES	2-(N-morpholino) ethanesulfonic acid
MgCl₂	Magnesium dichloride
MGE	Medial ganglionic eminence
MGH	Mixed genotype housing
Min	Minute (s)
mL	Millilitre (s)
mM	millimolar
mM	Millimolar
mm	Millimeter (s)
MW	Molecular weight
MZ	Marginal zone
Na₂HPO₄	Sodium phosphate dibasic
NaCl	Sodium chloride
NEAA	Non-Essential amino acids
NEC	Neural stem neuroepithelial cell

ng	Nanograms
OB	Olfactory bulb
OCT	Optimum cutting temperature
OTX1	Orthodenticle homeobox 1
P0	Postnatal day 0
PBS	Phosphate buffered saline
Pcdh10	Protocadherin 10
Pcdh17	Protocadherin 17
<i>Pcdh19</i>	Rodent protocadherin19 gene
<i>PCDH19</i>	Human protocadherin19 gene
PCDH19	Protocadherin19 protein
<i>Pcdh19FL</i>	<i>Protocadherin 19</i> full-length
PCR	Polymerase chain reaction
PFA	Paraformaldehyde
POD	Peroxidase
PV	Parvalbumin
RGC	Radial glial cell
RIPA	Radioimmunoprecipitation assay buffer
RNA	Ribonucleic acid
RORB	RAR related orphan receptor B

rpm	Revolutions per minute
RSNP	Regular spiking non-pyramidal cells
RT	Room temperature
S Probe	Sense probe
S.O.C.	Super optimal growth with catabolite repression
SASC	Salt and sodium citrate
SATB2	Special AT-rich sequence-binding protein 2
SDS	Sodium Dodecyl Sulfate
sec	Second (s)
SEM	Standard error of the mean
SGH	Single genotype housing
shRNA	Short hairpin ribonucleic acid
SSC	Somatosensory cortex
SST	Somatostatin
ST	Striatum
SV40	Simian virus 40
SVZ	Subventricular zone
TBE	Tris-Borate-EDTA
TBR1	T-box, brain 1

TBS	Tris-buffered saline
TH	Thalamus
UTR	Untranslated region
VIP	Vasoactive intestinal peptide
VZ	Ventricular zone
WAVE	Wiskott-Aldrich syndrome protein family verprolin-homologous protein
WIRS	WRC Interactive receptor sequence
WRC	WAVE regulatory complex
WT	Wild-type

Contents

Declaration	I
Acknowledgements	II
Abstract	IV
Abbreviations	V
Contents	XIII
List of Figures	XX
List of tables	XXVI
Chapter 1: Introduction.	1
1.1 The cadherin superfamily	1
1.2 The protocadherin family	5
1.3 <i>Pcdh19</i> structure	14
1.4 <i>Pcdh19</i> expression	15
1.5 Early Infantile Encephalopathy 9 (EIEE9).....	17
1.6 <i>Pcdh19</i> function	18
1.6.1 Role in cell-cell interaction.....	18
1.6.2 Role in intracellular signalling	20
1.6.3 Role in cortical development.....	22
1.6.4 Role in behaviour	22
1.7 Cortical development.....	23
1.8 Cortical lamination.....	28
1.9 Behaviour.....	36
1.10 Aims and hypothesis	37
Chapter 2: Material and methods.	39

2.1	Animal husbandry and legislation	39
2.1.1	Animal housing	39
2.1.2	Animals used	39
2.1.3	Animal matings	40
2.1.4	Mouse genotyping	40
2.1.4.1	DNA extraction.....	40
2.1.4.2	PCR analysis.....	41
2.2	Real-time quantitative polymerase chain reaction (PCR).....	43
2.2.1	Dissection	43
2.2.2	RNA extraction and reverse transcription.....	43
2.2.3	Quantitative PCR protocol and analysis.....	44
2.3	Histological techniques.....	48
2.3.1	Brain extraction and fixation	48
2.3.1.1	Embryonic brain extraction.....	48
2.3.1.2	Perfusion	48
2.3.2	Sectioning	49
2.3.2.1	Cryostat sectioning.....	49
2.3.2.2	Vibratome sectioning.....	50
2.3.3	Staining	50
2.3.3.1	ISH	50
2.3.3.2	Immunohistochemistry (IHC).....	60
2.3.3.3	<i>In situ</i> hybridization combined with immunohistochemistry	64
2.3.3.4	X-gal staining combined with IHC	64
2.3.4	Confocal microscopy	65
2.4	ShRNA effectiveness test.....	67
2.4.1	ShRNA preparation	67
2.4.2	HEK293T cell culture	72
2.4.3	Plasmid construction	73

2.4.4	Plasmid transfection	75
2.4.5	Cell lysis.....	76
2.4.6	BCA assay.....	76
2.4.7	Western blot	78
2.5	<i>In utero</i> electroporation	83
2.6	Behaviour.....	84
2.6.1	Open field.....	85
2.6.2	Elevated plus maze	86
2.6.3	Social interaction	86
2.6.4	24-hour activity.....	87
2.7	Statistical analysis.....	89

Chapter 3: Characterization of Protocadherin 19 expressing neurons in the developing cortex. 90

3.1	Introduction.....	90
3.2	Aims.....	92
3.3	Results	93
3.3.1	No antibodies could be optimised to detect PCDH19 by immunohistochemistry	93
3.3.2	<i>Pcdh19</i> mRNA is detected in the cortical wall at late embryonic and early postnatal stages.....	99
3.3.3	<i>Pcdh19</i> mRNA expressing cells partially colocalise with a diverse group of cortical excitatory and interneuronal markers.	110
3.3.3.1	Distribution of <i>Pcdh19</i> + cells in P10 and P20 cortices.....	110
3.3.3.2	Glutamatergic cortical markers at P10	114
3.3.3.3	Interneuronal cortical markers at P20.....	121
3.4	Discussion.....	124
3.4.1	Summary of results	124

3.4.2	Choice of methods.....	124
3.4.3	<i>Pcdh19</i> mRNA localization.....	126
3.4.4	<i>Pcdh19</i> colocalization with cortical excitatory and interneuronal markers	129
3.4.5	Conclusion.....	133
Chapter 4: Role of Protocadherin 19 in cortical migration.....		134
4.1	Introduction.....	134
4.2	Aims.....	135
4.3	Results	136
4.3.1	<i>Pcdh19</i> shRNAs effectively knockdown PCDH19.....	136
4.3.2	Analysis of cortical migration at E13.5.....	145
4.3.2.1	<i>Pcdh19</i> knockdown by shRNAs at E13.5 did not show any differences in migration with respect to the control.....	145
4.3.2.2	pCIG <i>in utero</i> electroporation experiments at E13.5 showed a decrease in migration in <i>Pcdh19</i> -KO animals with respect to the WT and <i>Pcdh19</i> -HET animals	161
4.3.3	Analysis of cortical migration at E15.5.....	165
4.3.3.1	<i>Pcdh19</i> knockdown by shRNAs at E15.5 in WT and <i>Pcdh19</i> -KO brains altered neuronal migration compared to the control	165
4.3.3.2	EGFP <i>in utero</i> electroporation on WT, <i>Pcdh19</i> -HET and <i>Pcdh19</i> -KO animals at E15.5 present differences in the cell migration of mutant animals with respect to the WT littermates.....	174
4.4	Discussion.....	178
4.4.1	Summary of results	178
4.4.2	Assessment of <i>Pcdh19</i> shRNAs effectiveness.....	178
4.4.3	Choice of methods.....	179
4.4.4	Analysis of migration in early-born neurons.....	181
4.4.4.1	ShRNA <i>in utero</i> electroporations: abnormal shRNA#2 results.	181
4.4.4.2	Comparison of results obtained with shRNA vs EGFP electroporations at E13.5	182

4.4.4.3	Possible causes of the abnormal positioning of the EGFP+ cells in the <i>Pcdh19</i> -KO brains.....	183
4.4.4.4	Absence of phenotype in the <i>Pcdh19</i> -HET brains and possible future experiments	184
4.4.5	Analysis of migration in late-born neurons	188
4.4.5.1	ShRNA <i>in utero</i> electroporations on WT and <i>Pcdh19</i> -KO animals.....	188
4.4.5.2	EGFP <i>in utero</i> electroporations on WT, <i>Pcdh19</i> -HET and <i>Pcdh19</i> -KO animals	190
4.4.6	Conclusion.....	194

Chapter 5: Characterization of the WT, *Pcdh19*-HET and *Pcdh19*-KO animals. 196

5.1	Introduction.....	196
5.2	Aims.....	197
5.3	Results	198
5.3.1	No differences in cortical width, total number and distribution of cells in the SSC among genotypes.....	201
5.3.2	Cell number and distribution of cortical excitatory neurons in the P10 SSC.....	205
5.3.2.1	CUX1-expressing cells showed a slight difference in distribution between WT and <i>Pcdh19</i> -HET	205
5.3.2.2	SATB2-positive cells were similar in number and distribution among genotypes.....	208
5.3.2.3	No significant differences were detected among the genotypes regarding the number or distribution of cells positive for RORB	210
5.3.2.4	Cells expressing CTIP2 did not present any differences among conditions.....	213
5.3.2.5	Analysis of TBR1-positive cells revealed a difference in distribution between the HET and KO animals.....	216
5.3.3	Cell number and distribution analysis of GABAergic interneurons in the SSC of P20 animals	220
5.3.3.1	Parvalbumin-expressing cells did not present any significant differences in their number or distribution amongst the genotypes.	220
5.3.3.2	Analysis of calretinin-positive cells showed no differences among the different genotypes.....	224

5.3.3.3	Cells expressing calbindin presented minor differences in distribution between <i>Pcdh19</i> -HET brains and <i>Pcdh19</i> -KO brains	228
5.3.3.4	Analysis of the SSC detects a difference among mutants in the distribution of somatostatin-expressing cells.....	232
5.4	Discussion.....	236
5.4.1	Results.....	236
5.4.2	Choice of methods.....	236
5.4.3	Analysis of glutamatergic neurons.....	237
5.4.4	Analysis of GABAergic neurons.....	241
5.4.5	Conclusion and future experiments.....	246
Chapter 6: Behavioural analysis of the WT, <i>Pcdh19</i>-HET and <i>Pcdh19</i>-KO animals.		251
6.1	Introduction.....	251
6.2	Aim	252
6.3	Results	253
6.3.1	Open field analysis in males.....	256
6.3.1.1	General locomotor activity does not reveal any differences among the conditions.....	256
6.3.1.2	No differences in thigmotaxis were observed between conditions... ..	258
6.3.1.3	An increase in the distance run in the 5-min slot was detected in the WT MGH compared to the WT SGH animals at P21	260
6.3.1.4	WT MGH males presented a failure in the habituation between trials at P21	263
6.3.2	The 24-hour activity test showed a delay in the increase of activity in the KO MGH mice at the onset of the dark period.....	265
6.3.3	No differences in the EPM test among conditions	269
6.3.4	Social behaviour analysis detected a decrease in the social interaction of MGH compared to SGH males.....	271
6.3.5	Open field analysis in females.....	273
6.3.5.1	General locomotor activity analysis detected an increase in the activity of MGH mice with respect to the WT SGH animals.....	273

6.3.5.2	Thigmotaxis of WT MGH females is increased compared to WT SGH at P60	275
6.3.5.3	MGH mice presented an increase in the total distance run in the 5-min slot compared to the WT SGH mice at both ages	277
6.3.5.4	WT MGH do not habituate at P21 and habituate at P60, unlike the other conditions	280
6.3.6	24-hour activity analysis revealed minor differences among the females	282
6.3.7	P21 HET MGH animals spent more time in the open arms of the EPM than WT mice	285
6.3.8	No differences are observed in social behaviour among females	287
6.4	Discussion	289
6.4.1	Summary of results	289
6.4.2	Choice of methods	293
6.4.3	Behavioural differences in the KO MGH males	297
6.4.4	Behavioural differences in the HET MGH females	299
6.4.5	Effects of housing (SGH vs MGH)	302
6.4.6	Conclusion	304
Chapter 7: General discussion.		305
7.1	Summary of results	305
7.2	Interpretation of the results in the general context of <i>Pcdh19</i>	309
7.3	The mouse as a model for the study of EIEE9	311
7.4	Future directions	316
7.5	Concluding remarks	321
References		322
Appendix		366

List of Figures

Figure 1. Classification of the cadherin family, according to Hulpiau and van Roy, 2009.....	3
Figure 2. Molecular structure of the subfamilies that belong to the cadherin family mentioned in this thesis, except for the protocadherin family.	4
Figure 3. Molecular structure of the subgroups that belong to the protocadherin subfamily.....	8
Figure 5. Neurogenesis and radial migration in mice.	27
Figure 6. Probe generation.....	55
Figure 7. A schematic showing where the different <i>Pcdh19</i> shRNAs bind to the <i>Pcdh19</i> mRNA.	68
Figure 8. The ANTI-B-GALACTOSIDASE antibody did not allow identification of individual cells in P2 <i>Pcdh19</i> -KO mice brains.....	97
Figure 9. No reliable co-detection of B-GALACTOSIDASE activity by X-gal staining and IHC against molecular markers.	98
Figure 10. <i>Pcdh19</i> is detected in the cortical plate at E16.5.....	101
Figure 11. <i>Pcdh19</i> mRNA is expressed in the cortical plate at P2.....	102
Figure 12. Expression of <i>Pcdh19</i> in the cortical plate of P6 mice.....	104
Figure 13. <i>Pcdh19</i> is detected in the cortical plate of P10 mice.	105
Figure 14. <i>Pcdh19</i> is detected in the cortical plate at P15.....	106
Figure 15. <i>Pcdh19</i> is expressed in the cortical plate at P20.	107
Figure 16. <i>Pcdh19</i> cortical expression in early postnatal mice peaks at P10.	109
Figure 17. <i>Pcdh19</i> mRNA is mainly detected in layers II/III and V and is more abundant in P10 than in P20 brains at the SSC.....	112
Figure 18. Almost half of <i>Pcdh19</i> mRNA expressing cells coexpress SATB2 in P10 SSC.....	116
Figure 19. <i>Pcdh19</i> mRNA expressing cells partially coexpress RORB in P10 SSC.....	117

Figure 20. Cells expressing <i>Pcdh19</i> mRNA partially coexpress CTIP2 in P10 SSC.....	118
Figure 21. Cells positive for <i>Pcdh19</i> mRNA partially coexpress TBR1 in P10 SSC.....	119
Figure 22. <i>Pcdh19</i> mRNA expression is specifically located in layer Va and part of layer Vb.....	120
Figure 23. <i>Pcdh19</i> mRNA-positive cells partially coexpress parvalbumin in P20 SSC.	122
Figure 24. <i>Pcdh19</i> mRNA-positive cells partially coexpress calbindin in P20 SSC, especially in layers II/III.	123
Figure 25. <i>Pcdh19</i> mRNA-positive cells partially colocalise with SATB2 expressing cells at P2 in mice.	128
Figure 26: HEK293T cells express the human <i>PCDH19</i> gene.	138
Figure 27: Sequence alignment of the binding regions of the mouse <i>Pcdh19</i> shRNAs#2, #3, #5 and #6 from Sigma with mouse and human <i>Pcdh19</i> gene.	139
Figure 28. CMV- <i>Pcdh19</i> -HA construct generation.	140
Figure 29: Assessment of gene knock-down by <i>Pcdh19</i> shRNAs.....	143
Figure 30. ShRNA control appears to reduce the quantity of PCDH19 protein at 48 hours.	144
Figure 31. Illustration of the strategy to decrease PCDH19 levels by shRNA <i>in utero</i> electroporation.	148
Figure 32: Reduction of PCDH19 by shRNA#3 at E13.5 does not affect migration, but the depletion by shRNA#2 does.....	151
Figure 33: Reduction of PCDH19 levels by shRNA#5 or shRNA#6 at E13.5 does not have an effect on neuronal migration.	153
Figure 34. <i>Pcdh19</i> shRNA <i>in utero</i> electroporation into <i>Pcdh19</i> -KO animals at E13.5 does not have an effect on migrating neurons compared to the control.	157

Figure 35. <i>Pcdh19</i> -KO neurons <i>in utero</i> electroporated with the shRNA control settle at deeper positions compared to the WT neurons electroporated with the same plasmid.....	159
Figure 36. <i>Pcdh19</i> -KO brains present an altered migration of neurons compared to their WT littermates when electroporated at E13.5.	163
Figure 37. Knock-down of PCDH19 increases the migration of late-born neurons.	169
Figure 38. <i>In utero</i> electroporation of the <i>Pcdh19</i> shRNAs into <i>Pcdh19</i> -KO brains at E15.5 also reveals an altered migration of late born neurons....	173
Figure 39. <i>Pcdh19</i> -KO brains presented an alteration in the migration of late-born neurons compared to their WT littermates.	176
Figure 40. Scheme of the suggested experiment to study the migration of WT and <i>Pcdh19</i> -KO cells within the <i>Pcdh19</i> -HET brain.	187
Figure 41. Overview of the immunohistochemical experiments conducted in WT, <i>Pcdh19</i> -HET and <i>Pcdh19</i> -KO mice analysed in Chapter 5.	200
Figure 42. There were no significant differences in the total number of cells and cortical width of the SSC amongst the different genotypes.	203
Figure 43. <i>Pcdh19</i> -HET and <i>Pcdh19</i> -KO animals showed no significant differences in the distribution of cells along the cortical wall with respect to their WT littermates.	204
Figure 44. Immunohistochemical analysis of mutant animals revealed a decrease in the percentage of CUX1-positive cells in bin 5 at P10 with respect to WT animals.	207
Figure 45. Number and distribution of cortico-cortical projecting cells is not altered in <i>Pcdh19</i> -HET and <i>Pcdh19</i> -KO animals with respect to their WT counterparts.	209
Figure 46. No differences in the proportion of RORB-positive cells or in their distribution at P10.	212
Figure 47. No differences in the total number of CTIP-positive cells with respect to DAPI and their distribution at P10 with respect to their WT counterparts.	215

Figure 48. Slight changes in the distribution, but not the overall proportion, of TBR1-expressing cells in <i>Pcdh19</i> -HET animals.....	218
Figure 49. Immunohistochemical analysis of <i>Pcdh19</i> -HET and <i>Pcdh19</i> -KO animals detected no differences at P20 in the total number of PV-expressing cells, nor their distribution, with respect to their WT counterparts.	222
Figure 50. Immunohistochemical analysis at P20 brains of mutant animals revealed no differences in the total number of CR-positive cells (normalised to DAPI) and the distribution of CR-positive cells with respect to WT animals.....	226
Figure 51. A difference is detected in the distribution of cells expressing CB at P20 in the SSC of <i>Pcdh19</i> -HET animals with respect to their WT littermates.....	230
Figure 52. Images of the immunohistochemical analysis of <i>Pcdh19</i> -HET and <i>Pcdh19</i> -KO animals showed no differences in the total number (normalised to DAPI) and the distribution of SST-positive cells at P20 with respect to their WT counterparts.	234
Figure 53. Immunohistochemical analysis of <i>Pcdh19</i> -HET and <i>Pcdh19</i> -KO animals showed a significant difference in the distribution of SST-positive cells at P20 between the mutants when the SSC was analysed.....	235
Figure 54. The distribution of CR, PV and SST interneurons observed in this thesis matches previously reported values.	244
Figure 55. Schematic illustrating the immunohistochemical analysis of female WT/XGFP and <i>Pcdh19</i> -HET/XGFP.	249
Figure 56. Schematic illustrating the behavioural analysis of WT, <i>Pcdh19</i> -HET and <i>Pcdh19</i> -KO mice.....	255
Figure 57. Open-field behavioural analysis revealed no differences in general locomotor activity among males.....	257
Figure 58. No differences in thigmotaxis among males.	259
Figure 59. Open-field behavioural test detected an increase in the distance run within the first 5 min in WT MGH male with respect to the WT SGH male on day 2.....	262

Figure 60. WT MGH males fail to habituate at P21 but habituate normally at P60.....	264
Figure 61. The increase of activity of KO MGH mice at the onset of the dark period is delayed with respect to WT mice in the 24-hour activity test...	268
Figure 62. No significant differences were detected among male mice in the EPM experiments conducted at P21 and P60.....	270
Figure 63. WT MGH males spend less time interacting with an adult female than WT SGH males at P21.....	272
Figure 64. General locomotion activity of WT MGH and HET MGH females in the open field test is increased compared to WT SGH females.	274
Figure 65. Open-field behavioural experiments detected a significant increase in thigmotaxis of the adult WT MGH females compared to the WT SGH animals.	276
Figure 66. Open-field behavioural analysis revealed an increase in the distance run by the WT MGH and HET MGH females with respect to the WT SGH female in the 5-min slot at P21 and P60.	279
Figure 67. Differences in the habituation of WT MGH females at P21 and P60.	281
Figure 68. 24-hour experiments performed in the adult female mice showed slight differences between MGH and SGH females and between the HET females and their WT counterparts.	284
Figure 69. <i>Pcdh19</i> -HET females spend more time in the open arms of the EPM than their WT peers at P21, but not at P60.....	286
Figure 70. Social behaviour analysis detected no differences among conditions in interaction time with a foreign mouse.	288
Figure 71. Schematic of the novel object recognition test.....	296
Figure A. 1. Anti-PCDH19 antibody A304-468A from Bethyl Laboratories could not detect clearly enough PCDH19 expression in P10 brains using IHC.	367

Figure A. 2. Anti-PCDH19 antibodies poly-41 and poly-42, generated by Icosagen, were unspecific..... 369

Figure A. 3. Anti-PCDH19 monoclonal antibodies 1A5, 1A8, 1F4 and 2G2, generated by Icosagen, did not detect PCDH19. 370

Figure A. 4. Antigen retrieval or higher antibody concentration did not improve the detection of PCDH19 by IHC using the monoclonal antibodies. 372

List of tables

Table 1. Summary of protocadherins functions and associated conditions in human and mouse.....	13
Table 2. PCR primers and protocol for genotyping.	42
Table 3. qPCR primer sequences and protocol.	47
Table 4. Primers to generate probes for the RNA ISH experiments.	51
Table 5. Restriction enzymes used to digest pCR TM -Blunt II-TOPO TM Vector to generate sense and antisense probe.	54
Table 6. Buffers used for probe detection in ISH.	59
Table 7. Characteristics of the primary antibodies used in ISH-IHC, IHC and BGAL detection.	61
Table 8. Secondary antibodies used for ISH-IHC, IHC and BGAL detection.	63
Table 9. Settings of the confocal microscope.	66
Table 10. ShRNA sequences.....	69
Table 11. Primers for shRNA sequencing confirmation.	71
Table 12. PCR primers and protocol for CMV- <i>Pcdh19</i> -HA vector generation.	74
Table 13. BSA dilutions to use in the standard curve.	77
Table 14. Western blot buffers.	80
Table 15. Primary antibodies used in western blots.	81
Table 16. Secondary antibodies used in western blots.	82
Table 17. Number of mice used in behavioural tests.	88
Table 18. Illustration of the results obtained in Chapter 6.	292
Table A. 1. Summary of all tried for the characterisation of <i>Pcdh19</i> -expressing cells.	373
Table A. 2. Details of the statistical analysis of shRNAs #2, #3 IUE at E13.5 in WT animals.	375
Table A. 3. Details of the statistical analysis of shRNAs #5, #6 IUE at E13.5 in WT animals.	376

Table A. 4. Details of the statistical analysis of shRNAs IUE at E13.5 in <i>Pcdh19</i> -KO animals.	377
Table A. 5. Details of the statistical analysis of shRNA control IUE at E13.5 in WT and <i>Pcdh19</i> -KO animals.....	378
Table A. 6. Details of the statistical analysis of EGFP IUE at E13.5 in WT, <i>Pcdh19</i> -HET and <i>Pcdh19</i> -KO animals.....	379
Table A. 7. Details of the statistical analysis of shRNAs IUE at E15.5 in WT animals.....	380
Table A. 8. Details of the statistical analysis of shRNAs IUE at E15.5 in <i>Pcdh19</i> -KO animals.	381
Table A. 9. Details of the statistical analysis of EGFP IUE at E15.5 in WT, <i>Pcdh19</i> -HET and <i>Pcdh19</i> -KO animals.....	382
Table A. 10. Details of the statistical analysis of DAPI distribution in P10 animals.....	383
Table A. 11. Details of the statistical analysis of CUX1 distribution in P10 animals.....	384
Table A. 12. Details of the statistical analysis of SATB2 distribution in P10 animals.....	385
Table A. 13. Details of the statistical analysis of RORB distribution in P10 animals.....	386
Table A. 14. Details of the statistical analysis of CTIP2 distribution in P10 animals.....	387
Table A. 15. Details of the statistical analysis of TBR1 distribution in P10 animals.....	388
Table A. 16. Details of the statistical analysis of DAPI distribution in P20 animals.....	389
Table A. 17. Details of the statistical analysis of PV distribution in P20 animals.....	390
Table A. 18. Details of the statistical analysis of CR distribution in P20 animals.....	391

Table A. 19. Details of the statistical analysis of CB distribution in P20 animals.....	392
Table A. 20. Details of the statistical analysis of SST distribution in P20 animals.....	393
Table A. 21. Details of the statistical analysis of open field behaviour in male mice.	394
Table A. 22. Details of the statistical analysis of open field behaviour in female mice.	395

Chapter 1: Introduction.

1.1 The cadherin superfamily

The cadherin superfamily is comprised by a vast group of transmembrane proteins characterised by the presence of extracellular cadherin domains (ECs) (Hatta et al. 1988). Using these domains, cadherins form heterophilic and homophilic bindings and, consequently, play important roles in Ca²⁺-dependent cell-cell interaction. (Hirano et al. 2012; Yoshida-Noro et al. 1984)

In vertebrates, there are over 100 members within the cadherin superfamily that can present very different structures. Several classifications into subfamilies have been attempted, dividing members according to function, structure, genomics or phylogenetics (Hulpiau et al. 2009; Nollet et al. 2000; Hirano et al. 2012). Even though a definitive classification does not exist yet, the division performed by Hulpiau and van Roy in 2009 is the one most cited in the field (Gerosa et al. 2019; Hirano et al. 2012; Brasch et al. 2012; Gul et al. 2017; Hayashi et al. 2017). In this classification, the cadherin superfamily was divided into 6 families and 21 subfamilies according to the phylogenetic analysis by sequence of the first ECs of cadherins from a wide variety of organisms (**Figure 1**).

As depicted in **Figure 1**, cadherins can be divided phylogenetically into two major branches: the cadherin major branch and the cadherin-related major branch (Hulpiau et al. 2009).

Within the cadherin major branch, the classical cadherins (type I and type II), the flamingo/*Celsr*¹ subfamily and the solitary cadherin *Cdh13* have known roles in neuronal development.

¹ Throughout the introduction, genes and proteins will in general be named using mouse gene nomenclature, except in concrete cases where the studies are centred exclusively in another specific organism.

Several type I and type II cadherins are expressed in the embryonic brain and participate in the processes of neural development. Cadherin 2 (CDH2), a binding partner of PCDH19 (Emond et al. 2011), has an essential role in the formation of the neural tube in mice (Radice et al. 1997) and zebrafish (Lele et al. 2002) and is important in cortical neuronal migration (Kawauchi et al. 2010; Martinez-Garay et al. 2016), migration and differentiation of cerebellar granule neurons (Rieger et al. 2009), neurite elongation and branching (Masai et al. 2003), axon guidance (Lele et al. 2002) and synapse formation (Aiga et al. 2011), morphogenesis (Kubota et al. 2009), signalling (Jüngling et al. 2006) and plasticity (Hirano et al. 2012; Jüngling et al. 2006; Mendez et al. 2010).

The CELSR are widely expressed in mouse neural tissue at developmental stages and are known to participate in several processes of neural development, such as planar cell polarity, dendritic survival and growth, axon guidance or neuronal migration (J. Feng et al. 2012). CDH13 is expressed strongly in the cortical preplate at early embryonic stages and within the cortex and striatum at later stages. It is involved in promoting the survival of interneuronal and late-born pyramidal cells in the cortex (Killen et al. 2017).

The other major branch, the cadherin-related branch, also harbours many subfamilies that participate in neural development, such as RET (Imai-Okano et al. 2016), Fat, Dachous, Fat-like, *Cdh23* (Avilés et al. 2017; Badouel et al. 2015; Zakaria et al. 2014), calsynenin (Steuble et al. 2010; Ponomareva et al. 2014; Imai-Okano et al. 2016) or the different protocadherins (Hirano et al. 2012). The molecular structure of the family is depicted in **Figure 2**.

Pcdh19, the focus of this thesis, belongs to the protocadherin subfamily (Wolverton et al. 2001). This subfamily contains the highest number of members within the cadherin superfamily, most of which participate in brain development. This group will be explained in detail in **section 1.2**.

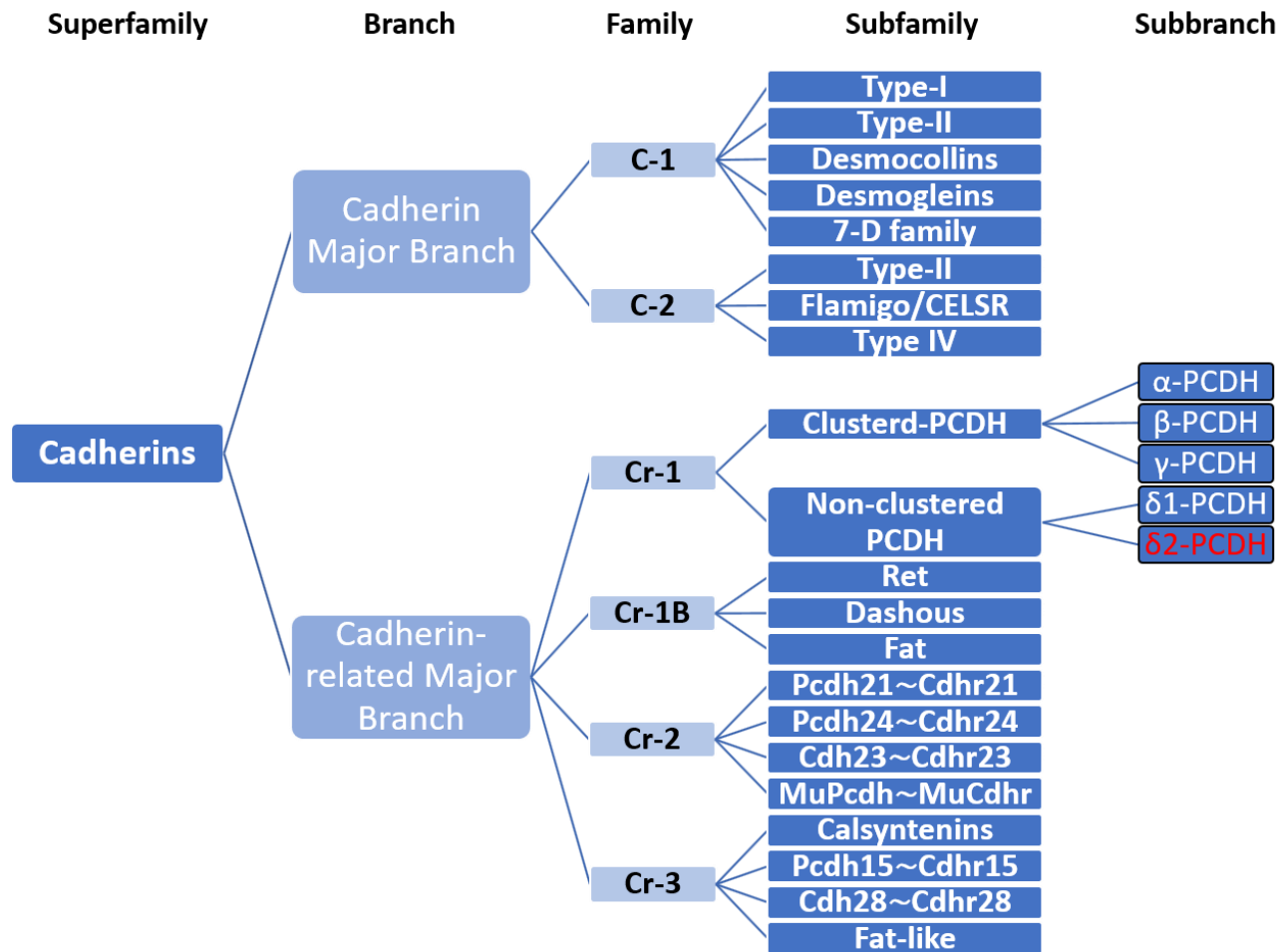


Figure 1. Classification of the cadherin family, according to Hulpiau and van Roy, 2009.

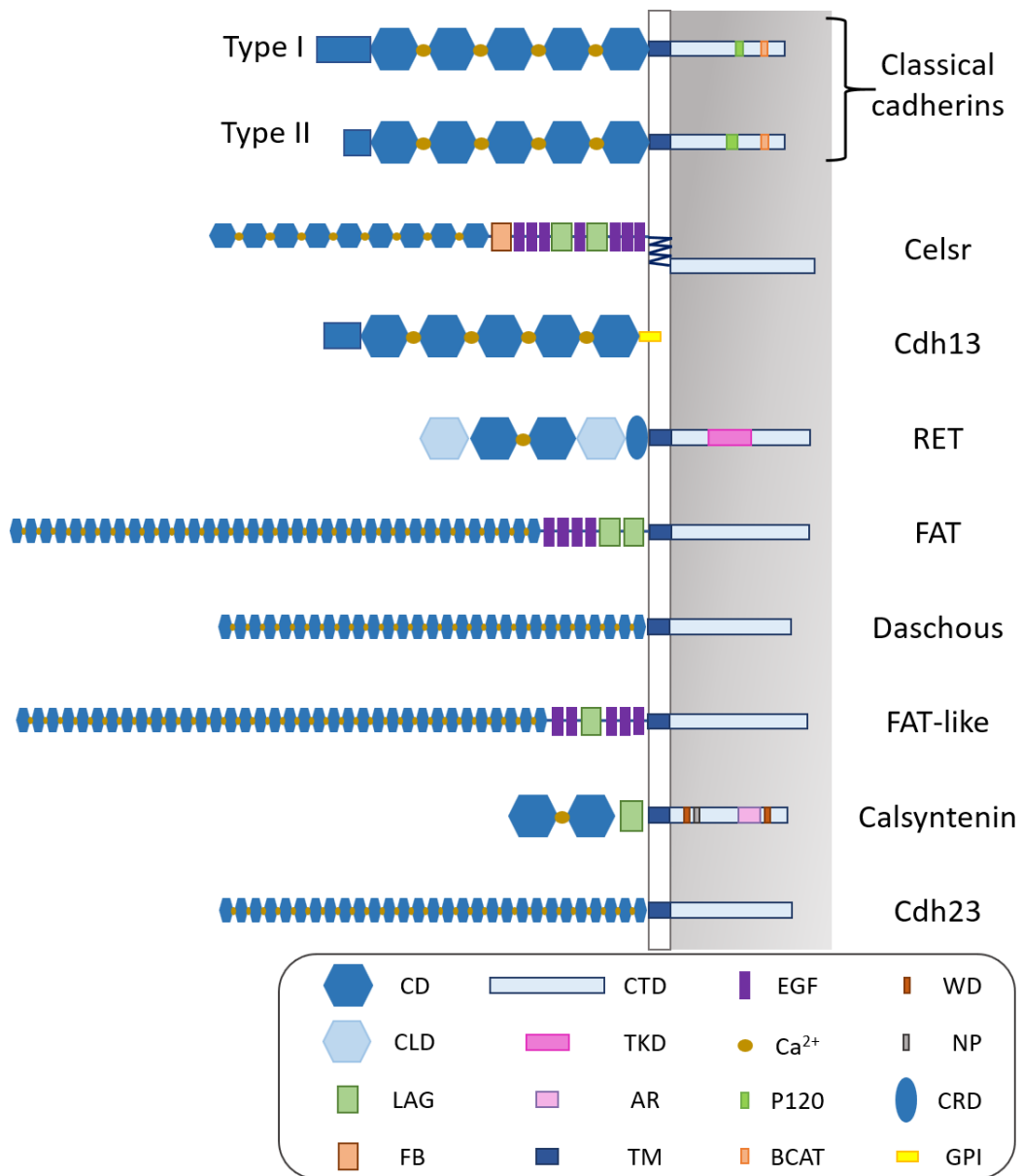


Figure 2. Molecular structure of the subfamilies that belong to the cadherin family mentioned in this thesis, except for the protocadherin family.

CD, cadherin domain; CLD, cadherin-like domain; Ca²⁺, calcium-binding region; TM, transmembrane domain; CTD, cytoplasmic domain; TKD, tyrosine kinase domain; CRD, cysteine-rich domain; GPI, glycosylphosphatidylinositol anchor; FB, flamingo box; LAG, laminin A-G domain; EGF, epidermal growth factor-like domain; P120, p120 binding; BCAT, B CATENIN binding; WD, kinesin light-chain-binding domain; NP, X11L binding site; AR, acidic region.

1.2 The protocadherin family

As mentioned in the previous section, the protocadherin subfamily is the largest among all groups in the cadherin superfamily. First discovered by Shintaro Suzuki in the 1990's, the proteins within this group possess a structure similar to the type I and type II cadherin subfamilies: extracellular domain with 6 or 7 EC repeats, single transmembrane domain and a cytoplasmic tail. However, they lack the catenin binding sites that type I and II cadherins contain in their cytoplasmic region (Keeler et al. 2015; Sano et al. 1993).

Protocadherins also participate in homophilic cell-cell adhesion, but this interaction is weaker, and the binding mechanism is different between cadherins and protocadherins. While EC1 in cadherins is responsible of mediating the interactions, it has been reported that other EC domains are also necessary in the homophilic binding of protocadherins, such as EC2, EC3, and/or EC4 (Nicoludis et al. 2015; Schreiner et al. 2010; Cooper et al. 2016; Hirano et al. 2012).

Most protocadherins are expressed in the nervous system, although not all their functions are currently known. However, they are essential in neural development and for proper functioning of neuronal circuits (Keeler et al. 2015; Hirano et al. 2012).

Protocadherins comprise two subfamilies, the clustered and the nonclustered protocadherins, according to their genomic organisation (Hulpiau et al. 2009). The genes of the clustered protocadherins are located in sequential arrays within chromosome 5 in human and chromosome 18 in mouse (Wu et al. 2001), while the nonclustered protocadherins are spread throughout the genome (Keeler et al. 2015; Hirano et al. 2012; Redies et al. 2005).

Clustered protocadherins contain 6 EC domains in their structure and are subdivided into three subgroups: α , β and γ (Hulpiau et al. 2009). The α

cluster positively regulates dendrite arborization and spine formation in hippocampus (Suo et al. 2012) and participates in the correct wiring of cortico-cortical connexions between the primary sensory cortices of both hemispheres (Yamashita et al. 2012). PCDHAC2, which belongs to this group, has been reported to mediate the spacing between axon terminals (axonal tiling) of serotonergic neurons, required for their proper wiring (W. V. Chen et al. 2017). The γ cluster, as the α cluster, regulates dendrite arborization in the hippocampus (Suo et al. 2012), it also participates in the dendritic branching in cortex (Garrett et al. 2012), in cell avoidance of Purkinje cells (Gibson et al. 2014) and in the promotion of the survival of spinal interneurons (Prasad et al. 2008). The β cluster also has a role in the survival of spinal interneurons. Together, the *Pcdha* and *Pcdhy* clusters contribute to cell survival in the retina and neural dendritic patterning in retina and cerebellum (S. Hasegawa et al. 2016) and all clusters are important to form the glomerular structure and correct axonal projections in the olfactory bulb (S. Hasegawa et al. 2016).

Nonclustered protocadherins are formed by the δ_1 and δ_2 subgroups, characterised by the presence of conserved cytoplasmic motifs (CM) in their aminoacidic sequence, and a couple of solitary protocadherins that lack said motifs, PCDH12 and PCDH20 (Wolverton et al. 2001; Hulpiau et al. 2009). PCDH12 contains 5ECs and is located in vascularised tissues, where it participates in the promotion of adhesion in endothelial cells, thus altering the function of the arteries, with no effects on neural development detected in mice (Philibert et al. 2012). PCDH20 contains 7 EC, its known to be involved in the regulation of the cell-fate and cortical lamination of layer IV neurons, and has been reported to act as a tumour suppressor too (Jennbacken et al. 2009).

The δ_1 subbranch is characterised by a structure with 7 EC domains in the extracellular region and three conserved motifs (CM) in the cytoplasmic domain. There are 4 members in mammals: *Pcdh1*, *Pcdh7*, *Pcdh9* and *Pcdh11*.

The δ_2 subbranch contains 6 EC cadherin domains in the extracellular part of the protein and two conserved motifs in its cytoplasmic region. In addition, δ_2 protocadherins also have a WIRS sequence, which is not present in most of the δ_1 members. The WIRS sequence mediates the interaction with the WAVE (Wiskott-Aldrich syndrome protein family verprolin-homologous protein) regulatory complex (WRC). In mammals, the δ_2 subfamily members are *Pcdh8*, *Pcdh10*, *Pcdh17*, *Pcdh18*, *Pcdh19* (Hulpiau et al. 2009). The molecular structure of the subgroups is illustrated in **Figure 3**.

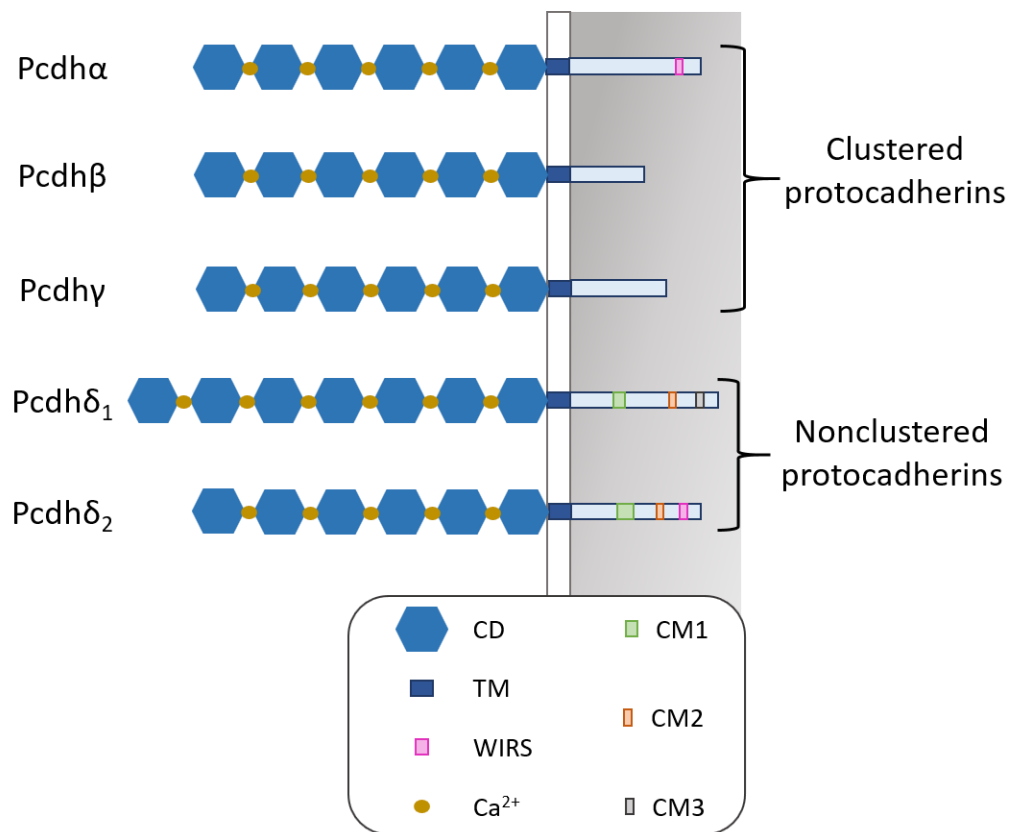


Figure 3. Molecular structure of the subgroups that belong to the protocadherin subfamily.

CD, cadherin domain; Ca²⁺, calcium-binding region; TM, transmembrane domain; WIRS, WRC-interacting receptor sequence; CM1, conserved motive 1; CM2, conserved motive 2; CM3, conserved motive 3.

The roles of all protocadherins, including the δ subfamilies, are still being studied, even though the fact that they are strongly expressed in neural tissues and that mutations in delta protocadherins usually cause neurodevelopmental disorders strongly suggest they have roles in the development of the nervous system (Keeler et al. 2015; Light et al. 2017).

Mutations in *PCDH1* are known to be associated with eczema, asthma and bronchial hyperresponsiveness in humans and the protein has been reported to participate in the establishment and maintenance of the bronchial epithelial barrier (Tellez et al. 2016). In *Xenopus*, however, *PCDH1* has been shown to participate in the morphogenesis of the notochord, probably by contributing to the determination of cells into a mesodermal fate (Yoder et al. 2011). In chicken, this protein has a role in the formation of the dorsal root ganglia of the peripheral nervous system by cell sorting the neural crest cells that correspond to this ganglia (Bononi et al. 2008).

PCDH7 has been revealed to be mutated in a patient with epilepsy (Lal et al. 2015) and to have its expression regulated by *MeCP2*, the gene responsible for Rett syndrome, which is a neurodevelopmental disorder (Miyake et al. 2011). In *Xenopus*, *PCDH7* is necessary for the growth, extension and pathfinding of axons in the retinal ganglion cells (Leung et al. 2015). A recent study of 2018 by Xiong *et al.* also revealed that overexpression of *PCDH7* in primary cortical neurons induces apoptosis *in vitro*, suggesting a role for this protein in cell survival (Xiao et al. 2018).

PCDH9 is the only δ_1 protocadherin that contains the WIRS motif (Light et al. 2017). *PCDH9* protein levels are reduced in brains with autistic spectrum disorder in humans (Parras et al. 2018). In mice, deletion of *Pcdh9* produces sensorimotor impairment and short-term and long-term learning deficits, together with a decrease in the number of lower-layer pyramidal neurons in the somatosensory cortex (SSC), reduced arborization of the dendrites

and increase of the spine density (Bruining et al. 2015); which strongly implies roles in neural circuit formation.

The *PCDH11* gene is located on both sex chromosomes in humans (*PCDH11X/PCDH11Y* pair, with some differences in genetic sequence), but only on the X-chromosome in the rest of mammals. *Pcdh11* is theorised to contribute to sexual dimorphism, even though that remains to be demonstrated. No differential expression has been detected so far between *PCDH11X* and *PCDH11Y* (Priddle et al. 2013), but *PCDH11X* levels are higher in females than in males (Lopes et al. 2006). In mice, *PCDH11X* has an important role in brain development, acting as a regulator of neural proliferation and stem cell neural differentiation in cortical development, which also causes premature migration (P. Zhang et al. 2014).

PCDH8 has been reported to participate in the regulation of spine density by promoting endocytosis of the classical cadherin *CDH2*, which is an essential component in spine remodelling, via the p39 MAPK signalling pathway in mouse hippocampal neurons (Yasuda et al. 2007).

PCDH10 has been suggested to play a role in autism (Bucan et al. 2009). This protocadherin has been shown to promote cell migration after cell-cell interaction by altering the adherens junctions (conformed by *CDH2* and actin) via the recruitment of the NAP1-WAVE complex *in vitro* (Nakao et al. 2008). In mice, the protein has been reported to be essential for the guidance of corticothalamic, thalamocortical and striatal axons, due to the alteration of the patterning of the guidance cells that assist in axon pathfinding that are positioned in the ventral telencephalon of mutant mice (Uemura et al. 2007). *PCDH10* has also been associated with synaptogenesis, since NAP1 is implicated in dendritic spine formation (Nakao et al. 2008) and synapse elimination, where it participates in PSD95 proteasomal degradation (Tsai et al. 2012). More recently, *Pcdh10* heterozygous male mice have been reported to present an increase in spine density and altered spine morphogenesis in the amygdala, which could imply defects in synaptic

plasticity or transmission. This effect was accompanied by abnormalities in mice social behaviour (Schoch et al. 2017).

PCDH17 has been recently revealed as a risk candidate gene for major mood disorders. In the same report, overexpression of the protein in primary neuronal cultures decreased spine density and altered the spine morphology, which suggests *PCDH17* could have a role in synapse transmission (H. Chang et al. 2018). This study supports the role of *PCDH17* in synaptic plasticity, that had already been reported in Hoshina *et al.*, who detected antidepressant-like behaviour in *Pcdh17*-KO mice, together with a reduction of efficacy in synapse function at the presynaptic level of the corticostriatal pathway (Hoshina et al. 2013). Hayashi *et al.* also discovered a role of this protocadherin in collective axonal growth in the amygdala, via the recruitment of the WAVE complex, lamellipodin and ENA/VASP proteins to axon-axon contacts, and that this mechanism also promotes the migration of U251 cells *in vitro* (Hayashi et al. 2014).

The role of *Pcdh18* in mammals is not known yet, even though the report of a patient with severe intellectual disability that presents a deletion of the *PCDH18* gene suggest a role in neuronal function in humans (Kasnauskiene et al. 2012). *PCDH18* also contains a binding site for DAB1, a protein that participates in the reelin signalling pathway and is implicated in neuronal migration (Homayouni et al. 2001). In zebrafish, *pcdh18* has been hypothesised to participate in the early stages of cell specification due to its interaction with B1 SOX transcription factors (Okuda et al. 2010) and to enhance axon arborization in the motor cortex together with the WAVE complex (Biswas et al. 2014).

Pcdh19 is one of the most studied protocadherins, since mutations of this gene produce early infantile encephalopathy 9 (EIEE9), a human developmental disorder. However, the role of *Pcdh19* in mammals and the causes behind the illness are not fully understood yet. Since this protein is

the focus of the project, detailed information about the protocadherin will be provided in the following sections.

A summary of the role of the different protocadherins and the conditions associated to mutations in said proteins in human and mouse is shown in **Table 1**.

PCDH	FUNCTIONS	ASSOCIATED CONDITIONS
PCDH12	- Promotion of adhesion in endothelial cells.	-
PCDH20	- Regulation of the cell-fate and cortical lamination of layer IV neurons. - Tumour suppressor.	-
PCDH1	- Participate in the establishment and maintenance of the bronchial epithelial barrier.	- Eczema. - Asthma. - Bronchial. Hyperresponsiveness.
PCDH7	- Possible role in cell survival.	- Epilepsy. - Rett syndrome.
PCDH9	- Probably implicated in neural circuit formation.	- Autistic spectrum disorder. - Sensorimotor impairment and short-term and long-term learning deficits in mice.
PCDH11	- Regulator of neural proliferation and stem cell neural differentiation in cortical development.	-
PCDH8	- Regulator of spine density in hippocampal neurons .	-
PCDH10	- Promoter of cell migration. - Essential for the guidance of corticothalamic, thalamocortical and striatal axons. - Possible role in synaptogenesis and synapse elimination.	- Possible role in autism. - Altered behaviour in mice.
PCDH17	- Possible role in synaptic plasticity. - Promoter of collective axonal growth in the amygdala.	- Candidate gene for major mood disorders. - Antidepressant-like behaviour in mice.
PCDH18	- Probably implicated in neuronal migration.	- Possible role in neuronal function.
PCDH19	- Possible roles in neurogenesis, neural differentiation and maturation, and cortical migration.	- EIEE9.

Table 1. Summary of protocadherins functions and associated conditions in human and mouse.

In the third column, the associated conditions relate to humans, unless otherwise stated; -, not known.

1.3 *Pcdh19* structure

The *Pcdh19* gene is located on the X-chromosome. Its mRNA consists of 6 exons, the first of which is unusually large and translates into the whole extracellular and transmembrane domains of the protein. Exon two can be alternatively spliced to form a new variant of *Pcdh19* (Dibbens et al. 2008).

As a member of the δ_2 subfamily of protocadherins, PCDH19 contains a signal peptide and six EC repeats in its extracellular region, a transmembrane domain and a cytoplasmic region with two conserved motives: CM1 and CM2 (Dibbens et al. 2008; Wolverson et al. 2001), and a WIRS (B. Chen et al. 2014). The WIRS is a weak six residue consensus motif that is necessary and sufficient for the binding of WRC, which happens through the surface of two of the proteins in the complex: *Sra1* and *Abi2* (B. Chen et al. 2014).

The aminoacidic sequence alignment and pairwise comparisons using *Pcdh19* from zebrafish, human and mice performed by Liu *et al.* showed the proteins are similar between species (71.28% between zebrafish and human, 71.76% between mouse and human and 96.46% between mouse and human; alignment performed between EC1 and CM2 regions of the protein). Particularly high degrees of identity are evident in the CMs: CM1 is identical among the three species, and the CM2 of zebrafish shares 88.2 % identity with respect to mouse and human, whose aminoacidic sequence is identical (Q. Liu et al. 2010). This degree of similarity points to a conserved function for those domains, either together or separately, shared by all delta protocadherins. However, no insight into their potential role has been gained so far, and no specific binding partners for those regions have been identified.

More recently, Cooper *et al.* analysed the structure of *Pcdh19* EC1-4 from zebrafish using crystallography. The study revealed each EC is formed by seven β strands, named from A to G, with a β sandwich fold in its ECs

(Greek-key), and calcium binding sites were located in the regions between the ECs. Both structures are common in other cadherins. In the EC1, however, there were structural traits that are typically found in clustered protocadherins: a disulphide bond detected at the E-F loop, as well as one of two α -helices at the B-C loop (Cooper et al. 2016).

1.4 *Pcdh19* expression

Pcdh19 is expressed in several non-neuronal tissues. In chicken, it has been detected in the lungs of embryos and P1 chicks (Bononi et al. 2008). In the developing mouse, expression is observed in kidney, olfactory system, eye, brain, stomach, dermomyotome, mesenteries, dermal papilla, presomitic mesoderm, pancreas and duodenum, usually when tissue morphogenesis takes place (Gaitan & Bouchard, 2006). In human, heart, kidney, lung and trachea express the transcript (Wolverton & Lalande, 2001).

However, as the rest of protocadherins, *Pcdh19* is mainly expressed in the nervous system of the different species studied so far, including zebrafish (Q. Liu et al. 2010), chicken (Tai et al. 2010), mouse (Gaitan et al. 2006; Hertel et al. 2008; Krishna-K et al. 2011), rat (Kim et al. 2007), ferret (Krishna et al. 2009) and human (Wolverton et al. 2001).

Pcdh19 expression has been reported in chicken brain, including the optic tectum (Lin, Yan, et al. 2012; Tai et al. 2010) and in the spinal cord of chicken embryos (Lin, Wang, et al. 2012). There is also expression in the cortex of developing and adult ferret, where layer V is strongly stained (Krishna et al. 2009).

In the embryonic zebrafish, *pcdh19* is expressed very early in development across the brain and spinal cord. The spinal cord expression is lost at later stages of development, and brain expression gets limited to the lateral and dorsal telencephalon. The eye primordium, developing retina, lens and otic vesicle also show *pcdh19* expression (Q. Liu et al. 2010).

In the developing mouse embryo, *Pcdh19* expression is weak at E9, but gets stronger at E9.5 (Gaitan et al. 2006). *Pcdh19* gets downregulated between E14.5 and E16.5 in the cortex, probably due to the destabilization of *Pcdh19* mRNA by miR-484, but in general PCDH19 expression increases during the development of the brain (Fujitani et al. 2017). The protein is also highly expressed in postmitotic neurons in the spinal cord between E15.5 and E18.5 (Gaitan et al. 2006). Expression is detected across several regions of the head and spinal cord, including the presomitic mesoderm at early stages, and dorsal cortex, lateral ganglionic eminence, retina, nasal cavity and prepituitary gland at later ones (Gaitan et al. 2006). In the adult, *Pcdh19* is strongly expressed in the cortex, hippocampus and cerebellum (Dibbens et al. 2008; Pederick et al. 2016), similar to the pattern detected in the developing rat brain at E18.5, where the strongest staining is located in cortex and limbic system, such as the amygdala, hippocampus and hypothalamus (Kim et al. 2007).

In human, as in rodent, *PCDH19* is strongly detected in the cortex and amygdala in the period between 8-21 weeks post-conception and in lower quantities in the adult brain (Miller et al. 2014; Pederick et al. 2018).

At the cellular level, *Pcdh19* expression has been detected in glial cells (oligodendrocytes and astrocytes) in mouse cortex postnatally (Y. Zhang et al. 2014). In addition, pyramidal neurons located in *cornu ammonis* (CA)1 and CA3 and dentate gyrus (DG) of the rat hippocampus (Bassani et al. 2018), and neurons in cortical layers II/III (low detection) and V and CA1 hippocampal neurons in mice (Hayashi et al. 2017; Pederick et al. 2016) also express PCDH19. In the neurons of rat and mouse, PCDH19 has been detected in the dendrites, and the protein partially colocalises with pre- and post-synaptic markers in mouse hippocampal neurons (Hayashi et al. 2017).

1.5 Early Infantile Encephalopathy 9 (EIEE9)

Mutations in the *PCDH19* gene cause Early Infantile Epileptic Encephalopathy 9 (EIEE9), also known as epilepsy and mental retardation in females (EFMR) or PCDH19-female epilepsy (Dibbens et al. 2008). The disorder was discovered by Juberg and Hellman in 1971 (Juberg et al. 1971), and is the second most prevalent monogenic cause of epilepsy after Dravet syndrome (Depienne et al. 2012). Apart from the characteristic seizures, that happen in clusters and are usually triggered by fever, the disorder is often accompanied by autistic spectrum disorders (25% approximately), language delays, cognitive impairment and/or behavioural disturbances including anxiety, obsessive-compulsive disorders, aggression and social withdrawal. The onset of the seizures occurs in infancy or early childhood, ranging from 4 to 60 months, and decreases or even disappears when reaching puberty. The cognitive and behavioural dysfunctions, if present, persist through adulthood, though (Scheffer et al. 2008; Duszyc et al. 2014; Depienne et al. 2012). The penetrance of the disorder is incomplete, and thought to be around 80% (Kolc et al. 2019).

Until recently, it was thought that in EIEE9 patients there was no correlation between the severity of the seizures and the degree of intellectual disability. The report from Kolc *et al.*, however, found that an early onset of the seizures was associated with a more severe cognitive impairment (Kolc et al. 2019).

Most of the mutations occur in the extracellular domain (more than 80%) and almost half of them are located in EC3 or EC4. With respect to the type of mutation, almost 50% were missense variants, while the rest were frameshift and nonsense ones. The mutations are thought to cause the loss of function of the mutated allele (Dibbens et al. 2008; Depienne et al. 2012; Kolc et al. 2019).

Even though half of the EIEE9 cases arise *de novo* (Kolc et al. 2019; Duszyc et al. 2014), the disease was originally discovered and recognised as a familial disorder. The inheritance pattern is highly intriguing. Contrary to most X-linked illnesses, EIEE9 is present in heterozygous females, while hemizygous males remain mostly unaffected. They act as carriers of the disease that can transmit the genetic defect to their daughters, and can present controlling, rigid and inflexible personalities, with obsessive traits and interests (Dibbens et al. 2008; Scheffer et al. 2008; Juberg et al. 1971). The molecular mechanism behind this unusual inheritance mode and the cause of the epileptic seizures is not well understood, but the model proposed is called “cellular interference”. In this model, the mosaic of *PCDH19*⁺ and *PCDH19*⁻ cells, brought about by random X-inactivation in the heterozygous females, would cause disruption of cell-cell communication, leading to the disease (Dibbens et al. 2008). This theory is supported by reports of ten cases of males affected with EIEE9-like phenotype that carry somatic mutations in the *PCDH19* gene (de Lange et al. 2017; Kolc et al. 2019).

1.6 *Pcdh19* function

Pcdh19 is known to have a role in neural development in zebrafish, but its role in mammals is still not well-understood. Its extracellular domain participates in cell-cell interactions and has been studied the most, while the intracellular cytoplasmic domain interacts with intracellular partners that could participate in signalling pathways.

1.6.1 Role in cell-cell interaction

PCDH19, as the rest of the protocadherins, is a cell-cell adhesion protein that forms calcium-dependent weak homophilic interactions.

In a crystallographic analysis, Cooper, Jontes and Sotomayor discovered a probable way of homophilic binding for *Pcdh19*, in which a fully overlapped

antiparallel dimer is formed by the EC1-EC4 domains of both proteins (EC1:EC4; EC2:EC3; EC3:EC2; EC4:EC1) (Cooper et al. 2016).

But the extracellular domain of PCDH19 not only forms homodimers. The zebrafish protein it was shown to interact in cis with *Cdh2* *in vitro*. The complex possesses strong adhesive properties, and *Pcdh19* seems to have the main role in this interaction with *Cdh2* acting as a cofactor. Sorting assays using *Cdh2*, *Cdh2-Pcdh19* and *Cdh2-Pcdh17* coated beads also showed an homophilic specificity that depended on the protocadherin *Cdh2* was partnered with (Emond et al. 2011). *In vivo*, *pcdh19* interacts with *cdh2* in zebrafish and both participate in the regulation of cell motility during brain development. The knockdown of any of the genes by antisense morpholinos causes disruption of the neural migration, including an increase of unproductive movements and a reduction of coordination in the trajectory of migration of neighbouring cells (Biswas et al. 2010).

Recently, *in vitro* assays from Pederick *et al.* and Bisogni *et al.* also revealed that combinatorial expression of non-clustered PCDHs, including PCDH19, influences cell adhesion affinity, and that these adhesive property is sensitive to differences in one single protocadherin or in the relative levels of expression among them (Pederick et al. 2018; Bisogni et al. 2018). Pederick *et al.* also reported an abnormal segregation of PCDH19⁺ and PCDH19⁻ cells in the cortex of *Pcdh19*-HET mice *in vivo* probably caused by the differences in cell adhesion affinity previously mentioned (Pederick et al. 2018).

Cell-cell interactions are essential in many neurodevelopmental processes: neuronal differentiation and migration, axon outgrowth, dendrite arborization, and synapse formation and maintenance (Weiner et al. 2013). In zebrafish, *pcdh19* is known to participate in the development of the neural tissues through cell adhesion. *Pcdh19* knockdown by antisense morpholino severely affects the formation of the neural tube by disrupting the morphogenesis and blocking the convergence cell movements of the neural

plate (Emond et al. 2009). A report from Cooper *et al.* did also reveal that *pcdh19* participates in the maintenance of the columnar organisation of the optic tectum. *Pcdh19*-KO elicited the loss of columns due to reduced cell cohesion and increase of cell production, affecting visually guided behaviours (Cooper et al. 2015).

Several reports also strongly suggest the involvement of *Pcdh19* in some neural development processes in mammals, even though the mechanisms have not been well-studied yet. Pederick *et al.* discovered that neurons from the developing cortex of *Pcdh19*-KO mice increased their migration with respect to the cells from WT animals *in vitro*, in an assay performed with neurospheres (Pederick et al. 2016). A recent article from Homan *at al.* also detected an enhanced neurogenesis, premature differentiation of neuronal progenitors and premature neuron maturation in cultures with either *Pcdh19*-KO cells or with a cell mosaic of WT/*Pcdh19*-KO cells, derived from mouse or human cortices. These defects are associated with a decrease of cell polarity in the progenitors (Homan et al. 2018).

The role of *Pcdh19* in cell adhesion has been the most studied so far, since the molecular mechanism proposed to be the cause of EIEE9 (cellular interference) is based on the disruption of cell-cell communication between the WT and *Pcdh19*-KO cells.

1.6.2 Role in intracellular signalling

Pcdh19, as the rest of the δ_2 protocadherins, contains a binding site for the WRC in its cytoplasmic domain, as described in **section 1.3**. *Pcdh19* only associates with the full WRC complex, that is composed by WAVE/SCAR, hematopoietic stem/progenitor cell protein 300 (HSPC300) /Brick1, cytoplasmic interactor of FMRP 1 and 2 (CYFIP1/2)/Sra1, Nck-associated protein (NAP1)/Hem2/Kette, and Abelson interactor 1 protein (*Abi1*), (B. Chen et al. 2014). WRC is known as a regulator of actin cytoskeleton dynamics. The complex contains a VCA region (verprolin homology domain, cofilin homology domain and acidic region). This is the surface the

Arp2/3 complex binds to, and the interaction triggers its activity as an actin nucleator (Kurisu et al. 2009). In fact, reports by Hayashi *et al.* and Bassani *et al.* have shown that PCDH19 fluorescent puncta colocalise with *Abi1* in the dendrites of neurons in hippocampal cultures (Hayashi et al. 2017; Bassani et al. 2018). Reduction of PCDH19 levels by shRNA *in utero* electroporation altered neuronal migration and dendritogenesis of CA1 hippocampal neurons, leading to an ectopic location of these cells, a decrease in their arborization and an aberrant spatial location of apical dendrites (Hayashi et al. 2017; Bassani et al. 2018). These results imply a role for PCDH19 in the regulation of actin cytoskeleton dynamics, probably in association with the WRC. However, no alterations of dendrite or spine morphology could be detected in layer V cells of *Pcdh19*-HET or *Pcdh19*-KO mice (Hayashi et al. 2017). Therefore, this role could be limited to certain neural types or the different results could be due to the use of different tools (siRNA vs mutant animals).

Pcdh19 has also been shown to associate with the non-POU-domain-containing octamer binding protein (NONO)/P54nrb, a paraspeckle protein which participates in transcriptional and posttranscriptional regulation and deoxyribonucleic acid (DNA) repair. This interaction has been shown to play a role in the regulation of genes via the oestrogen receptor alpha (ER α), a steroid hormone receptor (Pham et al. 2017). Disruption of this signalling pathway has been linked to EIEE9, as patients' fibroblasts show dysregulated genes that are controlled by the progesterone receptor and ER α receptor. In the same study, it was shown that patients present reduced levels of the neurosteroid allopregnanolone due to the downregulation of the gene *AKR1C*, whose protein transforms 5 α -hydroxyprogesterone into allopregnanolone (Tan et al. 2015). Allopregnanolone is a known anticonvulsant and therefore, reduction in its levels could be implicated in the epileptic seizures of the patients (Reddy 2010).

This neurosteroid is also a strong positive allosteric regulator of gamma aminobutyric acid (GABA)-A receptors (Reddy 2010). A recent report from Bassani *et al.* has revealed that PCDH19 interacts with the alpha subunits of the GABA-A receptor through its cytoplasmic domain, upstream of CM1. PCDH19 downregulation in hippocampal neurons caused a reduction in the levels of alpha subunits located at their surface, which affected their postsynaptic currents, implying a possible role of PCDH19 in the intracellular transport of GABA-A receptor units and modulation of its activity (Bassani *et al.* 2018). Failures in the GABAergic system alter inhibitory transmission in the adult brain and predispose the brain to epileptic activity (Ben-Ari 2015), which is consistent with EIEE9. Moreover, GABA has an excitatory function in the developmental brain and participates in neuronal proliferation, migration and (Deidda *et al.* 2014).

1.6.3 Role in cortical development

As explained in previous sections, *Pcdh19* could be involved in neural development through its cell adhesive properties (Weiner *et al.* 2013). *Pcdh19* could also have a role in cortical development due to its role as a regulator of cytoskeleton dynamics or its participation in GABAergic signalling (Bassani *et al.* 2018). The *in vitro* studies of Homan *et al.* and Pederick *et al.* also suggest a possible role for *Pcdh19* in neurogenesis, neural differentiation, cortical migration and neural maturation (Pederick *et al.* 2016; Homan *et al.* 2018). A recent article from Fujitani *et al.* also reported that reduction of PCDH19 levels by *in utero* electroporation of shRNA in the developing mouse caused an increase in the differentiation of radial glial cells (RGCs) to intermediate progenitors (IPs) (Fujitani *et al.* 2017). Moreover, cortical malformations have been detected in EIEE9 patients (Pederick *et al.* 2018).

1.6.4 Role in behaviour

EIEE9 patients can present cognitive impairment and behavioural disturbances in addition to clustered seizures (Dibbens *et al.* 2008). Even

though there are no reports of seizures in any of the *Pcdh19*-HET or *Pcdh19*-KO mouse models (Pederick et al. 2016; Hayashi et al. 2017), the *Pcdh19*-HET mouse model from Pederick *et al.* did show an abnormal brain network in the electrocorticogram analysis, with an increase in the number of spike-wave discharge events per hour and the duration of each event in P42 mice (Pederick et al. 2018).

Moreover, despite not observing any epileptic episodes in their *Pcdh19*-HET model, the study from Hayashi *et al.* did detect some differences between their mutant and WT mice in the performance of some behavioural tests. Both mutants showed abnormalities under stress conditions and hyperactivity at 34 weeks that was not present at 11-12 weeks (increased hyperactivity due to aging). Moreover, *Pcdh19*-HET females displayed a decrease in the contextual and cue responses to fear compared to WT and *Pcdh19*-KO animals. Anxiety-like behaviours, social interaction, working and spatial memory did not seem to be affected. These results suggest that, despite the lack of seizures, *Pcdh19*-HET animals might be useful to study the involvement of PCDH19 in brain function (Hayashi et al. 2017).

1.7 Cortical development

Cortical development is a process comprising several consecutive phases that result in a formed mature cortex (López-Bendito et al. 2008). *Pcdh19* could be participating in any of the phases or be involved in several of them.

In mice, which is the most common animal model for the study of cortical development, the cerebral cortex derives from the dorsal telencephalic vesicle that has originated from the neural tube at E9. This precortex is formed by neural stem neuroepithelial cells (NECs) and is composed by a single layer of these progenitors (Miyata et al. 2001; Fernández et al. 2016). These cells are characterised by their tight unions and they undergo interkinetic nuclear migration, a movement of the nucleus from the apical to basal part of the epithelium that follows their cell cycle (Taverna et al.

2010). They divide symmetrically, giving rise to two NEC daughters and amplifying the neuroepithelial pool (Miyata et al. 2010).

Around E10 neurogenesis starts and NECs transform into RGCs after losing the tight junctions and acquiring glial identity. RGCs go through symmetric divisions at this age (Misson et al. 1988; Fernández et al. 2016). However, these cells soon stop the cell-amplifying divisions and start to divide asymmetrically, generating an RGC and another cell, which can be an intermediate progenitor (IP) or a neuron (Miyata et al. 2001; Gal et al. 2006; Noctor et al. 2004). IPs do not undergo interkinetic nuclear migration, reside in a basal region compared to the RGCs called the subventricular zone (SVZ) and do not contact with the pial or basal surface. The zone where RGCs are located is called the ventricular zone (VZ). IPs undergo self-consuming divisions that give rise to two neurons in mice (Hirota et al. 2017b; Noctor et al. 2004; Fernández et al. 2016). The cerebral cortex is where most excitatory neurons are generated, while cortical inhibitory interneurons derive from subcortical regions: the lateral (Tamamaki et al. 1997), medial (Wichterle et al. 2001) and caudal ganglionic eminences (Kanatani et al. 2008; Wamsley et al. 2017), specifically.

Cortical excitatory neurons have to migrate from the SVZ/VZ to their correct laminar positions in a process called radial migration. Migration occurs in an inside-out pattern, where cells that are born later migrate radially outwards traversing the already positioned early-born neurons. At E11.5, the first neurons form the preplate, that is above the VZ. The following neurons migrate from the VZ/SVZ and split the preplate into the marginal zone (MZ) and the subplate, forming the cortical plate in between (Nadarajah et al. 2001; Hirota et al. 2017b; Marin-Padilla 1978).

Before neurons enter the cortical plate, they go through a multipolar cell phase, where cells extend and retract multiple processes very fast, moving slowly towards the cortical plate (Tabata et al. 2003). This characteristic movement is called multipolar migration. This phase lasts for 24 hours

approximately, and then the neurons get oriented towards the cortical plate via the *Reelin-Rap1-Cdh2* pathway (Jossin et al. 2011), acquire bipolar morphology and start migrating towards the cortical plate through other mechanisms (Tabata et al. 2016; Hirota et al. 2017b; Noctor et al. 2004).

Somal translocation is the mechanism used by early-born neurons, when the cortical plate is not very thick. In this mode of migration, neurons are attached to the pial surface by a long process, and the retraction of this process moves the cell soma until they reach their final position (Nadarajah et al. 2001; Hirota et al. 2017b).

Late-born neurons use glia-guided locomotion, using the fibres of the RGCs as a scaffold, as the cortex has thickened considerably over time. They traverse the early-born neurons, and when the neuronal leading process makes contact with the MZ, they switch their mode of migration to terminal translocation, a process morphologically similar to somal translocation, and then complete their migration to their final positions (Nadarajah et al. 2001; Hirota et al. 2017b). The process of neurogenesis and migration is depicted in **Figure 4**.

Cell migration requires the participation of the cytoskeleton, which *Pcdh19* is thought to be a regulator of. Cytoskeleton components are involved in the movement of the centrosome in the leading process and the movement of the nucleus. The promotion of actin polymerization via the *Cdk5-p27Kip1* and *Cdk5-Pak1* pathways (Kawauchi et al. 2006; Nikolic et al. 1998) is necessary for the extension and maintenance of the leading process. The growth of microtubules is needed to move the centrosome into the leading process and requires several microtubular proteins, such as APC, DCX or kinesins (Tanaka et al. 2004; Mimori-Kiyosue et al. 2000; Xie et al. 2003). Additionally, the *Lis1/Ndel1/dynein* complex is in charge of linking the microtubules with the nucleus to regulate the nucleokinesis (Shu et al. 2004). Lastly, proteins involved in cell polarity, like Par6 and aPKC contribute to cell migration too (Solecki et al. 2004; X. Jiang et al. 2016).

Reelin, secreted by the Cajal-Retzius cells in the MZ, is also essential in migration. This glycoprotein has been associated with cytoskeleton regulation, nucleokinesis, cell shape and cell adhesion via DAB1, nectins, Fyn or cadherins (Jossin et al. 2011; Franco et al. 2011; Gil-Sanz et al. 2013; Hirota et al. 2017a).

One of these cadherins is *Cdh2*, which is known to interact with *Pcdh19*. *Cdh2* participates in all the steps of radial migration of excitatory neurons. It regulates the orientation of multipolar neurons towards the cortical plate via *Rap1* as mentioned previously (Jossin et al. 2011). It is also involved in somal translocation by stabilizing the leading process that is contacting the MZ via a Reelin-*Dab1*-*Rap1*-*Cdh2* pathway (Franco et al. 2011), and promoting cell-cell interactions between the neurons that are migrating and the Cajal-Retzius cells in the MZ via Nectin 3 and afadin (Gil-Sanz et al. 2013). In glial-guided locomotion, *Cdh2* is critical for the attachment of the leading process of the migrating neuron to the RGC and is regulated via *Rab5/11* (Shikanai et al. 2011; Kawauchi et al. 2010). It also participates in nucleokinesis via the phosphatase PTPB1 and catenins α and β (Martinez-Garay et al. 2016). Degradation of this cadherin, which is at least partially regulated by the Reelin-*Fyn*-*Rab7* lysosomal degradation pathway, induces the terminal translocation of migrating cells (Kawauchi et al. 2010). In addition to adhesion proteins, other proteins secreted by the own migrating neuroblasts, such as Ephrin -B1, also promote migration (Dimidschstein et al. 2013).

Once the excitatory neurons achieve the correct positioning within the cortical layers, the terminal differentiation starts. Neurons increase their cell somas, grow their apical and basal dendrites, extend their axons, and form the spines and boutons that will be essential for synapses (X. Jiang et al. 2016).

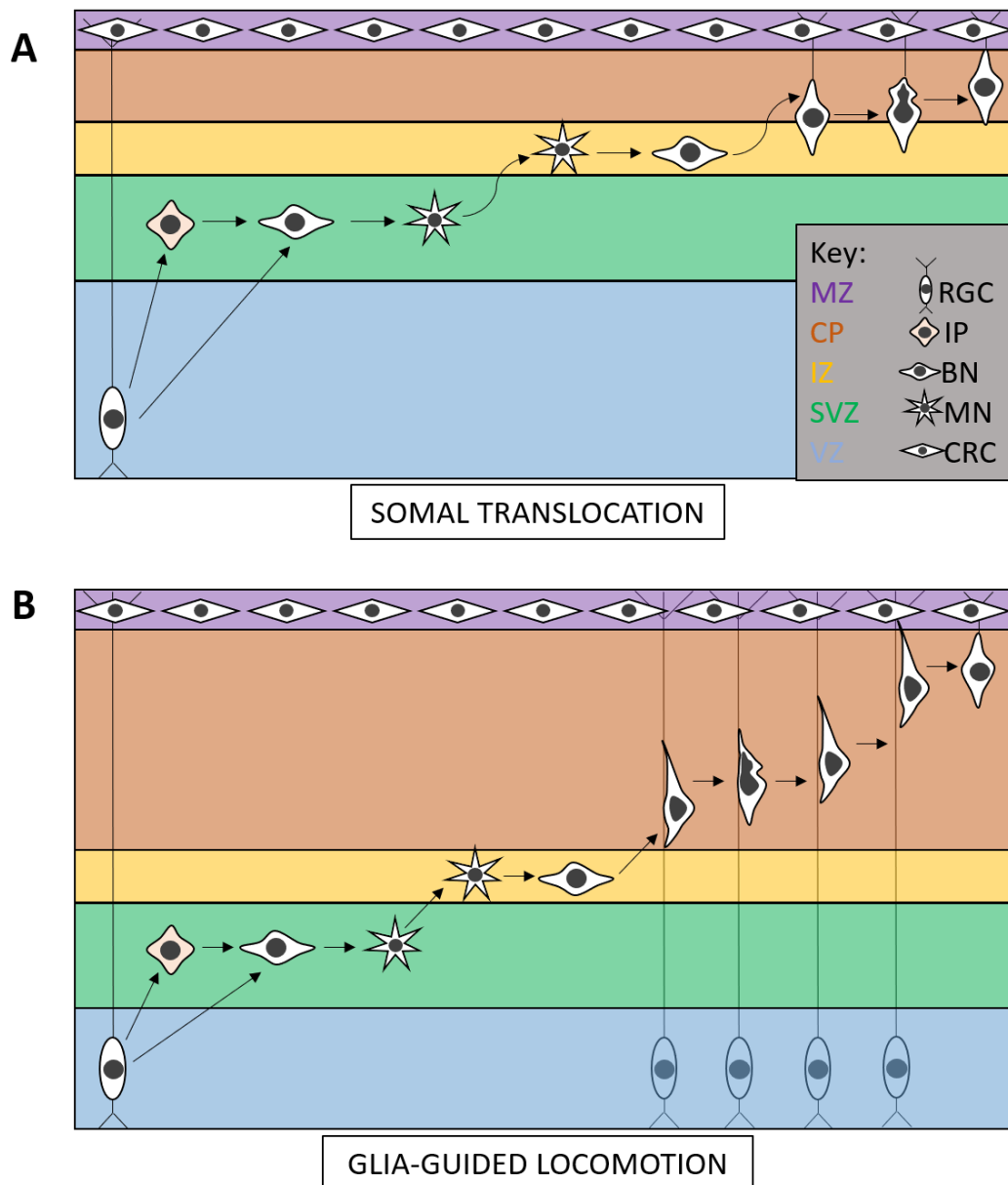


Figure 4. Neurogenesis and radial migration in mice.

MZ, marginal zone; CP, cortical plate; IZ, intermediate zone; SVZ, subventricular zone; VZ, ventricular zone; RGC, radial glial cell; IP, intermediate progenitor; BN, bipolar neuron; MN, multipolar neuron; CRC, Cajal-Retzius cells. Based on Jiang and Nardelli, 2015; Hirota and Nakajima, 2017.

After neurogenesis, the neuroprogenitors that generated the cortical neurons start to give rise to glial cells, such as astrocytes and oligodendrocytes. This process starts at E16 in mice and continues postnatally (X. Jiang et al. 2016; Qian et al. 2000).

In contrast to the migration of excitatory cells, GABAergic interneurons present a tangential migration (Lavdas et al. 1999; De Carlos et al. 1996). Interneurons migrate long distances from the ganglionic eminences extending a leading process that branches while migrating. The branches are generated and modified depending on the extracellular environmental cues that the leading process detects. These signals determine the direction of the interneuron, since the branching is followed by the movement of the nucleus towards the branching point (Martini et al. 2009).

Two migratory streams are the routes used for the majority of interneurons: they either go through the MZ or traverse the SVZ. A smaller group courses through the subplate, but interestingly, interneurons avoid migrating through the cortical plate during tangential migration (Tiveron et al. 2006; López-Bendito et al. 2008). When the invasion of the cortical plate occurs, interneurons switch to a radial migration mode (Polleux et al. 2002; Luhmann et al. 2015). Finally, they allocate their soma to specific layers of the cortex in the final phase of migration, likely by responding to chemical signals that are produced by the excitatory cells (Marín 2013; Miyoshi et al. 2011; Lodato et al. 2011).

1.8 Cortical lamination

Alterations in cortical development can cause defects in cortical lamination that lead to epilepsy (Marín 2012) and behavioural disturbances, as the ones seen in EIEE9 patients (Dibbens et al. 2008; Kurian et al. 2018).

The neocortex is the part of the brain in charge of high-order brain functions. In mammals, a large amount of areas that vary between species

can be identified. Each of the areas varies in its cell composition and circuits, and the thickness and cytoarchitecture of each of the cortical layers is also area specific (Kaas 1987). According to the way they process the different stimuli, the areas can be grouped into the visual cortex, for visual stimuli; the auditory cortex, involved in the processing of auditory information; the motor cortex, which controls the motor behaviour, and the somatosensory cortex, that processes different sensory modalities, specially from the whiskers (Lodato et al. 2015).

Apart from its organisation into areas, the mature cortex is also structured into 6 histologically different cortical layers that were generated in an inside-out pattern, as explained in **section 1.7**.

Layer I, also called the molecular layer, which during development is populated mainly by Cajal-Retzius cells (Germain et al. 2010), contains the apical dendritic tufts of cortical pyramidal neurons, whose inputs are necessary for the feedback interactions in the cerebral cortex that are involved in the cognitive process. This layer also receives input from the M-type thalamic cells (Rubio-Garrido et al. 2009).

Layers II/III, known as the external granular and external pyramidal layer are almost indistinguishable in mice. They contain medium-size pyramidal cells that extend cortico-cortical projections, either within the same hemisphere (associative) or to the opposite hemisphere (commissural). In rodents, the commissural projecting neurons usually traverse through the corpus callosum (callosal projecting neurons), while a small number extend their axons through the anterior commissure (Sabri et al. 2018; Molyneaux et al. 2007). In the somatosensory cortex, layer II/III receives excitatory inputs mainly from layer IV and propagates information to layer V, especially to layer Va (Hooks et al. 2011).

Layer IV, or internal granular layer, consists of spiny stellate excitatory neurons in the SSC of mice, while it is formed by pyramidal excitatory

neurons that project to layer I in the visual cortex. Several types of inhibitory interneurons are also present in both cortical areas, but they differ in the type of somatostatin-expressing interneurons located in the layer (Cadwell et al. 2018). This layer is the first step in the processing of sensory information, since it is the main target of the C-type cells (core) from the thalamus (Jones 1998) and distributes it to the other layers. The layer also receives cortico-cortical inputs (Hooks et al. 2011).

Layer V or internal pyramidal layer is comprised by larger pyramidal cells of heterogeneous morphology and electrophysiology that project to both corticocortical and subcortical targets (Hattox et al. 2007). Layer V can also be divided into two strata, layer Va and layer Vb, which possess different neuronal cell-types, functions and connexions (Schubert et al. 2006). In the somatosensory cortex of rodents, layer Va is mainly formed by intratelencephalic pyramidal neurons, that are electrophysiologically characterised by regular spiking action potential firing patterns and with a small dendritic arbour but a dense axonal ramifications, that usually are restricted to the supragranular layers (Schubert et al. 2006; Larsen et al. 2006; Naka et al. 2016). This stratum is the one that receives the strongest input from layer II/III (Hooks et al. 2011), but also from layer IV and from local neurons within layer Va. These neurons project intracortically to other layers too, but their intracortical output is mostly local (Schubert et al. 2006; Hooks et al. 2011; Larsen et al. 2006; Koralek et al. 1990). A group of cells from layer Va also present corticobulbar axon extensions and, thus, project subcerebrally (Hevner et al. 2003). On the contrary, layer Vb, which is more dense than layer Va, is composed by pyramidal tract, with a thickly-tufted dendritic arbour and a sparse axonal ramification that mostly descends into the infragranular layers. These neurons possess intrinsically bursting action potential firing patterns and project mostly extracortically (Hattox et al. 2007; Kasper et al. 1994; Larsen et al. 2006; Naka et al. 2016). The strongest input to this layer comes from layer II/III (Hooks et al. 2011), and layer Vb neurons extend axons to subcerebral targets, such as the pons and other

nuclei of the brainstem (cortico-pontine), the superior colliculus (corticotectal) or the spinal cord (corticospinal) (Molyneaux et al. 2007; Lévesque et al. 1996).

The deepest layer is layer VI, also called polymorphic layer. It contains neurons of diverse morphology, including pyramidal, spiny stellate or bipolar, that project both intra and extracortically. Layer VI receives strong inputs from layer IV, and also from layers Vb and VI (local inputs), and projects intracortically to these areas (Briggs 2010; Hooks et al. 2011). Neurons from this layer extend corticothalamic projections too (Hevner et al. 2003).

The cortical circuit can also be organised into columns in some parts of the neocortex, where the neurons connect with each other radially across the different layers. In the rodent somatosensory cortex, that can be clearly seen, with layer IV receiving the sensory input from the whiskers via the thalamus, and spreading the information to layers II/III, which pass it to layer V, the final processor of that sensory information (Petersen et al. 2001).

In summary, the cortex is composed by an heterogenous variety of neurons of different morphological and electrophysiological properties that project to different targets, and several types of glia, such as astrocytes, oligodendrocytes or microglia. To study its cell composition, cortical molecular markers are used. These markers are transcription factors, calcium-binding proteins and cytoskeletal proteins expressed by a specific layer or layers, or by a concrete subpopulation of cells (Molyneaux et al. 2007; Rudy et al. 2011). In a simplified way, the neuronal types within the cortex can be grossly divided into glutamatergic excitatory neurons that project either intracortically, subcortically or subcerebrally; and GABAergic inhibitory interneurons that form local connexions in the cortex (Gorski et al. 2002; Molyneaux et al. 2007).

Excitatory neurons can express different cortical markers according to their location within the cortex or where they project to. For example, cut like homeobox 1 (CUX1), CUX2 or LIM homeobox 2 (LHX2) are markers of the upper cortical layers and are expressed strongly in layers II-IV. LHX2 is also expressed in the most superficial part of layer V (Bulchand et al. 2003; Nieto et al. 2004), while RAR related orphan receptor B (RORB)-expressing cells are mainly located in layer IV of caudal areas of the cortex (Nakagawa et al. 2003). T-box, brain 1 (TBR1) is characteristic of layer VI neurons that also extend corticothalamic projections, but it is expressed postmitotically in layers II/III too (Hevner et al. 2001; Molyneaux et al. 2007). Most upper-layer excitatory neurons project callosally, but to characterise the corticocortical projecting cells in the deep layers, the special AT-rich sequence-binding protein 2 (SATB2) marker is used (Alcamo et al. 2008; Britanova et al. 2008; Jabaudon 2017). Within layer V, several markers can be used to determine the different subcerebrally-projecting cells: Orthodenticle homeobox 1 (OTX1)-positive cells extend their axons to the superior colliculus and pons in layer Va (Hevner et al. 2003), while chicken ovalbumin upstream promoter transcription factor interacting protein 2 (CTIP2) is expressed in corticospinal and corticotectal projecting cells in layer Vb and corticothalamic projecting neurons in layer VI (Arlotta et al. 2005; Molyneaux et al. 2007; Jabaudon 2017) for example.

Regarding the interneurons, three molecular markers can detect almost 100% of cortical interneurons in the mouse SSC: parvalbumin (PV), somatostatin (SST) and the ionotropic serotonin receptor 5HT3a (5HT3aR) (Rudy et al. 2011). PV-expressing interneurons, derived from the medial ganglionic eminence (MGE) (Fogarty et al. 2007) are composed of chandelier and basket cells with fast-spiking firing pattern and comprise 40% of the total number of interneurons, distributed in all layers except layer I (Woodruff et al. 2009; Rudy et al. 2011). Interneurons that express SST are originated in the MGE (Fogarty et al. 2007) and can be divided into Martinotti and non-Martinotti (X94) cells, which together make up 30% of

the total number of interneurons (Rudy et al. 2011). Martinotti cells display burst spiking nonpyramidal firing patterns, are mainly located in layer V (Uematsu et al. 2008) and target layer I. The X94 cells produce a firing pattern closer to the PV+ fast-spiking cells and different from Martinotti cells, are located in layers IV and Vb and target layer IV (Ma et al. 2006). 5HT3aR-positive interneurons, unlike the previously described interneurons, are mainly born in the caudal ganglionic eminence (CGE) and constitute the other 30% of interneurons. This 5HT3aR-expressing interneurons form the most diverse group with diverse morphology and electrophysiology. Around 40% of this cells coexpress vasoactive intestinal peptide (VIP), a marker that is expressed by interneurons mainly located in layers II/III with bipolar, bitufted and multipolar morphologies that comprise irregular spiking, fast-adapting, bursting nonadapting and delayed non-fast-spiking 3 firing patterns (Lee et al. 2010) that target pyramidal neurons or other interneurons (Rudy et al. 2011). The rest of the 5HT3aR cells mainly consist of reelin+ neurogliaform cells that reside in layer I and produce late-spiking firing patterns that target pyramidal neurons and other interneurons. These reelin+ cells comprise more than 80% of the VIP- cells, while other small populations of bursting nonadapting neurons (bNA) and multipolar irregular spiking (IS) neurons were also observed within this group (Lee et al. 2010; Rudy et al. 2011).

Before the discovery that almost 100% of the interneurons expressed one of these three molecular markers, GABAergic inhibitory neurons were usually studied using PV, calbindin (CB) and calretinin (CR) as interneuronal markers, since they comprise about 80% of the cortical interneurons in rodents (Gabbott et al. 1997). PV is expressed by fast-spiking cells, as has been explained in the previous paragraph. CB-positive cells consist of an important number of layer II/III cortical excitatory neurons (DeFelipe 1997) and a population of interneurons that can be regular spiking non-pyramidal (RSNP) or burst-spiking non-pyramidal (BSNP) cells of diverse morphology, fast-spiking (mostly PV positive) or irregular spiking (only

when co-expressed with SST) (Cauli et al. 1997; Markram et al. 2004; Flames et al. 2005) and derive from the MGE. Cells that express CR are originated in the CGE and can be divided into BSNP/IS bipolar cells; or RSNP multipolar cells, which are mostly located in layers II/III and target the rest of the layers (Barinka et al. 2010). CR colocalises with 5HT3aR in IS cells and with SST in some Martinotti cells (Rudy et al. 2011). CR is also detected at P8 in pyramidal neurons located in layer Va of the mouse SSC, but the expression decreased from that age on and disappeared by P30, where only a few interneurons were observed (J. Liu et al. 2014).

Another marker generally used to analyse interneurons is glutamic acid decarboxylase 65 and 67 (GAD65/67), the enzyme that produces GABA, the inhibitory neurotransmitter of the GABAergic inhibitory interneurons (Schousboe et al. 2007).

Recently, a new technique, single cell RNA-sequencing, has arisen as a powerful tool to conduct cell-type analysis. An analysis conducted by Ziesel *et al.* in 2015 in the somatosensory cortex and hippocampus of young adult mice (P21-P31) detected 15 GABAergic, 7 glutamatergic and 18 non-neuronal cell-types in the SSC. The 7 excitatory cell-type depended mainly on the layers: layers II/III, IV, VI and VIb contained one single subpopulation, while layer V was comprised by two. A subpopulation that expressed only common deep-layer markers was also found. The GABAergic interneurons were classified into 15 subclasses that expressed PV, SST or 5HT3aR, and did not overlap between them, as previously reported by immunohistochemical analysis (Rudy et al. 2011; Zeisel et al. 2015). PV was expressed in one subpopulation, SST in three and 5HT3aR contained the rest of the interneuronal cell-types. Non neuronal cell-types were comprised by two subtypes of astrocytes, two of microglia, two of perivascular macrophages, and six of oligodendrocytes, probably representing different states of maturity. A subclass of ependymal cells,

choroid plexus, vascular smooth muscle cells, pericytes and two types of endothelial cells were also identified (Zeisel et al. 2015).

Another study, performed by Tasic *et al.* in 2016 in the visual cortex of adult mice, revealed a total of 23 GABAergic, 19 glutamatergic and 7 non-neuronal subclasses of cells, according to their transcriptomic analysis. The experiment managed to detect most already known cortical markers and identified several new ones. Glutamatergic neurons, as in the SSC, were classified into six major classes depending on layers. GABAergic interneurons were divided into 23 subgroups, 18 of which contain PV, CB or VIP-expressing cells, markers that had previously been identified. The seven non neuronal subtypes corresponded to astrocytes, microglia, oligodendrocyte precursor cells, two types of oligodendrocytes, endothelial cells and smooth muscle cells, each with its own set of characteristic markers (Tasic et al. 2016). A more recent article from the same group showed that the better resolution of the single cell RNA-sequencing allowed the cells from the visual cortex to be classified into many more subtypes, but they corresponded well to the 49 identified in the previous study. Analysis using this technique in the motor and visual cortex of mice and comparison of both areas reported that most glutamatergic neuronal types were area specific, but interneuron and non-neuronal subclasses were shared between them, even though some interneuronal subpopulations did present some area-specific differences (Tasic et al. 2016). Some of the cell types identified possessed characteristic electrophysiological features and in the last report, glutamatergic cell-types classified by transcriptomic analyses could be matched according to their long-range specific axonal projections, thus posing single-cell transcriptomics as a great tool to classify all the unique cell populations within the cortex and to gain insight into the cortical circuitry.

1.9 Behaviour

As explained in **section 1.6.4**, the *Pcdh19*-mutant mouse model of Hayashi *et al.* presents some behavioural phenotypes (Hayashi *et al.* 2017). Mice share with humans many brain functions and emotional responses, one of the reasons why using mouse models to approach human behavioural responses under pathological conditions is very common. A very wide range of tests can be conducted to study mouse behaviour, but the experiments performed within one study depend on the particular phenotype that is analysed (Van Meer *et al.* 2005). Autism spectrum disorder (ASD) represents a good example, and a range of behavioural tests can be used to study this condition, which is present in around a quarter of EIEE9 patients (Camacho *et al.* 2012).

Because ASD is correlated with motor deficits, hyperactivity, anxiety and difficulties in adaptation to novel situations (Lai *et al.* 2014; Daenen *et al.* 2001), one of the chosen paradigms is the open field test. In this test, mice are let to run freely in an arena for a determined period of time, either in the dark or with lights on. Several parameters can be measured to test general locomotor activity, anxiety-like behaviour (Simon *et al.* 1994; Seibenhener *et al.* 2015), adaptation and habituation to the novel environment (Daenen *et al.* 2001).

Considering that autistic patients can present motor deficits, hyperactivity or sleep disturbances (Lai *et al.* 2014), 24-hour activity behavioural studies can also be carried out. Spontaneous locomotion of the mice in an open-field arena is analysed for 24 hours. Calculation of different parameters allows then to study the general activity of the mice and their circadian cycles (Paladino *et al.*, 2013; Kalbassi *et al.*, 2017).

Anxiety is seen in patients within the autistic spectrum (Lai *et al.* 2014). In the elevated plus maze (EPM) test, mice are placed into an elevated arena that consists of two closed arms and two open arms and are let to roam

around for a few minutes with lights on. Several parameters can be measured to analyse a type of anxiety-like behaviour that could correlate to the ASD patients.

Social interaction tests are highly important in the study of autism, since deficits in social communication and interaction are characteristic of this disease (Lai et al. 2014). Social interaction studies analyse the interest of a mouse in a peer and can be conducted within a novel environment (Kalbassi et al. 2017) or in their own cage (Silverman et al. 2010).

Other social interaction studies conducted in a three chamber arena analyse the time the subject mouse spends in a chamber with a novel mouse with respect to the time spent alone in an empty chamber, or study the mouse preference for social novelty by calculating the time spent by the subject mouse with a novel mouse respect to a familiar one (Silverman et al. 2010; Kaidanovich-Beilin et al. 2010).

1.10 Aims and hypothesis

As has been mentioned in the introduction, even though *Pcdh19* has been suggested to have a role in various steps during cortical development (Pederick et al. 2016; Fujitani et al. 2017; Bassani et al. 2018; Homan et al. 2018), its role in this process and the mechanisms that lead to EIEE9 are still not fully understood. The aim of this project was to expand the knowledge about *Pcdh19*, particularly regarding its expression throughout development, the characterization of the cell types expressing this gene and its role in migration, cortical lamination and behaviour in mice.

To achieve this aim, *Pcdh19* expression was detected by *in situ* hybridisation at the level of the cortex in late embryonic and early postnatal stages, followed by a characterisation of *Pcdh19* positive cells by *in situ* hybridisation combined with immunohistochemistry against several neuronal markers in the somatosensory cortex of P10 and P20 mouse brains.

Since some reports showed signs of cortical dysplasia in a patient, cortical migration was also analysed by performing *in utero* electroporation of shRNAs on wild type mice at E13.5 and E15.5, and by *in utero* electroporation of EGFP into WT, *Pcdh19*-HET and *Pcdh19*-KO embryos. Finally, to gain a better understanding of the potential functions of PCDH19, we conducted a detailed immunohistochemical and a basic behavioural characterization of a validated *Pcdh19* knock-out (KO) mouse model.

Chapter 2: Material and methods.

2.1 Animal husbandry and legislation

2.1.1 Animal housing

Mice were maintained on a 12 h light/dark cycle (with lights on from 6 am to 6 pm), in a controlled temperature environment of 21 ± 2 °C and a humidity of $50 \pm 10\%$. All mice had access to food and water *ad libitum*.

Animals were housed with at least one cardboard tube, one wooden chew stick, and nesting material. Animals were group housed (up to five per cage). To prevent fighting, males were only group housed if they belonged to the same litter and were weaned at the same time. Once the male was singly housed, he was never grouped housed again.

Animals were health checked regularly, and twice a day after an *in utero* electroporation procedure. Experiments were performed according to the UK Animal Scientific Procedures Act (1986). From 1st January 2013, the European Union (E.U.) Directive 2010/63/EU was implemented into UK law by an update of ASPA 1986.

2.1.2 Animals used

C57BL6/J wild-type (WT) animals were bought from Charles River Laboratories at 6-8 weeks of age and bred in Cardiff University School of Biosciences.

Pcdh19 knock-out (KO; TF2108) animals were purchased from Taconic Biosciences. These animals have a β -galactosidase and neomycin fusion (β -geo) cassette replacing the first three exons of the *Pcdh19* gene (Pederick et al. 2016). As seen in **Figure 6**, exon 1 is extremely large and codes for the extracellular and transmembrane domains of the protein. Thus, deletion of

the exons 1-3 results in the absence of the protein (Pederick et al. 2016). The background of the KO mouse is 129/SvEv-C57/BL6.

2.1.3 Animal matings

Females were paired individually or in duos with a male. Animals were mated at the start of the week and vaginal plugs were checked every morning. The day the plugs were observed was considered embryonic day (E)0.5. The day pups were born was designated as postnatal day (P)0. Pups were weaned between P30 and P35.

2.1.4 Mouse genotyping

All females were ear-notched for identification purposes.

Animals were sex genotyped if the animal was culled before P20 and genotyped to determine if the animal was *Pcdh19*-WT, *Pcdh19*-HET or *Pcdh19*-KO if required.

Ear notches and tail clips were stored at -20 °C until processing.

2.1.4.1 DNA extraction

For samples that only required sex genotyping, tail clips were digested in 100 µL of digestion buffer [50 mM Tris base pH 8.5 (Thermo Fisher Scientific, BP152), 2% Ethylenediaminetetraacetic acid (EDTA; Sigma-Aldrich, ED) and 5% Tween-20 (Sigma-Aldrich, P9416) in deionized water] at 56 °C overnight. Proteinase K was added to the buffer immediately before incubation at a 5 µg/µL concentration.

Samples that required *Pcdh19* allele identification or *Pcdh19* identification and sex genotyping were digested using the Mouse Direct PCR Kit (Biotool, B4001), following the manufacturer's protocol. In brief, ear notches were digested with buffer L and 2% protease plus for one hour at 55 °C and then incubated at 95 °C for 5 min.

If needed, samples were stored at -20 °C after digestion and before polymerase chain reaction (PCR) analysis.

2.1.4.2 PCR analysis

For sex determination, digested samples were heated at 100 °C for 10 minutes (min) before performing a PCR, using Taq DNA polymerase (QIAGEN, 201203). The protocol was performed according to the manufacturer's instructions. One μL of the lysate was added directly to a 24 μL PCR reaction [0.5 μL of 10 mM deoxynucleotide triphosphates (dNTPs; Promega, U1511), 5 μL of 5xQ solution, 1.25 μL of each primer (original concentration 10 mM), 2.5 μL of PCR buffer, 1.75 μL of 25 mM MgCl_2 , 0.5 μL of Taq DNA polymerase and Milli Q water up to 24 μL]. Primers used were Jarid 1c and d (Clapcote et al. 2005), as shown in **Table 2**. Samples were then put in a thermocycler (Biorad T100) following the programme outlined in **Table 2**. PCR products were loaded on a 2% agarose gel in Tris-Borate-EDTA (TBE) [0.22 M Tris base, 180 mM of boric acid (Sigma-Aldrich, B6768) and 5 mM of EDTA pH =8] solution at pH =8.3, and 0.005% of Ethidium Bromide (Sigma-Aldrich, E1510) in an electrophoresis chamber for 50 min at 110 V and visualized using an ultraviolet (UV) transilluminator (VWR GenoView, GenoSmart2).

For *Pcdh19* detection and sex genotyping, 1 μL of the sample plus 0.5 μL of each of the primers (10 μM) was added to 10 μL of 2xM-PCR OPTI™ mix (containing Taq DNA polymerase, dNTPs, MgCl_2 and reaction buffer). The mix was made up to 20 μL with Milli Q water. Samples were put in a thermocycler with the protocol described in **Table 2**. For *Pcdh19* genotyping, two different PCR protocols were used: one to detect the *Pcdh19*-WT allele and other to detect the *Pcdh19*-KO allele. Primers used to detect *Pcdh19*-WT alleles were TF2108-F and TF2108-R. To detect *Pcdh19*-KO alleles, TF2108-10 and GT-IRES primers were used. Sequences, annealing temperatures and molecular weights (MW) of the PCR products are shown in **Table 2**.

Genotyping	Primer sequences (forward and reverse)	PCR protocol	Product size
Sex genotyping	<p>Jarid 1c primer: 5'-CTGAAGCTTTTGGCTTTGAG-3'</p> <p>Jarid 1d primer: 5'-CCACTGCCAAATTCTTTGG-3'</p>	<p>Taq DNA polymerase (QIAGEN): - 94 °C 5'. - 40 cycles: • 94 °C 30". • 54 °C 1'. • 72 °C 40". - 72 °C 5'.</p> <p>Mouse Direct PCR Kit (Biotool): -94 °C 5'. -35 cycles: • 94 °C 20". • 54°C 20". • 72 °C 20". -72 °C 5'.</p>	<p>Jarid 1c: 331 bp</p> <p>Jarid 1d: 302 bp</p>
	<p><i>Pcdh19</i>-WT primers: <u>TF2108-F</u> 5'-TAGAGGTTCTTGCTGAAGACTTCC-3' <u>TF2108-R</u> 5'-TCAACTGTTTCGATGAGACACTGC-3'</p> <p><i>Pcdh19</i>-KO primers: <u>TF2108-10</u> 5'-GTGCGTACCAGGCGGGAGC-3' <u>GT-IRES</u> 5'-CCCTAGGAATGCTCGTCAAGA-3'</p>	<p><i>Pcdh19</i>-WT: -94 °C 5'. -35 cycles: • 94 °C 20". • 56.5°C 20". • 72 °C 20". -72 °C 5'.</p> <p><i>Pcdh19</i>-KO: -94 °C 5'. -35 cycles: • 94 °C 20". • 57.2°C 20". • 72 °C 20". -72 °C 5'.</p>	<p><i>Pcdh19</i>-WT: 123 bp</p> <p><i>Pcdh19</i>-KO: 437 bp</p>

Table 2. PCR primers and protocol for genotyping.

2.2 Real-time quantitative polymerase chain reaction (PCR)

Four mice of each age from at least three different litters were analysed in this experiment. Animals from the same litter were treated as independent biological replicates. All tissue was handled in an RNase free (RF) environment throughout the tissue preparation. All tools were sprayed with RNaseZAP (Sigma, R2020). Water and phosphate buffered saline [PBS; 13.7 mM NaCl (Sigma-Aldrich, S7653), 0.27 mM KCl (Sigma-Aldrich, P9333), 0.8 mM Na₂HPO₄ (Sigma-Aldrich, 71640), 0.146 mM KH₂PO₄ (Sigma-Aldrich, P9791) in distilled water] were treated with diethyl pyrocarbonate (DEPC; Sigma, D5758) at a 0.1% concentration and autoclaved the following day. All the rest of the solutions were maintained RF and diluted in DEPC water or DEPC PBS if required.

2.2.1 Dissection

Animals were culled at different ages (P2, P6, P10, P15 and P20), using cervical dislocation and confirming by decapitation in accordance with Schedule 1 (ASPA, Home Office 1986). The brain was extracted, placed in a mould (Electronic Microscopic Science, 69090-C) on ice and cut with blades (Electronic Microscopic Science, 70933-70) into coronal slices to facilitate the separation of its different parts. Samples were then snap frozen in liquid nitrogen and stored in a -80 °C freezer until ribonucleic acid (RNA) extraction. The brain sections isolated were olfactory bulb (OB), striatum (ST), cortex (CTX), hippocampus (HPC), thalamus (TH) and cerebellum (Cb). Only cortex samples had their RNA extracted.

2.2.2 RNA extraction and reverse transcription

To extract the RNA, cortical tissue from **Section 2.2.1** was thawed on ice and one mL of Trizol (Life technologies, 15596018) was added to the 1.5 ml tube. Tissue was triturated using a 1 mL pipette tip followed by a 16G gauge needle (BD Microlance™, 300637). The vial was centrifuged briefly at 4 °C,

the upper phase of the suspension was transferred to a new tube and 200 μ L of chloroform (Sigma, 372978) was added. The vial was shaken for 15 sec and then centrifuged at 12000 G for 15 min at 4 °C. The aqueous phase was transferred to another tube and 0.5 mL of 100% isopropanol (Sigma, 278475) was mixed with the sample. After inverting for 15 sec, the sample was loaded into a column from the RNeasy extraction kit (QIAGEN, 74104). Samples were processed according to the manufacturer's instructions from this point on. In summary, samples were washed in a series of buffers, treated with DNaseI mix (QIAGEN, 79254; 10 μ L of DNaseI stock in 70 μ L of buffer RDD) and eluted in 30 microliters of RF water. After elution, RNA was quantified using a Biospectrometer® basic (Eppendorf) and stored at -80 °C.

Once the RNA was extracted, samples were converted into coding deoxyribonucleic acid (cDNA) using the enzyme reverse transcriptase. 2 μ g of RNA was added into a mix of 0.67 μ L of Random Hexamer Primers (Promega, C1181) at a 300 ng/ μ L concentration and diluted in DEPC water up to 12 μ L. The mixture was then incubated for 3 min at 85 °C. Then, 1 μ L dNTP mix at 10 mM, 4 μ L of 5Xfirst strand buffer, 1 μ L of 0.1 M dithiothreitol (DTT; Invitrogen, 707265ML), 2 μ L SuperScript III reverse transcriptase (Invitrogen, 18080044) and 1 μ L RNase inhibitor (Applied Biosystems, N8080119) were added. The reaction was incubated for 5 min at room temperature (RT; 25 °C) and 1h30min at 50 °C. Lastly, cDNA was stored at -20 °C ready for qPCR.

2.2.3 Quantitative PCR protocol and analysis

After reverse transcription, a qPCR experiment was conducted to quantify the relative levels of cDNA present in each of them.

For each sample of the FAST SYBR® Green RT-qPCR, a qPCR mixture containing 12.5 μ L of FAST SYBR® Green Master mix (Applied Biosystems, 4385612), 0.625 μ L of 10 μ M forward and 10 μ M reverse primers and 10.25 μ L of Milli Q water were mixed. The primers used to perform the

quantitative PCR (Pcdh19-F, Pcdh19-R, B-actin-F and B-actin-R) were taken from a previous publication (Pederick et al. 2016). B-actin primers were used as an internal control. Primer sequences are shown in **Table 3**. 100 ng of cDNA was added to the mixture. Each reaction was prepared in triplicates, mixed in a tube and pipetted into a MicroAmp™ Fast Optical 96-well plate (Applied Biosystems, 4346906). The plate was placed in a 96-Well Support Base (Applied Biosystems, 4346906) covered with a clear adhesive film (Applied Biosystems, 4306311) and briefly centrifuged. Finally, the plate was placed into the StepOnePlus™ Real-Time PCR system (Applied Biosystems, 4379590) and the Sybr Green qPCR protocol conducted. The protocol consisted of 40 cycles of qPCR, using an annealing temperature of 60 °C for all primers. The number of PCR cycles the sample required to cross a fluorescent threshold was designated as the cycle threshold (Ct). Ct values were used to calculate the relative amount of cDNA. Raw data was extracted after qPCR completion and analysed using Microsoft Office Excel. Relative levels of cDNA were calculated using the $2^{-\Delta\Delta CT}$ method (Schmittgen, 2008). In this method, the fold change of the gene normalised to an internal control and relative to a calibrator were calculated using a series of formulas. To perform this analysis, two assumptions were made: that the efficiency of the target gene and the internal control is the same and that the efficiency is close to 1. First, the initial number of molecules (X_0) is equivalent to $X_0 = K_X \times (1 + E_X)^{-C_{T,X}}$, where K_X is a constant, E_X is the efficiency of target amplification and $C_{T,X}$ is the threshold cycle for target amplification. Second, to normalise to the internal control (β -actin), $X_0 = K_X \times (1 + E_X)^{-C_{T,X}}$ was divided by $R_0 = K_R \times (1 + E_R)^{-C_{T,R}}$, where R is the internal control. If $E_X = E_R$ is assumed, this results in the formula: $X_N = K \times (1 + E)^{-\Delta CT}$, where X_N is the normalized amount of target, and ΔCT is equal to the difference in threshold cycles for the target gene and the internal control. To relativise to the calibrator (P2), $X_{N,q} = K \times (1 + E)^{-\Delta CT,q}$ was divided by $X_{N,c} = K \times (1 + E)^{-\Delta CT,c}$, where q was the target sample and c the calibrator. If assumed $E=1$, $X_{N,q} / X_{N,c} = 2^{-\Delta\Delta CT}$, where $X_{N,q} / X_{N,c}$ is the initial quantity

of molecules normalised to an internal control and relative to a calibrator, and $-\Delta\Delta CT$ is $-(\Delta CT, q^{-\Delta CT}, c)$. Since all reactions were prepared in triplicates, values from each reaction were averaged.

Additionally, a melting curve was generated to check that only specific fluorescence signal could be detected. This curve indicates the melting temperature of the target, which depends on the cDNA length and its nucleotide sequence, thus confirming the primers amplified the correct product. Melting curve analysis is important in qPCR experiments that use SYBR Green, since the dye detects any double-stranded DNA (dsDNA), including unspecific products that could be generated in case the primers were not optimal, the annealing temperature was too low or the PCR got contaminated, among others. To generate this melting curve, the temperature was increased by 1°C per minute up to 99°C to detect the fluorescent signal released from the now denatured products. qPCR protocol is outlined in **Table 3**.

Target gene	Primer sequences (forward and reverse)	qPCR protocol
Pcdh19	Pcdh19-F: 5'-TGGCAATCAAATGCAAGCGT-3' Pcdh19-R: 5'-ACCGAGATGCAATGCAGACA-3'	- 95 °C 10'. - 40 cycles: • 95 °C 15'. • 60 °C 1'.
β-Actin	Bactin-F: 5'-CTGCCTGACGGCCAGG-3' Bactin-R: 5'-GATTCCATACCCAAGAAGGAAGG-3'	- 95 °C 15'. - 60 °C 1'. - 95 °C 15'+0.3 °C

Table 3. qPCR primer sequences and protocol.

2.3 Histological techniques

To characterise the *Pcdh19* positive cells, analyse the role of *Pcdh19* in cortical migration and determine if there were immunohistochemical differences among the *Pcdh19*-WT, *Pcdh19*-HET and *Pcdh19*-KO animals several immunohistochemical analysis were performed.

2.3.1 Brain extraction and fixation

Brains were extracted and fixed using different techniques according to the age of the animal. Embryonic animals were culled by decapitation while postnatal animals were perfused.

2.3.1.1 Embryonic brain extraction

When embryos reached E16.5 or E18.5, embryos were extracted, and their brains dissected in ice-cold PBS. Brains were then fixed overnight by immersion in 4% paraformaldehyde (PFA; diluted in PBS from 16% PFA; Thermo Fisher Scientific, 28908) at 4°C and subsequently stored in PBS at 4°C until cutting. Tails clips were used for genotyping purposes (described in **Section 2.1.4**).

In the cases where the samples were used to detect *Pcdh19* RNA, tissue was handled in an RF environment. As in **Section 2.2**, all tools were sprayed with RNaseZAP and all buffers were made RF.

2.3.1.2 Perfusion

To fix samples and prepare them for cutting, postnatal animals were perfused. If brains were to be used to detect RNA using *in situ* hybridization (ISH) techniques, tissue was handled in an RF environment. Animals were injected with 0.1 mL of Euthatal (Merial, R02701A). Once the animal lost the pedal withdrawal reflex, it was perfused with PBS followed by 4% PFA using a 26G needle (BD Microlance™, 300300). The tail clips were used for genotyping (explained in **Section 2.1.4**). Different quantities of PBS and 4%

PFA were used depending on the size of the animal: 5 mL for P2 and P6; 10 mL for P10, and 15 mL for P15 and P20. If the animal was an adult, 30 mL of PBS and 30 mL of PFA were infused using a pump (Ecoline; Bennet Scientific Limited). After perfusion, brains were extracted and immersed in PFA 4% for 24-hours (h) at 4 °C, and then stored in PBS also at 4 °C until cutting.

For X-gal staining, the procedure was very similar, but mice were perfused using 1% PFA and brains were fixed for 2 hours at 4°C, before immersing them in PBS.

2.3.2 Sectioning

Fixed brains were cut into slices using two different instruments. Slices that were going to be used for ISH analysis or X-gal staining were sectioned with the cryostat, while slices that were immunohistochemically stained or just counterstained with DAPI were cut with the vibratome.

2.3.2.1 Cryostat sectioning

In the cryostat sections that were used to detect RNA using ISH techniques, tissue was handled in an RF environment. Prior to cryostat sectioning, brains were immersed in 30% sucrose (Thermo Fisher Scientific, S/8600/60) until they sunk to the bottom of the tube. After cryoprotection, brains were embedded in optimum cutting temperature (OCT) compound (VWR, 361603E) and frozen on dry ice. Samples were kept at -80 °C until sectioning. Brains were cut into 12 or 20 µm coronal slices and mounted onto Polysine® microscope slides (VWR, 631-0107). Slides were labelled and stored at -80 °C until usage.

In the X-gal staining procedure, samples were cut into 25 µm coronal slices and didn't need to be RF.

2.3.2.2 Vibratome sectioning

To cut brains on the vibratome, brains were embedded in 4% Top Vision low melting-point agarose (Thermo Fisher Scientific, R0801) in PBS. Sections were cut at 100 µm or 50 µm, depending on their intended use, and collected into PBS with 0.05% sodium azide (Sigma-Aldrich, S2002).

2.3.3 Staining

Slices were stained using different techniques. ISH was performed when *Pcdh19* mRNA had to be detected, an IHC analysis was done to detect different molecular markers, and a combination of both techniques was performed to study the expression of the markers in *Pcdh19* mRNA positive cells. Brains used for migration analysis were only counterstained with DAPI.

2.3.3.1 ISH

The ISH technique consists of three steps: generation of a specific probe that binds to the target, probe hybridisation and probe detection.

2.3.3.1.1 Probe generation

Three riboprobes were designed to conduct ISH experiments: two against *Pcdh19* (exons 1 and 6, respectively) and the third against catenin delta-1 (*CTNND1*) as a positive control. All the steps required to generate the probes are illustrated in **Figure 5**. Sequences of the primers are shown in **Table 4**. PCR amplification was carried out using the specific primers (**Table 4**), a template of the gene of interest and the Phusion® High-Fidelity DNA Polymerase (New England Biolabs, M0530S). In brief, 250 ng of mouse brain cDNA was added into a PCR master mix containing 4 µL of the 5X Phusion HF buffer, 0.4 µL of 10 mM dNTPs, 1 µL of each of the primers, 0.2 µL of the Phusion® High-Fidelity DNA Polymerase. The mix was made up to 20 µL with Milli Q water and put in a thermocycler following the protocol in **Table 4**.

Probe	Primer sequences (Forward and reverse)	PCR protocol	Product size
Pcdh19 exon 1	<p>Pcdh19e1-F: 5'-CACCAAGCAGAAGATTGACCGAG-3'</p> <p>Pcdh19e1-R: 5'-GCCTCCCATCCACAAGAATAGTG-3'</p>	<p>- 98 °C 30".</p> <p>- 35 cycles:</p> <ul style="list-style-type: none"> • 98 °C 10". • 72 °C 1'. <p>- 72 °C 5'</p>	987 bp
Pcdh19 exon 6	<p>Pcdh19e6-F: 5'-GGATTCTTGGCCACTCTGATAG-3'</p> <p>Pcdh19e6-R: 5'-CTCTGTTTCCCCAACATCAAG-3'</p>	<p>- 98 °C 30".</p> <p>- 35 cycles:</p> <ul style="list-style-type: none"> • 98 °C 10". • 66.8 °C 30". • 72 °C 30". <p>- 72 °C 5'</p>	810 bp
CTNND1	<p>CTNND1-F: 5'-ATGGACGACTCAGAGGTGGA-3'</p> <p>CTNND1-R: 5'-GCACCTCTTCACCAATCATG-3'</p>	<p>- 98 °C 30".</p> <p>- 35 cycles:</p> <ul style="list-style-type: none"> • 94 °C 30". • 65 °C 30". • 72 °C 30". <p>- 72 °C 5'</p>	988 bp

Table 4. Primers to generate probes for the RNA ISH experiments.

Pcdh19, Protocadherin 19; *CTNND1*, Catenin delta-1.

The PCR product was cloned into a pCR™-Blunt II-TOPO™ Vector (Invitrogen, 45-0245). In brief, 1 µL of PCR product was mixed with 1 µL salt solution (Invitrogen, 45-0245), 1 µL of pCR™-Blunt II-TOPO™ and 3 µL of Milli-Q water, incubated for 5 min at RT and then transformed into One Shot™ TOP10 Chemically Competent E. coli cells (Thermo Fisher Scientific, C404006) as per manufacturer's instructions. TOP10 competent cells were thawed on ice and 2 µL of the cloning product was added to the 50 µL vial. The mix was incubated for 30 min, before a heat shock for 30 sec at 42 °C was performed and the sample was placed on ice again. Then, 250 µL of super optimal broth with catabolite repression (S.O.C.) medium (Sigma, 3522) were added to the TOP10 cells and incubated at 37 °C for 1 hour at 200 revolutions per minute (rpm) on a Thermomixer (Thermomixer C, Eppendorf) to allow the translation of the kanamycin resistance gene. After incubation, 100 and 150 µL of the product was spread onto LB (Sigma, 2897)-kanamycin agar plates (50 mg/mL) and incubated overnight at 37 °C.

6 colonies per transformation were selected for overnight culture into 3 mL LB + kanamycin. The following day, plasmid DNA was extracted using a QIAprep Spin miniprep kit (QIAGEN, 27104) following the manufacturer's protocol. Colonies were centrifuged at 5000 rpm for 2 min and the supernatant was discarded to collect the cultured bacteria. The pellet was resuspended in P1 buffer and an alkaline P2 solution was added and incubated for 5 min at RT to denature the genomic DNA. Then, N3 buffer was used to neutralise the acid solution. The solution was centrifuged at 14000 rpm for 10 min to precipitate the genomic DNA and cell debris to the bottom. The supernatant was collected, added into a column that contained a silica membrane for selective adsorption of plasmid DNA and centrifuged. The sample was washed with PE buffer twice to remove the salts and eluted with 30 µL of water. To check if the plasmid contained the correct insert in the correct orientation, 2 µL of each miniprep was digested with an enzyme for an hour and run on a 1% agarose gel. If the size of the bands was correct, one miniprep was selected for sequencing (see **Table 4**

for primers). Confirmed plasmids were retransformed (**Section 2.3.3.1.1**) for maxiprep (QIAGEN, 12362).

To generate sense and antisense probes, 25 to 50 µg of DNA were linearized using specific enzymes. To generate antisense and sense probes, the cloned pCR™-Blunt II-TOPO™ Vector was digested with a restriction enzyme that produced 5' overhangs to avoid transcription in the opposite sense. The restriction enzymes used are described in **Table 5**. The mix was incubated at 37 °C during the day and then left to incubate over-night after 4 µL more of the enzyme was added. After digestion, the DNA was purified using the QIA-quick PCR purification kit (QIAGEN, 28104) and the sample was eluted in 30 µL of RF water. All the steps performed after water elution were conducted in an RF environment. The digested sample was transcribed for 2 h at 37 °C in a water bath. The transcription reaction consisted of 4 µL of linearized DNA, 2 µL of RNA labelling mix, 2 µL of the RNA polymerase, 2 µL of a 10X transcription buffer specific to the RNA polymerase, and 10 µL of DEPC water. Probes were labelled with digoxigenin (DIG)-labelled 2'-deoxyuridine 5'-triphosphates (dUTPs) nucleotide mix (Sigma Aldrich, 11277073910). All sense probes were transcribed using SP6 RNA polymerase (New England-Biolabs, M0207S), and the three antisense probes were transcribed using T7 RNA polymerase (New England-Biolabs, M0251S). After transcription, the probes were purified using Illustra MicroSpin G50 columns (GE Healthcare Life Sciences, 27-5330-01) to eliminate the unincorporated labelled nucleotides. Finally, 0.5 µL of RNase inhibitor was added to each sample and 4 µL of each probe was loaded onto a gel (1-1.2% of agarose in TBE buffer) to check for RNA integrity.

Probe	Restriction enzymes	Manufacturer	Volume	Buffer
AS	Spe I, Hind III or BamH I	New England- Biolabs	4 μ L	CutSmart buffer
S	NotI, XbaI or XhoI			

Table 5. Restriction enzymes used to digest pCR™-Blunt II-TOPO™ Vector to generate sense and antisense probe.

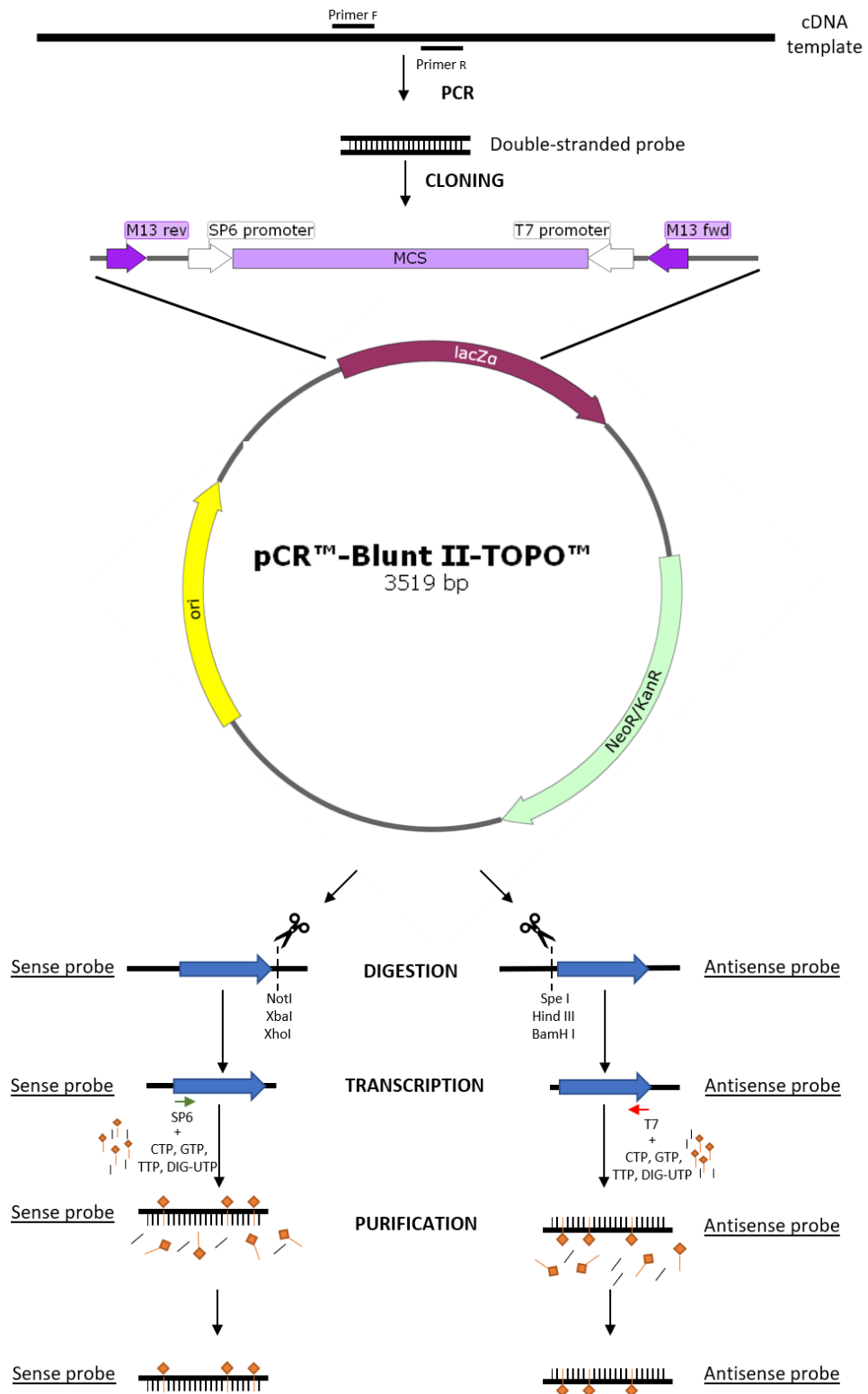


Figure 5. Probe generation.

Diagrammatic representation of the generation of riboprobes to detect *Pcdh19* and *CTNND1* mRNA using ISH techniques.

2.3.3.1.2 *In situ* hybridization

To detect *Pcdh19* mRNA in the tissues, ISH on E16.5, P2, P6, P10, P15, and P20 brains was performed. All the steps until the probe was hybridized were done in an RF environment. Frozen sections were thawed at RT for 20 min. The buffers used are depicted in **Table 6**. The slides were then placed in microscope slide mailers and post-fixed in 4% PFA for 15 min. Sections were then washed in PBS for 3 min 3 times and incubated in hydrogen peroxidase (Sigma-Aldrich, 216763) 3% diluted in PBS for 15 min to quench the endogenous peroxidases. Following the incubation, slides were rinsed in PBS again and acetylated in a 0.25% acetic anhydride solution (Sigma-Aldrich, 320102) for 10 min. After another 3 washes in PBS for 5 min, brain slices were pre-hybridized in a pre-warmed hybridization buffer [50% formamide (Sigma-Aldrich, 47671), 0.1% Tween-20, 0.25% CHAPS (Sigma-Aldrich, C5070), 250µg/ml yeast tRNA (Thermo Fisher Scientific, AM7119), 500µg/ml herring sperm (Invitrogen, 15634-017), 5x Denhardtts (Invitrogen, 750018), 5x SASC (diluted in Milli-Q water from 20xSASC; salt and sodium citrate; GIBCO, 15557-044), 50µg/ml heparin (Sigma-Aldrich, H4784), 2.5mM EDTA] for 1 h at 65 °C. Slices were hybridized with the probe overnight at 65 °C in a water bath (Julabo SW22). The slides were put in a closed humid chamber filled with a humidifier buffer to avoid the drying of the sample. Sense and antisense probes were used at a dilution of 2 µL of probe in 750 µL of hybridization buffer in all brains except for P15 and P20 brains, where the dilution used was 3 µL in 750 µL of buffer. Probes were denatured at 80 °C for 5 min before hybridization. Probes were then added to the slides, and hybridization coverslips (Grace Bio-Labs, GBL716024) were used to cover the slides.

2.3.3.1.3 Probe detection

For fluorescent detection, slides were removed from the bath on the following day and washed with 0.2xSASC 20 min for 3 times, followed by equilibration in buffer TN (preparation is described in **Table 6**) for 5 min and blocking in TNB (TN+0.5% Blocking Reagent; Perkin-Elmer) for 30 min. Slides were then incubated for 30 min in anti-DIG antibody coupled with horseradish peroxidase (HRP) (Sigma-Aldrich, 11207733910) in a 1 in 2000 dilution in TNB to detect the DIG-labelled probes. Following the incubation, tissue was rinsed in TNT (TN+ 0.5% Tween) 3 times for 5 min.

To amplify the fluorescence, each slide was incubated in 150 μ L of Cy3-Tyramide (TSATM Plus Cy3 Fluorescence kit, Perkin-Elmer, NEL744001KT) in a 1 in 50 dilution dissolved in the amplification diluent. TSA stands for Tyramide signal amplification. This amplification method uses the property of tyramide to bind to other proteins after oxidative radicalization. The incubation of the tissue labelled with an antibody coupled with HRP with tyramide and hydrogen peroxide (present in the diluent) produces the radicalization of tyramide. The radicalized tyramide binds covalently to proteins near the site of the radicalization. Tyramide is coupled with the fluorescent dye Cy3, thus amplifying the fluorescent signal and facilitating the detection of the probe.

The slide was then washed 3 times in TNT again. After the washes, the slices were equilibrated in PBS for 10 min, stained with 4',6- diamidino-2-phenylindole dihydrochloride (DAPI; Sigma-Aldrich, D9542) for 10 min in a 1 in 4000 dilution in PBS and then washed in PBS again. Finally, the slides were mounted in fluorescence mounting medium DAKO (Agilent, S3023). and stored at 4 °C before imaging.

If the probe was detected using a colourimetric reaction (CISH), on the second day, slides were removed from the bath and washed in a post-hybridization buffer (solution described in **Table 6**) for 1 h twice. To prepare for the blocking, brain slices were then rinsed twice for 15 min in

B1 buffer (components are shown in **Table 6**) and blocked for 1 h in CISH blocking buffer [10% goat serum (BIORAD, C07SA) dissolved in B1 buffer]. Tissue was then incubated overnight at 4 °C in anti-DIG-Alkaline phosphatase antibody (AP; Sigma-Aldrich, 11093274910) in a dilution of 1 in 2000. The following day, slides were washed twice in B1 for 5 min and once in B3 buffer (preparation detailed in **Table 6**) for 30 min to develop the *in situ* hybridization. The probe was detected using 5-bromo-4-chloro-3-indolyl-phosphate/nitro blue tetrazolium (BCIP/NBT) liquid substrate (Sigma, B1911). Tween-20 (Sigma, P9416) in a 1 in 1000 dilution was added to BCIP/NBT, and this mix was added onto the slide. The slide was incubated in the BCIP/NBT- Tween-20 mixture in darkness until the signal appeared (48-72 h). Finally, brain slices were rinsed in PBST (PBS + 0.1% TritonX-100) twice for 20 min, once with water and mounted with DAKO.

Buffer	Components	Final concentration	Manufacturer
Acetylation buffer	Triethanolamine	100 mM	Sigma-Aldrich
	Acetic anhydride	0.25%	Sigma-Aldrich
Humidifying buffer	Formamide	50%	Sigma-Aldrich
	20xSASC	10x	GIBCO
TN (1L)	1.5 M NaCl	150 mM	Sigma-Aldrich
	1 M Tris pH =7.5	100 mM	Thermo Fisher Scientific
Post-hybridization buffer (500 mL)	Formamide	50%	Sigma-Aldrich
	20xSASC	2x	GIBCO
	Tween-20	0.1%	Sigma-Aldrich
B1 (500 mL)	1.5 M NaCl	150 mM	Sigma-Aldrich
	1 M maleic acid buffer pH =7.5	100 mM	X
	Tween-20	0.1%	Sigma-Aldrich
B3 (50 mL) Prepared fresh	1 M Tris pH=9.5	100 mM	Thermo Fisher Scientific
	5M NaCl	100 mM	Sigma-Aldrich
	1 M MgCl ₂	50 mM	Sigma-Aldrich
	Tween-20	0.05%	Sigma-Aldrich

Table 6. Buffers used for probe detection in ISH.

SASC, salt and sodium citrate.

Images were taken on a confocal microscope. Details of the imaging are explained in **Section 2.3.4**.

2.3.3.2 Immunohistochemistry (IHC)

To detect molecular markers, IHC on P10 and P20 brains was performed. Cortical markers, such as chicken ovalbumin upstream promoter transcription factor interacting protein 2 (CTIP2), special AT-rich sequence-binding protein 2 (SATB2), cut like homeobox 1 (CUX1), T-box, brain 1 (TBR1) and RAR related orphan receptor B (RORB), were detected on P10 brains. Interneuronal markers, specifically parvalbumin (PV), calbindin (CB), calretinin (CR) and somatostatin (SST), were analysed in P20 brains. As explained in **Section 2.3.2.2**, brain slices were cut on the vibratome at 50 μm and stored in PBS with 0.05% sodium azide at 4 °C. The free-floating slices were selected and incubated in a blocking solution that contained 4% bovine serum albumin (BSA; Sigma-Aldrich, 7906), 3% donkey serum (DS; Sigma-Aldrich D9663) and 0.1% Triton X-100 (Sigma-Aldrich, T9284) in PBS at RT for 1 h. Tissue was then incubated in primary antibody diluted in blocking solution overnight at 4 °C. Incubation was performed in a humid chamber. Dilution and characteristics of the antibodies are shown in **Table 7**. Incubations with only the secondary antibody were used as negative controls. Antibodies against RORB, SATB2, PV and CR couldn't bind to their target antigens unless an antigen retrieval (AR) step was performed. In these cases, the tissue was either immersed in a 10 mM citrate buffer (Sigma-Aldrich, C2404) pH =6, at 95 °C for 5 min (RORB and SATB2) or 10 min (PV, CR) before the blocking was conducted. When optimization tests for the PCDH19 and BGAL antibodies were conducted, several ways of AR were tested: the tissue was immersed in 10 mM citrate buffer pH =6 in all cases. But then they were heated either in a waterbath or a microwave. The waterbath was at 70°C or 95°C and the time of incubation could be 10, 20 min or 30 min. When microwaved, the tissue was incubated for 5 min from room temperature or heat until boiling point and then heated for 5 minutes.

Primary antibody	Manufacturer	MAB/PAb	Dil.	Host	AR	Layer expression	Cell expression
Anti-CUX1	Proteintech, 11733	PAb	1:200	Rb	N	Layer II-IV	Cells of upper layers
	Santa Cruz Biotechnology, sc-13024						
Anti-CTIP2	Abcam, ab18465	MAB	1:250	Rt	N	Layers V and VI	Sub cerebral and corticothalamic projections.
Anti-SATB2	Abcam, ab51502	MAB	1:400	Ms	Y	Layers II-V	Corticocortical projections.
Anti-RORB	Proteintech, 17635-1AP	PAb	1:200	Rb	Y	Layer IV	Layer IV
Anti-TBR1	Abcam, ab31940	PAb	1:350	Rb	N	Layer VI	Layer VI
Anti-PV	Swant, PV27	PAb	1:10000 1:500 (ISH)	Rb	Y	All layers	Fast-spiking cells with narrow spike waveforms.
Anti-CB	Swant, CB38	PAb	1:5000	Rb	N	All layers	- Layer II-III pyramidal cells. - Some fast-spiking cells. - Some RSNP.
Anti-CR	Merck, AB5054	PAb	1:1000	Ms	Y	All layers, mainly II-III	- Bipolar neurons, BSNP. - Multipolar cells, RSNP.
Anti-SST	Merck, MAB354	MAB	1:200	Rt	N	All layers	Several inhibitory subpopulations, most known Martinotti cells
Anti-BGAL	Abcam, ab9361	PAb	1:500	Chk	Y	X	B-GALACTOSIDASE+ cells

Table 7. Characteristics of the primary antibodies used in ISH-IHC, IHC and BGAL detection.

MAB, monoclonal antibody; PAb, polyclonal antibody; Dil., dilution; Rb, rabbit; Ms, mouse; Rt, rat; AR, antigen retrieval; Y, yes; N, no; RSNP, regular spiking non-pyramidal cells; BSNP, burst spiking non-pyramidal cells.

The following day brain slices were rinsed in PBS for 10 min three times. The tissue was incubated with secondary antibody in a 1 in 1000 dilution for 1 h at RT. The secondary antibodies targeted the host of the primary antibody and were conjugated with Alexa Fluor dyes (Thermo Fisher Scientific), as specified in **Table 8**. Then, slices were washed in PBS, incubated in DAPI for 10 min and washed in PBS again. Finally, slices were mounted onto microscope slides (VWR, 631-1560) using DAKO. Mounted slides were stored at 4 °C until imaging.

Primary antibody	Secondary antibodies used	Experiment
Anti-CUX1 rabbit	Anti-rabbit Alexa 647	ISH-IHC
	Anti-rabbit Alexa 555	IHC
Anti-CTIP2 rat	Anti-rat Alexa 488	ISH-IHC, IHC
Anti-SATB2 mouse	Anti-mouse Alexa 488	ISH-IHC, IHC
Anti-RORB rabbit	Anti-rabbit Alexa 647	ISH-IHC
	Anti-rabbit Alexa 555	IHC
Anti-TBR1 rabbit	Anti-rabbit Alexa 488	ISH-IHC, IHC
Anti-PV rabbit	Anti-rabbit Alexa 647	ISH-IHC
	Anti-rabbit Alexa 555	IHC
Anti-CB rabbit	Anti-rabbit Alexa 647	ISH-IHC
	Anti-rabbit Alexa 555	IHC
Anti-CR mouse	Anti-mouse Alexa 488	ISH-IHC, IHC
Anti-SST rat	Anti-rat Alexa 488	ISH-IHC, IHC
Anti-BGAL chicken	Anti-chicken Alexa 488	BGAL detection
	Anti-chicken Alexa 555	BGAL detection

Table 8. Secondary antibodies used for ISH-IHC, IHC and BGAL detection.

2.3.3.3 *In situ* hybridization combined with immunohistochemistry

To visualise *Pcdh19* mRNA and detect different molecular markers at the same time, experiments combining ISH with IHC were performed on P10 and P20 brain slices. Slides were treated as in **Sections 2.3.3.1.2 and 2.3.3.1.3**, but on the second day, an IHC step was performed. In brief, slides were washed in PBST 3 times for 5 min each. Then, the tissue was blocked in ISH blocking solution (10% DS and 0.1% TritonX-100 in PBS) for 20 min at RT. After blocking, brain slices were incubated in primary antibody for 1 h at RT; washed in PBST again and incubated in secondary antibody for 1 h at RT. Primary and secondary antibodies were used as stated in **Table 7** and **Table 8** respectively, using the same dilutions, except for parvalbumin (dilution 1:500). However, no AR was required for these samples. Finally, slides were washed in PBST again. After the antibody detection was completed, slides were equilibrated in TN buffer. The rest of the probe's detection followed as explained in **Section 2.3.3.1.3**, except for the absence of a TNB blocking step previous to the incubation of the anti-DIG-HRP. This exception is due to the fact that the slide had already been blocked with the ISH blocking used prior to the incubation of the primary antibody.

2.3.3.4 X-gal staining combined with IHC

First, the IHC against the molecular marker, as described in **section 2.3.3.2**, was performed, followed by the X-gal staining. In the staining, the sample was washed for 5 min in X-gal wash buffer [Na-phosphate buffer pH 7.3 0.1 M (0.071 M sodium phosphate dibasic and 0.029 M sodium phosphate monobasic in deionised water), MgCl₂ 2mM, 0.01% deoxycholate and 0.02% NP-40] and incubated overnight at 37°C in X-gal staining solution [5mM potassium hexacyanoferrate(II) trihydrate (Sigma-Aldrich P-9387), 5mM potassium hexacyanoferrate(III) (Sigma-Aldrich, P-8131) in X-gal wash buffer, plus 1% of X-gal 100 mg/mL in N-N-dimethyl formamide (Sigma-Aldrich, D4551)]. On the next day, the slide was washed in PBS, fixated with

4% PFA for 10 min, counterstained with DAPI for another 10, washed and mounted.

2.3.4 Confocal microscopy

Stained slides from **Section 2.3.3** and **2.5** were acquired with the low (10x), intermediate (20x) or high (63x) magnification objectives on the confocal laser scanning microscope (LSM 780, Carl Zeiss) together with the ZEN Black software (version 2.0, Carl Zeiss). Imaging settings are shown in **Table 9**.

Experiment	Dye	Laser (nm)	Filter (nm)	Colour bit depth (per pixel)	Scan speed	General characteristics
ISH+IHC	A647	633	638-755	8 (256 grey levels)	7 (1.58 μ sec/pixel)	<ul style="list-style-type: none"> - <u>Averaging line-by-line by mean method.</u> - <u>Averaging number: 4</u> - <u>Frame size: 1024x1024 pixels</u> - <u>Tile scans.</u> - <u>.tif and .lsm images</u> - <u>Scan direction: Bi-directional</u>
	Cy3	561	570-624			
	A488	488	499-553			
	DAPI	405	410-496			
IHC	A647	633	638-755	8 (256 grey levels)	7 (1.58 μ sec/pixel)	
	A555	561	566-697			
	A488	488	499-553			
	DAPI	405	410-496			
IUE	EGFP	488	490-597	12 (4096 grey levels)	5 (6.30 μ sec/pixel)	
	DAPI	405	410-496			

Table 9. Settings of the confocal microscope.

To analyse the images, ImageJ Fiji software (Schindelin et al. 2012) was used. Images were stitched using the “image stitching” (Preibisch et al. 2009) plug-in. Cells were counted manually using the “Cell Counter” plug-in. In cases where cell distribution was analysed, images were divided in bins using the ‘rectangular select’ tool.

2.4 ShRNA effectiveness test

To test if the shRNAs significantly reduced the PCDH19 protein level, a western blot analysis was performed. The analysis compared the relative levels of PCDH19-HA in HEK293T lysates co-transfected with each of the *Pcdh19* shRNAs and a Cytomegalovirus (CMV)-*Pcdh19*- Human influenza hemagglutinin (HA) plasmid respective to the relative quantity of protein in HEK293T lysates co-transfected with the CMV-*Pcdh19*-HA plasmid and an shRNA control.

2.4.1 ShRNA preparation

MISSION shRNAs against mouse *Pcdh19* and the TRC2 pLKO.5-puro non-target shRNA control were obtained from Sigma. ShRNA TRCN0000252392 (ShRNA#2), TRCN0000252393 (ShRNA#3), TRCN0000252395 (ShRNA#5) and TRCN0000252396 (ShRNA#6) bind to *Pcdh19* exon 1, as seen in **Figure 6**. ShRNA sequences are shown in **Table 10**.

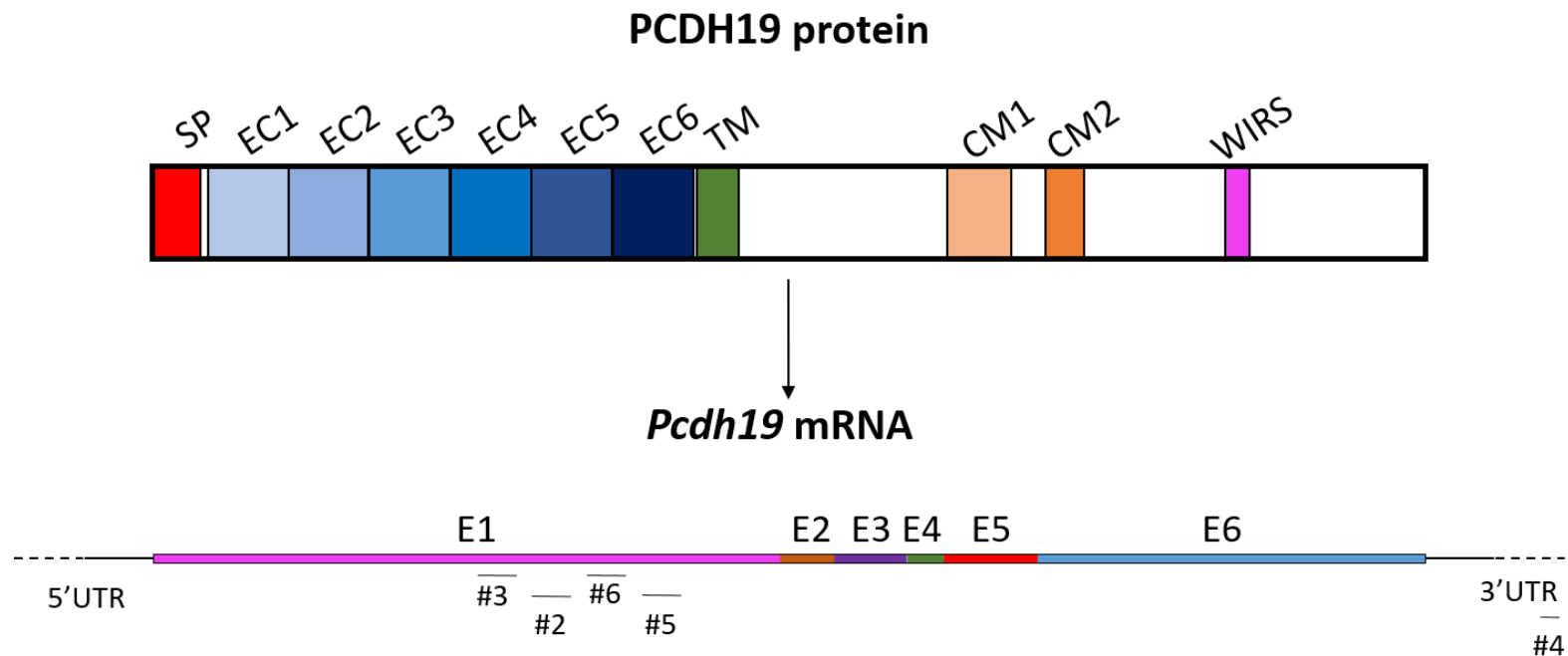


Figure 6. A schematic showing where the different *Pcdh19* shRNAs bind to the *Pcdh19* mRNA.

Pcdh19 mRNA is made up of 6 exons. ShRNA#2, shRNA#3, shRNA#5 and shRNA#6 bind to exon 1, which comprises the extracellular and transmembrane domain. ShRNA#4 binds to the 3'UTR. SP, signal peptide; EC, extracellular cadherin domain; TM, transmembrane domain; CM, conserved motive; WIRS, WRC interacting receptor sequence; E, exon; UTR, untranslated region; #2, ShRNA#2; #3, ShRNA#3; #4, ShRNA#4; #5, ShRNA#5; #6, ShRNA#6.

Pchd19 shRNA	Code name	Sequence
ShRNA control (ShC216)	ShRNA Ctr	5'-CCGGGCGCGATAGCGCTAATAATTTCTC GAGAAATTATTAGCGCTATCGCGCTTTTT-3'
TRCN0000252392	ShRNA #2	5'-CCGGGTAGTTAAGGCAGACGATTATCTCGA GATAATCGTCTGCCTTAACTACTTTTTG-3'
TRCN0000252393	ShRNA #3	5'-CCGGTCAACCTCCTGTCGGTCAATACTCGAG TATTGACCGACAGGAGGTTGATTTTTG-3'
TRCN0000252395	ShRNA #5	5'-CCGGTTCTGCCCTTGTCCTAATACTCGAG TATATTAGGACAAGGGCAGAATTTTTG-3'
TRCN0000252396	ShRNA #6	5'-CCGGGACCGAGGTTTCTTCGAAATACTCGAG TATTTCGAAGAAACCTCGGTCTTTTTG-3'

Table 10. ShRNA sequences.

The *Pcdh19* shRNAs came inserted in a TRC2-pLKO-puro vector harboured in a bacterial glycerol stock. 5 μ L of each shRNA stock was cultured in 500 μ L of LB at 37 °C at 300 rpm for 30 min in an incubator shaker and three-way streaked onto LB-Ampicillin (Amp; Sigma-Aldrich, A9518) plates. Plates were incubated overnight at 37 °C in an incubator (INCU-Line, VWR). 2 colonies from each shRNA were selected and a miniprep (**Section 2.3.3.1.1**) was performed. One miniprep was sent for sequencing using the primers seen in **Table 11**. Confirmed plasmids were retransformed for maxiprep (**Section 2.3.3.1.1**). To retransform the plasmid with ampicillin resistance, the miniprep was inoculated into 25 μ L of DH5 α cloning cells (Thermo Fisher Scientific, 18265-017) and left on ice for 10 min. Then the cloning product was heat-shocked at 42 °C for 30 sec and put on ice 2 min. Finally, 20 μ L of the bacterial plasmid were streaked on an Amp-agar plate and incubated at 37 °C in an incubator overnight. After performing the maxiprep, the construct's DNA was quantified and stored at -20 °C until transfection. A non-targeting shRNA was used as a control.

Primer	ShRNA	Sequence
TRC-F	ShRNA #3; shRNA #5	5'-CAAGGCTGTTAGAGAGATAATTGGA-3'
PLKOseq-R	ShRNA #2; shRNA #6	5'-AAACCCAGGGCTG CCTTGAAAAG-3'

Table 11. Primers for shRNA sequencing confirmation.

2.4.2 HEK293T cell culture

Human Embryonic Kidney cells experiment 293 transformed with large T antigen (HEK293T) cells were kindly provided by Dr Xinsheng Nan (Cardiff University). Cells were cultured in 10 cm² Nunclon Delta Surface Petri dishes (Fisher Scientific, 150350) until they reached confluency. To make the cells adhere to the surface, the dishes were coated with poly-lysine (Sigma, P2636) at a concentration of 0.5 mg/mL. Plates were incubated at 37 °C for 24 h in 7% CO₂ in Heracell 150i CO₂ Incubator (Thermo Fisher Scientific). The next day, the plates were emptied of poly-lysine, washed twice with Milli-Q water and dried for 5-10 min.

HEK293T cells were cultured in poly-lysine coated plates filled with 10 mL of Dulbecco's modified eagle media (DMEM; Gibco, 21969-035) based medium in a CO₂ incubator at 37 °C in 7% CO₂. This media contained 10% foetal bovine serum (FBS; Biosera, FB-1001/500-12251), 1% Glutamax (Gibco, 35050-038), 10% Penicillin/Streptomycin and 10% Non-Essential Amino acids (NEAA; Gibco, 11140-035) in DMEM. When cells reached 80% confluency (every 48 h approximately), a passaging of the cells was performed. In detail, the media was aspirated from the plate and rinsed in 10 mL of PBS. Cells were detached from the surface by incubating the plates in 1 mL of 0.25% trypsin (GIBCO, 25200056) for 2 min at 37 °C in the cell CO₂ incubator. 4 mL of the medium was then added to the dish to stop the trypsinization, and cells were collected into a 15 mL Falcon tube. Cells were centrifuged for 1 min 30 sec at 1500 rpm and the supernatant was aspirated, leaving the cell pellet at the bottom. Cells were then resuspended in 1 mL of fresh medium and 100 µL of the resuspension (1:10 split ratio) was added into a new plate with 10 mL of modified DMEM in it.

Some cells were stored frozen at liquid nitrogen as a back-up in case any contamination in the cultured cells occurred. To freeze the cells, the HEK293T cells were trypsinised for 2 min at 37 °C and centrifuged for 1 min 30 sec at 1500 rpm. The pellet was resuspended in 1mL of medium with 10%

of Dimethyl sulfoxide (DMSO; Sigma-Aldrich, D8418) in cryogenic vials (Starlab, E3110-6121). The tubes were frozen to -80 °C in a Mr Frosty freezing container (Thermo Fisher Scientific, 5100-0001) for 24-48 h and finally stored in liquid nitrogen until use. When these frozen cells had to be cultured, they were taken out from the liquid nitrogen and thawed at 37 °C in a water bath. Before the DMSO thawed, cells were pipetted and resuspended in 9 mL of DMEM medium. Cells were then placed in the CO₂ incubator at 37 °C to culture.

2.4.3 Plasmid construction

CMV-*Pcdh19*-HA plasmid and CMV-*Pcdh19*-myc were generated in the lab (section 4.3.1). A PCR, using 10 ng of a doublecortin (DCX)-*Protocadherin19* full-length (*Pcdh19*FL) template provided by Dr Isabel Martínez Garay (Cardiff University) and the Phusion® High-Fidelity DNA Polymerase, was performed. Primer sequences and PCR protocols are shown in **Table 12**. The PCR product was detected using an electrophoretic gel, extracted with the QIAquick gel extraction kit (QIAGEN, 28704) and purified. After that, the PCR product and the CMV-HA vector (provided by Dr Isabel Martínez Garay, Cardiff University) were digested for 4 h at 37 °C, gel electrophoresed, extracted and purified too. Then both products were ligated with a T4 DNA ligase (New England-Biolabs, M0202), transformed into DH5α cells and extracted with a miniprep kit. Identification of the colonies containing the correct product were conducted by digestion and analysis of the bands detected in an electrophoretic gel. The confirmation was done by sequencing. One miniprep containing the correct tagged construct was retransformed and extracted using a maxiprep kit to amplify the quantity of DNA. The maxiprep was used for the transfection.

Ligation components	Primer sequences	PCR protocol
<i>Pcdh19</i> insert	<p>Pcdh19-F-HindIII: 5'-GATCAAGCTTCCGCGCAGCCATGGAGTCTCTCC-3'</p> <p>Pcdh19-R2: 5'-GAGAACGATATCCTTCAGACGCTTC-3'</p>	<p>- 98 °C 30".</p> <p>- 30 cycles:</p> <ul style="list-style-type: none"> • 98 °C 10". • 72 °C 2'. - 72 °C 5'.
<p>CMV-<i>Pcdh19</i>-HA</p> <p>CMV-<i>Pcdh19</i>-myc</p>	<p>CMV forward: 5'-CGCAAATGGGCGGTAGGCGTG-3'</p> <p>Seq F: 5'-TGGTGTGCAGACCTACGAGC-3'</p> <p>Seq F2: 5'-CGACTGCAGGAGTATGAGAG-3'</p> <p>Seq F3: 5'-GAAGTCAGAACCACTCGTAC-3'</p> <p>Test F: 5'-CAGAATACCCGTAACACCACTGC-3'</p> <p>SV40 pA-R: 5'-GAAATTTGTGATGCTATTGC-3'</p>	-----

Table 12. PCR primers and protocol for CMV-*Pcdh19*-HA vector generation.

2.4.4 Plasmid transfection

Plasmids generated in **section 2.4.3** were transfected into HEK293T cells and detected by western blot. CMV-*Pcdh19*-HA detection was clearer and consequently was the vector used for the subsequent experiments.

To test the efficiency of the *Pcdh19* shRNAs, HEK293T cells were either transfected with the CMV-*Pcdh19*-HA plasmid or co-transfected with the plasmid and one of the shRNAs: control, #2, #3, #5 or #6.

One day before transfection, one million HEK293T cells were passaged and resuspended into 2 mL of DMEM with no modifications. The cell suspension was plated onto 6-well plates (Thermo Fisher Scientific, 140675), coated with 2mL of poly-lysine per well, and co-transfected on the following day.

For each transfection, either 1 μ g of the *Pcdh19* plasmid or 1 μ g of the plasmid and 7 μ g of the shRNAs were added to 250 μ L of Opti-MEM (Gibco, 31985-047) and mixed gently. In another tube, 8 μ L of Lipofectamine 2000 (Invitrogen, 11668-027) was added in 250 μ L of Opti-MEM and incubated for 5 mins at RT. After the incubation, the DNA and Lipofectamine were combined by adding the Lipofectamine to the DNA tube, gently mixing and incubating for 20 mins at RT. The complex was added to the well that contained the cells and mixed gently by rocking the plate back and forth. Transfected cells were incubated at 37°C in 7% CO₂ in a CO₂ incubator for 24, 48 or 72-h until lysis. Three independent transfections were performed for each condition and each timeslot.

Transfections using calcium phosphate as the reagent were also conducted but Lipofectamine 2000 showed a better transfection ratio, so it was selected as the reagent. To transfect using calcium phosphate, the plasmids are diluted in 250 μ L of 250 mM of CaCl₂ (Sigma-Aldrich, C1016). On another tube, 250 μ L of HeBS (50 mM of HEPES, 140 mM NaCl, 1.5 mM of Na₂HPO₄ diluted in water) at pH=7.04, 7.05 or 7.06 were added. Both tubes were

heated up and then the plasmids were added to the HeBS, mixed and incubated for a minute at 37°C. The complex was then added to the cells, incubated for 8 hours and then the media was changed.

2.4.5 Cell lysis

Cells were lysed 24-, 48- and 72-h post-transfection. Wells were washed twice in PBS and lysed in 100 µL of radioimmunoprecipitation assay buffer (RIPA) lysis buffer [50 mM of Tris base, 150 mM of NaCl, 1 mM of EDTA, 1% of Triton X-100 and 0.2% of sodium deoxycholate (Sigma-Aldrich, D6750), 10 % protease inhibitor cocktail (Sigma-Aldrich, P8340) and 10 % phosphatase inhibitor cocktail (Sigma-Aldrich, P0044) in deionised water] pH =7.4. Cells were scraped from the wells using pipette tips and the supernatant was transferred into an Eppendorf tube. The tubes were then placed on ice. Cells were resuspended with a 1 mL pipette, vortexed and sonicated. Sonication was performed at 50% amplitude for 10 sec twice with an ultrasonic processor (Sonic). After sonication, cells were vortexed, resuspended and centrifuged at 15000 rpm for 10 min at 4 °C. The supernatant was then collected into new Eppendorf tubes, split into 2 aliquots of 30 µL each approximately and an aliquot of 15 µL that was used for the BCA quantification.

2.4.6 BCA assay

To perform the western blot analysis, the quantity of the samples run had to be equal. The protein concentration of the lysates obtained in **Section 2.4.5** was measured using the Pierce™ BCA Protein assay kit (Thermo Fisher Scientific, 23225). Tubes containing different dilutions of BSA in water were prepared to use as a standard curve as shown in **Table 13**. Cell lysates were diluted 1 in 50 and 1 in 100 in Milli-Q water. 100 µL of the bicinchoninic acid (BCA) reagent was added into the 96-well clear polystyrene microplate (Sigma-Aldrich, CLS-3370). Then 100 µL of the standard was added into the wells, followed by 100 µL of the diluted samples. Standard and samples were measured in triplicates.

Tube	H ₂ O (μL)	BSA (2mg/mL)
A	1800	200 μL
B	496	1504 μL from tube A
C	666	1334 μL from tube B
D	496	1504 μL from tube C
E	666	1334 μL from tube D
F	400	400 μL from tube E
G	400	400 μL from tube F
H	400	400 μL from tube G
I	400	0

Table 13. BSA dilutions to use in the standard curve.

Plates were then incubated at 37 °C for 2 h in an incubator until the samples acquired a purple colour. Absorbance at 562 nm was analysed in a microplate reader (FLUOstar® Omega Microplate Reader, BMG Labtech). The data obtained were exported and analysed on Microsoft Office Excel. Since the program quantified the concentration of protein in the well, protein quantity in the sample was obtained using the formula: [protein in sample] = [protein in well (µg/mL)]x volume in well (0.2 mL)/(1000 µL x dilution).

2.4.7 Western blot

After the concentrations of the lysates were measured by the BCA assay (Section 2.4.6), a western blot analysis was performed.

20 µg of the lysate was mixed with lithium dodecyl sulphate (LDS) buffer [1 M Glycerol (Sigma-Aldrich, G9012), 140 mM Tris Base, 106 mM Tris HCl (Sigma-Aldrich, T3253), 0.5 mM EDTA, 0.22 mM Brilliant Blue G-250 (Sigma-Aldrich, B0770), 0.175 mM Phenol Red (Sigma-Aldrich, 114529), 74 mM LDS (Sigma-Aldrich, L4632), pH 8.] buffer and 10% 0.5 M DTT. To avoid distortion of the data, each lane of the gel was loaded with equal volumes of sample. Samples with a higher concentration of protein required to add less volume to the mixture than samples with a lower concentration, making the total volume of the mixtures unequal. To solve this issue, RIPA buffer was added to the loading mixtures with lower volumes. The mixture was heated for 5 min at 70°C, vortexed and centrifuged. Then, samples were loaded in a NuPAGE™ Novex™ 4-12% Bis-Tris gel (Novex Life Technologies, WC1020) alongside a Novex Sharp Pre-stained ladder (Invitrogen, LC5800) and run at 120 V for 1 h 45 min using a high current power supply (Power PAC HC, Biorad). Electrophoresis gels were immersed in 2-(N-morpholino) ethanesulfonic acid (MES) running buffer pH =7.3. All buffer preparations are detailed in **Table 14**. Afterwards, samples were passed to a membrane using a wet transfer technique. Run samples were transferred onto a nitrocellulose membrane with a 0.2 µm

pore size (GE Healthcare Life Sciences, 10600001) by applying 120 V for 90 min at 4 °C in an electrophoresis system (Xcell SureLock, Thermo Fisher Scientific). Gels were extracted from the electrophoresis chamber and encased in a transferring cassette. In the cassette, components were put in the following order: sponge, filter paper (Thermo Fisher Scientific, 88620), gel, membrane, filter paper and sponge. The cassette was placed in a transfer chamber filled with transfer buffer (NuPAGE dissolved in 10% isopropanol). Once the transfer was completed, the membrane was taken out and cut horizontally at approximately 55 kilodaltons (kDa), to detect the glyceraldehyde-3-phosphate dehydrogenase (GAPDH) loading control. Subsequently, both parts were placed in a dark box and stained with 1 mL of Ponceau to detect protein level. After staining, Ponceau was rinsed with Tris-buffered saline-Tween-20 (TBST; TBS plus 0.1% Tween-20) three times for 10 min each. Then, each piece was incubated with blocking buffer for 1 hour at RT, and with a primary antibody (**Table 15**) diluted in the same blocking reagent at 4 °C overnight. The next day, each piece was washed with TBST three times for 10 min each. Following the washes, an incubation of secondary antibodies (**Table 16**) in a 1 in 20000 dilution for 1 hour at RT was performed. Another three washes of TBST for 10 min were performed. For the development of the membrane, the Western Blotting Luminol Reagent kit (Santa Cruz Biotechnology, sc-2048) was used. If the previous kit was not sensitive enough and bands couldn't be detected or were very faint, the LumiGLO® Reserve Chemiluminescent Substrate kit (Seracare, 5430-0049), with a substrate that gives a stronger signal, was used. If the development was performed using the latter kit, two 20 min incubations with imidazole buffered saline with Tween-20, that is included in the kit, were done. One mL of the developing kit substrate was added to the membrane. After a 1 min incubation, the substrate was removed, and the signal was detected using a Medical Film Processor (Konica, SRX-101A).

Buffer	Components	Final concentration	Manufacturer
MES buffer	MES	0.05 M	Sigma-Aldrich
	Tris base	0.05 M	Sigma-Aldrich
	SDS	0.1%	Sigma-Aldrich
	EDTA	1 mM	Sigma-Aldrich
NuPAGE buffer	Bicine	25 mM	Sigma-Aldrich
	Bis-Tris	25 mM	Sigma-Aldrich
	EDTA	1 mM	Sigma-Aldrich
Ponceau buffer	Ponceau	2%	Sigma-Aldrich
	Sulfosalicylic acid	30%	Sigma-Aldrich
	Trichloroacetic acid	30%	Sigma-Aldrich
TBS buffer	Tris base	24.7 mM	Sigma-Aldrich
	NaCl	0.137 M	Sigma-Aldrich
	KCl	2.6 mM	Sigma-Aldrich
Blocking Buffer	ECL Prime blocking reagent	3%	GE Healthcare
	BSA	3%	Sigma-Aldrich
	TBS	94%	X

Table 14. Western blot buffers.

MES, 2-(N-morpholino) ethanesulfonic acid; SDS, Sodium Dodecyl Sulfate; EDTA, Ethylenediaminetetraacetic acid; TBS, Tris-buffered saline; ECL, enhanced chemiluminescence; BSA, bovine serum albumin

Primary antibody	Manufacturer	MAb/PAb	Dil.	Host
Anti-HA	Roche, 12013819001	MAb	1:2000	Rt
Anti-myc	Santa Cruz Biotechnology, sc-788	PAb	1:500	Rb
Anti-GAPDH	Abcam, ab8245	MAb	1:1000	Chk

Table 15. Primary antibodies used in western blots.

MAb, monoclonal antibody; PAb, polyclonal antibody; Dil., dilution; Rt, rat; Chk, chicken

Primary antibody	Secondary antibody used
Anti-HA rat	Anti-rat HRP
Anti-myc rabbit	Anti-rabbit HRP
Anti-GAPDH chicken	Anti-chicken HRP

Table 16. Secondary antibodies used in western blots.

Western blot data were quantified by densitometric analysis, using the Fiji Image J Analysis Software (Schindelin et al. 2012). In brief, the different lanes were selected with the 'rectangular select' tool. Using ImageJ gel analysis function and plot lanes, a profile plot of each lane was drawn. The profile plot represents the relative density of the bands over each lane. Each peak was closed with a straight line to allow quantification. The area under the curve (AUC) for each peak was calculated using the wand tool. This value was used to compare the relative quantity of protein respective to the control. To do that, the AUC of each sample was divided by the AUC of the internal control that was in the same lane as the sample. Finally, to analyse the changes of the sample relative to the control, the values of each sample were divided by the values obtained from the sample containing the shRNA control.

2.5 *In utero* electroporation

To analyse *Pcdh19* role in cortical migration, two different types of experiments were conducted. In the first, WT and *Pcdh19*-KO animals were *in utero* electroporated at two different ages with short hairpin ribonucleic acids (shRNAs) against *Pcdh19* and a pCIG plasmid. The pCIG plasmid contains a chicken beta actin promoter (CBA), an internal ribosomal entry site (IRES) and the enhanced green fluorescent protein (EGFP) (pCIG) plasmid that acted as a reporter to determine if knock-down of the protein alters cortical migration. In the second experiment; WT, *Pcdh19*-HET and *Pcdh19*-KO animals were *in utero* electroporated with a pCIG plasmid to detect if cortical migration was affected in the mutant animals compared to the WT controls.

In the first type, WT embryos were *in utero* electroporated with each shRNA individually at 1 $\mu\text{g}/\mu\text{L}$ together with 0.5 $\mu\text{g}/\mu\text{L}$ of pCIG plasmid that acted as a reporter. *Pcdh19*-KO embryos were *in utero* electroporated with a mixture of shRNA #3, #5, #6 at a 0.33 $\mu\text{g}/\mu\text{L}$ concentration for each shRNA,

together with the pCIG plasmid. After injection of the plasmids, 5 pulses of 35 V and 50 milliseconds were applied with paddle-type electrodes.

At E15.5, a mixture of shRNA #3, #5, #6 was electroporated into the embryos at a 0.33 $\mu\text{g}/\mu\text{L}$ concentration for each shRNA, together with the pCIG plasmid. After injection of the plasmids, 5 pulses of 45 V and 70 milliseconds were applied.

WT, *Pcdh19*-HET and *Pcdh19*-KO mice were *in utero* electroporated at E13.5 and E15.5 with 2 μg of the pCIG plasmid to mark the migrating cells at those time points. At E13.5, 5 pulses of 38 V and 50 milliseconds were applied after injection of the plasmid. At E15.5, 5 pulses were applied, at 45 V during 70 milliseconds per pulse.

All of the *in utero* electroporations were performed by Dr Isabel Martínez Garay (Cardiff University).

After electroporation, animals were health checked twice a day for at least three days and daily until culled, as mentioned in **Section 2.1.1**. Electroporated brains were extracted, fixed and cut as detailed in **Sections 2.3.1 and 2.3.2**. Brains were then counterstained with DAPI at a 1 in 4000 dilution for 10 min. Stained brains were imaged as shown in **Section 2.3.4** and analysed with ImageJ Fiji software (Schindelin et al. 2012).

2.6 Behaviour

Several behavioural tests were performed on experimental mice WT, HET and KO at P21 and P60 ages. WT animals were also subdivided into two groups: WT animals from pure WT litters, and WT animals from litters that also contained mutant pups. The latter subgroup was designated as WT MGH or WT from mixed genotyped housing to distinguish it from the WT animals from WT only litters, that were named SGH (Single genotype housing). The behavioural analysis consisted of four behavioural techniques: open field (**Section 2.6.1**), elevated plus maze (**Section 2.6.2**),

social interaction (**Section 2.6.3**), and 24-hour activity (**Section 2.6.4**). The equipment necessary to perform the experiments for the first three techniques was kindly provided by Dr Stéphane Badouin (Cardiff University). For 24-hour activity, the equipment from Professor Riccardo Brambilla (Cardiff University) was used, who kindly provided it. The number of mice used for each experiment is shown in **Table 17**. Mice were taken to the behavioural room 30 min prior to the behavioural analysis to habituate to the new environment. A maximum of one behavioural technique per day was conducted. Mice were handled with open hands to avoid raising stress levels. All experimental equipment was cleaned with ethanol between the testing of each individual and after use. All behaviour was recorded with a camera and analysed using the EthoVision XT software (Noldus) or the MED-PC® IV software suit (Med associates; 24-hour activity only). The experimenter was blind to the genotype of the animals during the behavioural tests in all experiments and during the scoring of the video in the social interaction analysis.

2.6.1 Open field

Open field behavioural analysis was performed on two consecutive days, using the first day to habituate the mice to the new environment. Mice were placed in an open field arena (40 cm x 40 cm) and were allowed to roam freely for 20 min in the dark. Infrared illumination (Tracksys) was located at the bottom of the arena. That illumination allowed the recording of the mouse spontaneous locomotion, using a computer-linked video camera (The Imaging Source) located above the arena. The mouse locomotion and trajectory travelled was tracked and quantified using the EthoVision XT software. The data analysed with the programme was total distance run, distance run in four slots of 5 min each and distance run by the mouse in the centre of the arena with respect to the distance run in the arena. Any distance 5 cm or further from the wall of the arena was defined as centre by the programme.

2.6.2 Elevated plus maze

The elevated plus maze has 4 arms (40 cm x 7 cm): two open arms (1 cm high) and two closed arms (16 cm high) and a centre (6 cm x 6 cm). Each mouse was deposited in one of the closed arms of the elevated plus maze and left to explore freely for 5 min in a well-lit room. The behaviour was recorded using a computer-linked video camera (The Imaging Source) located above the maze. EthoVision XT, Noldus automatically defined the different arms of the arena (open or closed) and analysed the time in sec the mouse spent in each of the open arms (centre not included). The total time the mice spent in both open arms was taken as the activity in the open arm.

2.6.3 Social interaction

At P21, WT, *Pcdh19*-HET and *Pcdh19*-KO pups were habituated to the arena (20 cm x 40 cm) for 3 min. After the habituation, WT females in oestrous, unfamiliar to the pups, were added to the cage and both mice were allowed to roam around and interact with each other with no restrictions for another 3 min. This experiment was performed in a well-lit room. The interaction between the pups and the females was recorded using a computer-linked video camera (The Imaging Source) located above the arena.

To determine whose females are in oestrus, around 10 WT females over P60 were taken to the behavioural room. Females were restrained with a scruff and 10 μ L of saline were mixed with vaginal fluids using a pipette tip. The mixture was smeared into a porta. After 30 min, porta slides were fixed for 3 min, stained with Giemsa solution (Polysciences inc., 24985) (Caligioni 2009) for 3 min and washed with water. Samples of females in oestrus presented big purple cell bodies.

At P60, WT and *Pcdh19*-HET females were tested for social interaction in the same settings used to conduct social interactions in the pups, with the difference that in this experiment the unknown WT females weren't required to be in oestrus.

Videos were analysed manually, and the time in sec the animals spent interacting during the 3 min was counted. Social interaction was scored when both mice were within 2 cm of each other, not including tail-tail interactions.

2.6.4 24-hour activity

P60 experimental mice were put in Perspex boxes (40cm x 24cm x 18cm) and recorded for 24 h. The cages were put into a structure that contained three infrared beams that traversed each cage at the bottom. Mice were let roam free for 24 h and *ad libitum* access to food and water. A lamp was left on, connected with a timer that turned off the lights at 6 am and turned on at 6 pm to maintain the mice on a 12 h light/dark cycle. Data were analysed using the MED-PC® IV software suit and extracted using the MPC2XL programme. Data analysed was the number of beams breaks by the mice in 24 h, in 1-hour slots; total number of beam breaks during light hours and total number of beam breaks during dark hours.

Age	Condition	Open field	EPM	Social interaction	24-H activity
P21	WT SGH M	19	19	19	---
	WT MGH M	11	11	11	---
	WT SGH F	18	18	18	---
	WT MGH F	13	13	13	---
	HET MGH F	12	12	12	---
	KO MGH M	14	14	14	---
P60	WT SGH M	17	17	---	17
	WT MGH M	11	11	---	10
	WT SGH F	18	18	18	18
	WT MGH F	13	13	13	13
	HET MGH F	12	12	12	12
	KO MGH M	13	13	---	13

Table 17. Number of mice used in behavioural tests.

WT: Wild-type; M: Male; F: Female; HET: Heterozygous; KO: Knock-out; SGH, single genotype housing; MGH, mixed genotype housing; EPM: Elevated plus maze; ---, experiment not performed. Animals from the same litter were treated as independent biological replicates.

2.7 Statistical analysis

Statistical analysis was performed using the IBM SPSS Statistics® 25 software. Normality was tested using the Shapiro-Wilk test. If this test was not significant ($p \geq 0.05$), ANOVA was considered for the analysis. If ANOVA tested as significant ($p \leq 0.05$), a Levene's test of equality of error variances was performed to test the homogeneity of variance. If equal variances were assumed ($p \geq 0.05$), a post-hoc Bonferroni correction for multiple comparisons followed. If equal variance was not assumed, a Games-Howell was performed. If the data were non-parametric, a Kruskal-Wallis test was considered. Kruskal-Wallis pair-wise comparisons were performed as a post-hoc if the Kruskal-Wallis showed significance.

For the open field behavioural test (**Section 2.6.1**), differences within the conditions between day 1 and day 2 were analysed by adding an EMMEANS subcommand on the SPSS syntax.

All statistical data were presented as mean \pm SEM.

Chapter 3: Characterization of Protocadherin 19 expressing neurons in the developing cortex.

3.1 Introduction

As previously mentioned in **section 1.4**, Protocadherin 19 is expressed early in development in neural tissues. *Pcdh19* mRNA is also expressed in a variety of non-neural tissues in the developing mouse embryo, such as kidney, dermomyotome, dorsal and urogenital mesenteries, forestomach, pancreas, duodenum and hair follicle, but its expression is most prominent in the central nervous system (CNS) (Gaitan et al. 2006). *Pcdh19* is present in the spinal cord and several regions of the brain, including the presomitic mesoderm at E9.5, and dorsal cortex, lateral ganglionic eminence, retina, nasal cavity and prepituitary gland by E12.5 (Gaitan et al. 2006). At E15.5, *Pcdh19* is located forming discrete clusters in the thalamus, hypothalamus, cortex, ganglionic eminence and olfactory bulbs and at P2 expression can be found in the cortex, thalamus and also in the CA1 and CA3 regions of the hippocampus (Dibbens et al. 2008). Both cortex and hippocampus are areas of the brain that participate in the cognitive process, and malfunctions of these regions can lead to epilepsy (Chatzikonstantinou 2014). The fact that EIEE9 patients present epileptic episodes accompanied frequently by intellectual disabilities with an early onset (Duszyc et al. 2014), together with the presence of cortical malformations in patients with the disease (Ryan et al. 1997; Kurian et al. 2018; Pederick et al. 2018), strongly suggest the participation of PCDH19 in cortical development and present the cortex as a main region to study in the search of a role for this protocadherin. Analyses so far have focused on laminar position at certain ages and have been conducted exclusively in a qualitative way. Therefore, despite the data about mouse *Pcdh19* expression from the Allen Brain Atlas, and the reports of Dibbens *et al.* and Pederick *et al.* that locate *Pcdh19* expression in layers

II/III and V (Dibbens et al. 2008; Pederick et al. 2016), no thorough characterisation of the neuronal types expressing *Pcdh19* in late embryonic and early postnatal mice in the cortex has been performed.

There are 3 main types of glutamatergic projection neurons in the cortex according to their axonal projections: associative, commissural and corticofugal. Within the corticofugal neurons, a main distinction is made between corticothalamic and subcerebral projection neurons (Molyneaux et al. 2007). Several markers have been discovered that allow identification of these different types of neurons: SATB2 labels subgroups of cells that project corticocortically through the corpus callosum (Alcamo et al. 2008; Britanova et al. 2008; Jabaudon 2017), CTIP2 positive cells in layer V have been identified as corticospinal neurons (Arlotta et al. 2005) and corticothalamic neurons are CTIP2 and TBR1 double positive cells located in layer VI (Arlotta et al. 2005; Molyneaux et al. 2007; Jabaudon 2017). RORB is characteristic of the layer IV neurons of caudal regions of the cortex (Nakagawa et al. 2003) and TBR1 is expressed by cells located in layer VI and is also expressed postmitotically in layers II/III (Hevner et al. 2001; Molyneaux et al. 2007). Because of their restriction to particular layers, these molecular markers can also be used to define layer boundaries in an accurate way.

Non-pyramidal GABAergic neurons are mainly generated in the ganglionic eminences in the mouse and migrate tangentially to reach the cortex between E9.5 and postnatal stages (Faux et al. 2012). *Pcdh19* is expressed in the ganglionic eminences of the mouse around that period (E12.5) (Gaitan et al. 2006), thus the interest in studying the interneuronal population, too. Almost all cortical interneurons in the mouse cortex can be detected with a combination of three molecular markers: PV, SST and 5HT3aR (Rudy et al. 2011). PV is expressed in fast-spiking interneurons (Wamsley et al. 2017). SST labels burst spiking nonpyramidal Martinotti cells and non-Martinotti (X94) cells with a similar firing pattern as the PV+ (Uematsu et al. 2008; Ma

et al. 2006), and 5HT3aR is composed by a very heterogenous group with varied electrophysiology and morphology (Rudy et al. 2011). However, there is a great diversity of interneurons and other markers are routinely used to identify particular subpopulations, such as CB and CR. CB-positive interneurons comprise several groups of regular spiking non-pyramidal cells (RSNP) or burst spiking non-pyramidal cells (BSNP) cells of diverse morphology, irregular spiking (IS) cells (only when co-expressed with SST) or fast-spiking interneurons (mostly PV positive) (Cauli et al. 1997; Markram et al. 2004; Flames et al. 2005). This marker is expressed in a significant number of pyramidal cells in layer II-III, too (DeFelipe 1997). CR is formed by a group of BSNP/IS bipolar cells; or RSNP multipolar cells (Barinka et al. 2010). Together, PV, CB and CR positive cells comprise about 80% of cortical interneurons in rodents (Gabbott et al. 1997).

Together, these neuronal markers can distinguish several subsets of cells that project to different locations of the CNS, are electrophysiologically diverse and have a restricted expression to certain layers. When combined with the detection of *Pcdh19*, it contributes to the expansion of the knowledge about the cell-specific expression of PCDH19, possibly giving insight into the role of the protein in cortical development.

3.2 Aims

The aim of this chapter was to determine the spatio-temporal pattern of expression of *Pcdh19* in late embryonic (E16.5) and early postnatal (P2, P6, P10, P15, P20) mice, and to characterise the *Pcdh19* positive cellular population by combining the detection of *Pcdh19* mRNA with immunohistochemistry against several cortical glutamatergic markers (SATB2, RORB, CTIP2 and TBR1) at P10, and several interneuronal markers (PV and CB) at P20.

3.3 Results

3.3.1 No antibodies could be optimised to detect PCDH19 by immunohistochemistry

To characterise PCDH19 expressing cells, the initial idea was to perform immunohistochemistry using antibodies against PCDH19 and several cortical molecular markers at different ages, since no thorough characterisation of cell- and region-specific protein expression had been reported in mammalian tissue so far, and all studies had been using ISH to detect *Pcdh19* mRNA.

Several optimization attempts with a rabbit polyclonal anti-PCDH19 antibody using P10 mouse brains were conducted. Unfortunately, even though this antibody was eventually optimised for western blot, all attempts to use it for immunohistochemistry on postnatal brain slices failed (**Figure A. 1** in Appendix).

Given these difficulties and a report describing commercial anti-PCDH19 antibodies to be incompatible for IHC (Pederick et al. 2016), a different strategy to characterise PCDH19⁺ cells was considered that would take advantage of the *Pcdh19*-KO mouse model. In this model from Taconic, the first three exons of *Pcdh19* have been replaced by a β -Geo cassette that contains the *β -galactosidase* gene (Pederick et al. 2016), allowing detection of BGAL as a proxy for PCDH19 expression.

However, for this strategy to work, the *Pcdh19*-KO should not have any alterations in its cortical lamination process. If any subset of cells that are expressing the molecular markers analysed are ectopically located or vary in number when *Pcdh19* is depleted, the cell characterisation of *Pcdh19*-expressing cells via the immunohistochemical characterisation of the cells positive for BGAL would be inaccurate.

This model, though, was validated by Pederick *et al.* and did not show any observable differences in the location of the β -Geo positive cells in the *Pcdh19*-KO animals with respect to the *Pcdh19* mRNA expressing cells in the WT counterparts (Pederick et al. 2016). In addition, quantitative analysis of number and distribution of cells positive for different cortical markers confirmed the lack of any major differences between *Pcdh19* WT and KO cortices (described in Chapter 5).

The immunohistochemical experiments were conducted using an anti-BGAL antibody that had been previously used in the lab by Dr. Jessica Griffiths (Cardiff University) to study PCDH19 mosaicism in *Pcdh19*-HET cortices at E11.5 (Abcam, ab9361). P2 cortices were chosen to test the antibody, as *Pcdh19* mRNA expression is highly detected at this age. Unfortunately, the antibody didn't detect BGAL at P2 clearly enough to allow characterisation of the cells, since the dotted fluorescent signal made it impossible to accurately assign the BGAL staining to a concrete cell, as observed in **Figure 7**.

Since detection of BGAL expression by IHC in postnatal brains had failed, direct X-gal staining combined with immunohistochemistry was attempted to detect the activity of the enzyme. X-gal (5-bromo-4-chloro-3-indolyl- β -D-galactopyranoside) is a colourless compound that gets hydrolysed by BGAL and forms an insoluble blue precipitate when in contact with oxygen, therefore detecting BGAL activity. To avoid inactivation of the enzyme due to excessive crosslinking during fixation, brains were perfused with 1% PFA and post-fixed for only 2 hours at 4°C. IHC against the molecular marker, as described in **section 2.3.3.2**, was performed at P2 (not shown) and P10 (**Figure 8**), followed by the X-gal staining, as explained in **section 2.3.3.4**. Although BGAL activity matched the expected location of *Pcdh19* mRNA within the cortical layers, the dotted, cytoplasmic nature of the precipitate again precluded the identification of individual cells when the staining was combined with IHC (**Figure 8**).

Given the difficulties with available commercial antibodies, it was decided to commission a company to generate monoclonal antibodies against PCDH19. The chosen company was Icosagen, as it uses a relatively new technology, HybriFree, which is robust and quick (Kivi et al. 2016). In total, two rabbit polyclonal antibodies (poly 41 and poly 42) and four human monoclonal antibodies (1A5, 1A8, 1F4 and 2G2) were created. By the time those antibodies were received, the commercial antibody had been optimised for embryonic stages by Dr. Jessica Griffiths (Cardiff university), and a combination of PCDH19 and BGAL immunostaining in *Pcdh19*-HET animals gave a non-overlapping columnar pattern of PCDH19+ and BGAL+ cells at E11.5, providing a positive control for PCDH19 staining. Therefore, the newly generated antibodies were tested initially using E11.5 WT, *Pcdh19*-HET and *Pcdh19*-KO embryos. However, neither the polyclonal (**Figure A. 2, Appendix**) nor the monoclonal antibodies (**Figure A. 3, Figure A. 4, Appendix**) were specific enough or detected the protein clearly at E11.5, independently of the titration or antigen retrieval used.

Table A. 1 in the Appendix summarises all attempts to detect PCDH19 protein.

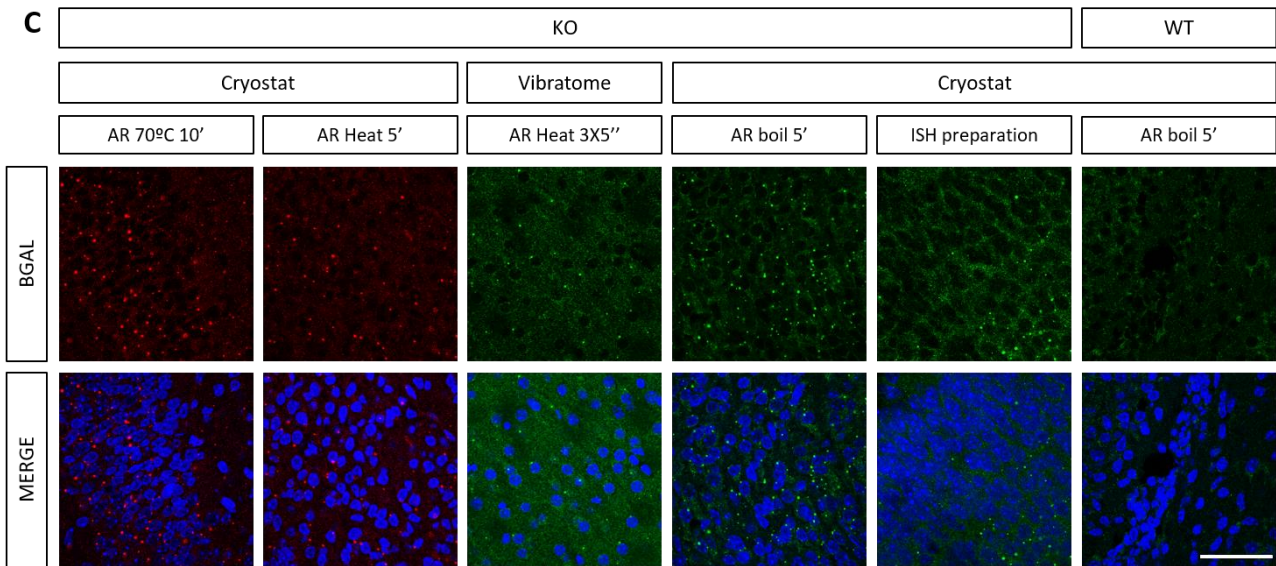
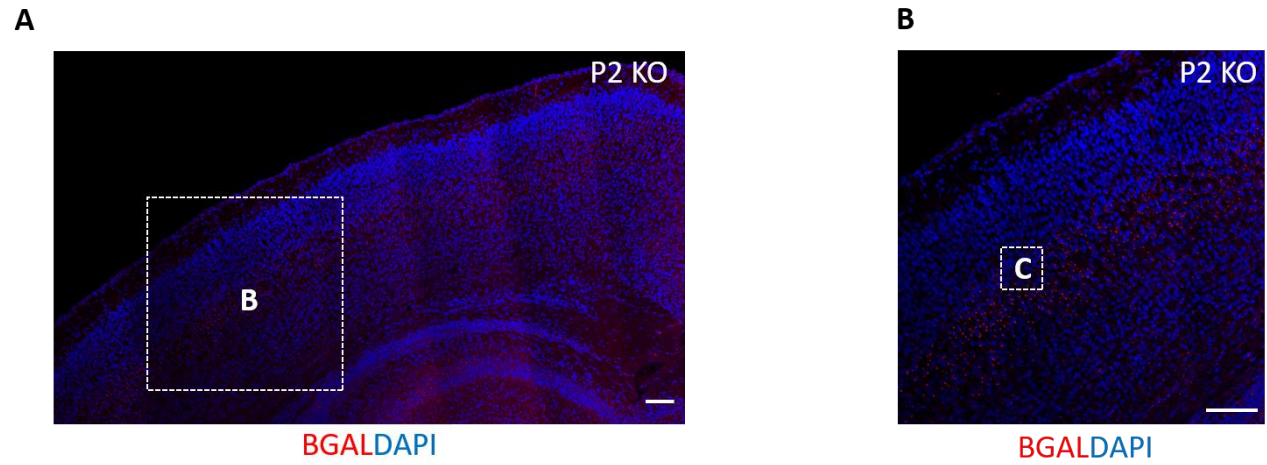


Figure 7. The ANTI-B-GALACTOSIDASE antibody did not allow identification of individual cells in P2 *Pcdh19*-KO mice brains.

Representative images of IHC tests against B-GALACTOSIDASE on *Pcdh19*-KO P2 mouse brains at 20x magnification (A, B) and 63x magnification (C), in the area that would correspond to future layer IV-V. BGAL was detected using a 1 in 500 dilution of the antibody. Slices cut on the cryostat were 20 μm , while slices cut on the vibratome were 50 μm . Antigen retrieval with citrate buffer was performed using different incubation methods and times. BGAL is shown in green or red, while DAPI counterstaining is indicated in blue. Scale bar: 50 μm . WT, Wild-type; KO, *Pcdh19*-Knockout; BGAL, B-GALACTOSIDASE.

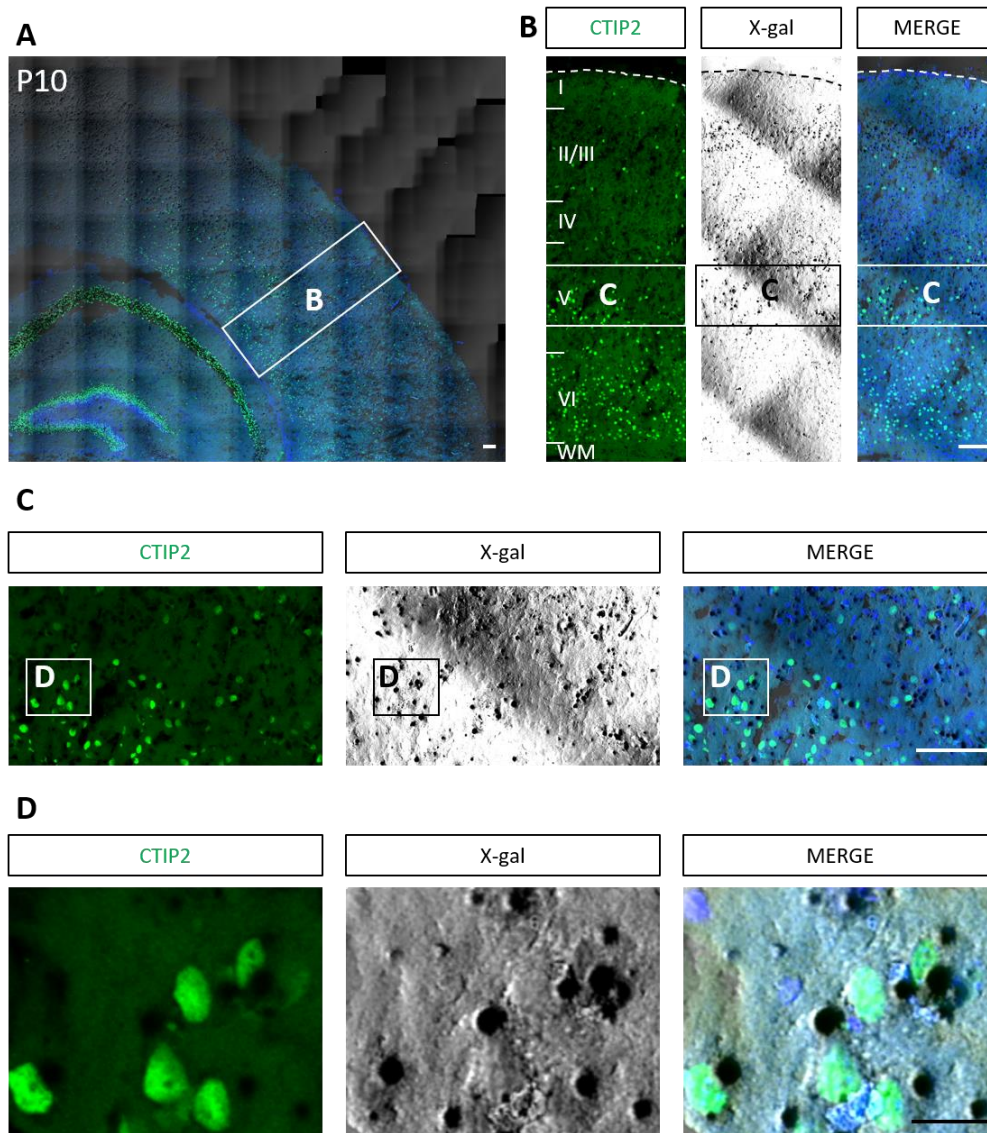


Figure 8. No reliable co-detection of B-GALACTOSIDASE activity by X-gal staining and IHC against molecular markers.

Representative images of X-gal staining in P2 KO mouse brains with a 10x objective (A). Images were magnified (B, C, D) to facilitate visualization. X-gal is indicated in black, CTIP2 is in green. Regions magnified are marked with a white rectangle. Scale bar: 100 μ m, magnified image C, 50 μ m, magnified image D, 20 μ m. KO, *Pcdh19*-Knockout.

3.3.2 *Pcdh19* mRNA is detected in the cortical wall at late embryonic and early postnatal stages.

Since all attempts to detect PCDH19 protein failed, the characterisation of *Pcdh19* expression was performed by identifying *Pcdh19* mRNA positive cells using RNA *in situ* hybridisation. The technique was conducted in mouse brains at E16.5 (**Figure 9**), P2 (**Figure 10**), P6 (**Figure 11**), P10 (**Figure 12**), P15 (**Figure 13**) and P20 (**Figure 14**) in rostral, medial and caudal regions. *Pcdh19* mRNA was detected using fluorescent *in situ* hybridization (fISH) at most ages. However, due to its low expression in P15 and P20 brains, colorimetric *in situ* hybridization (cISH) was performed instead at these two ages, since it generates a strong signal coming from an enzymatic reaction that does not diminish overtime, and can be developed during long periods of time, facilitating the visualisation.

Pcdh19 mRNA was detected at all ages studied, although expression was stronger at earlier (E16.5, P2, P6, P10) than at later ages (P15, P20).

At E16.5 (**Figure 9**), when cortical migration is ongoing and gliogenesis and synaptogenesis are starting, mRNA was detected throughout the whole cortical plate, and seemed to be expressed more intensely in medial and caudal regions than in the rostral area. No differences were observable in the lateral-medial axis in any of the areas.

The expression pattern changed at P2 (**Figure 10**), when a distinctive band could be identified in the cortex. Based on its position, this band probably corresponds to future layer V. No differences were seen among the different areas, but an intense expression of *Pcdh19* in the hippocampus was noted in the caudal region, and that expression was present at all later ages. At this age, the band of expression was wider medially than laterally.

At P6 (**Figure 11**) the band of expression was thinner but was still located in what could be future layer V, considering the position of the *Pcdh19*-expressing cells. The mRNA was expressed higher in the rostral (**Figure**

11A, A') and medial (**Figure 11B, B'**) regions than more caudally (**Figure 11C, C'**). As in P2 brains, the pattern of expression was wider medially than laterally, which was particularly noticeable in rostral (**Figure 11A, A'**) and caudal regions (**Figure 11C, C'**). In the hippocampus, expression was particularly strong in the CA1 region (**Figure 11C, C'**).

By P10, two distinct bands of expression were visible in the cortex (**Figure 12**), positioned in layers II/III and V. The band in layer V showed a higher fluorescence intensity. Rostral, medial and caudal regions didn't seem to show any differences in intensity or positioning of *Pcdh19* expression. However, as in P2 and P6, the band of cells expressing *Pcdh19* was wider in the medial side of the brain in comparison to the lateral sides, to the point in which both bands converged in the anterior cingulate area. These lateromedial differences were especially noticeable in the caudal region (**Figure 12C, C'**), where *Pcdh19* expression was almost not observable in the lateral side of the brain.

Pcdh19 expression did not vary much spatially at P15 (**Figure 13**) or P20 (**Figure 14**) with respect to the P10 brains, but fluorescence intensity in the cortex diminished considerably at those ages, leading to the choice of colorimetric detection. This will be further discussed in **section 3.4.3**. However, it is worth noting that *Pcdh19* mRNA could be detected by fISH at P20 in the experiments carried out to characterise the cellular types expressing *Pcdh19*, albeit with a higher concentration of the probe, as described in **section 2.3.3.1.2**. As in the rest of the postnatal ages, lateromedial expression was lower on the lateral part than in the medial, where the two bands merged into one. In the hippocampus, there was a noticeable increase in expression in the Dentate Gyrus compared to P10.

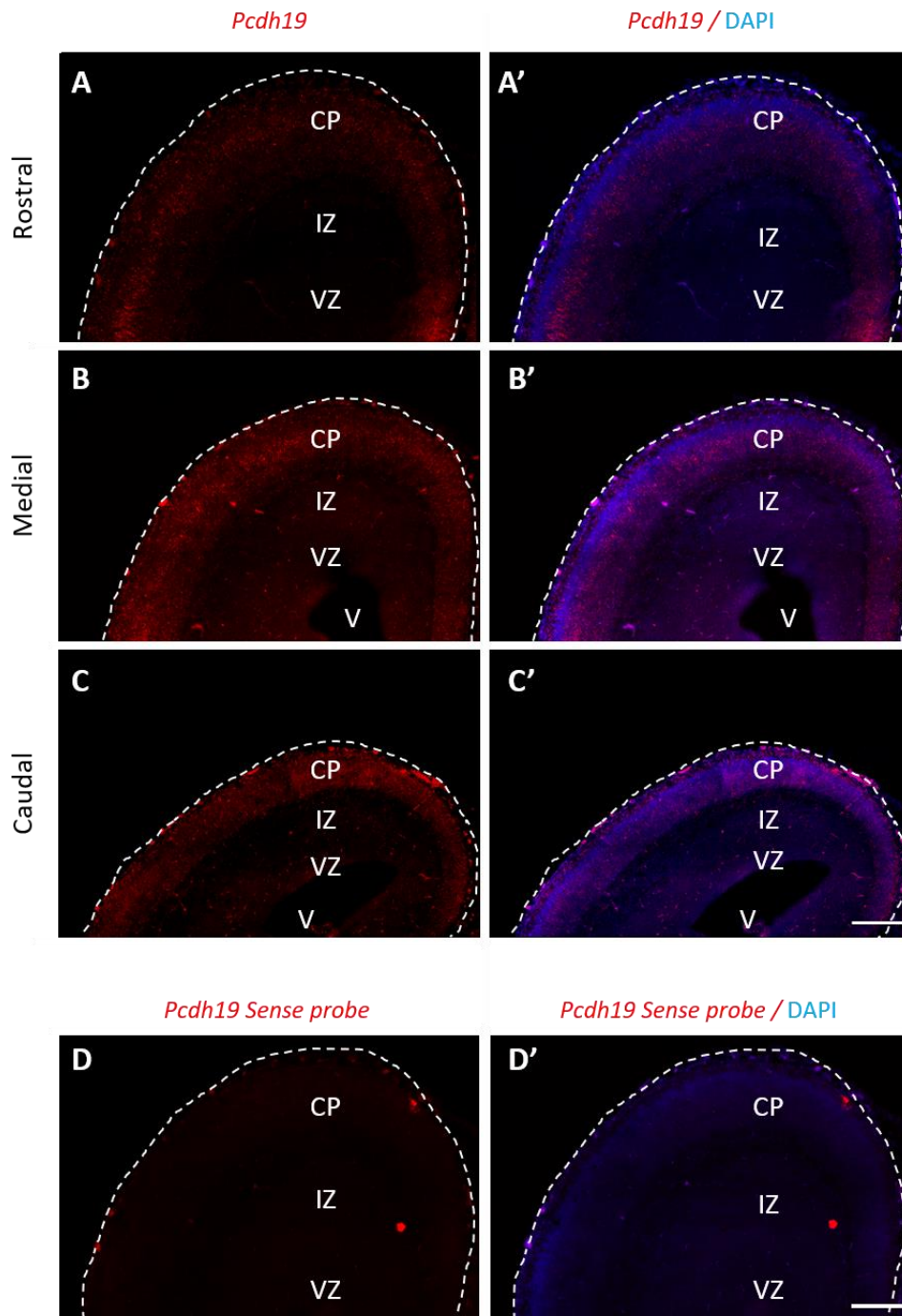


Figure 9. *Pcdh19* is detected in the cortical plate at E16.5.

Representative images of RNA *in situ* hybridisation with a *Pcdh19* antisense probe (red) on rostral (A, A'), medial (B, B') and caudal (C, C') cortical regions at E16.5. A sense probe was used as control (D, D'). Nuclei were counterstained with DAPI (blue in A' - D'). Brain slices are delineated with dashes. CP, cortical plate; IZ, intermediate zone; VZ, ventricular/subventricular zone; V, ventricle. Scale bar: 100 μ m.

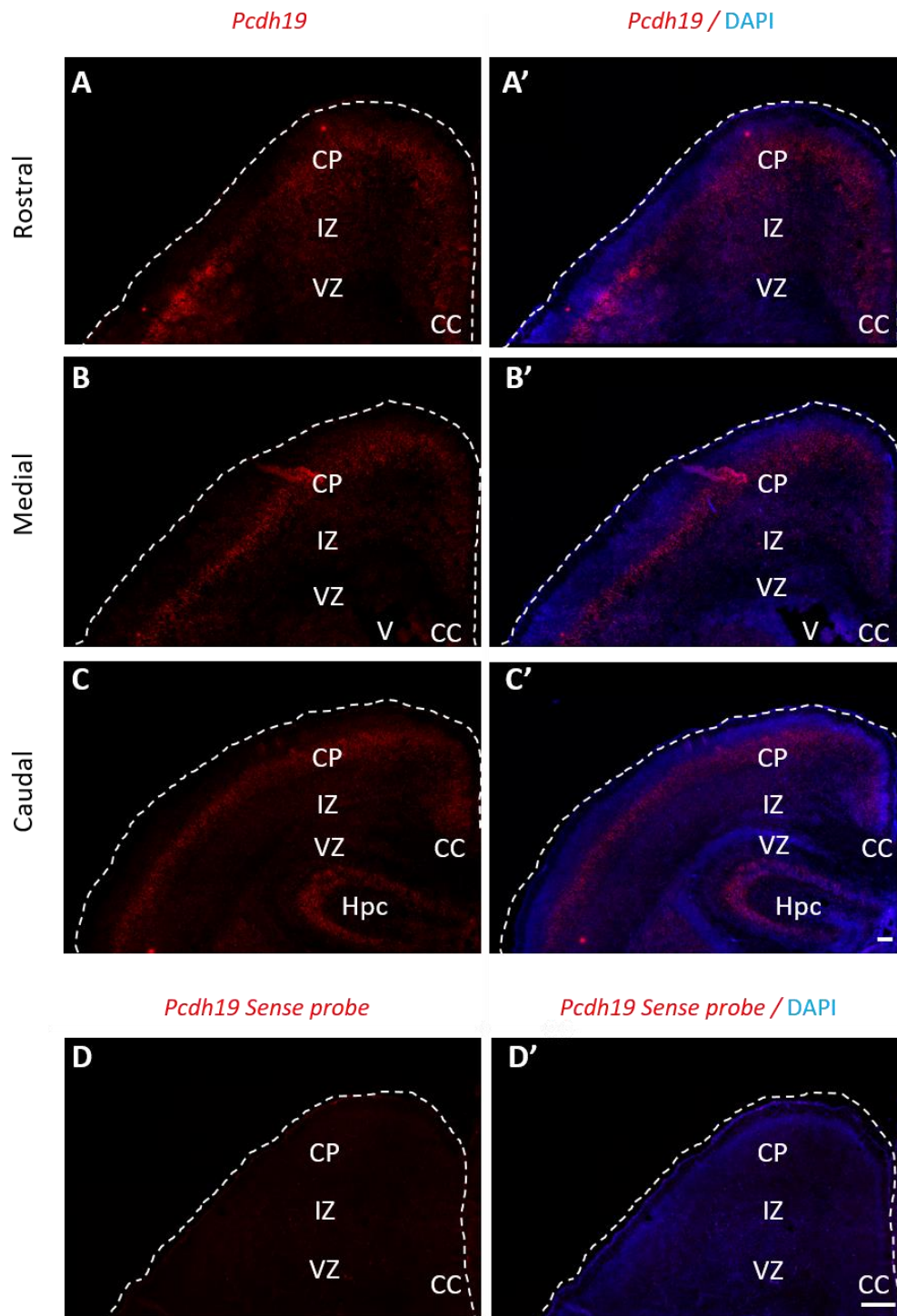


Figure 10. *Pcdh19* mRNA is expressed in the cortical plate at P2.

Representative images of RNA *in situ* hybridisation with a *Pcdh19* antisense probe (red) on rostral (A, A'), medial (B, B') and caudal (C, C') cortical areas at P2. Control was done using a sense probe (D, D'). Nuclei were counterstained with DAPI (blue in A' - D'). Brain slices are outlined with dashes. CP, cortical plate; IZ, intermediate zone; VZ,

ventricular/subventricular zone; V, ventricle; CC, corpus callosum; Hpc, hippocampus. Scale bar: 100 μ m.

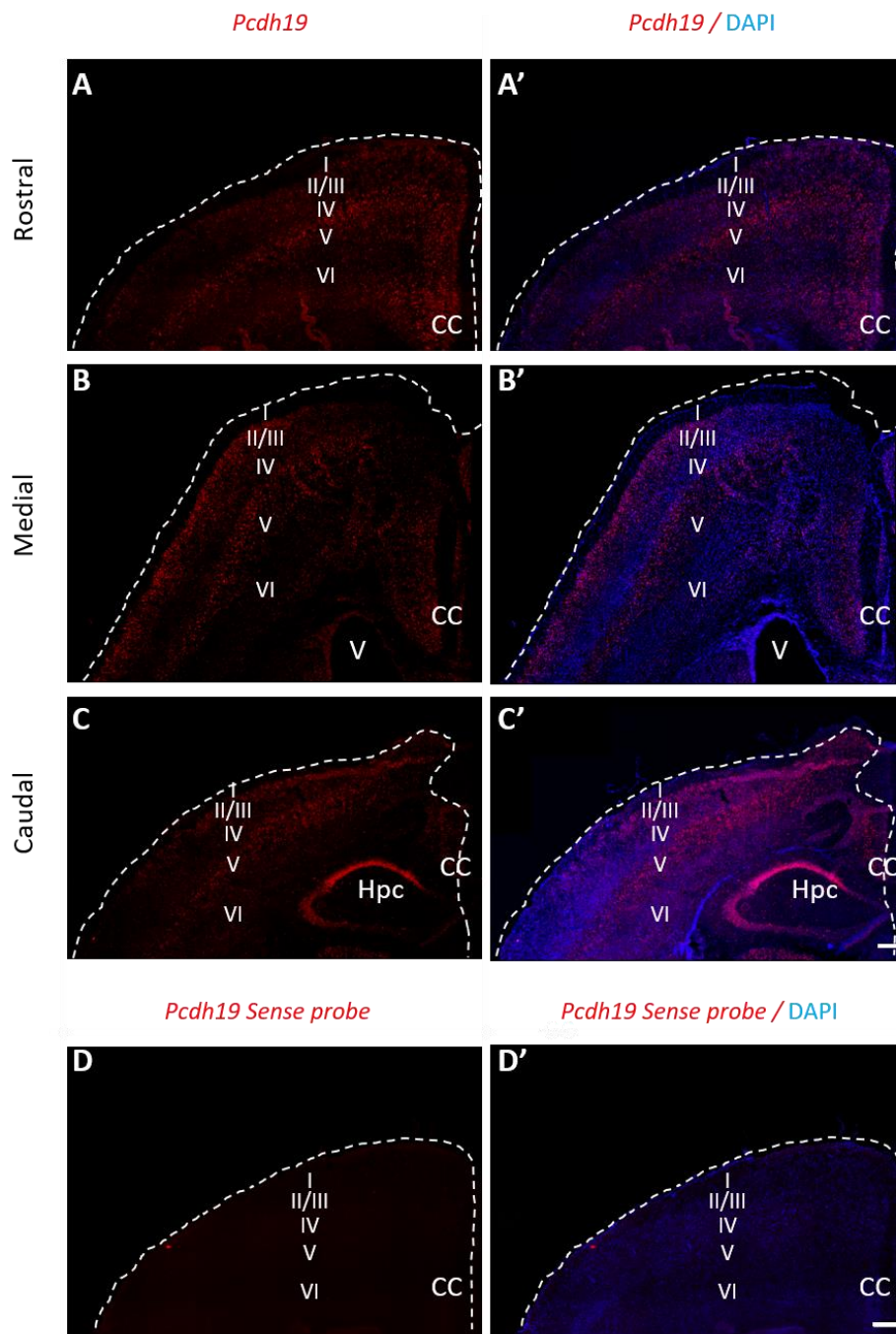


Figure 12. *Pcdh19* is detected in the cortical plate of P10 mice.

Representative images of RNA *in situ* hybridisation with a *Pcdh19* antisense probe (red) on rostral (A, A'), medial (B, B') and caudal (C, C') and a sense probe as control (D, D') in cortical regions at P10. Nuclei were counterstained with DAPI (blue in A' - D'). Brain slices are outlined with dashes. Cortical layers are indicated by roman numerals in the representative images. V, ventricle; CC, corpus callosum; Hpc, hippocampus. Scale bar: 100 μ m.

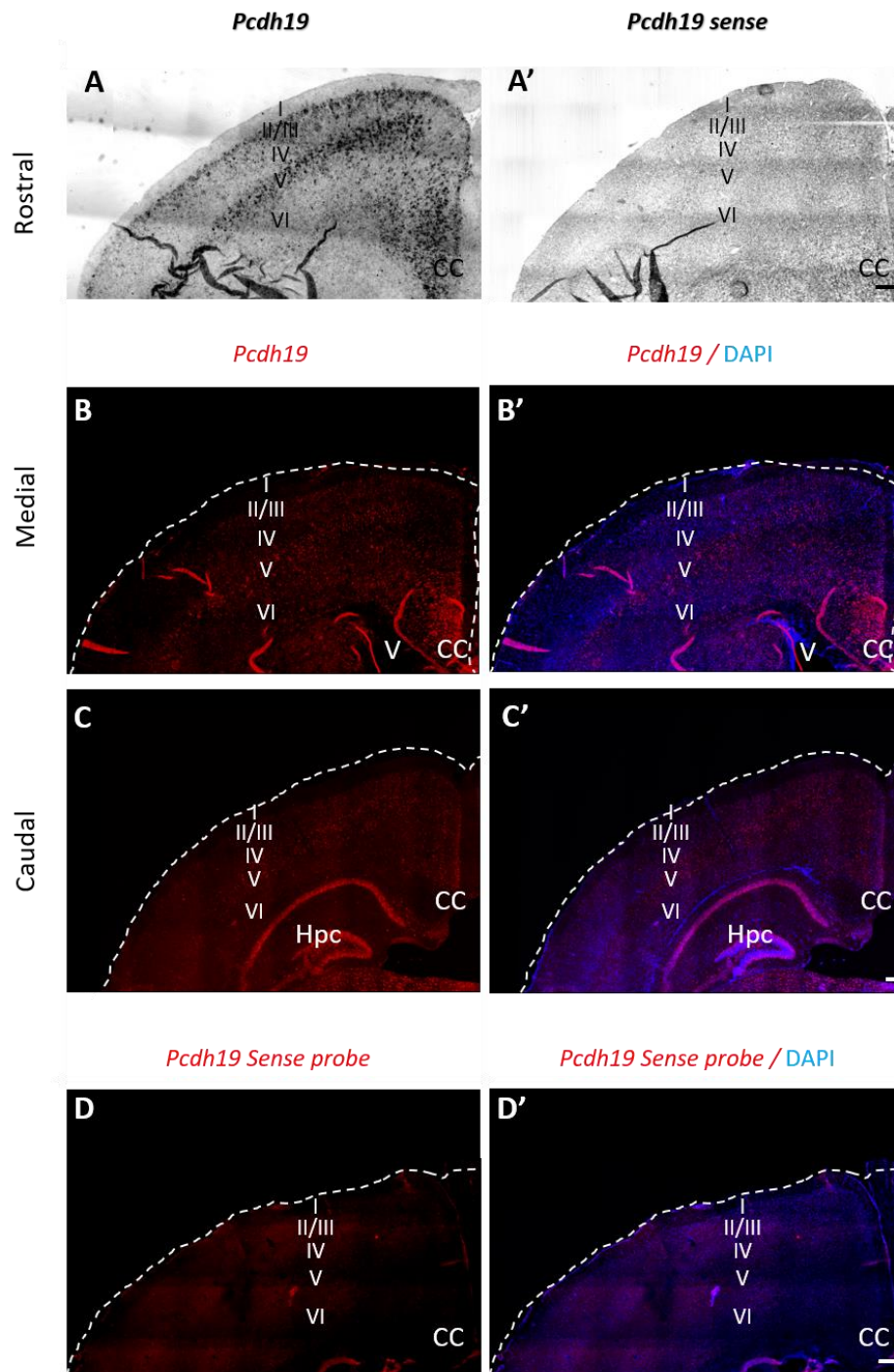


Figure 13. *Pcdh19* is detected in the cortical plate at P15.

Representative images of RNA *in situ* hybridisation with a *Pcdh19* antisense probe (red or black) on rostral (A, A'), medial (B, B') and caudal (C, C') cortical areas at P15. A sense probe was used as control (A', D, D'). Nuclei were counterstained with DAPI (blue in B' – D'). Brain slices are delimited by dashed lines. Darker areas reflect an illumination problem due to technical issues with the confocal. Cortical layers are indicated by roman numerals in the representative images. V, ventricle; CC, corpus callosum; Hpc, hippocampus. Scale bar: 100 μ m.

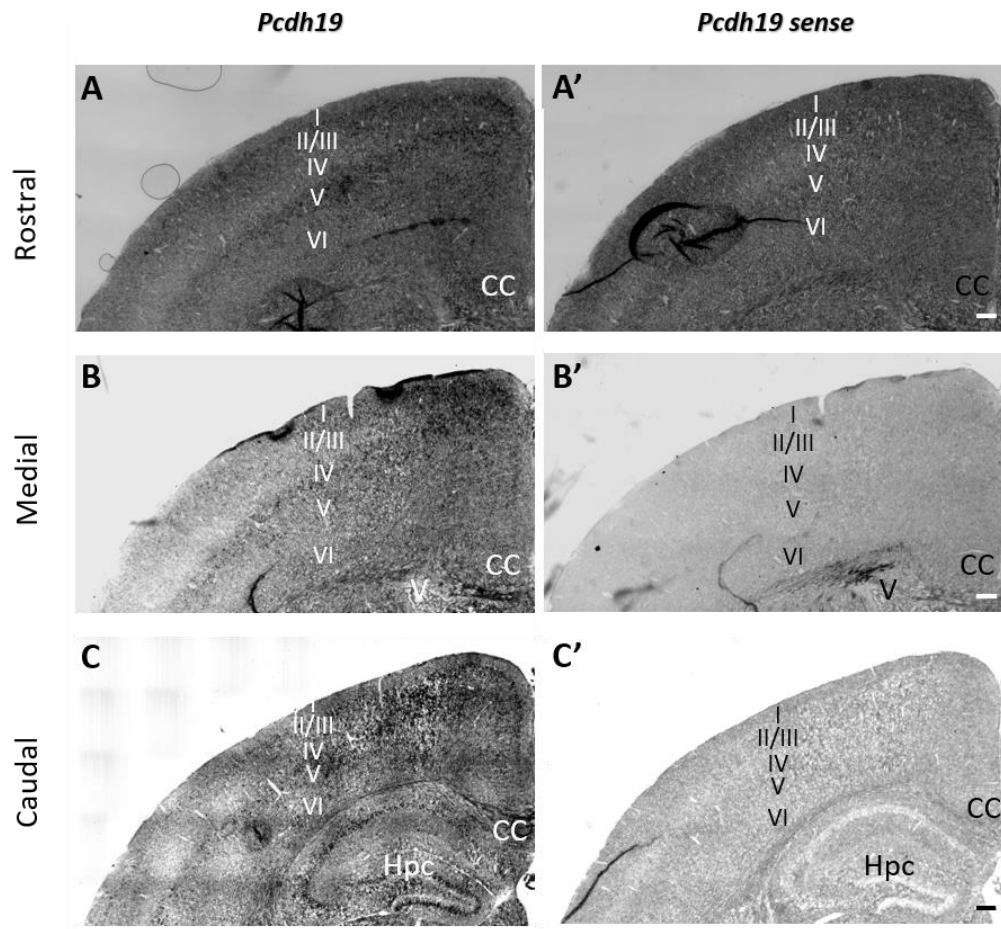


Figure 14. *Pcdh19* is expressed in the cortical plate at P20.

Representative images of RNA *in situ* hybridisation with a *Pcdh19* antisense probe (A-C) and sense probe (A' - C') on rostral (A, A'), medial (B, B') and caudal (C, C') cortical regions at P10. Brain slices are outlined with dashes. Cortical layers are indicated by roman numerals in the representative images. V, ventricle; CC, corpus callosum; Hpc, hippocampus. Scale bar: 100 μ m.

The decrease in signal intensity at P15 and P20 could represent lower *Pcdh19* expression levels. However, it could also be a consequence of differences in perfusion or fixation, or of the use of thicker tissue slices at those two ages (20 μm vs 12 μm). Therefore, to verify if the differences in intensity between the younger and older brains were due to different expression levels rather than a technical artefact, a quantitative PCR was carried out to quantify *Pcdh19* transcript levels at the different ages. Specifically, the relative fold change of *Pcdh19* cDNA levels at all ages with respect to P2 was calculated. As observed in **Figure 15**, *Pcdh19* expression levels increased by about 50% at P6 (1.45 ± 0.16) and P10 (1.57 ± 0.12) with respect to P2 (1 ± 0.03), whereas no such differences were present at P15 (0.96 ± 0.16) and P20 (1.1 ± 0.25). However, P2 is a much smaller brain with a lower number of cells than P15 or P20. If P15 or P20 brains and P10 brains were compared, there was a slight decrease in the total quantity of *Pcdh19* in the older brains. The interpretation of these results will be discussed in **section 3.4.3**.

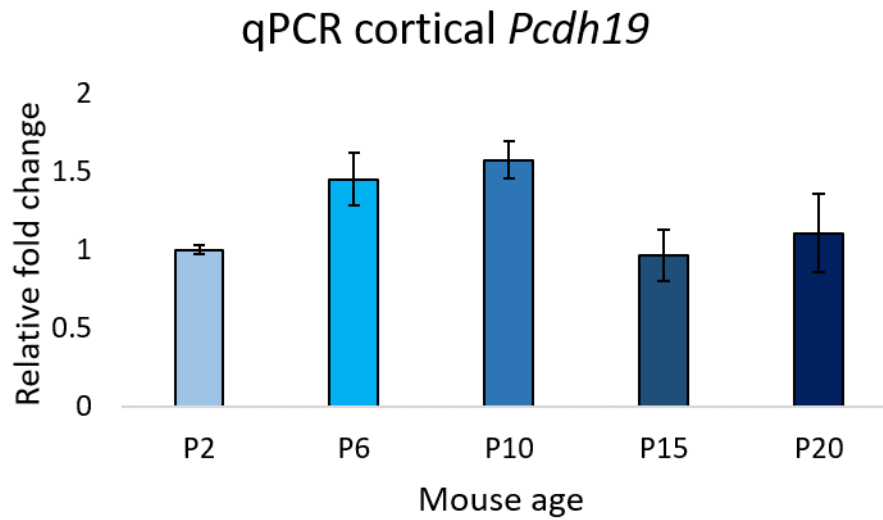


Figure 15. *Pcdh19* cortical expression in early postnatal mice peaks at P10.

The graph represents the relative fold change expression of *Pcdh19* in the entire cortex at different ages with respect to its expression at P2. Data are presented as mean \pm SEM. At least 4 animals from 3 different litters were used for the experiment. N was considered 4.

3.3.3 *Pcdh19* mRNA expressing cells partially colocalise with a diverse group of cortical excitatory and interneuronal markers.

Due to the difficulties mentioned in **section 3.3.1**, *Pcdh19* expressing cells were characterised by combining ISH and IHC. Even though *Pcdh19* mRNA is mainly cytoplasmic and therefore doesn't overlap with the nuclear signal of the cortical markers, *Pcdh19* mRNA in expressing cells was seen as fluorescent dots around the DAPI-counterstained nucleus. This allowed an analysis of whether *Pcdh19* mRNA co-localised with particular molecular markers. Cells with more than four dots located in close apposition to the nucleus were considered *Pcdh19*⁺, and any *Pcdh19*⁺ cell that was positive for the cortical marker that was being studied was counted as a double positive cell. Glutamatergic excitatory markers were analysed at P10, when the excitatory pyramidal neurons have achieved their final positions in the cortical wall (Alcamo et al. 2008; Jabaudon 2017). Analysis of inhibitory GABAergic markers was performed at P20 since the expression of most markers was very low before this age, as previously reported (J. del Rio et al. 1994).

3.3.3.1 Distribution of *Pcdh19*⁺ cells in P10 and P20 cortices

To thoroughly characterise *Pcdh19* expression at P10 and P20 (**Figure 16A**), an initial evaluation of the distribution of cells expressing the *Pcdh19* mRNA was performed in which three parameters were analysed: the percentage of total *Pcdh19*-positive cells with respect to DAPI (**Figure 16B**), the percentage of cells positive for *Pcdh19* with respect to DAPI in each layer and the distribution of *Pcdh19*-expressing cells throughout the cortical plate (**Figure 16C**).

At P10, a total of 12 images from 2 brains were analysed. One fifth of the total cells in the selected region were *Pcdh19*⁺ (20.81 ± 5.37 % cells), and those cells were mostly concentrated in layers II/III, V and VI. The analysis of the percentage of cells expressing *Pcdh19* per layer revealed that layers

II/III and V, but not VI, contained the highest proportion of *Pcdh19*-positive cells, as indicated in **Figure 16C**.

At P20, analysis was conducted using a total of 6 images from one brain. Therefore, the corresponding errors and error bars in **Figure 14** reflect the variation between technical replicates. In agreement with **section 3.3.2**, the total number of *Pcdh19*-expressing cells was lower at P20 than at P10 (13.66 % vs 20.81 ± 5.37 % cells). *Pcdh19*⁺ cells at P20 were distributed similarly to the cells at P10, except for layer VI where the percentage of *Pcdh19*⁺ cells decreased at P20. Regarding the percentages of *Pcdh19* positive cells per layer; they were generally lower in P20 brains than in P10 brains, but the layers with the highest percentage of *Pcdh19*-expressing cells were still layers II/III and V. All the percentages can be seen in **Figure 16C**.

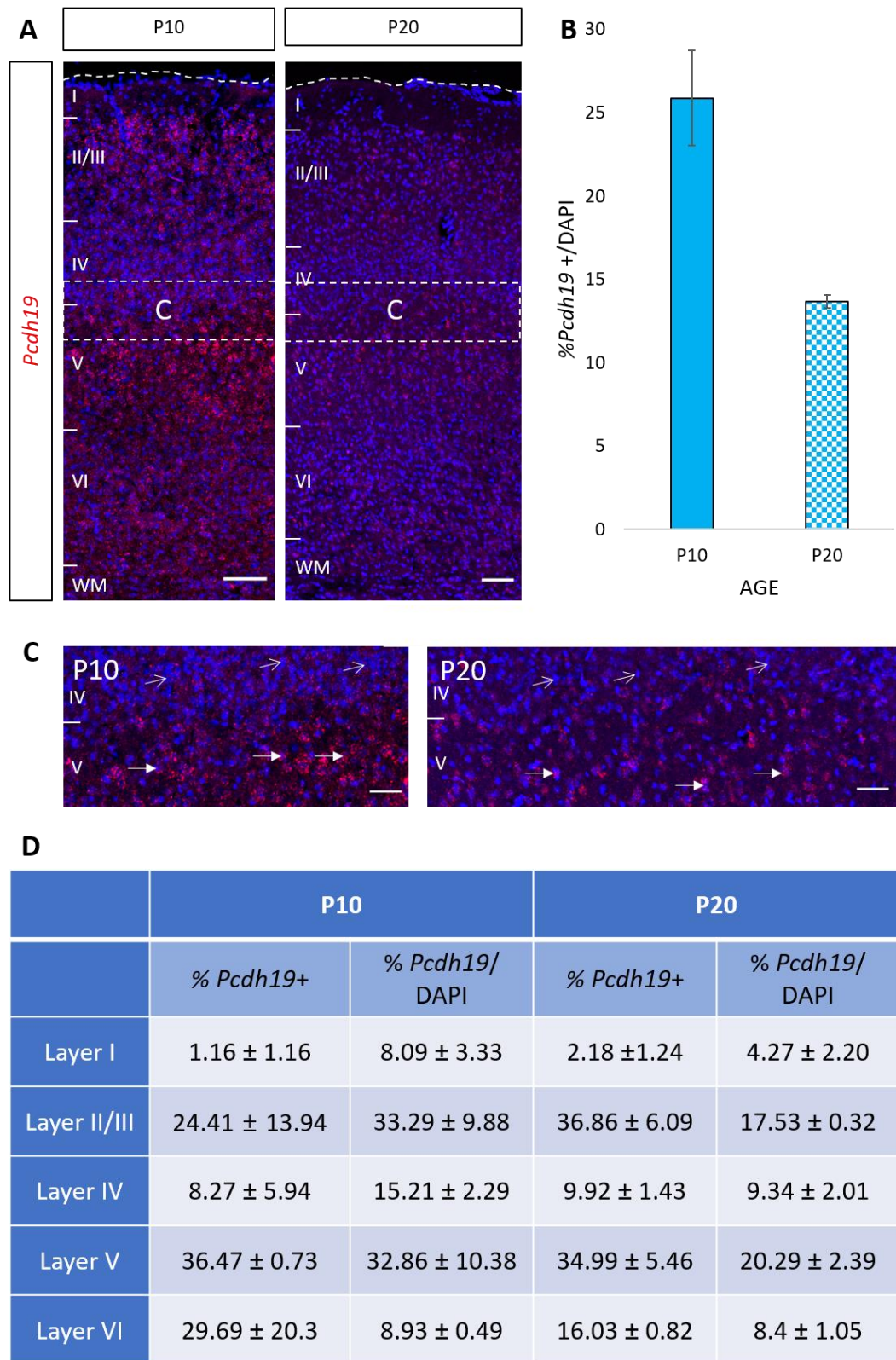


Figure 16. *Pcdh19* mRNA is mainly detected in layers II/III and V and is more abundant in P10 than in P20 brains at the SSC.

(A) Representative images of P10 and P20 mouse brains *in situ* hybridised for *Pcdh19* detection. *Pcdh19* is in red. (B) Quantification of the

Pcdh19⁺ cells/DAPI across the cortical span. (C) An area between layers IV/V are shown at higher magnification. (D) Table shows the %*Pcdh19*⁺ cells in each layer with respect to the total number of *Pcdh19*⁺ cells and the %*Pcdh19*⁺ cells with respect to DAPI in each layer at P10 and P20. Data presented as mean \pm SEM. WM, white matter. Cortical layers are indicated with roman numerals in the representative images. Dashed lines indicate the limit of the brain. White arrows reveal *Pcdh19*⁺ cells and white open arrows indicate *Pcdh19*⁻ cells. Scale bar on A: 100 μ m; scale bar on C: 50 μ m.

3.3.3.2 Glutamatergic cortical markers at P10

To perform the characterisation of *Pcdh19*-expressing cells at P10, ISH combined with immunohistochemistry against SATB2 (**Figure 17**), RORB (**Figure 18, Figure 21**), CTIP2 (**Figure 19, Figure 21**) and TBR1 (**Figure 20**) was conducted at P10. Four parameters were studied:

1. The percentage of *Pcdh19*⁺ cells with respect to DAPI in each layer (**Figure 17B, Figure 18B, Figure 19B, Figure 20B**).
2. The percentage of double positive cells (*Pcdh19*⁺; MARKER⁺) per layer (**Figure 17B, Figure 18B, Figure 19B, Figure 20B**).
3. The proportion of MARKER⁺ and MARKER⁻ cells with respect to the total number of *Pcdh19*⁺ cells (**Figure 17C, Figure 18C, Figure 19C, Figure 20C**).
4. The proportion of *Pcdh19*⁺ and *Pcdh19*⁻ cells with respect to the total number of MARKER⁺ cells (**Figure 17D, Figure 18D, Figure 19D, Figure 20D**).

Pcdh19⁺ cells partially colocalised with all glutamatergic markers tested. *Pcdh19*⁺SATB2⁺ cells (**Figure 17C**) represented $48.76 \pm 13.19\%$ of all *Pcdh19*⁺ cells and were present in all layers (**Figure 17B**). However, only $17.62 \pm 0.96\%$ of SATB2 expressing cells were *Pcdh19*⁺ (**Figure 17D**).

In the case of RORB, a layer IV marker, $15.18 \pm 7.02\%$ of the *Pcdh19*⁺ cells were also RORB⁺ (**Figure 18C**), and most of those double positive cells accumulated in layers IV and V of the cortex (**Figure 18B**). The percentage of RORB⁺ cells that were *Pcdh19*⁺RORB⁺ was less than a quarter, $22.6 \pm 5.6\%$.

CTIP2 is expressed in corticothalamic and corticospinal projecting cells located in layers V and VI, and the analysis revealed that the percentage of *Pcdh19*⁺ cells that co-expressed CTIP2 was $29.42 \pm 9.81\%$ (**Figure 19C**), the majority of which distributed between layers V and VI, as expected (**Figure 19B**). The percentage of CTIP2⁺ cells that colocalised with *Pcdh19* was only $28.61 \pm 5.28\%$ (**Figure 19D**).

Finally, the percentage of *Pcdh19*⁺ cells that colocalised with TBR1, a marker for layer VI neurons, was $17.83 \pm 1.28\%$ (**Figure 20C**) and those cells were positioned mainly in layers V and VI (**Figure 20B**). The percentage of TBR1⁺ cells that were *Pcdh19*⁺ was $15.65 \pm 4.86\%$ (**Figure 20D**).

The analysis of *Pcdh19* expression by combining detection of *Pcdh19* mRNA, RORB (layer IV) and CTIP2 (layer Vb) (**Figure 21**) showed that *Pcdh19*-positive cells are mainly located in layer Va, and part of layer Vb since the mRNA expression is almost complementary to RORB and partially overlaps with CTIP2, particularly in the upper part of layer Vb (**Figure 21B**).

As mentioned previously, two brains were studied at P10 but those brains were only used in the TBR1⁺ analysis. Thus, the error bars shown in the ISH+IHC against all molecular markers except TBR1 are of the technical replicates (three images or samples from one brain, N=1). In the case of TBR1 the error bars present in the graphic correspond to the biological replicates (three images from two biologically distinct samples, N=2).

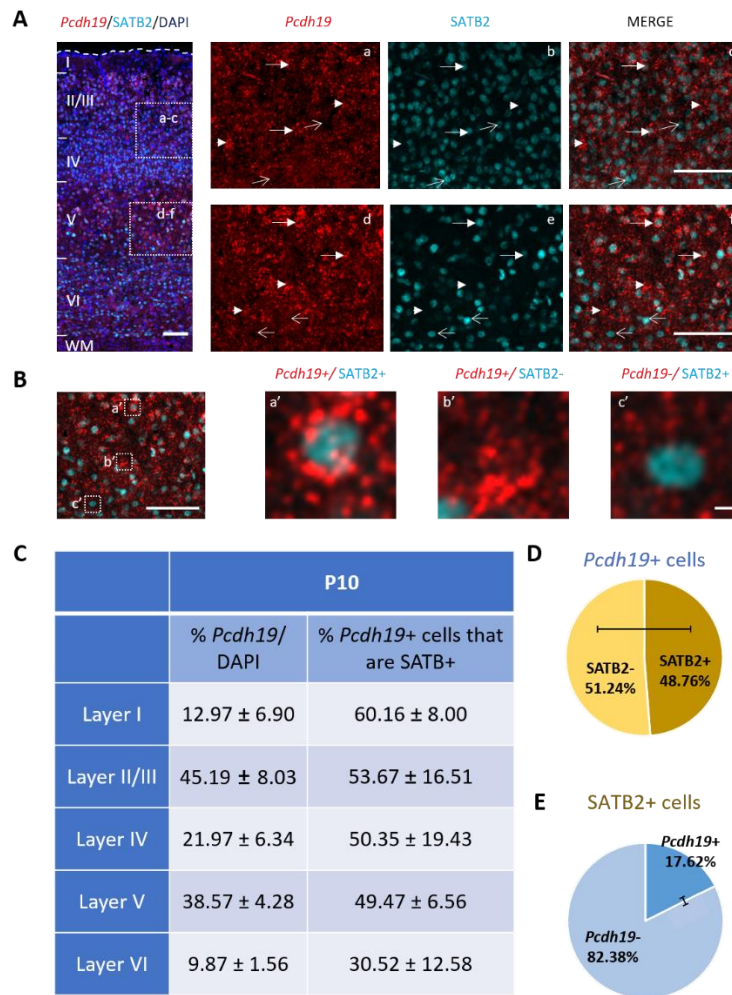


Figure 17. Almost half of *Pcdh19* mRNA expressing cells coexpress SATB2 in P10 SSC.

(A) Representative images of ISH+IHC experiments detecting *Pcdh19* (red) and SATB2 (cyan) in P10 SSC. Nuclei are counterstained with DAPI (blue). Layers II/III (a-c) and V (d-f) are shown at higher magnification. (B) Double positive (a'), *Pcdh19*+ (b') and SATB2+ (c') cells from layer V are shown at higher magnification. (C) Table shows the %*Pcdh19*+ cells with respect to DAPI in each layer, and the %*Pcdh19*+SATB2+ cells with respect to the total number of *Pcdh19*+ cells in each layer. (D) Quantification of the %*Pcdh19*+SATB2+ and *Pcdh19*+SATB2- cells with respect to the total number of *Pcdh19*+ cells. (E) Quantification of the %SATB2+*Pcdh19*+ and SATB2+*Pcdh19*- cells with respect to the total number of SATB2+ cells. Data presented as mean ± SEM. WM, white matter. Cortical layers are indicated with roman numerals in the representative images. Dashed lines indicate the brain limit. White arrows reveal *Pcdh19*+SATB2+ cells, white arrowheads highlight *Pcdh19*+SATB2- cells and white open arrows indicate *Pcdh19*-SATB2+ cells. Scale bar: 100 μm.

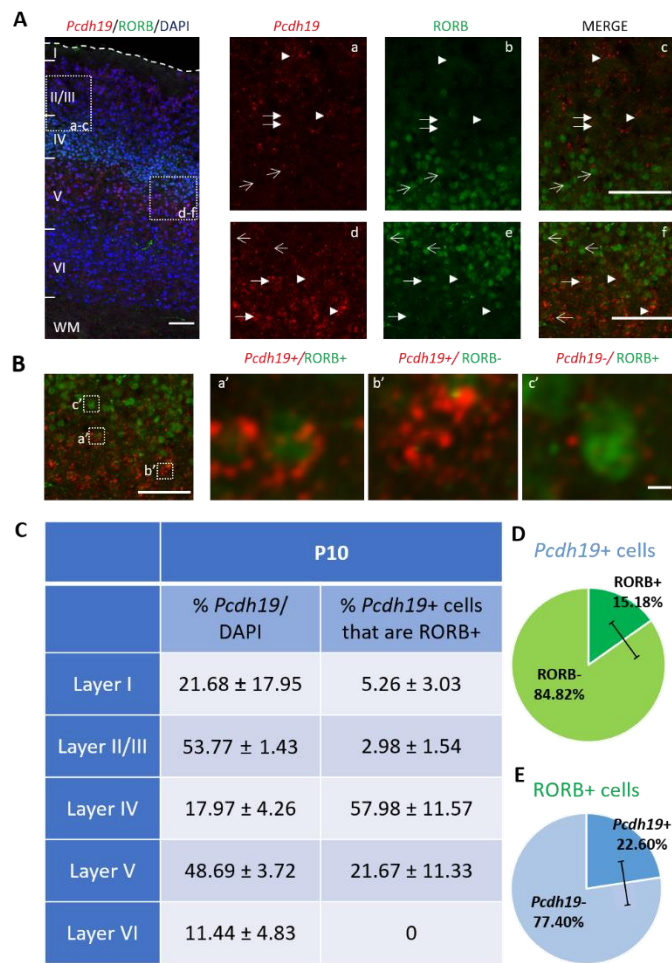


Figure 18. *Pcdh19* mRNA expressing cells partially coexpress RORB in P10 SSC.

(A) Representative images of P10 SSC detecting *Pcdh19* and RORB by ISH combined with IHC. *Pcdh19* shown in red, RORB cells are in green colour and DAPI is indicated in blue. Layers II/III-IV (a, b, c) and IV-V (d, e, f) are shown at higher magnification. (B) Double positive (a'), *Pcdh19*+ (b') and RORB+ (c') cells from layer V are shown at higher magnification. (C) Table shows the %*Pcdh19*+ cells with respect to DAPI per layer, and the % of *Pcdh19*+ cells that are also RORB+ in each layer. (D) Quantification of the %*Pcdh19*+RORB+ and *Pcdh19*+ RORB- cells with respect to the total number of *Pcdh19* mRNA expressing cells. (E) Quantification of the % RORB+ *Pcdh19*+ and RORB+*Pcdh19*- cells with respect to the total number of RORB+ expressing cells. Data presented as mean ± SEM. WM, white matter. Cortical layers are indicated with roman numerals in the representative images. Dashed line delimits the brain. White arrows indicate *Pcdh19*+RORB+ cells, white arrowheads show *Pcdh19*+RORB- cells and white open arrows highlight the *Pcdh19*-RORB+ cells. Scale bar: 100 μm.

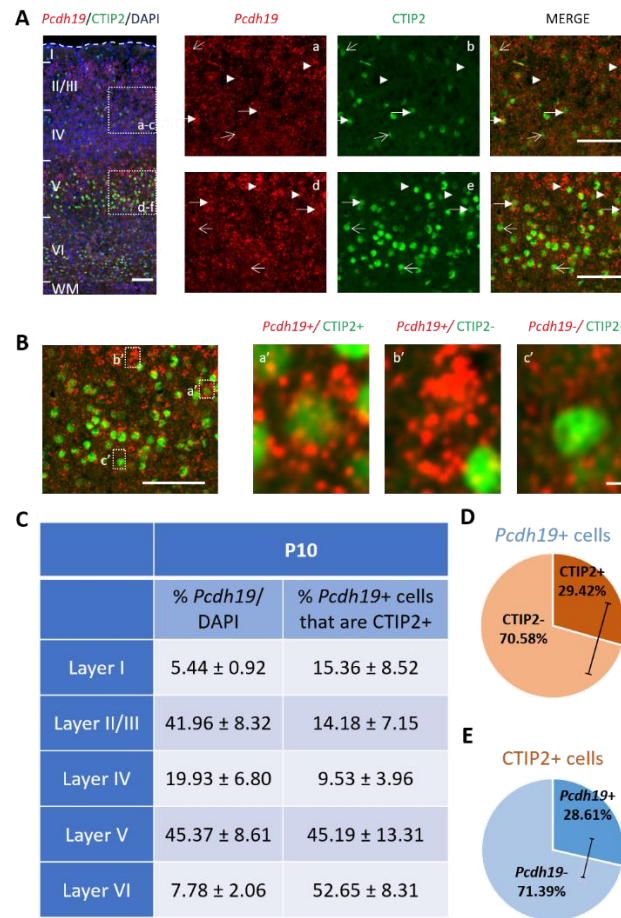


Figure 19. Cells expressing *Pcdh19* mRNA partially coexpress CTIP2 in P10 SSC.

(A) Representative images of *Pcdh19* and CTIP2 detected by ISH combined with IHC at P10 SSC. *Pcdh19* indicated in red, RORB cells are shown in green colour and DAPI is indicated in blue. Layers II/III (a, b, c) and V (d, e, f) are shown at higher magnification. (B) Double positive (a'), *Pcdh19*+ (b') and CTIP2+ (c') cells from layer V are shown at higher magnification. (C) Table shows the %*Pcdh19*+ cells with respect to DAPI per layer, and the % of *Pcdh19*+ cells that also express CTIP2 in each layer. (D) Quantification of the %*Pcdh19*+CTIP2+ and *Pcdh19*+CTIP2- cells with respect to the total number of *Pcdh19* mRNA expressing cells (E) Quantification of the %CTIP2+*Pcdh19*+ and CTIP2+*Pcdh19*- cells with respect to the total number of CTIP2 expressing cells. Data presented as mean ± SEM. WM, white matter. Cortical layers are specified with roman numerals in the representative images. Dashed line indicates the limits of the brain. White arrows highlight *Pcdh19*+CTIP2+ cells, white arrowheads indicate *Pcdh19*+CTIP2- cells and white open arrows signal the *Pcdh19*-CTIP2+ cells. Scale bar: 100 µm.

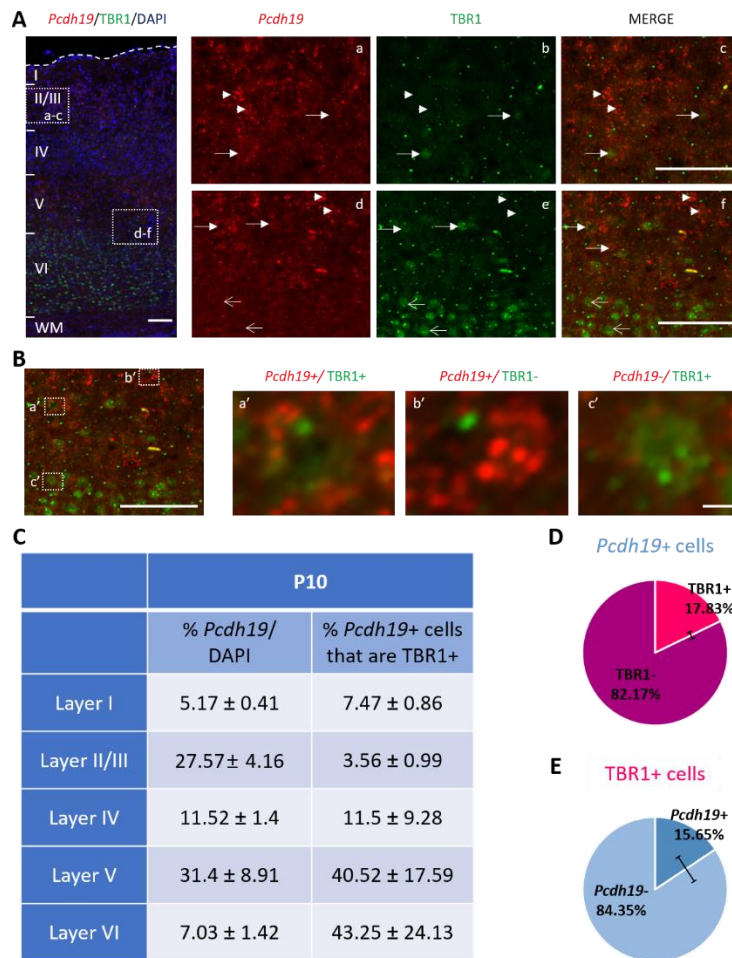


Figure 20. Cells positive for *Pcdh19* mRNA partially coexpress TBR1 in P10 SSC.

(A) Representative images of P10 SSC ISH combined with IHC that detected *Pcdh19* and TBR1. *Pcdh19* is in red, TBR1 cells are in green and DAPI is shown in blue. Layers II/III (a, b, c) and V (d, e, f) are shown at higher magnification. (B) Double positive (a'), *Pcdh19*+ (b') and TBR1+ (c') cells from layer V are shown at higher magnification. (C) Table shows the %*Pcdh19*-expressing cells with respect to DAPI in each layer, and the % of *Pcdh19*+ TBR1+ cells with respect to all *Pcdh19*+ cells in each layer. (D) Quantification of the %*Pcdh19*+TBR1+ and *Pcdh19*+TBR1- cells with respect to the total number of *Pcdh19* mRNA expressing cells (E) Quantification of the %TBR1+*Pcdh19*+ and TBR1+*Pcdh19*- cells with respect to the total number of cells expressing TBR1. The data are presented as mean ± SEM. WM, white matter. Cortical layers are indicated with roman numerals in the representative images. Dashed line reveals the limit of the brain. White arrows signal *Pcdh19*+TBR1+ cells, white arrowheads show *Pcdh19*+TBR1- cells and white open arrows highlight the *Pcdh19*-TBR1+ cells. Scale bar: 100 μ m.

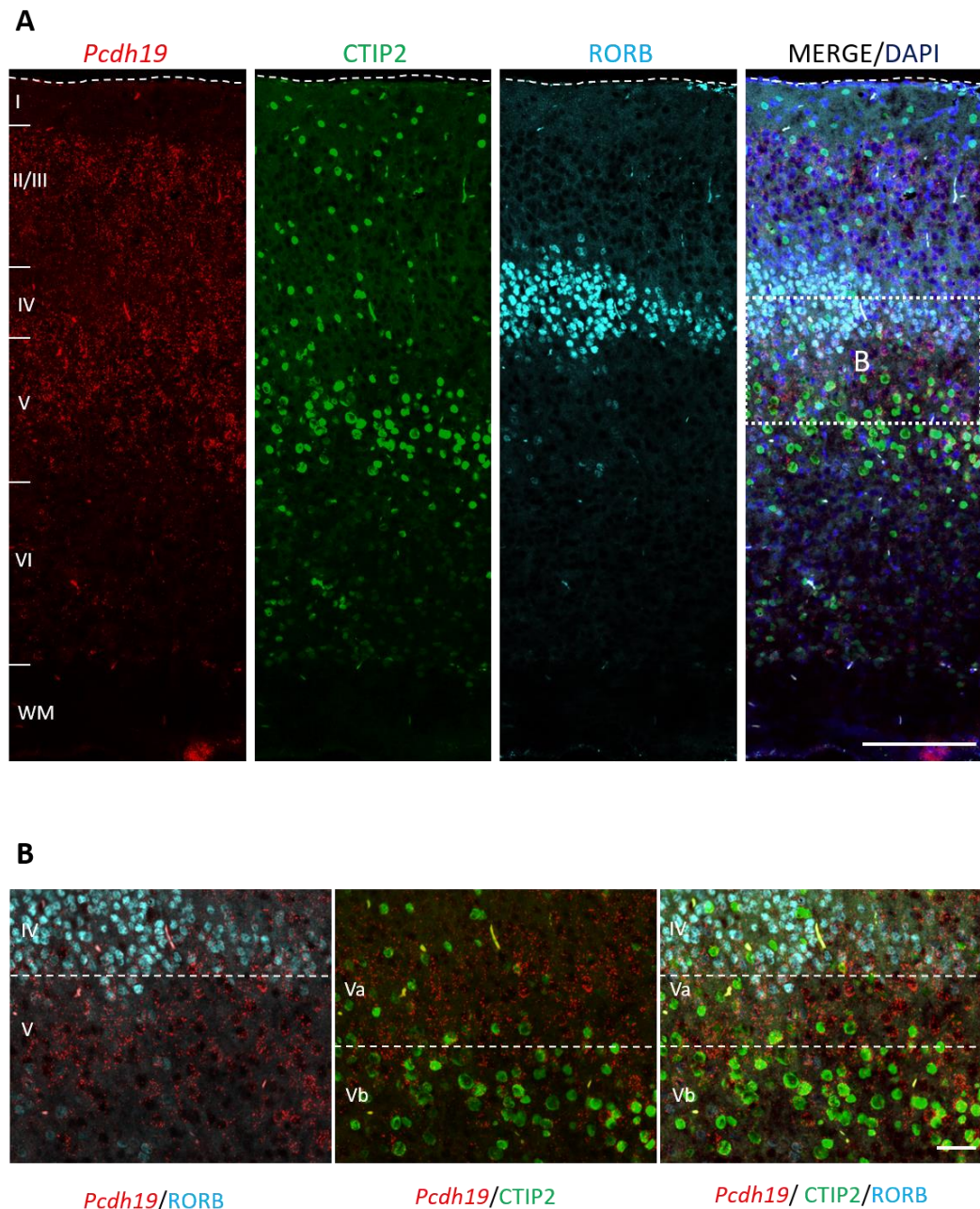


Figure 21. *Pcdh19* mRNA expression is specifically located in layer Va and part of layer Vb.

(A) Representative images of P10 SSC ISH combined with IHC that detected *Pcdh19*, RORB and CTIP2. *Pcdh19* is shown in red, CTIP2 cells are in green, RORB is indicated in cyan and DAPI counterstaining is in blue. (B) Magnification of an area that comprises lower layer IV and upper layer V. WM, white matter. Cortical layers are noted with roman numerals in the representative images. Dashed line indicates the limit of the brain. Scale bar: 100 μ m, in magnified images: 50 μ m.

3.3.3.3 Interneuronal cortical markers at P20

As mentioned in **section 3.1**, a combination of PV, SST and 5HT3aR can detect all cortical interneurons (Rudy et al. 2011). However, ionotropic serotonin receptor 5HT3a (5HT3aR) and SST could not be detected in combination with RNA ISH. Other commonly used interneuronal markers include CB and CR. Together, PV, CB and CR positive cells comprise about 80% of cortical interneurons in rodents (Gabbott et al. 1997). Unfortunately, the CR antibody did not work either, so PV (**Figure 22**) and CB (**Figure 23**), that comprise approximately 55% of the rodent cortical interneurons, were analysed in the experiments. The same four parameters as for the glutamatergic neurons were analysed.

Pcdh19⁺ cells partially colocalised with all interneuronal markers, too.

Of all *Pcdh19*⁺ cells, $9.30 \pm 1.78\%$ co-expressed PV (**Figure 22C**) and double positive cells were located mainly in layers IV and V (**Figure 22B**). Almost a third ($31.71 \pm 5.39\%$) of the cells expressing PV were positive for *Pcdh19* (**Figure 22D**).

On the other hand, *Pcdh19*⁺CB⁺ cells represented $28.49 \pm 6.19\%$ of the total *Pcdh19*⁺ cells (**Figure 21C**) and were located mainly in layers II/III (**Figure 23B**). Also, almost half ($45.7 \pm 9.24\%$) of the CB⁺ cells colocalised with *Pcdh19* (**Figure 21D**).

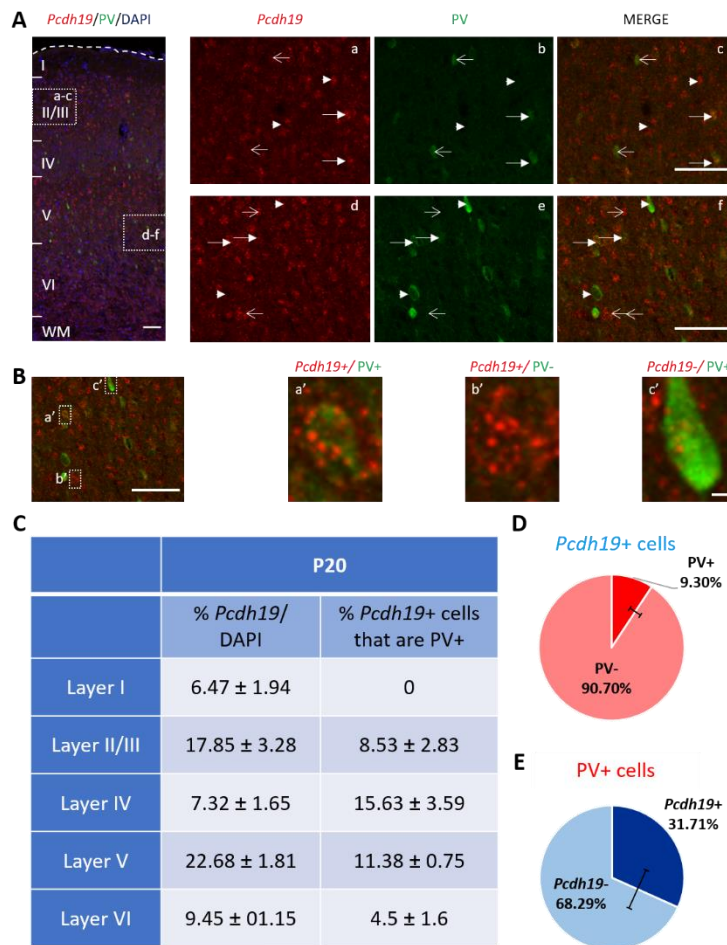


Figure 22. *Pcdh19* mRNA-positive cells partially coexpress parvalbumin in P20 SSC.

(A) Representative images of ISH+IHC experiments performed against *Pcdh19* and parvalbumin in the SSC area of P20 mice. *Pcdh19* is seen in red, PV+ cells are in green and DAPI counterstaining is in blue. Layers II/III (a, b, c) and V (d, e, f) are shown at higher magnification. (B) Double positive (a'), *Pcdh19*+ (b') and PV+ (c') cells from layer V are shown at higher magnification. (C) Table indicates the %*Pcdh19*+ cells with respect to DAPI in each layer, and the % of *Pcdh19*+ cells that are positive for PV too in each layer. (D) Quantification of the %*Pcdh19*+PV+ and *Pcdh19*+PV- cells with respect to the total number of *Pcdh19* mRNA expressing cells. (E) Quantification of the %PV+*Pcdh19*+ and the PV+*Pcdh19*- cells with respect to the total number of PV expressing cells. Data presented as mean ± SEM. WM, white matter. Cortical layers are designated by roman numerals in the representative images. Dashed line delimits the brain. White arrows indicate *Pcdh19*+PV+ cells, white arrowheads highlight *Pcdh19*+PV- cells and white open arrows designate the *Pcdh19*-PV+ cells. Scale bar: 100 μm.

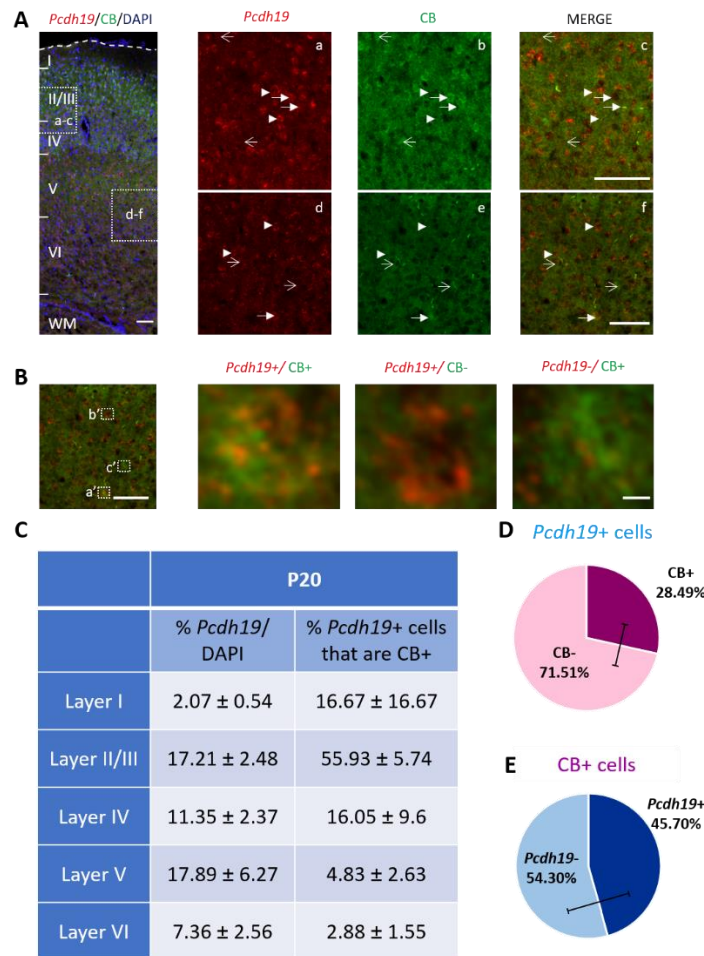


Figure 23. *Pcdh19* mRNA-positive cells partially coexpress calbindin in P20 SSC, especially in layers II/III.

(A) Representative pictures of ISH+IHC experiments conducted to detect *Pcdh19* mRNA and calbindin positive cells in the SSC area of P20 mice. *Pcdh19* is indicated in red, CB+ cells are shown in green and DAPI is in blue colour. Layers II/III (a, b, c) and V (d, e, f) are shown at higher magnification. (B) Double positive (a'), *Pcdh19*+ (b') and CB+ (c') cells from layer V are shown at higher magnification. (C) Table displays the %*Pcdh19*+ cells with respect to DAPI per layer, and the % of *Pcdh19*+ cells that also express in each layer. (D) Quantification of the %*Pcdh19*+CB+ and *Pcdh19*+CB- cells with respect to the total number of *Pcdh19* mRNA expressing cells (E) Quantification of the %CB+*Pcdh19*+ and CB+*Pcdh19*- cells with respect to the total number of CB expressing cells. Data presented as mean ± SEM. WM, white matter. Cortical layers are indicated by roman numerals in the representative images. Dashed line designates the limit of the brain. White arrows highlight *Pcdh19*+CB+ cells, white arrowheads show *Pcdh19*+CB- cells and white open arrows indicate the *Pcdh19*-CB+ cells. Scale bar: 100 µm.

3.4 Discussion

3.4.1 Summary of results

Characterisation of cortical *Pcdh19* expression during late embryonic and early postnatal stages was carried out using RNA *in situ* hybridisation due to the lack of suitable antibodies. *Pcdh19* is expressed primarily in layers II/III and V, a pattern that becomes clearly visible from P10 onwards, once the radial migration of cortical projection neurons is finished. However, *Pcdh19* is not only expressed by excitatory neurons in the cortex, but also by different types of interneurons, as demonstrated by combining RNA ISH for *Pcdh19* with IHC against different markers. This is of particular interest because it reveals that *Pcdh19* is not involved in the cortical development of just one or a few neuronal subtypes, but probably exerts its function in subsets of neurons that belong to a wide range of populations.

3.4.2 Choice of methods

The combination of IHC and ISH to characterise *Pcdh19*⁺ cells poses several challenges. The aggressive pre-treatment conducted to detect the target mRNA can alter epitopes in the proteins studied and block the binding of the antibody (Lopez 2014). Moreover, some antibodies cannot detect their epitopes in frozen samples, which was the type of samples used in ISH to cut thinner slices with the cryostat and detect the mRNA. This procedure also kills the GFP fluorescence, which is sensitive to the cell permeabilization and high temperatures required (Donadoni et al. 2004).

As shown in **section 3.3.1**, PCDH19 protein couldn't be detected using antibodies, thus only *Pcdh19* mRNA could be located by *in situ* hybridization of antisense probes for *Pcdh19*. However, mRNA and protein expression don't always correlate quantitatively or spatially, a phenomenon that has been described in several reports. Differences have been seen in the expression levels of proteins with respect to their mRNA due to the diversity of translation rates and post-translational modifications that alter

the half-life of the protein (Vogel et al. 2012; Y. Liu et al. 2016; Ghazalpour et al. 2011), and also in the location of the protein caused by the protein synthesis, half-life and transport. As protein synthesis takes time, changes in mRNA expression levels would affect protein levels with a certain delay in time; protein and mRNA half-lives might also differ. Consequently, variations in the quantity of mRNA expression might not be accurately reflected in the proteinic expression, and many proteins are transported to different locations within the cell, thus the spatial pattern of mRNA expression will, in many cases, not correspond to the protein pattern (Y. Liu et al. 2016). Recently, Moritz *et al.* also revealed that the anatomical and molecular polarity of neurons in the CNS is also one of the causes of low correlation between mRNA and protein expression. These differences are specially prominent in proteins involved in transport and in synaptic proteins (Moritz et al. 2019). Interestingly, PCDH19 has been found in the spines of chick and mouse hippocampal (Pederick et al. 2016; Hayashi et al. 2017) and cortical neurons *in vitro* (Hayashi et al. 2017).

It is to be noted that a *Pcdh19*^{HA-FLAG} mouse has been generated and validated by Pederick *et al.* (Pederick et al. 2018). Although protein expression in the brain was consistent with the *in situ* hybridisation data previously published, judging from the images available for a staining with anti-HA antibody at P7, this strategy does not look suitable for cell characterization, since it also does not allow the identification of individual PCDH19+ cells.

A potential solution to overcome the difficulties posed by both mRNA and protein detection in the characterisation of PCDH19 expressing cells would be to generate a nuclear EGFP mouse reporter strain (Stoller et al. 2008). Such a reporter would highlight the nucleus of PCDH19-expressing cells, preventing an investigation of the subcellular localization of the protein, but allowing detection of individual *Pcdh19*-expressing cells accurately. Since the fluorescence would be nuclear, it would overlap with the fluorescence

of the cortical molecular markers studied when immunohistochemical experiments were conducted. The fact that GFP fluorescence might be affected by antigen retrieval methods should be considered, because any molecular markers that can only be detected after antigen retrieval could be difficult to analyse. However, tests conducted in the Martinez-Garay laboratory have shown that detection of GFP by IHC works after short antigen retrieval (no longer than 10 min). Thus, so far, all of the markers studied in this thesis could be analysed (**section 2.3.3.2**) using this transgenic animal.

3.4.3 *Pcdh19* mRNA localization

Regarding the *Pcdh19* expression pattern, results in this chapter revealed that *Pcdh19* mRNA was detected at all ages in the cortex, but the expression pattern varied between the ages and also along the anterior-posterior and lateral-medial axes of the brains at some ages. Different expression in different areas of the cerebral cortex is not unusual, since this region of the brain is organised in different areas that perform a varied range of functions and have a different cellular composition (Lodato et al. 2015).

With respect to the age-dependent changes in *Pcdh19* expression, mRNA was detected in the cortical plate at E16.5, when neurogenesis of glutamatergic neurons is almost finished, and the migration of cortical neurons is in process (Nadarajah et al. 2001). By P2, expression was evident in a strong band that, according to its position within the cortical plate, would correspond to layers IV/V, whose neurons have finished migration and are starting to establish synaptic connections (Nadarajah et al. 2001). The pattern was similar at P6, when all glutamatergic neurons have almost finished migration (Farhy-Tselnicker et al. 2018). At P10, when migration of excitatory neurons is completely finished, two bands of expression could clearly be seen, one in layer II/III and a stronger one in layer V (Farhy-Tselnicker et al. 2018). These bands were clearly visible at P15 and P20 too, even though with a lower intensity. Therefore, *Pcdh19* seems to be

expressed both by cells that are undergoing migration and those establishing cortical circuits, suggesting a role for the protein in these two processes.

With regards to the expression of *Pcdh19* in specific cortical layers, one open question is if cells from layer II/III express *Pcdh19* from the beginning or if they do not start expressing *Pcdh19* mRNA until after P6. Earlier expression could be masked at earlier stages by a positional overlap during their migration with the already migrated layer V neurons that express *Pcdh19*. However, the wide expression of *Pcdh19* in the cortical plate at E16.5, when layer II/III neurons are starting migration, and the detection of *Pcdh19*⁺ cells in the intermediate zone at P2 (even if less intense), suggest that the mRNA is present in at least part of layer II/III neurons while they are migrating. In fact, combination of ISH to detect *Pcdh19* mRNA and IHC against SATB2 at P2 shows expression of *Pcdh19* in a zone of migrating cells. This observation shown in **Figure 24** also supports this hypothesis. To confirm this hypothesis, BrdU pulses could be given at E15.5 to label the cells born at that age that correspond to upper-layer neurons, and then conduct the ISH at P2, and analyse if the BrdU positive cells express *Pcdh19*.

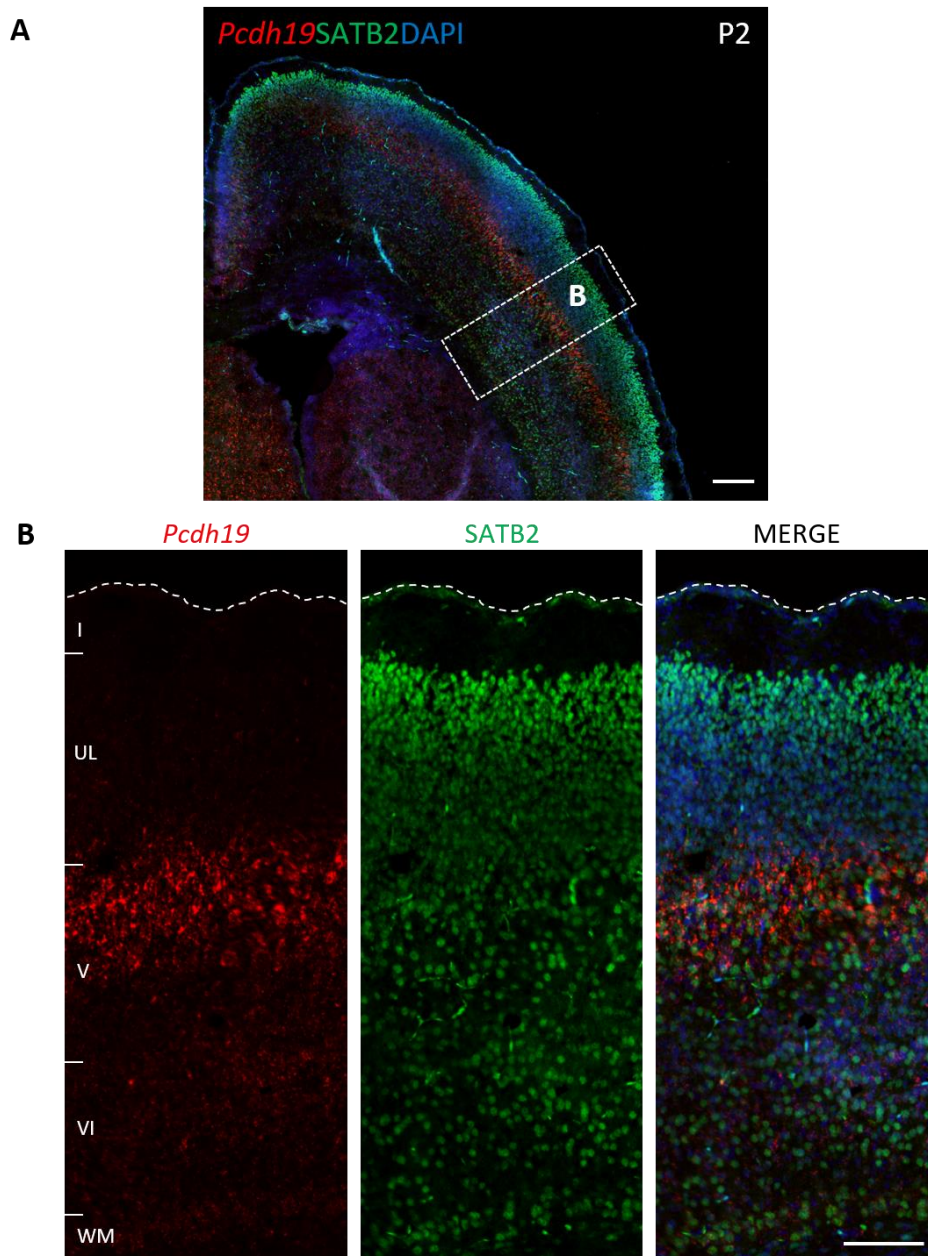


Figure 24. *Pcdh19* mRNA-positive cells partially colocalise with SATB2 expressing cells at P2 in mice.

(A) Representative images of P2 ISH combined with IHC that detected *Pcdh19* and SATB2. *Pcdh19* is shown in red, SATB2 cells are in green, and DAPI counterstaining is in blue. (B) Magnification of an area from A. WM, white matter; UL, upper layers; V, layer V, VI, layer VI. Dashed line indicates the limit of the brain. Scale bar: 200 μm , in magnified images: 100 μm .

To confirm if these upper-layer cells express *Pcdh19* before migration is finished, combination of ISH to detect *Pcdh19*⁺ expression and IHC against an upper-layer marker, such as CUX1 at P2 and P6 could be conducted. If

Pcdh19 mRNA co-localised with the marker, the theory would be validated. Unfortunately, the harsh conditions of the ISH made the detection of CUX1 impossible and attempts to make a probe to hybridise the marker and conduct double ISH to detect *Pcdh19* and *Cux1* were also unsuccessful so far. Thus, the generation of another probe for *Cux1* or the use of other upper-layer marker that is also expressed in cortical development, such as CUX2 or LHX2, whose antibody were compatible with IHC and resists the harsh conditions of the ISH, would be necessary to conduct this experiment (Bulchand et al. 2003; Nieto et al. 2004).

Moreover, cells from layer II/III are mainly callosal projection neurons, while the majority of cells located in layer V project subcerebrally; so *Pcdh19* seems to be expressed by different neuronal subtypes.

A decrease in the intensity of the fluorescence when detecting *Pcdh19* mRNA at P15 and P20 with respect to P10 was also observed in the ISH experiments. A stronger expression around P10 and a posterior reduction in the level of transcript could suggest a role of *Pcdh19* in processes that are very prominent during the second postnatal week, just after migration is finished, and decrease after that age, such as gliogenesis or synaptogenesis (Semple et al. 2013). However, variations in the perfusion or fixation of the brains, or the use of thicker slices of tissue could also have an impact on the detection of the mRNA. In fact, when the concentration of probe was increased the labelling became more intense in the P15 and P20 brains. To determine if the changes in fluorescence intensity were due to technical issues, a qPCR experiment was performed that showed a slight decrease in *Pcdh19* expression in P15 and P20 with respect to the P10 cortices. This result suggests that the reduction is not due to a technical problem.

3.4.4 *Pcdh19* colocalization with cortical excitatory and interneuronal markers

As shown in **section 3.3.3**, *Pcdh19* mRNA partially co-localises with all markers studied in the SSC. The SSC area was selected to perform these

experiments since it is an area that has been well-studied and widely used for experiments regarding cortical lamination (Jabaudon et al. 2012; Leone et al. 2015; Wang et al. 2017; M. Chang et al. 2018). However, other areas, such as the motor cortex, also express *Pcdh19* mRNA, and their analysis might be of interest, since, as explained in **section 3.3.2**, *Pcdh19* expression varied from medial to lateral areas within the same slice. This medial part of the cortex corresponds to the motor cortex, an area with different cytoarchitecture and function (Lodato and Arlotta, 2015), so *Pcdh19* could be involved in processes that are unique to this area, functionally different to the SSC. Following the same reasoning, the analysis in other parts of the brain, such as the hippocampus, where *Pcdh19* was strongly detected in these results, would help to gain further insight into the role of *Pcdh19* in the central nervous system.

The different molecular markers that were chosen to characterise *Pcdh19* expressing cells in the cortex cover different principal types of excitatory and inhibitory neurons and were described in **section 3.1**.

PV and CB only detect about 55% of the rodent cortical interneurons, but any attempts to optimise other antibodies against interneuronal markers, such as 5HT3aR, SST or CR, were not successful either. As with CUX1, finding antibodies compatible with the ISH process would be necessary to complete the characterisation. Another possibility would be to detect *Pcdh19*-expressing cells in another way, such as the generation of a PCDH19-nGFP reporter mouse strain, as described in **section 3.4.2**, that would allow the cell characterization using double immunohistochemistry.

When analysing the cortical glutamatergic markers, it was observed that almost 50% of the total *Pcdh19*⁺ cells were SATB2⁺ and this percentage was similar all the layers, except I and VI. This result establishes that a big percentage of *Pcdh19*⁺ are callosal projection neurons that are located in the different layers.

The percentage of *Pcdh19*⁺ cells expressing the other molecular markers (RORB, CTIP2 and TBR1) was not as high. Less than 20% in the case of RORB and TBR1, and less than 30% in the case of CTIP2. As expected, the layer with the highest percentage of double positive cells for each of the markers corresponded with the layer of higher expression of the marker: layer IV in RORB, layers V and VI in CTIP2, and layer VI in TBR1. The analysis of RORB and CTIP2 together, however, did determine that within layer V, *Pcdh19* was located mainly in sublayer Va, with a weaker expression in the upper part of layer Vb (**Figure 21**). Layer Va mainly contains medium-sized pyramidal neurons, that electrophysiologically present either regular spiking or intrinsically bursting action potential firing patterns. These neurons project intracortically to the upper layers II/III and IV, and subcortically to the superior colliculus and pons (OTX1+), and they receive strong intralaminar excitatory and inhibitory inputs in rodents (Schubert et al. 2006). Layer II/III, which also presents a strong expression of *Pcdh19*, contains corticocortically projecting neurons that receive inputs from layer IV and whose main output is layer V. In the somatosensory cortex, the pathway formed by layer IV, II/III and V is known to process sensory information coming from the thalamus, and alterations in the pathway can produce behavioural disturbances (Sabri et al. 2018). Thus, *Pcdh19* could be participating in the processing of somatosensory information intracortically and also in the output of information to the superior colliculus and pons. Because PCDH19 is a cell adhesion protein, it is also possible that it could be involved in the formation of the circuit and / or the synaptic transmission between both layers. The fact that *Pcdh19* has been found in the synapses of cortical neurons *in vitro* supports this hypothesis (Hayashi et al. 2017). Regarding the pathological mechanism, it has been reported that different combinations of protocadherins can alter cell-cell adhesion (Bisogni et al. 2018). Therefore, *Pcdh19*-HET mice could have a disrupted connexion between layers due to the alterations in cell-cell interaction between the cells that express *Pcdh19* and the *Pcdh19*-KO cells, a

phenomena called cellular interference (Dibbens et al. 2008). Independently of the circuit disrupted, alterations in the network could potentially cause behavioural problems. Therefore, a basic behavioural analysis was performed in chapter 6.

To analyse *Pcdh19*⁺ cells positioned in layer Va that project corticobulbary, *Otx1*, a molecular marker that is expressed by cells located in this sublayer was selected (Hevner et al. 2003). Unfortunately, the antibody was not compatible with ISH. Trying other antibodies to see if they are compatible for ISH or using a GFP-tagged *Otx1* mouse line, like the one from Fossat *et al.* for the IHC experiments, would be interesting to try in the future (Fossat et al. 2007).

Regarding the analysis of interneuronal cortical markers, *Pcdh19*⁺CB⁺ cells were almost 30% of the *Pcdh19*⁺ cells, a big percentage of which were in layers II/III, where the subset of CB⁺ cortical excitatory neurons are positioned (DeFelipe 1997), while more than half of *Pcdh19*-expressing cells colocalised with these CB⁺ neurons.

PV positive interneurons are not very abundant in the cortex (Rudy et al. 2011), so, accordingly, the percentage of *Pcdh19*⁺ cells that were positive for PV was also small. Interestingly, more than 30% of the PV⁺ cells expressed *Pcdh19*. PV neurons are comprised by basket and chandelier cells that target the soma and the axon initial segment, respectively, of projection neurons of all cortical layers (Rudy et al. 2011). *Pcdh19* has been shown to be expressed around the nucleus of cells (Lv et al. 2019), and experiments in the Martinez-Garay laboratory to target endogenous PCDH19 by a combination of CRISPR-Cas9 and *in utero* electroporation revealed PCDH19 protein to be located around the soma. Therefore, it is possible that PCDH19 could be mediating contact between PV⁺ interneurons and *Pcdh19*-expressing cells. Interestingly, a population of CB-expressing interneurons are also basket cells that target the soma of the glutamatergic neurons, suggesting that CB⁺*Pcdh19*⁺ interneurons could also regulate *Pcdh19*

expressing glutamatergic neurons as hypothesised for PV+*Pcdh19*+ interneurons.

Although the analysis performed in this chapter was focused on neuronal populations, as mentioned previously neurons are not the only cells in the neural tissues that express *Pcdh19* (Y. Zhang et al. 2014). A discussion of other relevant cell types that could be characterised is presented in **section 7.4**. However, it is also important to mention that, given the significant number of neuronal subtypes that have been recently discovered using single-cell RNA sequencing (Zeisel et al. 2015; Tasic et al. 2016; 2018), covering all the neuronal subpopulations of the cortex by ISH-IHC would be an impossible task. Nevertheless, reanalysing already published single cell RNA-seq datasets would represent a suitable alternative in the effort to dissect the *Pcdh19*+ cell population in the cortex.

3.4.5 Conclusion

In summary, *Pcdh19* positive cells comprise a heterogeneous group of neurons including excitatory neurons projecting both within and outside the cortex, and inhibitory neurons. This diversity in the composition of the *Pcdh19*+ cell population is particularly interesting considering the role of this protein in cell adhesion. Bisogni *et al.* showed that different combinations of PCDH19 with other δ_2 protocadherins, and their relative surface expression levels can influence cell affinity and impact cell adhesion (Bisogni et al. 2018). Thus, *Pcdh19* might be expressed in different combinations with other δ_2 protocadherins in each of the subpopulations studied. Mosaicism of the protein might then cause different effects in the different subpopulations of cells, due to disturbances in cell-cell communication caused by the changes in the cell adhesion between cells that expressed PCDH19 and cells that did not within their δ_2 protocadherin combinatorial expression. This model would fit with the 'cellular interference' hypothesis that is proposed to underpin the symptoms of EIEE9 (Dibbens et al. 2008).

Chapter 4: Role of Protocadherin 19 in cortical migration.

4.1 Introduction

As previously stated, the role of Protocadherin19 in mammals remains unknown. However, a neurofilament protein immunohistochemistry experiment conducted on a biopsy from a patient affected with EIEE9 revealed areas of cortical dysplasia, with the presence of abnormal neurons in the white matter and cortical neurons of abnormal morphology located in the frontal-lobe of the subject (Dibbens et al. 2008). Cortical dysplasia is characterised by a disorganised lamination in the cortex and cells with abnormal morphology (Taylor et al. 1971). Thus, this finding suggested Protocadherin19 might be required for cells to migrate and achieve their correct position in the cortical layers.

Other studies also support this hypothesis. For example, previous reports observed that cells transfected with *Pcdh10* (Taylor et al. 1971) or *Pcdh17* (Nakao et al. 2008) increased their migration compared with non-transfected cells. Both proteins belong to the δ -2 subfamily of protocadherins. Emond *et al.* (2011) also revealed that Protocadherin19 interacts with Cadherin2 *in vitro*, and Biswas *et al.* (2010) demonstrated this interaction exists *in vivo* in zebrafish (Emond et al. 2011; Biswas et al. 2010). *Cdh2* is known to be involved in glia-independent somal translocation (Franco et al. 2011; Gil-Sanz et al. 2013) and glia-guided migration (Kawauchi et al. 2010; Jossin et al. 2011; Martinez-Garay et al. 2016). A paper from Chen *et al.* (2014) also showed that PCDH19 contains a WIRS region that binds to the WRC. This complex participates, together with Arp2/3, in actin nucleation, which is important in cell division and migration (B. Chen et al. 2014). Recently, Pederick *et al.* (2016) reported an increase in neuronal migration of *Pcdh19*-KO cells compared to their WT counterparts in assays performed with neurospheres too (Pederick et al. 2016).

In addition, Allen Brain Atlas ISH data show *Pcdh19*-expressing cells at the cortical plate at E13.5 and E15.5, an expression pattern consistent with a role in migration. As seen in **Figure 9**, there is also expression of *Pcdh19* in the cortical plate at E16.5, supporting those findings. Moreover, the data from the Allen Brain Atlas (Miller et al. 2014) also shows *Pcdh19* expression is strong in humans at 15 and 16 weeks post-conception, when neurons are being generated and are migrating from the ventricular zone (Lenroot et al. 2006).

4.2 Aims

The main aim of this chapter was to explore the role of Protocadherin19 in migration, performing several *in utero* experiments on mice. For this purpose, WT mice were electroporated with *Pcdh19* shRNAs to knockdown the *Pcdh19* gene and an EGFP reporter to locate the electroporated migrating cells. Two different time-points (E13.5 and E15.5) were selected in which to perform the electroporations to target the two neuronal populations that express PCDH19 in the cortical plate (layers Va and II/III). To exclude that the results obtained were due to an shRNA off-target effect (Song et al. 2015), it was aimed to perform the same experiments on *Pcdh19*-KO mice. To study the migration in brains that had their *Pcdh19* gene altered from conception, *Pcdh19*-WT, *Pcdh19*-HET and *Pcdh19*-KO animals were electroporated with EGFP at E13.5 or E15.5.

4.3 Results

4.3.1 *Pcdh19* shRNAs effectively knockdown PCDH19

Prior to assessing the effect of the *Pcdh19* shRNAs in cell migration, it was first necessary to confirm their efficiency. Quantification of PCDH19 at the protein level was performed by western blot analyses in cells treated with non-targeting shRNA or shRNA against *Pcdh19*.

The HEK293T cell line was used for these experiments as it was available in the laboratory and it produces significant amounts of protein when transfected. *PCDH19* was detected by PCR in these cells, as seen in **Figure 25**. However, HEK293T cells originally derive from human embryonic kidney cells, so they express human PCDH19. The shRNAs in this study were designed to reduce the expression of mouse PCDH19, since the aim was to electroporate those shRNAs *in utero* and analyse cortical migration in the mouse. A comparison of the target regions for the different shRNAs between the murine and human mRNA sequences showed several mismatches (**Figure 26**), suggesting that most probably the shRNAs will bind to the mouse *Pcdh19* mRNA and not the human homolog. However, Jackson *et al.* showed that shRNAs could produce off-target effects by binding genes with similar sequences (Jackson et al. 2003). Consequently, it could not be ruled out completely that the mouse shRNAs might potentially reduce human PCDH19 protein levels as well. Therefore, to test the effectiveness of the shRNAs unequivocally on the mouse sequence, HEK293T cells were co-transfected with shRNAs and a construct containing mouse *Pcdh19*.

To assure western blot analysis only reflected knockdown of the transfected mouse *Pcdh19*, a tag was added to the *Pcdh19*FL during the generation of the construct. Two constructs were generated: CMV-*Pcdh19*-HA and CMV-*Pcdh19*-myc. As described in **Figure 27**, CMV-*Pcdh19*-HA was generated by amplifying *Pcdh19*FL from plasmid DCX-*Pcdh19*FL using the primers and

protocol depicted in **Table 12 (section 2.4.3, materials and methods)**. The PCR product was cloned into vector CMV-HA (provided by Dr Isabel Martínez Garay, Cardiff University), using enzymes HindIII and Bstz17I and T4 DNA ligase (detailed in **section 2.4.3**). 2 out of 6 clones obtained after transformation showed the expected pattern after digestion with *XcmI*. Further sequencing confirmed colony 1 presented no mutations and a maxiprep was conducted to amplify the vector quantity. **Figure 27** depicts the construction of CMV-*Pcdh19*-HA, but the generation of the other plasmid followed a very similar protocol.

Prior to transfecting with the tagged constructs, transfections with a pCIG reporter using different reagents (Calcium phosphate 1 M diluted in HEPES saline buffer (HeBS) and Lipofectamine 2000) were performed to optimise transfection efficiency (protocol shown in **section 2.4.3 of materials and methods**). Results showed the highest rate of transfection when Lipofectamine 2000 was used, thus this was the reagent selected for all transfections.

After optimisation of the reagents, tagged constructs were transfected into HEK293T cells, which were lysed 24 h post-transfection, and their protein analysed by immunoblotting with commercial antibodies (**Table 15 in materials and methods section**). Since the anti-HA antibody performed better in western blot experiments than the anti-myc antibody, the HA-tagged construct was used in the co-transfection experiments (**Figure 28A**).

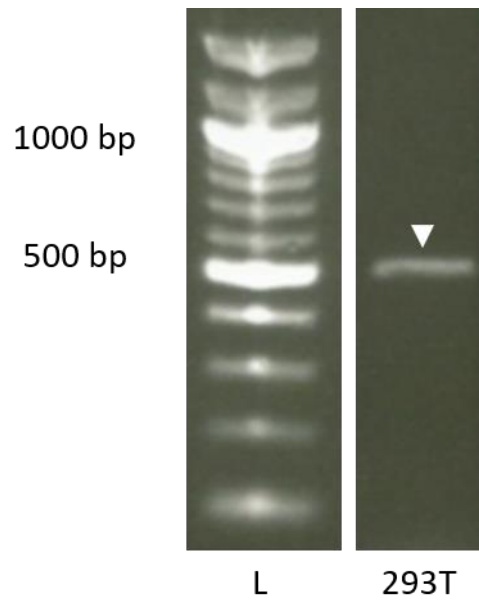


Figure 25: HEK293T cells express the human *PCDH19* gene.

Agarose gel (1%) electrophoresis of PCR products from HEK293T lysates. The band detected at approximately 500 bp corresponds to the expected amplicon which demonstrates that HEK293T cells express the gene. Band is indicated by a white arrowhead. bp, base pairs; L, ladder; 293T, HEK293T lysate.

<u><i>hPcdh19</i></u>	3441	GT T GT CA AGGCAGAA AGACTAC	3461
<u><i>mPcdh19</i></u>	3487	GTAGTTAAGGCAGACGATTAT	3507
<u><i>shRNA#2</i></u>	52	CATCAATTCCGTC TGCTAATA	32
<u><i>hPcdh19</i></u>	2712	ATCAACCT G CTGT CA GTCA CA	2733
<u><i>mPcdh19</i></u>	2758	ATCAACCTCC TGTCCGGTCAATA	2779
<u><i>shRNA#3</i></u>	53	TAGTTGGAGGACAGCCAGTTAT	32
<u><i>hPcdh19</i></u>	3638	CT CTG CTCT CG TCC TAAT CTAC	3659
<u><i>mPcdh19</i></u>	3684	TTCTGCCCTTGTCC TAATATAC	3705
<u><i>shRNA#5</i></u>	52	AAGACGGGAACAGGATTATATG	31
<u><i>hPcdh19</i></u>	3508	GACCG CGGCT TTC TTT GAA AATA	3528
<u><i>mPcdh19</i></u>	3553	GACCGAGGTTTC TTC GAA AATA	3573
<u><i>shRNA#6</i></u>	52	CTGGCTCCAAAGAAGCTTTAT	32

Figure 26: Sequence alignment of the binding regions of the mouse *Pcdh19* shRNAs#2, #3, #5 and #6 from Sigma with mouse and human *Pcdh19* gene.

Mouse *Pcdh19* gene and *Pcdh19* shRNAs showed a 100% nucleotide identity, while human *PCDH19* gene diverged in 3-5 nucleotides from the *Pcdh19* shRNAs. Alignments performed with Basic Local Alignment Search Tool (BLAST; Altschul *et al.*). shRNAs sequences were obtained from the Sigma-Aldrich webpage; *mPcdh19* sequence: ENSMUST00000149154.7; *hPcdh19* sequence: ENST00000373034.8. Letters in red show missalignments between sequences, numbers on the right and left of the sequence show, in base pairs, the location of the sequence aligned. *hPcdh19*, human Protocadherin 19; *mPcdh19*, mouse Protocadherin 19; shRNA, short haipin ribonucleic acid.

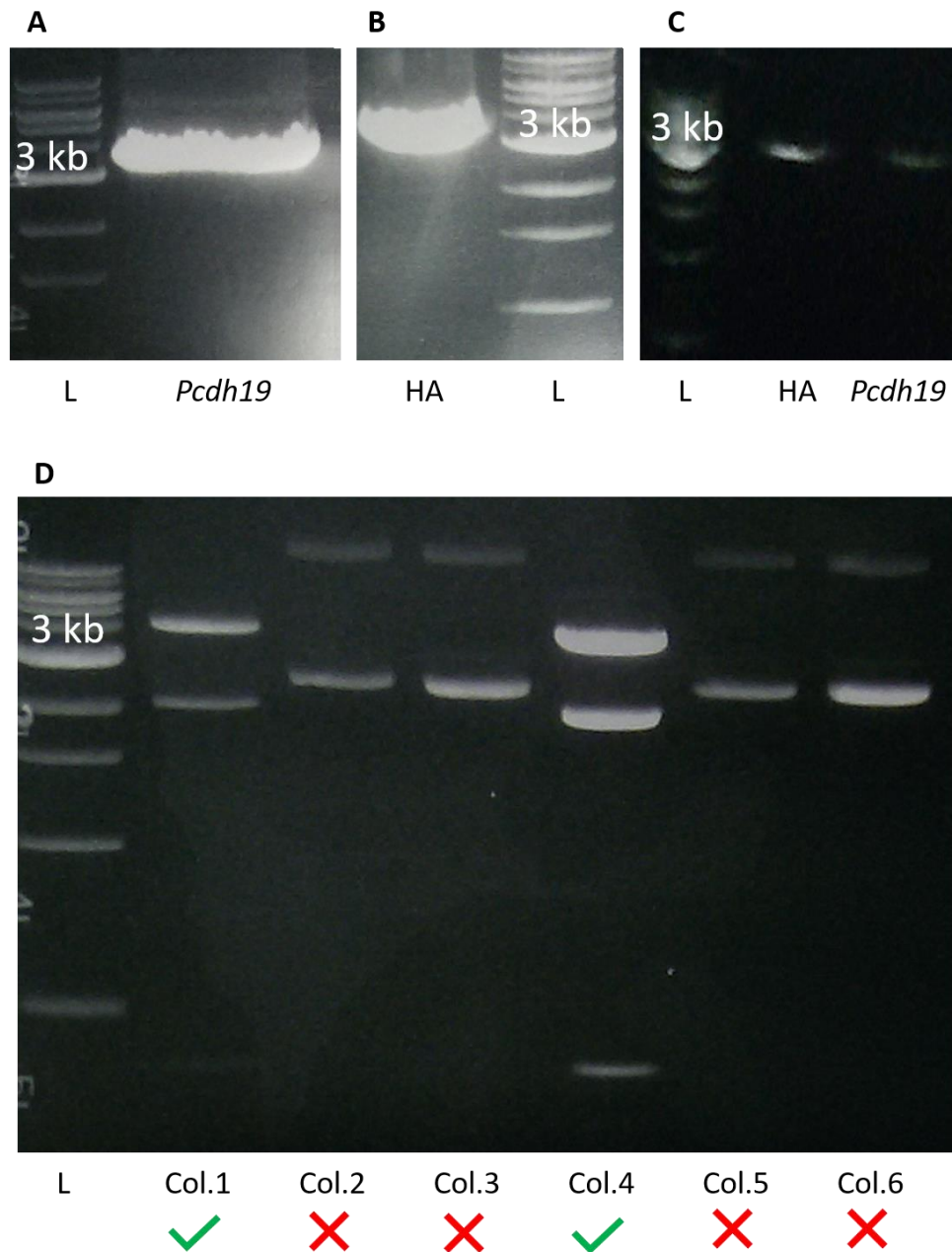


Figure 27. CMV-*Pcdh19*-HA construct generation.

(A) PCR product corresponding to the *Pcdh19* insert sequence with an added HindIII restriction site and a blunt end. (B) pCMV-HA digested with HindIII and Bstz17I. (C) After extraction and purification of both bands, the *Pcdh19* insert was digested with HindIII and purified again. Then, an electrophoresis with sample of both sequences was performed to detect the relative concentration between them. (D) *Pcdh19*-HA minipreps digested with *Xcm*I. Colonies 1 and 4 presented the 4193 bp, 2119 bp and 1717 bp bands that correspond to the CMV-*Pcdh19*-HA vector. L, ladder; kb, kilobases; *Pcdh19*, protocadherin 19; HA, CMV-HA vector; col., colony.

Five shRNAs against *Pcdh19* (#2, #3, #4, #5, #6) were purchased but only four were transfected into HEK293T cells. ShRNA#4, as shown in **section 2.4.1** from the materials and methods chapter, binds to the 3'UTR of the *Pcdh19* gene, while the other shRNAs bind to exon 1. The 3'UTR region of the gene is not contained in the mouse CMV-*Pcdh19*-HA construct, generated from an already available *Pcdh19FL* insert that did not contain the 3'UTR. Therefore, and considering the availability of four other shRNAs against *Pcdh19*, shRNA#4 was discarded since it cannot bind to the construct, making it more difficult to test its efficiency.

Cells were lysed at 24-, 48- or 72-hours post-transfection to determine how fast the shRNAs were able to decrease protein levels and whether the decrease of the protein was maintained over time. Three independent transfections were performed to conduct the analysis.

To perform the western blot, the gel was loaded with 20 μ g of protein to avoid saturation. Ponceau red, a reversible stain that detects protein bands, was used to confirm the transfer and detect any issues, such as saturation or bubbles in the region that was being analysed. To block the membrane to avoid unspecific binding, incubations were done with a BSA-ECL immunoblock for at least an hour. Other blockings, using only BSA or milk were tested, but the BSA-ECL mix gave the best detection results. Signal was detected using fluorescence or chemiluminescence. Detection of the chemiluminescent signal was clearer, so the membrane was developed using chemiluminescence. To analyse the western blot experiments, densitometric analysis was performed using Fiji Image J Analysis Software, as depicted in **Figure 28A** and detailed in **section 2.4.7**.

At 24-hours post-transfection, all *Pcdh19* shRNAs reduced the PCDH19 protein levels compared to the shRNA control (**Figure 28B, C**): shRNA#2 a $62 \pm 11.47\%$; shRNA#3 an $82.3 \pm 5.27\%$; shRNA#5 an $81.6 \pm 8.47\%$, and shRNA#6; a $76.8 \pm 1.57\%$. At 48-hours post-transfection, shRNA#2 and shRNA#5 showed similar decreases as after 24-hours ($69.7 \pm 14.81\%$ and

81.5 ± 6.71% respectively), shRNA#3 was still effective and the PCDH19 quantity was 72.9 ± 10.46% less than the control, and shRNA#6 decreased the protein quantity by at least 89.3 ± 5.25%, even more than that seen at 24-hours. At 72-hours post-transfection, all *Pcdh19* shRNAs produced a significant reduction of PCDH19 levels with respect to the shRNA control, slightly increasing the reduction seen at 48-hours post-transfection. Specifically, shRNA#2 decreased the protein level in comparison to the control a 72.2 ± 9.03%; shRNA#3 an 83.6 ± 7.88%; shRNA#5 an 84.4 ± 1.44%, and shRNA#6; a 93.3 ± 2.11%.

Also, to verify that the shRNA control was not affecting PCDH19 protein quantity, the experiment previously described was performed but transfecting only the CMV-*Pcdh19*-HA plasmid, or the tagged construct and the shRNA control and comparing PCDH19 protein levels of both transfections by western blot of the lysates at 24-h, 48-h and 72-h. As before, three independent transfections were conducted to perform the analysis. Results (**Figure 29**) revealed that at 24-hours (*Pcdh19*FL-HA=1 ± 0.21% and shRNA control= 0.78 ± 0.38%) and 72-hours (*Pcdh19*FL-HA=1 ± 0.12% and shRNA control= 0.47 ± 0.23%) post-transfection the quantity of PCDH19 did not decrease significantly between the cells transfected with the tagged construct only and the ones co-transfected with the shRNA control. At 48-hours, the level of protein when only the *Pcdh19*FL-HA was transfected was higher than when this construct was co-transfected with the shRNA control (*Pcdh19*FL-HA=1 ± 0.39% and shRNA control= 0.25 ± 0.04%). However, the variability in the quantity of protein detected at 24-, 48- and 72- hours post-transfection in the cells that only received the *Pcdh19*FL-HA was very high. This will be commented in the discussion at the end of the chapter (**section 4.4.2**).

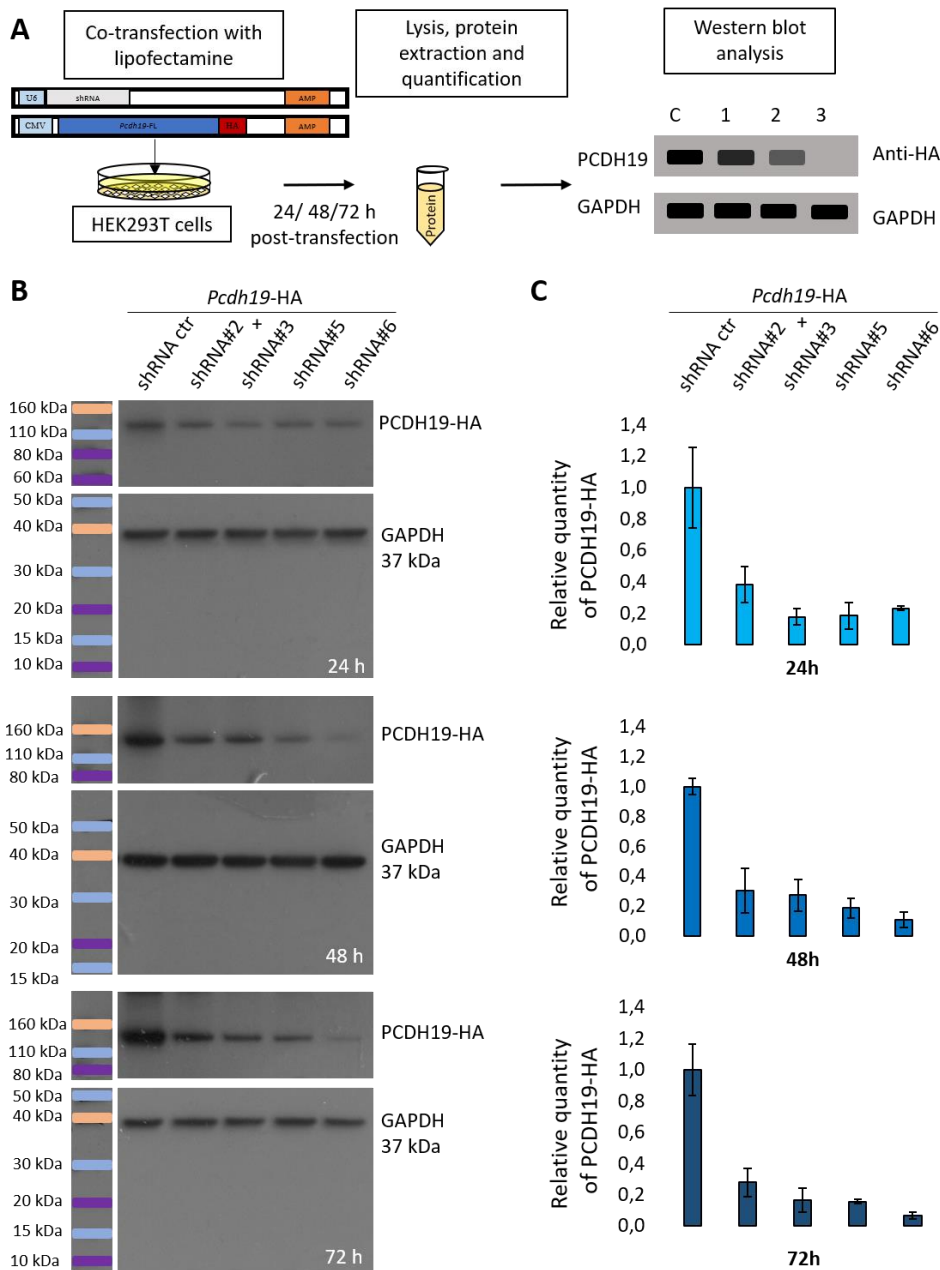


Figure 28: Assessment of gene knock-down by *Pcdh19* shRNAs.

Western blots detecting PCDH19-HA expression in HEK293T cells co-transfected with *Pcdh19*-HA and shRNAs. Schematic illustrating the transfection and western blot analysis (A). Western blot analysis (B) and quantification (C) at 24, 48 and 72-hours post-transfection. 20 μ g of protein was loaded per lane. An anti-HA antibody detected the tagged-PCDH19 band between 110 and 160 kDa. GAPDH (37 kDa) was used as a loading control. *Pcdh19* shRNAs significantly reduce PCDH19-HA protein quantity compared to the shRNA non-silencing control *in vitro*. shRNA ctr, shRNA control.

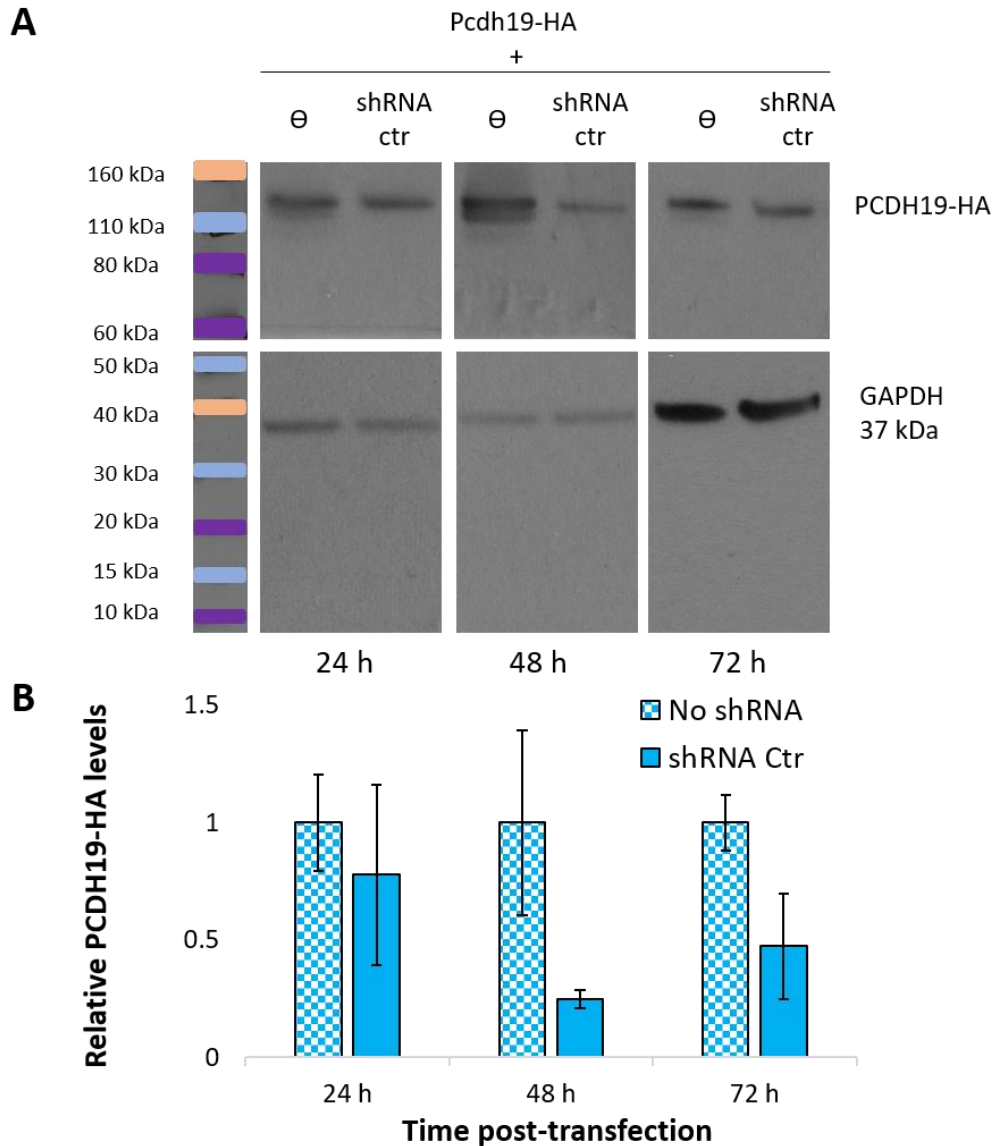


Figure 29. ShRNA control appears to reduce the quantity of PCDH19 protein at 48 hours.

Western blots detecting PCDH19-HA levels in HEK293T cells transfected with *Pcdh19*-HA or co-transfected with *Pcdh19*-HA and the shRNA control. Western blot analysis (**B**) and quantification (**C**) at 24, 48 and 72-hours post-transfection. 20 μ g of protein was loaded per lane. An anti-HA antibody detected the tagged-PCDH19 band between 110 and 160 kDa. GAPDH (37 kDa) was used as a loading control. shRNA ctr, shRNA control.

4.3.2 Analysis of cortical migration at E13.5

The aim of this section was to determine whether PCDH19 had a role in the cortical migration of early born neurons in mice. To achieve it, *Pcdh19* shRNAs were electroporated *in utero* to acutely knockdown *Pcdh19* at E13.5 and analysis of the electroporated cells was performed at E18.5. The migration of WT, *Pcdh19*-HET and *Pcdh19*-KO animals that have the *Pcdh19* gene altered from conception was also studied by *in utero* electroporating a pCIG reporter at E13.5 and analysing at E18.5.

4.3.2.1 *Pcdh19* knockdown by shRNAs at E13.5 did not show any differences in migration with respect to the control

WT embryos were *in utero* electroporated at E13.5 with 0.5 μ L pCIG plasmid or with pCIG and 1 μ g/ μ L of one shRNA. Electroporation of only the pCIG reporter was also performed to identify any off-target effects from the shRNA control. Specifically, no significant difference in cell migration analysis should be seen between pCIG-only electroporated brains and brains co-electroporated with both pCIG and the non-targeting shRNA.

To be able to analyse the effect of each shRNA individually, animals was electroporated with pCIG, or pCIG and one of the four shRNAs described previously. Due to the high number of plasmids that had to be electroporated, two different sets of electroporations were performed, I and II, as shown in **Figure 30A**. In electroporation I, WT embryos were electroporated with either pCIG, pCIG + shRNA control, pCIG + shRNA#2 or pCIG + shRNA#3. In electroporation II, pCIG, pCIG + shRNA control, pCIG + shRNA#5 or pCIG + shRNA#6 were electroporated into the E13.5 embryos. Each of the two experiments was analysed and quantified separately.

Two electroporation time-points were chosen based on the expression pattern of *Pcdh19* in the cortical plate. The vast majority of neurons born at E13.5 will form part layer V and layer IV (Angevine et al. 1961; Sidman et

al. 1973; Bayer et al. 1991). Since, as demonstrated in **3.3.3.2**, *Pcdh19* mRNA is expressed in layer Va at P10 in mouse, depletion of PCDH19 at E13.5 could affect the migration of these cells. At E13.5 the cortical plate is very thin, and most neurons migrate from the ventricular zone to the pial surface through somal translocation. In this process cells move their nuclei within a long basal process attached to the pial surface (Nadarajah et al. 2001).

E18.5 was the age selected to extract the brains since, by then, cells from layer V should already have reached their correct positions in the cortical plate. These experiments were analysed blindly, with the plasmids electroporated into each particular brain being revealed to the experimenter only after cell counting was finished.

After extraction, as explained in detail in **section 2.3** from materials and methods, brains were fixed, sectioned coronally into 100 μm slices and counterstained with DAPI, then mounted and imaged with a confocal microscope (shown in **Figure 30C**). Four animals from at least three different electroporations were analysed for each condition, with the exception of shRNA#2 IUEs, in which only 3 animals were analysed. Animals from the same litter were treated as independent biological replicates.

Analysis was performed manually and three images from each animal were quantified. Images were taken from the isocortex at rostral, medial and caudal regions within the electroporated area. Despite the fact that the brain shows a lateromedial and rostrocaudal gradient, where migration is more advanced in the rostromedial part of the brain than in the caudomedial part (Angevine et al. 1961; J. A. del Rio et al. 1989; Caviness 1982), the small size of the brain at E18.5 makes these differences minimal. A 373 μm wide area in the area of the future somatosensory cortex (SSC) was analysed. This region was selected because it was an easily identifiable location in all selected slices that also contained one of the largest numbers of GFP+ cells. Statistical analysis was performed using SPSS Statistics software. Images

were divided into ten horizontal bins of equal width, as illustrated in **Figure 30C**, and GFP+ cells were counted for each bin. Each bin was analysed individually and taken into consideration when reaching a general conclusion.

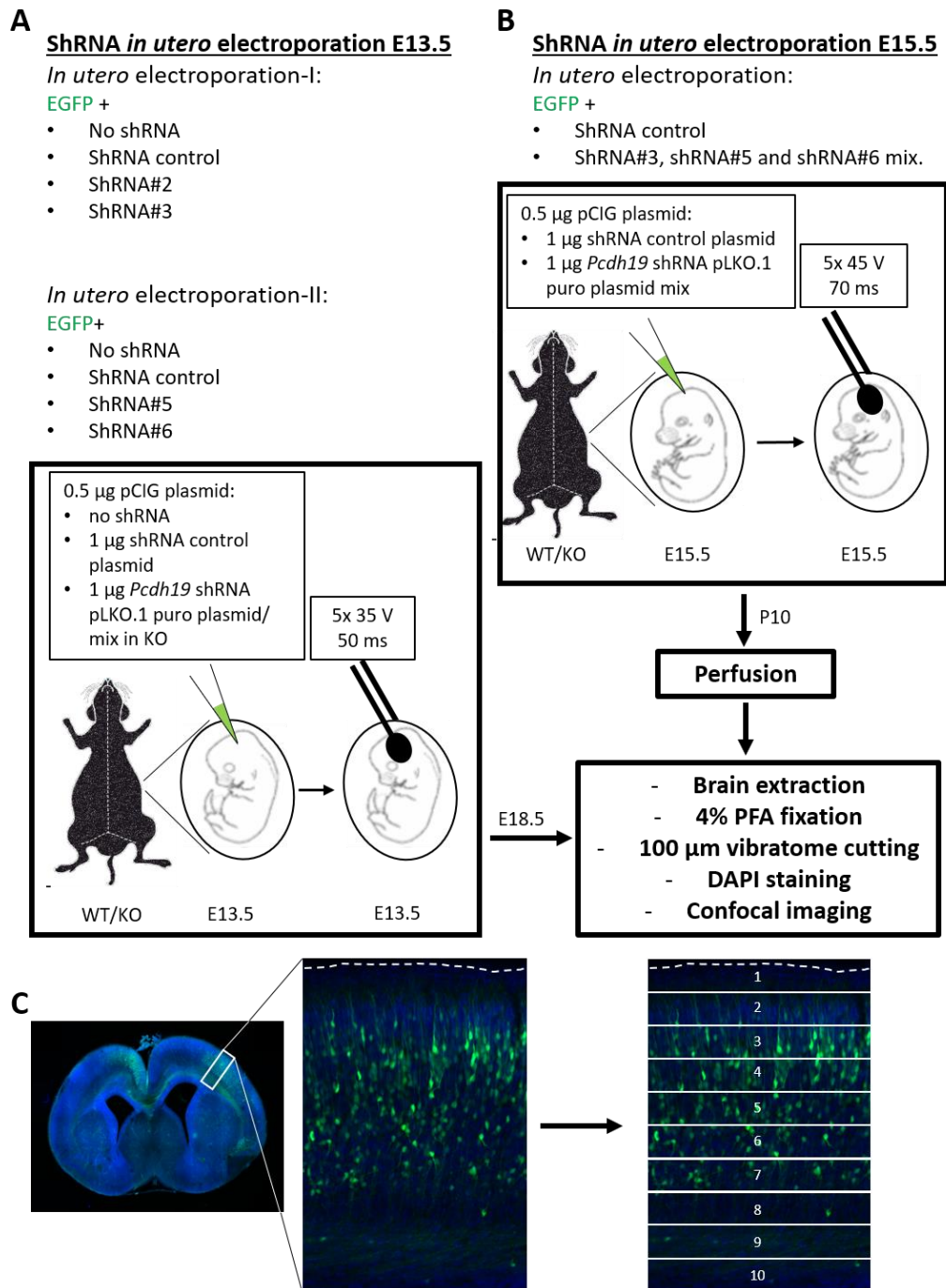


Figure 30. Illustration of the strategy to decrease PCDH19 levels by shRNA *in utero* electroporation.

At E13.5 (A), two sets of *in utero* electroporation experiments, I and II, were performed. WT or *Pcdh19*-KO embryos were electroporated at E13.5 with an shRNA control or a *Pcdh19* shRNA, and a pCIG reporter, and brains were extracted at E18.5. At E15.5 (B), brains were electroporated with the pCIG reporter, and the shRNA control or the shRNA mix; and brains extracted at P10. After processing, a section of the brain (C) was imaged and analysis was performed by dividing the section into ten bins of equal width and counting GFP+ cells for each bin.

4.3.2.1.1 ShRNA *in utero* electroporations on WT animals

WT brains co-electroporated with pCIG and shRNAs #2, #3, #5 and #6 did not show any differences in cortical migration with respect to the brains electroporated with just the pCIG reporter or co-electroporated with the pCIG plasmid and the shRNA control in the distribution of the cells within the cortical wall.

Images (**Figure 31A**, **Figure 32A**) of cortical sections of the electroporated brains illustrate that most GFP-positive cells were positioned in the cortical plate when analysed at E18.5. Quantifications of the images (**Figure 31B**, **Figure 32B**) showed that at least 76% of the electroporated cells were located between bins 2 and 6 in all conditions (pCIG = $93.85 \pm 1.31\%$ GFP+ cells; pCIG + shRNA control = $89.82 \pm 2.87\%$ GFP+ cells; pCIG + shRNA#2 = $76.06 \pm 7.93\%$ GFP+ cells; pCIG + shRNA#3 = $91.35 \pm 2.45\%$ GFP+ cells in electroporation I; pCIG = $93.66 \pm 1.1\%$ GFP+ cells; pCIG + shRNA control = $93.19 \pm 1.22\%$ GFP+ cells; pCIG + shRNA#5 = $94.07 \pm 0.86\%$ GFP+ cells; pCIG + shRNA#6 = $92.59 \pm 2.22\%$ GFP+ cells in electroporation II). Statistical analysis did not reveal any abnormalities in the distribution of electroporated cells in the brains between the different conditions.

As observed in **Figure 31B**, in bin 7 (pCIG = $5.16 \pm 1.83\%$ GFP+ cells; pCIG + shRNA control = $6.58 \pm 1.64\%$ GFP+ cells; pCIG + shRNA#2 = $12.75 \pm 1.33\%$ GFP+ cells; pCIG + shRNA#3 = $4.66 \pm 1.54\%$ GFP+ cells) there was a statistically significant difference in brains electroporated with shRNA#2 and those electroporated with just the reporter, and between the brains electroporated with shRNA#2 and those electroporated with shRNA#3 (ANOVA, $F(3, 12)=4.3$; $p=0.028$, post-hoc test Tukey HSD pCIG + shRNA#2 vs pCIG, $p=0.046$, pCIG + shRNA#2 vs. pCIG + shRNA#3, $p=0.025$).

However, significance in only 1 of the 10 bins was not sufficient to conclude that there was a difference in the distribution of the cells electroporated with shRNA#2. Even though other bins were not significantly different, the

position of the cells electroporated with shRNA#2 was slightly lower compared to the rest of the conditions. This was due to the fact that 2 out of the three brains electroporated with this shRNA presented a failure in the migration of some cells, which were positioned at E18.5 in the intermediate zone (IZ) and subventricular/ventricular zones (SVZ/VZ) forming cell clusters. The abnormal distribution is reflected in the graphic, where between bins 7-10, pCIG + shRNA#2 ($22.46 \pm 6.81\%$ GFP+ cells) contained a significantly higher number of cells than the rest of conditions (pCIG = $6.81 \pm 3.12\%$ GFP+ cells; pCIG + shRNA control = $8.05 \pm 2.23\%$ GFP+ cells; pCIG + shRNA#3 = $5.61 \pm 1.91\%$ GFP+ cells). These results will be discussed in **section 4.4.4**.

Details of the statistical analysis are shown in the appendix (**Table A. 2**, **Table A. 3**).

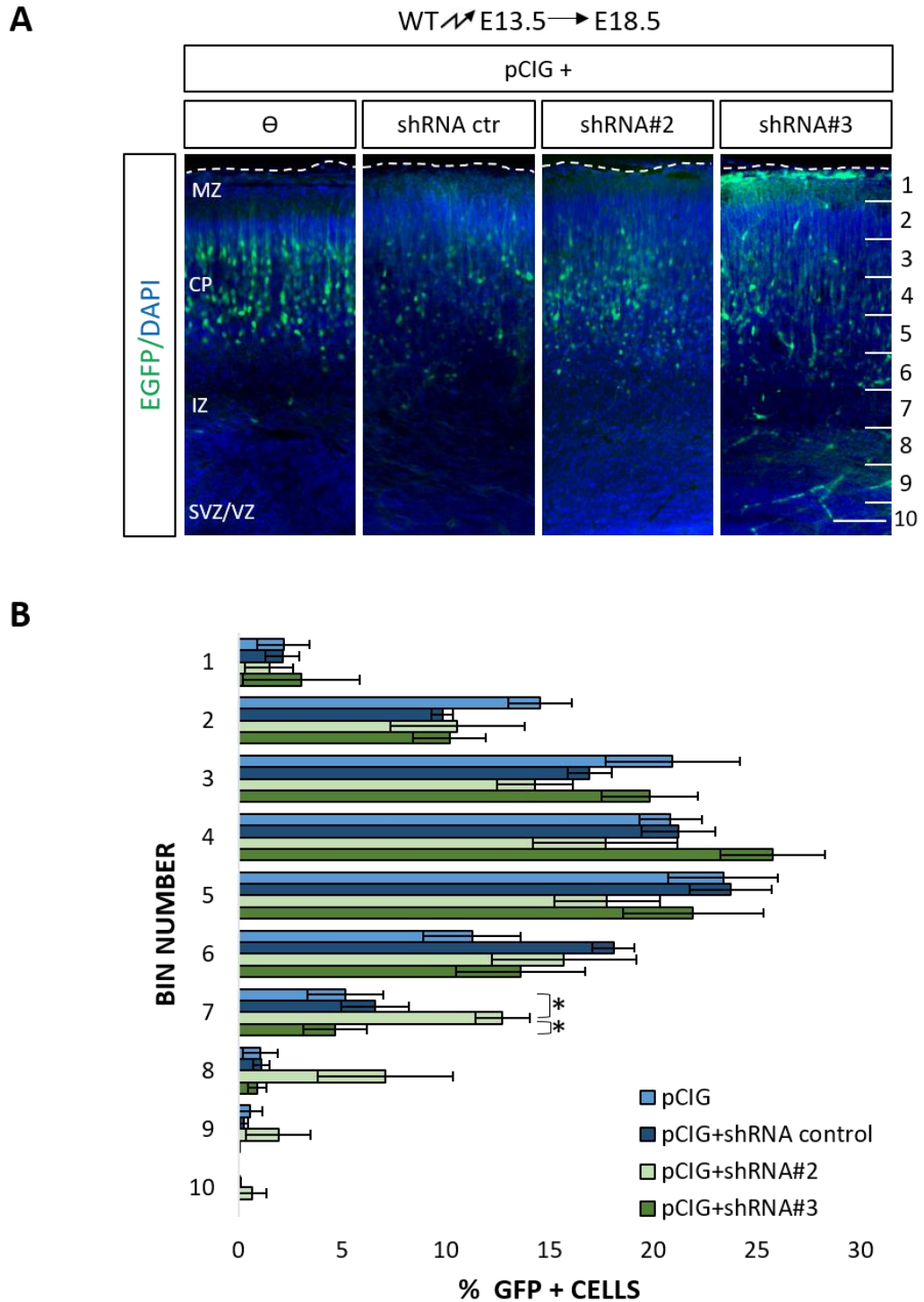


Figure 31: Reduction of PCDH19 by shRNA#3 at E13.5 does not affect migration, but the depletion by shRNA#2 does.

(A) Representative images of E13.5 *in utero* electroporated embryos analysed at E18.5. Electroporated neurons are in green. Nuclei were counterstained with DAPI (blue). Knockdown of PCDH19 does not alter the migration of deep layer neurons. (B) Quantification of the electroporated neurons from A. Graphs represent GFP+ cells in each of ten equal-size

horizontal bins expressed as % of total electroporated cells. The data are presented as mean \pm SEM. The horizontal bins used to perform the quantification are shown in arabic numerals on the right side of the image. Results, analysed by ANOVA or independent-samples Kruskal Wallis test, were only significant in bin 7 for shRNA#2 with respect to no shRNA electroporation and to shRNA#3, * $p < 0.05$. θ , no shRNA; ctr, control; MZ, marginal zone; CP, cortical plate; IZ, intermediate zone; SVZ/VZ, subventricular, ventricular zone. Scale bar: 100 μm .

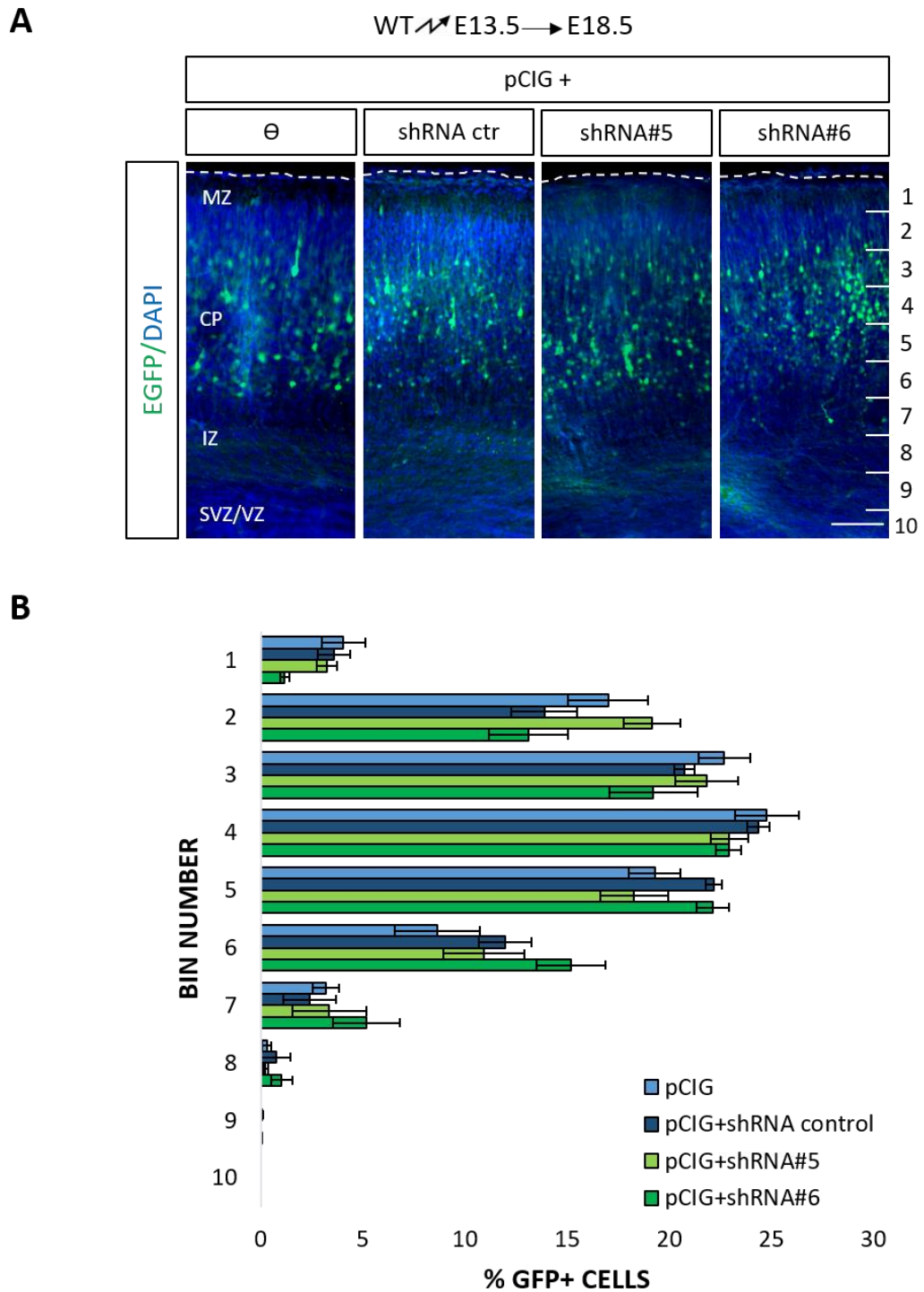


Figure 32: Reduction of PCDH19 levels by shRNA#5 or shRNA#6 at E13.5 does not have an effect on neuronal migration.

(A) Representative images of E13.5 *in utero* electroporated embryos analysed at E18.5. EGFP-positive neurons are in green. Nuclei were stained with DAPI (blue). Knockdown of PCDH19 does not affect the migration of deep layer neurons. (B) Quantification of the electroporated neurons from

A. Graphs represent the number of EGFP+ cells in each of ten equal-size horizontal bins expressed as % of total electroporated cells. The data are presented as mean \pm SEM. The horizontal bins used to perform the quantification are shown in arabic numerals on the right side of the image. Statistical analysis using ANOVA or independent-samples Kruskal Wallis test, was not significant. \emptyset , no shRNA; ctr, control; MZ, marginal zone; CP, cortical plate; IZ, intermediate zone; SVZ/VZ, subventricular, ventricular zone. Scale bar: 100 μ m.

4.3.2.1.2 ShRNA electroporations in *Pcdh19*-KO animals

Pcdh19 shRNAs were also electroporated into *Pcdh19*-KO animals as an additional control. In this case, embryos were co-electroporated at E13.5 with an shRNA control or an shRNA mix (shRNA#3, #5, #6) and a pCIG reporter. ShRNA#2 was not used in the mix because, as seen in **section 4.3.2.1.1**, when electroporated individually into WT animals at E13.5, it produced migration failure in some of the brains while in others migration was normal compared to the control.

The co-electroporation experiments were also changed from injecting each of the *Pcdh19* shRNAs individually at 1 $\mu\text{g}/\mu\text{L}$ to electroporating a mixture of all three shRNAs at a 0.33 $\mu\text{g}/\mu\text{L}$ each. The electroporating conditions remained the same.

Analysis of cortical migration in *Pcdh19*-KO brains electroporated *in utero* with the *Pcdh19* shRNA mix did not present reveal any differences between the conditions in the cell distribution among the cortical wall.

As seen in **Figure 33A**, EGFP-positive cells were positioned for the most part in the cortical plate in both types of electroporation. As illustrated in **Figure 33B**, approximately 80% of the electroporated cells were positioned between bins 3 and 7 (pCIG+shRNA ctr= $80.66 \pm 2.35\%$ EGFP+ cells; pCIG+shRNA mix= $83.36 \pm 3.45\%$ EGFP+ cells). Statistical analysis by IBM SPSS Statistics® 25 software did not reveal any differences between the *Pcdh19*-KO brains electroporated with *Pcdh19* shRNA mix and the brains electroporated with the shRNA control.

However, comparisons between the WT and *Pcdh19*-KO brains electroporated with pCIG+shRNA control (**Figure 34A**) showed a failure in the migration reflected in the images (**Figure 34A**) and in the quantification (**Figure 34B**) of bin 2 (WT= $2.88 \pm 0.66\%$ EGFP+ cells; *Pcdh19*-KO = $0.03 \pm 0.03\%$ EGFP+ cells), 4 (WT= $22.84 \pm 0.83\%$ EGFP+ cells; *Pcdh19*-KO = $17.57 \pm 1.16\%$ EGFP+ cells), 8 (WT= $1.06 \pm 0.42\%$ EGFP+ cells; *Pcdh19*-KO = 5.023

$\pm 0.63\%$ EGFP+ cells) and 9 (WT= $0.18 \pm 0.11\%$; *Pcdh19*-KO = $2.73 \pm 1.45\%$). The differences were statistically significant in all four bins (bin 2: independent samples Mann-Whitney U-test, $p=0.004$, bin 4: independent samples t-test, $t(10)=0.245$, $p=0.022$, bin 8: independent samples Mann-Whitney U-test, $p=0.004$ and bin 9: independent samples Mann-Whitney U-test, $p=0.028$).

Details of the statistical analysis are shown in the appendix (**Table A. 4**, **Table A. 5**).

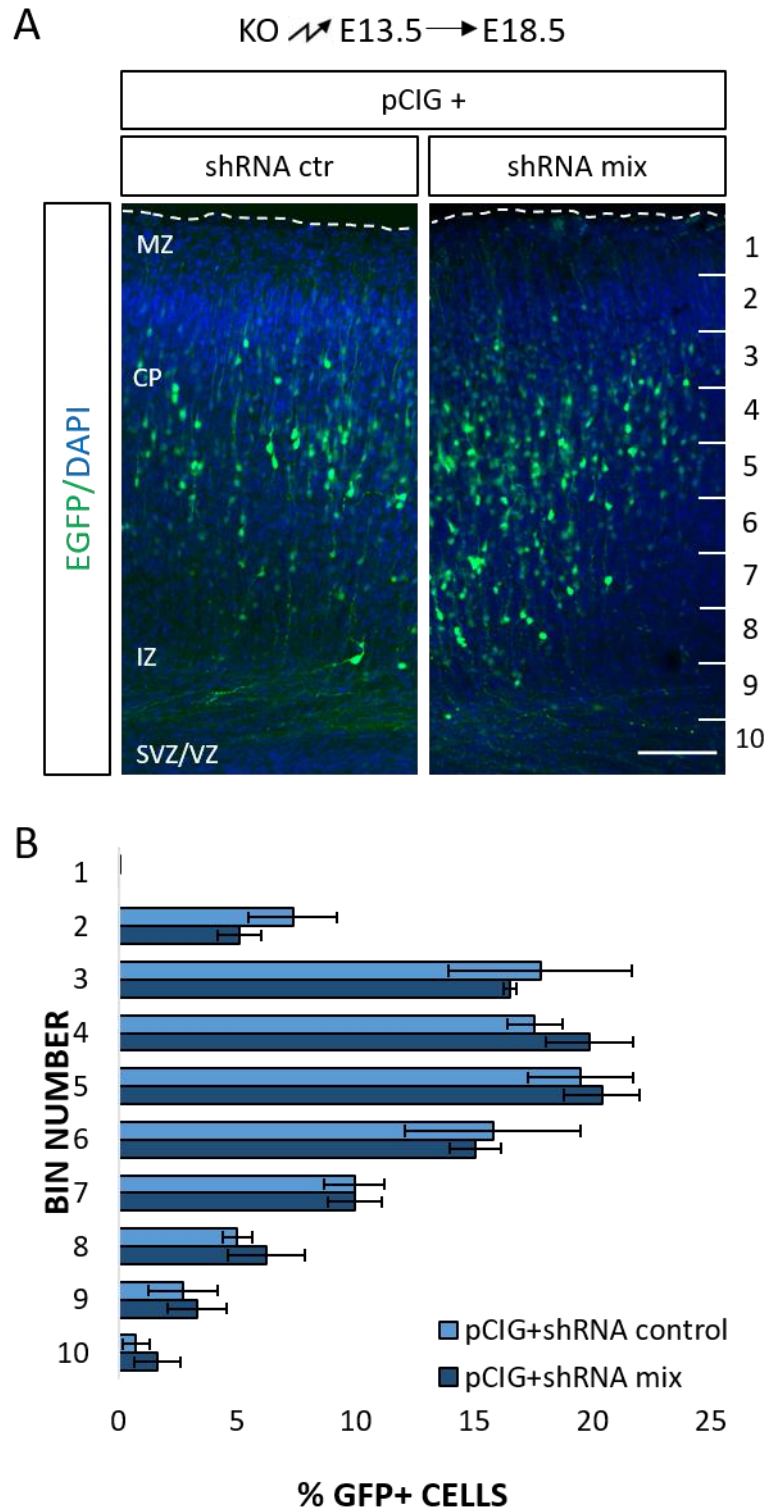


Figure 33. *Pcdh19* shRNA *in utero* electroporation into *Pcdh19*-KO animals at E13.5 does not have an effect on migrating neurons compared to the control.

(A) Representative images of E13.5 *in utero* electroporated *Pcdh19*-KO embryos analysed at E18.5. Electroporated neurons are EGFP-positive. Nuclei were stained with DAPI (blue). (B) Quantification of the

electroporated neurons from **A**. Graphs represent EGFP⁺ cells in each of ten equal-size horizontal bins expressed as % of total electroporated cells. The data are presented as mean \pm SEM. The horizontal bins used to perform the quantification are shown in arabic numerals on the right side of the image. θ , no shRNA; ctr, control; MZ, marginal zone; CP, cortical plate; IZ, intermediate zone; SVZ/VZ, subventricular, ventricular zone. Scale bar: 100 μ m.

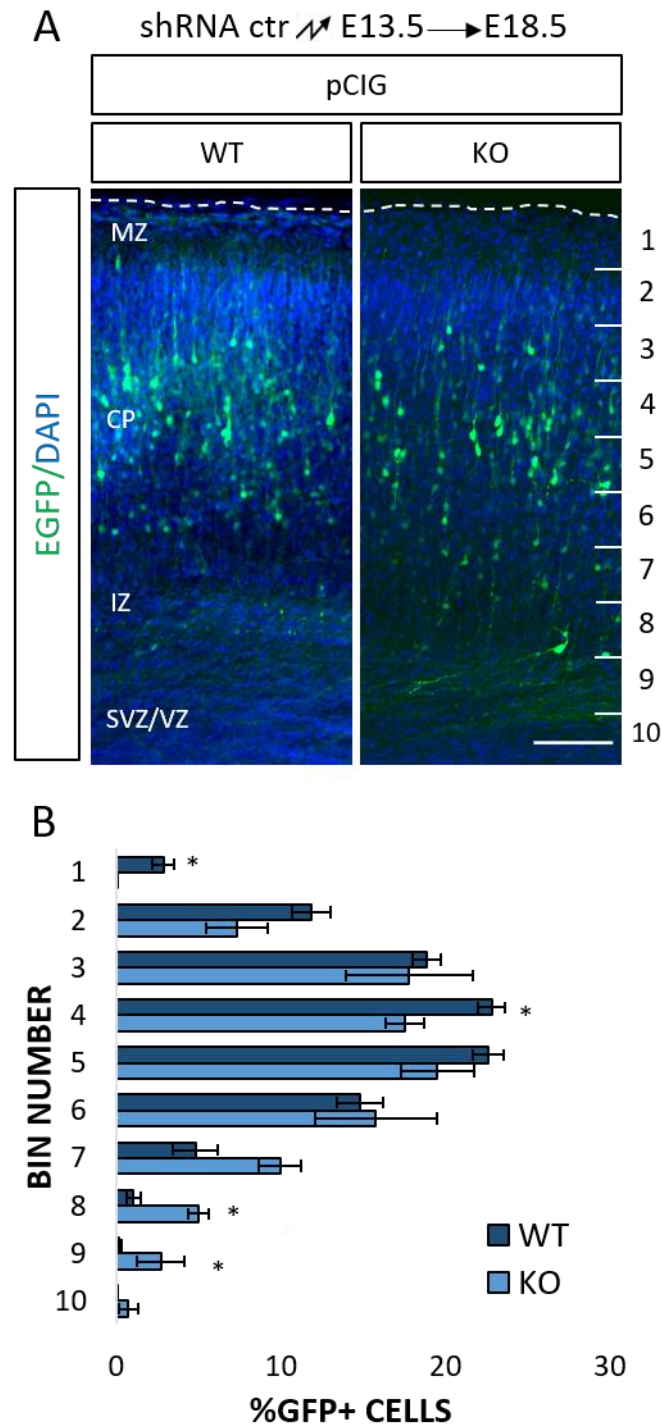


Figure 34. *Pcdh19*-KO neurons *in utero* electroporated with the shRNA control settle at deeper positions compared to the WT neurons electroporated with the same plasmid.

(A) Representative images of electroporated E13.5 embryos with pCIG+shRNA control embryos analysed at E18.5. EGFP expressing neurons are shown in green. Nuclei were counterstained with DAPI (blue). (B) Quantifications of the electroporated neurons of A. Graphs represent each EGFP+ cells in each of ten equal-size vertical bins expressed as % of total

electroporated cells. The data are presented as mean \pm SEM. The horizontal bins used to perform the quantification are shown in arabic numerals on the right side of the image. Statistical significance is indicated with * $p < 0.05$. WT brains present a different migration than *Pcdh19*-KO brains. MZ, marginal zone; CP, cortical plate; IZ, intermediate zone; SVZ/VZ, subventricular/ventricular zone; WT, wild-type; KO, *Pcdh19* knock-out. Scale bar: 100 μ m.

4.3.2.2 pCIG *in utero* electroporation experiments at E13.5 showed a decrease in migration in *Pcdh19*-KO animals with respect to the WT and *Pcdh19*-HET animals

To assess the role of PCDH19 in the cortical migration of neurons in mice that have a genetic alteration in the *Pcdh19* gene, *in utero* electroporations of the pCIG reporter plasmid were performed at E13.5 in mutant animals and their WT littermates. This experiment was also meant to provide further clarification on the difference detected between the WT and *Pcdh19*-KO animals electroporated with the pCIG plasmid and the shRNA control.

Embryos were obtained from matings between a WT male and a *Pcdh19*-HET female, that produced the genetic backgrounds necessary for the experiment (WT males and females, *Pcdh19*-HET F and *Pcdh19*-KO M). Unlike in the co-electroporations with shRNAs, 2 µg/µl of pCIG plasmid were injected instead of 0.5 µg/µl. This keeps the total concentration of DNA the same across experiments but increases the amount of cells that get electroporated. After injection of the plasmid, 5 pulses of 38 V and 50 milliseconds were applied on E13.5 animals. The change of the settings was decided because when electroporations were performed on these animals, there was a decrease in the intensity of the fluorescence and in the number of electroporated cells with respect to the shRNA electroporations, increasing the probability of type II errors and biased results. Higher voltage pulses increase the effectivity of transfection, consequently increasing the fluorescence.

Images (**Figure 35A**) revealed that, in *Pcdh19*-KO brains electroporated at E13.5 and analysed 5 days later, some EGFP-positive cells were still located in the intermediate zone (IZ) and the subventricular/ventricular zones (SVZ/VZ), while the vast majority of electroporated cells in WT and *Pcdh19*-HET brains were positioned in the cortical plate (CP). Quantitative analysis of these electroporations (**Figure 35B**) showed differences in bins 2 (WT=

14.38 ± 1.17%; *Pcdh19*-KO = 9.77 ± 1.16%) and 3 (WT= 5.23 ± 0.56%; *Pcdh19*-KO = 2.08 ± 0.33%) that were statistically significant in bin 3 (ANOVA, F (2, 12)=4.352, p=0.038; post-hoc test Tukey HSD, p=0.031) and almost significant in bin 2 (independent samples Kruskal-Wallis test, p=0.019; pair-wise comparisons, p=0.059) between WT and *Pcdh19*-KO brains. Although the difference only reached statistical significance in bin 3, there was a tendency of the *Pcdh19*-KO cells to migrate to lower positions within the cortical plate with respect to the WT cells. In fact, more *Pcdh19*-KO cells were located between bins 7 and 8 than WT cells (WT= 18.37 ± 1.57%; *Pcdh19*-KO = 27.05 ± 4.57%).

Unlike the decrease noted in the migration of neurons in *Pcdh19*-KO brains, electroporated neurons in *Pcdh19*-HET brains tended to concentrate in the central bins 4 and 5 (**Figure 35A**; WT= 39.43 ± 0.84%; *Pcdh19*-HET = 47.1 ± 4.91%), with less neurons present in top and bottom bins 3 and 7-10 (WT= 35.97 ± 1.4%; *Pcdh19*-HET= 24.11 ± 2.91%). This could explain the difference between the genotypes in bin 8 (WT= 5.19 ± 0.71% EGFP+ cells; *Pcdh19*-HET = 1.98 ± 0.53% EGFP+ cells) that analysis revealed to be statistically significant (ANOVA, F (2, 12)=4.933, p=0.027; post-hoc test Games-Howell, p=0.014).

Since a higher percentage of cells from *Pcdh19*-KO brains were positioned in the lower bins, and cells from *Pcdh19*-HET brains accumulated more in the central bins, statistically significant differences between those two genotypes could also be detected in bins 2 (*Pcdh19*-HET= 6.32 ± 1.21%; *Pcdh19*-KO= 2.08 ± 0.33%; independent samples Kruskal-Wallis test, p=0.019; pair-wise comparisons post-hoc test, p=0.027) and 7 (*Pcdh19*-HET= 8.58 ± 1.96%; *Pcdh19*-KO= 17.75 ± 1.64%; ANOVA, F (2, 12)=7.382, p=0.008; post-hoc test Tukey HSD, p=0.006) (**Figure 35B**).

Details of the statistical analysis are shown in the appendix (**Table A. 6**).

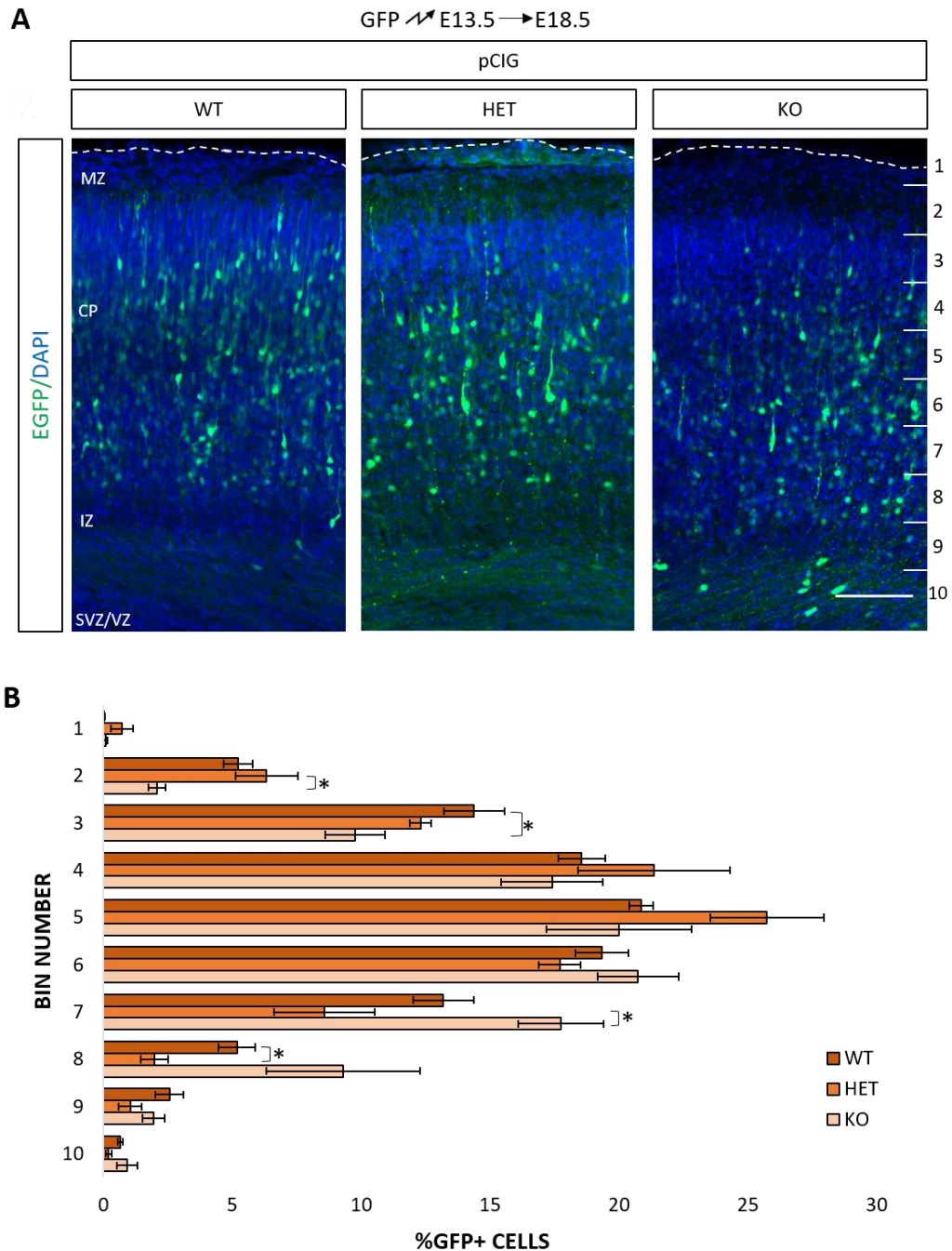


Figure 35. *Pcdh19*-KO brains present an altered migration of neurons compared to their WT littermates when electroporated at E13.5.

(A) Representative images of E13.5 embryos electroporated *in utero* with an EGFP plasmid and analysed at E18.5. Electroporated neurons are EGFP-positive. Nuclei were counterstained with DAPI (blue). PCDH19 mutation affects the migration of early born neurons. *Pcdh19*-KO neurons fail to migrate as much as the WT neurons. **(B)** Quantification of the electroporated brains from A. Graphs represent EGFP+ cells in each of ten equal-size horizontal bins expressed as % of total electroporated cells. The data are presented as mean \pm SEM. The horizontal bins used to perform the

quantification are shown in arabic numerals on the right side of the image. Results were analysed using ANOVA or independent-samples Kruskal Wallis test. Statistical significance was reached in bins 2 and 7 between *Pcdh19*-HET and *Pcdh19*-KO, in bin 3 between WT and *Pcdh19*-KO and in bin 8 between WT and *Pcdh19*-HET, * $p < 0.05$. WT, wild-type; HET, *Pcdh19*-heterozygous, KO, *Pcdh19*-knock-out; MZ, marginal zone; CP, cortical plate; IZ, intermediate zone; SVZ/VZ, subventricular, ventricular zone. Scale bar: 100 μm .

4.3.3 Analysis of cortical migration at E15.5

The aim of this section was to analyse the function of PCDH19 in the cortical migration of upper layer neurons in mouse. To achieve it, *in utero* electroporation experiments using *Pcdh19* shRNAs that acutely knockdown *Pcdh19* at E15.5 and an analysis of the migration of the electroporated cells at P10 were conducted. The migration of genetically modified animals that have their *Pcdh19* gene altered was also analysed by *in utero* electroporating a pCIG reporter at E15.5 and analysing at P10.

4.3.3.1 *Pcdh19* knockdown by shRNAs at E15.5 in WT and *Pcdh19*-KO brains altered neuronal migration compared to the control

4.3.3.1.1 ShRNA *in utero* electroporations on WT animals

WT embryos were electroporated *in utero* at E15.5 with the same plasmids than at E13.5 (pCIG, shRNA control and a mix of *Pcdh19* shRNAs #3,5,6). E15.5 was the age selected to electroporate the brains since cells generated at this time-point would migrate and reach their final position in the upper layers of the cortex, layers II and III (Hatten 1999; Bayer et al. 1991; Sidman et al. 1973; Britanova et al. 2008; Hirota et al. 2017b; Jabaudon 2017). *Pcdh19* mRNA is expressed in layers II/III at P10 in mouse, as illustrated in **Figure 12**. Thus, if *Pcdh19* was expressed during the migration of late-born cells, reduction of PCDH19 protein levels could alter the process. To analyse migration of these upper-layer cells, brains were perfused at P10, when migration to the cortical plate has finished.

In this case, mothers gave birth to the electroporated embryos and pups were perfused at P10, their brains fixed, cut, counterstained with DAPI, and imaged on a confocal microscope. An area of 830 μm was analysed as detailed in **section 2.3** from materials and methods.

Analysis was again performed blind to avoid experimenter's bias. Labelling the animals according to their position in the uterus, as when

electroporating at E13.5, was not possible due to the birth of the pups. Brains were therefore electroporated with two different set of plasmids (pCIG+shRNA control or pCIG+shRNA mix) and each set of vectors was electroporated in either the right or the left cerebral hemisphere. When those electroporated brains were cut, the location of the green fluorescence was noted, and the brains were labelled accordingly. The plasmids electroporated into each hemisphere were only revealed after cell counting was completed.

Unlike at E18.5, at P10 EGFP+ cells reveal differences in their positioning within the cortical plate depending on the area of the brain they are located in, probably due to the lateromedial and rostrocaudal gradient of migration, (Angevine et al. 1961; J. A. del Rio et al. 1989; Caviness 1982). Therefore, migration was analysed in a selected region of the SSC in medial parts of the brain, making sure the regions were equivalent in all the brains.

WT brains co-electroporated with pCIG and the mix of shRNAs presented an altered migration of the EGFP-positive cells with respect to the cells from brains co-electroporated with the pCIG plasmid and the shRNA control. At P10, cells that received the shRNA mix at E15.5 occupy the very top of the cortical plate, in contrast to cells that received the control shRNA, which are located slightly deeper (**Figure 36A**). Quantification of the percentage of cells in each of 10 horizontal bins spanning the whole cortical width showed that $96.58 \pm 1.24\%$ of the cells electroporated with *Pcdh19* shRNAs were located between bins 1 and 3, while only $71.87 \pm 5.7\%$ of the EGFP-positive cells from brains electroporated with shRNA control are contained within those bins (**Figure 36B**).

Quantifications revealed an increase in the percentage of the EGFP-expressing cells positioned in the upper bins in the brains with reduced levels of PCDH19 when compared to the brains with an unaltered PCDH19 (bin 1: pCIG + shRNA control= $2.85 \pm 1.93\%$ EGFP+ cells; pCIG + shRNAmix= $18.1 \pm 2.11\%$ EGFP+ cells; bin 2: pCIG + shRNA control= 34.67

$\pm 8.75\%$ EGFP+ cells; pCIG + shRNAmix= $56.84 \pm 2.74\%$ EGFP+ cells). Conversely, fewer EGFP-positive cells were located in the lower bins in these brains (bin 4: pCIG + shRNA control= $3.95 \pm 0.95\%$ EGFP+ cells; pCIG + shRNAmix= $0.57 \pm 0.18\%$ EGFP+ cells; bin 7: pCIG + shRNA control= $2.06 \pm 0.28\%$ EGFP+ cells; pCIG + shRNAmix= $0.17 \pm 0.1\%$ EGFP+ cells; bin 8: pCIG + shRNA control= $3.47 \pm 0.57\%$ EGFP+ cells; pCIG + shRNAmix= $0.33 \pm 0.11\%$ EGFP+ cells; bin 9: pCIG + shRNA control= $6.38 \pm 1.03\%$ EGFP+ cells; pCIG + shRNAmix= $0.6 \pm 0.19\%$ EGFP+ cells, and bin 10: pCIG + shRNA control= $10.55 \pm 3.39\%$ EGFP+ cells; pCIG + shRNAmix= $0.86 \pm 0.36\%$ EGFP+ cells). Statistical analysis detected significant differences in bins 1 (independent samples t-test, $t(6) = -5.334$; $p=0.002$), 4 (independent samples t-test, $t(6) = 3.507$; $p=0.013$), 7 (independent samples Mann-Whitney U test, $p=0.029$), 8 (independent samples Mann-Whitney U test, $p=0.029$), 9 (independent samples t-test, $t(6) = 5.506$; $p=0.002$) and differences that tended towards significance in bin 10 (independent samples t-test with equal variances not assumed, $t(2.825) = 3.065$, $p=0.062$).

However, it is important to mention that the differences in bins 7, 8, and 9 were mainly due to the abnormal location of some EGFP-positive cells in brains electroporated with the shRNA control. This anomaly will be discussed in **section 4.4.5**.

Details of the statistical analysis are shown in the appendix (**Table A. 7**).

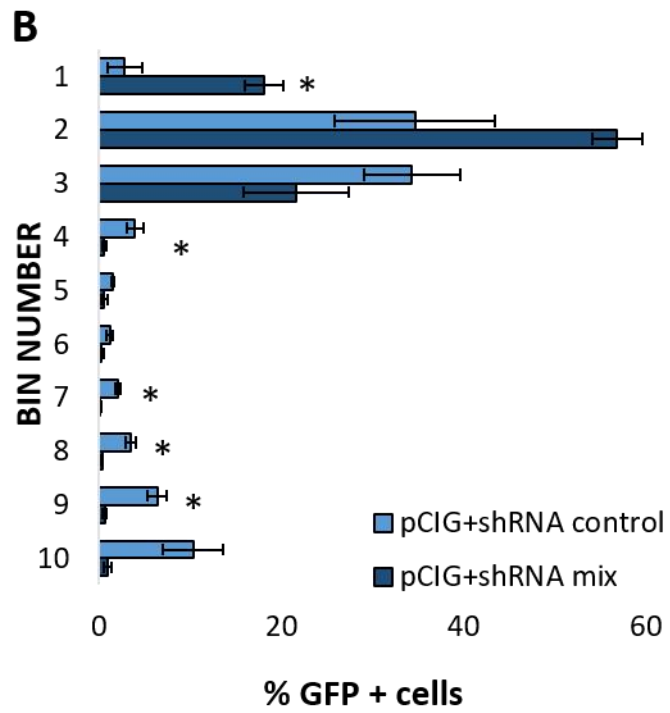
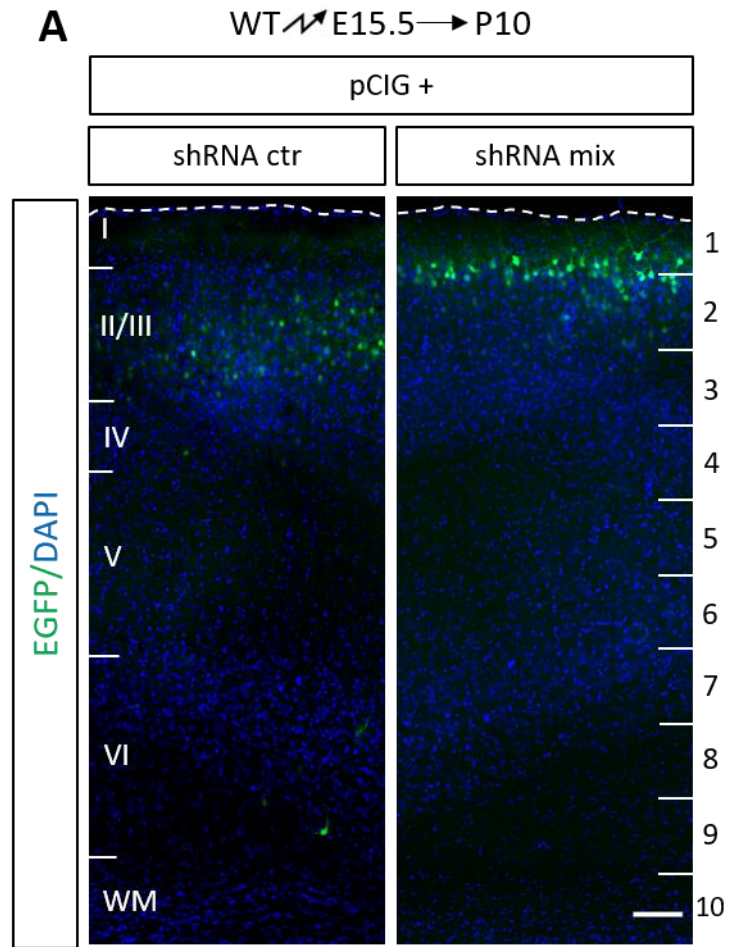


Figure 36. Knock-down of PCDH19 increases the migration of late-born neurons.

(A) Representative images of E15.5 WT embryos *in utero* co-electroporated with shRNA control or an shRNA mix (shRNA#3, #5 and #6) and an EGFP reporter, and analysed at P10. Targeted neurons express EGFP. Nuclei were counterstained with DAPI (blue). Darker areas reflect an illumination problem due to technical issues with the confocal. The problem did not affect the migration analysis. Neurons transfected with shRNA mix migrated more than neurons migrated with the shRNA control. **(B)** Quantification of the electroporated brains from **A**. Graphs represent EGFP+ cells in each of ten equal-size horizontal bins expressed as % of total electroporated cells. Data are presented as mean \pm SEM. The horizontal bins used to perform the quantification are indicated in arabic numerals on the right side of the image. Statistical analysis was performed using a t-test of independent samples or independent-samples Mann-Whitney U test. Analysis was significant in bins 1, 4, 7, 8 and 9, * $p < 0.05$. WT, wild-type; ctr, control; WM, white matter. Cortical layers are indicated with roman numerals in the representative images. Scale bar: 100 μm .

4.3.3.1.2 ShRNA *in utero* electroporations on *Pcdh19*-KO animals

To validate that the increase in migration was due to *Pcdh19* knockdown, *in utero* electroporations of E15.5 *Pcdh19*-KO embryos using the same settings as the electroporations from **section 4.3.3.1.1** and analysis at P10 were performed.

Images from the *Pcdh19*-KO brains analysed at P10 (**Figure 37A**) illustrated that the vast majority of electroporated cells with the *Pcdh19* shRNA mix were located at the top of layer II, like the cells observed in the WT brains electroporated with the same plasmid. However, the *Pcdh19*-KO brains electroporated with the *Pcdh19* shRNA control showed a great number of cells positioned in the lower part of layers II/III and some cells in the lower part of layer VI and WM.

Quantification of the images (**Figure 37B**) showed differences in all bins except 7 and 8 (bin 1: pCIG + shRNA control= $1.76 \pm 0.78\%$ EGFP+ cells; pCIG + shRNAmix= $32.28 \pm 7.35\%$ EGFP+ cells; bin 2: pCIG + shRNA control= $19.03 \pm 2.27\%$ EGFP+ cells; pCIG + shRNAmix= $47.49 \pm 7.34\%$ EGFP+ cells; bin 3: pCIG + shRNA control= $45.25 \pm 2.84\%$ EGFP+ cells; pCIG + shRNAmix= $22.82 \pm 9.9\%$ EGFP+ cells; bin 4: pCIG + shRNA control= $9.77 \pm 3.17\%$ EGFP+ cells; pCIG + shRNAmix= $3.12 \pm 1.66\%$ EGFP+ cells; bin 5: pCIG + shRNA control= $3.81 \pm 0.7\%$ EGFP+ cells; pCIG + shRNAmix= $1.21 \pm 0.92\%$ EGFP+ cells; bin 6: pCIG + shRNA control= $1.52 \pm 0.5\%$ EGFP+ cells; pCIG + shRNAmix= $0.14 \pm 0.09\%$ EGFP+ cells; bin 9: pCIG + shRNA control= $6.08 \pm 2.25\%$ EGFP+ cells; pCIG + shRNAmix= $0.79 \pm 0.36\%$ EGFP+ cells, and bin 10: pCIG + shRNA control= $8.49 \pm 2.26\%$ EGFP+ cells; pCIG + shRNAmix= $1.52 \pm 0.3\%$ EGFP+ cells).

Overall, the positioning of the cells is very similar as the positions shown in **Figure 36B**. These results were unexpected because *in utero* electroporation of *Pcdh19* KO brains with *Pcdh19* shRNAs should not present any differences in migration respect to the brains electroporated with the

shRNA control, since *Pcdh19* shRNA cannot affect the quantity of PCDH19 in brains that do not express the gene. These results will be discussed in **section 4.4**.

Details of the statistical analysis are shown in the appendix (**Table A. 8**).

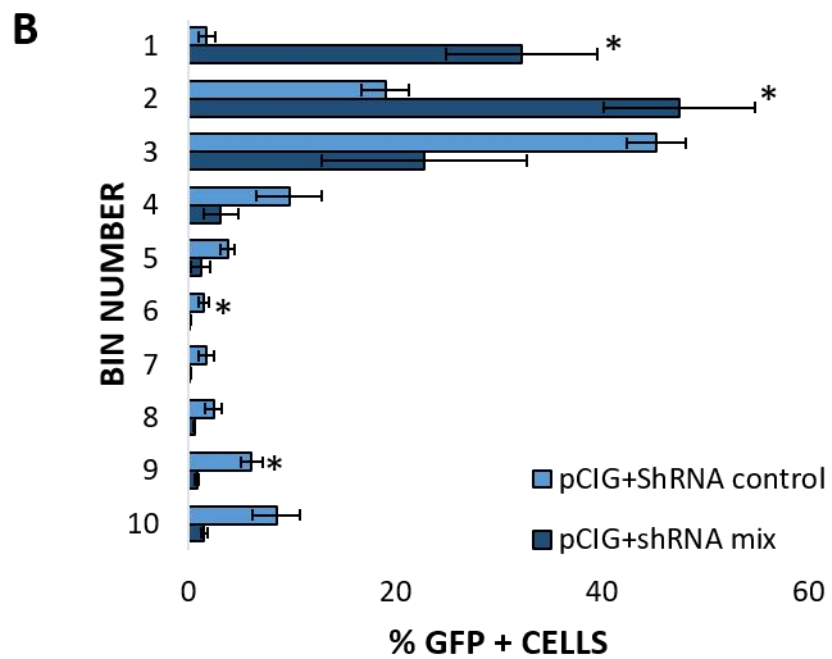
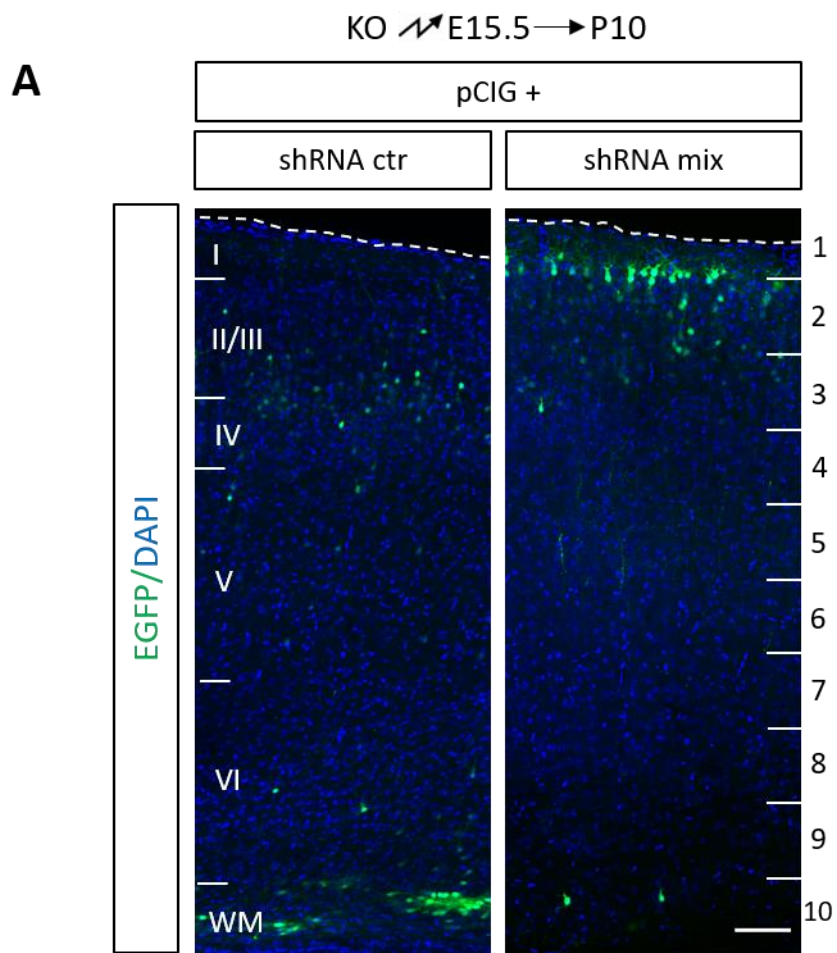


Figure 37. *In utero* electroporation of the *Pcdh19* shRNAs into *Pcdh19*-KO brains at E15.5 also reveals an altered migration of late born neurons.

(A) Representative images of E15.5 *Pcdh19*-KO embryos *in utero* co-electroporated with shRNA control or shRNA mix (shRNA#3, #5 and #6) and an EGFP reporter, and analysed at P10. Electroporated neurons are shown in green. Nuclei were counterstained with DAPI (blue). *Pcdh19*-KO brains transfected with the shRNA mix against *Pcdh19* presented an effect in migration with respect to the ones electroporated with the shRNA control. (B) Quantification of the electroporated brains from A. Graphs represent EGFP⁺ cells in each of ten equal-size horizontal bins expressed as % of total electroporated cells. Data are presented as mean \pm SEM. The horizontal bins used to perform the quantification are shown in arabic numerals on the right side of the image. Results were analysed using a t-test of independent samples or independent-samples Mann-Whitney U test. Results were significant in bins 1, 2, 6 and 9, * $p < 0.05$. KO, knock-out; ctr, control; WM, white matter. Cortical layers are indicated with roman numerals in the representative images. Scale bar: 100 μ m.

4.3.3.2 EGFP *in utero* electroporation on WT, *Pcdh19*-HET and *Pcdh19*-KO animals at E15.5 present differences in the cell migration of mutant animals with respect to the WT littermates

To examine the role of PCDH19 in the cortical migration of layer II/III neurons in *Pcdh19*-HET and *Pcdh19*-KO mice that present a chronic knockdown of the *Pcdh19* gene, *in utero* electroporation experiments were conducted with a pCIG reporter plasmid at E15.5 in the mutant animals and their WT littermates. This experiment was also particularly relevant given the unexpected results obtained in the shRNA control electroporations performed in WT and KO animals.

Embryos from matings between a WT male and a *Pcdh19*-HET female, were electroporated at E15.5 with 2 µg/µl of pCIG reporter and analysed at P10. Electroporation settings applied are shown in **Figure 30**.

Images of P10 coronal sections (**Figure 38A**) revealed that most of the EGFP-positive cells in *Pcdh19*-KO animals were positioned in a higher region of layer II/III compared to the electroporated cells from their WT counterparts. On the contrary, EGFP-electroporated cells in *Pcdh19*-HET brains were located in a lower part of layers II/III with respect to the WT littermates. Quantifications of the images (**Figure 38B**) showed differences in bins 2 (WT= 23.13 ± 4.24% EGFP+ cells, *Pcdh19*-HET = 17.15 ± 4.36% EGFP+ cells, *Pcdh19*-KO = 42.67 ± 4.75% EGFP+ cells; ANOVA, F (2, 11)=9.037, p=0.005; post-hoc test Tukey HSD WT vs KO, p=0.023; post-hoc test Tukey HSD WT vs HET, p=0.577; post-hoc test Tukey HSD HET vs KO, p=0.004) and 4 (WT= 7.54 ± 2.81% EGFP+ cells; *Pcdh19*-HET = 19.26 ± 6.25% EGFP+ cells, *Pcdh19*-KO = 1.36 ± 0.47% EGFP+ cells; ANOVA, F (2, 11)=5.699, p=0.02; post-hoc test Games-Howell WT vs KO, p=0.186; post-hoc test Games-Howell WT vs HET, p=0.207; post-hoc test Games-Howell HET vs KO, p=0.06) between the mutant and the WT animals that reflected

what was observed in the images, and that were only significant between the *Pcdh19*-KO and the other genotypes in bin 2.

Details of the statistical analysis are shown in the appendix (**Table A. 9**).

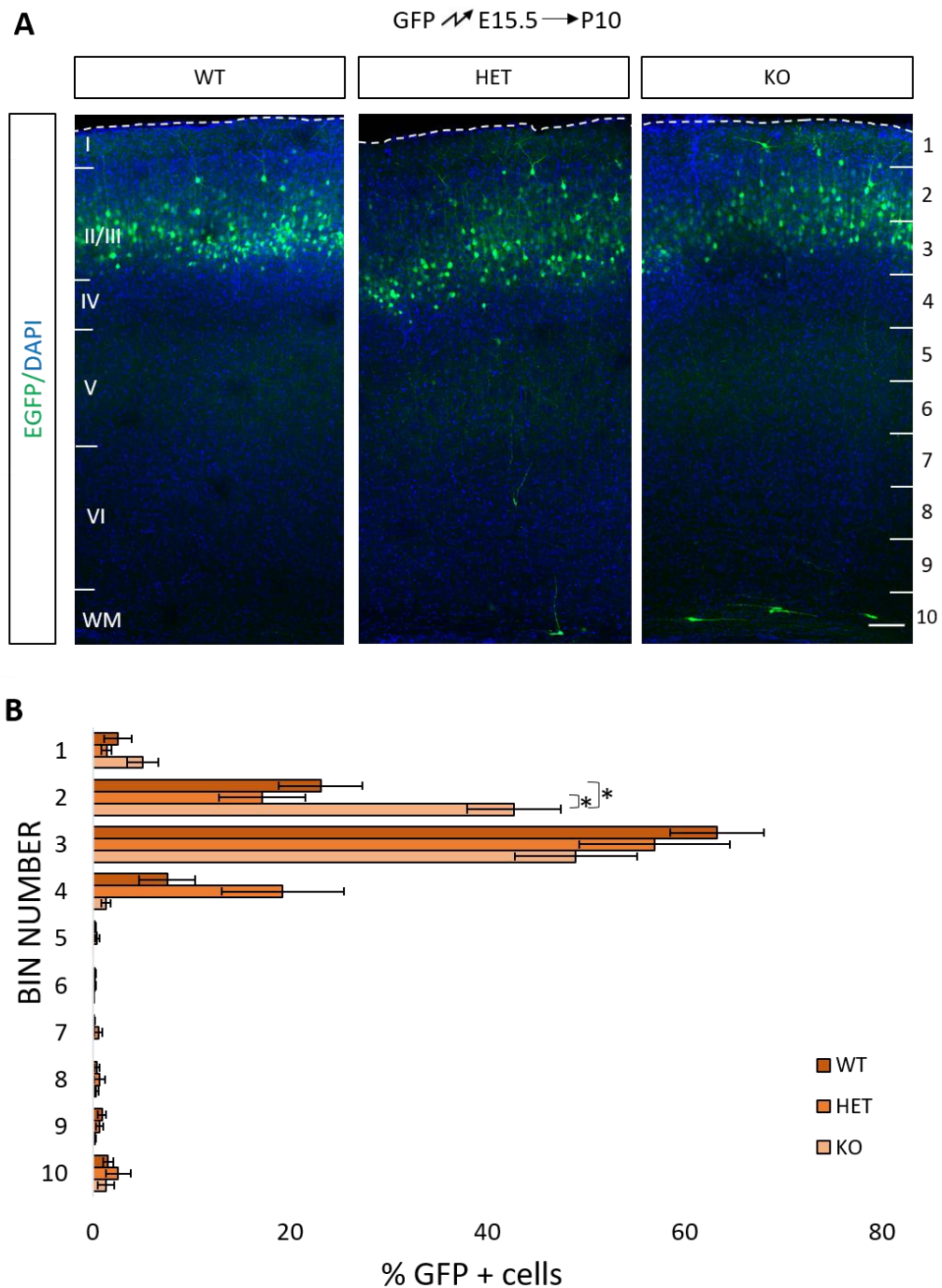


Figure 38. *Pcdh19*-KO brains presented an alteration in the migration of late-born neurons compared to their WT littermates.

(A) Representative images of E15.5 embryos *in utero* electroporated with an EGFP vector and analysed at P10. Electroporated neurons express EGFP. Nuclei were counterstained with DAPI (blue). PCDH19 mutation alters the migration of upper layer neurons. Neurons from *Pcdh19*-HET brains were located in lower positions within the cortical plate with respect to the cells from WT brains, while *Pcdh19*-KO neurons from *Pcdh19*-KO brains were in higher positions with respect to the WT neurons. **(B)** Quantification of the electroporated brains from **A**. Graphs represent EGFP+ cells in each of ten

equal-size horizontal bins expressed as % of total electroporated cells. Data are presented as mean \pm SEM. The horizontal bins used to perform the quantification are indicated in arabic numerals on the right side of the image. Results, analysed by ANOVA or independent-samples Kruskal Wallis test, were only significant in bin 2, between *Pcdh19*-KO and the other animals, * $p < 0.05$. WT, wild-type; HET, *Pcdh19*-heterozygous; KO, *Pcdh19*-knock-out; WM, white matter. Cortical layers are indicated with roman numerals in the representative images. Scale bar: 100 μm .

4.4 Discussion

4.4.1 Summary of results

In this chapter, the aim was to determine whether PCDH19 had a role in cortical neuronal migration in mice.

In western blot experiments, it was demonstrated that *Pcdh19* shRNAs reduce PCDH19 protein levels significantly 24 hours post-transfection, and that this reduction is maintained 48 and 72 hours later. As expected, the shRNA control does not reduce significantly the level of PCDH19 at 24- or 72-hours. However, a reduction in protein quantity was seen at 48-hours. Experiments conducted by *in utero* electroporation of *Pcdh19* shRNAs at E13.5 suggested that *Pcdh19* knock-down did not affect cortical migration in early-born neurons and that *Pcdh19* shRNAs could be producing an off-target effect when electroporations were performed at E15.5, making impossible to conclude if *Pcdh19* had an effect in the migration of late-born neurons. However, EGFP *in utero* electroporation experiments conducted in WT and *Pcdh19*-mutant embryos revealed that cortical migration of early-born neurons is affected in *Pcdh19*-KO animals and migration of late-born neurons is affected in *Pcdh19*-KO mice.

4.4.2 Assessment of *Pcdh19* shRNAs effectiveness

Western blot experiments demonstrate that *Pcdh19*-shRNAs reduced PCDH19 protein levels in cells at least by 60%, an effect occurring as soon as 24h post-transfection and still after 72h *in vitro*. These results show the effectiveness of the shRNA in knocking down PCDH19, and, consequently, their suitability to be used to decrease the expression of PCDH19 *in vivo* by *in utero* electroporation. However, it needs to be taken into account that, although western blot analysis indicates a reduction of PCDH19, those data come from *in vitro* transfections, in a cellular context that is different from the *in vivo* model. Moreover, as expected in the knocking down conditions,

there is not a total loss of PCDH19 in *Pcdh19*-shRNA transfected cells. A similar scenario would be occurring in *Pcdh19*-shRNA electroporated cells.

Transfection of control shRNA seemed to decrease PCDH19-HA protein levels at 48-hours. This result was unexpected, since the control was a Sigma bought shRNA that targets no known mammalian genes. This control shRNA has been used previously for western blot, but none of the previous reports used a non-treated lysate as a control (Santer et al. 2017; Conn et al. 2015; Pu et al. 2017). It is worth noting, however, that the *Pcdh19*-HA transfection data show unusually high error bars, suggesting that this result might be due to excess PCDH19-HA in the control transfection, rather than decreased levels in the control shRNA samples. Alternatively, it could be argued that the difference is due to a higher number of copies received of the *Pcdh19*-HA plasmid in the cells transfected with only this vector. It is possible the cells can only admit a certain number of copies, and since the cells transfected with the shRNA control have to incorporate two plasmids instead of just one, they might be receiving less *Pcdh19*-HA copies. To see if this hypothesis is true, these experiments could be performed in mouse cells that expressed mouse PCDH19, so the comparisons would be between cells transfected with an empty vector and cells transfected with the shRNA control, using an antibody to detect the PCDH19 protein in western blot. This would be possible to perform now, however at the time, no anti-PCDH19 antibody was available that could be used for western blot.

4.4.3 Choice of methods

In *Pcdh19* shRNA *in utero* electroporation experiments, as mentioned in **section 4.3**, shRNA#4 was not co-transfected with EGFP since its effectiveness couldn't be tested. ShRNA#4 binds to the 3'UTR of the *Pcdh19* mRNA, which allows the possibility of performing rescue experiments by introducing a cDNA plasmid that contains the protein sequence lacking the 3'UTR. *In utero* electroporation experiments using the shRNA#4 could have been performed after testing the effectiveness of the shRNA by western blot

analysis. In this case, the shRNA could have either been co-transfected with a PCDH19FL that contained the 3'UTR; or selecting a mouse cell line that expressed PCDH19 and detecting the protein with an antibody (this method was already described in the previous section).

After the co-electroporation of shRNAs into WT animals at E13.5, the rest of experiments were changed from injecting each of the *Pcdh19* shRNAs individually at 1 $\mu\text{g}/\mu\text{L}$ to electroporating a mixture of all three shRNAs at a 0.33 $\mu\text{g}/\mu\text{L}$ each. Because WB results showed that all shRNAs reduce the quantity of PCDH19 to a similar level and the individual electroporations performed on WT animals also showed no differences between shRNAs #3, #5 and #6, the electroporation of a mixture of shRNA was considered the best way to conduct the experiments. The diminished concentration of each individual shRNA reduces the possibility of unspecific effects that could alter migration, since lower quantities of the plasmid implies less possibility of unspecific binding without increasing the possibility of saturation of the RNA interference machinery because the total concentration of shRNA introduced remained the same as in the previous experiment (1 $\mu\text{g}/\mu\text{L}$). This strategy also allowed a reduction in the number of animals used in the experiment.

The electroporation of shRNAs against *Pcdh19*, that allowed us to acutely knock-down the protein at specific times in the neurodevelopment, was used at the beginning of the project in order to study the role of *Pcdh19* in cortical migration, before *Pcdh19* mutant animals were obtained. However, as *Pcdh19*-KO animals became available, a different option was chosen that would mimic better what is happening in patients with EIEE9: to perform electroporations of EGFP to follow cells in a context of presence or absence of *Pcdh19* and in *Pcdh19*-HET animals in which the population of both *Pcdh19*⁺ and *Pcdh19*⁻ cells coexists, as happens in affected individuals.

At E15.5, the different shRNA conditions (shRNA control and *Pcdh19*-shRNA mix) were electroporated into the left or right hemisphere,

respectively, as explained in **section 4.3.3.1.1**. When this experiment was set, it was discussed to use several reporters to differentiate which plasmid was electroporated in each P10 embryo to be able to electroporate more than two different conditions per litter. However, comparisons between different colours are not the best option, due to differences in brightness and photobleaching amongst other things (Shaner et al. 2004; Barondeau et al. 2002). For these reasons, injecting each set of vectors either in the left or right hemisphere was determined to be better and used for these experiments.

4.4.4 Analysis of migration in early-born neurons

4.4.4.1 ShRNA *in utero* electroporations: abnormal shRNA#2 results.

In **section 4.3.2.1.1**, results showed that WT brains electroporated with *Pcdh19* shRNAs #3, #5 and #6 at E13.5 and analysed at E18.5 did not present any alterations in the distribution of their EGFP⁺ cells with respect to those receiving the shRNA control. Therefore, it was initially considered that the downregulation of *Pcdh19* probably did not have an effect in the final positions of neurons targeted at this age.

However, some WT brains electroporated with shRNA#2 showed a migration failure. Since western blot studies demonstrated that all shRNAs knocked down the levels of PCDH19 similarly but no defects in migration were observed with any of the other shRNAs, it is fair to assume that the failure in migration is due to an off-target effect produced by the *Pcdh19* shRNA#2 and is not related to the decrease of PCDH19. Consequently, shRNA#2 was excluded from the experiments that followed.

4.4.4.2 Comparison of results obtained with shRNA vs EGFP electroporations at E13.5

Electroporation of single *Pcdh19* shRNAs into WT brains, or of the shRNA mix into KO brains at E13.5 did not give rise to any disturbances in the distribution of the EGFP-positive cells compared to the cells receiving the shRNA control. However, the migration analysis in WT and *Pcdh19*-KO animals electroporated with control shRNAs that was conducted revealed that a higher proportion of cells appeared to be present in lower positions (mainly intermediate zone) in *Pcdh19*-KO with respect to WT animals. This result suggests that *Pcdh19* might affect migration only when completely knocked-out since conception or in all cell-types. Analysis at E18.5 of EGFP+ cells distribution in WT and *Pcdh19*-mutant embryos electroporated at E13.5 also supported that hypothesis. Results revealed that, as explained in **section 4.3.2.2**, a higher percentage of EGFP-positive cells in *Pcdh19*-KO animals were located in lower bins, corresponding mainly to the intermediate zone, than in WT brains. On the contrary, this effect was not observed in *Pcdh19*-HET animals.

The fact that *Pcdh19* shRNA electroporations in WT do not alter cortical migration while EGFP electroporations in mutants reveal a defect in the position of the cells could be explained considering that only a percentage of the cells will receive the *Pcdh19*-shRNAs and get their protein level reduced, while other cells will maintain the original quantity of protein. This situation is more comparable to what happens in *Pcdh19*-HET mice, that possesses a mixture of WT cells and *Pcdh19*-KO cells. However, in the *Pcdh19*-shRNA electroporation the only cells labelled will be the ones who are *Pcdh19*-KO, while in the *Pcdh19*-HET both WT and KO cells were analysed together. Nevertheless, *Pcdh19*-HET mice do not present any disruption in the position of their EGFP+ cells compared to the WT, which is in accordance to what is seen in the brains electroporated with the shRNAs.

4.4.4.3 Possible causes of the abnormal positioning of the EGFP+ cells in the *Pcdh19*-KO brains

The reasons why there is a higher number of EGFP-expressing cells positioned in the intermediate zone in the *Pcdh19*-KO mice than in WT mice could be several and would need further investigation.

When a plasmid containing GFP is electroporated at E13.5, RGC located in the VZ take up the reporter and pass on the plasmid to the IP or neurons they generate when they go through asymmetric divisions. The GFP will also be passed on to the immature neurons that will be generated by the self-consuming division of IP in the SVZ (Gal et al. 2006; Noctor et al. 2004). Then, these neurons migrate radially from this germinal zone to their correct positions within the cortical plate.

If *Pcdh19* plays a role in the cortical migration of excitatory neurons that are born from E13.5 onwards, the knockout of the protein could cause said neurons to fail their migration. The results obtained in the EGFP IUE of the *Pcdh19*-KO animals imply that neurons might not be able to enter the cortical plate, or their speed is slower than that of the WT cells. To determine which of them is causing the alteration in cortical migration at E18.5, WT, *Pcdh19*-HET and *Pcdh19*-KO mice could be electroporated at E13.5 and analysed at P10. If some of the cells from the *Pcdh19*-KO brains were still positioned lower within the cortical plate compared to the WT cells, it is probable that the depletion of *Pcdh19* causes a failure in migration. Then, immunohistochemistry against cortical markers corresponding to upper layers (CUX1) or lower layers (CTIP2, TBR1) could be used to detect the type of cells they are. In fact, this IHC experiment could be performed using different markers on the EGFP electroporated *Pcdh19*-KO brains analysed at E18.5 to determine which populations do the cells that are located in lower positions at this age in the *Pcdh19*-KO belong to.

Three different mechanisms could be affected. As detailed in **section 1.7**, somal translocation is used mainly by early-born neurons to traverse the cortical plate; and glia-guided locomotion and terminal translocation, which is similar to somal translocation, are used in the migration of late-born neurons (Nadarajah et al. 2001). The multipolar migration that both cell-types go through while in the SVZ/IZ could also be altered (Tabata et al. 2003).

Since multipolar migration requires *Cdh2* to orient these cells towards the cortical plate before switching to bipolar morphology (Jossin et al. 2011) and *Pcdh19* has been shown to interact with *Cdh2* (Emond et al. 2011), a role for *Pcdh19* in multipolar migration is a possibility. Although studying an implication of *Pcdh19* in multipolar migration was outside the boundaries of this thesis, experiments that analyse the cell morphology and time-lapse experiments that analysed speed, migration patterns, time to enter the cortical plate or number of processes, such as the ones conducted by Inoue *et al.* or Fan *et al.* could be performed in the future (Inoue et al. 2019; Fan et al. 2018).

Changes in neurogenesis could also impact the final position of neurons in the cortex, but the experiments conducted in this thesis were not informative into that aspect. Moreover, unpublished data from obtained by Dr. Jessica Griffiths (Cardiff university) did not detect any differences in the neurogenesis of *Pcdh19*-KO brains compared to the WT, which makes this possibility unlikely.

4.4.4.4 Absence of phenotype in the *Pcdh19*-HET brains and possible future experiments

Analysis of *Pcdh19*-HET brains revealed a different phenotype from the *Pcdh19*-KO. Analysis of cellular distribution was made by dividing the cortical plates into bins of equal size and a significant difference with respect to the WT brains was detected in bin 8. The results suggest that

migrating cells from *Pcdh19*-HET animals might accumulate in the central bins (4 and 5) more than the cells from WT brains, thus reducing the number of cells accumulating in the lower bins which explains the significant difference in bin 8. But, overall, *Pcdh19*-HET brains did not seem to present a significant alteration of migration with respect to their WT counterparts.

However, we also have to take into account the fact that *Pcdh19*-HET brains contain a mixture of WT and *Pcdh19*-KO cells. Cells are not isolated entities and there are a lot of biological processes (including cortical migration) where cells influence the behaviour of other cells, such as the Cajal-Retzius cells who secrete reelin, regulating the final positioning of the cortical neurons (Ogawa et al. 1995), or the external cues interneurons follow to reach the cortex (Martini et al. 2009). In consequence, it remains a possibility that WT cells within the *Pcdh19*-HET brains could get influenced by the *Pcdh19*-KO cells and vice versa, altering the cortical migration of both cell types differently with respect to the WT neurons from WT brains. Such a mechanism would also fit with the 'cellular interference' hypothesis, that has also been proposed to be the cause of craniofrontonasal syndrome (CFNS), which shows the same abnormal pattern of inheritance as *EIEE9* (Wieland et al. 2004). Since both *Pcdh19*-KO and WT cells were analysed together in the *Pcdh19*-HET brain the differences could get masked and any differences between brains from WT animals and from *Pcdh19*-HET mice would not be detectable.

To test this hypothesis, it would be necessary to be able to distinguish between WT and KO cells within *Pcdh19*-HET brains. An elegant way to do so would be through the use of the D4/XGFP (XGFP) mouse strain (Hadjantonakis et al. 1998), which harbours a transgene containing EGFP in its X chromosome. By mating XGFP and *Pcdh19* mutant animals, heterozygous females could be obtained with WT *Pcdh19* and XGFP on one X chromosome and mutant *Pcdh19* and no XGFP on the other. After random X-inactivation, these mice would have green fluorescence in their WT cells,

while *Pcdh19*-KO cells would not express EGFP. *In utero* electroporations with a plasmid expressing a different reporter, such as RFP, could be performed at E13.5 to analyse differences among cellular populations at E18.5 to study any possible differences among the populations (**Figure 39**).

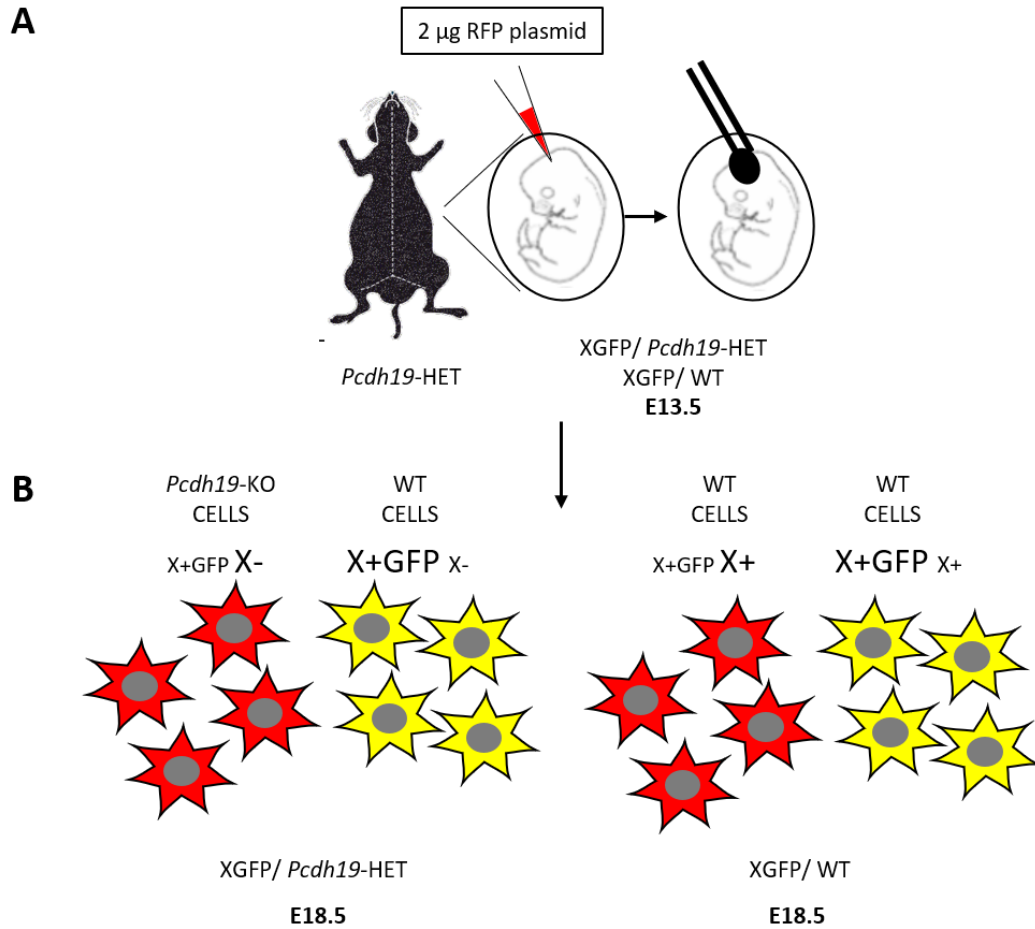


Figure 39. Scheme of the suggested experiment to study the migration of WT and *Pcdh19*-KO cells within the *Pcdh19*-HET brain.

Embryos from a mating between an XGFP male and a *Pcdh19*-HET female would be *in utero* electroporated with an RFP plasmid at E13.5 (A). Migration of WT and *Pcdh19*-KO cells would be analysed within the *Pcdh19*-HET brains and would be compared to the WT cells from WT brains. In the *Pcdh19*-HET brains, WT cells would be green and red (depicted as yellow) and *Pcdh19*-KO cells would be red while in the WT brains there would be a mix of green and green and red WT cells (B). X-chromosome which is active in each set of cells is shown in a bigger font size. WT, wild-type; HET, *Pcdh19*-heterozygous; KO, *Pcdh19*-knock-out.

4.4.5 Analysis of migration in late-born neurons

4.4.5.1 ShRNA *in utero* electroporations on WT and *Pcdh19*-KO animals

The results of **section 4.3.3.1** revealed that EGFP+ neurons in the WT and *Pcdh19*-KO P10 brains co-electroporated with *Pcdh19* shRNAs had a tendency to localise in higher positions within layers II/III with respect to the brains electroporated with the control. There was a higher presence of EGFP+ cells localised in lower regions in the brains electroporated with the shRNA control compared to the brains electroporated with the *Pcdh19* shRNAs too, which is an anomaly and should not be present in shRNA control electroporations.

These results could be caused by an off-target effect due to unspecific binding and silencing of another target, which would produce the alteration in the migration observed in the experiment. Even though migration was not affected by the shRNA control in the brains *in utero* electroporated at E13.5 and analysed at E18.5 (**Figure 31, Figure 32**), the control could be altering the distribution of cells from E15.5 onwards or the effect might not be observed at E18.5 yet. As explained in **section 4.4.2**, this shRNA had been previously used in WB experiments, but not in *in utero* electroporation studies (Santer et al. 2017; Conn et al. 2015; Pu et al. 2017). Despite the fact that shRNA controls are one of the recommended negative controls by the companies, there have been reports describing effects produced by shRNAs that are widely used as such, like the luciferase shRNA that affects voltage-gated ion channels in the hippocampus of mice (Y. Hasegawa et al. 2017). In addition to that, Ghazalpour *et al.* and Liang, Hart, & Crooke demonstrated that the transfection of siRNAs (which use part of the same machinery as the shRNAs) *in vitro* altered the levels of some mRNA and proteins (Ghazalpour et al. 2011) by competing with the endogenous miRNAs (Liang et al. 2013). This change of levels is transitory, but any kind of alteration at the developmental stages of the brain could produce some

effects. Another possibility could be that, despite careful handling, the maxiprep of the shRNA control got contaminated at some point during the experiments, probably when the electroporations at E15.5 started, explaining why E13.5 brains electroporated with the control are not affected.

To test these hypotheses, *in utero* electroporation experiments with only EGFP and EGFP plus the shRNA control at E15.5 in WT animals could be performed to see if there is a difference in the migration of the brains electroporated with the shRNA control with respect to the brains electroporated with EGFP. Some experiments could be conducted using the old maxiprep of the shRNA control and others using a new one. If the electroporation were aberrant only in the brains electroporated with the old maxiprep, the problem would be due to a contamination; if cortical migrations were affected in both conditions (old and new maxiprep), the migration failure would be due to an off-target effect.

In any case, the migration defect caused by the shRNA control render these results unreliable and not amenable to interpretation.

Therefore, only the EGFP *in utero* electroporations on WT and *Pcdh19*-mutants will be discussed. The use of shRNAs allows to acutely knockdown a protein at different time-points, which permits the study of its role in different phases of cortical development and the investigation of the effects of knocking down proteins that are lethal in early development or are redundant with other genes (Reiner et al. 2012). On the other hand, EGFP *in utero* electroporations in WT and mutant animals, despite being expensive and slow due to the necessity to generate the mutant animals, are much cleaner experiments where only a reporter that is innocuous for the cells is received, and does not produce off-target effects (Reiner et al. 2012). Moreover, as explained in **section 4.4.3**, they reflect better the conditions of the EIEE9 compared to the electroporations with shRNAs.

4.4.5.2 EGFP *in utero* electroporations on WT, *Pcdh19*-HET and *Pcdh19*-KO animals

EGFP *in utero* electroporations at E15.5 in WT, *Pcdh19*-HET and *Pcdh19*-KO animals showed that GFP-expressing cells from *Pcdh19*-KO animals were located in higher positions with respect to their WT counterparts at P10. This result was consistent with the data obtained *in vitro* by Pederick *et al.*, where some *Pcdh19*-KO cells displayed increased migration with respect to the WT cells (Pederick *et al.* 2016). However, when the animals were electroporated earlier in development (E13.5), most cells were detected in lower areas of the cortical plate compared to the WT. These results are not paradoxical since cells were electroporated at different time-points. Due to the inside-out pattern of cortical lamination, the progenitor cells that were electroporated at E13.5 are still generating some deep layer neurons and start generating upper layer neurons not long after; while cells electroporated at E15.5 give rise only to upper layer neurons (Bayer *et al.* 1991; Sidman *et al.* 1973; Angevine *et al.* 1961; Hatten 1999). Depending on their time of birth, neurons present different characteristics and migrate with different mechanisms (Nadarajah *et al.* 2001). Since *Pcdh19*-KO presented altered cortical positioning of cells electroporated at E13.5 and E15.5, it is possible both lower and upper layer neurons are affected by the lack of *Pcdh19*. However, as mentioned previously, IUE at E13.5 also labels a percentage of upper-layer neurons, so it is also possible that upper layer neurons are the only ones whose cortical positioning is altered. If *Pcdh19* only had a role in the migration of late-born neurons, the mechanism it would be participating in would be glia-guided locomotion. On the other hand, if *Pcdh19* was involved in the migration of early- and late-born neurons, it is probable that the protein had a role in one of the common mechanisms (multipolar migration, somal translocation) used by both types of cells to migrate. As has been seen with *Cdh2* (Martinez-Garay *et al.* 2016;

Gil-Sanz et al. 2013; Jossin et al. 2011), *Pcdh19* might be involved in several of these mechanisms and not just one.

Another explanation of the phenotype observed, where the *Pcdh19*-KO cells that were electroporated at E13.5 seemed to be failing migration at E18.5, but then *Pcdh19*-KO cells electroporated at E15.5 were located in higher positions with respect to the WT at P10, would be a compensatory mechanism. In a compensatory mechanism, other genes or extracellular migration guides are upregulated to compensate for the loss of another gene. In this case, the loss of *Pcdh19* would cause the lower positioning of cells in the cortical plate compared to WT cells at E18.5, but by P10 another gene or guide related to *Pcdh19* would be compensating for the lack of *Pcdh19* (El-Brolosy et al. 2017). If it overcompensated it could end up generating the opposing phenotype, as it is the case in monoamine oxidase A (MAO-A) knockout mice whose chronic increase of 5-HT causes an alteration of the cerebral cortical blood flow that is not consistent with the results obtained when this neurotransmitter is acutely increased (Holschneider et al. 2001). So an upregulation of genes could cause the alteration in the migration. Compensatory mechanisms are exerted by genes that are related to the one that has been depleted, so to investigate this hypothesis, an analysis of the levels of expression of delta protocadherin genes by qPCR, that are the most closely related to *Pcdh19* could be conducted, using WT *Pcdh19* as a control. The study of the expression levels of the genes could be performed at several ages between E15.5, when the cells that acquire higher positions within the cortical plate in the *Pcdh19*-KO are born, and P7, when migration is finished approximately. The upregulation of any of the delta protocadherin genes at these ages in the *Pcdh19*-KO with respect to the WT animals would suggest a compensatory mechanism is taking place.

Pcdh19-HET brains do not show any overall differences in migration compared to their WT counterparts at E18.5 or P10. This is an interesting

result, since in humans mosaic females are the most affected by the illness, while only slight behavioural characteristics have been reported in hemizygous males, as described in **section 1.5**. This could imply that cellular interference, that is the model proposed to lead to the disease, is not present in the radial cortical migration, hence the lack of phenotype in the *Pcdh19*-HET females.

However, the slight decrease is interesting because the total lack of *Pcdh19* produces an increase in the migration of late-born neurons with respect to the WT, but the mosaicism does not cause an intermediate phenotype as expected but has a tendency to oppose the phenotype of the *Pcdh19*-KO. In fact, the results are so contrasting that the difference in the percentage of EGFP+ cells in bin 2 is significant between *Pcdh19*-HET and *Pcdh19*-KO. This result could actually be caused by the cellular interference mechanism, which could give the phenotype observed even if there was a compensatory mechanism present.

At E13.5, the migration in the *Pcdh19*-HET brains isn't altered, which could mean the cellular interference is not at play during the migration of early-born neurons or the mixture of WT and *Pcdh19*-KO cells could be masking any phenotypes.

To explore more about the migration of cells in *Pcdh19*-HET brains at E15.5, the experiment using XGFP/*Pcdh19*-HET and XGFP WT mice described at the end of **section 4.4.4** could be performed, electroporating at E15.5 and analysing at P10.

PCDH19 also contains a WAVE regulatory complex (WRC) binding site, the WIRS (B. Chen et al. 2014). As detailed in **section 1.6.1**, the WRC participates in the regulation of actin cytoskeleton dynamics via the Arp2/3 complex (Kurusu et al. 2009). Since actin polymerization through the *Cdk5-p27Kip1* and *Cdk5-Pak1* pathways is essential in the extension and maintenance of the leading process of migrating cells (Kawauchi et al. 2006; Nikolic et al.

1998), it could be also important to consider if PCDH19 exerts its role in migration through the WAVE complex. Interestingly, PCDH17 has been reported to participate in cell and axonal migration via the WAVE complex. Hayashi *et al.* revealed that the increased cell-motility due to PCDH17 expression *in vitro* shown by Nakao *et al.* (Nakao et al. 2008) disappeared when *Pcdh17* was mutated and the binding sites for *Nap1*, one of the components of the WAVE complex, was deleted (Hayashi et al. 2014). A general experiment to determine if *Pcdh19* is involved in cell migration via the WAVE complex would be *in vitro* migration assays. Neurospheres derived from *Pcdh19*-KO embryos, such as the ones obtained by Pederick *et al.* (Pederick et al. 2016) could be transfected with a *Pcdh19*FL plasmid. The migration of these cells could be compared to untransfected controls. If *Pcdh19* had an effect on the migration of the cells, another test could be conducted in which cells were transfected with a *Pcdh19* that lacks the WIRS, using the cells transfected with the *Pcdh19*FL as a control. A different migration of the cells transfected with the mutant gene with respect to the migration of the cells transfected with the full-length *Pcdh19* would support a role in migration via the WAVE complex.

To determine if *Pcdh19* exerts a role in cortical migration specifically, *Pcdh19*-KO animals could be electroporated with a *Pcdh19* that lacked the WIRS or with a full-length *Pcdh19*. The full-length *Pcdh19* should rescue the phenotype and would be used as a control. If the *Pcdh19* that lacks the WIRS does not rescue the phenotype or the rescue is smaller than the observed in the brains of *Pcdh19*-KO animals electroporated with the full-length *Pcdh19*, the hypothesis will be validated. Even though this experiment can be conducted *in vivo* and is more specific, it has a couple of problems that need to be taken into account. The *Pcdh19* that is introduced as a rescue could be overexpressed or ectopically expressed in cells that do not normally contain the protein, which could cause an undesired phenotype. In addition, electroporation of *Pcdh19* into the *Pcdh19*-KO would generate mosaicism, which could also complicate interpretation.

Other cadherins apart from PCDH17 have been previously reported to have roles in cell migration, regulating multipolar migration, glial-guided motility or somal translocation (Franco et al. 2011; Kawauchi et al. 2010). One of this cadherins is cadherin 2 (CDH2), which has been reported to interact with protocadherin 19 (Emond et al. 2011) and to regulate cell movement in neurulation in zebrafish when forming complexes (Biswas et al. 2010). Thus, it is possible that PCDH19 cooperates with CDH2 in the regulation of migration. CDH2 function has been reported to be regulated by the *Dab1* effector *Rap1* (Franco et al. 2011; Jossin et al. 2011). To analyse if PCDH19 is also regulated by *Rap1*, an experiment similar to the one conducted by Franco *et al.* could be performed to study if effects in migration caused by *Rap1* inactivation can be rescued by *Pcdh19* overexpression (Franco et al. 2011). The rescue, partial or total of the phenotype, would demonstrate that *Rap1* contributes to the regulation of *Pcdh19* function in migration. However, rescue experiments can be very tricky. When electroporating, the gene could be expressed either ectopically or at much higher levels than in normal conditions which could generate a new phenotype that is not seen when the protein is active in a WT animal (Moriya 2015). This aspect of the experiment should be taken into account when performing this kind of experiments.

Moreover, PCDH20 has been shown to regulate the positioning and cell-type specification of layer IV neurons after the radial migration is finished via the small GTPase Rhoa (Oishi et al. 2016), which is also a possible role of *Pcdh19* that would need to be considered. As detailed in **section 4.4.4.3**, time-lapse experiments would determine when *Pcdh19* is exerting its role.

4.4.6 Conclusion

In summary, the *in utero* electroporation experiments performed in this chapter demonstrate that cortical migration is affected at different time-points during corticogenesis (E13.5 and E15.5) in *Pcdh19*-KO and at E15.5 in *Pcdh19*-HET, suggesting *Pcdh19* might have a role in this process. Even

though some differences can be detected, cells located at lower positions in the *Pcdh19*-KO mice at E18.5 could end up acquiring their final positions within the cortical plate later, and the disruptions in cortical positioning at P10 observed in the *Pcdh19*-HET and *Pcdh19*-KO animals were relatively subtle, so it is unknown if the alterations in cortical migration are causing a phenotype in cortical lamination. Therefore, an analysis of cortical lamination in WT and *Pcdh19*-mutant animals was conducted (Chapter 5). Moreover, further experiments would have to be conducted to explore which mechanism or mechanisms *Pcdh19* could be participating in to generate the observed phenotype. Since one of the possibilities is that a compensatory mechanism is taking place, studying candidate genes for that role could be an interesting path to follow.

Chapter 5: Characterization of the WT, *Pcdh19*-HET and *Pcdh19*-KO animals.

5.1 Introduction

As shown in the previous chapter, *Pcdh19*-HET and *Pcdh19*-KO animals presented an altered migration phenotype compared to their WT littermates. During development, the cortical wall is generated in an 'inside-out' manner, where early-born cells form the deep layers and late-born cells, using radial glia cells as scaffolds, migrate past the deep layer neurons and position themselves in the upper part of the cortical plate, forming the upper layers (Rakic 1974; Nadarajah et al. 2001; Franco et al. 2011). Thus, an alteration in the migration of early-born neurons (**Figure 35**) and late-born neurons (**Figure 38**) could impact the positioning of the different cell types in the cortex leading to cortical dysplasia, a malformation that has been reported in some EIEE9 patients in the (Ryan et al. 1997; Kurian et al. 2018). Alterations in the number of cortical glutamatergic neurons or GABAergic interneurons could also affect the excitatory-inhibitory balance, which leads to epilepsy and has also been described in patients with autistic spectrum disorder (Marín 2012).

In fact, other members of the cadherin superfamily have been reported to participate in processes regulating neuronal position and numbers. CDH2, a known interacting partner of PCDH19 (Emond et al. 2011), is involved in neurogenesis and migration of cortical projection neurons. When knocked out, it leads to premature neuronal differentiation and migration defects (Kadowaki et al. 2007; J. Zhang et al. 2010; Franco et al. 2011). CDH13 has been shown to play a role in cell survival of interneurons and pyramidal cells in the mouse cortex, probably by preventing apoptosis via the Akt/GSK β signalling pathway (Killen et al. 2017). Studies in mouse have also revealed the involvement of the protocadherin alpha cluster in cortical migration through interactions with the WAVE regulatory complex (Fan et

al. 2018). Interestingly, *Pcdh19* can also bind to this complex through its WIRS region. Within the nonclustered protocadherins, Xiao *et al.* showed that overexpression of *Pcdh7* promotes cortical neuronal death *in vitro* that can be rescued by eliminating the CM2 motif from the gene. Uemura *et al.* revealed that *Pcdh10* knockout produces a failure of striatal axonal projections that leads to the disappearance of the mouse barrel cortex at P8, and Oishi *et al.* also demonstrated that *Pcdh20* acts as a regulator in the cortical lamination of layer IV neurons (Uemura *et al.* 2007; Xiao *et al.* 2018; Oishi *et al.* 2016).

Although Pederick *et al.* reported no severe alterations in the cortex of *Pcdh19*-HET or *Pcdh19*-KO animals (Pederick *et al.* 2016), that observation was based on an analysis of the gross morphology of the brain. No quantifications were performed, and no markers were used to differentiate between different neuronal types. To date, no thorough immunohistochemical characterization of the mutant animals has been conducted. Such an analysis is necessary, though, because small differences regarding cell number or positioning, which might not be detected qualitatively by observation, might still lead to phenotypic consequences.

5.2 Aims

The aim of this chapter was to conduct an immunohistochemical characterisation of *Pcdh19*-HET and *Pcdh19*-KO animals by performing a thorough analysis of five cortical markers (CUX1, SATB2, RORB, CTIP2 and TBR1) at P10 and four interneuronal markers (PV, CB, CR, SST) at P20. The number of cells positive for the marker with respect to DAPI and the distribution of cells along the cortical wall was compared between mutant and WT animals. Total number of cells, distribution and cortical width of the somatosensory cortex (SSC) were also analysed.

5.3 Results

To analyse if the mutant animals presented differences in the number or distribution of the cell types present within the cortical wall, several immunohistochemical experiments were conducted in WT, *Pcdh19*-HET and *Pcdh19*-KO animals, using markers for different cortical projection neuronal subtypes, as well as different interneurons. An overview of the experiments is provided in **Figure 40**.

As explained in Chapter 3, glutamatergic excitatory markers were studied at P10, when the excitatory pyramidal neurons have reached their final positions within the cortex (Alcamo et al. 2008; Jabaudon 2017). Regarding the inhibitory GABAergic markers, the analysis was conducted at P20 since most markers present a very low expression before this age, as previously reported (J. del Rio et al. 1994).

Cortical glutamatergic markers assessed were the ones used in Chapter 3, namely CTIP2, SATB2, RORB and TBR1, plus CUX1 (**Figure 40C**). CUX1, which was not analysed in Chapter 3 experiments due to the lack of an antibody that detected the marker under the harsh conditions of the ISH, is a marker of upper layer neurons that project intracortically (Nieto et al. 2004; Molyneaux et al. 2007; Jabaudon 2017).

Interneuronal GABAergic markers analysed were PV, CB, CR and SST (**Figure 40C**). PV and CB were already used and described in Chapter 3, but CR and SST could not be detected by the antibody after the ISH treatment, so they were not used in Chapter 3. CR-expressing cells are either bipolar interneurons with a bursting firing pattern or multipolar neurons with a regular firing pattern (Barinka et al. 2010). CR is also expressed in a subset of pyramidal neurons in layer Va at P8 in mouse (J. Liu et al. 2014). In contrast, SST-positive interneurons are a diverse group that is comprised by different interneuronal subpopulations (Rudy et al. 2011; Wamsley et al. 2017). Similar to what happened in Chapter 3, 5HT3aR-expressing cells

could not be detected by the antibody. Consequently, not 100% of the cortical interneurons were analysed. This will be discussed in **section 5.4**.

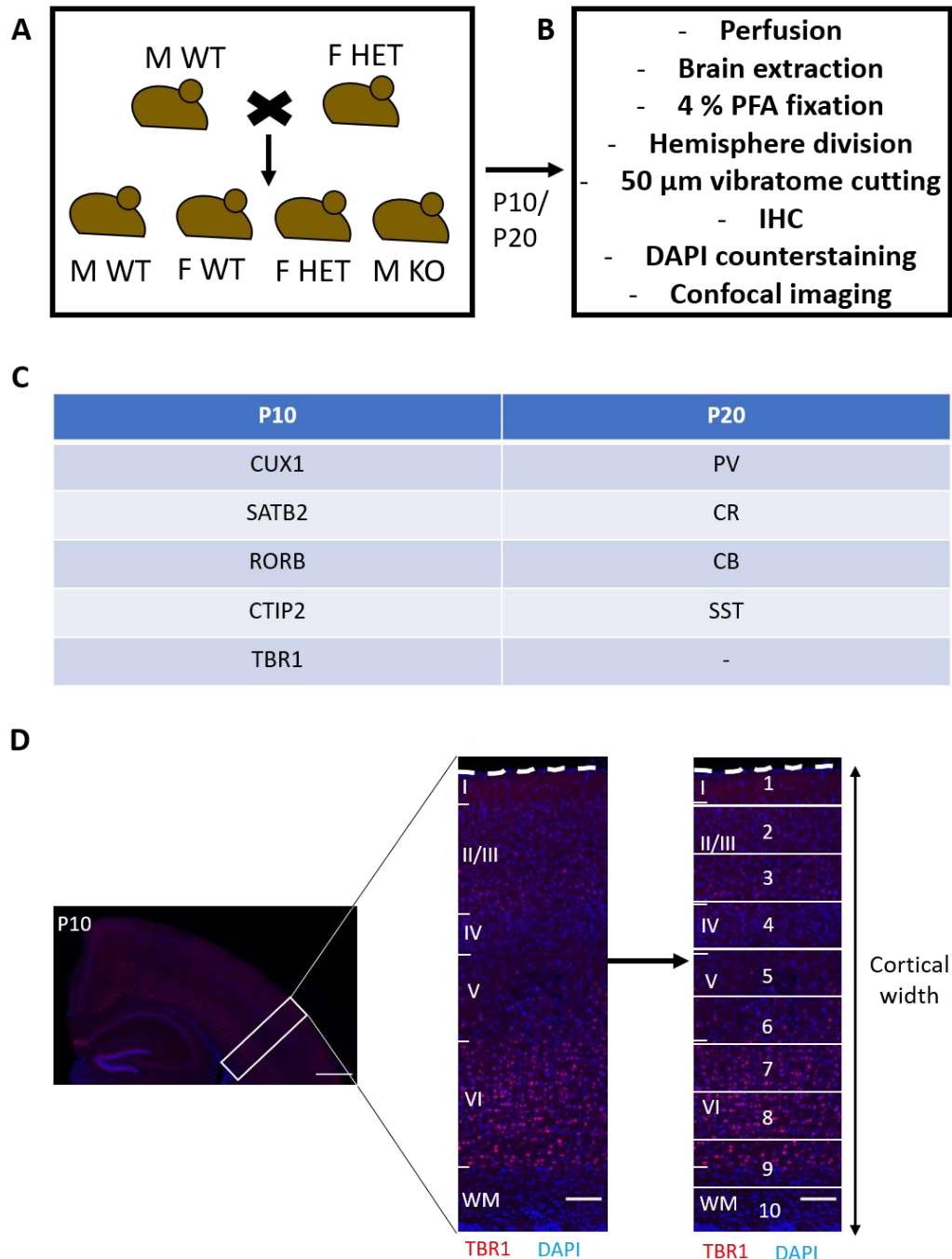


Figure 40. Overview of the immunohistochemical experiments conducted in WT, *Pcdh19*-HET and *Pcdh19*-KO mice analysed in Chapter 5.

Cortical layers are indicated with roman numerals in the representative images. White dotted lines delimit the marginal zones. M WT, wild-type male; F WT, wild-type female; F HET, *Pcdh19*-heterozygous female; M KO, *Pcdh19*-knock-out male; WM, white matter. Scale bar of right hemisphere: 500 μ m; scale bar of selection: 100 μ m.

5.3.1 No differences in cortical width, total number and distribution of cells in the SSC among genotypes.

To test the possibility that alteration of the *Pcdh19* gene caused an effect in the overall number of cells or their distribution, nuclei from P10 and P20 animals were stained with DAPI and counted using Image J analysis software. The cortical width from the selected region of the SSC was also measured. In total, a minimum of 3 images of 6 WT brains, 9 *Pcdh19*-HET brains and 5 *Pcdh19*-KO from at least 3 different litters were analysed at P10. At P20, 6 images of 4 brains from each condition, from at least three different litters were used. Animals from the same litter were treated as independent biological replicates. The selected region had a width of 1000 pixels in P10 images and 1500 pixels in P20 images, which is equivalent to 415 μm and 622 μm , respectively.

Images and posterior quantification did not reveal any clear differences in the overall number of DAPI-positive cells or their distribution amongst the genotypes in P10 (WT= 1985 \pm 114 cells, *Pcdh19*-HET= 1991 \pm 174 cells and *Pcdh19*-KO= 2065 \pm 193 cells) or P20 (WT= 2342 \pm 114 cells, *Pcdh19*-HET= 2239 \pm 42 cells and *Pcdh19*-KO= 2064 \pm 147 cells). Cortical width did not present any major changes in the mutant animals respective to their WT counterparts at P10 (WT= 1321.09 \pm 21.59 μm , *Pcdh19*-HET= 1354.23 \pm 33.78 μm and *Pcdh19*-KO= 1305.41 \pm 30.62 μm) or P20 (WT= 1417.18 \pm 32.71 μm , *Pcdh19*-HET= 1402.97 \pm 42.92 μm and *Pcdh19*-KO= 1387.02 \pm 9.88 μm) either (**Figure 41**).

Statistical analysis confirmed these results. At P10, one-way ANOVA showed no difference among genotypes in cortical width (F (2, 17) =0.699, p>0.05) or number of DAPI-positive cells (F=0.61, df=2, p>0.05). As with P10 results; at P20 no differences between mutant animals and their WT littermates were detected in the statistical analysis of cortical width (F (2, 9) =1.61, p>0.05) or in number of DAPI-positive cells (F (2, 9) =1.348, p>0.05).

When performing the analysis, it was noticeable that the number of DAPI cells did not increase between P10 and P20 in *Pcdh19*-KO brains. However, statistical analysis did not show any significant differences between WT, *Pcdh19*-HET and *Pcdh19*-KO regarding the increase of the total number of DAPI positive cells between ages P10 and P20 (**Figure 42A**).

Distribution of cells at P10 and P20 (**Figure 42B, C**) showed no statistical differences in any bins for any of the conditions. The results are shown in the appendix (**Table A. 10, Table A. 16**).

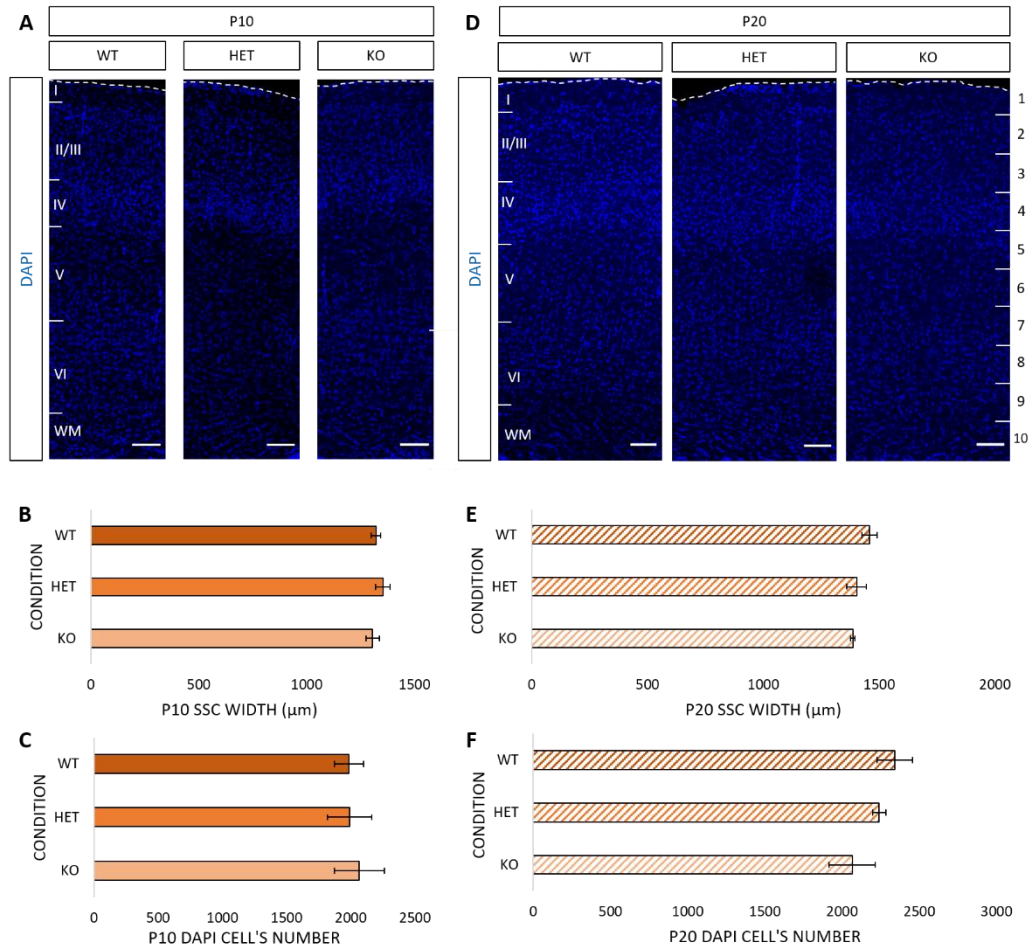


Figure 41. There were no significant differences in the total number of cells and cortical width of the SSC amongst the different genotypes.

Representative images of P10 (A) and P20 (D) animals counterstained with DAPI (blue). (B, C) Quantification of the stained images from A. (E, F) Quantification of the counterstained images from D. Data are presented as mean \pm SEM. Results showed no statistical differences in number of cells (B, E) or cortical width (C, F) at P10 or P20. Cortical layers are indicated with roman numerals in the representative images. The horizontal bins used to perform the quantification are shown in arabic numerals on the right side of the image. White dotted lines mark the limit of the marginal zones. WT, wild-type; HET, *Pcdh19*-heterozygous, KO, *Pcdh19*-knock-out; WM, white matter; SSC, somatosensory cortex. Scale bar: 100 μ m.

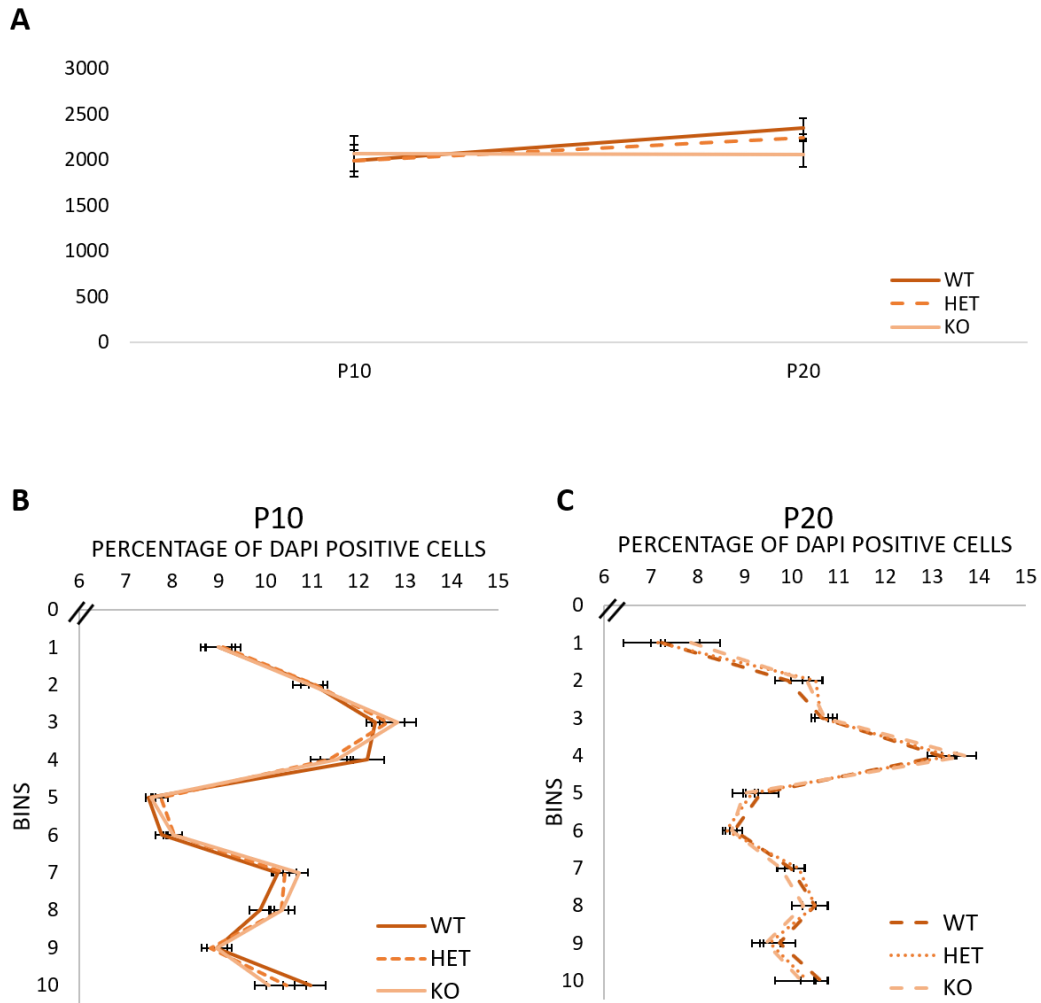


Figure 42. *Pcdh19*-HET and *Pcdh19*-KO animals showed no significant differences in the distribution of cells along the cortical wall with respect to their WT littermates.

(A) Graph shows the increment in number of DAPI counterstained nuclei between P10 and P20 among the animals. Results detected no statistical differences among the mice (B, C) Quantification of the stained images from **Figure 13**. Graphs represent DAPI-positive nuclei in each of ten equal-size horizontal bins expressed as % of total DAPI-positive cells. The data are presented as mean \pm SEM. Results revealed no statistical differences in the distribution of cells in P10 (B) or P20 (C) mice. WT, wild-type; HET, *Pcdh19*-heterozygous; KO, *Pcdh19*-knock-out.

5.3.2 Cell number and distribution of cortical excitatory neurons in the P10 SSC

5.3.2.1 CUX1-expressing cells showed a slight difference in distribution between WT and *Pcdh19*-HET

To analyse if alteration of *Pcdh19* affected the relative proportion of upper layer, intracortically-projecting neurons or their distribution within the cortex, brain sections from P10 WT, *Pcdh19*-HET and *Pcdh19*-KO were immunostained for CUX1 and counterstained with DAPI (Figure 43). CUX1-positive and DAPI-positive cells from an SSC region were then counted using Image J analysis software.

As seen in Figure 43A, no obvious differences in the number of CUX1-expressing cells could be seen between the genotypes, except for a small number of CUX1 cells in the lower layers that were more prominently stained in the WT than in the *Pcdh19*-HET or *Pcdh19*-KO animals.

Quantification showed that total number of CUX1-expressing cells with respect to DAPI in the SSC of WT, *Pcdh19*-HET and *Pcdh19*-KO animals (Figure 43B) was slightly increased in *Pcdh19*-KO brains with respect to the WT (WT=21.45 ± 1.2%, *Pcdh19*-HET=22.36 ± 1.65% and *Pcdh19*-KO=24.82 ± 2.13%). However, statistical analysis revealed there were no significant differences among the genotypes (ANOVA, F (2, 9) =2.461, p>0.05). Quantification of the distribution of CUX1-positive cells at P10 throughout the cortical plate (Figure 43C) revealed a decrease in the percentage of CUX1+ cells in the mutant animals compared to the WT in bins 5 (WT=2.08 ± 0.18%, *Pcdh19*-HET=0.86 ± 0.27% and *Pcdh19*-KO=1.14 ± 0.32%), 6 (WT=2.24 ± 0.41%, *Pcdh19*-HET=0.75 ± 0.32% and *Pcdh19*-KO=1.43 ± 0.43%) and 7 (WT=2.32 ± 0.73%, *Pcdh19*-HET=0.87 ± 0.1% and *Pcdh19*-KO=0.86 ± 0.25%). Those differences were significant in bin 5 between WT brains and *Pcdh19*-HET brains and trended towards significance between WT and *Pcdh19*-KO mice (ANOVA, F (2, 9) =5.82, p=0.024; Tukey HSD post hoc test,

p=0.024 WT vs HET; p=0.077 WT vs KO). In bins 6 (ANOVA, F (2, 9) =3.65, p=0.069) and 7 (ANOVA, F (2, 9) =3.55, p=0.073) the difference was treading towards significance.

Details of the statistical analysis are shown in the appendix (**Table A. 11**).

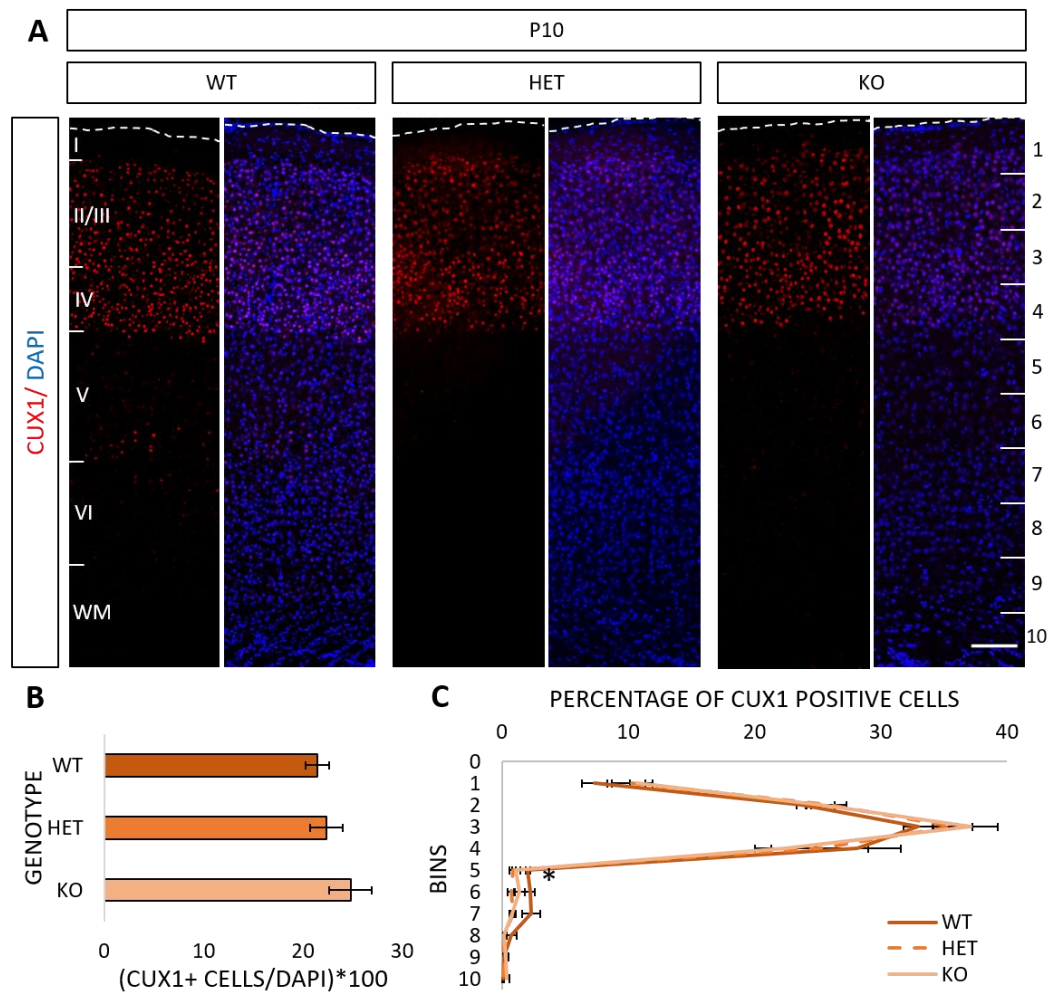


Figure 43. Immunohistochemical analysis of mutant animals revealed a decrease in the percentage of CUX1-positive cells in bin 5 at P10 with respect to WT animals.

(A) Representative images of P10 animals stained with CUX1. Nuclei were counterstained with DAPI (blue). (B-C) Quantification of the images stained with CUX1 from (A). Data are presented as mean \pm SEM. Results revealed no statistically significant differences in the number of CUX1-expressing cells with respect to DAPI (B). Distribution of CUX1-positive cells in the cortex (C) showed a statistical difference in bin 5 between WT and *Pcdh19*-HET animals. Cortical layers are indicated with roman numerals in the representative images. The horizontal bins used to perform the quantification are shown in arabic numerals on the right side of the image. White dotted lines delimit the marginal zone. Graphs represent CUX1-expressing cells in each of ten equal-size horizontal bins expressed as % of total CUX1-positive cells. 3 images of 4 brains of each genotype from at least 3 different litters were analysed. WT, wild-type; HET, *Pcdh19*-heterozygous; KO, *Pcdh19*-knock-out; WM, white matter. Scale bar: 100 μ m.

5.3.2.2 SATB2-positive cells were similar in number and distribution among genotypes

The number and cortical distribution of corticocortical (callosal) projecting neurons was analysed by immunostaining for SATB2 in the SSC of WT, *Pcdh19*-HET and *Pcdh19*-KO animals at P10.

No observable differences were detected in the mutant animals with respect to the WT in the percentage of SATB2-expressing cells with respect to DAPI or their distribution in the cortex, as outlined in **Figure 44**. Cells expressing SATB2 were located throughout layers II-VI. When images were quantified, no differences were apparent in the total number of the SATB2-positive cells with respect to DAPI (WT=59.08 ± 0.92%, *Pcdh19*-HET=58.08 ± 3.62% and *Pcdh19*-KO=57.82 ± 2.74%), as seen in **Figure 44A**, or in the distribution of cells in any of the bins (**Figure 44B**). Statistical analysis confirmed these results.

Details of the statistical analysis are shown in the appendix (**Table A. 12**).

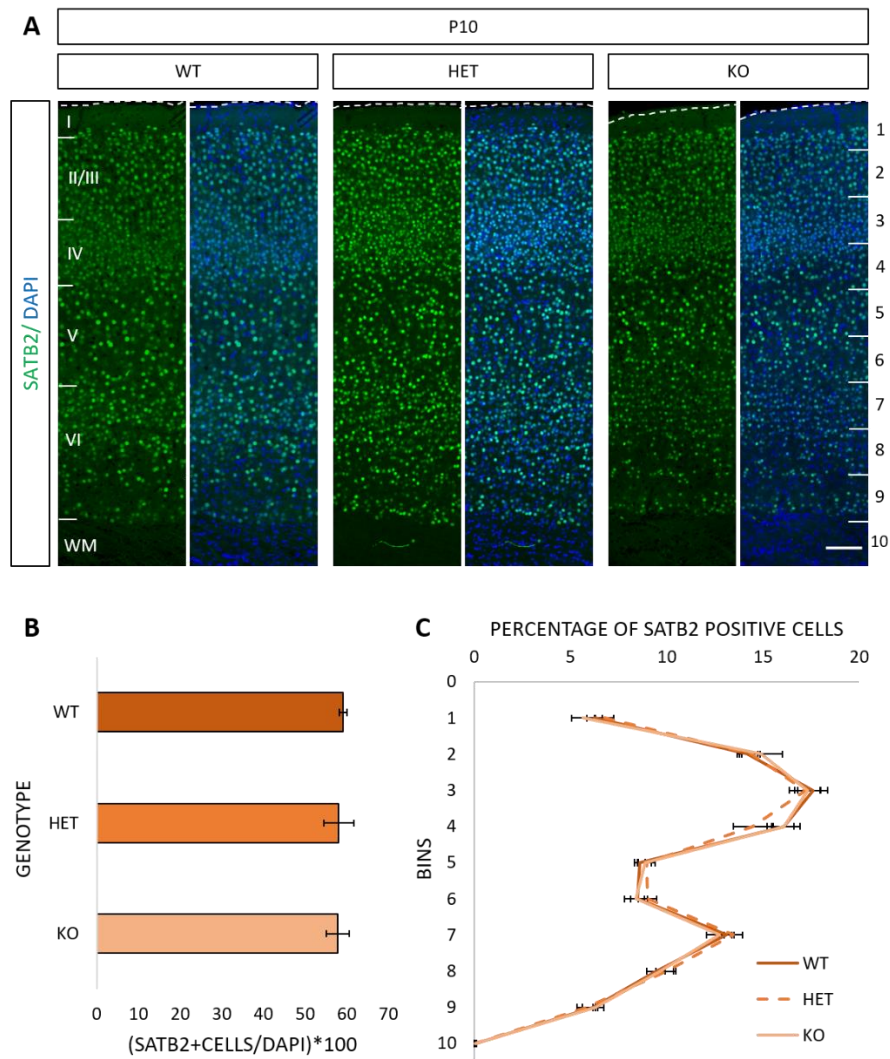


Figure 44. Number and distribution of cortico-cortical projecting cells is not altered in *Pcdh19*-HET and *Pcdh19*-KO animals with respect to their WT counterparts.

(A) Representative images of brains stained with SATB2 at P10. Nuclei were counterstained with DAPI (blue). (B-C) Quantification of the images stained with SATB2 from (A). Data are presented as mean \pm SEM. Analysis presented no differences in number of SATB2-positive cells with respect to DAPI (B). Distribution of cells expressing SATB2 in the cortex (C) showed no statistical differences between the conditions. Graphs represent SATB2-expressing cells in each of ten equal-size horizontal bins expressed as % of total SATB2-positive cells. 3 images of 4 brains of each condition from at least 3 different litters were analysed. Cortical layers are indicated with roman numerals in the representative images. The horizontal bins used to perform the quantification are shown in arabic numerals on the right side of the image. White dotted lines mark the limit of the marginal zones. WM, white matter. WT, wild-type; HET, *Pcdh19*-heterozygous; KO, *Pcdh19*-knock-out. Scale bar: 100 μ m.

5.3.2.3 No significant differences were detected among the genotypes regarding the number or distribution of cells positive for RORB

Analysis of the number of layer IV neurons was performed using immunostaining for RORB and counterstaining with DAPI. WT, *Pcdh19*-HET and *Pcdh19*-KO brains were studied at P10 at the level of the SSC and the percentage of RORB-positive cells with respect to DAPI and distribution of those cells spanning the cortical wall were calculated (**Figure 45**).

No differences were observed in the *Pcdh19*-HET or *Pcdh19*-KO animals compared to the WT littermates either in the RORB-expressing/DAPI ratio or in the distribution of the cells (**Figure 45A**).

Quantification of the images (**Figure 45B**) revealed a decrease in the relative proportion of RORB-positive neurons present in the *Pcdh19*-KO with respect to their WT littermates (WT=27.73 ± 1.75%, *Pcdh19*-HET=24.43 ± 2.5% and *Pcdh19*-KO=18.98 ± 3.7%). This difference was not significant when the statistical analysis was conducted (independent samples Kruskal-Wallis test, p=0.092).

Regarding the distribution of the neurons throughout the cortical plate (**Figure 45C**), quantifications revealed that at least 60% (WT=62.5 ± 3.67%, *Pcdh19*-HET=63.46 ± 8.55% and *Pcdh19*-KO=79.26 ± 9.85%) of the cells expressing RORB were located between bins 3 and 4, that would correspond to low layer II/III and layer IV, as seen in **Figure 40**.

Also, the percentage of cells expressing RORB in the *Pcdh19*-KO brains with respect to the WT counterparts was increased in bin 4 (WT=33.03 ± 1.50%, *Pcdh19*-HET=31.02 ± 7.08% and *Pcdh19*-KO=45.37 ± 7.58%) and slightly decreased in bins 5 (WT=9.51 ± 0.51%, *Pcdh19*-HET=8.12 ± 0.66% and *Pcdh19*-KO=7.33 ± 1.27%), 6 (WT=6.28 ± 0.71%, *Pcdh19*-HET=5.75 ± 1.33% and *Pcdh19*-KO=3.62 ± 1.6%), 7 (WT=3.56 ± 0.62%, *Pcdh19*-HET=4.58 ±

1.83% and *Pcdh19*-KO=1.54 ± 1.3%), 8 (WT=3.61 ± 1.14%, *Pcdh19*-HET=3.85 ± 1.38% and *Pcdh19*-KO=1.31 ± 1%) and 9 (WT=2.66 ± 0.85%, *Pcdh19*-HET=3.06 ± 1.1% and *Pcdh19*-KO=1.17 ± 0.84%). Despite that, no significant differences were detected in any of the bins when the statistical analysis was conducted.

Details of the statistical analysis are shown in the appendix (**Table A. 13**).

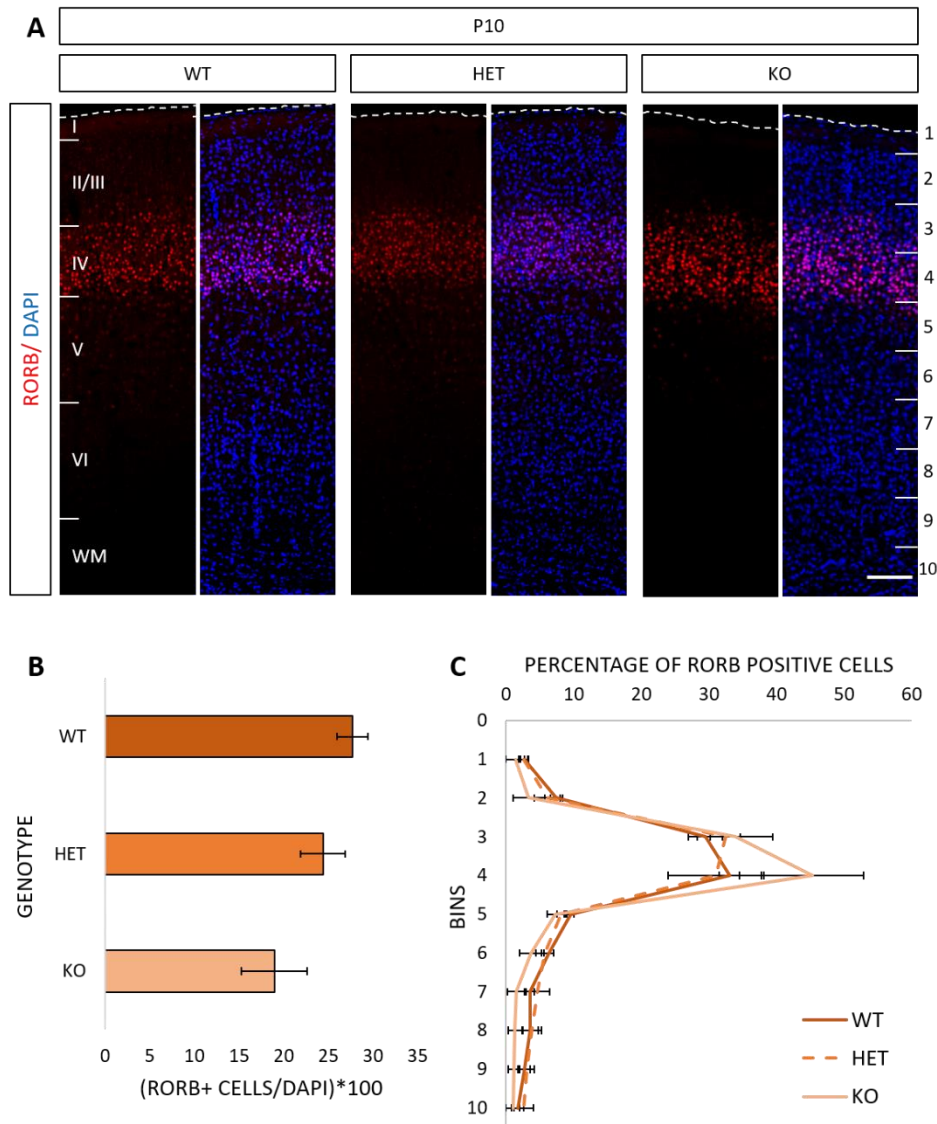


Figure 45. No differences in the proportion of RORB-positive cells or in their distribution at P10.

(A) Representative images of brains stained with RORB at P10. Nuclei were counterstained with DAPI (blue). (B, C) Quantification of the images stained with RORB from A. Data are presented as mean \pm SEM. Analysis revealed no significant differences in the number of RORB-expressing cells with respect to DAPI (B). Distribution of RORB-positive cells at P10 within the cortex (C) showed no statistical differences amongst the genotypes. Graphs represent RORB-expressing cells in each of ten equal-size horizontal bins expressed as % of total RORB-positive cells. 3 images of 4 brains of each condition from at least 3 different litters were counted. Cortical layers are indicated with roman numerals in the representative images. The horizontal bins used to perform the quantification are shown in arabic numerals on the right side of the image. White dotted lines delimit the marginal zones. WM, white matter; WT, wild-type; HET, *Pcdh19*-heterozygous; KO, *Pcdh19*-knock-out. Scale bar: 100 μ m.

5.3.2.4 Cells expressing CTIP2 did not present any differences among conditions

CTIP2 is a marker for corticospinal projecting neurons in layer V. In addition, layer VI neurons that extend axons to the thalamus also express CTIP2, albeit at lower levels. Analysis of these neurons by immunostaining for CTIP2 and counterstaining with DAPI was performed in WT, *Pcdh19*-HET and *Pcdh19*-KO animals at P10. The percentage of CTIP2-positive cells with respect to DAPI and distribution of those neurons within the cortex were determined (**Figure 46**).

Images from *Pcdh19*-HET and *Pcdh19*-KO brains presented similar numbers of CTIP2-expressing cells and distribution as in WT animals (**Figure 46A**).

Quantifications of the images detected no differences in the percentage of CTIP2 neurons normalised to DAPI between mutant and WT animals (**Figure 46B**; WT=13.33 ± 0.46%, *Pcdh19*-HET=13.82 ± 1.32% and *Pcdh19*-KO=13.61 ± 1.14%). As expected, statistical analysis confirmed these results (ANOVA, F (2, 9) =0.57, p>0.05).

When the distribution of the CTIP2-positive cells in the cortical wall was analysed (**Figure 46C**), at least 82% of the neurons positive for CTIP2 were present within bins 5 to 9 (WT=84.68 ± 0.91%, *Pcdh19*-HET=84 ± 1.07% and *Pcdh19*-KO=82.73 ± 0.55%), which correspond to layers V and VI (**Figure 40**).

Quantifications also revealed that *Pcdh19*-HET had a slight decrease in the percentage of CTIP2-positive neurons in bin 5 (WT=15.13 ± 1.59%, *Pcdh19*-HET=12.3 ± 2.41% and *Pcdh19*-KO=16.32 ± 2.41%) and bin 6 (WT=20.21 ± 1.47%, *Pcdh19*-HET=17.89 ± 1.71% and *Pcdh19*-KO=19.24 ± 2.58%); respectively and slight increase in the percentage of said neurons in bin 9 (WT=15.44 ± 1.38%, *Pcdh19*-HET=18.85 ± 1.27% and *Pcdh19*-KO=14.45 ± 2.17%). None of those differences were significant when the statistical

analysis was performed (bin 5= ANOVA, $F(2, 9) = 0.907$, $p = 0.438$; bin 6= ANOVA, $F(2, 9) = 0.347$, $p = 0.716$; bin 9= ANOVA, $F(2, 9) = 1.943$, $p = 0.199$).

Details of the statistical analysis are shown in the appendix (**Table A. 14**).

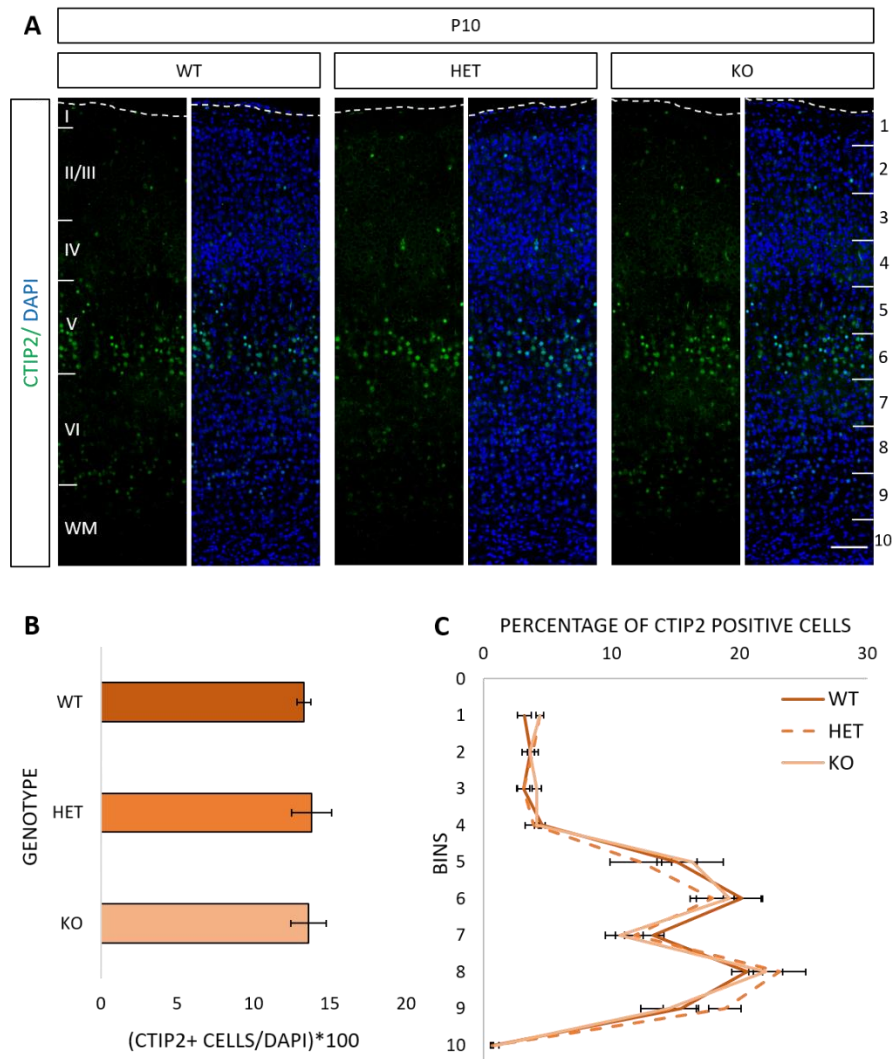


Figure 46. No differences in the total number of CTIP-positive cells with respect to DAPI and their distribution at P10 with respect to their WT counterparts.

(A) Representative images of brains stained with CTIP2 at P10. Nuclei were counterstained with DAPI (blue). (B) Quantification of the images stained with CTIP2 from (A). Data are presented as mean \pm SEM. Analysis revealed no differences in number of CTIP2-expressing cells with respect to DAPI (B). Distribution of cells expressing CTIP2 at P10 in the cortex (C) was not statistically significant amongst the genotypes. Graphs represent CTIP2-expressing cells in each of ten equal-size horizontal bins expressed as % of total CTIP2-positive cells. 3 images of 4 brains of each condition from at least 3 different litters were used. Cortical layers are indicated with roman numerals in the representative images. The horizontal bins used to perform the quantification are shown in arabic numerals on the right side of the image. White dotted lines mark the limit of the marginal zones. WM, white matter; WT, wild-type; HET, *Pcdh19*-heterozygous; KO, *Pcdh19*-knock-out. Scale bar: 100 μ m.

5.3.2.5 Analysis of TBR1-positive cells revealed a difference in distribution between the HET and KO animals

To perform the characterisation of layer VI neurons, WT, *Pcdh19*-HET and *Pcdh19*-KO brains were immunostained with the layer VI cortical marker TBR1 and counterstained with DAPI. TBR1- and DAPI-positive cells were counted and the percentage of TBR1-positive cells with respect to DAPI and distribution of those neurons within the cortical wall amongst the different genotypes was analysed (**Figure 47**).

Results detected no gross differences in the images taken from WT, *Pcdh19*-HET and *Pcdh19*-KO brains (**Figure 47A**), neither in the TBR1-positive/DAPI ratio nor in the distribution within the cortical wall of the TBR1-expressing cells.

Quantification of the images revealed a very similar percentage of neurons expressing TBR1 with respect to DAPI (**Figure 47B**) when comparing the genotypes (WT=33.65 ± 2.92%, *Pcdh19*-HET=34.03 ± 2.64% and *Pcdh19*-KO=38.51 ± 1.7%). No differences were detected when conducting the statistical analysis either (independent samples Kruskal-Wallis test, $p > 0.05$).

When studying the distribution of TBR1-expressing cells (**Figure 47C**), quantifications detected that bins 7 to 9, that would approximately correspond to layer VI, accounted for 50% of all TBR1-expressing cells (WT=58.99 ± 4.94%, *Pcdh19*-HET=54.84 ± 3.02% and *Pcdh19*-KO=52.63 ± 1.84%). A peak of cells in bin 3, corresponding to the upper layers, is also present (WT=12.76 ± 2.35%, *Pcdh19*-HET=11.1 ± 0.92% and *Pcdh19*-KO=14.58 ± 0.37%). Interestingly, an increase in the percentage of TBR1+ cells was detected in bin 5 between *Pcdh19*-HET and the other genotypes when the images were quantified (WT=4.97 ± 0.71%, *Pcdh19*-HET=7.46 ± 0.35% and *Pcdh19*-KO=4.34 ± 0.41%). Slight increases in the percentage of cells expressing TBR1 in the *Pcdh19*-KO animal with respect to the WT were

seen in bins 1 (WT=2.71 ± 0.78%, *Pcdh19*-HET=2.03 ± 0.87% and *Pcdh19*-KO=4.5 ± 0.33%), 2 (WT=5.6 ± 1.68%, *Pcdh19*-HET=7.55 ± 0.65% and *Pcdh19*-KO=8.97 ± 1.09%) and 3 (WT=12.77 ± 2.35%, *Pcdh19*-HET=11.1 ± 0.92% and *Pcdh19*-KO=14.58 ± 0.37%), and a slight decrease of said cells in mutant brains compared to WT brains were revealed in bins 7 (WT=21.87 ± 1.92%, *Pcdh19*-HET=20.4 ± 2.19% and *Pcdh19*-KO=19.58 ± 1.46%) and 8 (WT=21.8 ± 1.74%, *Pcdh19*-HET=20.29 ± 1.19% and *Pcdh19*-KO=19.25 ± 0.69%).

Statistical analysis revealed a significant difference in bin 5 only between *Pcdh19*-HET and *Pcdh19*-KO (independent samples Kruskal-Wallis test p=0.018; pairwise comparison post-hoc test, p=0.018 between *Pcdh19*-HET and *Pcdh19*-KO) and a trend towards significance in bin 1 (ANOVA, F (2, 9) =3.294, p=0.084).

Since TBR1 was being used as a marker for layer VI, an analysis selecting only the cells in bins 7 to 9, that as mentioned previously correspond roughly to layer VI, was conducted. Neither quantifications nor statistical analysis showed any differences in the percentage of TBR1-positive cells with respect to DAPI (**Figure 47D**) or in the distribution of said cells within bins 7 to 9 amongst the genotypes (**Figure 47E**).

Details of the statistical analysis are shown in the appendix (**Table A. 15**).

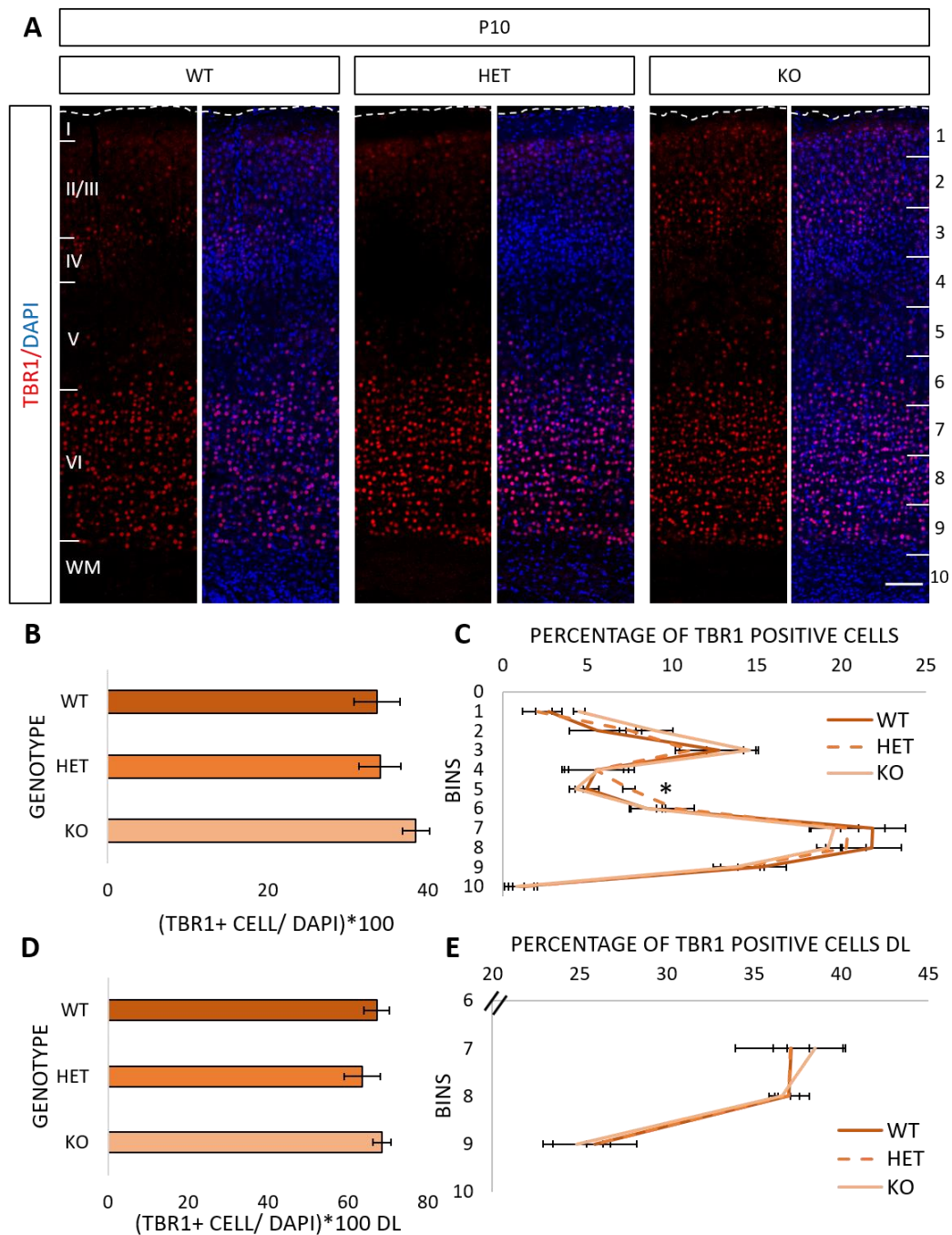


Figure 47. Slight changes in the distribution, but not the overall proportion, of TBR1-expressing cells in *Pcdh19*-HET animals.

(A) Representative images of brains stained with TBR1 at P10. Nuclei were counterstained with DAPI (blue). (B-E) Quantification of the images stained with TBR1 from (A). Data are presented as mean \pm SEM. Analysis presented no differences in number of TBR1-positive cells with respect to DAPI in the cortical wall (B) or only in bins 7 to 9 (D). Distribution of cells expressing TBR1 within the cortex (C) or in bins 7-9 (E) showed only one statistical difference between the conditions in bin 5 ($p < 0.05$) between *Pcdh19*-HET and *Pcdh19*-KO. Graphs represent TBR1-expressing cells in each of ten equal-size horizontal bins expressed as % of total TBR1-positive cells. 3

images of 4 brains of each condition from at least 3 different litters were included in the analysis. Cortical layers are indicated with roman numerals in the representative images. The horizontal bins used to perform the quantification are shown in arabic numerals on the right side of the image. White dotted lines delimit the marginal zones. WM, white matter; WT, wild-type; HET, *Pcdh19*-heterozygous; KO, *Pcdh19*-knock-out. Scale bar: 100 μ m.

5.3.3 Cell number and distribution analysis of GABAergic interneurons in the SSC of P20 animals

5.3.3.1 Parvalbumin-expressing cells did not present any significant differences in their number or distribution amongst the genotypes.

At P20, analysis of PV-expressing interneurons in WT, *Pcdh19*-HET and *Pcdh19*-KO cortex was conducted by immunostaining for PV and counterstaining with DAPI. The percentage of PV-positive cells with respect to DAPI and the distribution of those cells spanning the cortical wall were analysed in the SSC region of the brain (**Figure 48**).

The percentage of PV-positive cells normalised to DAPI and their distribution throughout the cortical layers looked similar among the genotypes (**Figure 48A**).

Quantification of the images showed a small increase in the percentage of interneurons expressing PV with respect to DAPI (**Figure 48B**) in *Pcdh19*-HET animals compared to the other genotypes (WT=3 ± 0.29%, *Pcdh19*-HET=3.7 ± 0.2% and *Pcdh19*-KO=2.99 ± 0.25%). Statistical analysis showed this difference was not significant (ANOVA, F (2, 9) =2.687, p=0.122).

Analysis of the distribution of PV-positive interneurons within the cortex (**Figure 48C**) revealed that more than 70% of PV-positive cells were located between bins 4 to 8 (WT=73.86 ± 7.38%, *Pcdh19*-HET=78.18 ± 0.48% and *Pcdh19*-KO=75.03 ± 1.35%), which corresponds to layers IV to VI of the cortex, as illustrated in **Figure 40**.

A slight increase in the percentage of cells in *Pcdh19*-HET brains compared to the WT and *Pcdh19*-KO brains was detected in bin 5 when quantifying (WT=17.27 ± 1.67%, *Pcdh19*-HET=19.96 ± 2.91% and *Pcdh19*-KO=17.72 ± 0.87%). Statistical analysis proved the increase was not significant (ANOVA, F (2, 9) =0.523, p>0.05).

Details of the statistical analysis are shown in the appendix (**Table A. 17**).

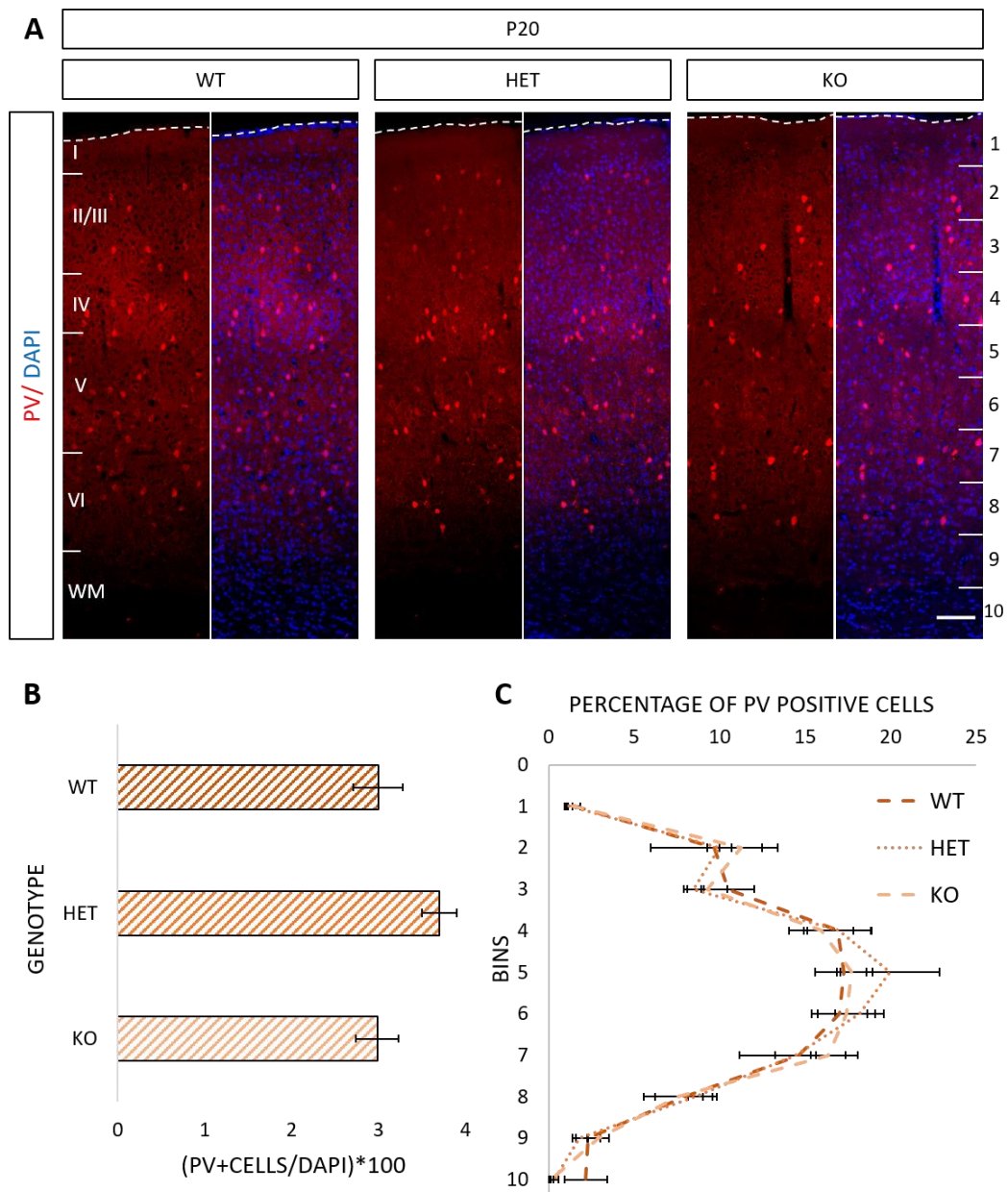


Figure 48. Immunohistochemical analysis of *Pcdh19*-HET and *Pcdh19*-KO animals detected no differences at P20 in the total number of PV-expressing cells, nor their distribution, with respect to their WT counterparts.

(A) Representative images of brains stained with PV at P20. Nuclei were counterstained with DAPI (blue). (B-C) Quantification of the images from A. Data are presented as mean \pm SEM. Analysis presented no differences in number of PV-positive cells with respect to DAPI (B). Distribution of cells expressing PV in the cortex (C) showed no statistical differences between the conditions. Graphs represent PV-expressing cells in each of ten equal-size horizontal bins expressed as % of total PV-positive cells. Cortical layers are indicated with roman numerals in the representative images. The horizontal bins used to perform the quantification are shown in arabic

numerals on the right side of the image. 3 images of 4 brains of each condition from at least 3 different litters were included in the analysis. White dotted lines delimit the marginal zones. WM, white matter; WT, wild-type; HET, *Pcdh19*-heterozygous; KO, *Pcdh19*-knock-out. Scale bar: 100 μ m.

5.3.3.2 Analysis of calretinin-positive cells showed no differences among the different genotypes

CR-positive interneurons were analysed by immunostaining for CR and counterstaining with DAPI in WT, *Pcdh19*-HET and *Pcdh19*-KO brain slices at P20 and quantifying the percentage of cells expressing CR normalised to DAPI and the distribution of those cells in the cortical wall at the SSC region (**Figure 49**).

The percentage of CR-expressing cells with respect to DAPI and their distribution throughout the cortical layers did not reveal visible differences between the WT and the mutant animals (**Figure 49A**).

Quantifications of the images (**Figure 49B**) detected a small decrease in the percentage of interneurons expressing CR with respect to DAPI in the mutant animals compared to the WT counterparts (WT=1.62 ± 0.42%, *Pcdh19*-HET=1.14 ± 0.04% and *Pcdh19*-KO=1.13 ± 0.25%). This decrease was not significant (ANOVA, F (2, 9) =0.952, p>0.05).

Analysis of the distribution of CR-expressing interneurons within the cortical wall (**Figure 49C**) showed that around 40% of the cells positive for calretinin were positioned in bins 2 and 3 (WT=43.94 ± 6.17%, *Pcdh19*-HET=39.1 ± 3.37% and *Pcdh19*-KO=48.33 ± 3.89%), which roughly correspond to layers II and III.

The quantification did detect an increase in the percentage of CR+ cells in bin 9 in the *Pcdh19*-HET brains with respect to the other mice (WT=5.83 ± 1.66%, *Pcdh19*-HET=9.84 ± 1.78% and *Pcdh19*-KO=5.34 ± 0.8%). However, this difference was not significant when the statistical analysis was performed (independent samples Kruskal-Wallis test, p=0.087).

During this analysis, it was noticed that the overall number of cells expressing calretinin in the selected region was very low (WT=36.42 ± 7.79 CR+ cells, *Pcdh19*-HET=25.42 ± 2.09 CR+ cells and *Pcdh19*-KO=21.33 ± 1.86

CR+ cells). This made it very difficult to interpret the results, especially those regarding the distribution of the CR cells. Therefore, it was decided to analyse the total number of cells expressing CR and their distribution over a larger area of the cortex, adding the motor cortex. This extended analysis was performed calculating the percentage of CR+ cells per layer with respect to the total number of CR+ cells counted in the region selected, since due to the size of the region selected, the total number of DAPI positive cells was not counted.

Quantification of the total number of cells positive for CR throughout the MC and SSC (**Figure 49D**) revealed a slight decrease in the mutant with respect to the WT littermates (WT=132.25 ± 12.02 CR+ cells, *Pcdh19*-HET=105.75 ± 18 CR+ cells and *Pcdh19*-KO=100.75 ± 8.33 CR+ cells). The statistical analysis revealed this difference was not significant (ANOVA, F(2, 9) =1.598, p>0.05).

Regarding the distribution of the cells expressing the CR marker (**Figure 49E**), at least half of the cells accumulated in bin 2 (WT=52.36 ± 3.66%, *Pcdh19*-HET=50.01 ± 4.49% and *Pcdh19*-KO=52.7 ± 1.56%), which corresponds to layers II/III, as seen in the analysis of a selected region of the SSC. No differences among the genotypes were detected in the quantification or statistical analysis.

Details of the statistical analysis are shown in the appendix (**Table A. 18**).

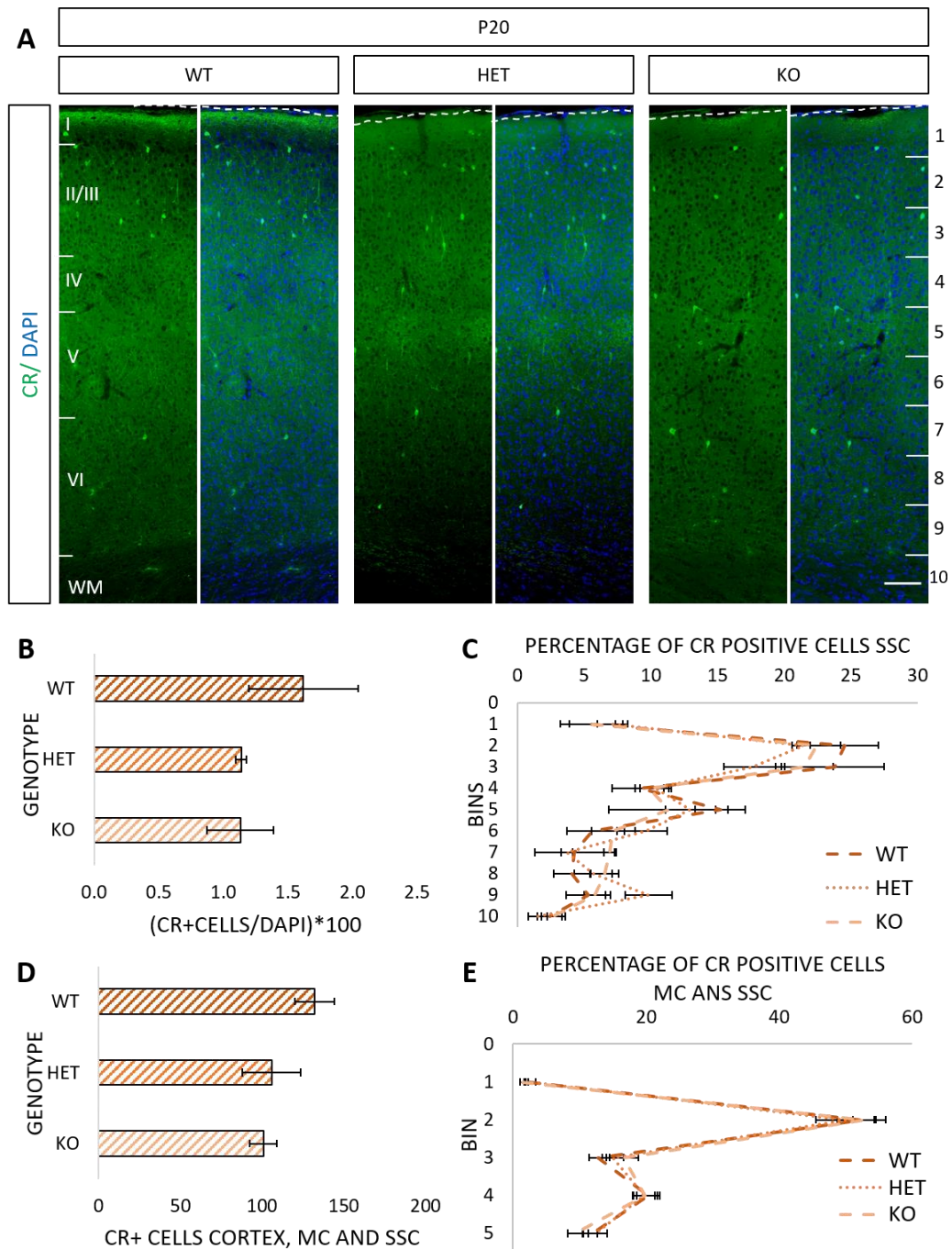


Figure 49. Immunohistochemical analysis at P20 brains of mutant animals revealed no differences in the total number of CR-positive cells (normalised to DAPI) and the distribution of CR-positive cells with respect to WT animals.

(A) Representative images of P20 animals stained with CR. Brains showed no differences in the percentage of CR+ cells with respect to DAPI or distribution of CR-positive cells in the SSC. Nuclei were counterstained with DAPI (blue). (B-C) Quantification of the images stained with CR from (A). Data are presented as mean \pm SEM. Results revealed no statistical differences in the number of CR-expressing cells with respect to DAPI (B). Distribution of CR-positive cells within the cortex (C) showed no

differences among the genotypes. Graphs represent CR-expressing cells in each of ten equal-size horizontal bins expressed as % of total CR-positive cells. (D-E) Quantification of a larger region of the cortex, that includes the motor cortex (MC) and most of the SSC. Total number (D) or distribution (E) of the CR+ cells were similar amongst the conditions. Graphs represent cells positive CR in each of the cortical layers expressed as % of total CR-positive cells. Layers were determined by the DAPI counterstaining. 3 images of 4 brains of each condition from at least 3 different litters were included in the analysis. Cortical layers are indicated with roman numerals in the representative images. The horizontal bins used to perform the quantification are shown in arabic numerals on the right side of the image. White dotted lines mark the limit of the marginal zones. WM, white matter; WT, wild-type; HET, *Pcdh19*-heterozygous; KO, *Pcdh19*-knock-out. Scale bar: 100 μ m.

5.3.3.3 Cells expressing calbindin presented minor differences in distribution between *Pcdh19*-HET brains and *Pcdh19*-KO brains

Analysis of the cells expressing CB was performed in WT, *Pcdh19*-HET and *Pcdh19*-KO animals at P20 by immunostaining for CB and counterstaining with DAPI. The percentage of CB-positive cells normalised to DAPI and their distribution in the cortex at the SSC area was calculated and statistically analysed (**Figure 50**).

Images from this region (**Figure 50A**) showed similar percentage of neurons expressing CB with respect to DAPI and similar distribution within the cortical wall among all genotypes.

Quantification of the images did reveal a slight decrease in the percentage of cells expressing CB with respect to DAPI in the *Pcdh19*-HET brains compared to the WT (WT=19.12 ± 1.06%, *Pcdh19*-HET=16.17 ± 1.23% and *Pcdh19*-KO=18.76 ± 0.18%). No statistically significant differences between the mutant and the WT animals were detected when the statistical analysis was conducted, though (ANOVA, F (2, 9) =2.881, p=0.108). Regarding the distribution of cells positive for CB within the cortical wall (**Figure 50C**), the analysis revealed more than 80% of the cells were positioned between bins 2 to 5 (WT=87.92 ± 1.65%, *Pcdh19*-HET=88.08 ± 2.07% and *Pcdh19*-KO=87.99 ± 0.48%). This corresponds to a group of glutamatergic neurons expressing CB in layers II-IV, as explained in **section 3.1**.

Analysis of the distribution in the whole cortical wall showed a slight increase in the percentage of CB+ cells in bin 7 in the *Pcdh19*-HET animals with respect to the other genotypes (WT=2.17 ± 0.17%, *Pcdh19*-HET=2.95 ± 0.26% and *Pcdh19*-KO=1.98 ± 0.26%). The difference was significant between *Pcdh19*-HET and *Pcdh19*-KO mice, but not with respect to WT (ANOVA, F (2, 9) =5.023, p=0.034; Tukey HSD post hoc test, p=0.037

between *Pcdh19*-HET and *Pcdh19*-KO; $p=0.089$ between WT and *Pcdh19*-HET).

Since expression in layers II-IV corresponds mostly to a group of glutamatergic neurons, as mentioned previously, an analysis was conducted selecting bins 6-10 to study exclusively interneurons that populate the lower layers. No differences among the genotypes were detected when quantifying the percentage of CB-expressing interneurons normalised to DAPI (WT= $2.9 \pm 0.17\%$, *Pcdh19*-HET= $2.72 \pm 0.35\%$ and *Pcdh19*-KO= $3.16 \pm 0.33\%$) as seen in **Figure 50D**. The statistical analysis confirmed this result (ANOVA, $F(2, 9)=0.571$, $p>0.05$).

In the distribution of these interneuronal types throughout bins 6 to 10 (**Figure 50E**), there was an increase in the percentage of CB-positive cells in bin 7 in the *Pcdh19*-HET mice with respect to the WT and a slight decrease of these cells in the *Pcdh19*-KO compared to the WT (WT= $28.56 \pm 1.45\%$, *Pcdh19*-HET= $35.06 \pm 1.39\%$ and *Pcdh19*-KO= $23.27 \pm 2.43\%$), which is the same trend seen when all bins were analysed. When statistical analysis was performed, the difference was significant between the *Pcdh19*-HET and the *Pcdh19*-KO and it almost reached significance between WT and *Pcdh19*-HET (ANOVA, $F(2, 9)=10.634$, $p=0.004$; Tukey HSD post hoc test, $p=0.003$ between *Pcdh19*-HET and *Pcdh19*-KO; $p=0.073$ between WT and *Pcdh19*-HET).

Details of the statistical analysis are shown in the appendix (**Table A. 19**).

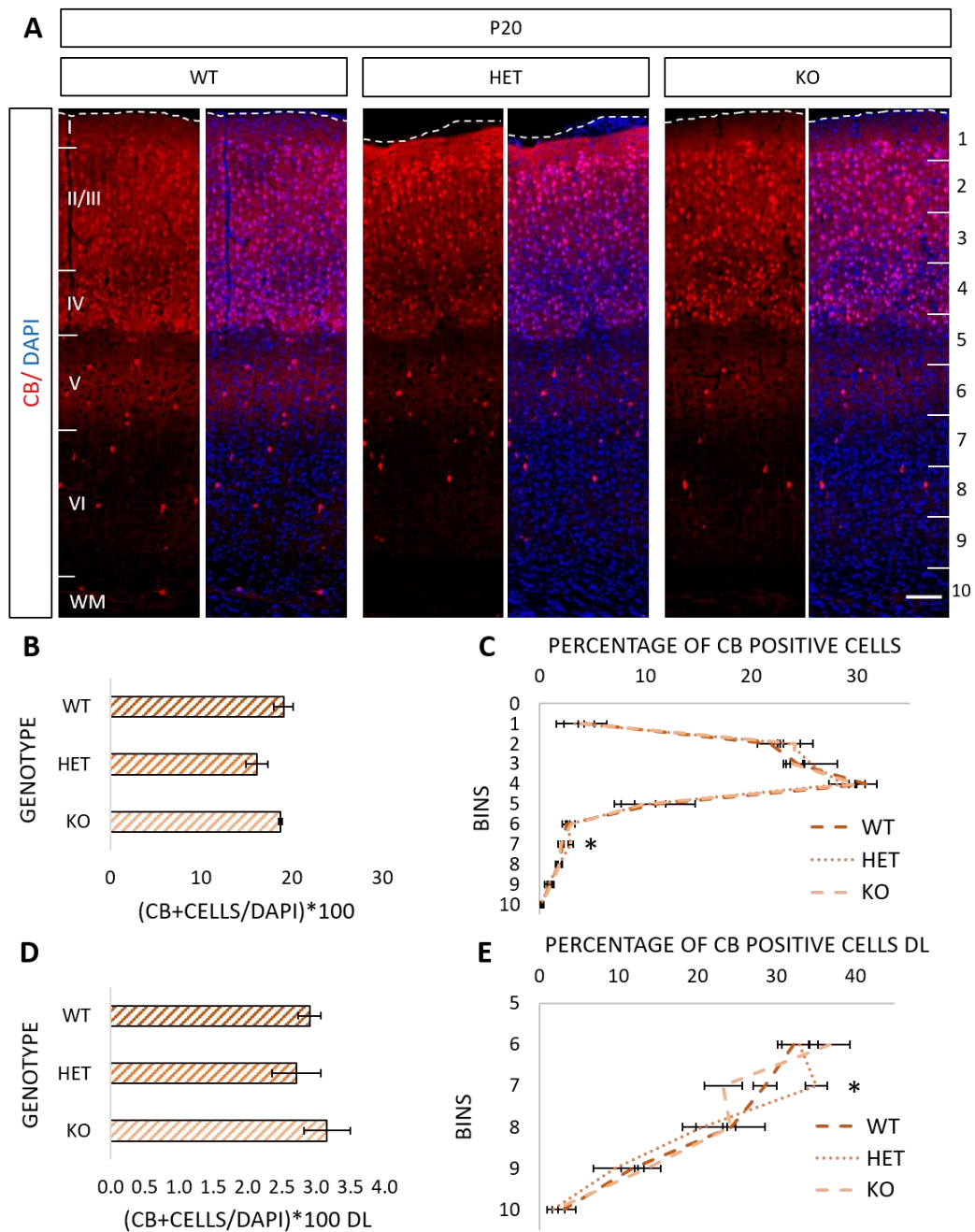


Figure 50. A difference is detected in the distribution of cells expressing CB at P20 in the SSC of *Pcdh19*-HET animals with respect to their WT littermates.

(A) Representative images of brains stained with CB at P20. Nuclei were counterstained with DAPI (blue). (B-E) Quantification of the images stained with CB from A. Data are presented as mean \pm SEM. Analysis revealed no differences among the genotypes in the number of CB-expressing cells with respect to DAPI within the whole cortical wall (B), or between bins 6-10 (D). Distribution of CB-positive cells at P20 in the cortex (C) and between bins 6-10 (E) only showed a statistical difference in bin 7 between *Pcdh19*-HET

and *Pcdh19*-KO brains. Graphs represent CB-expressing cells in each of ten equal-size horizontal bins expressed as % of total CB-positive cells. 3 images of 4 brains of each condition from at least 3 different litters were included in the analysis. Cortical layers are indicated with roman numerals in the representative images. The horizontal bins used to perform the quantification are shown in arabic numerals on the right side of the image. White dotted lines delimit the marginal zones. WM, white matter; WT, wild-type; HET, *Pcdh19*-heterozygous; KO, *Pcdh19*-knock-out; AL, all layers; DL, deep layers. Scale bar: 100 μ m.

5.3.3.4 Analysis of the SSC detects a difference among mutants in the distribution of somatostatin-expressing cells

To analyse if mutations in the *Pcdh19* gene alter the number or distribution of SST-expressing interneurons, WT, *Pcdh19*-HET and *Pcdh19*-KO brain slices at P20 were immunostained for SST and counterstained with DAPI. The percentage of SST-positive cells with respect to DAPI and the distribution of these interneurons within the cortex in the SSC area was calculated and a statistical analysis was performed (**Figure 51, Figure 52**).

Images (**Figure 51A, B**) revealed no observable differences in the percentage of SST-positive interneurons normalised to DAPI or their distribution throughout the cortical wall between the mutant animals and the WT.

Quantification of images (**Figure 52A**) detected a decrease in the percentage of SST-positive interneurons relative to DAPI in the mutant animals compared to the WT littermates (WT=2.21 ± 0.25%, *Pcdh19*-HET=1.32 ± 0.11% and *Pcdh19*-KO=1.61 ± 0.32%). This decrease trended towards significance (ANOVA, F (2, 9) =3.5, p=0.075).

Regarding the distribution of interneurons positive for SST (**Figure 52B**), an increase in the percentage of SST+ cells was revealed in *Pcdh19*-KO brains compared to the other genotypes in bin 5 (WT=11.21 ± 1.34%, *Pcdh19*-HET=10.58 ± 1.62% and *Pcdh19*-KO=17.71 ± 2.12%). This difference was statistically significant between *Pcdh19*-HET and *Pcdh19*-KO (ANOVA, F (2, 9) =5.257, p=0.031; Tukey HSD post hoc test, p=0.04 between *Pcdh19*-HET and *Pcdh19*-KO; p=0.06 between WT and *Pcdh19*-KO).

As happened in **section 5.3.3.2**, the small number of SST-positive cells difficulted the analysis, so it was again decided to perform the analysis on a larger section of the cortex, using the same criteria as in **section 5.3.3.2**.

In this analysis, no differences were detected among the genotypes in the number of cells expressing SST (**Figure 52C**) or in the distribution of said

cells within the cortical layers (**Figure 52D**). SST+ cells were mainly located in layers II/III, V and VI.

Details of the statistical analysis are shown in the appendix (**Table A. 20**).

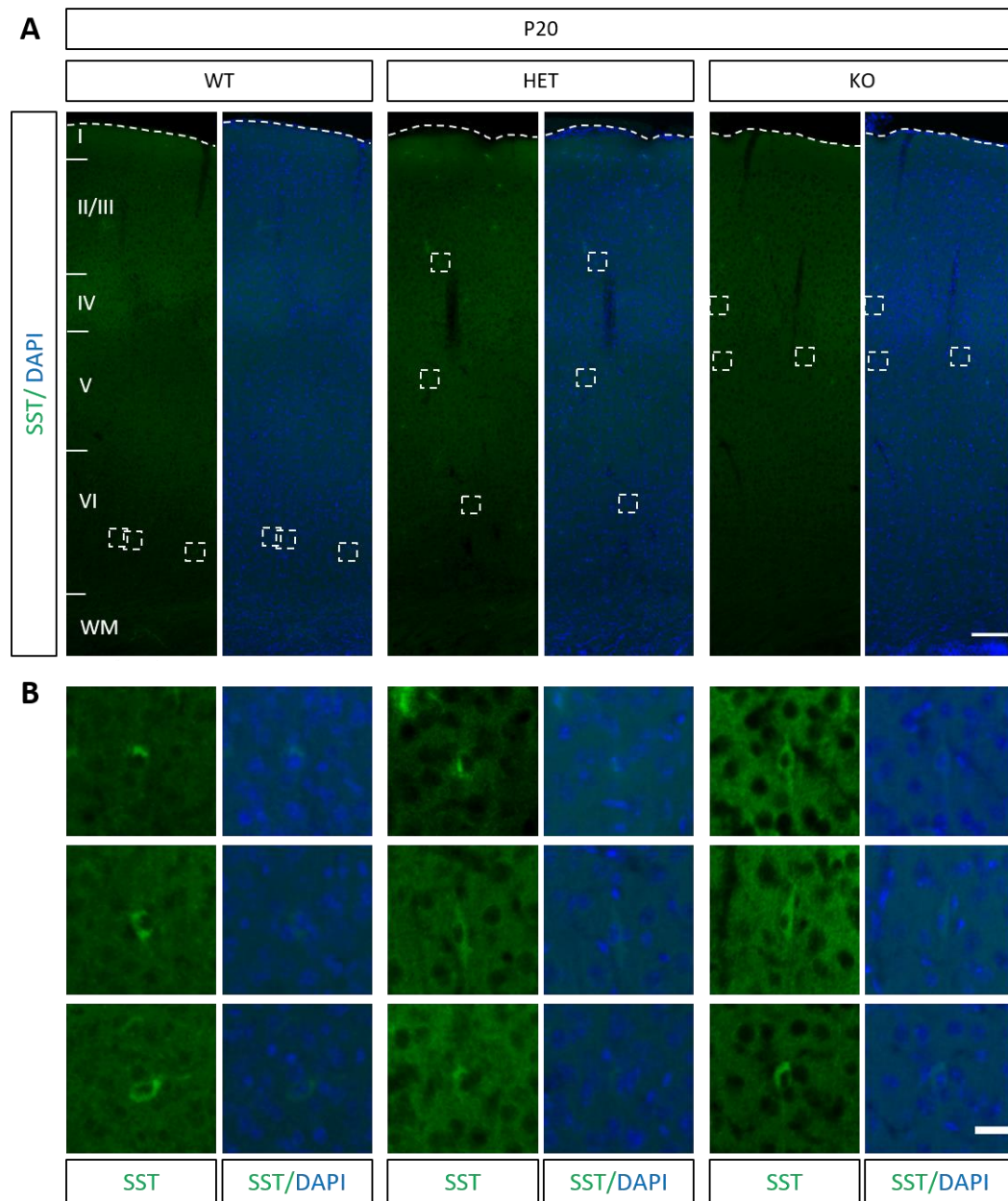


Figure 51. Images of the immunohistochemical analysis of *Pcdh19*-HET and *Pcdh19*-KO animals showed no differences in the total number (normalised to DAPI) and the distribution of SST-positive cells at P20 with respect to their WT counterparts.

(A) Representative images of brains stained with SST at P20. Nuclei were counterstained with DAPI (blue). (B) High magnification of the images shown in A, each of them showing individual SST+ cells. Cortical layers are indicated with roman numerals in the representative images. White dashed lines mark the limit of the marginal zones. White dashed squares reveal the areas amplified. WM, white matter; WT, wild-type; HET, *Pcdh19*-heterozygous; KO, *Pcdh19*-knock-out; SST, somatostatin. Scale bar: 100 μ m in A and 20 μ m in B.

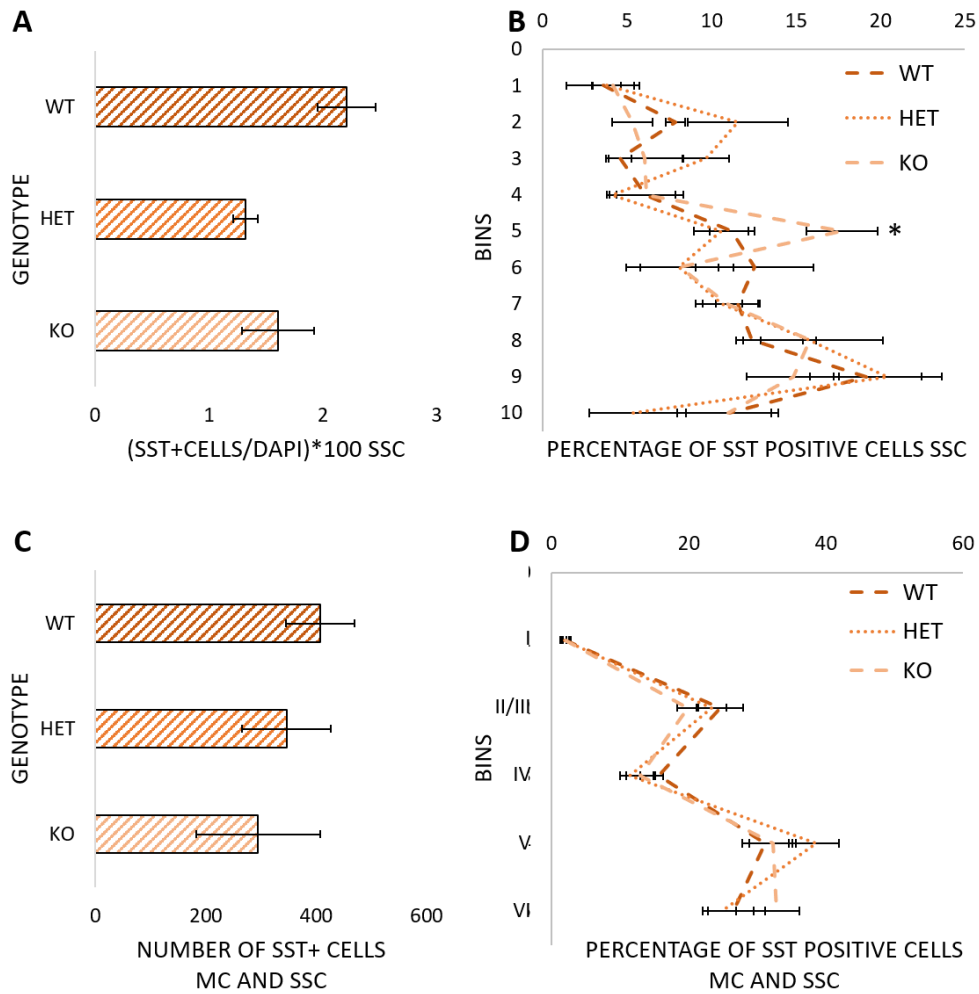


Figure 52. Immunohistochemical analysis of *Pcdh19*-HET and *Pcdh19*-KO animals showed a significant difference in the distribution of SST-positive cells at P20 between the mutants when the SSC was analysed.

(A-B) Quantification of the images stained with SST from **Figure 51**. Data are presented as mean \pm SEM. Analysis revealed no differences in number of SST-positive cells with respect to DAPI among the genotypes (A). Distribution of cells expressing SST at P20 in the SSC cortex (B) were statistically significant between *Pcdh19*-HET and *Pcdh19*-KO at bin 5. Graphs represent SST-expressing cells in each of ten equal-size horizontal bins expressed as % of total SST-positive cells. (C-D) Quantification of a bigger area of the cortex, including the motor cortex (MC) and most of the SSC. Total number (C) or distribution (D) of the SST+ cells did not show differences among conditions. Graphs represent cells positive for SST in each the cortical layers noted as % of total SST-expressing cells. 3 images of 4 brains of each condition from at least 3 different litters were included in the analysis. Cortical layers are indicated with roman numerals in the representative images. WT, wild-type; HET, *Pcdh19*-heterozygous; KO, *Pcdh19*-knock-out; MC, motor cortex; SSC, somatosensory cortex.

5.4 Discussion

5.4.1 Results

The aim of this chapter was to immunohistochemically characterise the *Pcdh19* mutant animals to determine if there was any difference in the number or distribution of the specific subtypes of neurons studied between mutant and WT mice.

Results showed no statistical differences between the animals in the total number of cells, their distribution or the cortical width. Proportion or overall distribution of cells expressing cortical layer markers CUX1, SATB2, CTIP2, RORB and TBR1 at P10, or cells expressing markers for interneurons PV, CB, CR or SST at P20 in the SSC area were mostly unaltered, although there were slight differences that were significant in the case of CUX1, TBR1 and CB-positive cells. However, those differences do not seem to be relevant in the general context of the immunohistochemical characterisation.

5.4.2 Choice of methods

The SSC area was selected to perform these experiments since it was the area that was studied to determine which cell types co-localised with *Pcdh19* mRNA in **Chapter 3**; and also corresponded to the area where migration experiments were conducted in **Chapter 4**. It is also an area that has been well-studied and widely used for experiments regarding cortical lamination (Jabaudon et al. 2012; Leone et al. 2015; Prasad et al. 2008; H. Chang et al. 2018; M. Chang et al. 2018). However, other areas, such as the motor cortex, also express *Pcdh19* mRNA, as showed in **section 3.3.2**. Experiments of the molecular markers in other areas of the cortex where *Pcdh19* is expressed could be conducted in the future to determine if there are differences between *Pcdh19*-mutant and WT animals in those areas.

5.4.3 Analysis of glutamatergic neurons

For the three genotypes, cells positive for all cortical glutamatergic markers tested occupied locations similar to those reported in the past (Molyneaux et al. 2007; Harb et al. 2016). CUX1, a marker of upper layer neurons, detected a higher percentage of cells in bins 1 to 4, corresponding to layers II to IV. SATB2, a marker for corticocortical projecting neurons, stained layers II to IV and a subset of cells located in layers V and VI (bins 1 to 9). RORB staining was located mainly between bins 3 and 4, corresponding roughly to layer IV, and CTIP2, a marker of subcortically-projecting neurons positioned in layers V and VI, stained cells in bins 5 to 9. Finally, TBR1, a molecular marker expressed mainly in layers Vb and VI and, to a lesser degree in layers II-III (Karpagam Srinivasan et al. 2012) stained cells mainly in bins 3 and 7 to 9, which correspond to those layers.

Analysis of cells positive for CUX1 revealed a significant difference between WT and *Pcdh19*-HET animals in bin 5, corresponding to layer V. Immunostaining of CUX1 in lower layers has been described (Nieto et al. 2004; Jabaudon 2017; M. Chang et al. 2018), but the percentage of cells accumulated in those layers was very small (WT=7.72 ± 1.55%, *Pcdh19*-HET=2.88 ± 0.23% and *Pcdh19*-KO=4.37 ± 0.85%), representing less than 10 % of the total CUX1+ cells. The fact that the only bin that shows a significant difference for CUX1 contains a low percentage of positive cells questions its relevance in the overall distribution of cells expressing this marker. However, bin 5 corresponds approximately to the upper part of layer V. This means that some of the CUX1 upper-layer glutamatergic cells from the *Pcdh19*-HET animals are positioned in higher regions within the cortical plate compared to the WT animals.

Interestingly, CUX2, which is a second mammalian homolog of the homeobox gene *Cut* from *Drosophila* (Quaggin et al. 1996; Nieto et al. 2004), is expressed by some interneurons originated mainly from the medial ganglionic eminences that reside in the lower layers of the cortical plate

(Zimmer et al. 2004). Thus, it could be that the CUX1 positive cells detected in the lower layers in these experiments are interneurons too. Indeed, even though the differences between WT and *Pcdh19*-HET were only significant in bin 5, *Pcdh19*-HET also presented a decrease in the percentage of CUX1+ cells in bins 6 and 7. Moreover, when looking at the percentage of CUX1-expressing cells with respect to DAPI in the lower layers (bins 5-10), differences between the *Pcdh19*-mutant animals and the WT were apparent in the quantification (WT=3.08 ± 0.65%, *Pcdh19*-HET=1.22 ± 0.17% and *Pcdh19*-KO=2.14 ± 0.56%), and were almost significant when statistically analysed (ANOVA, F (2, 9) =3.391, p=0.08; Tukey HSD post hoc test, p=0.0517 between *Pcdh19*-HET and *Pcdh19*-KO; p=0.064 between WT and *Pcdh19*-KO).

To test this hypothesis, a double immunohistochemical experiment could be conducted using antibodies against CUX1 and an interneuronal marker. A good choice would be GAD65/67, as it labels all GABAergic interneurons. However, if detection using immunohistochemistry proved to be difficult, as was the case in this thesis (**section 5.4.4**), another marker would have to be used. *Dlx5* is expressed in cortical interneurons (Stühmer et al. 2002), and a pan-DLX antibody was used by Zimmer *et al.* to determine that CUX2 was also expressed in a subpopulation of interneurons (Zimmer et al. 2004), therefore this could be an interesting marker to test for future investigations. Double immunohistochemistry against CUX1 and PV/CR/SST/CB could also be conducted to analyse the nature of those cells.

If the difference detected in bin 5 is due to alterations in the distribution of CUX1 positive interneurons, this could imply a role for *Pcdh19* in the cortical migration of this subset of cells, either in their radial migration or in the cortical allocation of the soma. Due to the low number of cells expressing CUX1 in the deep layers compared with the upper layers, an alteration in the number of these cells could also be masked. A decrease or

increase in the number of CUX1-expressing possible interneurons would suggest a role for *Pcdh19* in the neurogenesis of these interneurons (*Pcdh19* is expressed in the ganglionic eminences in embryonic development, as described by Gaitan and Bouchard) or in the tangential migration these neurons go through to reach the cortical plate. The switch between radial and tangential migration could also be affected (Gaitan et al. 2006; Marín 2013). This could be studied by culling WT, *Pcdh19*-HET and *Pcdh19*-KO animals at different stages of development and performing immunohistochemistry using the CUX1 antibody to identify them and the pan-DLX antibody to determine their GABAergic nature. The earliest timepoint for the analysis could be E11.5 since CUX2+ expression can already be seen in the subpallium at that age (Zimmer et al. 2004). Numbers and location would then be analysed and compared between mutants and WT. The stage of development in which the first differences were observed would be the one *Pcdh19* was participating in.

No significant alterations were detected in the numbers or distribution of SATB2, RORB and CTIP2-expressing cells between the mutant and the WT, implying *Pcdh19* is not implicated in the cortical positioning of corticocortical projection cells (Britanova et al. 2008), layer IV cells (Schaeren-Wiemers et al. 1997) or the CTIP2-positive subcortical projection cells from layers V and VI (Arlotta et al. 2005). However, a significant difference in distribution was detected in TBR1-expressing cells in bin 5. This bin corresponds to layer V of the cortex, an area where TBR1 is not usually expressed (Hevner et al. 2001). This fact, together with the low percentage of cells expressing TBR1 in said bin, that no other changes in distribution were present in the other bins and that the statistically significant difference is only between *Pcdh19*-HET and *Pcdh19*-KO, suggests that this difference might not be relevant for this study. However, sometimes subtle differences in a subpopulation can alter the neuronal network and cause a phenotype.

TBR1 is expressed by the corticothalamic neurons of layer VI embryonically and postnatally, and in upper layers only postnatally (Hevner et al. 2001). An increase in the percentage of TBR1 positive neurons in layer 5 of the *Pcdh19*-HET animals with respect to *Pcdh19*-KO and (even though not significant) WT mice could imply an abnormal positioning of the neurons expressing TBR1. Either TBR1-positive layer VI neurons could be located in higher positions within the cortical plate, or TBR1-expressing upper layer neurons could be positioned in lower layers. Another possibility is that those TBR1+ cells are not ectopically located, but their cell subtype specification is altered. Some layer V neurons that do not normally express TBR1 could have become TBR1+. Experiments using BrdU pulses at different ages and an immunohistochemical analysis against TBR1 could be used to determine the nature of these cells.

Even though not significant, the percentage of CTIP2-expressing cells in bin 5 was slightly decreased in *Pcdh19*-HET animals with respect to the other mice. CTIP2 knockout mutants have been reported to present an increased expression of TBR1 (K. Srinivasan et al. 2012), so it is possible that a decrease, albeit small, in the percentage of CTIP2-positive cells in the bin 5 of *Pcdh19*-HET, could increase the percentage of cells expressing TBR1. This result could imply that the mosaicism of *Pcdh19* affects the cortical lamination or composition of layer V corticospinal and VI thalamocortical projecting neurons, but more experiments would need to be performed to test this theory.

No differences were detected in the total number of cells or cortical width at P10 among genotypes, suggesting *Pcdh19* mutation does not alter the number of cortical neurons overall. Considering the results for all glutamatergic markers, the mutants do not present big defects in the number or distribution of the subpopulations studied.

In summary, the mosaicism of *Pcdh19* could be subtly altering the location or numbers of specific subpopulations of neurons and that could potentially

have an effect in neuronal connectivity. Since the diversity of glutamatergic cells is considerable and the markers studied are expressed in large populations, it would be possible that one of the neuronal subpopulations is affected.

This project did not cover all the subsets of glutamatergic neurons that populate the cortex. Thus, other markers could be used to expand this characterization. One of the markers that was attempted to be used was OTX1 that is expressed by cells located in the Va sublayer (Hevner, 2003), an area where *Pcdh19* mRNA is expressed in the SSC (**Figure 21**). Unfortunately, the antibody used to perform the immunohistochemical analysis was unspecific despite the optimisation experiments conducted. Trying other antibodies or use of a GFP-tagged *Otx1* mouse line, as the one used by Fossat to conduct the immunohistochemical characterisation of this marker would be a useful investigation to perform in the future (Fossat, 2007).

5.4.4 Analysis of GABAergic neurons.

As explained in chapter 3, a report from Rudy *et al.* concluded that immunostaining for PV, SST and the ionotropic serotonin receptor 5HT3a (5HT3aR) detected almost 100% of cortical interneurons in the mouse SSC (Rudy *et al.* 2011). Unfortunately, there was no specific antibody against 5HT3aR available at the moment these experiments were performed, as mentioned previously by Rudy *et al.* Indeed, the immunohistochemical analysis using antibody against this marker was attempted with no success. Performing these experiments with a mouse line that uses GFP as a reporter, such as the mouse lines used in the experiments of Rudy *et al.* or Inta *et al.* to detect 5HT3aR expression would be necessary to complete the characterisation (Rudy *et al.* 2011; Inta *et al.* 2008).

To be able to study the overall number and distribution of all interneurons, the use of an antibody against glutamic acid decarboxylase (GAD65/67), the enzyme that produces GABA (Schousboe *et al.* 2007), was also

considered as an alternative but an optimisation of the antibody that achieved sufficient specificity was never reached. As explained in **section 5.4.3**, a pan-DLX antibody could be used as an alternative to GAD65/67 to detect the general population of interneurons.

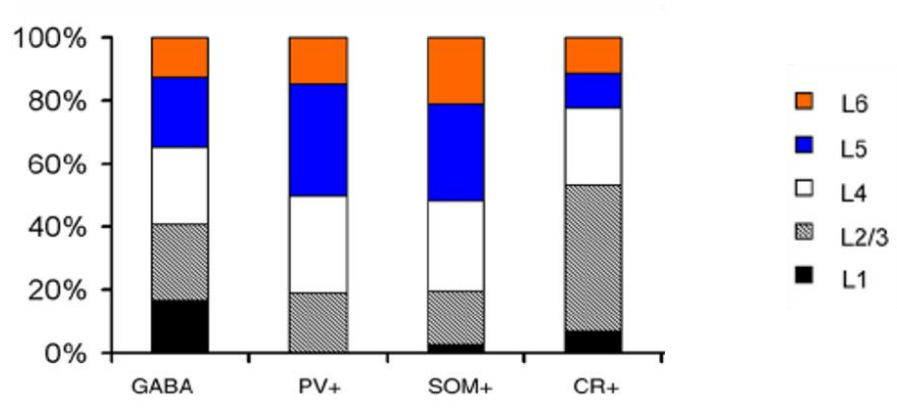
The interneuronal markers PV, CB and CR that were used collectively stain for 80% of the total number of interneurons expressed in the cortex in rat (Gabbott et al. 1997; Ueno et al. 2015). The SST marker, that partially overlaps with calretinin (Rudy et al. 2011), was also analysed.

Like in P10 animals, no differences were detected in the total number or distribution of DAPI positive cells at P20 or in the cortical width of the brains at this age. Surprisingly, the number of cells did not increase between P10 and P20 in the *Pcdh19*-KO animals, opposite to the WT and *Pcdh19*-HET mice. However, this difference was not significant because the total number of cells at P20 does not differ much from P10 in WT and *Pcdh19*-HET animals. Nevertheless, the absence of an increment of the total number of DAPI+ cells (neurons and glia) between P10 and P20 could imply that these populations are slightly decreased in the P20 knock-out and, even though not significant, as previously mentioned, subtle changes in cell subtypes can potentially alter cortical connectivity.

The migration of cortical glutamatergic neurons is finished by P10, but the migration of interneurons into the cortical plate is not. Thus, it is possible that neurogenesis or migration of the interneurons that acquire their final positioning between P10 and P20 is altered. Another possibility is that the survival of the glutamatergic neurons already located within the cortical plate is affected. Glial cells are also DAPI+, so alterations in gliogenesis could also cause the phenotype seen. In conclusion, if this lack of increase of DAPI+ cells in the *Pcdh19*-KO animals between those ages is relevant, PCDH19 could be involved in any of those processes and further experimentation would be needed to determine which one is affected.

The percentages of cells expressing the different interneuronal markers used in the experiments were slightly low but otherwise similar to that reported in the past (X. Xu et al. 2010; Rudy et al. 2011). This percentage depends on age and cortical area, which makes comparisons complicated. In this analysis, the percentage of PV-positive cells is 3% in the WT mice, compared to a percentage of expressing cells that ranges between 3.7% to 8% (X. Xu et al. 2010; Rudy et al. 2011). CR analysis detects a percentage of 1.62% of cells expressing CR in the WT animals in comparison to the reports that observe around 1.32% to 2.6% of total CR-positive cortical neurons (X. Xu et al. 2010). Cells expressing CB are located mainly in layers II-IV and are a subset of glutamatergic neurons (DeFelipe, 1997). In total, they comprise 19.17% of the neurons in the SSC. SST-expressing cells were 2.21% of the total cortical cells which is within the range of 1.4 to 6% that experiments from other laboratories have shown (X. Xu et al. 2010; Rudy et al. 2011). Distribution of the interneuronal markers within the cortex other than CB, which wasn't included in the analysis of Xu, Roby and Callaway, also corresponded with what has been reported: CR is more prominent in upper layers II-III (bins 2-3) and PV and SST are more prominent in lower layers (bins 4 to 7 and 5 to 9, respectively). A report from Xu, Roby and Callaway quantified the distribution of different interneuronal molecular markers in the somatosensory cortex of adult mice (X. Xu et al. 2010). Even though the mice used for the interneuronal analysis of this project are P20, the distributions were similar in all the common markers (CR, PV and SST), with the highest variations in layers IV and VI (**Figure 53**).

A ADULT MICE RESULTS FROM Xu, Roby and Callaway (2010)



B P20 MICE RESULTS OF CHAPTER 5 ANALYSIS

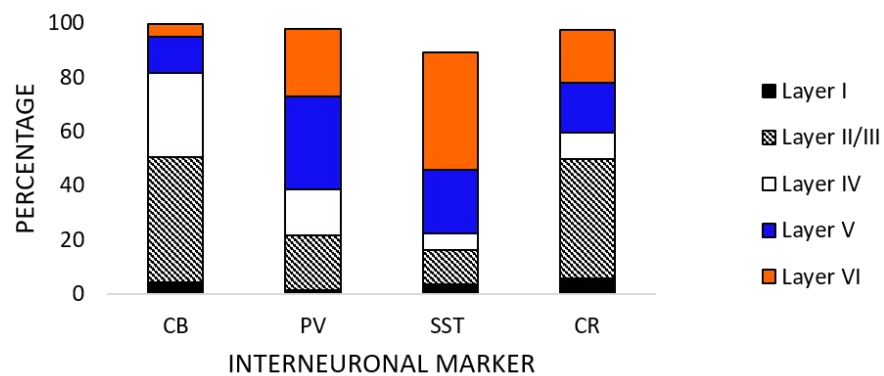


Figure 53. The distribution of CR, PV and SST interneurons observed in this thesis matches previously reported values.

Graphics represent the percentage of MARKER+ cells in each layer with respect to the total number of MARKER+ cells in the area analysed in the somatosensory cortex of adult (A) and P20 (B) mice. Graphic A was extracted from Xu, Roby and Callaway (2010) and contains the distribution of GABA+ cells, which is absent in graphic B. Graphic B reflects the values obtained in this work. GABA, gamma-aminobutyric acid; PV, parvalbumin; CR, calretinin; SST or SOM, somatostatin; CB, calbindin; L, layer.

Analysis of the numbers and distribution of interneurons expressing PV, CR, CB or SST revealed only a statistically significant difference in the distribution of CB-positive cells, specifically in bin 7, that corresponds roughly to layer VI. *Pcdh19*-HET animals present a slight increase in the percentage of cells accumulated in bin 7 with respect to WT and *Pcdh19*-KO counterparts. As happened with the differences in the glutamatergic cortical markers, the low percentage of cells that expressed CB in bin 7 and the fact that no other significant alteration can be detected in other bins questions how relevant this difference is for the overall distribution of CB positive cells. However, CB-expressing interneurons are an heterogeneous population of varied morphology and physiology, with double bouquet, Martinotti and neurogliaform cells as the subtypes more observed (Gabbott et al. 1997; Cauli et al. 1997) that is detected in the lower layers of the cortex. Therefore, this result could also reflect that *Pcdh19* mosaicism affects the cortical lamination of a particular subtype of CB positive interneurons.

In contrast to *Pcdh19*-HET mice, *Pcdh19*-KO presented a slight decrease in the percentage of CB+ cells located in bin 7 with respect to WT, but only when bins 6 to 9 (that contain the CB+ interneurons) were analysed.

Even though not significant, *Pcdh19*-KO brains also showed a slight decrease in the numbers of CR and SST interneurons. A third of the SST-positive cells coexpress CR (Rudy et al. 2011), so it is possible that the depletion of *Pcdh19* decreases the number of SST+/CR+ interneurons. To test this hypothesis, a double immunohistochemistry against SST and CR could be conducted, and the number and distribution of the double positive cells could be analysed in WT, *Pcdh19*-HET and *Pcdh19*-KO.

Pcdh19-HET also presented minor not significant differences with respect to WT. PV neurons were slightly increased, while CR and CB percentages were slightly decreased. Regarding the distribution, *Pcdh19*-HET reveals a small increase of PV interneurons in bin 5 and of interneurons expressing CB in bin 7.

As happened with the glutamatergic cortical analysis, the lack or mosaicism of *Pcdh19* could be slightly affecting the ratio of the different subsets of interneurons or producing discrete populations of ectopically located neurons that would affect neuronal wiring. As suggested in **section 5.4.3**, a behavioural analysis was considered as an indirect way to assess potential changes in network activity.

5.4.5 Conclusion and future experiments

In general, the results in this chapter support the finding that there are no dramatic alterations in the number or distribution of the populations of cortical glutamatergic and GABAergic neurons studied in the somatosensory cortex of P10 and P20 animals. This is in accordance to Pederick *et al.*, that didn't observe any gross abnormalities in the *Pcdh19*-HET or *Pcdh19*-KO mice with respect to the WT animals (Pederick et al. 2016), as detailed in **section 5.1**.

Nevertheless, given the number of glutamatergic and GABAergic cell-types that have been recently discovered, especially with single-cell RNA sequencing (Tasic et al. 2016), covering all the neuronal subpopulations of the cortex would be an almost impossible task. Therefore, it was decided to conduct a behavioural analysis to detect if there were functional differences caused by possible circuit disruptions in the *Pcdh19*-mutants with respect to the WT animals (Chapter 6).

However, there were some minor differences in some subsets of both glutamatergic and GABAergic neurons that could potentially affect cortical connectivity. In *Pcdh19*-HET animals most of these alterations were detected in bin 5 (CUX1, CTIP2, TBR1, PV), which corresponds to layer Va, where *Pcdh19* expression is strongest at both ages (**Figure 16**) This suggests that *Pcdh19* mosaicism could be altering, albeit slightly, the composition of this particular layer in the SSC area.

Moreover, as described in **section 4.4.4**, *Pcdh19*-HET brains are formed by a mixed population of WT and *Pcdh19*-KO cells that can influence each other; and could potentially present a different cortical lamination compared to WT cells from WT brains and *Pcdh19*-KO cells from *Pcdh19*-KO brains. Since *Pcdh19*-HET brains were analysed as a unit, alterations in the cortical lamination of the WT or *Pcdh19*-KO cell subsets could get masked. Moreover, a recent report from Pederick *et al.* revealed an abnormal cell sorting between WT and *Pcdh19*-KO cells in the cortex of *Pcdh19*-HET mice that resulted in a striking columnar pattern in the cortex that doesn't appear in WT mice or in animals where *Pcdh19* is uniformly deleted. The cortical wall was segmented into columns that were either mostly composed by WT cells, or mostly populated with *Pcdh19*-KO cells (Pederick *et al.* 2018). Therefore, the immunohistochemical characterisation of WT and *Pcdh19*-KO cells within the *Pcdh19*-HET brains would be an exciting project to conduct to gain more knowledge about the divergences in these two populations. As explained in **section 4.4.4**, this could be achieved mating D4/XEGFP (XGFP) male mice with *Pcdh19*-HET females (**Figure 54A**).

When performing this experiment, a columnar pattern of GFP+WT cells and GFP-*Pcdh19*-KO cells as the one seen by Pederick *et al.* would be expected. Animals would be culled either at P10 or P20, perfused, brains extracted and cut, and immunohistochemistry against several cortical markers performed as described in **section 2.3** (**Figure 51B, C**). Next, GFP+ cells in the cortex would be counted and classified in 4 groups: MARKER+GFP+ in GFP+ columns; MARKER+GFP- in GFP+ columns; MARKER-GFP+ in GFP- columns or MARKER-GFP- in GFP- columns. Then, the percentage of each of the groups with respect to the total number of GFP+ cells would be calculated (**Figure 51D, E**) in the whole cortex from both hemispheres and also within the different layers. Differences in those percentages in *Pcdh19*-HET brains with respect to the WT brains would imply the mosaicism of *Pcdh19* is affecting cortical lamination.

Two facts need to be taken into account when considering this experiment. First, definition of GFP+ column and GFP- column in the WT cortices would be difficult because the columnar pattern is not present in these animals. Consequently, the columns would need to be established randomly, utilising the pattern of one of the *Pcdh19*-HET brains as a model (**Figure 51D**). Second, in this experiment XGFP+ cells are WT cells and XGFP- cells are *Pcdh19*-KO cells, but that is not equivalent to *Pcdh19*-expressing cells and *Pcdh19*-non expressing cells.

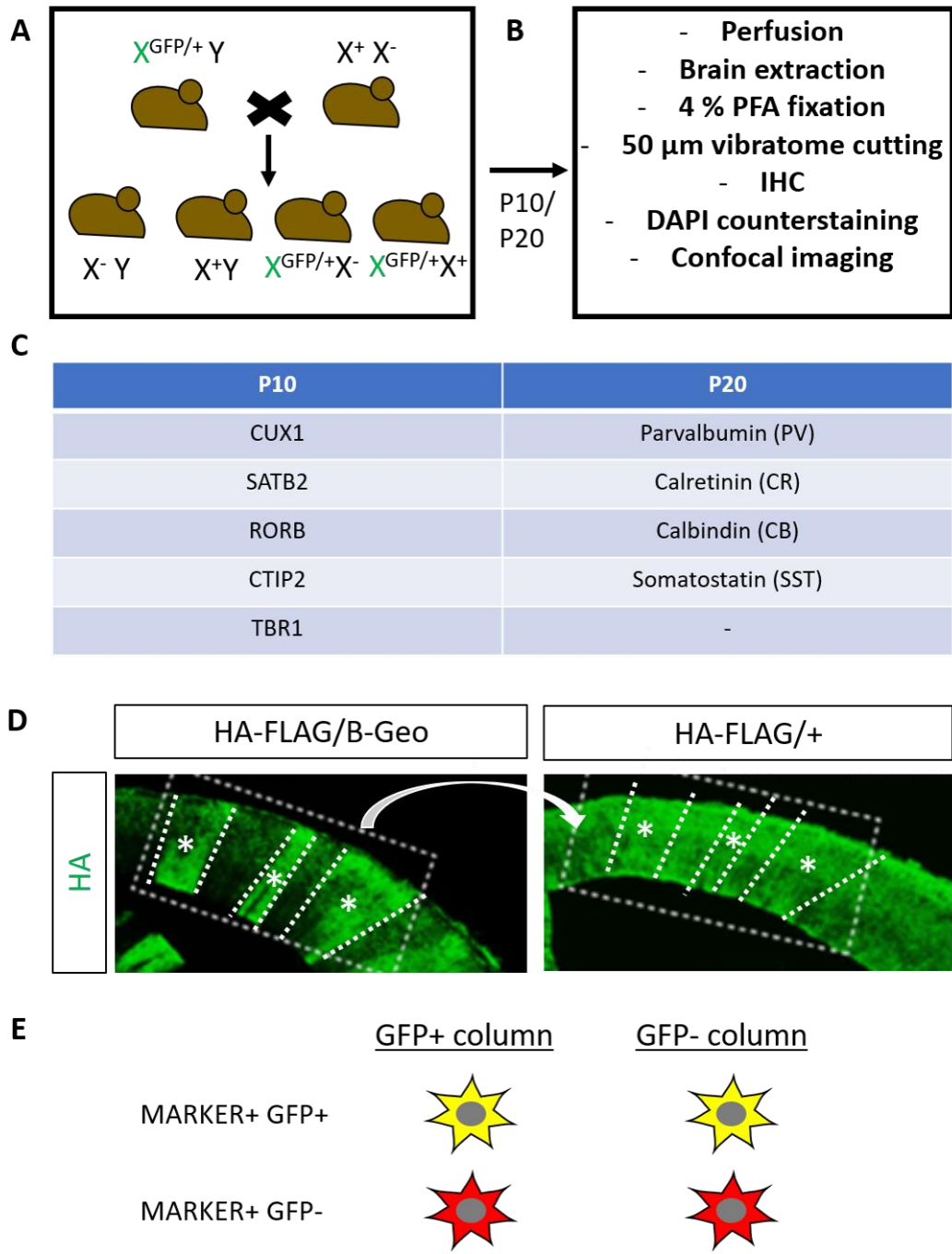


Figure 54. Schematic illustrating the immunohistochemical analysis of female WT/XGFP and *Pcdh19*-HET/XGFP.

(A) Depiction of XGFP males and *Pcdh19*-HET matings. (B) Delineation of the experimental procedures to obtain the images that would be analysed (C) Table shows the markers to study. (D) Pictures extracted from Pederick *et al.* (2018), that show the columnar pattern of WT and *Pcdh19*-KO cells in the *Pcdh19*-HET brain. White dashed lines separate GFP+ from GFP- columns. GFP+ columns are indicated with an asterisk. (E) Cells would be classified into 4 groups: MARKER+GFP+ in GFP+ mainly columns; MARKER+GFP- in GFP+ mainly columns; MARKER+GFP+ in GFP- mainly columns or MARKER+GFP- in GFP- mainly columns. MARKER+GFP+

cells are depicted in yellow, reflecting a red and green fluorescence, MARKER+GFP- cells are shown in red. $X^{GFP/+} Y$, wild-type male for *Pcdh19* gene that contains the reporter GFP in the X chromosome; $X^+ X^-$, heterozygous female for *Pcdh19*; $X^- Y$, knock-out male for *Pcdh19*; $X^{GFP/+} X^+$, WT female for *Pcdh19* that contains GFP in one of the X-chromosomes; $X^{GFP/+} X^-$, *Pcdh19*-heterozygous females that contains GFP in the X-chromosome that is a WT for the *Pcdh19* gene; WM, white matter.

Chapter 6: Behavioural analysis of the WT, *Pcdh19*-HET and *Pcdh19*-KO animals.

6.1 Introduction

Previous studies have reported that EIEE9 patients present a heterogeneous phenotype, characterised by epileptic episodes that occur in clusters. Most patients also display cognitive impairment of variable severity and behavioural disturbances, such as autistic-like features, aggressiveness, schizophrenia, hysteria, panic attacks or self-mutilation (Scheffer et al. 2008; Dibbens et al. 2008; Duszyc et al. 2014). In fact, a meta-analysis performed by Camacho *et al.* using 10 different papers that detailed the behaviour of the affected females showed that 55.4% of the *Pcdh19*-HET patients studied presented behavioural issues and almost half of said patients (44.2%) were within the autistic spectrum (Camacho et al. 2012). In addition, even though male carriers (*Pcdh19*-KO) are considered phenotypically normal, they have been shown to have rigid, controlling, obsessive and inflexible personalities (Scheffer et al. 2008; Kolc et al. 2019).

No epileptic episodes have been detected in the *Pcdh19*-mutant mice (Pederick et al. 2016; Hayashi et al. 2017). However, spontaneous recurrent seizures are very difficult to detect by observation since they can be rare and the changes in the behaviour of the mice when they happen can be very subtle (Yang et al. 2004; Gu et al. 2017). In fact, Pederick *et al.* did detect abnormal neuronal activity, albeit not seizures, when conducting intracranial electroencephalographic recordings in *Pcdh19*-HET mice backcrossed into a background that was more sensitive to seizures (Pederick et al. 2018). Moreover, the results from Bassani *et al.* demonstrated that rats electroporated with shRNAs against *Pcdh19* were more susceptible to pharmacologically induced seizures than their WT counterparts (Bassani et al. 2018). These results support the hypothesis that mosaicism of *Pcdh19* alters neuronal connectivity.

Even though the analysis conducted in chapter 5 did not reveal any gross alterations in cortical lamination, some subtle but significant differences could be detected in some cortical subpopulations of cells between *Pcdh19*-mutants and WT mice. These subtle differences could be causing some network activity disruption that could translate into unusual behavioural responses. Although the behaviour of the Taconic *Pcdh19*-KO mouse model has not been studied, a behavioural analysis of a different *Pcdh19* mutant animal model was published during the completion of this thesis (Hayashi et al. 2017). It revealed that both mutants presented abnormal behaviour under stress conditions and hyperactivity at 34 weeks but not at 11-12 weeks (increased hyperactivity due to aging). Moreover, *Pcdh19*-HET females showed a decrease in the contextual and cue responses to fear compared to WT and *Pcdh19*-KO animals. However, different mouse models can reveal different behavioural characteristics. Moreover, the experiments performed by Hayashi *et al.* were conducted in mice no younger than 10 weeks of age and mouse behaviour can present differences in behaviour depending on age.

6.2 Aim

The objective of this chapter was to carry out a behavioural characterisation of the *Pcdh19*-mutant animals using paradigms commonly employed in the analysis of autistic mouse models: open-field, EPM, social interaction and activity during 24h. It was aimed to examine *Pcdh19*-HET female and *Pcdh19*-KO male mice and compare them to WT animals. Furthermore, given reports of the influence of single versus multiple genotype housing on the behaviour of another X-linked gene mutant, an additional aim to compare to WT animals from pure WT litters was included.

6.3 Results

Considering that around 25% EIEE9 patients present autistic-like behaviours (Camacho et al. 2012), a battery of four experiments used to study mouse models related to autism was conducted. Autistic spectrum disorders are characterised by difficulty in social communication and interaction, together with repetitive and restrictive patterns of behaviour and interests. The disorder is usually accompanied by other conditions, that can be developmental (atypical language development, intellectual disability, hyperactivity, tic disorders or motor deficits), medical (epilepsy, gastrointestinal problems, immune dysregulation, genetic syndromes and sleep disorders) or psychiatric (such as anxiety or depression) (Lai et al. 2014). Consequently, the chosen experimental paradigms included 24-hour activity, open field, elevated plus maze (EPM) and social interaction, designed to study activity, anxiety-related behaviour and social behaviour, respectively.

In the open field, mice were tested for their general locomotor activity, their anxiety-like behaviour or thigmotaxis (Simon et al. 1994; Seibenhener et al. 2015), their adaptation to the open-field arena and their habituation between two trials separated by 24-hours (Daenen et al. 2001). The EPM analysed the mice's anxiety-like behaviour related to fear of open, bright spaces, together with the fear of height (van Meer et al. 2005). The social interaction studied the mouse's interest in another mouse when both were put in a novel environment (Kalbassi et al. 2017). 24-hour activity experiments were performed to detect alterations in the spontaneous general locomotor activity or disruptions in the circadian cycle (Paladino et al. 2013; Kalbassi et al. 2017).

Since Kalbassi *et al.* showed that the presence of mutant and WT mice in the same cage altered each other's behaviour (Kalbassi et al. 2017), two groups of WT animals were studied. WT of single genotype housing (WT SGH)

were WT animals derived from WT matings, so that they had only been housed with other WT animals, while WT of mixed genotype housing (WT MGH) came from the mating of a WT male and a *Pcdh19*-HET female, so that mutant and WT littermates were housed together. Since the mutant animals analysed in this chapter were together with their WT littermates, they will be named as KO MGH and HET MGH too. Since it is known that sex and age can influence the behavioural performance, analysis of the results was performed by comparing the *Pcdh19*-KO males with their WT counterparts and the *Pcdh19*-HET females with their WT counterparts in experiments conducted at two different ages for the most part: P21 (preweaning) and P60 (young adult).

An overview of the experiments performed is outlined in **Figure 55**.

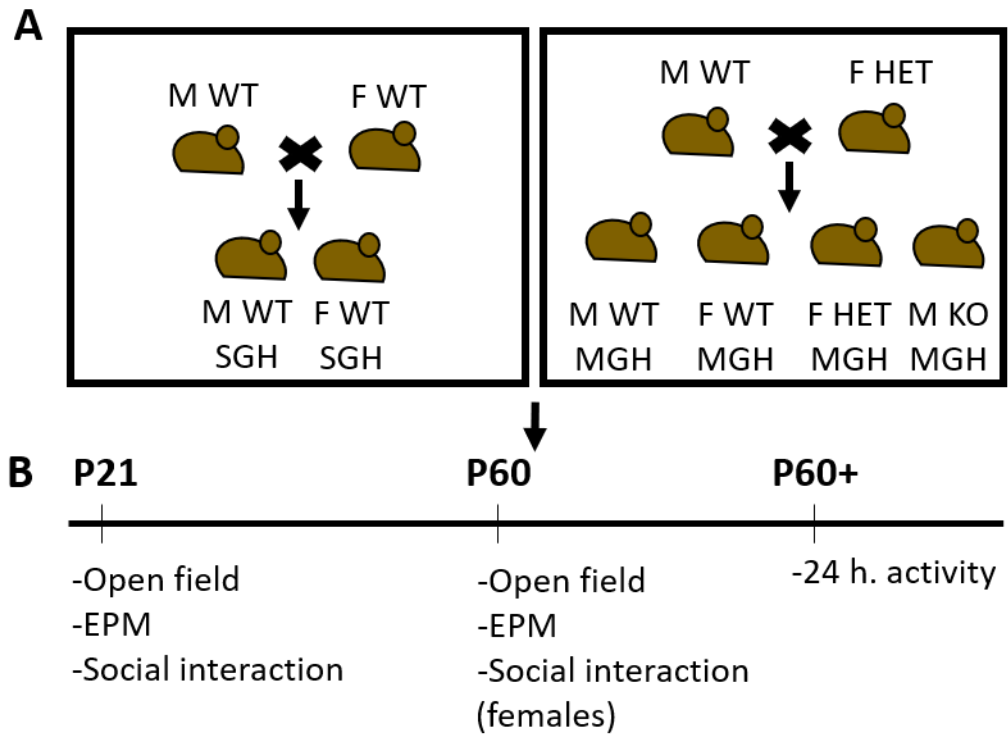


Figure 55. Schematic illustrating the behavioural analysis of WT, *Pcdh19*-HET and *Pcdh19*-KO mice.

M, male; F, female; WT, wild-type; HET, *Pcdh19*-heterozygous; KO, *Pcdh19*-knock-out; SGH, single genotype housing; MGH, mixed genotype housing; EPM, elevated plus maze.

6.3.1 Open field analysis in males

6.3.1.1 General locomotor activity does not reveal any differences among the conditions

The open-field paradigm tests general locomotor activity by measuring the total distance run by the mice when introduced in a novel environment during a certain period of time (Simon et al. 1994). Changes in the general locomotor activity are influenced by alterations in motor activity, exploratory behaviour or anxiety (Seibenhener et al. 2015).

To analyse if the depletion of *Pcdh19* affected the ambulation of the male mice, animals were tested at P21 and P60. Mice were habituated to the open-field arena (novel environment) 24 hours prior to the experiments and then let to run freely in the same arena for 20 min on the second day in the dark (**Figure 56A**). Total distance run was recorded and calculated using the EthoVision XT software, as detailed in **section 2.6.1**. Animal numbers were 19 WT SGH, 11 WT MGH and 14 KO MGH at P21, and 17 WT SGH, 11 WT MGH and 13 KO MGH at P60.

As seen in **Figure 56B**, the total distance run by the WT MGH males was higher than the distance run by the WT SGH males at P21 (WT SGH=2829.37 ± 127.31 cm, WT MGH=3677.46 ± 347.63 cm and *Pcdh19*-KO MGH=3174.78 ± 186.19 cm), but the increase did not reach statistical significance (independent-samples Kruskal-Wallis test, $p=0.081$).

There were no observable differences (WT SGH=4469.58 ± 229.22 cm, WT MGH=4387 ± 268.93 cm and *Pcdh19*-KO MGH=4336.89 ± 187.07 cm) in the total distance run in 20 min among the different P60 male mice (**Figure 56C**). Statistical analysis did not reveal any significant differences among the conditions either (ANOVA, $F(2, 38) = 1.214$; $p>0.05$).

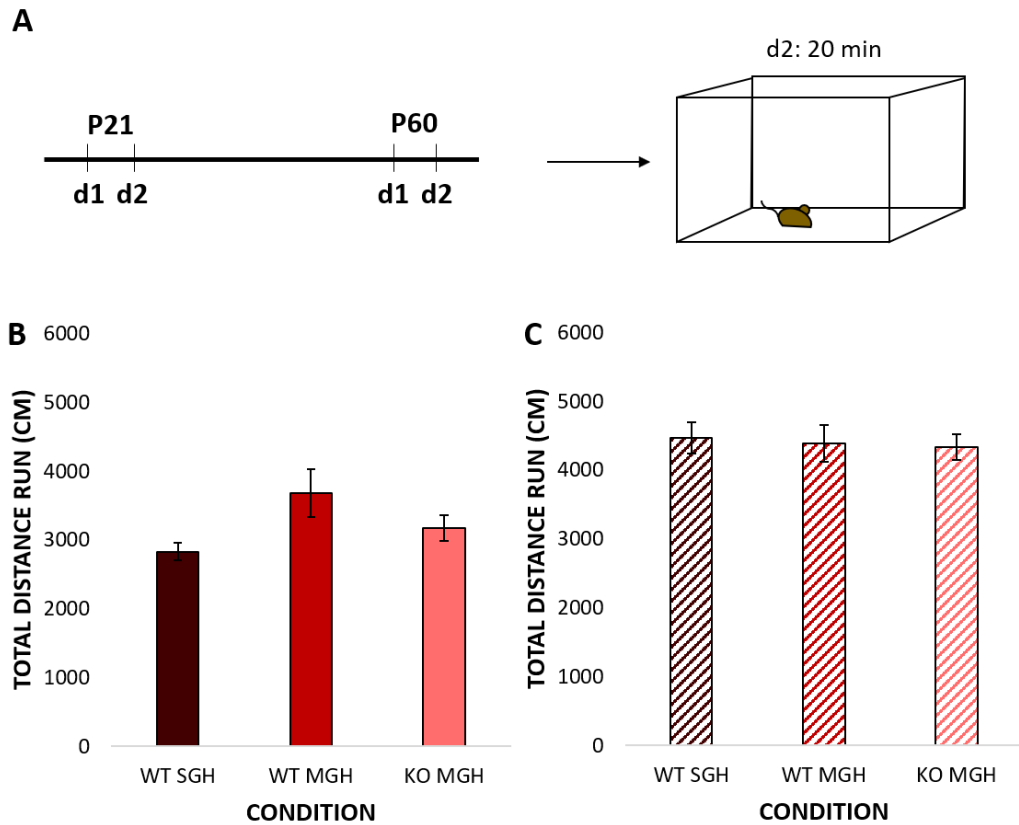


Figure 56. Open-field behavioural analysis revealed no differences in general locomotor activity among males.

Illustration of the general locomotor activity in the open field (A). Graphs represent total distance run for 20 min in P21 (B) and P60 (C) animals on day 2. Data are presented as mean \pm SEM. d1, day1; d2, day2; WT SGH, wild-type from single genotype housing; WT MGH, wild-type from mixed genotype housing; KO MGH, *Pcdh19*-knock-out male from mixed genotype housing.

6.3.1.2 No differences in thigmotaxis were observed between conditions

Thigmotaxis, or the tendency of the animal to remain close to the walls of the open field arena when introduced to it, is a measure for anxiety-like behaviour (Simon et al. 1994). This is due to their fear of open space, probably because they consider they can be easily preyed upon in those locations (Seibenhener et al. 2015). This behaviour can be determined by analysing the distance run in the centre with respect to the total distance run in the open-field arena. The open field test data from P21 and P60 mice (**section 6.3.1.1**) were analysed for this anxiety-like behaviour to determine if the depletion of *Pcdh19* affected this parameter. Thigmotaxis was calculated manually as detailed in **section 2.6.1**.

P21 males showed no differences (WT SGH=0.24 ± 0.01, WT MGH=0.24 ± 0.02 and *Pcdh19*-KO MGH=0.24 ± 0.01; ANOVA, F (2, 41) = 0.01, p>0.05) in thigmotaxis among the conditions (**Figure 57B**).

Thigmotaxis in the P60 males (**Figure 57C**) was also very similar among conditions (WT SGH=0.24 ± 0.01, WT MGH=0.26 ± 0.02 and *Pcdh19*-KO MGH=0.23 ± 0.01). No differences were detected after the statistical analysis was conducted either (ANOVA, F (2, 38) = 0.001, p>0.05).

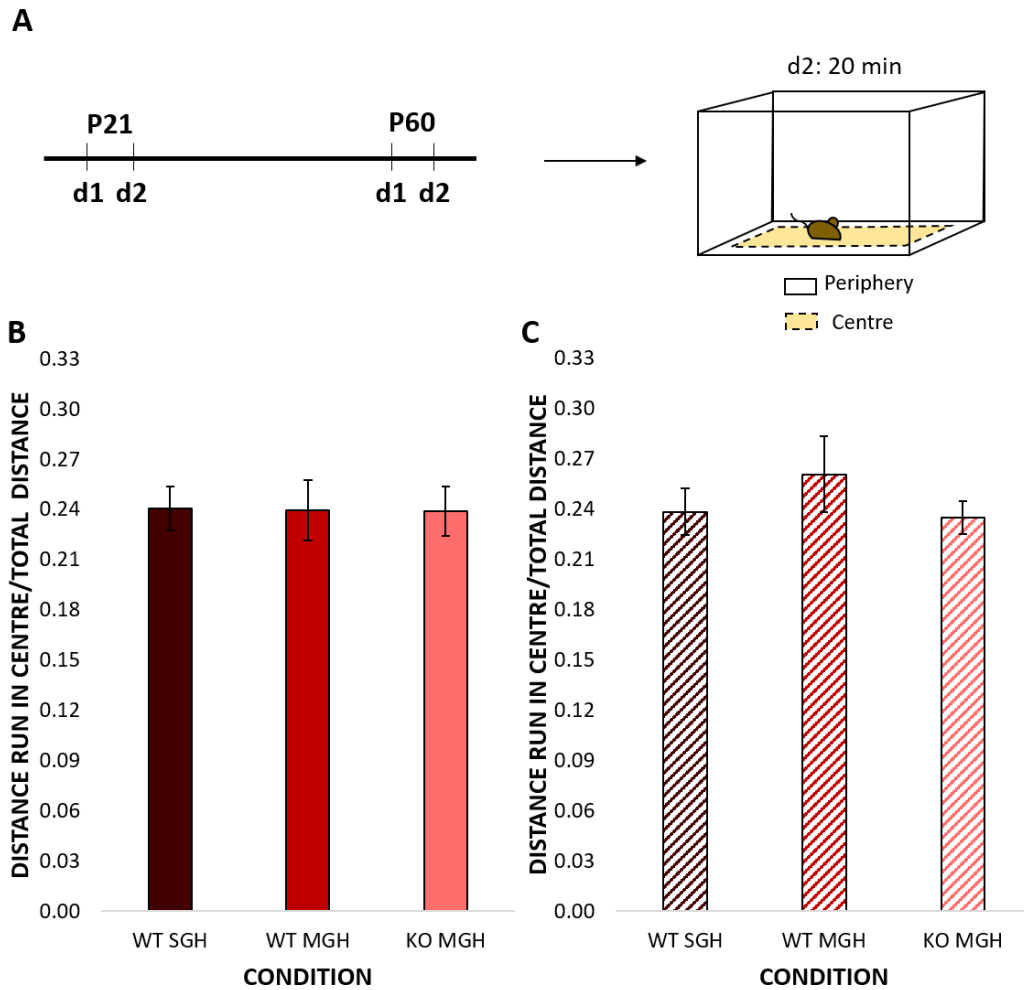


Figure 57. No differences in thigmotaxis among males.

Illustration of the thigmotaxis test in the open field arena (A). Graphs represent thigmotaxis in P21 (B) and P60 (C) animals on day 2. The data are presented as mean \pm SEM. Dashed black lines and light-yellow colour signal the centre of the box. d1, day1; d2, day2; WT SGH, wild-type from single genotype housing; WT MGH, wild-type from mixed genotype housing; KO MGH, *Pcdh19*-knock-out male from mixed genotype housing.

6.3.1.3 An increase in the distance run in the 5-min slot was detected in the WT MGH compared to the WT SGH animals at P21

To determine the ability of a mouse to adapt to the open-field arena over time within the same session, the distance run in the arena every 5-min over a 20-min session is recorded. Mice usually display exploratory behaviour during the first minutes of being in a novel environment and then this activity decreases over time as they habituate to it, a process called adaptation or intrasession habituation (Kondratova et al. 2010; Daenen et al. 2001). Patients with neurodevelopmental disorders, including autism, have shown difficulty to adapt to novel situations, thus it was interesting to study this parameter (Daenen et al. 2001).

To determine if deletion of *Pcdh19* altered the adaptation of the animals to the arena, the open field test data from P21 and P60 mice (**section 6.3.1.1**) were re-analysed to calculate the total distance run in every 5-min slot.

Analysis of P21 males (**Figure 58B**) showed a higher distance run by the WT MGH compared to the WT SGH and the KO MGH animals in the first 5-min slot (WT SGH=585.9 ± 39.31 cm, WT MGH=996.73 ± 136.47 cm and *Pcdh19*-KO MGH=722.14 ± 76.94 cm). This difference was significant between the WT MGH and the WT SGH (ANOVA, $F(2, 41) = 6.607$, $p=0.003$; Games-Howell post-hoc test, WT MGH vs. WT SGH, $p=0.034$). The distance run by the WT MGH males at the 10-min slot was still higher in comparison to the WT SGH males (WT SGH=692.84 ± 61.22 cm, WT MGH=929.38 ± 118.05 cm and *Pcdh19*-KO MGH=806.51 ± 67.58 cm) but statistical analysis revealed no significant differences among the conditions (independent-samples Kruskal-Wallis test, $p>0.05$). Distance run by the mice was similar among all conditions at the 15-min slot (WT SGH=810.48 ± 63.26 cm, WT MGH=860.55 ± 77.13 cm and *Pcdh19*-KO MGH=831.95 ± 60.75 cm) and the

20-min slot (WT SGH=759.74 ± 53.7 cm, WT MGH=890.8 ± 106.27 cm and *Pcdh19*-KO MGH=814.17 ± 63.84 cm).

At P60 (**Figure 58C**), the distance run by male mice of the different conditions was similar in each of the four slots (5-min slot: WT SGH=1290.46 ± 74.43 cm, WT MGH=1230.58 ± 89.57 cm and *Pcdh19*-KO MGH=1383.32 ± 71.29 cm; 10-min slot: WT SGH=1121.99 ± 67.98 cm, WT MGH=1150.98 ± 68.13 cm and *Pcdh19*-KO MGH=1042.61 ± 55.2 cm; 15-min slot: WT SGH=1081.52 ± 78.31 cm, WT MGH=1054.52 ± 54.57 cm and *Pcdh19*-KO MGH=1044.68 ± 60.61 cm; and 20-min slot: WT SGH=975.61 ± 60.61 cm, WT MGH=950.92 ± 108.13 cm and *Pcdh19*-KO MGH=866.27 ± 64.75 cm). Statistical analysis confirmed the absence of differences among conditions.

Details of the statistical analysis are shown in the appendix (**Table A. 21**).

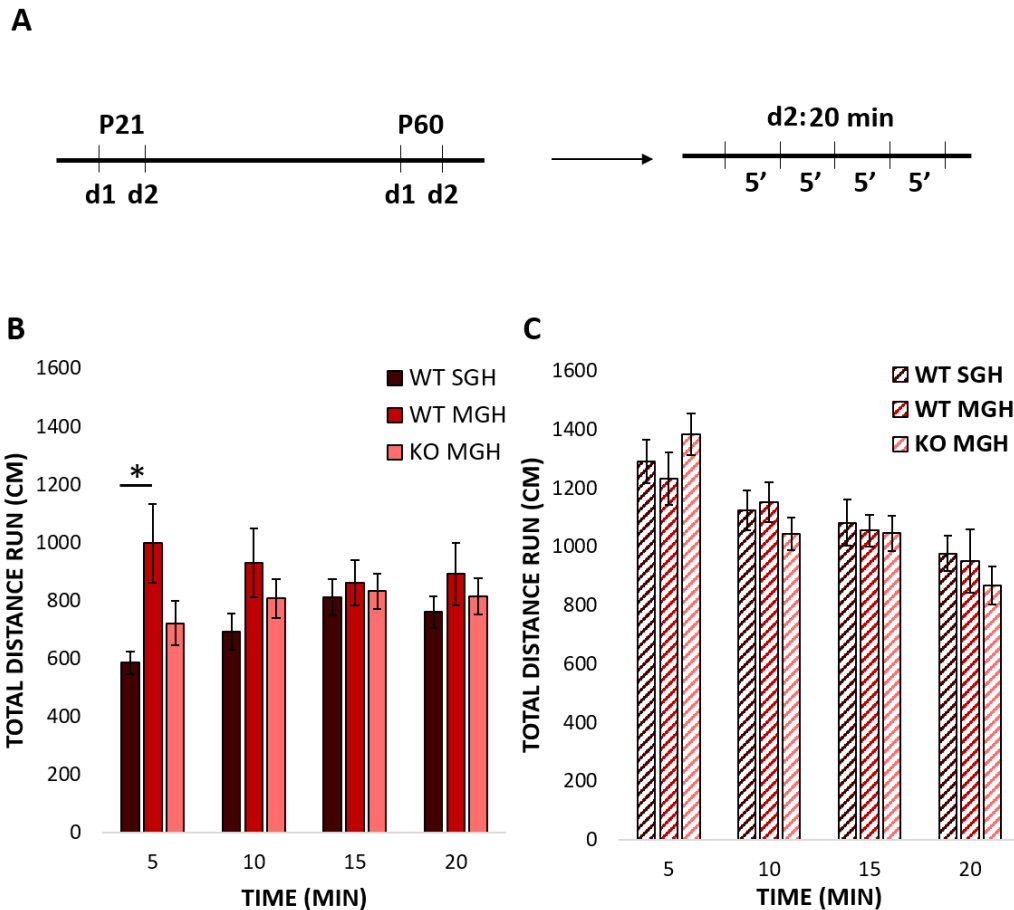


Figure 58. Open-field behavioural test detected an increase in the distance run within the first 5 min in WT MGH male with respect to the WT SGH male on day 2.

Scheme of the adaptation to the arena in the open-field behavioural test (A). Graphs represent distance run in cm per 5-min slot by the P21 (B) and the P60 (C) animals on day 2. The data are presented as mean \pm SEM. $P^* < 0.05$. d1, day1; d2, day2; WT SGH, wild-type from single genotype housing; WT MGH, wild-type from mixed genotype housing; KO MGH, *Pcdh19*-knock-out male from mixed genotype housing.

6.3.1.4 WT MGH males presented a failure in the habituation between trials at P21

Similar to adaptation, habituation or intersessional habituation measures the decrease in the exploratory behaviour of the mice in the arena between consequent days, due to the recognition of this environment as not novel anymore (Kondratova et al. 2010; Daenen et al. 2001). Therefore, habituation studies another way of adaptation to novel situations, that as mentioned in **section 6.3.1.3**, can be impaired in neurodevelopmental disorders (Daenen et al. 2001).

To determine if knock-out of the *Pcdh19* gene in mice affected their habituation, the open field test data from P21 and P60 mice (section **6.3.1.1**) were re-analysed. Total distance run on day 1 (trial 1) and day 2 (trial 2) was recorded and calculated using the EthoVision XT software and differences of habituation between trials were calculated using the IBM SPSS Statistics® 25 software, as explained in **section 2.6.1 (Figure 59A)**.

At P21 (**Figure 59B**), WT MGH males showed a failure in habituation between trials since the distance run between days 1 and 2 did not decrease (trial 1: 3671.31 ± 162.25 cm, trial 2: 3677 ± 347.63 cm; $p > 0.05$), unlike the WT SGH males (trial 1: 3820.81 ± 129.57 cm, trial 2: 2829.37 ± 127.31 cm; $p = 0$) and the KO MGH males (trial 1: 3761.22 ± 212.13 cm, trial 2: 3174.78 ± 186.19 cm; $p = 0.016$).

The differences observed at P21 in the WT MGH male were not present at P60 (**Figure 59C**), where all males habituated (WT SGH, trial 1: 5223.48 ± 341.1 cm, trial 2: 4469.58 ± 229.22 cm; $p = 0.004$; WT MGH, trial 1: 5173.02 ± 362.3 cm, trial 2: 4387 ± 268.93 cm; $p = 0.01$; KO MGH, trial 1: 5288.55 ± 272.67 cm, trial 2: 4336.89 ± 187.07 cm; $p = 0.001$).

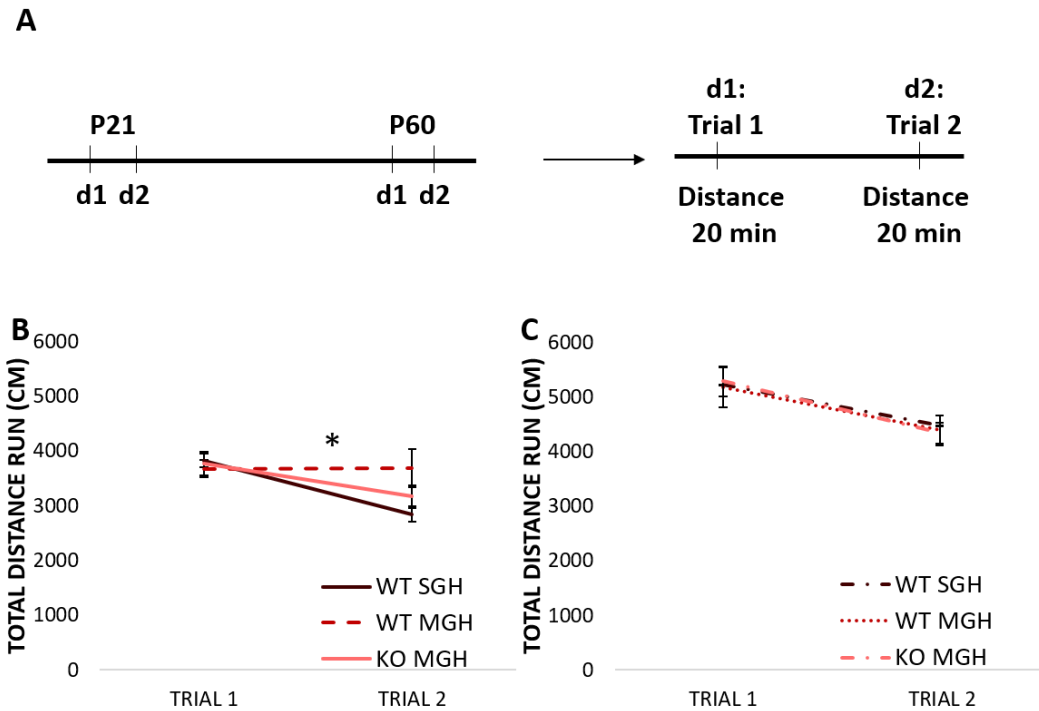


Figure 59. WT MGH males fail to habituate at P21 but habituate normally at P60.

Scheme of the habituation between trials in the open-field behavioural test (A). Graphs represent distance run in cm on day 1 (trial 1) and day 2 (trial 2) by the P21 (B) and the P60 (C) animals. The data are presented as mean \pm SEM. $P^* < 0.05$. d1, day1; d2, day2; WT SGH, wild-type from single genotype housing; WT MGH, wild-type from mixed genotype housing; KO MGH, *Pcdh19*-knock-out male from mixed genotype housing.

6.3.2 The 24-hour activity test showed a delay in the increase of activity in the KO MGH mice at the onset of the dark period

Analysing spontaneous activity of mice during 24 hours in an open-field arena allows the study of general locomotion and the circadian cycle of the animals (Paladino et al. 2013; Kalbassi et al. 2017).

Regarding the circadian cycle, in mammals it comprises a 24-hour oscillation that regulates behavioural, physiological and metabolic processes of the animal. The oscillations are controlled by peripheral circadian clocks. These are regulated by a master clock located in the hypothalamic suprachiasmatic nucleus (SCN) of the anterior hypothalamus, which is in turn synchronised by the light/dark period. Disruption of this system has been reported to affect human health, and is particularly associated with sleep disorders (Kondratova et al. 2010; Kondratov et al. 2007). Since sleep dysregulation has been observed in EIEE patients, the analysis of this cycle was considered important (Smith et al. 2018).

Analysing general locomotion during 24-hours studies mouse activity not induced by novelty, taking into account that the locomotor activity is also influenced by the circadian cycle, and that mice increase their activity during the dark period (Paladino et al. 2013).

24-hour activity experiments were conducted in males older than P60 to assert if depletion of *Pcdh19* affected these parameters. Mice were let to roam freely for 24-hours in an arena with infrared beams positioned at the bottom of the cage, following a 12-hour light-dark cycle. Number of beam breaks during light period, number of beam breaks during dark period, total number of beam breaks and number of beams breaks per hour during 24-hours were recorded and analysed using the MED-PC® IV software, (**Figure 60A**), as stated in **section 2.6.4**. To avoid the general locomotion to be influenced by the exploratory behaviour of the novel environment,

animals stayed in the arena for at least 26-hours, and the first two hours of activity were not considered for the analysis. Animal numbers were 17 WT SGH, 10 WT MGH and 10 KO MGH.

No differences among conditions were appreciated in the number of beam breaks during the dark period (**Figure 60C**; WT SGH=2060.76 ± 128.08 breaks, WT MGH=1940.3 ± 205.73 breaks and KO MGH=1888.7 ± 185.89 breaks) or the total number of beam breaks (**Figure 60D**; WT SGH=2852 ± 162.94 breaks, WT MGH=2599.4 ± 244.49 breaks and KO MGH=2812.4 ± 159.14 breaks), and only a small increase in the number of beam breaks was detected in the KO MGH with respect to the rest of the conditions during the light period (**Figure 60B**; WT SGH=791.24 ± 63.11 breaks, WT MGH=659.1 ± 65.43 breaks and KO MGH=923.7 ± 74.14 breaks). Although an ANOVA between the 3 groups did not reach statistical significance, a difference among conditions in the number of beam breaks during the light period was detected between WT MGH and KO MGH (ANOVA, F (2, 38) = 3.031, p=0.061, Tukey HSD post hoc test, WT MGH vs KO MGH, p=0.049). Statistical analysis programs consider the post-hoc test results to be valid, since occasionally they are powerful enough to detect significant differences between groups when ANOVA cannot. No differences were detected either in the number of beam breaks during the dark period (ANOVA, F (2, 38) = 0.314, p>0.05) or in the total number of beam breaks (ANOVA, F (2, 38) = 0.483, p>0.05).

When analysing the number of beam breaks per hour, the KO MGH males presented a lower number of beam breaks on the first and second hours of the dark period: at 19:00 (WT SGH=148.18 ± 28.27 breaks, WT MGH=268.3 ± 37.49 breaks and KO MGH=56.8 ± 14.84 breaks) and 20:00 (WT SGH=276.76 ± 29.09 breaks, WT MGH=256.2 ± 45.2 breaks and KO MGH=128.9 ± 27.07 breaks) respect to their WT peers. This decrease was statistically significant at 19:00 between the WT MGH and the KO MGH and almost significant between WT SGH and WT MGH (independent-

samples Kruskal-Wallis test, $p=0.00$; pairwise comparison post-hoc test, WT MGH vs KO MGH, $p=0.000$, WT SGH vs WT MGH, $p=0.056$) and at 20:00 between the WT SGH and the KO MGH and tended towards significance between WT MGH and KO MGH (ANOVA, $F(2, 38) = 5.178$, $p=0.011$; Tukey HSD post hoc test, WT SGH vs KO MGH, $p=0.01$, WT MGH vs KO MGH, $p=0.056$).

In the light period, there was also a decrease of the activity of WT MGH mice with respect to the other animals at 8:00 (WT SGH= 56.24 ± 13.31 breaks, WT MGH= 22.4 ± 8.85 breaks and KO MGH= 93.8 ± 33.9 breaks) and at 10:00 (WT SGH= 59.59 ± 21.25 breaks, WT MGH= 27.5 ± 5.78 breaks and KO MGH= 98.6 ± 15.75 breaks). At 8:00, the difference was significant between the WT MGH and the KO MGH and a tendency towards significance between WT SGH and WT MGH (independent-samples Kruskal-Wallis test, $p=0.028$; pairwise comparison post-hoc test, WT MGH vs KO MGH, $p=0.036$, WT SGH vs WT MGH, $p=0.088$). The statistical analysis at 10:00 revealed the difference was significant between the KO MGH and the other animals (independent-samples Kruskal-Wallis test, $p=0.005$; pairwise comparison post-hoc test, WT SGH vs KO MGH, $p=0.027$, WT MGH vs KO MGH, $p=0.006$).

6.3.3 No differences in the EPM test among conditions

Elevated-plus maze (EPM) test was conducted as an indicator of another anxiety-like behaviour different from the thigmotaxis analysed in **section 6.3.1.2**. This maze is a structure comprised by two closed arms and two open arms forming a cross, located at a certain height. This experiment is performed with lights on, so open arms are an elevated, open and bright area that mice try to avoid probably because they feel more vulnerable in those regions. However, open arms are also a novel area that mice tend to explore. Thus, less anxious, hyperactive or more explorative mice will spend more time in the open arms (van Meer et al. 2005; Walf et al. 2007).

To determine if the absence of *Pcdh19* altered the behaviour of the mice in the EPM test, WT SGH males, WT MGH males and KO MGH males were used at P21 and P60. Mice were introduced into the EPM and let to explore freely for 5 min with the lights on. Time in the open arms was recorded and calculated using the EthoVision XT software, as explained in **section 2.6.2 (Figure 61A)**. Animal numbers were 19 WT SGH, 11 WT MGH and 14 KO MGH at P21, and 17 WT SGH, 11 WT MGH and 13 KO MGH at P60.

At P21 (**Figure 61B**), WT MGH male mice spent less time in the open arms than the rest of their peers (WT SGH=70.21 ± 7.92 s, WT MGH=50.85 ± 7.84 s and KO MGH=81.44 ± 10.07 s), but the difference was not statistically significant (ANOVA, $F(2, 41) = 2.577$, $p=0.09$; Tukey HSD post hoc test, WT MGH vs KO MGH, $p=0.075$).

P60 males (**Figure 61C**) showed no differences in the time spent in the open arms among conditions (WT SGH=73.34 ± 8.56 s, WT MGH=72.75 ± 10.05 s and KO MGH=83.05 ± 8.94 s) and statistical analysis did not detect any differences either (ANOVA, $F(2, 38) = 0.383$, $p>0.05$).

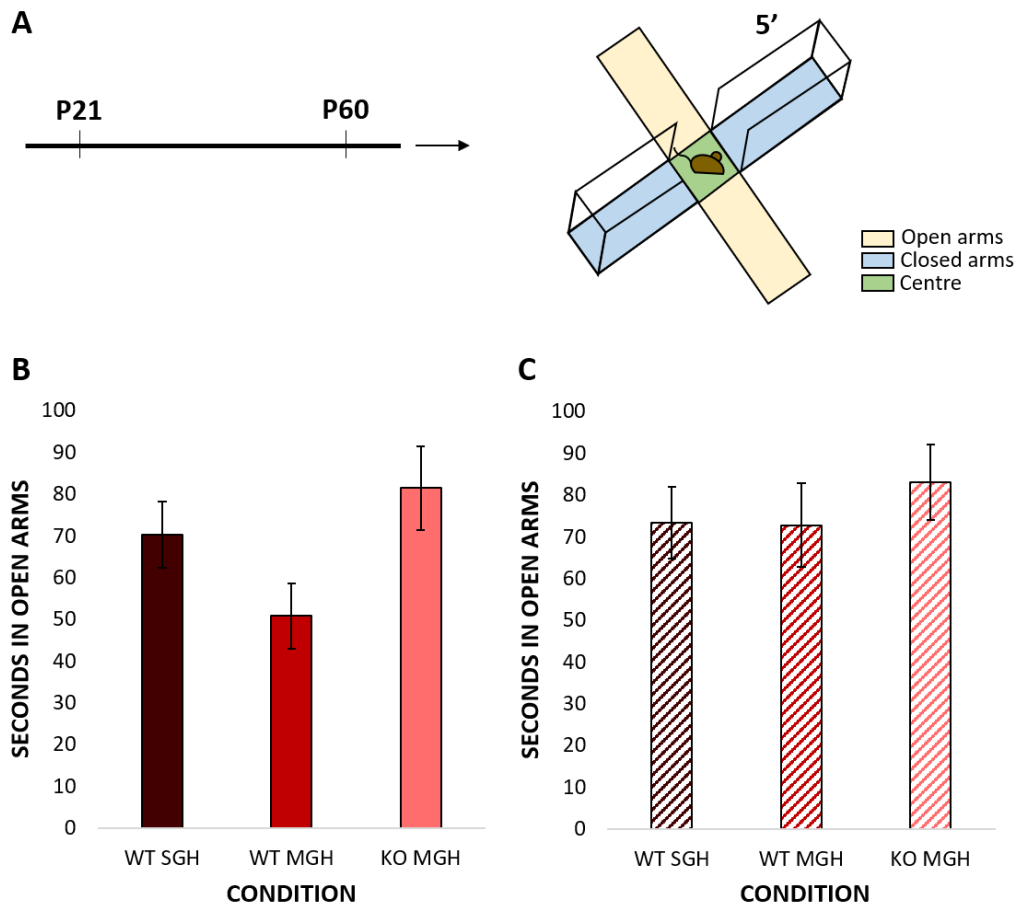


Figure 61. No significant differences were detected among male mice in the EPM experiments conducted at P21 and P60.

Scheme depicting the EPM behavioural test in males (A). Graphs represent the quantification of the number of seconds spent on the open arms in EPM at P21 (B) and P60 (C). Data are presented as means \pm SEM. Light yellow indicates the open arms of the EPM. Light blue signals the closed arms in the EPM. Light green indicates the centre of the EPM. WT SGH, wild-type from single genotype housing; WT MGH, wild-type from mixed genotype housing; KO MGH, *Pcdh19*-knock-out male from mixed genotype housing.

6.3.4 Social behaviour analysis detected a decrease in the social interaction of MGH compared to SGH males

Mice are a highly social species, making them good models to study social behaviour and detect possible deficits that could be similar to the behaviour seen in autism (Moy et al. 2004).

To investigate if the absence of *Pcdh19* leads to any defects in the interaction between animals, social behaviour analysis was carried out.

To conduct the test, P21 male mice were habituated to the arena 3 minutes prior to the experiment. Then an adult female mouse that had been confirmed to be in oestrus was added into the box and both mice were let to roam freely for another 3 minutes with lights on. The interaction was videotaped using the EthoVision XT software and time of interaction was calculated manually (**Figure 62A**), as explained in **section 2.6.3**. Male adult mice were not used for this experiment due to the aggressiveness some male mice show towards other animals (males and females) in adult ages. Animal numbers were 19 WT SGH, 11 WT MGH and 14 KO MGH.

Analysis of P21 male social behaviour (**Figure 62B**) revealed that WT MGH and KO MGH males interact less time with the female in oestrus than their WT SGH peers (WT SGH=115.32 ± 4.76 s, WT MGH=93.18 ± 6.94 s and *Pcdh19*-KO MGH=101.64 ± 7.42 s). Statistical analysis showed that the difference was significant only between the WT SGH and the WT MGH animals (ANOVA, $F(2, 41) = 3.296$, $p=0.047$; Tukey HSD post hoc test, WT SGH vs WT MGH, $p=0.046$; WT SGH vs KO MGH, $p>0.05$).

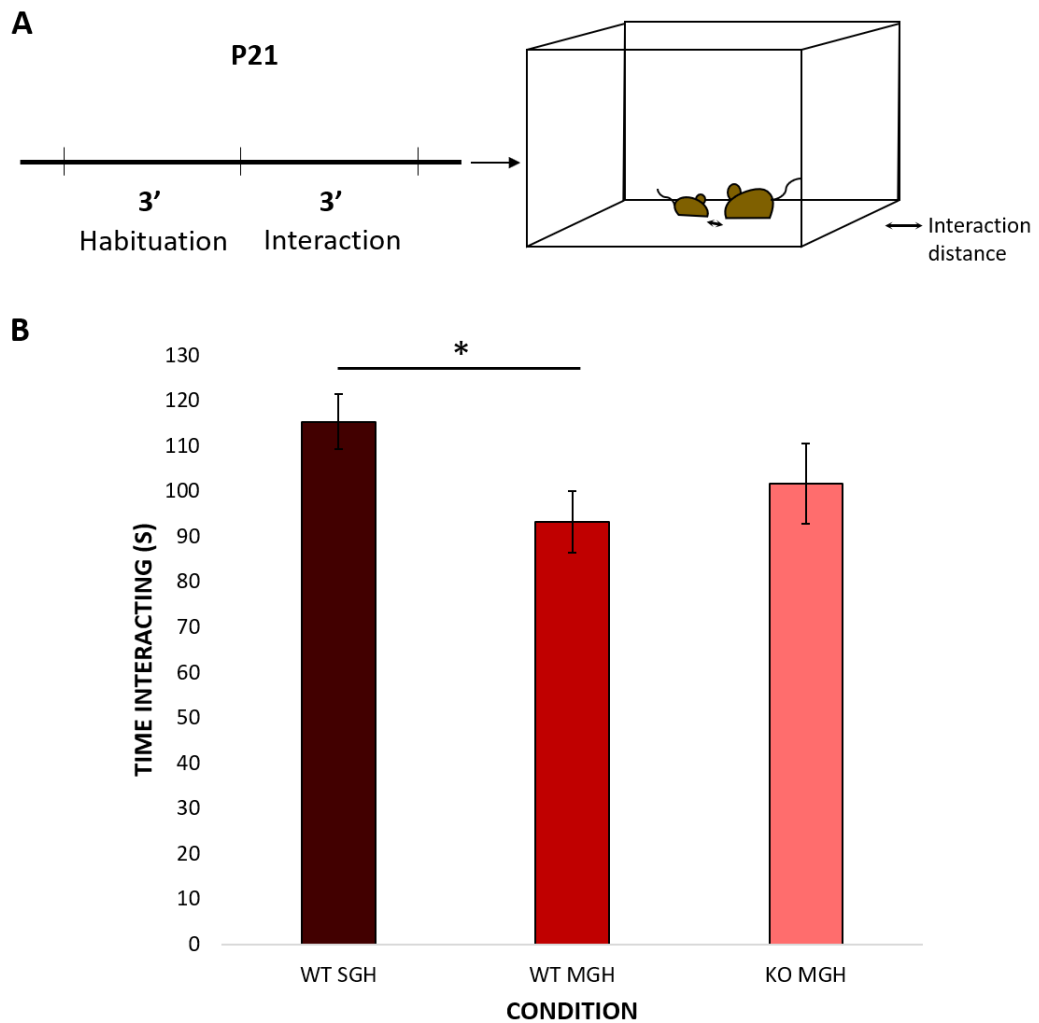


Figure 62. WT MGH males spend less time interacting with an adult female than WT SGH males at P21.

Scheme illustrating the social interaction behavioural test in males (A). Graphs represent the time of interaction between mice (B). Double arrow vector shows the interaction distance. The data are presented as mean \pm SEM. $P^* < 0.05$. WT SGH, wild-type from single genotype housing; WT MGH, wild-type from mixed genotype housing; KO MGH, *Pcdh19*-knock-out male from mixed genotype housing.

6.3.5 Open field analysis in females

6.3.5.1 General locomotor activity analysis detected an increase in the activity of MGH mice with respect to the WT SGH animals

To study if the mosaic expression of *Pcdh19* altered the locomotor activity of female mice, experiments were conducted on P21 and P60 animals. Mice were introduced to the arena for 20 min 24-hours prior to the experiments to get habituated, and then let to explore freely in the box for 20 min in the dark on the second day (**Figure 63A**). Total distance run was recorded and analysed using the EthoVision XT software, as detailed in **section 2.6.1**. Animal numbers were 18 WT SGH, 13 WT MGH and 12 HET MGH both at P21 and P60.

MGH females presented a higher total distance run in the arena with respect to the WT SGH animals (WT SGH=2508.26 ± 160.21 cm, WT MGH=3368.79 ± 178.24 cm and HET MGH=3693.76 ± 194.98 cm) at P21 (**Figure 63B**). This increase was statistically significant between WT SGH and WT MGH and between WT SGH and HET MGH (ANOVA, $F(2, 40) = 12.87$; $p=0.000$; Tukey HSD post-hoc test, WT SGH vs. WT MGH, $p=0.003$, WT SGH vs. HET MGH, $p=0.000$).

At P60 (**Figure 63C**), MGH females also showed a higher distance run in the arena for the 20 min with respect to their WT SGH peers (WT SGH=3661.28 ± 223.53 cm, WT MGH=4211.62 ± 234.87 cm and HET MGH=4262.88 ± 235.11 cm), but this increase was not statistically significant (ANOVA, $F(2, 40) = 2.229$; $p=0.121$).

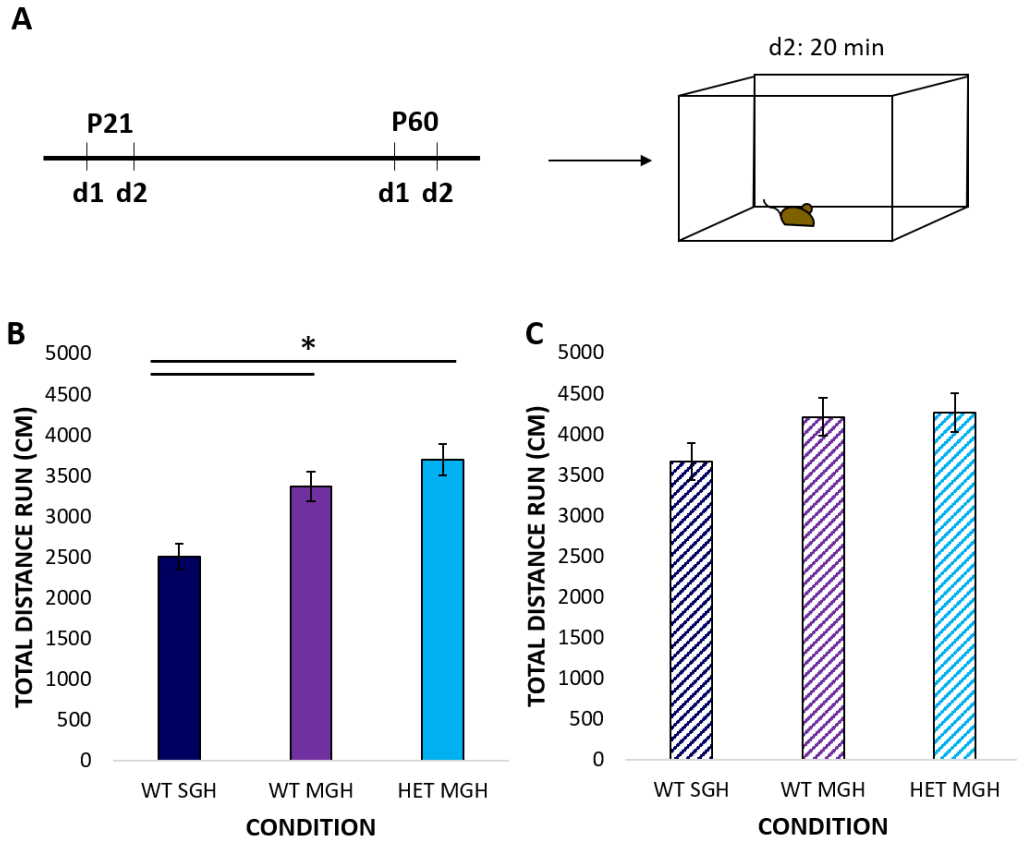


Figure 63. General locomotion activity of WT MGH and HET MGH females in the open field test is increased compared to WT SGH females.

Scheme of the general locomotor activity in open field (A). Graphs represent total distance run for 20 min in P21 (B) and P60 (C) animals on day 2. The data are presented as mean \pm SEM. $P^* < 0.05$. d1, day1; d2, day2; WT SGH, wild-type from single genotype housing; WT MGH, wild-type from mixed genotype housing; HET MGH, *Pcdh19*-heterozygous female from mixed genotype housing.

6.3.5.2 Thigmotaxis of WT MGH females is increased compared to WT SGH at P60

P21 and P60 female mice were tested to determine if the mosaicism of the *Pcdh19* gene in the animals affected their thigmotaxis. Open field test data were analysed to record distance run in the centre and periphery, and the distance run in the centre with respect to the total distance run was calculated manually, as mentioned in **section 2.6.1**.

As explained in **section 6.3.1.2** thigmotaxis is the tendency of the animal to remain close to the walls of the open field arena when introduced to it (Simon et al. 1994). As thigmotaxis is calculated as the time spent in the centre of the arena with respect to the total time spent in it, a decreased thigmotaxis would be reflected with a higher bar and vice versa.

As seen in **Figure 64B**, P21 HET MGH females presented a lower thigmotaxis than their WT counterparts (WT SGH=0.22 ± 0.02, WT MGH=0.22 ± 0.02 and HET MGH=0.28 ± 0.02). However, statistical analysis revealed this difference was not significant (ANOVA, $F(2, 40) = 2.607$, $p=0.086$).

At P60 (**Figure 64C**), WT MGH females show a higher thigmotaxis compared to the WT SGH and the HET MGH animals (WT SGH=0.26 ± 0.01, WT MGH=0.2 ± 0.02 and HET MGH=0.23 ± 0.02). This increase was statistically significant between WT SGH and WT MGH animals (independent-samples Kruskal-Wallis test, $p=0.015$; pairwise comparison post-hoc test, WT SGH vs WT MGH, $p=0.011$).

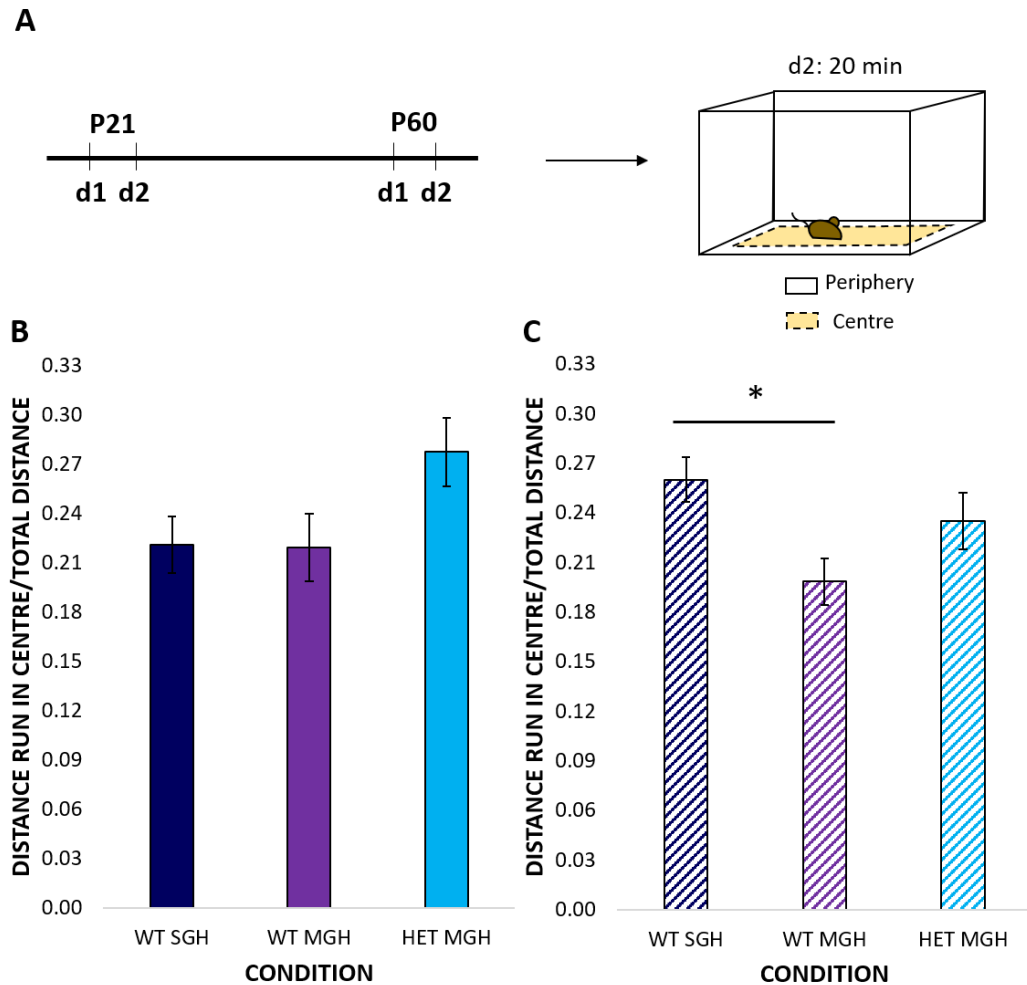


Figure 64. Open-field behavioural experiments detected a significant increase in thigmotaxis of the adult WT MGH females compared to the WT SGH animals.

Illustration of the test for thigmotaxis in open field (A). Graphs represent the distance run in the centre with respect to the total distance run in P21 (B) and P60 (C) animals on day 2. The data are presented as mean \pm SEM. $P^* < 0.05$. Dashed black lines and light-yellow colour signal the centre of the box. d1, day1; d2, day2; WT SGH, wild-type from single genotype housing; WT MGH, wild-type from mixed genotype housing; HET MGH, *Pcdh19*-heterozygous female from mixed genotype housing.

6.3.5.3 MGH mice presented an increase in the total distance run in the 5-min slot compared to the WT SGH mice at both ages

To determine if the mosaicism of the *Pcdh19* gene caused an alteration in the adaptation to the open-field arena, total distance run in the arena in each 5-min slot during the 20 min long open field test was calculated from the open field data.

At P21 (**Figure 65B**), it was observed that WT MGH and WT HET females showed a higher distance run at the 5-min slot (WT SGH=441.46 ± 47.42 cm, WT MGH=867.3 ± 89.87 cm and HET MGH=1121.25 ± 99.45 cm), the 10-min slot (WT SGH=740.27 ± 63.61 cm, WT MGH=908.23 ± 82.32 cm and HET MGH=963.56 ± 48.81 cm) and the 15-min slot (WT SGH=637.38 ± 71.41 cm, WT MGH=817.2 ± 76.45 cm and HET MGH=863.61 ± 66.05 cm) with respect to the WT SGH animals. Statistical analysis revealed that the difference in the 5-min slot was significant between the WT SGH and the MGH animals, and the difference between WT MGH and WT HET trended towards significance (ANOVA F (2, 40) = 21.772, p=0.000; Tukey HSD post-hoc test, WT SGH vs. WT MGH, p=0.001, WT SGH vs. WT HET, p=0.000, WT MGH vs WT HET, p=0.079), while in the 10-min slot (ANOVA, F (2, 40) = 3.181, p=0.052) and in the 15-min slot (ANOVA, F (2, 40) = 2.893, p=0.067) differences did not reach significance. Distance run in the 20-min slot was similar among conditions (WT SGH=668.47 ± 70.05 cm, WT MGH=776.04 ± 60.16 cm and HET MGH=745.33 ± 63.28 cm), and statistical analysis detected no differences among conditions either (independent-samples Kruskal-Wallis test, p>0.05).

At P60 (**Figure 65C**), WT MGH and HET MGH females also presented a higher distance run in the 5-min slot compared to the WT SGH counterparts (WT SGH=882.14 ± 63.85 cm, WT MGH=1331.95 ± 88.07 cm and *Pcdh19*-HET MGH=1273.9 ± 68.51 cm), that was statistically significant (ANOVA, F

(2, 40) = 12.246, $p=0.000$; Tukey HSD post-hoc test, WT SGH vs. WT MGH, $p=0.001$, WT SGH vs. WT HET, $p=0.000$). There were no differences in the distance run among conditions in the 10-min slot (WT SGH= 972.25 ± 64.08 cm, WT MGH= 1031.21 ± 80.82 cm and HET MGH= 989.46 ± 59.63 cm), the 15-min slot (WT SGH= 904.1 ± 70.92 cm, WT MGH= 914.24 ± 59.6 cm and HET MGH= 1019.99 ± 90.90 cm) or the 20-min slot (WT SGH= 902.79 ± 75.44 cm, WT MGH= 934.21 ± 84.72 cm and HET MGH= 979.53 ± 7.62 cm).

Details of the statistical analysis are shown in the appendix (**Table A. 22**).

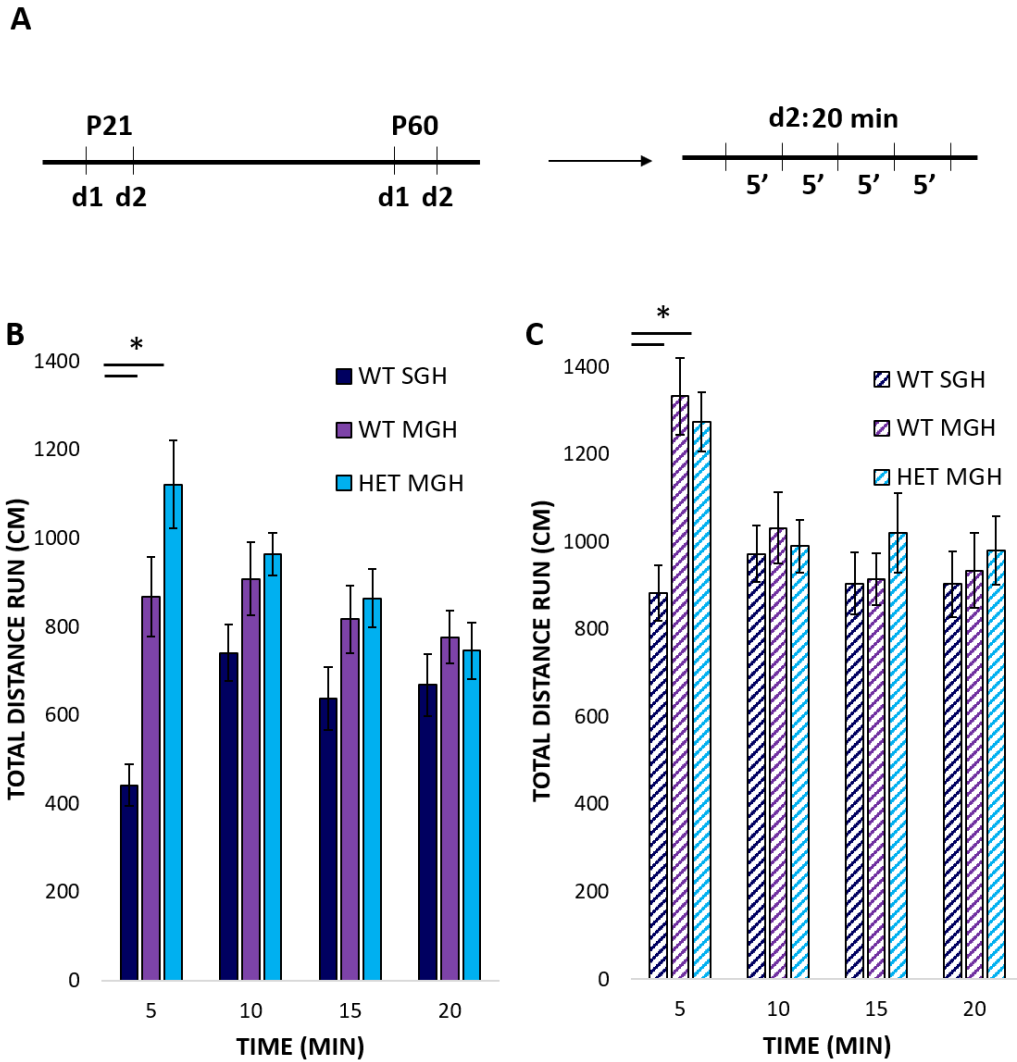


Figure 65. Open-field behavioural analysis revealed an increase in the distance run by the WT MGH and HET MGH females with respect to the WT SGH female in the 5-min slot at P21 and P60.

Scheme of the adaptation to the arena in the open-field behavioural test (A). Graphs represent distance run in cm per 5-min slot by the P21 (B) and the P60 (C) animals on day 2. The data are presented as mean \pm SEM. $P^* < 0.05$. d1, day1; d2, day2; WT SGH, wild-type from single genotype housing; WT MGH, wild-type from mixed genotype housing; HET MGH, *Pcdh19*-heterozygous female from mixed genotype housing.

6.3.5.4 WT MGH do not habituate at P21 and habituate at P60, unlike the other conditions

To assess if *Pcdh19* mosaicism had an effect in the habituation between trials in the open-field test, total distance run on day 1 (trial 1) and day 2 (trial 2) was measured and differences of habituation between trials were calculated as explained in **section 2.6.1**.

P21 (**Figure 66B**) WT MGH females presented a failure in habituation between trials (trial 1: 3586.32 ± 148.31 cm, trial 2: 2508.26 ± 160.21 cm; $p > 0.05$). However, WT SGH females (trial 1: 3459.41 ± 204.36 cm, trial 2: 3368.79 ± 178.24 cm; $p = 0$) and HET MGH females (trial 1: 4366.69 ± 258.17 cm, trial 2: 3693.76 ± 194.98 cm; $p = 0.013$) adapted normally.

At P60 (**Figure 66C**), WT MGH was the only condition that habituated, while WT SGH and HET MGH females did not (WT SGH, trial 1: 3915 ± 263.76 cm, trial 2: 3661.28 ± 223.53 cm; $p > 0.05$; WT MGH, trial 1: 4909.44 ± 356.69 cm, trial 2: 4211.62 ± 234.87 cm; $p = 0.016$; HET MGH, trial 1: 4672.72 ± 226.64 cm, trial 2: 4262.88 ± 235.11 cm; $p > 0.05$).

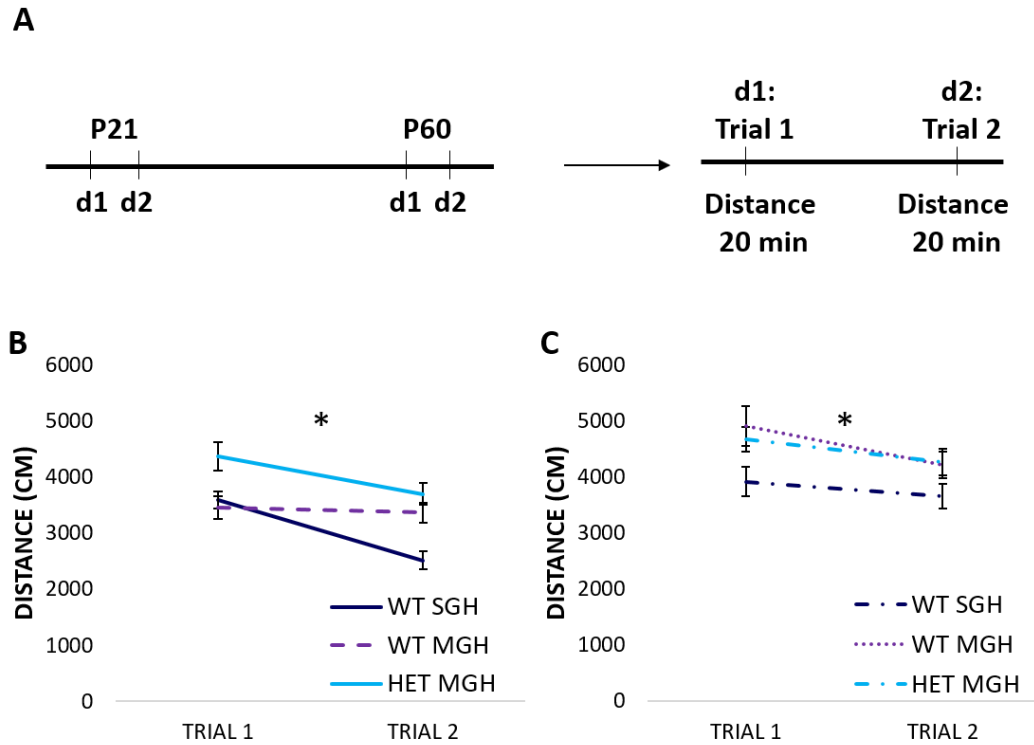


Figure 66. Differences in the habituation of WT MGH females at P21 and P60.

Scheme of the habituation between trials in the open-field behavioural test (A). Graphs represent distance run in cm on day 1 (trial 1) and day 2 (trial 2) by the P21 (B) and the P60 (C) animals. The data are presented as mean \pm SEM. $P^* < 0.05$. d1, day1; d2, day2; WT SGH, wild-type from single genotype housing; WT MGH, wild-type from mixed genotype housing; HET MGH, *Pcdh19*-heterozygous female from mixed genotype housing.

6.3.6 24-hour activity analysis revealed minor differences among the females

To determine if the mosaic expression of *Pcdh19* altered the 24-hour activity of the mice, P60 animals were let to roam freely in an arena with infrared beams positioned at the bottom of the cage for 24-hours, following a 12-hour light-dark cycle. Number of beam breaks during light period, number of beam breaks during dark period, total number of beam breaks and number of beams breaks per hour were calculated using the MED-PC® IV software (**Figure 67A**), as explained in **section 2.6.4**. Animal numbers were WT SGH=18; WT MGH=11; HET MGH= 10.

Number of beam breaks during the light period (**Figure 67B**; WT SGH=802 ± 70.7 breaks, WT MGH=856.73 ± 103.53 breaks and *Pcdh19*-HET MGH=1068.2 ± 104.01 breaks) and during the dark period (**Figure 67C**; WT SGH=1928.39 ± 142.55 breaks, WT MGH=2278.45 ± 210.19 breaks and *Pcdh19*-HET MGH=2060.9 ± 169.25 breaks) were similar among conditions. Total number of beam breaks (**Figure 67D**; WT SGH=2730.39 ± 184.03 breaks, WT MGH=3135.18 ± 296.72 breaks and *Pcdh19*-HET MGH=3129.1 ± 260.58 breaks) was higher in WT MGH and HET MGH with respect to WT SGH mice. However, statistical analysis of all three parameters did not detect any significant differences.

The analysis of the number of beam breaks per hour (**Figure 67E**) showed a higher activity of the MGH females compared to the WT SGH animals at two consecutive hours in the dark period: 21:00 (WT SGH=204.33 ± 29.09 breaks, WT MGH=284.82 ± 37.57 breaks and *Pcdh19*-HET MGH=260.8 ± 20.27 breaks) and 22:00 (WT SGH=204.17 ± 26.34 breaks, WT MGH=314.27 ± 31.55 breaks and *Pcdh19*-HET MGH=286.8 ± 37.23 breaks), and a lower activity of the HET MGH compared to the WT females at 4:00, also in the dark period (WT SGH=116.78 ± 21.74 breaks, WT MGH=118.09 ± 13.43 breaks and *Pcdh19*-HET MGH=52.9 ± 10.46 breaks).

The statistical analysis revealed that the difference at the 22:00 mark was significant between the WT SGH and the WT MGH (ANOVA, $F(2, 40) = 3.837$, $p=0.031$; Tukey HSD post hoc test, WT SGH vs WT MGH, $p=0.036$), and at 4:00 was significant between HET MGH and the rest of the animals (ANOVA, $F(2, 40) = 3.184$, $p=0.053$; Games-Howell post-hoc test, WT SGH vs. HET MGH, $p=0.037$, WT MGH vs. HET MGH, $p=0.003$).

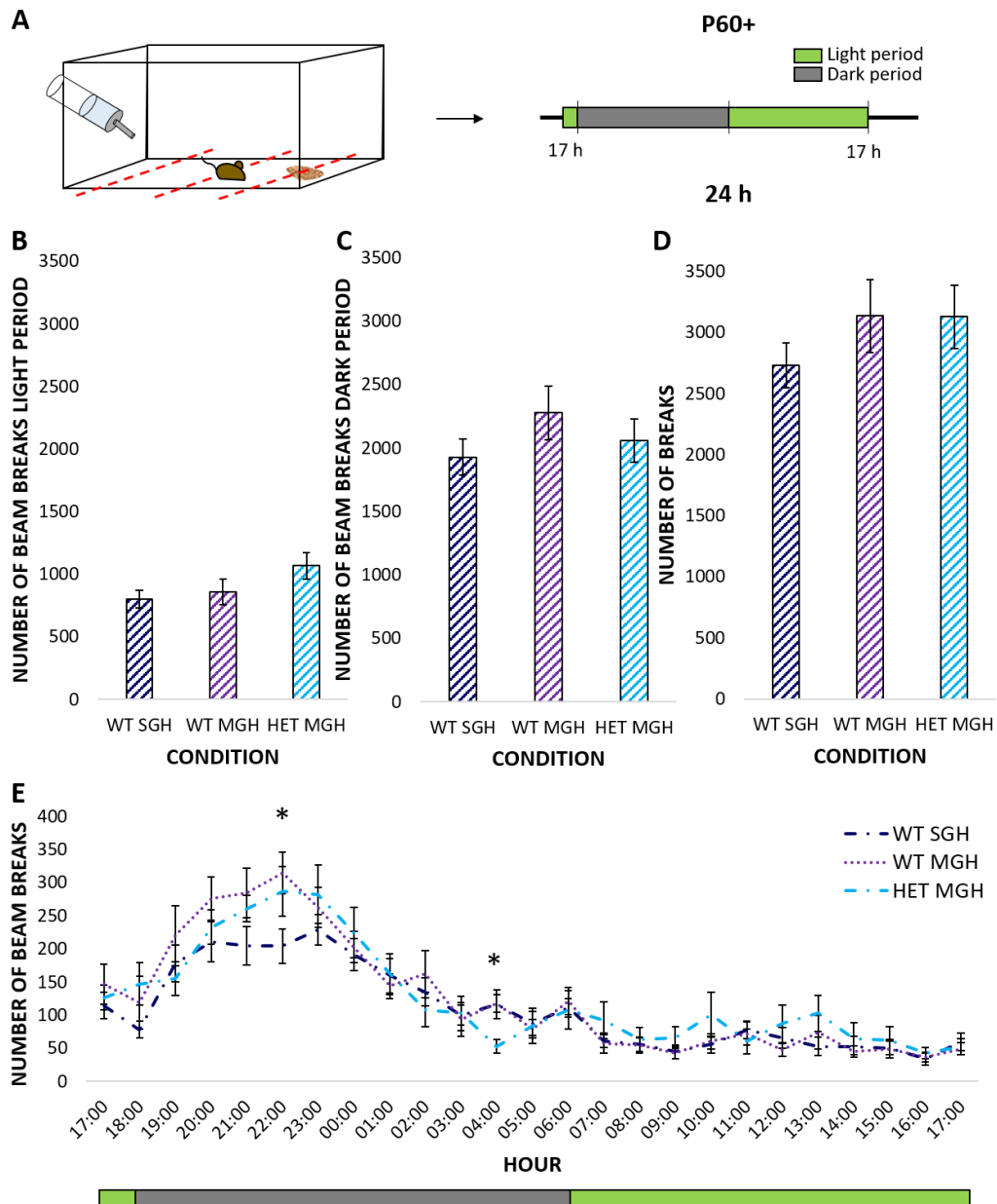


Figure 67. 24-hour experiments performed in the adult female mice showed slight differences between MGH and SGH females and between the HET females and their WT counterparts.

Scheme of the 24-hour activity test (A). Graphs represented the number of beam breaks during the light period (B), the dark period (C), the total number of beam breaks during the 24-hour cycle (D) and number of beams broken per hour during the experiment (E). Dashed red lines mark the lasers that cross the activity box. $P^* < 0.05$. WT SGH, wild-type from single genotype housing; WT MGH, wild-type from mixed genotype housing; HET MGH, *Pcdh19*-heterozygous female from mixed genotype housing.

6.3.7 P21 HET MGH animals spent more time in the open arms of the EPM than WT mice

To detect any changes in the EPM test behaviour caused by the mosaic expression of *Pcdh19*, WT SGH, WT MGH and HET MGH females were used at P21 and P60. Mice were let to freely explore for 5 min in the EPM arena with light on. Time in the open arms was measured using the EthoVision XT software (**Figure 68A**), as described in **section 2.6.2**. Animal numbers were 18 WT SGH, 13 WT MGH and 12 HET MGH, both at P21 and P60.

P21 analysis (**Figure 68B**) revealed that HET MGH females spent more time in the open arms than WT mice (WT SGH=62.59 ± 7.25 s, WT MGH=56.57 ± 6.26 s and HET MGH=105.19 ± 6.18 s). This difference was statistically significant between WT SGH and HET MGH and between WT MGH and HET MGH (ANOVA, $F(2, 40) = 13.125$, $p=0.00$; Tukey HSD post hoc test, WT SGH vs HET MGH, $p=0.00$, WT MGH vs HET MGH, $p=0.00$).

The alteration was not present at P60 (**Figure 68C**). Although both WT MGH and HET MGH animals spent more time in the open arms of the EPM compared to the WT SGH adult female mice (WT SGH=59.74 ± 6.64 s, WT MGH=76.39 ± 9.82 s and HET MGH=76.29 ± 8.45 s), statistical analysis showed the difference was not significant.

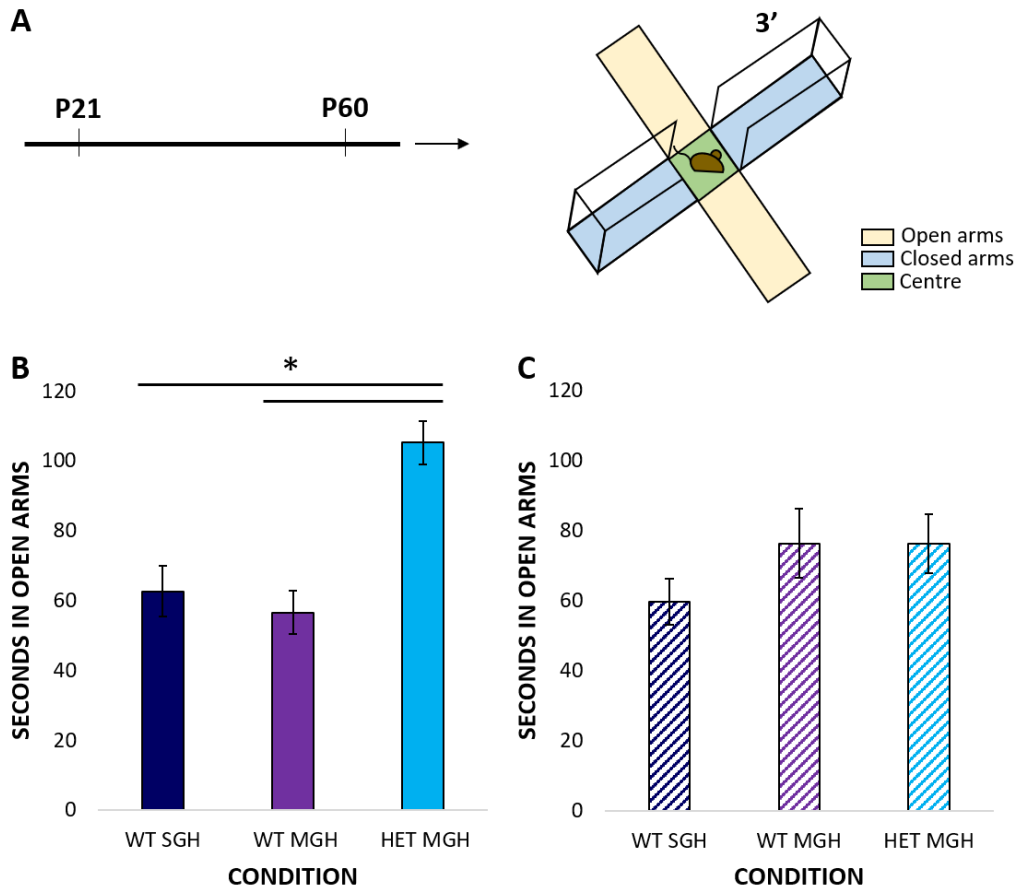


Figure 68. *Pcdh19*-HET females spend more time in the open arms of the EPM than their WT peers at P21, but not at P60.

Illustration of the EPM behavioural test in females (A). Graphs represent the quantification of the number of seconds spent on the open arms in EPM at P21 (B) and P60 (C). Light yellow indicates the open arms of the EPM. Light blue signals the closed arms in the EPM. Light green indicates the centre of the EPM. $P^* < 0.05$. WT SGH, wild-type from single genotype housing; WT MGH, wild-type from mixed genotype housing; HET MGH, *Pcdh19*-heterozygous female from mixed genotype housing.

6.3.8 No differences are observed in social behaviour among females

To determine possible alterations in the social behaviour of mice with mosaicism of the *Pcdh19* gene, P21 female mice were habituated to the arena 3 minutes prior to the experiment. Then an adult female mouse that had been confirmed to be in oestrus was added into the box and both mice were let to roam freely for another 3 minutes. The interaction was videotaped using the EthoVision XT software and time of interaction was calculated manually. At P60, the procedure was identical, but foreign female mice were not tested for oestrus condition (**Figure 69A**). Animal numbers were 18 WT SGH, 13 WT MGH and 12 HET MGH, both at P21 and P60.

No differences among the conditions were observed regarding the time of interaction at P21 (WT SGH=112.28 ± 8.41 s, WT MGH=105.92 ± 8.42 s and *Pcdh19*-HET MGH=103.83 ± 8.03 s) or P60 (WT SGH=83.72 ± 6.4 s, WT MGH=74.08 ± 6.87 s and *Pcdh19*-HET MGH=85.83 ± 5.98 s) and statistical analysis confirmed it (**Figure 69B, C**).

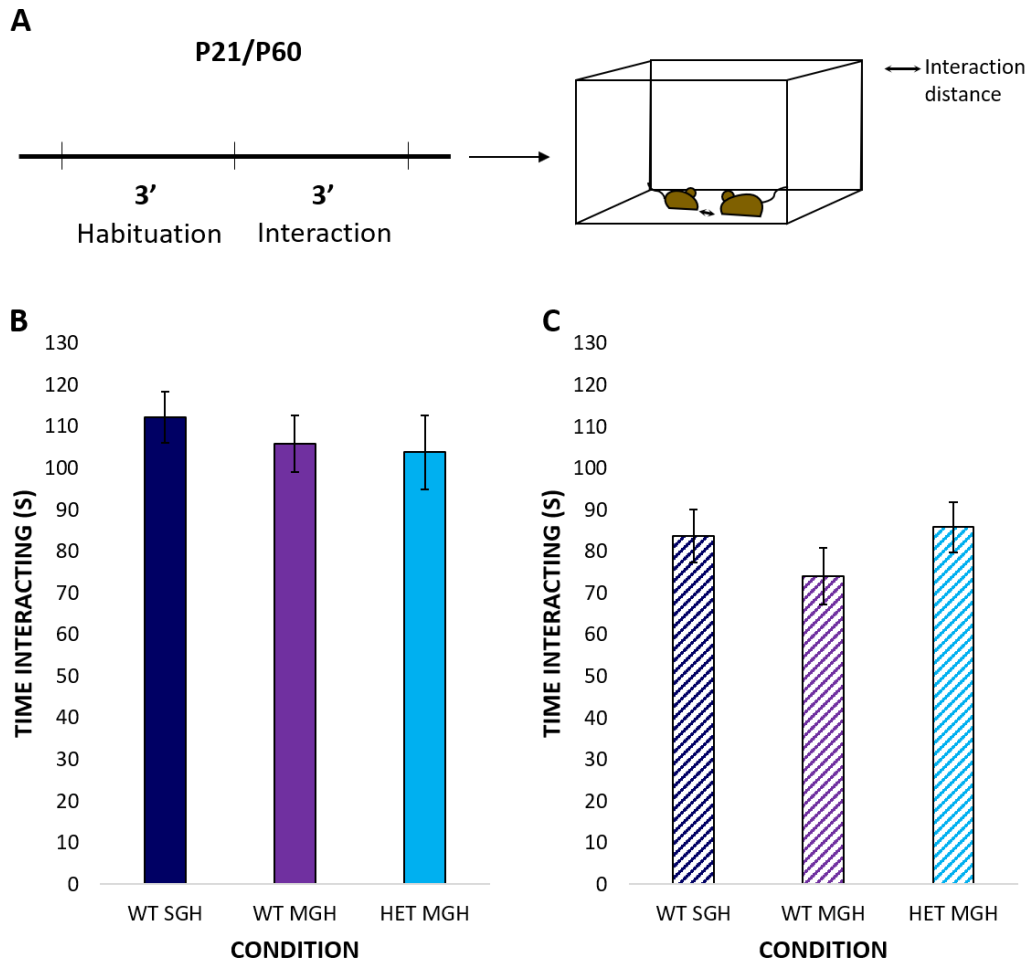


Figure 69. Social behaviour analysis detected no differences among conditions in interaction time with a foreign mouse.

Scheme illustrating the social interaction behavioural test in females (A). Graphs represent the time of interaction between mice at P21 (B) and P60 (C). Double arrow vector shows the interaction distance. The data are presented as mean \pm SEM. WT SGH, wild-type from single genotype housing; WT MGH, wild-type from mixed genotype housing; HET MGH, *Pcdh19*-heterozygous female from mixed genotype housing.

6.4 Discussion

6.4.1 Summary of results

The aim of this chapter was to assess if *Pcdh19* mutant animals presented alterations in their behaviour with respect to WT mice, and if as observed by Kalbassi *et al.* the presence of mutant littermates (MGH) affected the behaviour of WT animals (Kalbassi et al. 2017).

KO MGH males only showed differences in the 24-h activity behavioural test. These animals presented a significant increase of activity with respect to the WT MGH mice during the light period, which was reflected by an increase of activity at 8:00 and 10:00. A delay in the increase of activity at the start of the dark period (19:00 and 20:00) with respect to the WT MGH was also revealed. The analysis only detected one significant difference between the KO MGH males and the WT SGH mice, which was the increase of activity in the second hour of the dark period (20:00).

HET MGH females presented significant differences in the open field analysis, 24-hour activity and the EPM compared to the WT mice, most of them at P21. In the open field experiments conducted at P21, these females showed a significant increase in the total locomotor activity with respect to the P21 WT SGH, that is originated from the significantly high ambulation in the first 5-min slot and the non-significant increases in the 10- and 15-min slots. The thigmotaxis is also slightly decreased compared to both types of WT animals. At P60, analysis revealed an increase in the distance run by HET MGH during the first 5-min slot with respect to the WT SGH that was statistically significant. In the 24-hour activity analysis, an increase in the activity of the HET MGH animals compared to the WT was seen in one of the slots during the dark period. In the EPM study, there was an increase in the time spent in the open arms compared to the WT SGH and the WT MGH at P21, and a slight, non-significant increase at P60 with respect to WT SGH.

As in Kalbassi *et al.* WT MGH animals presented behavioural differences with respect to WT SGH mice (Kalbassi *et al.* 2017).

In males, P21 WT MGH showed differences in open field and social interaction. WT MGH analysis in the open field detected a failure in the habituation between trials at P21, unlike the WT SGH and the KO MGH mice. This failure probably leads to the significant increase of the activity of these animals in the 5-min slot on trial 2 compared to the WT SGH animals, and the increase of the total distance run by the mice, that is not significant. There was also a significant decrease in the time the WT MGH mice spent interacting with the foreign female at P21 with respect to the WT SGH animals. In the EPM, the differences between WT SGH and WT MGH were not significant. However, 3 WT SGH males stood out when performing the analysis, as their time in the open arms was almost non-existent. Those three males belonged to the same litter, were analysed within the same session and were also the first three to be analysed on that particular day. Re-analysis of the EPM behaviour omitting those three samples showed a statistically significant between the WT MGH and the rest of the animals (ANOVA, $F(2, 38) = 2.577$, $p=0.024$; Tukey HSD post hoc test, WT SGH vs WT MGH, $p=0.036$, WT MGH vs KO MGH, $p=0.041$), but exclusion of those three animals could not really be justified and consequently, EPM results will be considered as not significant.

In females, statistically significant differences were detected in open field at P21 and P60; and in the 24 h. activity experiments. The WT MGH females presented a failure of habituation between trials compared to the WT SGH that translated into a significant increase in the total distance run by the mice in trial 2. This increase was observed in the first 5-min slot, when it was significant, and in the 10- and 15- min slots, when it was not. At P60, the increase in activity at the 5-min slot compared to the WT SGH was still present, together with an increase in the thigmotaxis. WT MGH females also adapt between trials at P60, unlike the WT SGH and HET MGH animals. In

the 24-hour activity experiments, a significant increase at one of the hours of the dark period, and a slight non-significant increase in the number of beams broken during the dark period, were detected between the WT MGH animals and the other conditions. A higher time spent in the open arms of the EPM by the P60 WT MGH compared to the WT SGH appeared to be seen, but it was not statistically significant.

Results are depicted in **Table 18**.

		OPEN FIELD	24H ACTIVITY	EPM	SOCIAL BEHAVIOUR
MALES	KO vs WT	n.d.	<ul style="list-style-type: none"> • ↑ Total breaks light period * • ↑ Total breaks at 8:00, 10:00, 19:00 and 20:00 * 	n.d.	n.d.
	WT MGH vs WT SGH	<ul style="list-style-type: none"> • ↑ 5-min slot P21 * • No habituation P21 • ↑ Total distance run (n.s.) 	n.d.	• ↓ Total time in OA P21 (n.s.)	• ↓ Time P21
FEMALES	HET vs WT	<ul style="list-style-type: none"> • ↑ Total distance run * • ↑ 5-min slot P21 * • ↑ 5-min slot P60 * • ↑ 10- and 15-min slot P21 (n.s.) • ↓ Thigmotaxis (n.s.) 	<ul style="list-style-type: none"> • ↑ Total breaks light (n.s.) • ↑ Total breaks at 4:00* 	<ul style="list-style-type: none"> • ↑ Total time in OA P21 * • ↑ Total time in OA P60 (n.s.) 	n.d.
	WT MGH vs WT SGH	<ul style="list-style-type: none"> • ↑ Total distance run * • ↑ 5-min slot P21 * • ↑ 5-min slot P60 * • ↑ Thigmotaxis P60* • No habituation P21 • Habituation P60 • ↑ 10- and 15-min slot P21 (n.s.) 	<ul style="list-style-type: none"> • ↑ Total breaks dark (n.s.) • ↑ Total breaks at 22:00* 	• ↑ Total time in OA P60 (n.s.)	n.d.

Table 18. Illustration of the results obtained in Chapter 6.

EPM, elevated plus maze; WT SGH, wild-type from single genotype housing; WT MGH, wild-type from mixed genotype housing; HET, *Pcdh19*-heterozygous female from mixed genotype housing; KO, *Pcdh19*-knockout male from mixed genotype housing; ↑ increase; ↓, decrease; *, significant; n.s., not significant; n.d., no differences; OA, open arms.

6.4.2 Choice of methods

As mentioned in **section 6.1**, *Pcdh19*-mutant mice do not seem to present epileptic episodes (Pederick et al. 2016; Hayashi et al. 2017), even though a more recent paper from Pederick *et al.* has reported alterations in the brain network activity of *Pcdh19*-HET mice. Thus, it was decided to study other possible alterations in the mouse phenotype, particularly in behaviour.

Other KO mouse models for different delta-protocadherins have been reported to present behavioural alterations: *Pcdh9*-KO animals revealed changes in locomotor activity in young adults, sensorimotor behaviours, touch-evoked biting, and long-term social recognition and novel object recognition (Bruining et al. 2015); male *Pcdh10*-HET mice showed atypical social behaviour, not present in the *Pcdh10*-HET female mice (Schoch et al. 2017) and behavioural tests in *Pcdh17*-KO animals detected antidepressant-like behaviours in comparison to the WT animals (Hoshina et al. 2013).

In this chapter, 4 tests (open-field, social interaction, EPM and 24-hour activity) were conducted to analyse spontaneous locomotor activity, alteration of the circadian rhythms, social and anxiety-like behaviour. Even though these experiments do not cover all the phenotypes seen in other delta-protocadherins, they were chosen as a simple way to analyse altered behaviours that correlate to autism (Lai et al. 2014), which is present in around 25% of EIEE9 patients (Camacho et al. 2012). Moreover, these experiments induce little stress to the mice and the equipment was readily available from Dr. Stéphane Badouin (Cardiff University).

Novel object recognition, which was altered in *Pcdh9*-KO mice (Bruining et al. 2015), was also tested, as outlined in **Figure 70**. However, control mice failed to perform the task and did not spend more time with the unfamiliar object. Three different versions of the experiment were attempted using different objects. First, objects of different shape; then objects with different size and shape; and finally objects with different size, shape and materials. These experiments were performed using the WT MGH, since these

experiments were conducted before the differences between WT SGH and WT MGH mice were detected. It could be possible WT MGH mice fail this behavioural test and WT SGH do not. However, these mice have a 129/SvEv-C57/BL6 background that needs to be considered. It has previously been reported that mice performance in behavioural tasks varies among strains, including the novel object recognition task (Brooks et al. 2004). In fact, the 129S6 strain from Taconic has been reported to have a low performance in novel object recognition (Wolf et al. 2016), so it is also possible this particular strain does not perform the novel object recognition task well.

Male and female mice were pooled and analysed separately since in many cases there are differences in male and female behaviour mainly due to hormonal variations (Van Meer et al. 2005). For example, sleep regulation is partially controlled by hormonal variations related to the oestrus cycle in females (Koehl et al. 2003). Also, the *Pcdh19*-mutant mice studied are exclusively *Pcdh19*-KO males and *Pcdh19*-HET females so separating and analysing the WT males with the *Pcdh19*-KO males and the WT females with the *Pcdh19*-HET females seemed to be the most adequate option.

Mice were studied at ages P21 and P60, which are preweaning ages and young adult respectively, since behaviour can also be age-dependant (Van Meer et al. 2005). Hayashi *et al.* did a behavioural characterization, even though on another model of *Pcdh19*-mutant animal, but their analysis was never performed in animals younger than 10-weeks old (Hayashi et al. 2017). Since EIEE9 is a neurodevelopmental disorder with infancy or early childhood onset (Duszyc et al. 2014), it was decided to study the behaviour at earlier ages, too.

Several factors can alter animal behaviour independently of genotype: general genetic background, age, animal health and animal care, housing conditions, environment or environmental stress, among others (Van Meer et al. 2005). Therefore, all these conditions were kept as homogeneous as

possible across litters: animals were from the same background and were subjected to the same environment and the minimal stress possible in each experiment. Subjects were of very similar ages (P20-P24 and P58-P67), apart from the 24-h. activity experiments, that were conducted between P67 and P80. Housing conditions were identical in temperature, humidity or cage type, but varied between the WT SGH and the WT MGH. This last factor is altered to study the possible influence of *Pcdh19*-mutant mice on the WT when housed together (Kalbassi et al. 2017), as explained in **section 6.3**.

Since the presence of *Pcdh19*-mutant animals seemed to be influencing the behaviour of the WT littermates, the possibility of the WT animals influencing their *Pcdh19*-mutant peers was considered. Open-field and EPM tests were performed on litters that consisted of *Pcdh19*-HET and KO animals only (HET SGH and KO SGH). Unfortunately, animals had to be relocated due to construction work around that time of the experimental period of this thesis, so tests had to be performed in another location with different apparatus. As a result, a meaningful comparison between the two sets of data was unfortunately not possible. Time constraints prevented the repetition of these experiments, but they will be essential to complete the characterisation of the *Pcdh19*-mutant animals.

6.4.3 Behavioural differences in the KO MGH males

As described in the results, KO MGH mice do not present major differences in behaviour with respect to the WT SGH males. The only statistically significant differences were an increase in the number of beam breaks during the light period, an increase in the activity during two of the hours of the light period, and a delay in the increase of activity at the onset of the dark period in the 24-hour activity test. With respect to this last result, five of the ten KO MGH males tested belonged to the same litter, which contained no WT males. Those 5 littermates were tested on the same day, so the possibility of the difference being due to a timing error in the switching of the lights was considered. However, analysis performed after the removal of those mice from the experiment did not alter the tendency, even though, with only 5 animals, statistical significance was not achieved. These results could indicate an alteration in the circadian rhythms of the *Pcdh19*-KO male mice; however, the apparatus used was more oriented to detect general locomotor activity than circadian rhythms. Specific tests for circadian rhythms, such as wheel runners or infrared thermal sensors, could be used to validate these results. Wheel runners have been widely used to study circadian rhythms (Wisor et al. 2007; P. Jiang et al. 2012; Y. Xu et al. 2005), this analysis has less 'noise' during the rest phase (light period) than other tests, facilitating the determination of the onset of activity during the dark period, even though the bias generated due to the 'willingness' of the mice to run the wheel needs to be taken into account (Eckel-Mahan et al. 2015). Both characteristics would be useful to validate the significant increase in the number of beam breaks observed during the light phase and the shift in the increase of activity at the start of the dark period respectively. The infrared thermal sensors, as the one used by Ono, Honma and Honma, detect changes in thermal radiation of the animal due to movement, and the amount of movement can be recorded every minute (Ono et al. 2016), making the readings much more accurate than the infrared laser beams. The

detectors might perceive more 'noise' during the rest phase but eliminate the bias the wheel runner experiments possess (Eckel-Mahan et al. 2015).

The circadian clock in mammals is located in the hypothalamic suprachiasmatic nuclei (SCN) and controlled by extrinsic and intrinsic neurotransmitters (Reghunandanan et al. 2006). The function of the circadian clock is very complex, thus further experiments would need to be conducted to determine the molecular mechanisms behind this delay if it is confirmed to be due to alterations in the circadian rhythm.

In 2017, Hayashi *et al.* also conducted a behavioural study in *Pcdh19*-mutant animals (Hayashi et al. 2017). Those mice have a C57Bl6/J, CBA/J and CFW background, unlike the mice studied in this chapter, which are 129/SvEv-C57/BL6 and experiments were not performed in mice younger than 10 weeks of age. Also, the comparisons were done without taking into account the housing effect and using the WT MGH animals as a control.

The Taconic *Pcdh19*-KO studied in this chapter did not show any significant differences in the open field analysis, the time spent in the open arms of the EPM or in the social interaction with another mouse in a novel environment, which agrees with what Hayashi *et al.* reported in those behavioural tests.

Interestingly, human males that lack the *Pcdh19* gene are mostly phenotypically normal (Scheffer et al. 2008), which seem to correlate with the result obtained in this analysis.

6.4.4 Behavioural differences in the HET MGH females

P21 HET MGH females presented a significantly higher total distance run in the open field test, which when divided into 5-min slots revealed to be significantly higher in the 5-slot and still high at 10- and 15-min. In addition, a significant increase in the number of beam breaks at one of the hour slots during the light period in the 24-hour activity analysis was detected, as well as a significant increase in the time spent in the open arms of the EPM with respect to the WT animals. The results obtained could be due to several causes: hyperactivity, a decrease in anxiety or a higher exploratory behaviour.

Hyperactivity would increase the distance run by the animals and also correlate to spending more time in the open arms of the EPM, but results of the 24-hour activity test suggested that the HET MGH mice were not hyperactive since the total number of beam breaks within 24-hours was not significantly higher in the mutants than in the WT animals. Even though the EPM result could be explained by a decrease in fear response (anxiety), that would not explain why there is an increase of activity in the first 5 min in the open field arena, but not an increase in the total activity within 20 min. Thus, the results obtained in the open field, EPM and 24-hour activity were more consistent with the HET MGH presenting a higher exploratory behaviour caused by a hypersensitivity to novel environments. This hypersensitivity could possibly be due to higher levels of stress or anxiety caused by the environment being novel, or by an inability to recognise a familiar territory. In case of the HET MGH females, the thigmotaxis analysis revealed that P21 HET MGH female tended to spend more time in the centre compared to the WT animals, which implied the mutant animals were less anxious than their WT counterparts. This result strongly suggested the HET MGH females present a higher exploratory behaviour that might be due to an inability to recognise the familiar territory, leading them to explore it as if it was a novel environment. The fact that the activity increase in the 5-

min slot in the mutant animals was also present in at P60 also supports this hypothesis.

Potential cognitive deficits in HET MGH animals, leading to an inability to remember known environments could correlate with the human phenotype, since a high percentage of affected patients present cognitive impairments that persist into adulthood (Scheffer et al. 2008). Also, in the model studied by Hayashi *et al.*, the HET MGH females showed a lower fear response after fear-conditioning tests (Hayashi et al. 2017), which could be a sign of memory deficits.

However, further experiments should be performed to validate this hypothesis, such as T-maze tests or cue discrimination experiments. The T-maze experiment is one of the most common tests used to analyse spatial working memory and one of the less stressful ones. The maze is comprised of three arms that are positioned forming a T-shape. If rodents are placed in the arm that is the base of the T and let them explore one of the other arms, they will switch arms if two consecutive trials are conducted, a phenomenon called 'spontaneous alternation', and is reinforced by mildly depriving the animal of food and rewarding it with a the food if it alternates (Hussein et al. 2018). Mice with memory defects have an impaired spontaneous alternation. Cue discrimination experiments is another test that analyses cognitive function. Animals are placed in a special cage (IntelliCage) that contains cues that can be positive (gain access to water) or negative (an air-puff punishment) and can be accessed by nose poking. The animal has to discriminate between them to be able to drink. Mice with deficits in memory will make more errors when trying to discriminate between the cues. The cage allows a wide range of conditioning experiments that can study spatial referential memory, spatial working memory, passive avoidance and non-spatial alternation (Voikar et al. 2018).

As mentioned previously, *Pcdh19*-HET mice also present a high exploratory behaviour in the open arms of the EPM, which does not correspond to an

inability to recognise a familiar environment. In this case, the exploratory behaviour could be caused by a hypersensitivity to the new environment, both phenotypes would be present in the *Pcdh19*-HET animals.

The study of 24-hour activity experiments revealed an increase in the HET MGH activity at one of the hours during the light period, but the overall locomotion over 24-hours wasn't altered, questioning the relevance of this statistically significant result.

There were no differences between the HET MGH females studied in this chapter and the model from Hayashi *et al.* in any of the parameters. The significant differences in the time spent in the open arms of the EPM and the increment of total activity in the open-field arena were observed at P21 and had disappeared by P60, which is the age closer to the mice studied by Hayashi *et al.* No differences in the social interaction with another mouse in a novel environment at P60 were observed in the analysis conducted in this chapter or in the results of Hayashi *et al.* either.

The only difference detected in P60 females in this analysis was an increase in the total distance run in the 5-min slot of the open field test between the HET MGH mice and the WT SGH female. However, as mentioned in **section 6.4.3**, Hayashi *et al.* used the WT MGH animals as a control. Since there was no difference between the HET MGH and the WT MGH female, which would correspond to the animals studied in Hayashi *et al.*, no differences between both models of *Pcdh19*-HET mice were observed (Hayashi *et al.* 2017). Hayashi *et al.* did report behavioural disturbances under stress conditions, hyperactivity at 34-weeks and a lower contextual and cue responses to fear in the *Pcdh19*-HET compared to the WT, but these behavioural tests were not conducted for this thesis (Hayashi *et al.* 2017).

Interestingly, both WT MGH and HET MGH female littermates appear to present a higher exploratory behaviour in the open field arena. However, HET MGH females spend a significant more time in the open arms of the

EPM and a tendency to a decreased thigmotaxis at P21, a phenotype that corresponds with lower anxiety, while WT MGH analysis present a significantly higher thigmotaxis at P60 in the open field arena, which is an anxiety-related behaviour.

6.4.5 Effects of housing (SGH vs MGH)

In both males and females, there were differences between the WT SGH and the WT MGH animals.

P21 WT MGH males presented a significant increase in the total distance run in the 5-min slot leading to an increase in the total activity that was not significant, and failures in habituation between trials in the open field analysis with respect to the WT SGH. The social interaction was also decreased in the WT MGH compared to the WT SGH males at P21. The phenotypes from the open field and EPM experiments were not present at P60. Social interaction was not studied in P60 males, as explained in **section 6.3.4**.

WT MGH females showed an increase in the total activity that was significant, a significant increase in the total distance run in the 5-min slot and a failure in habituation between trials in the open field analysis at P21 with respect to the WT SGH females. The significant increase in the ambulation of the mice in the 5-min slot is still present at P60, together with an increase in thigmotaxis. P60 females also habituate between trials, unlike the SGH female mice. In the 24-hour activity, there was an increase in activity in one of the hours of the dark period in the WT MGH female mice with respect to the other conditions too.

The open field analysis results suggest both WT MGH males and females could be failing to recognise the territory as familiar, hence the lack of habituation and the increased exploration in the second trial. The decreased time spent in the open arms in the EPM in WT MGH males at P21 could be due to higher levels of anxiety and these animals also seem to present

deficits in social interaction. Taking into account all the data from the 24-hour activity analysis, the increase in activity in one of the hours of the dark period in the WT MGH female mice does not seem relevant.

The differences in behaviour between WT SGH and WT MGH mice were noticeable but surprising, since those animals were the same genotype, sex, age, strain, and were housed in the same animal room, so environmental conditions were very similar.

One possibility is that these differences are due to the different genotype of the mother, since WT SGH animals come from a WT mother, while WT MGH animals come from a *Pcdh19*-HET mother. Tests like pup retrieval could be performed in the future with the WT and *Pcdh19*-HET mothers to assess the possibility that impaired maternal behaviour could be influencing the pups.

Another possibility is the housing condition. WT MGH animals are housed with their mutant littermates, and the presence of the HET and KO animals could be affecting their WT littermates.

In fact, Kalbassi *et al.* reported differences between WT SGH and WT MGH mice from litters with Neuroligin 3 (*Nlg3*)-HET and KO animals in social behaviour, and that WT MGH have an increased anxiety with respect to the WT SGH animals. Experiments like ultrasonic vocalisation and tube test could be performed to demonstrate if, as revealed by Kalbassi *et al.* in the *Nlg3* model mouse, litters with WT and mutant pups do not develop a clear social hierarchy, which causes the phenotypes observed in the WT MGH mice (Kalbassi *et al.* 2017).

It is also interesting to notice that in Kalbassi's work, like in this chapter's results, one of the sexes presented more differences between single and mixed housed WT animals (Kalbassi *et al.* 2017). In both studies, this is the case for the sex most affected by the illness (females for *Pcdh19*, males for *Nlg3*, which is also an X-linked gene). This could imply that the housing

effect is more severe in the gender most affected by the mutations in the gene.

Since most of the differences are evident at P21 but disappear by P60, it is also possible that the only pups influencing the WT MGH are the HET MGH, which would explain the maintenance of some of the phenotypes in P60 WT MGH females, who are still housed together as adults. To test this hypothesis, WT MGH and HET MGH females could be separated into different cages when weaned, and their behaviours analysed at P60. The disappearance of the phenotypes at P60 would support this theory.

6.4.6 Conclusion

To sum up, the behavioural analysis conducted in this chapter revealed behavioural disturbances in the *Pcdh19*-mutant mice compared to the WT, that were minor in the *Pcdh19*-KO and more severe in the *Pcdh19*-HET. The behavioural abnormalities suggest there might be some differences in the circuitry. Interestingly, the fact that *Pcdh19*-HET females present more behavioural differences than *Pcdh19*-KO males correlates with what is seen in humans. Further experiments would be needed to understand the pathological mechanisms causing the phenotypes. The effect of housing was also an interesting discovery and brought up the possibility that the mutant mice could also be influenced by their WT littermates. More experiments would need to be conducted to explore this hypothesis.

Chapter 7: General discussion.

The results obtained in this thesis show that PCDH19 depletion or mosaicism cause an effect in neuronal migration, but cortical lamination remains mostly unaffected. *Pcdh19*-mutant animals also present some behavioural disturbances with respect to their WT counterparts.

7.1 Summary of results

In situ hybridization experiments revealed a specific spatio-temporal expression pattern of *Pcdh19* mRNA in the mouse developing cortex. *Pcdh19* was expressed throughout the cortical plate at E16.5, when neurons are migrating to reach their position in the cortex, suggesting the protein might have a role in the cortical migration of glutamatergic neurons. Because *Pcdh19* was expressed in layers II/III and V by P10, the involvement of this protein in migration was analysed by *in utero* electroporation at E13.5 and E15.5. Interestingly, it was found that although *Pcdh19* knockdown via shRNAs did not alter migration at E13.5, neurons electroporated with EGFP in *Pcdh19*-KO animals settled in lower positions than in WT counterparts. The results of the shRNA electroporations at E15.5 were considered unreliable due to the unusual migration of WT cells electroporated with control plasmid. Nevertheless, cells in *Pcdh19*-KO animals were located higher within the cortical plate compared to their WT littermates. No significant differences were found in *Pcdh19*-HET mice, although neurons were positioned slightly lower with respect to the WTs.

As detailed in **section 4.4.4.3**, these results could imply that *Pcdh19* has a role in neuronal migration. *Pcdh19* could be participating in several of the phases of radial migration, and that could explain why cells are positioned deeper or higher than in WT brains when electroporated at E13.5 and E15.5, respectively. However, *in utero* electroporations with EGFP to analyse deep-layer neurons also label a percentage of upper-layer neurons, so it is

possible the cells positioned lower within the cortical plate at E13.5 are cells that migrate to the upper-layers.

Another explanation for the opposing results found in the E18.5 and P10 analysis is that a compensatory mechanism exerted by a related gene in response to the lack of *Pcdh19* ends up overcompensating and producing a phenotype at P10 (El-Brolosy et al. 2017; Holschneider et al. 2001).

Regarding *Pcdh19*-HET animals, the migration at E13.5 was not affected, or the mice presented a very subtle disruption that was undetectable when the lower layer cells' analysis was conducted. Interestingly, some of the GFP-labelled cells of the *Pcdh19*-HET mice at P10 were located into slightly lower positions than their WT littermates, even though the differences were not significant. This defect is the opposite of that seen in *Pcdh19*-KO animals, which could imply that the mixture of WT and *Pcdh19*-KO cells within the *Pcdh19*-HET is affecting the function of *Pcdh19* in the cortical migration. This phenomenon is called cellular interference and has been proposed to be the cause of the unusual inheritance of EIEE9.

Analysis of cortical lamination in the SSC by IHC revealed no alterations in cell number of the subpopulations of cells studied, and only minor differences in distribution between mutant and WT mice. The markers analysed corresponded to the markers that coexpressed *Pcdh19* in the cell-type characterisation performed in chapter 3.

The initial characterisation of *Pcdh19*-expressing cells represents the first detailed characterisation of the cell-types expressing *Pcdh19*. Several markers, including some that were not characteristic of layers II/III and V were used, since *Pcdh19*⁺ cells are positioned in all layers, albeit most of the expression is located in layers II/III and V.

The results revealed that *Pcdh19* colocalised partially with all of the markers used, both excitatory and inhibitory. Therefore, several subgroups of excitatory and inhibitory neurons were included in the lamination study.

The analysis detected no differences among the genotypes in the total number or distribution of DAPI+ cells or in cortical width. WT, *Pcdh19*-HET and *Pcdh19*-KO animals presented similar number and distribution of cells expressing glutamatergic neuronal markers SATB2, CTIP2, RORB and inhibitory neuronal markers PV, CR and SST. Some slight but significant differences were found in the distribution of CUX1-, TBR1- and CB- positive cells between *Pcdh19*-HET and *Pcdh19*-KO in the analysis of TBR1 and CB, and between WT and *Pcdh19*-KO in the study of CUX1. As discussed in **section 5.4**, the number or distribution of other subpopulations of cells that were not analysed in this study could be disrupted in the mutant. Also, even though subtle, these differences, if relevant, could be altering the cortical circuitry of the mouse and point to the possibility of alterations in other brain regions. Abnormal connexions between neurons could have an impact on mouse behaviour.

Indeed, *Pcdh19*-KO male mice showed an increase in the total number of beam breaks during the light period and a delay in the increase of activity at the start of the dark period with respect to the WT mice in the 24 h. activity test, which could imply a possible disturbance of circadian rhythms. *Pcdh19*-HET females also presented some differences in their behaviour with respect to WT mice, their phenotype more severe than in *Pcdh19*-KO males. At P21, a higher total distance run and an increase in ambulation within the first 5 minutes in the open field arena could be detected, together with an increase of time spent in the open arms in the EPM study. The increase of activity in the 5-min slot of the open field was maintained over time, being also present at P60, alongside with an increase in ambulation in one of the hours during the dark period (of questionable relevance). These results signal an increase in the exploratory behaviour of the *Pcdh19*-HET females, that as detailed in **section 6.4.4**, could be caused by a high reactivity of these mice to novel environments and the inability to recognise a familiar territory, even though further studies would be needed to substantiate these theories.

In summary, *Pcdh19*-KO animals present some abnormalities in radial migration of glutamatergic neurons, but only subtle differences in cortical lamination. These mice also show behavioural disturbances, that are more severe in *Pcdh19*-HET females than in *Pcdh19*-KO males, and which may correlate with disruptions in brain circuitry. As explained in the introduction, *Pcdh19* is strongly detected in the cortex, hippocampus, cerebellum (Dibbens et al. 2008; Pederick et al. 2016), amygdala, and hypothalamus (Kim et al. 2007) of the adult rodent, therefore the alterations in the circuitry may not be cortical. Further experiments would need to be conducted to determine the molecular mechanisms behind the alterations in migration and the behavioural abnormalities.

During the behavioural study, another intriguing discovery was made. WT animals from litters including mutant mice animals (WT MGH) presented differences in their behaviour with respect to WT animals from litters of just WT mice (WT SGH), as had been observed by Kalbassi *et al.* (Kalbassi et al. 2017). At P21, the analysis of WT MGH males showed a failure in the adaptation between trials and an increase in the activity of the first 5 mins in the open field, coupled with a lower time spent interacting with a foreign adult female compared to WT SGH males. Regarding the females, P21 WT MGH mice presented a failure in habituation between trials, a higher total distance run and an increased ambulation during the first 5-min of the open field test with respect to P21 WT SGH females. The higher distance run in the 5-min slot was also detected at P60, accompanied by an increase in the thigmotaxis compared to the WT SGH mice. WT MGH females also adapted between trials, unlike the WT SGH females. A significant increase in activity at one of the hours of the dark period was also detected in the MGH females with respect to the WT SGH peers in the 24-hour activity experiments, although the relevance of this observation is questionable. With respect to the differences between WT MGH and HET MGH female littermates, both seem to present a higher exploratory behaviour in the open field arena. However, HET MGH females present a phenotype

corresponding with lower anxiety (significant more time spent in the open arms and a tendency to lower thigmotaxis at P21) while WT MGH analysis did reveal an increase in the thigmotaxis at P60 in the open field arena, which is an anxiety-related behaviour.

In any case, the differences between WT SGH and WT MGH animals strongly suggest that the presence of mutant animals within the cage, and/or the parenting by a *Pcdh19*-HET mother is influencing the behaviour of the WT pups, and some of the behaviour is maintained in WT MGH female adults, as detailed in **section 6.4.5**. All in all, these results, together with those of Kalbassi *et al.*, highlight the complexity and potential difficulties of choosing the appropriate controls in behavioural studies. Considering that both genes are X-linked, experiments to determine if this effect of housing is present in all mutant mice, or only in those with mutations in the X-chromosome would be important to conduct.

The following sections will discuss the results of this work in the wider *Pcdh19* context, the advantages and disadvantages of the mouse model to study EIEE9 and potential future developments of this project to elucidate the role of *Pcdh19* in cortical development.

7.2 Interpretation of the results in the general context of *Pcdh19*

In vitro and *in vivo* studies conducted mainly in mouse models have begun to decipher the role of *Pcdh19* in mammalian cortical development. *In vitro* analysis have suggested roles of *Pcdh19* in neurogenesis, differentiation and maturation of neurons and cortical migration (Pederick *et al.* 2016; Homan *et al.* 2018). *In vivo* studies have shown that alterations in the levels of PCDH19 promote neurogenesis and alter the surface levels of GABA-A receptor, which strongly suggests a participation in GABAergic signalling (Fujitani *et al.* 2017; Gerosa *et al.* 2019). Cortical malformations detected in humans with EIEE9 confirm the role of *Pcdh19* in cortical development

(Pederick et al. 2018). The disruptions in cortical development translate into behavioural disturbances that can be maintained into adulthood in both human (Dibbens et al. 2008) and mice (Hayashi et al. 2017).

In this work, the results provide an insight into the cell types that co-express *Pcdh19* in young mice, into the possible roles of *Pcdh19* in cortical migration and lamination, and a behavioural characterisation of the Taconic mouse model.

Regarding the characterisation of *Pcdh19*-expressing cells, it has to be considered that the great variety of neuronal and non-neuronal subtypes within the cortex makes the full characterisation of all the subpopulations using the ISH-IHC technique almost unachievable. However, it was still revealed that *Pcdh19*⁺ was partially coexpressed in a varied range of glutamatergic and GABAergic interneurons, which supports a role in a mechanism mediated by the cell adhesive properties of *Pcdh19*. The differences detected in migration were minor in the *Pcdh19*-KO and not significant in the *Pcdh19*-HET, implying migration is not the main mechanism *Pcdh19* exerts its main role in. Nonetheless, the slightly increased migration of *Pcdh19*-KO electroporated neurons *in vivo* is in agreement with the observed increase in the distance migrated by *Pcdh19*-KO neurons *in vitro* (Pederick *et al.*, 2016), suggesting an involvement of PCDH19 in this process. As expected from the migration results, no dramatic abnormalities were observed in the cortical lamination of *Pcdh19*-mutant brains either. However, both *Pcdh19*-HET and *Pcdh19*-KO mutants presented an altered behavioural phenotype as explained in chapter 6. Disruptions in behaviour are related to aberrant network activity, that has been reported in *Pcdh19*-HET mice by Pederick *et al.* (Pederick et al. 2018). Unpublished data generated by Dr. Jessica Griffiths also revealed that *Pcdh19*-KO neurons presented a decrease in KCl-evoked calcium response with respect to WT cells *in vitro* and that WT cells co-cultured with *Pcdh19*-KO neurons showed that same reduction, which would be consistent with

disrupted neuronal activity. All these results substantiate the hypothesis that *Pcdh19* might be involved in the neuronal circuit formation. Indeed, PCDH19 can be detected in the spines of cortical neurons (Hayashi et al. 2017) which supports this hypothesis. As explained in chapter 3, the fact that *Pcdh19* is mainly expressed in layers II/III and V (Sabri et al. 2018; Schubert et al. 2006), which are connected to each other as part of the basic cortical circuit, reinforces this thesis. If *Pcdh19* participated in the development of brain circuits, the 'cellular interference' (Dibbens et al. 2008) caused by the presence of PCDH19+ and PCDH19- mixture of cells in mosaic females could alter the neuronal connectivity and be the cause of EIEE9. This disruption in the cell-cell interaction of WT and *Pcdh19*-KO cells that alters synaptic transmission could be due to the change in cell adhesive properties cells experience depending on their combinatorial expression of protocadherins (Bisogni et al. 2018). This disruption in cell adhesion is the presumed cause of the cell sorting between both cell types, that results in an abnormal patterning of the cortex with WT and *Pcdh19*-KO cells segregated into columns (Pederick et al. 2018). The synaptic transmission would likely be altered due to this failure in cell-cell interaction and the segregation of both populations. Therefore, it would be important to focus on this process when conducting future experiments aimed to discern the role of *Pcdh19* in cortical development.

7.3 The mouse as a model for the study of EIEE9

As detailed in **section 1.5**, patients affected with EIEE9 develop seizures in infancy or early childhood that occur in clusters, usually accompanied by language delays, intellectual disability and behavioural disorders (Duszyc et al. 2014). Regarding cortical migration and lamination, some areas of cortical dysplasia were detected in one patient from Ryan *et al.* and in all five EIEE9 patients studied in the Kurian *et al.* paper (Ryan et al. 1997; Kurian et al. 2018).

However, no cortical disorganisation was observable in the mouse models studied (Pederick et al. 2016; Hayashi et al. 2017) and only very minor differences in the distribution of particular cell subgroups were detected in chapter 5. Even though mice are the most common animal model in the study of cortical development, some differences exist between both species. Rodents are lissencephalic, while humans are gyrencephalic (Gertz et al. 2015). This difference in brain architecture reflects variability in the cortical development of mice and human, like an expanded VZ and SVZ, and a difference in the size between the pial and ventricular surfaces, due to an increase in the number of cortical neurons in the pial one. These contrast in size between both surfaces leads to the formation of the folds. The increase in the number of basal radial glial cells (bRGCs) in the folded cortex is considered essential in the cortical expansion and folding, and represents another considerable difference between lissencephalic and gyrencephalic species (Fernández et al. 2016). The folding is also related to variability in the amplification of IPs (Lamonica et al. 2013), and amplification, production and diversity of neurons and glia (Borrell et al. 2014; Sun et al. 2014).

All of these differences between mouse and human can lead to different effects in cortical development when the same protein is mutated in both species. Mutations in *Tuba1*, which produce slightly abnormal migration in mice but lissencephaly in humans (Keays et al. 2007), or *Nde1*, whose knockout in mouse presents a reduced cerebral cortex and a lissencephalic brains in humans (Y. Feng et al. 2004) could be examples of this phenomenon.

Thus, the reports that some EIEE9 patients present disruptions in cortical sulcation (Pederick et al. 2018), that cannot be mimicked in mouse, support the idea that species like the mouse cannot accurately reproduce what is observed in the EIEE9 patients. Further experiments using a gyrencephalic animal model, such as the ferret, might be needed to fully understand the

role of *Pcdh19* in cortical development (Gertz et al. 2015; Fernández et al. 2016). To be able to analyse cortical development in the ferret, *Pcdh19*-mutant animals would need to be generated, for example by using CRISPR-Cas9 technology (Kou et al. 2015).

No epileptic episodes have been detected in the two published mouse models of *Pcdh19* either (Pederick et al. 2016; Hayashi et al. 2017). However, this is not uncommon, since spontaneous recurrent seizures in mice can be rare and unpredictable. They may vary depending on the genetic background of particular mouse strains and present with very little change in behaviour, making their characterisation just by observation very challenging (Yang et al. 2004; Gu et al. 2017). Moreover, not all mouse models can recapitulate the epileptic symptoms of the human disease, as exemplified by some mouse models for Dravet syndrome, whose spontaneous seizures strongly depend on the background strain of the mouse used (Griffin et al. 2018). Consequently, distinguishing if the mouse model lacks seizure activity or is simply very difficult to observe can be a hard task. Nevertheless, rodents tend to be excellent models for epilepsy since many of the characteristics of seizures and most of the ways of inducing them are common between both species. Even if spontaneous seizures are not present, seizures can be induced in animal models by electroconvulsive currents, chemoconvulsants or loud acoustic stimuli, and the seizure threshold can be compared between mutant and WT animals (Yang et al. 2004). Detection of spontaneous seizures can also be conducted by electroencephalography, in which the brain wave patterns of the mice are constantly recorded by electrodes placed intracranially while they are freely roaming in the cage (Gu et al. 2017). In fact, intracranial electroencephalographic recordings conducted by Pederick *et al.* in a *Pcdh19*-mutant model revealed an unusual network activity in *Pcdh19*-HET animals with respect to the WT or *Pcdh19*-KO mice (Pederick et al. 2018). Despite not being an epileptic seizure, altered neuronal connectivity that is only present in *Pcdh19*-HET mice does correlate with EIEE9, where mosaic

females are affected and males that lack PCDH19 are spared. In addition, in an experiment of pharmacologically induced seizures, Bassani *et al.* reported a reduced time latency to the first generalised tonic-clonic seizure in P7 rat pups electroporated in the hippocampus with shRNA against *Pcdh19* and treated with pentylenetetrazol (Bassani *et al.*, 2018).

With respect to the behavioural characterisation, mice are good models to study diseases with behavioural disturbances due to shared brain functions and emotional responses (Van Meer *et al.* 2005), as explained in **section 6.1**. However, mice can also present phenotypes that in some behavioural tests could cause artefacts and lead to a misinterpretation of the results, such as olfactory deficits in mice reducing social interaction, which needs to be considered. Some human phenotypes cannot be mimicked by mouse models either, so mouse models generally partially recapitulate the human behaviour (Silverman *et al.* 2010).

Pcdh19-mutant mouse models present altered behaviours, as reported by Hayashi *et al.* (Hayashi *et al.* 2017) and the results shown in this thesis. In these models, both *Pcdh19*-HET and *Pcdh19*-KO animals showed unusual behavioural responses, but the phenotype was more severe in *Pcdh19*-HET females, which partially correlates with the observations in EIEE9 patients. However, the fact that *Pcdh19*-KO males are affected implies that, in mouse, the loss of *Pcdh19* produces behavioural disturbances, which does not completely correlate with EIEE9, where only minor symptoms are observed (Dibbens *et al.* 2008; Scheffer *et al.* 2008). Further experiments to characterise homozygous *Pcdh19*-KO females could be conducted to distinguish which behavioural anomalies are due to the loss of protein and which to the mosaicism. The behavioural analysis conducted in chapter 6 also detected that the behaviour of WT animals is probably influenced by the presence of mutant littermates, as detailed in **section 6.4.5**. This result leads to the question of whether the mutant animals' behaviour was also influenced by their WT littermates. Therefore, a behavioural characterisation of *Pcdh19*-

mutant animals from *Pcdh19*-mutant litters would pose an interesting experiment to conduct in the future.

In summary, the mouse model appears to be good to recapitulate the behavioural phenotype of EIEE9, but migration and cortical lamination studies would probably benefit from a gyrencephalic species, such as the ferret, to have a better phenotypic correlation and complete understanding of the molecular mechanisms behind the illness.

7.4 Future directions

As explained in **section 7.2**, the characterisation of all of the *Pcdh19*-expressing cell-types is unattainable by ISH-IHC and cortical lamination did only present minor differences between mutants and WT animals. Thus, further extension of those studies would be indicated only if other experiments suggested the mutation of *Pcdh19* affects a concrete population of neurons. Should that be the case, other approaches to detect PCDH19 expression or the use of recently developed tools could aid understand fully the cell types of *Pcdh19*-expressing cells that populate the cortical plate.

For example, the generation of a mouse model that facilitated protein detection at cellular level would be an option in the performance of these studies. However, the creation of mouse lines is not an easy task. The generation of a PCDH19-IRES-DDCre mouse model, that would allow selective labelling of PCDH19+ cells at specific time-points, was attempted by PhD student Sylvia Newbold (Cardiff University). In this model, the delivery of trimethoprim helps to maintain the destabilised Cre (DDCre) expression, which can then recombine a reporter allele that has been crossed into the strain (Sando et al. 2013). Unfortunately, the DD-Cre targeted cells necessary to conduct the blastocyst injection did not express PCDH19 nor CRE after the nucleofection, so the experiment could not be continued. Although generation of mouse models is expensive and can be difficult, the creation of a nuclear EGFP PCDH19 reporter mouse that detected PCDH19 expression in individual cells would pose a great advantage towards the characterisation of the cell-types that express the protein.

Another recently developed tool that could be used and has implied a great advancement in the study of cortical cell types, as mentioned in **section 3.4.4**, is single cell RNA-sequencing. This technique has allowed the identification of several glutamatergic, GABAergic and non-neuronal cell subtypes within the cortex and hippocampus of young postnatal and adult

mice. The different subclasses contain already known markers but also new ones, and this type of analysis could potentially identify all the cell subgroups within the cortex. The analysis also shows differences in the cellular composition between the cortex and the hippocampus, and the common and unique groups among different areas within the cortex, such as motor and visual (Zeisel et al. 2015; Tasic et al. 2018; 2016). Analysis by single cell RNA-sequencing of the *Pcdh19*-expressing cells was considered an important experiment to identify all the cell-types that express PCDH19. In fact, a reanalysis of the data set obtained by Tasic *et al.* in 2016 (Tasic et al. 2016) to determine PCDH19 levels in the cell clusters, conducted by PhD student Sylvia Newbold, revealed that PCDH19 was expressed in different subtypes of glutamatergic and GABAergic neurons, which is in accordance with the results obtained in Chapter 3. Specifically, PCDH19 is coexpressed in cells positive for SATB2, CUX1, CR, SST, CB and PV, but not in RORB or TBR1; which is very similar to the data revealed by the ISH-IHC analysis from Chapter 3. *Pcdh19* was partially coexpressed in RORB+ and TBR1+ cells in P10 animals but the single cell RNA-sequencing was conducted in adult animals and in a different area of the cortex (visual vs SSC), which could explain the differences. Reanalysis of other datasets that focus in the cortex of younger animals could be conducted to characterise cell-type PCDH19-expression in the developing mouse.

The characterisation of *Pcdh19*+ astrocytes and oligodendrocytes, that have been shown to express *Pcdh19* at P7 and P17 in mice, respectively (Y. Zhang et al. 2014), would be important, too. This study would be a first step to explore the participation of *Pcdh19* into the development of glial cells. The characterisation of the glial cells could be conducted using antibodies against aquaporin 4 or glial fibrillary acidic protein for astrocytes, and Olig 2 and opalin for oligodendrocytes (precursor and mature cells respectively) (Yokoo et al. 2004; Tasic et al. 2018). To conduct a better analysis of the *Pcdh19*+ cells, the development of a PCDH19-nGFP mouse reporter, as described in **section 3.4.2** would be extremely useful.

Only minor differences were detected in cortical migration between *Pcdh19*-KO and WT mice, with no significant defects in *Pcdh19*-HET animals. In conclusion, *Pcdh19* doesn't seem to be exerting a very important role in this process, so any further analysis into this process would not be a priority.

However, Dr. Jessica Griffiths (Cardiff University) made a very interesting observation during her thesis. She found out that *Pcdh19*-KO and WT RG progenitors differ in their neurogenic behaviour in *Pcdh19*-HET animals. This difference, which does not lead to overall changes in the heterozygous cortex as a whole, is also not present between RGCs in *Pcdh19*-KO and WT animals.

Consequently, another important aspect to ascertain would be if WT and *Pcdh19*-KO cells in the *Pcdh19*-HET brains present different migratory behaviours or acquire distinct laminar positions from each other and in comparison, to their WT counterparts. The generation of an XGFP/*Pcdh19*-HET mouse model that permits the identification of WT and *Pcdh19*-KO cells, as described in **section 4.4.4.4**, would provide an excellent tool for the study of cell migration and cortical lamination in *Pcdh19*-HET animals.

Moreover, since *Pcdh19* is known to be expressed in the ganglionic eminences during the generation of interneurons, and *Pcdh19* is partially co-expressed with several subsets of interneurons, the analysis of tangential migration would also be interesting. Such an analysis could be conducted by IUE of EGFP into the GE of WT and *Pcdh19*-mutant animals at the different ages interneurons are generated, followed by an analysis of the distribution of EGFP+ cells at P20. In fact, the XGFP/*Pcdh19*-HET animal described above would also allow a very interesting study to determine if WT and *Pcdh19*-KO interneurons show any preference for WT and *Pcdh19*-KO columns in the heterozygous cortex.

The behavioural analysis revealed differences between the mutant and WT animals. Thus, experiments to further characterise the behaviour of the

mutant animals and investigate the causes underlying the behavioural disturbances should be conducted. As detailed in **section 6.4**, the possible alteration of the circadian rhythms in *Pcdh19*-KO mouse could be confirmed using behavioural tests more oriented to the study of this parameter, such as wheel runners or infrared thermal sensors. The possible inability to recognise new territory detected in the *Pcdh19*-HET could be further explored by using T-maze tests or cue discrimination experiments that would determine if the animals present cognitive deficits with respect to the WT (Hussein et al. 2018; Voikar et al. 2018).

The effects of housing seen in WT, where WT MGH mice showed different responses to the SGH animals raised the question whether the *Pcdh19*-mutant animals could be getting influenced by the WTs too, thus performing the behavioural tests in *Pcdh19*-mutant animals that come from pure mutant litters would be important too.

As mentioned in **section 7.2**, *Pcdh19* might be involved in the neuronal circuit formation. Therefore, further experiments should be conducted to explore this hypothesis. First, the connectivity between WT and *Pcdh19*-KO cells could be studied *in vitro*. A cell line generated by Garcia *et al.* containing a TdTomato, the Rabies G glycoprotein and the avian TVA receptor, called ROSA26-tomRITVA could be used for these experiments (Garcia et al. 2012). The embryonic stem cells from this line could be differentiated into neurons and get mixed with *Pcdh19*-KO cells. The ROSA26-tomRITVA can be distinguished from the *Pcdh19*-KO due to its red fluorescence. Cells would then get infected with the EnvA-pseudotyped G-deleted EGFP rabies virus (SADDG-EGFP RV). This virus can only infect ROSA26-tomRITVA neurons that express the TVA receptor, but not the *Pcdh19*-KO neurons, which do not. However, the virus performs one presynaptic jump, so any neurons connected to an infected cell become green. A comparison between the number of presynaptic neurons between

ROSA26-tomRITVA-*Pcdh19*-WT and ROSA26-tomRITVA-*Pcdh19*-KO cultures could indicate whether PCDH19 plays a role in circuit formation.

To conduct the neuronal tracing *in vivo*, a PCDH19-IRES-DdCRE animal as the one mentioned in **section 7.2**, would have to be crossed with a *Pcdh19*-KO animal to generate *Pcdh19*-HET animals. These animals would then be injected with a Cre-dependant AAV virus encoding for the TVA receptor and the G protein, necessary for virus reception and the synaptic jump, respectively, and mCherry to label PCDH19-expressing starting cells. Finally, the animals would be injected with the SADDG-EGFP RV virus. Therefore, the first cells labelled that will be *Pcdh19*⁺ will express red fluorescence, while the presynaptic neurons to the *Pcdh19*-expressing cells would be green. Unfortunately, as previously mentioned, the generation of the DdCre mouse was unsuccessful. Instead of a PCDH19-IRES-DdCre mouse, a conditional *Pcdh19*-CreERT2 could possibly be generated to conduct the experiments.

To determine differences in the electrophysiological and anatomical properties of the synaptic connections of WT and *Pcdh19*-KO cells, the whole-cell patch clamp technique could be conducted in individual cells of WT, *Pcdh19*-KO and mixed cultures (Harrison et al. 2015). In the mixed cultures, WT cells will be fluorescent to distinguish them from *Pcdh19*-KO cells. This technique can also be conducted *in vivo*, so cortical WT cells from WT animals, *Pcdh19*-KO cells from *Pcdh19*-KO animals and WT and *Pcdh19*-KO neurons from *Pcdh19*-HET mice could be analysed by *in vivo* patch clamp too. All the cells will be non-fluorescent except for the WT cells in *Pcdh19*-HET animals, that could come from an XGFP/*Pcdh19*-HET mouse model. For this *in vivo* experiment, it has to be considered that patch-clamping at deep depths, thus the recordings in layer IV, V and VI are more complicated, albeit not impossible.

7.5 Concluding remarks

EIEE9 is a disorder that causes epilepsy in young girls and can be accompanied by a variety of other symptoms, including cognitive impairment of varying severity and behavioural disturbances. It is thought that cellular interference, brought about by the mosaic of *Pcdh19*⁺ and *Pcdh19*⁻ cells is a critical factor in the illness, but the mechanism underpinning EIEE9 remains undiscovered. In this thesis, it is shown that the lack of *Pcdh19* causes small alterations in the positioning of cortical cells, that do not result in blatant alterations of cortical lamination. However, behavioural disturbances are seen in the mutant mice, with *Pcdh19*-HET mice presenting a more severe behavioural phenotype than *Pcdh19*-KO littermates. This suggests that cellular interference is also playing a role in mice and underscores the usefulness of this model system to investigate the pathophysiology of PCDH19 mosaicism. Since migration disturbances and behavioural anomalies are related to disruptions in cortical circuitry, further experimentation in that direction could provide better understanding on the pathological molecular and cellular mechanisms underpinning EIEE9. A better understanding of the pathophysiology of this disorder is the first step towards the development of treatments to improve quality of life for patients and their families.

References

- Aiga, Mytyl, Joshua N. Levinson, and Shernaz X. Bamji. 2011. "N-Cadherin and Neuroligins Cooperate to Regulate Synapse Formation in Hippocampal Cultures." *Journal of Biological Chemistry* 286 (1): 851–58. <https://doi.org/10.1074/jbc.M110.176305>.
- Alcamo, Elizabeth A., Laura Chirivella, Marcel Dautzenberg, Gergana Dobрева, Isabel Fariñas, Rudolf Grosschedl, and Susan K. McConnell. 2008. "Satb2 Regulates Callosal Projection Neuron Identity in the Developing Cerebral Cortex." *Neuron* 57 (3): 364–77. <https://doi.org/10.1016/j.neuron.2007.12.012>.
- Angevine, J. B., and R. L. Sidman. 1961. "Autoradiographic Study of Cell Migration during Histogenesis of Cerebral Cortex in the Mouse." *Nature* 192 (4804): 766–68. <https://doi.org/10.1038/192766b0>.
- Arlotta, Paola, Bradley J. Molyneaux, Jinhui Chen, Jun Inoue, Ryo Kominami, and Jeffrey D. MacKlis. 2005. "Neuronal Subtype-Specific Genes That Control Corticospinal Motor Neuron Development in Vivo." *Neuron* 45 (2): 207–21. <https://doi.org/10.1016/j.neuron.2004.12.036>.
- Avilés, Evelyn C., and Lisa V. Goodrich. 2017. "Configuring a Robust Nervous System with Fat Cadherins." *Seminars in Cell and Developmental Biology*. <https://doi.org/10.1016/j.semcdb.2017.06.001>.
- Badouel, Caroline, Mark A. Zander, Nicole Liscio, Mazdak Bagherie-Lachidan, Richelle Sopko, Etienne Coyaud, Brian Raught, Freda D. Miller, and Helen McNeill. 2015. "Fat1 Interacts with Fat4 to Regulate Neural Tube Closure, Neural Progenitor Proliferation and Apical Constriction during Mouse Brain Development." *Development (Cambridge)* 142 (16): 2781–91. <https://doi.org/10.1242/dev.123539>.
- Barinka, F., and R. Druga. 2010. "Calretinin Expression in the Mammalian Neocortex: A Review." *Physiological Research* 59 (5): 665–77.

- Barondeau, David P., Carey J. Kassmann, John A. Tainer, and Elizabeth D. Getzoff. 2002. "Structural Chemistry of a Green Fluorescent Protein Zn Biosensor." *Journal of the American Chemical Society* 124 (14): 3522–24. <https://doi.org/10.1021/ja0176954>.
- Bassani, Silvia, Andrzej W. Cwetsch, Laura Gerosa, Giulia M. Serratto, Alessandra Folci, Ignacio F. Hall, Michele Mazzanti, Laura Cancedda, and Maria Passafaro. 2018. "The Female Epilepsy Protein PCDH19 Is a New GABAAR-Binding Partner That Regulates GABAergic Transmission as Well as Migration and Morphological Maturation of Hippocampal Neurons." *Human Molecular Genetics*. <https://doi.org/10.1093/hmg/ddy019>.
- Bayer, Shirley A., Joseph Altman, Raymond J. Russo, Xiaofeng Dai, and James A. Simmons. 1991. "Cell Migration in the Rat Embryonic Neocortex." *Journal of Comparative Neurology* 307 (3): 499–516. <https://doi.org/10.1002/cne.903070312>.
- Ben-Ari, Yehezkel. 2015. "Is Birth a Critical Period in the Pathogenesis of Autism Spectrum Disorders?" *Nature Reviews Neuroscience*. <https://doi.org/10.1038/nrn3956>.
- Bisogni, Adam J., Shila Ghazanfar, Eric O. Williams, Heather M. Marsh, Jean Y.H. Yang, and David M. Lin. 2018. "Tuning of Delta-Protocadherin Adhesion through Combinatorial Diversity." *ELife* 7. <https://doi.org/10.7554/eLife.41050>.
- Biswas, Sayantane, Michelle R. Emond, Phan Q. Duy, Le T. Hao, Christine E. Beattie, and James D. Jontes. 2014. "Protocadherin-18b Interacts with Nap1 to Control Motor Axon Growth and Arborization in Zebrafish." *Molecular Biology of the Cell* 25 (5): 633–42. <https://doi.org/10.1091/mbc.E13-08-0475>.
- Biswas, Sayantane, Michelle R. Emond, and James D. Jontes. 2010. "Protocadherin-19 and N-Cadherin Interact to Control Cell Movements during Anterior Neurulation." *Journal of Cell Biology* 191

(5): 1029–41. <https://doi.org/10.1083/jcb.201007008>.

Bononi, Judy, Angela Cole, Paul Tewson, Andrew Schumacher, and Roger Bradley. 2008. "Chicken Protocadherin-1 Functions to Localize Neural Crest Cells to the Dorsal Root Ganglia during PNS Formation." *Mechanisms of Development* 125 (11–12): 1033–47. <https://doi.org/10.1016/j.mod.2008.07.007>.

Borrell, Victor, and Federico Calegari. 2014. "Mechanisms of Brain Evolution: Regulation of Neural Progenitor Cell Diversity and Cell Cycle Length." *Neuroscience Research*. <https://doi.org/10.1016/j.neures.2014.04.004>.

Brasch, Julia, Oliver J. Harrison, Barry Honig, and Lawrence Shapiro. 2012. "Thinking Outside the Cell: How Cadherins Drive Adhesion." *Trends in Cell Biology*. <https://doi.org/10.1016/j.tcb.2012.03.004>.

Briggs, Farran. 2010. "Organizing Principles of Cortical Layer 6." *Frontiers in Neural Circuits* 4 (FEB). <https://doi.org/10.3389/neuro.04.003.2010>.

Britanova, Olga, Camino de Juan Romero, Amanda Cheung, Kenneth Y. Kwan, Manuela Schwark, Andrea Gyorgy, Tanja Vogel, et al. 2008. "Satb2 Is a Postmitotic Determinant for Upper-Layer Neuron Specification in the Neocortex." *Neuron* 57 (3): 378–92. <https://doi.org/10.1016/j.neuron.2007.12.028>.

Brooks, S. P., T. Pask, L. Jones, and S. B. Dunnett. 2004. "Behavioural Profiles of Inbred Mouse Strains Used as Transgenic Backgrounds. I: Motor Tests." *Genes, Brain and Behavior* 3 (4): 206–15. <https://doi.org/10.1111/j.1601-183X.2004.00072.x>.

Bruining, Hilgo, Asuka Matsui, Asami Oguro-Ando, René S. Kahn, Heleen M. Van'T Spijker, Guus Akkermans, Oliver Stiedl, et al. 2015. "Genetic Mapping in Mice Reveals the Involvement of Pcdh9 in Long-Term Social and Object Recognition and Sensorimotor Development." *Biological Psychiatry* 78 (7): 485–95. <https://doi.org/10.1016/j.biopsych.2015.01.017>.

- Bucan, Maja, Brett S. Abrahams, Kai Wang, Joseph T. Glessner, Edward I. Herman, Lisa I. Sonnenblick, Ana I. Alvarez Retuerto, et al. 2009. "Genome-Wide Analyses of Exonic Copy Number Variants in a Family-Based Study Point to Novel Autism Susceptibility Genes." *PLoS Genetics* 5 (6). <https://doi.org/10.1371/journal.pgen.1000536>.
- Bulchand, Sarada, Lakshmi Subramanian, and Shubha Tole. 2003. "Dynamic Spatiotemporal Expression of LIM Genes and Cofactors in the Embryonic and Postnatal Cerebral Cortex." *Developmental Dynamics* 226 (3): 460–69. <https://doi.org/10.1002/dvdy.10235>.
- Cadwell, C.R., Z.H. Tan, and A.S. Tolias. 2018. "Neocortical Layer 4 in Adult Mouse Differs in Major Cell Types and Circuit Organization between Primary Sensory Areas." *BioRxiv*: 507293. <https://doi.org/10.1101/507293>.
- Caligioni, Claudia S. 2009. "Assessing Reproductive Status/Stages in Mice." *Current Protocols in Neuroscience* (SUPPL. 48). <https://doi.org/10.1002/0471142301.nsa04is48>.
- Camacho, Ana, Rogelio Simón, Raúl Sanz, Antonio Viñuela, Antonio Martínez-Salio, and Fernando Mateos. 2012. "Cognitive and Behavioral Profile in Females with Epilepsy with PDCH19 Mutation: Two Novel Mutations and Review of the Literature." *Epilepsy and Behavior* 24 (1): 134–37. <https://doi.org/10.1016/j.yebeh.2012.02.023>.
- Carlos, J. A. De, L. López-Mascaraque, and F. Valverde. 1996. "Dynamics of Cell Migration from the Lateral Ganglionic Eminence in the Rat." *Journal of Neuroscience* 16 (19): 6146–56. <https://doi.org/10.1523/jneurosci.16-19-06146.1996>.
- Cauli, Bruno, Etienne Audinat, Bertrand Lambolez, Maria Cecilia Angulo, Nicole Ropert, Keisuke Tsuzuki, Shaul Hestrin, and Jean Rossier. 1997. "Molecular and Physiological Diversity of Cortical Nonpyramidal Cells." *Journal of Neuroscience* 17 (10): 3894–3906. <https://doi.org/10.1523/jneurosci.17-10-03894.1997>.

- Caviness, Verne S. 1982. "Neocortical Histogenesis in Normal and Reeler Mice: A Developmental Study Based upon [3H]Thymidine Autoradiography." *Developmental Brain Research* 4 (3): 293-302. [https://doi.org/10.1016/0165-3806\(82\)90141-9](https://doi.org/10.1016/0165-3806(82)90141-9).
- Chang, H., N. Hoshina, C. Zhang, Y. Ma, H. Cao, Y. Wang, D. D. Wu, et al. 2018. "The Protocadherin 17 Gene Affects Cognition, Personality, Amygdala Structure and Function, Synapse Development and Risk of Major Mood Disorders." *Molecular Psychiatry* 23 (2): 400-412. <https://doi.org/10.1038/mp.2016.231>.
- Chang, Minzi, and Hideki Derek Kawai. 2018. "A Characterization of Laminar Architecture in Mouse Primary Auditory Cortex." *Brain Structure and Function* 223 (9): 4187-4209. <https://doi.org/10.1007/s00429-018-1744-8>.
- Chatzikonstantinou, Anastasios. 2014. "Epilepsy and the Hippocampus." In *The Hippocampus in Clinical Neuroscience*, 34:121-42. <https://doi.org/10.1159/000356435>.
- Chen, Baoyu, Klaus Brinkmann, Zhucheng Chen, Chi W. Pak, Yuxing Liao, Shuoyong Shi, Lisa Henry, Nick V. Grishin, Sven Bogdan, and Michael K. Rosen. 2014. "The WAVE Regulatory Complex Links Diverse Receptors to the Actin Cytoskeleton." *Cell* 156 (1-2): 195-207. <https://doi.org/10.1016/j.cell.2013.11.048>.
- Chen, Weisheng V., Chiamaka L. Nwakeze, Christine A. Denny, Sean O'Keeffe, Michael A. Rieger, George Mountoufaris, Amy Kirner, et al. 2017. "Pcdhac2 Is Required for Axonal Tiling and Assembly of Serotonergic Circuitries in Mice." *Science* 356 (6336): 406-11. <https://doi.org/10.1126/science.aal3231>.
- Clapcote, Steven J., and John C. Roder. 2005. "Simplex PCR Assay for Sex Determination in Mice." *BioTechniques* 38 (5): 702-6. <https://doi.org/10.2144/05385BM05>.
- Conn, Simon J., Katherine A. Pillman, John Toubia, Vanessa M. Conn,

- Marika Salmanidis, Caroline A. Phillips, Suraya Roslan, Andreas W. Schreiber, Philip A. Gregory, and Gregory J. Goodall. 2015. "The RNA Binding Protein Quaking Regulates Formation of CircRNAs." *Cell* 160 (6): 1125–34. <https://doi.org/10.1016/j.cell.2015.02.014>.
- Cooper, Sharon R., Michelle R. Emond, Phan Q. Duy, Brandon G. Liebau, Marc A. Wolman, and James D. Jontes. 2015. "Protocadherins Control the Modular Assembly of Neuronal Columns in the Zebrafish Optic Tectum." *Journal of Cell Biology* 211 (4): 807–14. <https://doi.org/10.1083/jcb.201507108>.
- Cooper, Sharon R, James D Jontes, and Marcos Sotomayor. 2016. "Structural Determinants of Adhesion by Protocadherin-19 and Implications for Its Role in Epilepsy." *ELife* 5: 1–22. <https://doi.org/10.7554/elife.18529>.
- Daenen, E. W.P.M., J. A. Van der Heyden, C. G. Kruse, G. Wolterink, and J. M. Van Ree. 2001. "Adaptation and Habituation to an Open Field and Responses to Various Stressful Events in Animals with Neonatal Lesions in the Amygdala or Ventral Hippocampus." *Brain Research* 918 (1–2): 153–65. [https://doi.org/10.1016/S0006-8993\(01\)02987-0](https://doi.org/10.1016/S0006-8993(01)02987-0).
- DeFelipe, Javier. 1997. "Types of Neurons, Synaptic Connections and Chemical Characteristics of Cells Immunoreactive for Calbindin-D28K, Parvalbumin and Calretinin in the Neocortex." *Journal of Chemical Neuroanatomy*. [https://doi.org/10.1016/S0891-0618\(97\)10013-8](https://doi.org/10.1016/S0891-0618(97)10013-8).
- Deidda, Gabriele, Ignacio F. Bozarth, and Laura Cancedda. 2014. "Modulation of GABAergic Transmission in Development and Neurodevelopmental Disorders: Investigating Physiology and Pathology to Gain Therapeutic Perspectives." *Frontiers in Cellular Neuroscience*. <https://doi.org/10.3389/fncel.2014.00119>.
- Depienne, Christel, and Eric Leguern. 2012. "PCDH19-Related Infantile Epileptic Encephalopathy: An Unusual X-Linked Inheritance Disorder." *Human Mutation* 33 (4): 627–34. <https://doi.org/10.1002/humu.22029>.

- Dibbens, Leanne M., Patrick S. Tarpey, Kim Hynes, Marta A. Bayly, Ingrid E. Scheffer, Raffaella Smith, Jamee Bomar, et al. 2008. "X-Linked Protocadherin 19 Mutations Cause Female-Limited Epilepsy and Cognitive Impairment." *Nature Genetics* 40 (6): 776–81. <https://doi.org/10.1038/ng.149>.
- Dimidschstein, Jordane, Lara Passante, Audrey Dufour, Jelle vandenAmeele, Luca Tiberi, Tatyana Hrechdakian, Ralf Adams, et al. 2013. "Ephrin-B1 Controls the Columnar Distribution of Cortical Pyramidal Neurons by Restricting Their Tangential Migration." *Neuron* 79 (6): 1123–35. <https://doi.org/10.1016/j.neuron.2013.07.015>.
- Donadoni, Chiara, Stefania Corti, Federica Locatelli, Dimitra Papadimitriou, Michela Guglieri, Sandra Strazzer, Patrizia Bossolasco, Sabrina Salani, and Giacomo P. Comi. 2004. "Improvement of Combined FISH and Immunofluorescence to Trace the Fate of Somatic Stem Cells after Transplantation." *Journal of Histochemistry and Cytochemistry* 52 (10): 1333–39. <https://doi.org/10.1369/jhc.4A6320.2004>.
- Duszyc, Kinga, Iwona Terczynska, and Dorota Hoffman-Zacharska. 2014. "Epilepsy and Mental Retardation Restricted to Females: X-Linked Epileptic Infantile Encephalopathy of Unusual Inheritance." *Journal of Applied Genetics*. <https://doi.org/10.1007/s13353-014-0243-8>.
- Eckel-Mahan, Kristin, and Paolo Sassone-Corsi. 2015. "Phenotyping Circadian Rhythms in Mice." *Current Protocols in Mouse Biology* 5 (3): 271–81. <https://doi.org/10.1002/9780470942390.mo140229>.
- El-Brolosy, Mohamed A., and Didier Y.R. Stainier. 2017. "Genetic Compensation: A Phenomenon in Search of Mechanisms." *PLoS Genetics*. <https://doi.org/10.1371/journal.pgen.1006780>.
- Emond, Michelle R., Sayantane Biswas, Cheasequah J. Blevins, and James D. Jontes. 2011. "A Complex of Protocadherin-19 and n-Cadherin Mediates a Novel Mechanism of Cell Adhesion." *Journal of Cell Biology*

195 (7): 1115–21. <https://doi.org/10.1083/jcb.201108115>.

- Emond, Michelle R., Sayantane Biswas, and James D. Jontes. 2009. "Protocadherin-19 Is Essential for Early Steps in Brain Morphogenesis." *Developmental Biology* 334 (1): 72–83. <https://doi.org/10.1016/j.ydbio.2009.07.008>.
- Fan, Li, Yichao Lu, Xiulian Shen, Hong Shao, Lun Suo, and Qiang Wu. 2018. "Alpha Protocadherins and Pyk2 Kinase Regulate Cortical Neuron Migration and Cytoskeletal Dynamics via Rac1 GTPase and WAVE Complex in Mice." *ELife* 7. <https://doi.org/10.7554/eLife.35242>.
- Farhy-Tselnicker, Isabella, and Nicola J. Allen. 2018. "Astrocytes, Neurons, Synapses: A Tripartite View on Cortical Circuit Development." *Neural Development*. <https://doi.org/10.1186/s13064-018-0104-y>.
- Faux, Clare, Sonja Rakic, William Andrews, and Joanne M. Britto. 2012. "Neurons on the Move: Migration and Lamination of Cortical Interneurons." *NeuroSignals*. <https://doi.org/10.1159/000334489>.
- Feng, Jia, Qi Han, and Libing Zhou. 2012. "Planar Cell Polarity Genes, Celsr1-3, in Neural Development." *Neuroscience Bulletin*. <https://doi.org/10.1007/s12264-012-1232-8>.
- Feng, Yuanyi, and Christopher A. Walsh. 2004. "Mitotic Spindle Regulation by Nde1 Controls Cerebral Cortical Size." *Neuron* 44 (2): 279–93. <https://doi.org/10.1016/j.neuron.2004.09.023>.
- Fernández, Virginia, Cristina Llinares-Benadero, and Víctor Borrell. 2016. "Cerebral Cortex Expansion and Folding: What Have We Learned?" *The EMBO Journal* 35 (10): 1021–44. <https://doi.org/10.15252/emj.201593701>.
- Flames, Nuria, and Oscar Marín. 2005. "Developmental Mechanisms Underlying the Generation of Cortical Interneuron Diversity." *Neuron*. <https://doi.org/10.1016/j.neuron.2005.04.020>.
- Fogarty, Matthew, Matthew Grist, Diego Gelman, Oscar Marín, Vassilis

- Pachnis, and Nicoletta Kessaris. 2007. "Spatial Genetic Patterning of the Embryonic Neuroepithelium Generates GABAergic Interneuron Diversity in the Adult Cortex." *Journal of Neuroscience* 27 (41): 10935–46. <https://doi.org/10.1523/JNEUROSCI.1629-07.2007>.
- Fossat, Nicolas, Coralie Le Greneur, Francis Béby, Stéphane Vincent, Pierre Godement, Gilles Chatelain, and Thomas Lamonerie. 2007. "A New GFP-Tagged Line Reveals Unexpected Otx2 Protein Localization in Retinal Photoreceptors." *BMC Developmental Biology* 7. <https://doi.org/10.1186/1471-213X-7-122>.
- Franco, Santos J., Isabel Martinez-Garay, Cristina Gil-Sanz, Sarah R. Harkins-Perry, and Ulrich Müller. 2011. "Reelin Regulates Cadherin Function via Dab1/Rap1 to Control Neuronal Migration and Lamination in the Neocortex." *Neuron* 69 (3): 482–97. <https://doi.org/10.1016/j.neuron.2011.01.003>.
- Fujitani, M., S. Zhang, R. Fujiki, Y. Fujihara, and T. Yamashita. 2017. "A Chromosome 16p13.11 Microduplication Causes Hyperactivity through Dysregulation of MiR-484/Protocadherin-19 Signaling." *Molecular Psychiatry* 22 (3): 364–74. <https://doi.org/10.1038/mp.2016.106>.
- Gabbott, Paul L.A., Brian G.M. Dickie, R. Roy Vaid, Anthony J.N. Headlam, and Sarah J. Bacon. 1997. "Local-Circuit Neurones in the Medial Prefrontal Cortex (Areas 25, 32 and 24b) in the Rat: Morphology and Quantitative Distribution." *Journal of Comparative Neurology* 377 (4): 465–99. [https://doi.org/10.1002/\(SICI\)1096-9861\(19970127\)377:4<465::AID-CNE1>3.0.CO;2-0](https://doi.org/10.1002/(SICI)1096-9861(19970127)377:4<465::AID-CNE1>3.0.CO;2-0).
- Gaitan, Yaned, and Maxime Bouchard. 2006. "Expression of the δ -Protocadherin Gene Pcdh19 in the Developing Mouse Embryo." *Gene Expression Patterns* 6 (8): 893–99. <https://doi.org/10.1016/j.modgep.2006.03.001>.
- Gal, Jonathan S., Yury M. Morozov, Albert E. Ayoub, Mitali Chatterjee,

- Pasko Rakic, and Tarik F. Haydar. 2006. "Molecular and Morphological Heterogeneity of Neural Precursors in the Mouse Neocortical Proliferative Zones." *Journal of Neuroscience* 26 (3): 1045–56. <https://doi.org/10.1523/JNEUROSCI.4499-05.2006>.
- Garcia, Isabella, Longwen Huang, Kevin Ung, and Benjamin R. Arenkiel. 2012. "Tracing Synaptic Connectivity onto Embryonic Stem Cell-Derived Neurons." *Stem Cells* 30 (10): 2140–51. <https://doi.org/10.1002/stem.1185>.
- Garrett, Andrew M., Dietmar Schreiner, Mark A. Lobas, and Joshua A. Weiner. 2012. "γ-Protocadherins Control Cortical Dendrite Arborization by Regulating the Activity of a FAK/PKC/MARCKS Signaling Pathway." *Neuron* 74 (2): 269–76. <https://doi.org/10.1016/j.neuron.2012.01.028>.
- Germain, No lle, Erin Banda, and Laura Grabel. 2010. "Embryonic Stem Cell Neurogenesis and Neural Specification." *Journal of Cellular Biochemistry* 111 (3): 535–42. <https://doi.org/10.1002/jcb.22747>.
- Gerosa, Laura, Maura Francolini, Silvia Bassani, and Maria Passafaro. 2019. "The Role of Protocadherin 19 (PCDH19) in Neurodevelopment and in the Pathophysiology of Early Infantile Epileptic Encephalopathy-9 (EIEE9)." *Developmental Neurobiology*. <https://doi.org/10.1002/dneu.22654>.
- Gertz, Caitlyn C., and Arnold R. Kriegstein. 2015. "Neuronal Migration Dynamics in the Developing Ferret Cortex." *Journal of Neuroscience* 35 (42): 14307–15. <https://doi.org/10.1523/JNEUROSCI.2198-15.2015>.
- Ghazalpour, Anatole, Brian Bennett, Vladislav A. Petyuk, Luz Orozco, Raffi Hagopian, Imran N. Mungrue, Charles R. Farber, et al. 2011. "Comparative Analysis of Proteome and Transcriptome Variation in Mouse." *PLoS Genetics* 7 (6). <https://doi.org/10.1371/journal.pgen.1001393>.
- Gibson, Daniel A., Stephen Tymanskyj, Rachel C. Yuan, Haiwen C. Leung,

- Julie L. Lefebvre, Joshua R. Sanes, Alain Chédotal, and Le Ma. 2014. "Dendrite Self-Avoidance Requires Cell-Autonomous Slit/Robo Signaling in Cerebellar Purkinje Cells." *Neuron* 81 (5): 1040–56. <https://doi.org/10.1016/j.neuron.2014.01.009>.
- Gil-Sanz, Cristina, Santos J. Franco, Isabel Martinez-Garay, Ana Espinosa, Sarah Harkins-Perry, and Ulrich Müller. 2013. "Cajal-Retzius Cells Instruct Neuronal Migration by Coincidence Signaling between Secreted and Contact-Dependent Guidance Cues." *Neuron* 79 (3): 461–77. <https://doi.org/10.1016/j.neuron.2013.06.040>.
- Gorski, Jessica A., Tiffany Talley, Mengsheng Qiu, Luis Puelles, John L.R. Rubenstein, and Kevin R. Jones. 2002. "Cortical Excitatory Neurons and Glia, but Not GABAergic Neurons, Are Produced in the Emx1-Expressing Lineage." *Journal of Neuroscience* 22 (15): 6309–14. <https://doi.org/10.1523/jneurosci.22-15-06309.2002>.
- Griffin, Aliesha, Kyla R. Hamling, Soon Gweon Hong, Mana Anvar, Luke P. Lee, and Scott C. Baraban. 2018. "Preclinical Animal Models for Dravet Syndrome: Seizure Phenotypes, Comorbidities and Drug Screening." *Frontiers in Pharmacology*. <https://doi.org/10.3389/fphar.2018.00573>.
- Gu, Bin, and Katherine A. Dalton. 2017. "Models and Detection of Spontaneous Recurrent Seizures in Laboratory Rodents." *Zoological Research*. <https://doi.org/10.24272/j.issn.2095-8137.2017.042>.
- Gul, Ismail Sahin, Paco Hulpiau, Yvan Saeys, and Frans van Roy. 2017. "Evolution and Diversity of Cadherins and Catenins." *Experimental Cell Research*. <https://doi.org/10.1016/j.yexcr.2017.03.001>.
- Hadjantonakis, A. K., M. Gertsenstein, M. Ikawa, M. Okabe, and A. Nagy. 1998. "Non-Invasive Sexing of Preimplantation Stage Mammalian Embryos [2]." *Nature Genetics*. <https://doi.org/10.1038/893>.
- Harb, Kawssar, Elia Magrinelli, Céline S. Nicolas, Nikita Lukianets, Laura Frangeul, Mariel Pietri, Tao Sun, et al. 2016. "Area-Specific

Development of Distinct Projection Neuron Subclasses Is Regulated by Postnatal Epigenetic Modifications." *ELife* 5 (JANUARY2016). <https://doi.org/10.7554/eLife.09531>.

Harrison, Reid R., Ilya Kolb, Suhasa B. Kodandaramaiah, Alexander A. Chubykin, Aimei Yang, Mark F. Bear, Edward S. Boyden, and Craig R. Forest. 2015. "Microchip Amplifier for in Vitro, in Vivo, and Automated Whole Cell Patch-Clamp Recording." *Journal of Neurophysiology* 113 (4): 1275–82. <https://doi.org/10.1152/jn.00629.2014>.

Hasegawa, Sonoko, Makiko Kumagai, Mitsue Hagihara, Hiroshi Nishimaru, Keizo Hirano, Ryosuke Kaneko, Atsushi Okayama, et al. 2016. "Distinct and Cooperative Functions for the Protocadherin- α , β and γ Clusters in Neuronal Survival and Axon Targeting." *Frontiers in Molecular Neuroscience* 9 (DEC2016). <https://doi.org/10.3389/fnmol.2016.00155>.

Hasegawa, Yuto, Wenjie Mao, Sucharita Saha, Georgia Gunner, Jenya Kolpakova, Gilles E. Martin, and Kensuke Futai. 2017. "Luciferase ShRNA Presents Off-Target Effects on Voltage-Gated Ion Channels in Mouse Hippocampal Pyramidal Neurons." *ENeuro* 4 (5). <https://doi.org/10.1523/ENEURO.0186-17.2017>.

Hatta, K., A. Nose, A. Nagafuchi, and M. Takeichi. 1988. "Cloning and Expression of cDNA Encoding a Neural Calcium-Dependent Cell Adhesion Molecule: Its Identity in the Cadherin Gene Family." *Journal of Cell Biology* 106 (3): 873–81. <https://doi.org/10.1083/jcb.106.3.873>.

Hatten, Mary E. 1999. "Central Nervous System Neuronal Migration." *Annual Review of Neuroscience* 22 (1): 511–39. <https://doi.org/10.1146/annurev.neuro.22.1.511>.

Hattox, Alexis M., and Sacha B. Nelson. 2007. "Layer V Neurons in Mouse Cortex Projecting to Different Targets Have Distinct Physiological Properties." *Journal of Neurophysiology* 98 (6): 3330–40.

<https://doi.org/10.1152/jn.00397.2007>.

Hayashi, Shuichi, Yoko Inoue, Satoko Hattori, Mari Kaneko, Go Shioi, Tsuyoshi Miyakawa, and Masatoshi Takeichi. 2017. "Loss of X-Linked Protocadherin-19 Differentially Affects the Behavior of Heterozygous Female and Hemizygous Male Mice." *Scientific Reports* 7 (1). <https://doi.org/10.1038/s41598-017-06374-x>.

Hayashi, Shuichi, Yoko Inoue, Hiroshi Kiyonari, Takaya Abe, Kazuyo Misaki, Hiroyuki Moriguchi, Yo Tanaka, and Masatoshi Takeichi. 2014. "Protocadherin-17 Mediates Collective Axon Extension by Recruiting Actin Regulator Complexes to Interaxonal Contacts." *Developmental Cell* 30 (6): 673–87. <https://doi.org/10.1016/j.devcel.2014.07.015>.

Hertel, Nicole, Krishna-K, Monique Nuernberger, and Christoph Redies. 2008. "A Cadherin-Based Code for the Divisions of the Mouse Basal Ganglia." *Journal of Comparative Neurology* 508 (4): 511–28. <https://doi.org/10.1002/cne.21696>.

Hevner, Robert F., Ray A.M. Daza, John L.R. Rubenstein, Henk Stunnenberg, Jaime F. Olavarria, and Chris Englund. 2003. "Beyond Laminar Fate: Toward a Molecular Classification of Cortical Projection/Pyramidal Neurons." *Developmental Neuroscience* 25 (2–4): 139–51. <https://doi.org/10.1159/000072263>.

Hevner, Robert F., Limin Shi, Nick Justice, Yi Ping Hsueh, Morgan Sheng, Susan Smiga, Alessandro Bulfone, André M. Goffinet, Anthony T. Campagnoni, and John L.R. Rubenstein. 2001. "Tbr1 Regulates Differentiation of the Preplate and Layer 6." *Neuron* 29 (2): 353–66. [https://doi.org/10.1016/S0896-6273\(01\)00211-2](https://doi.org/10.1016/S0896-6273(01)00211-2).

Hirano, Shinji, and Masatoshi Takeichi. 2012. "Cadherins in Brain Morphogenesis and Wiring." *Physiological Reviews* 92 (2): 597–634. <https://doi.org/10.1152/physrev.00014.2011>.

Hirota, Yuki, and Kazunori Nakajima. 2017a. "Control of Neuronal Migration and Aggregation by Reelin Signaling in the Developing

- Cerebral Cortex." *Frontiers in Cell and Developmental Biology*.
<https://doi.org/10.3389/fcell.2017.00029>.
- — —. 2017b. "Control of Neuronal Migration and Aggregation by Reelin Signaling in the Developing Cerebral Cortex." *Frontiers in Cell and Developmental Biology*. <https://doi.org/10.3389/fcell.2017.00040>.
- Holschneider, D. P., K. Chen, I. Seif, and J. C. Shih. 2001. "Biochemical, Behavioral, Physiologic, and Neurodevelopmental Changes in Mice Deficient in Monoamine Oxidase A or B." In *Brain Research Bulletin*, 56:453–62. [https://doi.org/10.1016/S0361-9230\(01\)00613-X](https://doi.org/10.1016/S0361-9230(01)00613-X).
- Homan, Claire C., Stephen Pederson, Thu Hien To, Chuan Tan, Sandra Piltz, Mark A. Corbett, Ernst Wolvetang, Paul Q. Thomas, Lachlan A. Jolly, and Jozef Gecz. 2018. "PCDH19 Regulation of Neural Progenitor Cell Differentiation Suggests Asynchrony of Neurogenesis as a Mechanism Contributing to PCDH19 Girls Clustering Epilepsy." *Neurobiology of Disease* 116: 106–19. <https://doi.org/10.1016/j.nbd.2018.05.004>.
- Homayouni, Ramin, Dennis S. Rice, and Tom Curran. 2001. "Disabled-1 Interacts with a Novel Developmentally Regulated Protocadherin." *Biochemical and Biophysical Research Communications* 289 (2): 539–47. <https://doi.org/10.1006/bbrc.2001.5998>.
- Hooks, B. M., S. Andrew Hires, Ying Xin Zhang, Daniel Huber, Leopoldo Petreanu, Karel Svoboda, and Gordon M.G. Shepherd. 2011. "Laminar Analysis of Excitatory Local Circuits in Vibrissal Motor and Sensory Cortical Areas." *PLoS Biology* 9 (1). <https://doi.org/10.1371/journal.pbio.1000572>.
- Hoshina, Naosuke, Asami Tanimura, Miwako Yamasaki, Takeshi Inoue, Ryoji Fukabori, Teiko Kuroda, Kazumasa Yokoyama, et al. 2013. "Protocadherin 17 Regulates Presynaptic Assembly in Topographic Corticobasal Ganglia Circuits." *Neuron* 78 (5): 839–54. <https://doi.org/10.1016/j.neuron.2013.03.031>.

- Hulpiau, Paco, and Frans van Roy. 2009. "Molecular Evolution of the Cadherin Superfamily." *International Journal of Biochemistry and Cell Biology*. <https://doi.org/10.1016/j.biocel.2008.09.027>.
- Hussein, Ahmed, Mekite Bezu, and Volker Korz. 2018. "Evaluating Working Memory on a T-Maze in Male Rats." *Bio-Protocol* 8 (14). <https://doi.org/10.21769/bioprotoc.2930>.
- Imai-Okano, Keiko, and Shinji Hirano. 2016. "Various Atypical Cadherins: T-Cadherin, RET, Calsyntenin, and 7D-Cadherin." In *The Cadherin Superfamily: Key Regulators of Animal Development and Physiology*, 277–311. https://doi.org/10.1007/978-4-431-56033-3_11.
- Inoue, Seika, Kanehiro Hayashi, Kyota Fujita, Kazuhiko Tagawa, Hitoshi Okazawa, Ken-ichiro Kubo, and Kazunori Nakajima. 2019. "Drebrin-like (Dbnl) Controls Neuronal Migration via Regulating N-Cadherin Expression in the Developing Cerebral Cortex." *The Journal of Neuroscience*. <https://doi.org/10.1523/jneurosci.1634-18.2018>.
- Inta, D., J. Alfonso, J. von Engelhardt, M. M. Kreuzberg, A. H. Meyer, J. A. van Hooft, and H. Monyer. 2008. "Neurogenesis and Widespread Forebrain Migration of Distinct GABAergic Neurons from the Postnatal Subventricular Zone." *Proceedings of the National Academy of Sciences*. <https://doi.org/10.1073/pnas.0807059105>.
- Jabaudon, Denis. 2017. "Fate and Freedom in Developing Neocortical Circuits." *Nature Communications*. <https://doi.org/10.1038/ncomms16042>.
- Jabaudon, Denis, Sara J. Shnider, David J. Tischfield, Maria J. Galazo, and Jeffrey D. MacKlis. 2012. "ROR β Induces Barrel-like Neuronal Clusters in the Developing Neocortex." *Cerebral Cortex* 22 (5): 996–1006. <https://doi.org/10.1093/cercor/bhr182>.
- Jackson, Aimee L., Steven R. Bartz, Janell Schelter, Sumire V. Kobayashi, Julia Burchard, Mao Mao, Bin Li, Guy Cavet, and Peter S. Linsley. 2003. "Expression Profiling Reveals Off-Target Gene Regulation by RNAi."

Nature Biotechnology 21 (6): 635–37. <https://doi.org/10.1038/nbt831>.

Jennbacken, Karin, Heléne Gustavsson, Tajana Tešan, Michael Horn, Christina Vallbo, Karin Welén, and Jan Erik Damber. 2009. “The Prostatic Environment Suppresses Growth of Androgen-Independent Prostate Cancer Xenografts: An Effect Influenced by Testosterone.” *Prostate* 69 (11): 1164–75. <https://doi.org/10.1002/pros.20965>.

Jiang, Peng, Kathleen M. Franklin, Marilyn J. Duncan, Bruce F. O’Hara, and Jonathan P. Wisor. 2012. “Distinct Phase Relationships between Suprachiasmatic Molecular Rhythms, Cerebral Cortex Molecular Rhythms, and Behavioral Rhythms in Early Runner (CAST/EiJ) and Nocturnal (C57BL/6J) Mice.” *Sleep* 35 (10): 1385–94. <https://doi.org/10.5665/sleep.2120>.

Jiang, Xiangning, and Jeannette Nardelli. 2016. “Cellular and Molecular Introduction to Brain Development.” *Neurobiology of Disease*. <https://doi.org/10.1016/j.nbd.2015.07.007>.

Jones, E. G. 1998. “Viewpoint: The Core and Matrix of Thalamic Organization.” *Neuroscience*. [https://doi.org/10.1016/S0306-4522\(97\)00581-2](https://doi.org/10.1016/S0306-4522(97)00581-2).

Jossin, Yves, and Jonathan A. Cooper. 2011. “Reelin, Rap1 and N-Cadherin Orient the Migration of Multipolar Neurons in the Developing Neocortex.” *Nature Neuroscience* 14 (6): 697–703. <https://doi.org/10.1038/nn.2816>.

Juberg, Richard C., and C. David Hellman. 1971. “A New Familial Form of Convulsive Disorder and Mental Retardation Limited to Females.” *The Journal of Pediatrics* 79 (5): 726–32. [https://doi.org/10.1016/S0022-3476\(71\)80382-7](https://doi.org/10.1016/S0022-3476(71)80382-7).

Jüngling, Kay, Volker Eulenburg, Robert Moore, Rolf Kemler, Volkmar Lessmann, and Kurt Gottmann. 2006. “N-Cadherin Transsynaptically Regulates Short-Term Plasticity at Glutamatergic Synapses in Embryonic Stem Cell-Derived Neurons.” *Journal of Neuroscience* 26 (26):

6968–78. <https://doi.org/10.1523/JNEUROSCI.1013-06.2006>.

Kaas, J. 1987. "The Organization Of Neocortex In Mammals: Implications For Theories Of Brain Function." *Annual Review of Psychology* 38 (1): 129–51. <https://doi.org/10.1146/annurev.psych.38.1.129>.

Kadowaki, Masakazu, Shoko Nakamura, Ondrej Machon, Stefan Krauss, Glenn L. Radice, and Masatoshi Takeichi. 2007. "N-Cadherin Mediates Cortical Organization in the Mouse Brain." *Developmental Biology* 304 (1): 22–33. <https://doi.org/10.1016/j.ydbio.2006.12.014>.

Kaidanovich-Beilin, Oksana, Tatiana Lipina, Igor Vukobradovic, John Roder, and James R. Woodgett. 2010. "Assessment of Social Interaction Behaviors." *Journal of Visualized Experiments*. <https://doi.org/10.3791/2473>.

Kalbassi, Shireene, Sven O. Bachmann, Ellen Cross, Victoria H. Roberton, and Stéphane J. Baudouin. 2017. "Male and Female Mice Lacking Neuroligin-3 Modify the Behavior of Their Wild-Type Littermates." *ENeuro* 4 (4). <https://doi.org/10.1523/ENEURO.0145-17.2017>.

Kanatani, Shigeaki, Masato Yozu, Hidenori Tabata, and Kazunori Nakajima. 2008. "COUP-TFII Is Preferentially Expressed in the Caudal Ganglionic Eminence and Is Involved in the Caudal Migratory Stream." *Journal of Neuroscience* 28 (50): 13582–91. <https://doi.org/10.1523/JNEUROSCI.2132-08.2008>.

Kasnauskiene, Jurate, Zivile Ciuladaite, Egle Preiksaitiene, Aušra Matulevičiene, Angelos Alexandrou, George Koumbaris, Carolina Sismani, Ingrida Pepalyte, Philippos C. Patsalis, and Vaidutis Kučinskis. 2012. "A Single Gene Deletion on 4q28.3: PCDH18 - A New Candidate Gene for Intellectual Disability?" *European Journal of Medical Genetics* 55 (4): 274–77. <https://doi.org/10.1016/j.ejmg.2012.02.010>.

Kasper, Ekkehard M., Alan U. Larkman, Joachim Lübke, and Colin Blakemore. 1994. "Pyramidal Neurons in Layer 5 of the Rat Visual Cortex. I. Correlation among Cell Morphology, Intrinsic

Electrophysiological Properties, and Axon Targets." *Journal of Comparative Neurology* 339 (4): 459–74. <https://doi.org/10.1002/cne.903390402>.

Kawauchi, Takeshi, Kaori Chihama, Yo Ich Nabeshima, and Mikio Hoshino. 2006. "Cdk5 Phosphorylates and Stabilizes P27kip1 Contributing to Actin Organization and Cortical Neuronal Migration." *Nature Cell Biology* 8 (1): 17–26. <https://doi.org/10.1038/ncb1338>.

Kawauchi, Takeshi, Katsutoshi Sekine, Mima Shikanai, Kaori Chihama, Kenji Tomita, Ken ichiro Kubo, Kazunori Nakajima, Yo ichi Nabeshima, and Mikio Hoshino. 2010. "Rab GTPases-Dependent Endocytic Pathways Regulate Neuronal Migration and Maturation through N-Cadherin Trafficking." *Neuron* 67 (4): 588–602. <https://doi.org/10.1016/j.neuron.2010.07.007>.

Keays, David A., Guoling Tian, Karine Poirier, Guo Jen Huang, Christian Siebold, James Cleak, Peter L. Oliver, et al. 2007. "Mutations in α -Tubulin Cause Abnormal Neuronal Migration in Mice and Lissencephaly in Humans." *Cell* 128 (1): 45–57. <https://doi.org/10.1016/j.cell.2006.12.017>.

Keeler, Austin B., Michael J. Molumby, and Joshua A. Weiner. 2015. "Protocadherins Branch out: Multiple Roles in Dendrite Development." *Cell Adhesion and Migration*. <https://doi.org/10.1080/19336918.2014.1000069>.

Killen, Abigail C., Melissa Barber, Joshua J.W. Paulin, Barbara Ranscht, John G. Parnavelas, and William D. Andrews. 2017. "Protective Role of Cadherin 13 in Interneuron Development." *Brain Structure and Function* 222 (8): 3567–85. <https://doi.org/10.1007/s00429-017-1418-y>.

Kim, S. Y., H. Sun Chung, W. Sun, and H. Kim. 2007. "Spatiotemporal Expression Pattern of Non-Clustered Protocadherin Family Members in the Developing Rat Brain." *Neuroscience* 147 (4): 996–1021. <https://doi.org/10.1016/j.neuroscience.2007.03.052>.

- Kivi, Gaily, Kaupo Teesalu, Jüri Parik, Elen Kontkar, Mart Ustav, Liis Noodla, Mart Ustav, and Andres Männik. 2016. "HybriFree: A Robust and Rapid Method for the Development of Monoclonal Antibodies from Different Host Species." *BMC Biotechnology* 16 (1). <https://doi.org/10.1186/s12896-016-0232-6>.
- Koehl, Muriel, Sally E. Battle, and Fred W. Turek. 2003. "Sleep in Female Mice: A Strain Comparison across the Estrous Cycle." *Sleep* 26 (3): 267–72. <https://doi.org/10.1093/sleep/26.3.267>.
- Kolc, Kristy L., Lynette G. Sadleir, Ingrid E. Scheffer, Atma Ivancevic, Rachel Roberts, Duyen H. Pham, and Jozef Gecz. 2019. "A Systematic Review and Meta-Analysis of 271 PCDH19-Variant Individuals Identifies Psychiatric Comorbidities, and Association of Seizure Onset and Disease Severity." *Molecular Psychiatry*. <https://doi.org/10.1038/s41380-018-0066-9>.
- Kondratov, Roman V., Victoria Y. Gorbacheva, and Marina P. Antoch. 2007. "The Role of Mammalian Circadian Proteins in Normal Physiology and Genotoxic Stress Responses." *Current Topics in Developmental Biology*. [https://doi.org/10.1016/S0070-2153\(06\)78005-X](https://doi.org/10.1016/S0070-2153(06)78005-X).
- Kondratova, Anna A., Yuliya V. Dubrovsky, Marina P. Antoch, and Roman V. Kondratov. 2010. "Circadian Clock Proteins Control Adaptation to Novel Environment and Memory Formation." *Aging* 2 (5): 285–97. <https://doi.org/10.18632/aging.100142>.
- Koralek, Katherine-Ann -A, Jaime Olavarria, and Herbert P. Kellackey. 1990. "Areal and Laminar Organization of Corticocortical Projections in the Rat Somatosensory Cortex." *Journal of Comparative Neurology* 299 (2): 133–50. <https://doi.org/10.1002/cne.902990202>.
- Kou, Zhaohui, Qian Wu, Xiaochen Kou, Chonghai Yin, Hong Wang, Zhentao Zuo, Yan Zhuo, Antony Chen, Shaorong Gao, and Xiaoqun Wang. 2015. "CRISPR/Cas9-Mediated Genome Engineering of the Ferret." *Cell Research*. <https://doi.org/10.1038/cr.2015.130>.

- Krishna-K, K., N. Hertel, and C. Redies. 2011. "Cadherin Expression in the Somatosensory Cortex: Evidence for a Combinatorial Molecular Code at the Single-Cell Level." *Neuroscience* 175: 37–48. <https://doi.org/10.1016/j.neuroscience.2010.11.056>.
- Krishna, K., Monique Nuernberger, Franco Weth, and Christoph Redies. 2009. "Layer-Specific Expression of Multiple Cadherins in the Developing Visual Cortex (V1) of the Ferret." *Cerebral Cortex* 19 (2): 388–401. <https://doi.org/10.1093/cercor/bhn090>.
- Kubota, Kyoko, Kiyoshi Inoue, Ryota Hashimoto, Natsuko Kumamoto, Asako Kosuga, Masahiko Tatsumi, Kunitoshi Kamijima, et al. 2009. "Tumor Necrosis Factor Receptor-Associated Protein 1 Regulates Cell Adhesion and Synaptic Morphology via Modulation of N-Cadherin Expression." *Journal of Neurochemistry* 110 (2): 496–508. <https://doi.org/10.1111/j.1471-4159.2009.06099.x>.
- Kurian, Mary, Christian M. Korff, Emmanuelle Ranza, Andrea Bernasconi, Anja Lübbig, Srishti Nangia, Gian Paolo Ramelli, Gabriele Wohlrab, Douglas R. Nordli, and Thomas Bast. 2018. "Focal Cortical Malformations in Children with Early Infantile Epilepsy and PCDH19 Mutations: Case Report." *Developmental Medicine and Child Neurology* 60 (1): 100–105. <https://doi.org/10.1111/dmcn.13595>.
- Kurusu, Shusaku, and Tadaomi Takenawa. 2009. "The WASP and WAVE Family Proteins." *Genome Biology*. <https://doi.org/10.1186/gb-2009-10-6-226>.
- Lai, Meng Chuan, Michael V. Lombardo, and Simon Baron-Cohen. 2014. "Autism." *The Lancet* 383 (9920): 896–910. [https://doi.org/10.1016/S0140-6736\(13\)61539-1](https://doi.org/10.1016/S0140-6736(13)61539-1).
- Lal, Dennis, Ann Kathrin Ruppert, Holger Trucks, Herbert Schulz, Carolien de Kovel, Dorothée Kasteleijn-Nolst Trenité, Anja C.M. Sonsma, et al. 2015. "Burden Analysis of Rare Microdeletions Suggests a Strong Impact of Neurodevelopmental Genes in Genetic Generalised

Epilepsies.”

PLoS

Genetics.

<https://doi.org/10.1371/journal.pgen.1005226>.

Lamonica, Bridget E., Jan H. Lui, David V. Hansen, and Arnold R. Kriegstein. 2013. “Mitotic Spindle Orientation Predicts Outer Radial Glial Cell Generation in Human Neocortex.” *Nature Communications* 4. <https://doi.org/10.1038/ncomms2647>.

Lange, I. M. de, P. Rump, R. F. Neuteboom, P. B. Augustijn, K. Hodges, A. I. Kistemaker, O. F. Brouwer, et al. 2017. “Male Patients Affected by Mosaic PCDH19 Mutations: Five New Cases.” *Neurogenetics* 18 (3): 147–53. <https://doi.org/10.1007/s10048-017-0517-5>.

Larsen, De Laine D., and Edward M. Callaway. 2006. “Development of Layer-Specific Axonal Arborizations in Mouse Primary Somatosensory Cortex.” *Journal of Comparative Neurology* 494 (3): 398–414. <https://doi.org/10.1002/cne.20754>.

Lavdas, Alexandros A., Maria Grigoriou, Vassilis Pachnis, and John G. Parnavelas. 1999. “The Medial Ganglionic Eminence Gives Rise to a Population of Early Neurons in the Developing Cerebral Cortex.” *Journal of Neuroscience* 19 (18): 7881–88. <https://doi.org/10.1523/jneurosci.19-18-07881.1999>.

Lee, Soo Hyun, Jens Hjerling-Leffler, Edward Zagher, Gord Fishell, and Bernardo Rudy. 2010. “The Largest Group of Superficial Neocortical GABAergic Interneurons Expresses Ionotropic Serotonin Receptors.” *Journal of Neuroscience* 30 (50): 16796–808. <https://doi.org/10.1523/JNEUROSCI.1869-10.2010>.

Lele, Zsolt, Anja Folchert, Miguel Concha, Gerd Jörg Rauch, Robert Geisler, Frédéric Rosa, Steve W. Wilson, Matthias Hammerschmidt, and Laure Bally-Cuif. 2002. “Parachute/ n-Cadherin Is Required for Morphogenesis and Maintained Integrity of the Zebrafish Neural Tube.” *Development*.

Lenroot, Rhoshel K., and Jay N. Giedd. 2006. “Brain Development in

Children and Adolescents: Insights from Anatomical Magnetic Resonance Imaging." *Neuroscience and Biobehavioral Reviews*. <https://doi.org/10.1016/j.neubiorev.2006.06.001>.

Leone, Dino P., Whitney E. Heavner, Emily A. Ferenczi, Gergana Dobрева, John R. Huguenard, Rudolf Grosschedl, and Susan K. McConnell. 2015. "Satb2 Regulates the Differentiation of Both Callosal and Subcerebral Projection Neurons in the Developing Cerebral Cortex." *Cerebral Cortex* 25 (10): 3406–19. <https://doi.org/10.1093/cercor/bhu156>.

Leung, Louis C., William A. Harris, Christine E. Holt, and Michael Piper. 2015. "NF-Protocadherin Regulates Retinal Ganglion Cell Axon Behaviour in the Developing Visual System." *PLoS ONE* 10 (10). <https://doi.org/10.1371/journal.pone.0141290>.

Lévesque, Martin, Ali Charara, Serge Gagnon, André Parent, and Martin Deschênes. 1996. "Corticostriatal Projections from Layer V Cells in Rat Are Collaterals of Long-Range Corticofugal Axons." *Brain Research* 709 (2): 311–15. [https://doi.org/10.1016/0006-8993\(95\)01333-4](https://doi.org/10.1016/0006-8993(95)01333-4).

Liang, Xue hai, Christopher E. Hart, and Stanley T. Crooke. 2013. "Transfection of SiRNAs Can Alter MiRNA Levels and Trigger Non-Specific Protein Degradation in Mammalian Cells." *Biochimica et Biophysica Acta - Gene Regulatory Mechanisms* 1829 (5): 455–68. <https://doi.org/10.1016/j.bbagr.2013.01.011>.

Light, Sarah E.W., and James D. Jontes. 2017. "δ-Protocadherins: Organizers of Neural Circuit Assembly." *Seminars in Cell and Developmental Biology*. <https://doi.org/10.1016/j.semcdb.2017.07.037>.

Lin, Juntang, Congrui Wang, and Christoph Redies. 2012. "Expression of Delta-Protocadherins in the Spinal Cord of the Chicken Embryo." *Journal of Comparative Neurology* 520 (7): 1509–31. <https://doi.org/10.1002/cne.22808>.

Lin, Juntang, Xin Yan, Congrui Wang, Zhikun Guo, Arndt Rolfs, and Jiankai Luo. 2012. "Anatomical Expression Patterns of Delta-Protocadherins in

- Developing Chicken Cochlea." *Journal of Anatomy* 221 (6): 598–608. <https://doi.org/10.1111/j.1469-7580.2012.01568.x>.
- Liu, Junhua, Bin Liu, Xiao Yun Zhang, Baocong Yu, Wuqiang Guan, Kun Wang, Yang Yang, et al. 2014. "Development of the Paralemniscal Pathway in the Barrel Cortex." *Molecular Brain* 7 (1). <https://doi.org/10.1186/s13041-014-0084-8>.
- Liu, Qin, Yun Chen, Fumitaka Kubota, Jean J. Pan, and Tohru Murakami. 2010. "Expression of Protocadherin-19 in the Nervous System of the Embryonic Zebrafish." *International Journal of Developmental Biology* 54 (5): 905–11. <https://doi.org/10.1387/ijdb.092882ql>.
- Liu, Yansheng, Andreas Beyer, and Ruedi Aebersold. 2016. "On the Dependency of Cellular Protein Levels on mRNA Abundance." *Cell*. <https://doi.org/10.1016/j.cell.2016.03.014>.
- Lodato, Simona, and Paola Arlotta. 2015. "Generating Neuronal Diversity in the Mammalian Cerebral Cortex." *Annual Review of Cell and Developmental Biology* 31 (1): 699–720. <https://doi.org/10.1146/annurev-cellbio-100814-125353>.
- Lodato, Simona, Caroline Rouaux, Kathleen B. Quast, Chanati Jantrachotechatchawan, Michèle Studer, Takao K. Hensch, and Paola Arlotta. 2011. "Excitatory Projection Neuron Subtypes Control the Distribution of Local Inhibitory Interneurons in the Cerebral Cortex." *Neuron* 69 (4): 763–79. <https://doi.org/10.1016/j.neuron.2011.01.015>.
- Lopes, Alexandra M., Norman Ross, James Close, Adam Dagnall, António Amorim, and Timothy J. Crow. 2006. "Inactivation Status of PCDH11X: Sexual Dimorphisms in Gene Expression Levels in Brain." *Human Genetics* 119 (3): 267–75. <https://doi.org/10.1007/s00439-006-0134-0>.
- López-Bendito, Guillermina, Juan Antonio Sánchez-Alcañiz, Ramón Pla, Víctor Borrell, Esther Picó, Miguel Valdeolmillos, and Oscar Marín. 2008. "Chemokine Signaling Controls Intracortical Migration and Final Distribution of GABAergic Interneurons." *Journal of Neuroscience* 28 (7):

1613–24. <https://doi.org/10.1523/JNEUROSCI.4651-07.2008>.

Lopez, Manuel. 2014. “Combined in Situ Hybridization/Immunohistochemistry (ISH/IH) on Free-Floating Vibratome Tissue Sections.” *Bio-Protocol* 4 (18). <https://doi.org/10.21769/bioprotoc.1243>.

Luhmann, Heiko J., A. Fukuda, and W. Kilb. 2015. “Control of Cortical Neuronal Migration by Glutamate and GABA.” *Frontiers in Cellular Neuroscience*. <https://doi.org/10.3389/fncel.2015.00004>.

Lv, Xiaohui, Si Qiang Ren, Xin Jun Zhang, Zhongfu Shen, Tanay Ghosh, Anjin Xianyu, Peng Gao, et al. 2019. “TBR2 Coordinates Neurogenesis Expansion and Precise Microcircuit Organization via Protocadherin 19 in the Mammalian Cortex.” *Nature Communications* 10 (1). <https://doi.org/10.1038/s41467-019-11854-x>.

Ma, Yunyong, Hang Hu, Albert S. Berrebi, Peter H. Mathers, and Ariel Agmon. 2006. “Distinct Subtypes of Somatostatin-Containing Neocortical Interneurons Revealed in Transgenic Mice.” *Journal of Neuroscience* 26 (19): 5069–82. <https://doi.org/10.1523/JNEUROSCI.0661-06.2006>.

Marin-Padilla, Miguel. 1978. “Dual Origin of the Mammalian Neocortex and Evolution of the Cortical Plate.” *Anatomy and Embryology* 152 (2): 109–26. <https://doi.org/10.1007/BF00315920>.

Marín, Oscar. 2012. “Interneuron Dysfunction in Psychiatric Disorders.” *Nature Reviews Neuroscience*. <https://doi.org/10.1038/nrn3155>.

— — —. 2013. “Cellular and Molecular Mechanisms Controlling the Migration of Neocortical Interneurons.” *European Journal of Neuroscience* 38 (1): 2019–29. <https://doi.org/10.1111/ejn.12225>.

Markram, Henry, Maria Toledo-Rodriguez, Yun Wang, Anirudh Gupta, Gilad Silberberg, and Caizhi Wu. 2004. “Interneurons of the Neocortical Inhibitory System.” *Nature Reviews Neuroscience*.

<https://doi.org/10.1038/nrn1519>.

- Martinez-Garay, Isabel, Cristina Gil-Sanz, Santos J. Franco, Ana Espinosa, Zoltán Molnár, and Ulrich Mueller. 2016. "Cadherin 2/4 Signaling via PTP1B and Catenins Is Crucial for Nucleokinesis during Radial Neuronal Migration in the Neocortex." *Development (Cambridge)* 143 (12): 2121–34. <https://doi.org/10.1242/dev.132456>.
- Martini, Francisco J., Manuel Valiente, Guillermina López Bendito, Gábor Szabó, Fernando Moya, Miguel Valdeolmillos, and Oscar Marín. 2009. "Biased Selection of Leading Process Branches Mediates Chemotaxis during Tangential Neuronal Migration." *Development* 136 (1): 41–50. <https://doi.org/10.1242/dev.025502>.
- Masai, Ichiro, Zsolt Lele, Masahiro Yamaguchi, Atsuko Komori, Asuka Nakata, Yuko Nishiwaki, Hironori Wada, et al. 2003. "N-Cadherin Mediates Retinal Lamination, Maintenance of Forebrain Compartments and Patterning of Retinal Neurites." *Development*. <https://doi.org/10.1242/dev.00465>.
- Meer, Peter Van, and Jacob Raber. 2005. "Mouse Behavioural Analysis in Systems Biology." *Biochemical Journal* 389 (3): 593–610. <https://doi.org/10.1042/BJ20042023>.
- Mendez, Pablo, Mathias De Roo, Lorenzo Pogli, Paul Klauser, and Dominique Muller. 2010. "N-Cadherin Mediates Plasticity-Induced Long-Term Spine Stabilization." *Journal of Cell Biology* 189 (3): 589–600. <https://doi.org/10.1083/jcb.201003007>.
- Miller, Jeremy A., Song Lin Ding, Susan M. Sunkin, Kimberly A. Smith, Lydia Ng, Aaron Szafer, Amanda Ebbert, et al. 2014. "Transcriptional Landscape of the Prenatal Human Brain." *Nature* 508 (7495): 199–206. <https://doi.org/10.1038/nature13185>.
- Mimori-Kiyosue, Yuko, Nobuyuki Shiina, and Shoichiro Tsukita. 2000. "Adenomatous Polyposis Coli (APC) Protein Moves along Microtubules and Concentrates at Their Growing Ends in Epithelial

Cells." *Journal of Cell Biology* 148 (3): 505–17.
<https://doi.org/10.1083/jcb.148.3.505>.

Misson, Jean Paul, Michael A. Edwards, Miyuki Yamamoto, and Verne S. Caviness. 1988. "Mitotic Cycling of Radial Glial Cells of the Fetal Murine Cerebral Wall: A Combined Autoradiographic and Immunohistochemical Study." *Developmental Brain Research* 38 (2): 183–90. [https://doi.org/10.1016/0165-3806\(88\)90043-0](https://doi.org/10.1016/0165-3806(88)90043-0).

Miyake, Kunio, Takae Hirasawa, Masaki Soutome, Masayuki Itoh, Yu Ichi Goto, Kazushi Endoh, Kenichiro Takahashi, et al. 2011. "The Protocadherins, PCDHB1 and PCDH7, Are Regulated by MeCP2 in Neuronal Cells and Brain Tissues: Implication for Pathogenesis of Rett Syndrome." *BMC Neuroscience* 12. <https://doi.org/10.1186/1471-2202-12-81>.

Miyata, Takaki, Ayano Kawaguchi, Hideyuki Okano, and Masaharu Ogawa. 2001. "Asymmetric Inheritance of Radial Glial Fibers by Cortical Neurons." *Neuron* 31 (5): 727–41.
[https://doi.org/10.1016/S0896-6273\(01\)00420-2](https://doi.org/10.1016/S0896-6273(01)00420-2).

Miyata, Takaki, Daichi Kawaguchi, Ayano Kawaguchi, and Yukiko Gotoh. 2010. "Mechanisms That Regulate the Number of Neurons during Mouse Neocortical Development." *Current Opinion in Neurobiology*.
<https://doi.org/10.1016/j.conb.2010.01.001>.

Miyoshi, Goichi, and Gord Fishell. 2011. "GABAergic Interneuron Lineages Selectively Sort into Specific Cortical Layers during Early Postnatal Development." *Cerebral Cortex* 21 (4): 845–52.
<https://doi.org/10.1093/cercor/bhq155>.

Molyneaux, Bradley J., Paola Arlotta, Joao R.L. Menezes, and Jeffrey D. Macklis. 2007. "Neuronal Subtype Specification in the Cerebral Cortex." *Nature Reviews Neuroscience*.
<https://doi.org/10.1038/nrn2151>.

Moritz, Christian P., Timo Mühlhaus, Stefan Tenzer, Thomas Schulenburg,

- and Eckhard Friauf. 2019. "Poor Transcript-Protein Correlation in the Brain: Negatively Correlating Gene Products Reveal Neuronal Polarity as a Potential Cause." *Journal of Neurochemistry* 149 (5): 582–604. <https://doi.org/10.1111/jnc.14664>.
- Moriya, Hisao. 2015. "Quantitative Nature of Overexpression Experiments." *Molecular Biology of the Cell* 26 (22): 3932–39. <https://doi.org/10.1091/mbc.E15-07-0512>.
- Moy, S. S., J. J. Nadler, A. Perez, R. P. Barbaro, J. M. Johns, T. R. Magnuson, J. Piven, and J. N. Crawley. 2004. "Sociability and Preference for Social Novelty in Five Inbred Strains: An Approach to Assess Autistic-like Behavior in Mice." *Genes, Brain and Behavior* 3 (5): 287–302. <https://doi.org/10.1111/j.1601-1848.2004.00076.x>.
- Nadarajah, Bagirathy, Janice E. Brunstrom, Jaime Grutzendler, Rachel O.L. Wong, and Alan L. Pearlman. 2001. "Two Modes of Radial Migration in Early Development of the Cerebral Cortex." *Nature Neuroscience* 4 (2): 143–50. <https://doi.org/10.1038/83967>.
- Naka, Alexander, and Hillel Adesnik. 2016. "Inhibitory Circuits in Cortical Layer 5." *Frontiers in Neural Circuits*. <https://doi.org/10.3389/fncir.2016.00035>.
- Nakagawa, Yasushi, and Dennis D.M. O'Leary. 2003. "Dynamic Patterned Expression of Orphan Nuclear Receptor Genes ROR α and ROR β in Developing Mouse Forebrain." *Developmental Neuroscience* 25 (2–4): 234–44. <https://doi.org/10.1159/000072271>.
- Nakao, Shinsuke, Anna Platek, Shinji Hirano, and Masatoshi Takeichi. 2008. "Contact-Dependent Promotion of Cell Migration by the OL-Protocadherin-Nap1 Interaction." *Journal of Cell Biology* 182 (2): 395–410. <https://doi.org/10.1083/jcb.200802069>.
- Nicoludis, John M., Sze Yi Lau, Charlotta P.I. Schärfe, Debora S. Marks, Wilhelm A. Weihofen, and Rachelle Gaudet. 2015. "Structure and Sequence Analyses of Clustered Protocadherins Reveal Antiparallel

Interactions That Mediate Homophilic Specificity." *Structure* 23 (11): 2087–98. <https://doi.org/10.1016/j.str.2015.09.005>.

Nieto, Marta, Edwin S. Monuki, Hua Tang, Jaime Imitola, Nicole Haubst, Samia J. Khoury, Jim Cunningham, Magdalena Gotz, and Christopher A. Walsh. 2004. "Expression of Cux-1 and Cux-2 in the Subventricular Zone and Upper Layers II-IV of the Cerebral Cortex." *Journal of Comparative Neurology* 479 (2): 168–80. <https://doi.org/10.1002/cne.20322>.

Nikolic, Margareta, Margaret M. Chou, Wange Lu, Bruce J. Mayer, and Li Huei Tsai. 1998. "The P35/Cdk5 Kinase Is a Neuron-Specific Rac Effector That Inhibits Pak1 Activity." *Nature* 395 (6698): 194–98. <https://doi.org/10.1038/26034>.

Noctor, Stephen C., Verónica Martínez-Cerdeño, Lidija Ivic, and Arnold R. Kriegstein. 2004. "Cortical Neurons Arise in Symmetric and Asymmetric Division Zones and Migrate through Specific Phases." *Nature Neuroscience* 7 (2): 136–44. <https://doi.org/10.1038/nn1172>.

Nollet, Friedel, Patrick Kools, and Frans Van Roy. 2000. "Phylogenetic Analysis of the Cadherin Superfamily Allows Identification of Six Major Subfamilies besides Several Solitary Members." *Journal of Molecular Biology*. <https://doi.org/10.1006/jmbi.2000.3777>.

Ogawa, Masaharu, Takaki Miyata, Kazunori Nakajima, Kenichi Yagyu, Masahiro Seike, Kazuhiro Ikenaka, Hiroshi Yamamoto, and Katsuhiko Mikoshiba. 1995. "The Reeler Gene-Associated Antigen on Cajal-Retzius Neurons Is a Crucial Molecule for Laminar Organization of Cortical Neurons." *Neuron* 14 (5): 899–912. [https://doi.org/10.1016/0896-6273\(95\)90329-1](https://doi.org/10.1016/0896-6273(95)90329-1).

Oishi, Koji, Nao Nakagawa, Kashiko Tachikawa, Shinji Sasaki, Michihiko Aramaki, Shinji Hirano, Nobuhiko Yamamoto, Yumiko Yoshimura, and Kazunori Nakajima. 2016. "Identity of Neocortical Layer 4 Neurons Is Specified through Correct Positioning into the Cortex."

ELife 5 (FEBRUARY2016). <https://doi.org/10.7554/eLife.10907>.

Okuda, Yuichi, Eri Ogura, Hisato Kondoh, and Yusuke Kamachi. 2010. "B1 SOX Coordinate Cell Specification with Patterning and Morphogenesis in the Early Zebrafish Embryo." *PLoS Genetics* 6 (5): 36. <https://doi.org/10.1371/journal.pgen.1000936>.

Ono, Daisuke, Sato Honma, and Ken ichi Honma. 2016. "Differential Roles of AVP and VIP Signaling in the Postnatal Changes of Neural Networks for Coherent Circadian Rhythms in the SCN." *Science Advances* 2 (9). <https://doi.org/10.1126/sciadv.1600960>.

Paladino, Natalia, José M. Duhart, Malena L. Mul Fedele, and Diego A. Golombek. 2013. "Characterization of Locomotor Activity Circadian Rhythms in Athymic Nude Mice." *Journal of Circadian Rhythms* 11 (1). <https://doi.org/10.1186/1740-3391-11-2>.

Parras, Alberto, Héctor Anta, María Santos-Galindo, Vivek Swarup, Ainara Elorza, José L. Nieto-González, Sara Picó, et al. 2018. "Autism-like Phenotype and Risk Gene mRNA Deadenylation by CPEB4 Mis-Splicing." *Nature* 560 (7719): 441–46. <https://doi.org/10.1038/s41586-018-0423-5>.

Pederick, Daniel T., Claire C. Homan, Emily J. Jaehne, Sandra G. Piltz, Bryan P. Haines, Bernhard T. Baune, Lachlan A. Jolly, James N. Hughes, Jozef Gecz, and Paul Q. Thomas. 2016. "Pcdh19 Loss-of-Function Increases Neuronal Migration In Vitro but Is Dispensable for Brain Development in Mice." *Scientific Reports* 6. <https://doi.org/10.1038/srep26765>.

Pederick, Daniel T., Kay L. Richards, Sandra G. Piltz, Raman Kumar, Stefka Mincheva-Tasheva, Simone A. Mandelstam, Russell C. Dale, et al. 2018. "Abnormal Cell Sorting Underlies the Unique X-Linked Inheritance of PCDH19 Epilepsy." *Neuron* 97 (1): 59-66.e5. <https://doi.org/10.1016/j.neuron.2017.12.005>.

Petersen, Carl C.H., and Bert Sakmann. 2001. "Functionally Independent Columns of Rat Somatosensory Barrel Cortex Revealed with Voltage-

- Sensitive Dye Imaging." *Journal of Neuroscience* 21 (21): 8435–46.
<https://doi.org/10.1523/jneurosci.21-21-08435.2001>.
- Pham, Duyen H., Chuan C. Tan, Claire C. Homan, Kristy L. Kolc, Mark A. Corbett, Dale McAninch, Archa H. Fox, Paul Q. Thomas, Raman Kumar, and Jozef Gecz. 2017. "Protocadherin 19 (PCDH19) Interacts with Paraspeckle Protein NONO to Co-Regulate Gene Expression with Estrogen Receptor Alpha (ER α)." *Human Molecular Genetics* 26 (11): 2042–52. <https://doi.org/10.1093/hmg/ddx094>.
- Philibert, C., S. Bouillot, P. Huber, and G. Faury. 2012. "Protocadherin-12 Deficiency Leads to Modifications in the Structure and Function of Arteries in Mice." *Pathologie Biologie* 60 (1): 34–40.
<https://doi.org/10.1016/j.patbio.2011.11.005>.
- Polleux, Franck, Kristin L. Whitford, Paul A. Dijkhuizen, Tania Vitalis, and Anirvan Ghosh. 2002. "Control of Cortical Interneuron Migration by Neurotrophins and PI3-Kinase Signaling." *Development*.
- Ponomareva, Olga Y., Ian C. Holmen, Aiden J. Sperry, Kevin W. Eliceiri, and Mary C. Halloran. 2014. "Calsyntenin-1 Regulates Axon Branching and Endosomal Trafficking during Sensory Neuron Development in Vivo." *Journal of Neuroscience* 34 (28): 9235–48.
<https://doi.org/10.1523/JNEUROSCI.0561-14.2014>.
- Prasad, Tuhina, Xiaozhong Wang, Paul A. Gray, and Joshua A. Weiner. 2008. "A Differential Developmental Pattern of Spinal Interneuron Apoptosis during Synaptogenesis: Insights from Genetic Analyses of the Protocadherin- γ Gene Cluster." *Development*.
<https://doi.org/10.1242/dev.026807>.
- Preibisch, Stephan, Stephan Saalfeld, and Pavel Tomancak. 2009. "Globally Optimal Stitching of Tiled 3D Microscopic Image Acquisitions." *Bioinformatics* 25 (11): 1463–65.
<https://doi.org/10.1093/bioinformatics/btp184>.
- Priddle, Thomas H., and Tim J. Crow. 2013. "Protocadherin 11X/Y a

- Human-Specific Gene Pair: An Immunohistochemical Survey of Fetal and Adult Brains." *Cerebral Cortex* 23 (8): 1933–41. <https://doi.org/10.1093/cercor/bhs181>.
- Pu, Jing, Tal Keren-Kaplan, and Juan S. Bonifacino. 2017. "A Ragulator-BORC Interaction Controls Lysosome Positioning in Response to Amino Acid Availability." *Journal of Cell Biology* 216 (12): 4183–97. <https://doi.org/10.1083/jcb.201703094>.
- Qian, Xueming, Qin Shen, Susan K. Goderie, Wenlei He, Alexandra Capela, Andrew A. Davis, and Sally Temple. 2000. "Timing of CNS Cell Generation: A Programmed Sequence of Neuron and Glial Cell Production from Isolated Murine Cortical Stem Cells." *Neuron* 28 (1): 69–80. [https://doi.org/10.1016/S0896-6273\(00\)00086-6](https://doi.org/10.1016/S0896-6273(00)00086-6).
- Quaggin, Susan E., Gregory B. Vanden Heuvel, Krista Golden, Rolf Bodmer, and Peter Igarashi. 1996. "Primary Structure, Neural-Specific Expression, and Chromosomal Localization of Cux-2, a Second Murine Homeobox Gene Related to Drosophila Cut." *Journal of Biological Chemistry* 271 (37): 22624–34. <https://doi.org/10.1074/jbc.271.37.22624>.
- Radice, Glenn L., Helen Rayburn, Hiroaki Matsunami, Karen A. Knudsen, Masatoshi Takeichi, and Richard O. Hynes. 1997. "Developmental Defects in Mouse Embryos Lacking N-Cadherin." *Developmental Biology* 181 (1): 64–78. <https://doi.org/10.1006/dbio.1996.8443>.
- Rakic, Pasko. 1974. "Neurons in Rhesus Monkey Visual Cortex: Systematic Relation between Time of Origin and Eventual Disposition." *Science* 183 (4123): 425–27. <https://doi.org/10.1126/science.183.4123.425>.
- Reddy, Doodipala Samba. 2010. "Neurosteroids. Endogenous Role in the Human Brain and Therapeutic Potentials." In *Progress in Brain Research*, 186:113–37. <https://doi.org/10.1016/B978-0-444-53630-3.00008-7>.
- Redies, C., K. Vanhalst, and F. Van Roy. 2005. "δ-Protocadherins: Unique Structures and Functions." *Cellular and Molecular Life Sciences*.

<https://doi.org/10.1007/s00018-005-5320-z>.

Reghunandanan, Vallath, and Rajalaxmy Reghunandanan. 2006. "Neurotransmitters of the Suprachiasmatic Nuclei." *Journal of Circadian Rhythms*. <https://doi.org/10.1186/1740-3391-4-2>.

Reiner, Orly, Anna Gorelik, and Raanan Greenman. 2012. "Use of RNA Interference by in Utero Electroporation to Study Cortical Development: The Example of the Doublecortin Superfamily." *Genes*. <https://doi.org/10.3390/genes3040759>.

Rieger, Sandra, Niklas Senghaas, Axel Walch, and Reinhard W. Köster. 2009. "Cadherin-2 Controls Directional Chain Migration of Cerebellar Granule Neurons." *PLoS Biology* 7 (11). <https://doi.org/10.1371/journal.pbio.1000240>.

Rio, Jose A. del, and Eduardo Soriano. 1989. "Immunocytochemical Detection of 5'-Bromodeoxyuridine Incorporation in the Central Nervous System of the Mouse." *Developmental Brain Research* 49 (2): 311-17. [https://doi.org/10.1016/0165-3806\(89\)90033-3](https://doi.org/10.1016/0165-3806(89)90033-3).

Rio, JoséAntonio del, L. de Lecea, Isidro Ferrer, and Eduardo Soriano. 1994. "The Development of Parvalbumin-Immunoreactivity in the Neocortex of the Mouse." *Developmental Brain Research* 81 (2): 247-59. [https://doi.org/10.1016/0165-3806\(94\)90311-5](https://doi.org/10.1016/0165-3806(94)90311-5).

Rubio-Garrido, Pablo, Flor Pérez-De-Manzo, César Porrero, Maria J. Galazo, and Francisco Clascá. 2009. "Thalamic Input to Distal Apical Dendrites in Neocortical Layer 1 Is Massive and Highly Convergent." *Cerebral Cortex* 19 (10): 2380-95. <https://doi.org/10.1093/cercor/bhn259>.

Rudy, Bernardo, Gordon Fishell, Soo Hyun Lee, and Jens Hjerling-Leffler. 2011. "Three Groups of Interneurons Account for Nearly 100% of Neocortical GABAergic Neurons." *Developmental Neurobiology* 71 (1): 45-61. <https://doi.org/10.1002/dneu.20853>.

- Ryan, Stephen G., Phillip F. Chance, Chang Hua Zou, Nancy B. Spinner, Jeffrey A. Golden, and Susan Smietana. 1997. "Epilepsy and Mental Retardation Limited to Females: An X-Linked Dominant Disorder with Male Sparing." *Nature Genetics* 17 (1): 92–95. <https://doi.org/10.1038/ng0997-92>.
- Sabri, Mohammad Mahdi, and Ehsan Arabzadeh. 2018. "Information Processing across Behavioral States: Modes of Operation and Population Dynamics in Rodent Sensory Cortex." *Neuroscience*. <https://doi.org/10.1016/j.neuroscience.2017.09.016>.
- Sando, Richard, Karsten Baumgaertel, Simon Pieraut, Nina Torabi-Rander, Thomas J. Wandless, Mark Mayford, and Anton Maximov. 2013. "Inducible Control of Gene Expression with Destabilized Cre." *Nature Methods* 10 (11): 1085–91. <https://doi.org/10.1038/nmeth.2640>.
- Sano, K., H. Tanihara, R.L. Heimark, S. Obata, M. Davidson, T. St John, S. Taketani, and S. Suzuki. 1993. "Protocadherins: A Large Family of Cadherin-Related Molecules in Central Nervous System." *The EMBO Journal* 12 (6): 2249–56. <https://doi.org/10.1002/j.1460-2075.1993.tb05878.x>.
- Santer, Deanna M., Gillian E.S. Minty, Adil Mohamed, Lesley Baldwin, Rakesh Bhat, Michael Joyce, Adrian Egli, D. Lorne J. Tyrrell, and Michael Houghton. 2017. "A Novel Method for Detection of IFN-Lambda 3 Binding to Cells for Quantifying IFN-Lambda Receptor Expression." *Journal of Immunological Methods* 445: 15–22. <https://doi.org/10.1016/j.jim.2017.03.001>.
- Schaeren-Wiemers, Nicole, Elisabeth André, Josef P. Kapfhammer, and Michael Becker-André. 1997. "The Expression Pattern of the Orphan Nuclear Receptor ROR β in the Developing and Adult Rat Nervous System Suggests a Role in the Processing of Sensory Information and in Circadian Rhythm." *European Journal of Neuroscience* 9 (12): 2687–2701. <https://doi.org/10.1111/j.1460-9568.1997.tb01698.x>.

- Scheffer, Ingrid E., Samantha J. Turner, Leanne M. Dibbens, Marta A. Bayly, Kathryn Friend, Bree Hodgson, Linda Burrows, et al. 2008. "Epilepsy and Mental Retardation Limited to Females: An under-Recognized Disorder." *Brain* 131 (4): 918–27. <https://doi.org/10.1093/brain/awm338>.
- Schindelin, Johannes, Ignacio Arganda-Carreras, Erwin Frise, Verena Kaynig, Mark Longair, Tobias Pietzsch, Stephan Preibisch, et al. 2012. "Fiji: An Open-Source Platform for Biological-Image Analysis." *Nature Methods* 9 (7): 676–82. <https://doi.org/10.1038/nmeth.2019>.
- Schoch, Hannah, Arati S. Kreibich, Sarah L. Ferri, Rachel S. White, Dominique Bohorquez, Anamika Banerjee, Russell G. Port, et al. 2017. "Sociability Deficits and Altered Amygdala Circuits in Mice Lacking Pcdh10, an Autism Associated Gene." *Biological Psychiatry* 81 (3): 193–202. <https://doi.org/10.1016/j.biopsych.2016.06.008>.
- Schousboe, Arne, and Helle S. Waagepetersen. 2007. "GABA: Homeostatic and Pharmacological Aspects." *Progress in Brain Research*. [https://doi.org/10.1016/S0079-6123\(06\)60002-2](https://doi.org/10.1016/S0079-6123(06)60002-2).
- Schreiner, Dietmar, and Joshua A. Weiner. 2010. "Combinatorial Homophilic Interaction between γ -Protocadherin Multimers Greatly Expands the Molecular Diversity of Cell Adhesion." *Proceedings of the National Academy of Sciences of the United States of America*. <https://doi.org/10.1073/pnas.1004526107>.
- Schubert, D., R. Kötter, H. J. Luhmann, and J. F. Staiger. 2006. "Morphology, Electrophysiology and Functional Input Connectivity of Pyramidal Neurons Characterizes a Genuine Layer Va in the Primary Somatosensory Cortex." *Cerebral Cortex* 16 (2): 223–36. <https://doi.org/10.1093/cercor/bhi100>.
- Seibenhener, Michael L., and Michael C. Wooten. 2015. "Use of the Open Field Maze to Measure Locomotor and Anxiety-like Behavior in Mice." *Journal of Visualized Experiments* (96). <https://doi.org/10.3791/52434>.

- Semple, Bridgette D., Klas Blomgren, Kayleen Gimlin, Donna M. Ferriero, and Linda J. Noble-Haeusslein. 2013. "Brain Development in Rodents and Humans: Identifying Benchmarks of Maturation and Vulnerability to Injury across Species." *Progress in Neurobiology*. <https://doi.org/10.1016/j.pneurobio.2013.04.001>.
- Shaner, Nathan C., Robert E. Campbell, Paul A. Steinbach, Ben N.G. Giepmans, Amy E. Palmer, and Roger Y. Tsien. 2004. "Improved Monomeric Red, Orange and Yellow Fluorescent Proteins Derived from *Discosoma* Sp. Red Fluorescent Protein." *Nature Biotechnology* 22 (12): 1567-72. <https://doi.org/10.1038/nbt1037>.
- Shikanai, Mima, Kazunori Nakajima, and Takeshi Kawauchi. 2011. "N-Cadherin Regulates Radial Glial Fiber-Dependent Migration of Cortical Locomoting Neurons." *Communicative & Integrative Biology* 4 (3): 326-30. <https://doi.org/10.4161/cib.4.3.14886>.
- Shu, Tianzhi, Ramses Ayala, Minh Dang Nguyen, Zhigang Xie, Joseph G. Gleeson, and Li Huei Tsai. 2004. "Ndel1 Operates in a Common Pathway with LIS1 and Cytoplasmic Dynein to Regulate Cortical Neuronal Positioning." *Neuron* 44 (2): 263-77. <https://doi.org/10.1016/j.neuron.2004.09.030>.
- Sidman, Richard L., and Pasko Rakic. 1973. "Neuronal Migration, with Special Reference to Developing Human Brain: A Review." *Brain Research*. [https://doi.org/10.1016/0006-8993\(73\)90617-3](https://doi.org/10.1016/0006-8993(73)90617-3).
- Silverman, Jill L., Mu Yang, Catherine Lord, and Jacqueline N. Crawley. 2010. "Behavioural Phenotyping Assays for Mouse Models of Autism." *Nature Reviews Neuroscience*. <https://doi.org/10.1038/nrn2851>.
- Simon, P., R. Dupuis, and J. Costentin. 1994. "Thigmotaxis as an Index of Anxiety in Mice. Influence of Dopaminergic Transmissions." *Behavioural Brain Research* 61 (1): 59-64. [https://doi.org/10.1016/0166-4328\(94\)90008-6](https://doi.org/10.1016/0166-4328(94)90008-6).
- Smith, Lacey, Nilika Singhal, Christelle M. El Achkar, Gessica Truglio, Beth

- Rosen Sheidley, Joseph Sullivan, and Annapurna Poduri. 2018. "PCDH19-Related Epilepsy Is Associated with a Broad Neurodevelopmental Spectrum." *Epilepsia* 59 (3): 679–89. <https://doi.org/10.1111/epi.14003>.
- Solecki, David J., Lynn Model, Jedidiah Gaetz, Tarun M. Kapoor, and Mary E. Hatten. 2004. "Par6 α Signaling Controls Glial-Guided Neuronal Migration." *Nature Neuroscience* 7 (11): 1195–1203. <https://doi.org/10.1038/nn1332>.
- Srinivasan, K., D. P. Leone, R. K. Bateson, G. Dobрева, Y. Kohwi, T. Kohwi-Shigematsu, R. Grosschedl, and S. K. McConnell. 2012. "A Network of Genetic Repression and Derepression Specifies Projection Fates in the Developing Neocortex." *Proceedings of the National Academy of Sciences*. <https://doi.org/10.1073/pnas.1216793109>.
- Srinivasan, Karpagam, Dino P. Leone, Rosalie K. Bateson, Gergana Dobрева, Yoshinori Kohwi, Terumi Kohwi-Shigematsu, Rudolf Grosschedl, and Susan K. McConnell. 2012. "A Network of Genetic Repression and Derepression Specifies Projection Fates in the Developing Neocortex." *Proceedings of the National Academy of Sciences of the United States of America* 109 (47): 19071–78. <https://doi.org/10.1073/pnas.1216793109>.
- Steuble, Martin, Bertran Gerrits, Alexander Ludwig, José María Mateos, Tu My Diep, Mitsuo Tagaya, Alexander Stephan, et al. 2010. "Molecular Characterization of a Trafficking Organelle: Dissecting the Axonal Paths of Calsyntenin-1 Transport Vesicles." *Proteomics* 10 (21): 3775–88. <https://doi.org/10.1002/pmic.201000384>.
- Stoller, Jason Z., Karl R. Degenhardt, Li Huang, Diane D. Zhou, Min Lu Min, and Jonathan A. Epstein. 2008. "Cre Reporter Mouse Expressing a Nuclear Localized Fusion of GFP and β -Galactosidase Reveals New Derivatives of Pax3-Expressing Precursors." *Genesis* 46 (4): 200–204. <https://doi.org/10.1002/dvg.20384>.

- Stühmer, Thorsten, Stewart A. Anderson, Marc Ekker, and John L.R. Rubenstein. 2002. "Ectopic Expression of the Dlx Genes Induces Glutamic Acid Decarboxylase and Dlx Expression." *Development* 129 (1): 245-52.
- Sun, Tao, and Robert F. Hevner. 2014. "Growth and Folding of the Mammalian Cerebral Cortex: From Molecules to Malformations." *Nature Reviews Neuroscience*. <https://doi.org/10.1038/nrn3707>.
- Suo, Lun, Huinan Lu, Guoxin Ying, Mario R. Capecchi, and Qiang Wu. 2012. "Protocadherin Clusters and Cell Adhesion Kinase Regulate Dendrite Complexity through Rho GTPase." *Journal of Molecular Cell Biology* 4 (6): 362-76. <https://doi.org/10.1093/jmcb/mjs034>.
- Tabata, Hidenori, and Koh Ichi Nagata. 2016. "Decoding the Molecular Mechanisms of Neuronal Migration Using in Utero Electroporation." *Medical Molecular Morphology*. <https://doi.org/10.1007/s00795-015-0127-y>.
- Tabata, Hidenori, and Kazunori Nakajima. 2003. "Multipolar Migration: The Third Mode of Radial Neuronal Migration in the Developing Cerebral Cortex." *Journal of Neuroscience* 23 (31): 9996-10001. <https://doi.org/10.1523/jneurosci.23-31-09996.2003>.
- Tai, Kiyoto, Masaki Kubota, Kohei Shiono, Hitoshi Tokutsu, and Shintaro T. Suzuki. 2010. "Adhesion Properties and Retinofugal Expression of Chicken Protocadherin-19." *Brain Research* 1344: 13-24. <https://doi.org/10.1016/j.brainres.2010.04.065>.
- Tamamaki, Nobuaki, Kazuhiro E. Fujimori, and Rumiko Takauji. 1997. "Origin and Route of Tangentially Migrating Neurons in the Developing Neocortical Intermediate Zone." *Journal of Neuroscience* 17 (21): 8313-23. <https://doi.org/10.1523/jneurosci.17-21-08313.1997>.
- Tan, Chuan, Chloe Shard, Enzo Ranieri, Kim Hynes, Duyen H. Pham, Damian Leach, Grant Buchanan, et al. 2015. "Mutations of Protocadherin 19 in Female Epilepsy (PCDH19-FE) Lead to

Allopregnanolone Deficiency." *Human Molecular Genetics* 24 (18): 5250–59. <https://doi.org/10.1093/hmg/ddv245>.

Tanaka, Teruyuki, Finley F. Serneo, Christine Higgins, Michael J. Gambello, Anthony Wynshaw-Boris, and Joseph G. Gleeson. 2004. "Lis1 and Doublecortin Function with Dynein to Mediate Coupling of the Nucleus to the Centrosome in Neuronal Migration." *Journal of Cell Biology* 165 (5): 709–21. <https://doi.org/10.1083/jcb.200309025>.

Tasic, Bosiljka, Vilas Menon, Thuc Nghi Nguyen, Tae Kyung Kim, Tim Jarsky, Zizhen Yao, Boaz Levi, et al. 2016. "Adult Mouse Cortical Cell Taxonomy Revealed by Single Cell Transcriptomics." *Nature Neuroscience* 19 (2): 335–46. <https://doi.org/10.1038/nn.4216>.

Tasic, Bosiljka, Zizhen Yao, Lucas T. Graybuck, Kimberly A. Smith, Thuc Nghi Nguyen, Darren Bertagnolli, Jeff Goldy, et al. 2018. "Shared and Distinct Transcriptomic Cell Types across Neocortical Areas." *Nature* 563 (7729): 72–78. <https://doi.org/10.1038/s41586-018-0654-5>.

Taverna, Elena, and Wieland B. Huttner. 2010. "Neural Progenitor Nuclei IN Motion." *Neuron*. <https://doi.org/10.1016/j.neuron.2010.08.027>.

Taylor, D. C., M. A. Falconer, C. J. Bruton, and J. A. Corsellis. 1971. "Focal Dysplasia of the Cerebral Cortex in Epilepsy." *Journal of Neurology, Neurosurgery, and Psychiatry* 34 (4): 369–87. <https://doi.org/10.1136/jnnp.34.4.369>.

Tellez, Grissel Faura, Brigitte W.M. Willemse, Uilke Brouwer, Susan Nijboer Brinksma, Karl Vandepoele, Jacobien A. Noordhoek, Irene Heijink, et al. 2016. "Protocadherin-1 localization and Cell adhesion function in Airway Epithelial cells in Asthma." *PLoS ONE*. <https://doi.org/10.1371/journal.pone.0163967>.

Tiveron, Marie Catherine, Mireille Rossel, Barbara Moepps, Li Zhang Yong, Ralph Seidenfaden, Jack Favor, Norbert König, and Harold Cremer. 2006. "Molecular Interaction between Projection Neuron Precursors and Invading Interneurons via Stromal-Derived Factor 1

(CXCL12)/CXCR4 Signaling in the Cortical Subventricular Zone/Intermediate Zone." *Journal of Neuroscience* 26 (51): 13273–78. <https://doi.org/10.1523/JNEUROSCI.4162-06.2006>.

Tsai, Nien Pei, Julia R. Wilkerson, Weirui Guo, Marina A. Maksimova, George N. Demartino, Christopher W. Cowan, and Kimberly M. Huber. 2012. "Multiple Autism-Linked Genes Mediate Synapse Elimination via Proteasomal Degradation of a Synaptic Scaffold PSD-95." *Cell* 151 (7): 1581–94. <https://doi.org/10.1016/j.cell.2012.11.040>.

Uematsu, Masakazu, Yasuharu Hirai, Fuyuki Karube, Satoe Ebihara, Megumi Kato, Kuniya Abe, Kunihiro Obata, et al. 2008. "Quantitative Chemical Composition of Cortical GABAergic Neurons Revealed in Transgenic Venus-Expressing Rats." *Cerebral Cortex* 18 (2): 315–30. <https://doi.org/10.1093/cercor/bhm056>.

Uemura, Masato, Shinsuke Nakao, Shintaro T. Suzuki, Masatoshi Takeichi, and Shinji Hirano. 2007. "OL-Protocadherin Is Essential for Growth of Striatal Axons and Thalamocortical Projections." *Nature Neuroscience* 10 (9): 1151–59. <https://doi.org/10.1038/nn1960>.

Ueno, Hiroshi, Shunsuke Suemitsu, Yosuke Matsumoto, and Motoi Okamoto. 2015. "Sensory Deprivation during Early Postnatal Period Alters the Density of Interneurons in the Mouse Prefrontal Cortex." *Neural Plasticity* 2015. <https://doi.org/10.1155/2015/753179>.

van Meer, Peter, and Jacob Raber. 2005. "Mouse Behavioural Analysis in Systems Biology." *Biochemical Journal*. <https://doi.org/10.1042/BJ20042023>.

Vogel, Christine, and Edward M. Marcotte. 2012. "Insights into the Regulation of Protein Abundance from Proteomic and Transcriptomic Analyses." *Nature Reviews Genetics*. <https://doi.org/10.1038/nrg3185>.

Voikar, Vootele, Sven Krackow, Hans Peter Lipp, Anton Rau, Giovanni Colacicco, and David P. Wolfer. 2018. "Automated Dissection of Permanent Effects of Hippocampal or Prefrontal Lesions on

- Performance at Spatial, Working Memory and Circadian Timing Tasks of C57BL/6 Mice in IntelliCage." *Behavioural Brain Research* 352: 8–22. <https://doi.org/10.1016/j.bbr.2017.08.048>.
- Walf, Alicia A., and Cheryl A. Frye. 2007. "The Use of the Elevated plus Maze as an Assay of Anxiety-Related Behavior in Rodents." *Nature Protocols* 2 (2): 322–28. <https://doi.org/10.1038/nprot.2007.44>.
- Wamsley, Brie, and Gord Fishell. 2017. "Genetic and Activity-Dependent Mechanisms Underlying Interneuron Diversity." *Nature Reviews Neuroscience*. <https://doi.org/10.1038/nrn.2017.30>.
- Wang, Zhi Liang, Wei Zhou, Zheng Ai Xiong, Teng Hua Yu, Li Mei Wu, Cheng Xiang Li, Cheng Guo Yao, Yu Tong Wu, and Yuan Yuan Hua. 2017. "Irreversible Electroporation-Mediated ShRNA Knockdown of the HPV18 E6 Gene Suppresses Cervical Cancer Growth in Vitro and in Vivo." *Oncology Letters* 14 (2): 1943–49. <https://doi.org/10.3892/ol.2017.6405>.
- Weiner, Joshua A., and James Jontes. 2013. "Protocadherins, Not Prototypical: A Complex Tale of Their Interactions, Expression, and Functions." *Frontiers in Molecular Neuroscience*. <https://doi.org/10.3389/fnmol.2013.00004>.
- Wichterle, H., D. H. Turnbull, S. Nery, G. Fishell, and A. Alvarez-Buylla. 2001. "In Utero Fate Mapping Reveals Distinct Migratory Pathways and Fates of Neurons Born in the Mammalian Basal Forebrain." *Development* 128 (19): 3759–71.
- Wieland, Ilse, Sibylle Jakubiczka, Petra Muschke, Monika Cohen, Hannelore Thiele, Klaus L. Gerlach, Ralf H. Adams, and Peter Wieacker. 2004. "Mutations of the Ephrin-B1 Gene Cause Craniofrontonasal Syndrome." *American Journal of Human Genetics* 74 (6): 1209–15. <https://doi.org/10.1086/421532>.
- Wisor, Jonathan P., Martin Striz, Jason DeVoss, Greer M. Murphy, Dale M. Edgar, and Bruce F. O'Hara. 2007. "A Novel Quantitative Trait Locus

- on Mouse Chromosome 18, 'Era1,' Modifies the Entrainment of Circadian Rhythms." *Sleep* 30 (10): 1255–63. <https://doi.org/10.1093/sleep/30.10.1255>.
- Wolf, Andrea, Björn Bauer, Erin L. Abner, Tal Ashkenazy-Frolinger, and Anika M.S. Hartz. 2016. "A Comprehensive Behavioral Test Battery to Assess Learning and Memory in 129S6/ Tg2576 Mice." *PLoS ONE* 11 (1). <https://doi.org/10.1371/journal.pone.0147733>.
- Wolverton, Thomas, and Marc Lalande. 2001. "Identification and Characterization of Three Members of a Novel Subclass of Protocadherins." *Genomics* 76 (1–3): 66–72. <https://doi.org/10.1006/geno.2001.6592>.
- Woodruff, Alan, Qing Xu, Stewart A. Anderson, and Rafael Yuste. 2009. "Depolarizing Effect of Neocortical Chandelier Neurons." *Frontiers in Neural Circuits* 3 (OCT). <https://doi.org/10.3389/neuro.04.015.2009>.
- Wu, Qiang, Theresa Zhang, Jan Fang Cheng, Youngwook Kim, Jane Grimwood, Jeremy Schmutz, Mark Dickson, et al. 2001. "Comparative DNA Sequence Analysis of Mouse and Human Protocadherin Gene Clusters [3]." *Genome Research*. <https://doi.org/10.1101/gr.167301>.
- Xiao, Huajuan, Ziling Sun, Jun Wan, Shengtao Hou, and Yi Xiong. 2018. "Overexpression of Protocadherin 7 Inhibits Neuronal Survival by Downregulating BIRC5 in Vitro." *Experimental Cell Research* 366 (1): 71–80. <https://doi.org/10.1016/j.yexcr.2018.03.016>.
- Xie, Zhigang, Kamon Sanada, Benjamin Adam Samuels, Heather Shih, and Li Huei Tsai. 2003. "Serine 732 Phosphorylation of FAK by Cdk5 Is Important for Microtubule Organization, Nuclear Movement, and Neuronal Migration." *Cell* 114 (4): 469–82. [https://doi.org/10.1016/S0092-8674\(03\)00605-6](https://doi.org/10.1016/S0092-8674(03)00605-6).
- Xu, Xiangmin, Keith D. Roby, and Edward M. Callaway. 2010. "Immunochemical Characterization of Inhibitory Mouse Cortical Neurons: Three Chemically Distinct Classes of Inhibitory Cells."

Journal of Comparative Neurology 518 (3): 389–404.
<https://doi.org/10.1002/cne.22229>.

Xu, Ying, Quasar S. Padiath, Robert E. Shapiro, Christopher R. Jones, Susan C. Wu, Noriko Saigoh, Kazumasa Saigoh, Louis J. Ptáček, and Ying Hui Fu. 2005. “Functional Consequences of a CKI δ Mutation Causing Familial Advanced Sleep Phase Syndrome.” *Nature* 434 (7033): 640–44.
<https://doi.org/10.1038/nature03453>.

Yamashita, Haruyoshi, Shanlin Chen, Seiji Komagata, Ryuichi Hishida, Takuji Iwasato, Shigeyoshi Itohara, Takeshi Yagi, Naoto Endo, Minoru Shibata, and Katsuei Shibuki. 2012. “Restoration of Contralateral Representation in the Mouse Somatosensory Cortex after Crossing Nerve Transfer.” *PLoS ONE* 7 (4).
<https://doi.org/10.1371/journal.pone.0035676>.

Yang, Yan, and Wayne N. Frankel. 2004. “Genetic Approaches to Studying Mouse Models of Human Seizure Disorders.” *Advances in Experimental Medicine and Biology*. https://doi.org/10.1007/978-1-4757-6376-8_1.

Yasuda, Shin, Hidekazu Tanaka, Hiroko Sugiura, Ko Okamura, Taiki Sakaguchi, Uyen Tran, Takako Takemiya, et al. 2007. “Activity-Induced Protocadherin Arcadlin Regulates Dendritic Spine Number by Triggering N-Cadherin Endocytosis via TAO2 β and P38 MAP Kinases.” *Neuron* 56 (3): 456–71.
<https://doi.org/10.1016/j.neuron.2007.08.020>.

Yoder, Michael D., and Barry M. Gumbiner. 2011. “Axial Protocadherin (AXPC) Regulates Cell Fate during Notochordal Morphogenesis.” *Developmental Dynamics* 240 (11): 2495–2504.
<https://doi.org/10.1002/dvdy.22754>.

Yokoo, Hideaki, Sumihito Nobusawa, Hirohide Takebayashi, Kazuhiro Ikenaka, Koji Isoda, Makoto Kamiya, Atsushi Sasaki, Junko Hirato, and Yoichi Nakazato. 2004. “Anti-Human Olig2 Antibody as a Useful Immunohistochemical Marker of Normal Oligodendrocytes and

- Gliomas." *American Journal of Pathology* 164 (5): 1717–25. [https://doi.org/10.1016/S0002-9440\(10\)63730-3](https://doi.org/10.1016/S0002-9440(10)63730-3).
- Yoshida-Noro, Chikako, Noboru Suzuki, and Masatoshi Takeichi. 1984. "Molecular Nature of the Calcium-Dependent Cell-Cell Adhesion System in Mouse Teratocarcinoma and Embryonic Cells Studied with a Monoclonal Antibody." *Developmental Biology* 101 (1): 19–27. [https://doi.org/10.1016/0012-1606\(84\)90112-X](https://doi.org/10.1016/0012-1606(84)90112-X).
- Zakaria, Sana, Yaopan Mao, Anna Kuta, Catia Ferreira De Sousa, Gary O. Gaufo, Helen McNeill, Robert Hindges, Sarah Guthrie, Kenneth D. Irvine, and Philippa H. Francis-West. 2014. "Regulation of Neuronal Migration by Dchs1-Fat4 Planar Cell Polarity." *Current Biology* 24 (14): 1620–27. <https://doi.org/10.1016/j.cub.2014.05.067>.
- Zeisel, Amit, Ana B. Mōz-Manchado, Simone Codeluppi, Peter Lōnnerberg, Gioele La Manno, Anna Juréus, Sueli Marques, et al. 2015. "Cell Types in the Mouse Cortex and Hippocampus Revealed by Single-Cell RNA-Seq." *Science* 347 (6226): 1138–42. <https://doi.org/10.1126/science.aaa1934>.
- Zhang, Jianing, Gregory J. Woodhead, Sruthi K. Swaminathan, Stephanie R. Noles, Erin R. McQuinn, Anna J. Pisarek, Adam M. Stocker, Christopher A. Mutch, Nobuo Funatsu, and Anjen Chen. 2010. "Cortical Neural Precursors Inhibit Their Own Differentiation via N-Cadherin Maintenance of β -Catenin Signaling." *Developmental Cell* 18 (3): 472–79. <https://doi.org/10.1016/j.devcel.2009.12.025>.
- Zhang, Peng, Cuiying Wu, Ning Liu, Lijun Niu, Zhongjie Yan, Yanyan Feng, and Ruxiang Xu. 2014. "Protocadherin 11 X Regulates Differentiation and Proliferation of Neural Stem Cell In Vitro and In Vivo." *Journal of Molecular Neuroscience* 54 (2): 199–210. <https://doi.org/10.1007/s12031-014-0275-x>.
- Zhang, Y., K. Chen, S. A. Sloan, M. L. Bennett, A. R. Scholze, S. O’Keeffe, H. P. Phatnani, et al. 2014. "An RNA-Sequencing Transcriptome and

Splicing Database of Glia, Neurons, and Vascular Cells of the Cerebral Cortex." *Journal of Neuroscience*.
<https://doi.org/10.1523/jneurosci.1860-14.2014>.

Zimmer, Céline, Marie Catherine Tiveron, Rolf Bodmer, and Harold Cremer. 2004. "Dynamics of Cux2 Expression Suggests That an Early Pool of SVZ Precursors Is Fated to Become Upper Cortical Layer Neurons." *Cerebral Cortex* 14 (12): 1408–20.
<https://doi.org/10.1093/cercor/bhh102>.

Appendix

Optimising an anti-PCDH19 antibody for immunohistochemistry

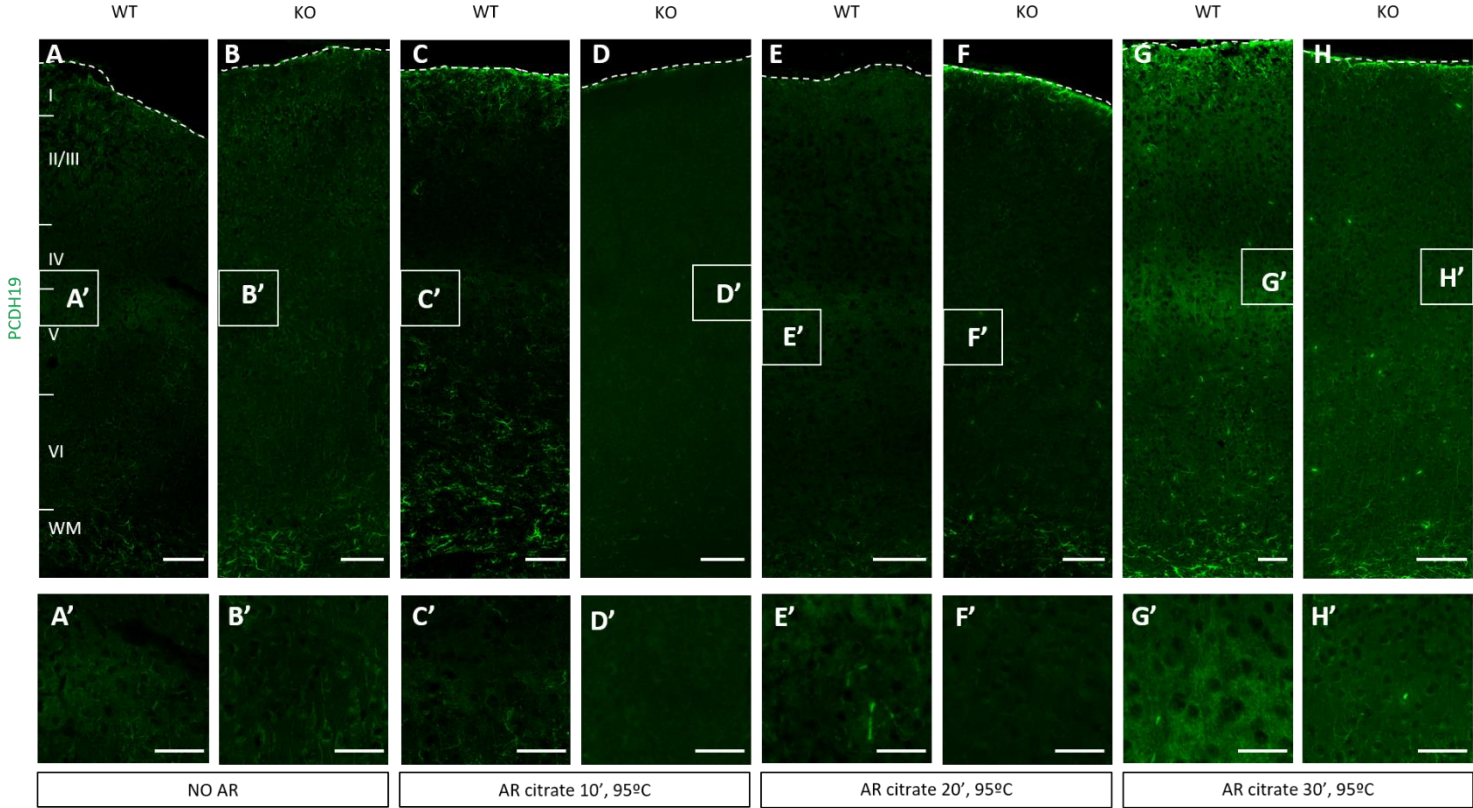


Figure A. 1. Anti-PCDH19 antibody A304-468A from Bethyl Laboratories could not detect clearly enough PCDH19 expression in P10 brains using IHC.

Representative images of PCDH19 detection by IHC on P10 WT (**A, A', C, C', E, E', G, G'**) and KO (**B, B', D, D', F, F', H, H'**) mouse brains at 10x (**A**). Regions amplified are signalled with a white square and a letter. PCDH19 could be detected specifically by the antibody when AR was used for 20 or 30 min. In layer Va, where *Pcdh19* mRNA is detected, the PCDH19 antibody detects some expression in WT but not in KO tissue. Unspecific binding can be detected in the WM though. Despite the specific detection of the PCDH19 protein, it was not possible to clearly assign the expression to a particular cell or sometimes even a particular layer, since the expression could simply be signalling neuronal projections and not cell bodies.

Dashed lines indicate the limits of the brains. Cortical layers are indicated with roman numerals in the representative images. PCDH19 is in green. Scale bar: full image, 100 μm ; amplified images, 50 μm . WM, white matter; WT, Wild-type; KO, *Pcdh19*-Knockout.

Generating and optimising an anti-PCDH19 antibody for immunohistochemistry

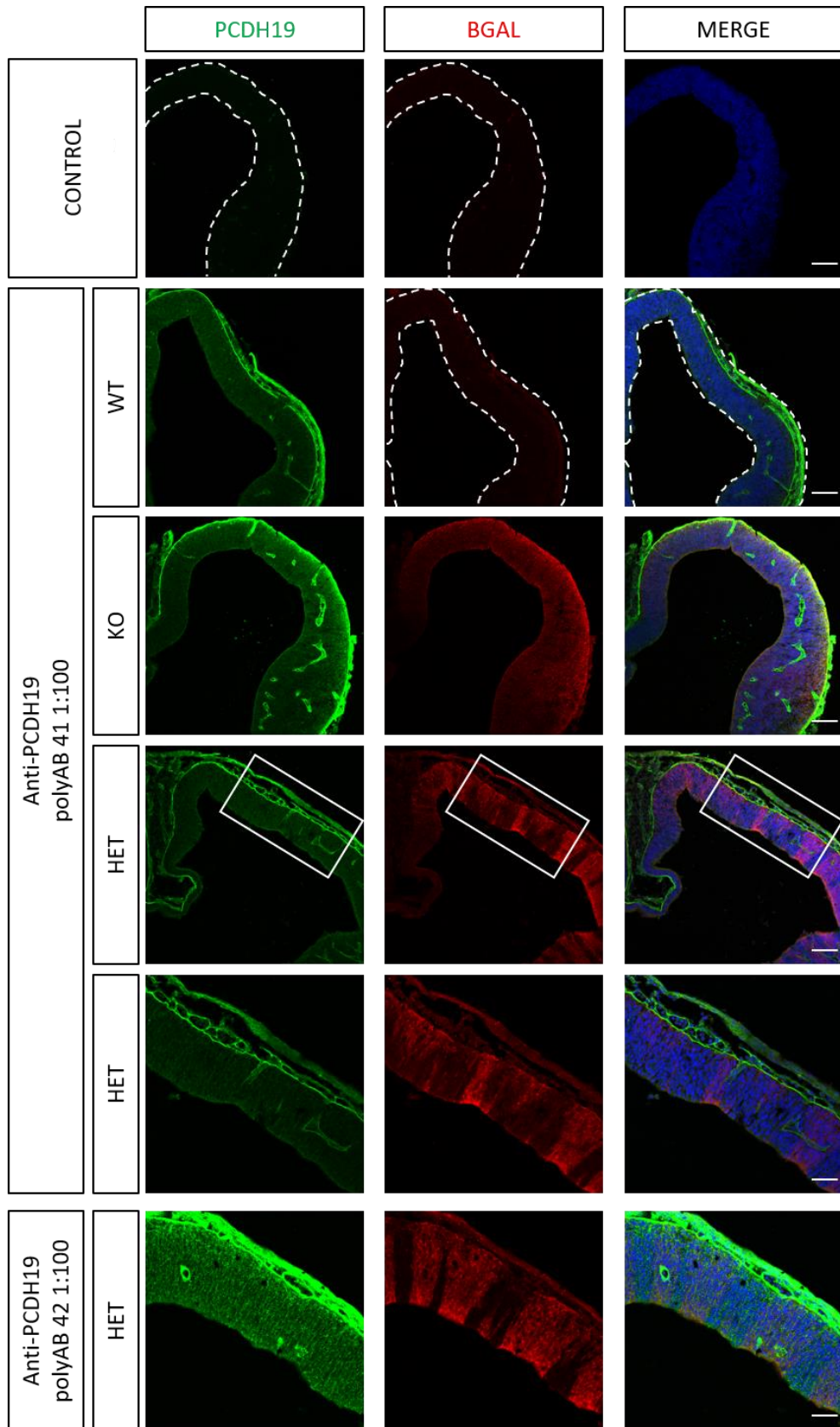


Figure A. 2. Anti-PCDH19 antibodies poly-41 and poly-42, generated by Icosagen, were unspecific.

Representative images of IHC tests against PCDH19 and B-GALACTOSIDASE on E11.5 WT, HET and KO mouse brains at 10x. Brains were subjected to AR with citrate for 10 min at 95 °C, PCDH19 was detected using either poly-41 or poly-42 ab at 1:100 dilution, while BGAL was detected using a BGAL antibody at 1:500 dilution. Dashed lines indicate the limits of the brains. Regions amplified are indicated by a white rectangle. PCDH19 is in green, BGAL is shown in red and DAPI counterstaining is in blue. Scale bar: 100 µm, magnified images: 50 µm. WT, Wild-type; KO, *Pcdh19*-Knockout. HET, *Pcdh19*-heterozygous; BGAL, B-GALACTOSIDASE.

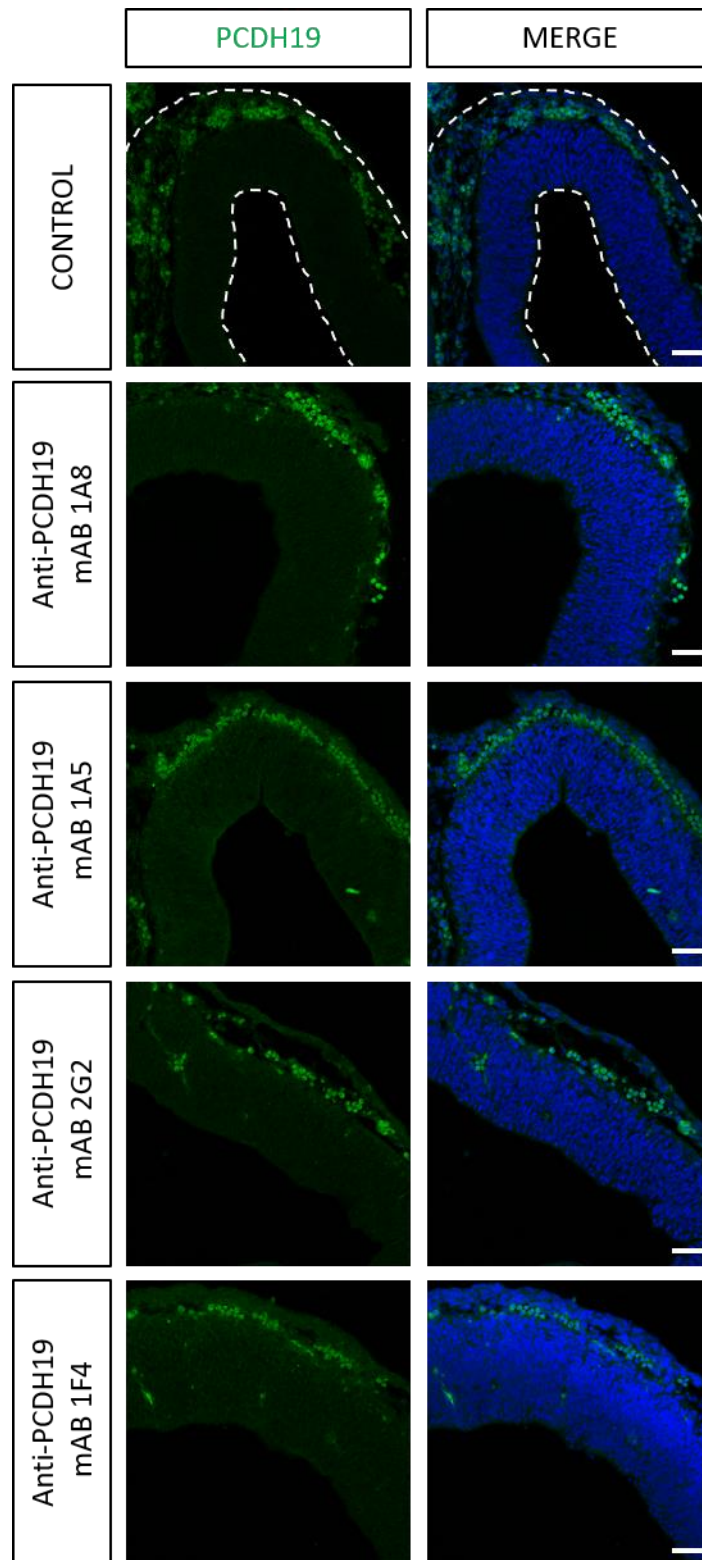


Figure A. 3. Anti-PCDH19 monoclonal antibodies 1A5, 1A8, 1F4 and 2G2, generated by Icosagen, did not detect PCDH19.

Representative images of IHC tests against PCDH19 on WT mouse brains at E11.5 at 20x. Monoclonal antibodies were used at a 1:100 dilution. Dashed lines signal the limits of the brains. PCDH19 is indicated in green, and DAPI counterstaining is in blue. Scale bar: 50 μ m. WT, Wild-type.

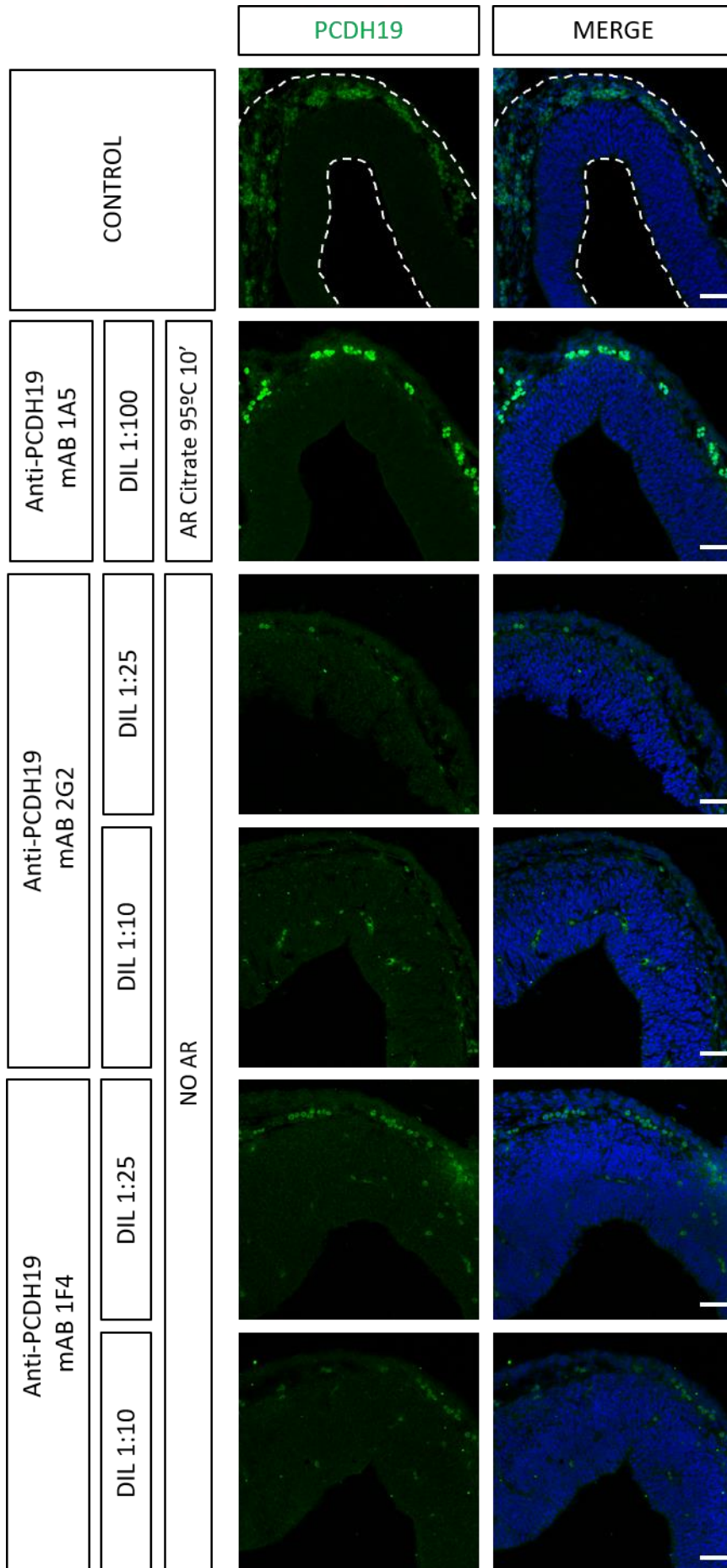


Figure A. 4. Antigen retrieval or higher antibody concentration did not improve the detection of PCDH19 by IHC using the monoclonal antibodies.

Representative images of IHC tests against PCDH19 on E11.5 WT mouse brains at 20x. Dashed lines signal the limits of the brains. PCDH19 is indicated in green, and DAPI counterstaining is in blue. Scale bar: 50 μm . WT, Wild-type.

	E11.5		P2				P10			
	Cryostat		Vibratome		Cryostat		Vibratome		Cryostat	
	No AR	AR	No AR	AR	No AR	AR	No AR	AR	No AR	AR
Commercial Ab	-	-	-	-	-	-	Y	- 70°C for 10' - 95° for 10', 20' or 30'	-	-
BGAL Ab	-	-	Y	- 3x5'' heat - 95°C for 30'	Y	-3x5'' boil -Heat 5' -ISH procedure -70°C, 10'	-	-	Y	95° for 10', 20' or 30'
X-gal	-	-	-	-	Y	-	-	-	Y	-
Generated Polyclonal Ab	Y, up to 1:100 dil	95° for 10', 20' or 30'	Y	-	Y	-	-	-	-	-
Generated Monoclonal Ab	Y, up to 1:10 dil	95° for 10', 20' or 30'	-	-	-	-	-	-	-	-

Table A. 1. Summary of all tried for the characterisation of *Pcdh19*-expressing cells.

AR, antigen retrieval with sodium citrate; Ab, antibody; dil, dilution; ISH, *in situ* hybridisation; Y, yes; -, not attempted.

E13.5 shRNA#2, #3 IUE in WT

BIN	QUANTIFICATION	STATISTICAL ANALYSIS
1	pCIG = 2.18 ± 1.24 %	Independent-samples Kruskal Wallis test, p = 0.53
	pCIG + shRNA control = 2.13 ± 0.81 %	
	pCIG + shRNA #2 = 1.49 ± 1.14 %	
	pCIG + shRNA #3 = 3.04 ± 2.82 %	
2	pCIG = 14.57 ± 1.53 %	ANOVA, F (3, 12) =1.509; p=0.262
	pCIG + shRNA control = 9.83 ± 0.51 %	
	pCIG + shRNA #2 = 10.57 ± 3.25 %	
	pCIG + shRNA #3 = 10.19 ± 1.76 %	
3	pCIG = 20.95 ± 3.26 %	ANOVA, F (3, 12) =1.434; p=0.281
	pCIG + shRNA control = 16.94 ± 1.05 %	
	pCIG + shRNA #2 = 14.29 ± 1.82 %	
	pCIG + shRNA #3 = 19.84 ± 2.31 %	
4	pCIG = 20.85 ± 1.51 %	ANOVA, F (3, 12) =2.019; p=0.165
	pCIG + shRNA control = 21.23 ± 1.8 %	
	pCIG + shRNA #2 = 17.71 ± 3.49 %	
	pCIG + shRNA #3 = 25.76 ± 2.51 %	
5	pCIG = 23.38 ± 2.63 %	ANOVA, F (3, 12) =0.736; p=0.551
	pCIG + shRNA control = 23.73 ± 1.99 %	
	pCIG + shRNA #2 = 17.78 ± 2.55 %	
	pCIG + shRNA #3 = 21.94 ± 3.37 %	
6	pCIG = 11.27 ± 2.36 %	ANOVA, F (3, 12) =1.175; p=0.36
	pCIG + shRNA control = 18.09 ± 1.01 %	
	pCIG + shRNA #2 = 15.71 ± 3.5 %	
	pCIG + shRNA #3 = 13.61 ± 3.11 %	
7	pCIG = 5.16 ± 1.83 %	ANOVA, F (3, 12)=4.3; p=0.028 Post-hoc test Tukey HSD, pCIG vs pCIG + shRNA control, p=0.927; pCIG vs pCIG + shRNA #2, p=0.046 ; pCIG vs pCIG + shRNA #3, p=0.996; pCIG + shRNA control vs pCIG + shRNA #2, p=0.119; pCIG + shRNA control vs pCIG + shRNA #3, p=0.821; pCIG + shRNA #2 vs pCIG + shRNA #3, p=0.025
	pCIG + shRNA control = 6.58 ± 1.64 %	
	pCIG + shRNA #2 = 12.75 ± 1.33 %	
	pCIG + shRNA #3 = 4.66 ± 1.54 %	
8	pCIG = 1.06 ± 0.83 %	Independent-samples Kruskal Wallis test, p = 0.102
	pCIG + shRNA control = 1.11 ± 0.38 %	
	pCIG + shRNA #2 = 7.11 ± 3.26 %	
	pCIG + shRNA #3 = 0.90 ± 0.44 %	
9	pCIG = 0.58 ± 0.58 %	Independent-samples Kruskal Wallis test, p = 0.464
	pCIG + shRNA control = 0.27 ± 0.22 %	
	pCIG + shRNA #2 = 1.93 ± 1.57 %	
	pCIG + shRNA #3 = 0.04 ± 0.04 %	
10	pCIG = 0 %	Independent-samples Kruskal Wallis test, p = 0.214
	pCIG + shRNA control = 0.09 ± 0.06 %	
	pCIG + shRNA #2 = 0.68 ± 0.68 %	
	pCIG + shRNA #3 = 0 %	

Table A. 2. Details of the statistical analysis of shRNAs #2, #3 IUE at E13.5 in WT animals.

E13.5 shRNA#5, #6 IUE in WT

BIN	QUANTIFICATION	STATISTICAL ANALYSIS
1	pCIG = 4.06 ± 1.06 %	ANOVA, F (3, 13) =3.17; p=0.06
	pCIG + shRNA control = 3.6 ± 0.81 %	
	pCIG + shRNA #5 = 3.23 ± 0.49 %	
	pCIG + shRNA #6 = 1.17 ± 0.22 %	
2	pCIG = 17.01 ± 1.96 %	ANOVA, F (3, 13) =2.834; p=0.079
	pCIG + shRNA control = 13.88 ± 1.6 %	
	pCIG + shRNA #5 = 19.16 ± 1.39 %	
	pCIG + shRNA #6 = 13.13 ± 1.94 %	
3	pCIG = 22.71 ± 1.25 %	Independent-samples Kruskal-Wallis test, p = 0.479
	pCIG + shRNA control = 20.76 ± 0.49 %	
	pCIG + shRNA #5 = 21.85 ± 1.53 %	
	pCIG + shRNA #6 = 19.23 ± 2.16 %	
4	pCIG = 24.77 ± 1.56 %	ANOVA, F (3, 13) =0.938; p=0.45
	pCIG + shRNA control = 24.36 ± 0.54 %	
	pCIG + shRNA #5 = 22.95 ± 0.91 %	
	pCIG + shRNA #6 = 22.91 ± 0.64 %	
5	pCIG = 19.29 ± 1.25 %	ANOVA, F (3, 13) =2.669; p=0.091
	pCIG + shRNA control = 22.2 ± 0.39 %	
	pCIG + shRNA #5 = 18.29 ± 1.67 %	
	pCIG + shRNA #6 = 22.13 ± 0.81 %	
6	pCIG = 8.66 ± 2.08 %	ANOVA, F (3, 13) =2.09; p=0.151
	pCIG + shRNA control = 11.99 ± 1.28 %	
	pCIG + shRNA #5 = 10.92 ± 1.98 %	
	pCIG + shRNA #6 = 15.19 ± 1.69 %	
7	pCIG = 3.19 ± 0.66 %	ANOVA, F (3, 13) =0.59; p=0.663
	pCIG + shRNA control = 2.39 ± 1.3 %	
	pCIG + shRNA #5 = 3.36 ± 1.8 %	
	pCIG + shRNA #6 = 5.18 ± 1.63 %	
8	pCIG = 0.30 ± 0.23 %	Independent-samples Kruskal-Wallis test, p = 0.571
	pCIG + shRNA control = 0.75 ± 0.72 %	
	pCIG + shRNA #5 = 0.24 ± 0.13 %	
	pCIG + shRNA #6 = 1.03 ± 0.52 %	
9	pCIG = 0 %	Independent-samples Kruskal-Wallis test, p = 0.492
	pCIG + shRNA control = 0.07 ± 0.07 %	
	pCIG + shRNA #5 = 0 %	
	pCIG + shRNA #6 = 0.04 ± 0.04 %	
10	pCIG = 0 %	Independent-samples Kruskal-Wallis test, p = 1
	pCIG + shRNA control = 0 %	
	pCIG + shRNA #5 = 0 %	
	pCIG + shRNA #6 = 0 %	

Table A. 3. Details of the statistical analysis of shRNAs #5, #6 IUE at E13.5 in WT animals.

E13.5 shRNA IUE in *Pcdh19*-KO

BIN	QUANTIFICATION	STATISTICAL ANALYSIS
1	pCIG + shRNA control = 0.03 ± 0.03 % and pCIG + shRNAmix = 0 %	independent samples t-test with equal variances not assumed, $t(3) = 1, p = 0.391$
2	pCIG + shRNA control = 7.36 ± 1.87 % and pCIG + shRNAmix = 5.12 ± 0.91 %	independent samples t-test, $t(7) = 1.149, p = 0.288$
3	pCIG + shRNA control = 17.81 ± 3.86 % and pCIG + shRNAmix = 16.53 ± 0.27 %	independent samples t-test with equal variances not assumed, $t(3.03) = 0.332, df = 3.03, p = 0.761$
4	pCIG + shRNA control = 17.57 ± 1.16 % and pCIG + shRNAmix = 19.89 ± 1.84 %	independent samples t-test, $t(7) = -1.000, p = 0.351$
5	pCIG + shRNA control = 19.52 ± 2.22 % and pCIG + shRNAmix = 20.41 ± 1.6 %	independent samples t-test with equal variances not assumed, $t(5.754) = -0.327, p = 0.755$
6	pCIG + shRNA control = 15.8 ± 3.72 % and pCIG + shRNAmix = 15.07 ± 1.09 %	independent samples t-test, $t(7) = 0.209, p = 0.84$
7	pCIG + shRNA control = 9.96 ± 1.27 % and pCIG + shRNAmix = 9.99 ± 1.13 %	independent samples t-test, $t(7) = -0.023, p = 0.983$
8	pCIG + shRNA control = 5.02 ± 0.64 % and pCIG + shRNAmix = 6.23 ± 1.63 %	independent samples t-test, $t(7) = -0.622, p = 0.554$
9	pCIG + shRNA control = 2.73 ± 1.45 % and pCIG + shRNAmix = 3.34 ± 1.24 %	independent samples t-test with equal variances not assumed, $t(6.41) = -0.321, p = 0.758$
10	pCIG + shRNA control = 0.74 ± 0.58 % and pCIG + shRNAmix = 1.64 ± 0.98 %	independent samples t-test, $t(7) = -0.731, p = 0.489$

Table A. 4. Details of the statistical analysis of shRNAs IUE at E13.5 in *Pcdh19*-KO animals.

IUE of shRNA control in WT and *Pcdh19*-KO

BIN	QUANTIFICATION	STATISTICAL ANALYSIS
1	WT = 2.88 ± 0.66 % and <i>Pcdh19</i> -KO = 0.03 ± 0.03 %	independent samples Mann-Whitney U test, p=0.004
2	WT = 11.84 ± 1.16 % and <i>Pcdh19</i> -KO = 7.36 ± 1.87 %	independent samples t-test, $t(10) = 2.122$, $df = 10$, $p = 0.06$
3	WT = 18.86 ± 0.87 % and <i>Pcdh19</i> -KO = 17.81 ± 3.86 %	independent samples t-test, $t(10) = 0.475$, $p = 0.645$
4	WT = 22.84 ± 0.83 % and <i>Pcdh19</i> -KO = 17.57 ± 1.16 %	independent samples t-test, $t(10) = 2.702$, p = 0.022
5	WT = 22.62 ± 0.95 % and <i>Pcdh19</i> -KO = 19.52 ± 2.22 %	independent samples t-test, $t(10) = 0.622$, $p = 0.548$
6	WT = 14.83 ± 1.4 % and <i>Pcdh19</i> -KO = 15.8 ± 3.72 %	independent samples t-test, $t(10) = -0.917$, $p = 0.381$
7	WT = 4.83 ± 1.36 % and <i>Pcdh19</i> -KO = 9.96 ± 1.27 %	independent samples Mann-Whitney U test, $p=0.109$
8	WT = 1.06 ± 0.42 % and <i>Pcdh19</i> -KO = 5.02 ± 0.64 %	independent samples Mann-Whitney U test, p=0.004
9	WT = 0.18 ± 0.11 % and <i>Pcdh19</i> -KO = 2.73 ± 1.45 %	independent samples Mann-Whitney U test, p=0.028
10	WT = 0.05 ± 0.03 % and <i>Pcdh19</i> -KO = 0.74 ± 0.58 %	independent samples Mann-Whitney U test, $p=0.214$

Table A. 5. Details of the statistical analysis of shRNA control IUE at E13.5 in WT and *Pcdh19*-KO animals.

E13.5 EGFP IUE

BIN	QUANTIFICATION	STATISTICAL ANALYSIS
1	WT = 0.04 ± 0.04 %, <i>Pcdh19</i> -HET = 0.72 ± 0.43 % and <i>Pcdh19</i> -KO = 0.08 ± 0.08 %	Independent-samples Kruskal-Wallis test, $p = 0.295$
2	WT = 5.23 ± 0.56 %, <i>Pcdh19</i> -HET = 6.33 ± 1.21 % and <i>Pcdh19</i> -KO = 2.08 ± 0.33 %	Independent-samples Kruskal-Wallis test, $p = 0.019$. Pair-wise comparisons post-hoc test WT vs <i>Pcdh19</i> -HET, $p=1$; WT vs <i>Pcdh19</i> -KO, $p=0.059$; <i>Pcdh19</i> -HET vs. <i>Pcdh19</i> -KO, $p=0.027$
3	WT = 14.38 ± 1.17 %, <i>Pcdh19</i> -HET = 12.31 ± 0.41 % and <i>Pcdh19</i> -KO = 9.77 ± 1.16 %	ANOVA, $F(2, 12)=4.352$; $p=0.038$ Post-hoc test Tukey HSD, WT vs <i>Pcdh19</i> -HET, $p=0.411$; WT vs <i>Pcdh19</i> -KO, $p=0.031$; <i>Pcdh19</i> -HET vs. <i>Pcdh19</i> -KO, $p=0.356$
4	WT = 18.55 ± 0.92 %, <i>Pcdh19</i> -HET = 21.36 ± 2.96 % and <i>Pcdh19</i> -KO = 17.41 ± 1.97 %	Independent-samples Kruskal-Wallis test, $p = 0.363$
5	WT = 20.87 ± 0.47 %, <i>Pcdh19</i> -HET = 25.74 ± 2.2 % and <i>Pcdh19</i> -KO = 20 ± 2.8 %	ANOVA, $F(2, 12) = 3.002$; $p=0.088$
6	WT = 19.33 ± 1.03 %, <i>Pcdh19</i> -HET = 17.7 ± 0.81 % and <i>Pcdh19</i> -KO = 20.75 ± 1.58 %	Independent-samples Kruskal-Wallis test, $p = 0.144$
7	WT = 13.19 ± 1.17 %, <i>Pcdh19</i> -HET = 8.58 ± 1.96 % and <i>Pcdh19</i> -KO = 17.75 ± 1.65 %	ANOVA, $F(2, 12) = 7.382$; $p=0.008$ Post-hoc test Tukey HSD, WT vs <i>Pcdh19</i> -HET, $p=0.305$; WT vs <i>Pcdh19</i> -KO, $p=0.159$; <i>Pcdh19</i> -HET vs. <i>Pcdh19</i> -KO, $p=0.006$
8	WT = 5.19 ± 0.71 %, <i>Pcdh19</i> -HET = 1.98 ± 0.53 % and <i>Pcdh19</i> -KO = 9.3 ± 2.98 %	ANOVA, $F(2, 12) = 4.933$; $p=0.027$ Post-hoc test Games-Howell, WT vs <i>Pcdh19</i> -HET, $p=0.116$; WT vs <i>Pcdh19</i> -KO, $p=0.12$; <i>Pcdh19</i> -HET vs. <i>Pcdh19</i> -KO, $p=0.022$
9	WT = 2.57 ± 0.55 %, <i>Pcdh19</i> -HET = 1.05 ± 0.45 % and <i>Pcdh19</i> -KO = 1.94 ± 0.43 %	ANOVA, $F(2, 12) = 2.036$; $p=0.173$
10	WT = 0.65 ± 0.1 %, <i>Pcdh19</i> -HET = 0.2 ± 0.11 % and <i>Pcdh19</i> -KO = 0.92 ± 0.4 %	ANOVA, $F(2, 12) = 2.596$; $p=0.116$

Table A. 6. Details of the statistical analysis of EGFP IUE at E13.5 in WT, *Pcdh19*-HET and *Pcdh19*-KO animals.

E15.5 shRNA IUE in WT

BIN	QUANTIFICATION	STATISTICAL ANALYSIS
1	pCIG + shRNA control = 2.84 ± 1.95 % and pCIG + shRNAmix = 16.67 ± 1.65 %	independent samples t-test, $t(6) = -5.334$; p=0.002
2	pCIG + shRNA control = 34.56 ± 8.60 % and pCIG + shRNAmix = 58.77 ± 3.85 %	independent samples t-test, $t(6) = -2.417$; p=0.052
3	pCIG + shRNA control = 33.31 ± 5.11 % and pCIG + shRNAmix = 21.26 ± 5.95 %	independent samples Mann-Whitney U test, p=0.2
4	pCIG + shRNA control = 3.93 ± 0.91 % and pCIG + shRNAmix = 0.54 ± 0.18 %	independent samples t-test, $t(6) = 3.507$; p=0.013
5	pCIG + shRNA control = 1.55 ± 0.12 % and pCIG + shRNAmix = 0.58 ± 0.39 %	independent samples Mann-Whitney U test, p=0.2
6	pCIG + shRNA control = 1.13 ± 0.35 % and pCIG + shRNAmix = 0.28 ± 0.17 %	independent samples t-test, $t(6) = 2.098$; p=0.089
7	pCIG + shRNA control = 2.10 ± 0.29 % and pCIG + shRNAmix = 0.19 ± 0.11 %	independent samples Mann-Whitney U test, p=0.029
8	pCIG + shRNA control = 3.52 ± 0.61 % and pCIG + shRNAmix = 0.32 ± 0.11 %	independent samples Mann-Whitney U test, p=0.029
9	pCIG + shRNA control = 6.50 ± 1.03 % and pCIG + shRNAmix = 0.54 ± 0.18 %	independent samples t-test, $t(6) = 5.506$; p=0.002
10	pCIG + shRNA control = 10.55 ± 3.39 % and pCIG + shRNAmix = 0.86 ± 0.36 %	independent samples t-test with equal variances not assumed, $t(2.825) = 3.065$, p=0.062

Table A. 7. Details of the statistical analysis of shRNAs IUE at E15.5 in WT animals.

E15.5 shRNA IUE in *Pcdh19*-KO

BIN	QUANTIFICATION	STATISTICAL ANALYSIS
1	pCIG + shRNA control = 1.76 ± 0.78 % and pCIG + shRNAmix = 32.28 ± 7.35 %	independent samples t-test, t (6) = -4.13, p = 0.006
2	pCIG + shRNA control = 19.03 ± 2.27 % and pCIG + shRNAmix = 47.49 ± 7.34 %	independent samples t-test, t (6) = -3.703, p = 0.01
3	pCIG + shRNA control = 45.25 ± 2.84 % and pCIG + shRNAmix = 22.82 ± 9.91 %	independent samples t-test, t (6) = 2.177, p = 0.072
4	pCIG + shRNA control = 9.77 ± 3.17 % and pCIG + shRNAmix = 3.12 ± 1.66 %	independent samples Mann-Whitney U test, p = 0.057
5	pCIG + shRNA control = 3.81 ± 0.70 % and pCIG + shRNAmix = 1.21 ± 0.92 %	independent samples Mann-Whitney U test, p = 0.057
6	pCIG + shRNA control = 1.52 ± 0.50 % and pCIG + shRNAmix = 0.15 ± 0.09 %	independent samples t-test with equal variances not assumed, t (6) = 2.679, p = 0.037
7	pCIG + shRNA control = 1.71 ± 0.75 % and pCIG + shRNAmix = 0.15 ± 0.09 %	independent samples t-test with equal variances not assumed, t (6) = 2.079, p = 0.127
8	pCIG + shRNA control = 2.40 ± 0.79 % and pCIG + shRNAmix = 0.56 ± 0.05 %	independent samples t-test with equal variances not assumed, t (6) = 2.328, p = 0.102
9	pCIG + shRNA control = 6.08 ± 1.07 % and pCIG + shRNAmix = 0.79 ± 0.21 %	independent samples t-test with equal variances not assumed, t (6) = 4.852, df = 3.231, p = 0.014
10	pCIG + shRNA control = 8.49 ± 2.26 % and pCIG + shRNAmix = 1.52 ± 0.30 %	independent samples t-test with equal variances not assumed, t (3.108) = 3.065, p = 0.052

Table A. 8. Details of the statistical analysis of shRNAs IUE at E15.5 in *Pcdh19*-KO animals.

E15.5 EGFP IUE

BIN	QUANTIFICATION	STATISTICAL ANALYSIS
1	WT = 2.56 ± 1.37 %, <i>Pcdh19</i> -HET = 1.41 ± 0.53 % and <i>Pcdh19</i> -KO = 5.09 ± 1.6 %	Independent-samples Kruskal-Wallis test, $p = 0.166$
2	WT = 23.13 ± 4.24 %, <i>Pcdh19</i> -HET = 17.15 ± 4.36 % and <i>Pcdh19</i> -KO = 42.67 ± 4.75 %	ANOVA, $F(2, 11) = 9.037$; $p = 0.005$ Post-hoc test Tukey HSD, WT vs <i>Pcdh19</i> -HET, $p = 0.577$; WT vs <i>Pcdh19</i> -KO, $p = 0.023$; <i>Pcdh19</i> -HET vs. <i>Pcdh19</i> -KO, $p = 0.004$
3	WT = 63.25 ± 4.76 %, <i>Pcdh19</i> -HET = 56.95 ± 7.64 % and <i>Pcdh19</i> -KO = 48.96 ± 6.19 %	Independent-samples Kruskal-Wallis test, $p = 0.277$
4	WT = 7.54 ± 2.81 %, <i>Pcdh19</i> -HET = 19.26 ± 6.15 % and <i>Pcdh19</i> -KO = 1.36 ± 0.47 %	ANOVA, $F(2, 11) = 9.037$; $p = 0.02$ Post-hoc test Games-Howell, WT vs <i>Pcdh19</i> -HET, $p = 0.207$; WT vs <i>Pcdh19</i> -KO, $p = 0.186$; <i>Pcdh19</i> -HET vs. <i>Pcdh19</i> -KO, $p = 0.06$
5	WT = 0.22 ± 0.11 %, <i>Pcdh19</i> -HET = 0.46 ± 0.22 % and <i>Pcdh19</i> -KO = 0 %	Independent-samples Kruskal-Wallis test, $p = 0.072$
6	WT = 0.21 ± 0.11 %, <i>Pcdh19</i> -HET = 0.26 ± 0.06 % and <i>Pcdh19</i> -KO = 0.05 ± 0.05 %	Independent-samples Kruskal-Wallis test, $p = 0.292$
7	WT = 0.16 ± 0.08 %, <i>Pcdh19</i> -HET = 0.58 ± 0.41 % and <i>Pcdh19</i> -KO = 0 %	Independent-samples Kruskal-Wallis test, $p = 0.144$
8	WT = 0.43 ± 0.26 %, <i>Pcdh19</i> -HET = 0.65 ± 0.56 % and <i>Pcdh19</i> -KO = 0.34 ± 0.24 %	Independent-samples Kruskal-Wallis test, $p = 0.912$
9	WT = 0.94 ± 0.42 %, <i>Pcdh19</i> -HET = 0.67 ± 0.39 % and <i>Pcdh19</i> -KO = 0.18 ± 0.11 %	ANOVA, $F(2, 11) = 1.124$; $p = 0.359$
10	WT = 1.56 ± 0.53 %, <i>Pcdh19</i> -HET = 2.57 ± 1.24 % and <i>Pcdh19</i> -KO = 1.35 ± 0.82 %	ANOVA, $F(2, 11) = 0.561$; $p = 0.586$

Table A. 9. Details of the statistical analysis of EGFP IUE at E15.5 in WT, *Pcdh19*-HET and *Pcdh19*-KO animals.

P10 DAPI

BIN	QUANTIFICATION	STATISTICAL ANALYSIS
1	WT = 9 ± 0.28 %, <i>Pcdh19</i> -HET = 9.09 ± 0.37 % and <i>Pcdh19</i> -KO = 8.99 ± 0.37 %	Independent-samples Kruskal-Wallis test, $p = 0.844$
2	WT = 11.05 ± 0.28 %, <i>Pcdh19</i> -HET = 11.09 ± 0.15 % and <i>Pcdh19</i> -KO = 10.96 ± 0.37 %	ANOVA, $F(2, 17) = 0.063$; $p = 0.94$
3	WT = 12.36 ± 0.18 %, <i>Pcdh19</i> -HET = 12.63 ± 0.35 % and <i>Pcdh19</i> -KO = 12.85 ± 0.38 %	Independent-samples Kruskal-Wallis test, $p = 0.56$
4	WT = 12.19 ± 0.36 %, <i>Pcdh19</i> -HET = 11.37 ± 11.37 % and <i>Pcdh19</i> -KO = 11.54 ± 0.36 %	ANOVA, $F(2, 17) = 1.239$; $p = 0.315$
5	WT = 7.49 ± 0.05 %, <i>Pcdh19</i> -HET = 7.75 ± 0.16 % and <i>Pcdh19</i> -KO = 7.54 ± 0.11 %	ANOVA, $F(2, 17) = 1.176$; $p = 0.332$
6	WT = 7.78 ± 0.13 %, <i>Pcdh19</i> -HET = 8.04 ± 0.16 % and <i>Pcdh19</i> -KO = 8.01 ± 0.2 %	ANOVA, $F(2, 17) = 0.732$; $p = 0.495$
7	WT = 10.26 ± 0.13 %, <i>Pcdh19</i> -HET = 10.42 ± 0.24 % and <i>Pcdh19</i> -KO = 10.72 ± 0.2 %	ANOVA, $F(2, 17) = 0.932$; $p = 0.413$
8	WT = 9.89 ± 0.23 %, <i>Pcdh19</i> -HET = 10.34 ± 0.15 % and <i>Pcdh19</i> -KO = 10.36 ± 0.27 %	ANOVA, $F(2, 17) = 1.606$; $p = 0.23$
9	WT = 8.96 ± 0.22 %, <i>Pcdh19</i> -HET = 8.83 ± 0.19 % and <i>Pcdh19</i> -KO = 8.96 ± 0.32 %	ANOVA, $F(2, 17) = 0.126$; $p = 0.882$
10	WT = 10.96 ± 0.33 %, <i>Pcdh19</i> -HET = 10.45 ± 0.43 % and <i>Pcdh19</i> -KO = 10.08 ± 0.3 %	ANOVA, $F(2, 17) = 1.001$; $p = 0.388$

Table A. 10. Details of the statistical analysis of DAPI distribution in P10 animals.

P10 CUX1

BIN	QUANTIFICATION	STATISTICAL ANALYSIS
1	WT = 7.36 ± 1.03 %, <i>Pcdh19</i> -HET = 10.32 ± 1.64 % and <i>Pcdh19</i> -KO = 10.74 ± 0.62 %	ANOVA, F (2, 9) =2.461; p=0.14
2	WT = 23.74 ± 0.36 %, <i>Pcdh19</i> -HET = 25.91 ± 1.41 % and <i>Pcdh19</i> -KO = 25.22 ± 1.12 %	Independent-samples Kruskal-Wallis test, p = 0.39
3	WT = 32.98 ± 1.19 %, <i>Pcdh19</i> -HET = 35.7 ± 1.56 % and <i>Pcdh19</i> -KO = 37.15 ± 2.16 %	ANOVA, F (2, 9) =1.574; p=0.259
4	WT = 28.18 ± 3.4 %, <i>Pcdh19</i> -HET = 25.17 ± 0.27 % and <i>Pcdh19</i> -KO = 22.52 ± 2.44 %	ANOVA, F (2, 9) =0.744; p=0.502
5	WT = 2.08 ± 0.18 %, <i>Pcdh19</i> -HET = 0.86 ± 0.13 % and <i>Pcdh19</i> -KO = 1.14 ± 0.32 %	ANOVA, F (2, 9) =5.82; p=0.024 Post-hoc test Tukey HSD, WT vs <i>Pcdh19</i> -HET, p=0.024 ; WT vs <i>Pcdh19</i> -KO, p=0.077; <i>Pcdh19</i> -HET vs. <i>Pcdh19</i> -KO, p=0.75
6	WT = 2.24 ± 0.41 %, <i>Pcdh19</i> -HET = 0.75 ± 0.32 % and <i>Pcdh19</i> -KO = 1.43 ± 0.43 %	ANOVA, F (2, 9) =3.651; p=0.069
7	WT = 2.32 ± 0.73 %, <i>Pcdh19</i> -HET = 0.87 ± 0.1 % and <i>Pcdh19</i> -KO = 0.86 ± 0.25 %	ANOVA, F (2, 9) =3.547; p=0.073
8	WT = 0.78 ± 0.41 %, <i>Pcdh19</i> -HET = 0.19 ± 0.07 % and <i>Pcdh19</i> -KO = 0.21 ± 0.07 %	ANOVA, F (2, 9) =1.851; p=0.212
9	WT = 0.2 ± 0.1 %, <i>Pcdh19</i> -HET = 0.14 ± 0.03 % and <i>Pcdh19</i> -KO = 0.34 ± 0.18 %	Independent-samples Kruskal-Wallis test, p = 0.793
10	WT = 0.11 ± 0.05 %, <i>Pcdh19</i> -HET = 0.08 ± 0.08 % and <i>Pcdh19</i> -KO = 0.39 ± 0.22 %	Independent-samples Kruskal-Wallis test, p = 0.276

Table A. 11. Details of the statistical analysis of CUX1 distribution in P10 animals.

P10 SATB2

BIN	QUANTIFICATION	STATISTICAL ANALYSIS
1	WT = 2.71 ± 0.78 %, <i>Pcdh19</i> -HET = 2.03 ± 0.87 % and <i>Pcdh19</i> -KO = 4.5 ± 0.33 %	ANOVA, F (2, 9) =1.28; p=0.324
2	WT = 5.6 ± 1.68 %, <i>Pcdh19</i> -HET = 7.55 ± 0.65 % and <i>Pcdh19</i> -KO = 8.97 ± 1.09 %	ANOVA, F (2, 9) =0.228; p=0.8
3	WT = 12.77 ± 2.35 %, <i>Pcdh19</i> -HET = 11.1 ± 0.92 % and <i>Pcdh19</i> -KO = 14.58 ± 0.37 %	ANOVA, F (2, 9) =0.072; p=0.931
4	WT = 5.52 ± 1.9 %, <i>Pcdh19</i> -HET = 5.49 ± 1.63 % and <i>Pcdh19</i> -KO = 5.63 ± 2.13 %	ANOVA, F (2, 9) =1.266; p=0.328
5	WT = 4.97 ± 0.71 %, <i>Pcdh19</i> -HET = 7.46 ± 0.35 % and <i>Pcdh19</i> -KO = 4.34 ± 0.41 %	ANOVA, F (2, 9) =0.272; p=0.768
6	WT = 8.47 ± 0.92 %, <i>Pcdh19</i> -HET = 10.21 ± 1.11 % and <i>Pcdh19</i> -KO = 8.55 ± 1.06 %	ANOVA, F (2, 9) =0.418; p=0.671
7	WT = 21.87 ± 1.92 %, <i>Pcdh19</i> -HET = 20.4 ± 2.19 % and <i>Pcdh19</i> -KO = 19.58 ± 1.46 %	Independent-samples Kruskal-Wallis test, p = 0.232
8	WT = 21.8 ± 1.74 %, <i>Pcdh19</i> -HET = 20.29 ± 1.19 % and <i>Pcdh19</i> -KO = 19.25 ± 0.69 %	ANOVA, F (2, 9) =0.19; p=0.83
9	WT = 15.32 ± 1.45 %, <i>Pcdh19</i> -HET = 14.15 ± 1.3 % and <i>Pcdh19</i> -KO = 13.81 ± 1.39 %	ANOVA, F (2, 9) =0.349; p=0.714
10	WT = 0.97 ± 0.87 %, <i>Pcdh19</i> -HET = 1.33 ± 0.73 % and <i>Pcdh19</i> -KO = 0.8 ± 0.46 %	ANOVA, F (2, 9) =0.43; p=0.663

Table A. 12. Details of the statistical analysis of SATB2 distribution in P10 animals.

P10 RORB

BIN	QUANTIFICATION	STATISTICAL ANALYSIS
1	WT = 2.74 ± 0.57 %, <i>Pcdh19</i> -HET = 2.57 ± 0.63 % and <i>Pcdh19</i> -KO = 1.38 ± 1.38 %	Independent-samples Kruskal-Wallis test, p = 0.385
2	WT = 7.43 ± 0.87 %, <i>Pcdh19</i> -HET = 6.06 ± 1.95 % and <i>Pcdh19</i> -KO = 3.36 ± 2.37 %	ANOVA, F (2, 9) = 1.269; p=0.327
3	WT = 29.47 ± 2.52 %, <i>Pcdh19</i> -HET = 32.43 ± 2.22 % and <i>Pcdh19</i> -KO = 33.89 ± 5.57 %	ANOVA, F (2, 9) = 0.36; p=0.707
4	WT = 33.03 ± 1.5 %, <i>Pcdh19</i> -HET = 31.02 ± 7.08 % and <i>Pcdh19</i> -KO = 45.37 ± 7.58 %	ANOVA, F (2, 9) = 1.647; p=0.246
5	WT = 9.51 ± 0.51 %, <i>Pcdh19</i> -HET = 8.12 ± 0.66 % and <i>Pcdh19</i> -KO = 7.33 ± 1.27 %	ANOVA, F (2, 9) = 1.585; p=0.257
6	WT = 6.28 ± 0.71 %, <i>Pcdh19</i> -HET = 5.75 ± 1.34 % and <i>Pcdh19</i> -KO = 3.62 ± 1.6 %	ANOVA, F (2, 9) = 1.228; p=0.338
7	WT = 3.56 ± 0.62 %, <i>Pcdh19</i> -HET = 4.58 ± 1.83 % and <i>Pcdh19</i> -KO = 1.54 ± 1.3 %	Independent-samples Kruskal-Wallis test, p = 0.383
8	WT = 3.61 ± 1.14 %, <i>Pcdh19</i> -HET = 3.85 ± 1.38 % and <i>Pcdh19</i> -KO = 1.31 ± 1 %	Independent-samples Kruskal-Wallis test, p = 0.39
9	WT = 2.66 ± 0.85 %, <i>Pcdh19</i> -HET = 3.06 ± 1.1 % and <i>Pcdh19</i> -KO = 1.17 ± 0.84 %	Independent-samples Kruskal-Wallis test, p = 0.39
10	WT = 1.72 ± 0.93 %, <i>Pcdh19</i> -HET = 2.57 ± 1.46 % and <i>Pcdh19</i> -KO = 1.03 ± 1.03 %	Independent-samples Kruskal-Wallis test, p = 0.339

Table A. 13. Details of the statistical analysis of RORB distribution in P10 animals.

P10 CTIP2

BIN	QUANTIFICATION	STATISTICAL ANALYSIS
1	WT = 3.2 ± 0.54 %, <i>Pcdh19</i> -HET = 4.42 ± 0.29 % and <i>Pcdh19</i> -KO = 4.41 ± 0.32 %	ANOVA, F (2, 9) =3.091; p=0.095
2	WT = 3.7 ± 0.28 %, <i>Pcdh19</i> -HET = 3.88 ± 0.43 % and <i>Pcdh19</i> -KO = 3.66 ± 0.6 %	ANOVA, F (2, 9) =0.071; p=0.932
3	WT = 3.15 ± 0.48 %, <i>Pcdh19</i> -HET = 3.12 ± 0.5 % and <i>Pcdh19</i> -KO = 4.17 ± 0.34 %	ANOVA, F (2, 9) =1.786; p=0.222
4	WT = 4.61 ± 0.2 %, <i>Pcdh19</i> -HET = 3.92 ± 0.63 % and <i>Pcdh19</i> -KO = 4.15 ± 0.17 %	ANOVA, F (2, 9) =0.783; p=0.486
5	WT = 15.13 ± 1.59 %, <i>Pcdh19</i> -HET = 12.3 ± 2.41 % and <i>Pcdh19</i> -KO = 16.32 ± 2.41 %	ANOVA, F (2, 9) =0.907; p=0.438
6	WT = 20.21 ± 1.47 %, <i>Pcdh19</i> -HET = 17.89 ± 1.71 % and <i>Pcdh19</i> -KO = 19.24 ± 2.58 %	ANOVA, F (2, 9) =0.347; p=0.716
7	WT = 13.29 ± 0.83 %, <i>Pcdh19</i> -HET = 11.82 ± 2.27 % and <i>Pcdh19</i> -KO = 10.68 ± 0.34 %	ANOVA, F (2, 9) =0.86; p=0.455
8	WT = 20.61 ± 1.2 %, <i>Pcdh19</i> -HET = 23.14 ± 2.07 % and <i>Pcdh19</i> -KO = 22.04 ± 1.33 %	ANOVA, F (2, 9) =0.642; p=0.549
9	WT = 15.44 ± 1.38 %, <i>Pcdh19</i> -HET = 18.85 ± 1.27 % and <i>Pcdh19</i> -KO = 14.45 ± 2.17 %	ANOVA, F (2, 9) =1.943; p=0.199
10	WT = 0.66 ± 0.05 %, <i>Pcdh19</i> -HET = 0.66 ± 0.12 % and <i>Pcdh19</i> -KO = 0.9 ± 0.33 %	ANOVA, F (2, 9) =0.456; p=0.648

Table A. 14. Details of the statistical analysis of CTIP2 distribution in P10 animals.

P10 TBR1

BIN	QUANTIFICATION	STATISTICAL ANALYSIS
1	WT = 2.71 ± 0.78 %, <i>Pcdh19</i> -HET = 2.03 ± 0.87 % and <i>Pcdh19</i> -KO = 4.5 ± 0.33 %	ANOVA, F (2, 9) =3.294; p=0.084
2	WT = 5.6 ± 1.68 %, <i>Pcdh19</i> -HET = 7.55 ± 0.65 % and <i>Pcdh19</i> -KO = 8.97 ± 1.09 %	ANOVA, F (2, 9) =1.929; p=0.201
3	WT = 12.77 ± 2.35 %, <i>Pcdh19</i> -HET = 11.1 ± 0.92 % and <i>Pcdh19</i> -KO = 14.58 ± 0.37 %	ANOVA, F (2, 9) =1.398; p=0.296
4	WT = 5.52 ± 1.9 %, <i>Pcdh19</i> -HET = 5.49 ± 1.63 % and <i>Pcdh19</i> -KO = 5.63 ± 2.13 %	ANOVA, F (2, 9) =0.002; p=0.998
5	WT = 4.97 ± 0.71 %, <i>Pcdh19</i> -HET = 7.46 ± 0.35 % and <i>Pcdh19</i> -KO = 4.34 ± 0.41 %	Independent-samples Kruskal-Wallis test, p = 0.018 . Pair-wise comparisons post-hoc test WT vs <i>Pcdh19</i> -HET, p=0.15; WT vs <i>Pcdh19</i> -KO, p=1; <i>Pcdh19</i> -HET vs. <i>Pcdh19</i> -KO, p=0.018
6	WT = 8.47 ± 0.92 %, <i>Pcdh19</i> -HET = 10.21 ± 1.11 % and <i>Pcdh19</i> -KO = 8.55 ± 1.06 %	ANOVA, F (2, 9) =0.905; p=0.438
7	WT = 21.87 ± 1.92 %, <i>Pcdh19</i> -HET = 20.4 ± 2.19 % and <i>Pcdh19</i> -KO = 19.58 ± 1.46 %	ANOVA, F (2, 9) =0.381; p=0.694
8	WT = 21.8 ± 1.74 %, <i>Pcdh19</i> -HET = 20.29 ± 1.19 % and <i>Pcdh19</i> -KO = 19.25 ± 0.69 %	Independent-samples Kruskal-Wallis test, p = 0.735
9	WT = 15.32 ± 1.45 %, <i>Pcdh19</i> -HET = 14.15 ± 1.3 % and <i>Pcdh19</i> -KO = 13.81 ± 1.39 %	ANOVA, F (2, 9) =0.33; p=0.727
10	WT = 0.97 ± 0.87 %, <i>Pcdh19</i> -HET = 1.33 ± 0.73 % and <i>Pcdh19</i> -KO = 0.8 ± 0.46 %	Independent-samples Kruskal-Wallis test, p = 0.695

P10 TBR1 DL

BIN	QUANTIFICATION	STATISTICAL ANALYSIS
7	WT = 37.14 ± 1.05 %, <i>Pcdh19</i> -HET = 37.1 ± 3.16 % and <i>Pcdh19</i> -KO = 38.51 ± 1.6 %	ANOVA, F (2, 9) =2.093; p=0.179
8	WT = 36.99 ± 0.62 %, <i>Pcdh19</i> -HET = 37.01 ± 1.14 % and <i>Pcdh19</i> -KO = 36.64 ± 0.46 %	ANOVA, F (2, 9) =0.272; p=0.768
9	WT = 25.88 ± 0.47 %, <i>Pcdh19</i> -HET = 25.89 ± 2.4 % and <i>Pcdh19</i> -KO = 24.85 ± 1.94 %	Independent-samples Kruskal-Wallis test, p = 0.147

Table A. 15. Details of the statistical analysis of TBR1 distribution in P10 animals.

P20 DAPI

BIN	QUANTIFICATION	STATISTICAL ANALYSIS
1	WT = 7.22 ± 0.81 %, <i>Pcdh19</i> -HET = 7.15 ± 0.16 % and <i>Pcdh19</i> -KO = 7.84 ± 0.64 %	ANOVA, F (2, 9) =0.395; p=0.685
2	WT = 9.94 ± 0.29 %, <i>Pcdh19</i> -HET = 10.51 ± 0.14 % and <i>Pcdh19</i> -KO = 10.33 ± 0.33 %	Independent-samples Kruskal-Wallis test, p = 0.236
3	WT = 10.65 ± 0.23 %, <i>Pcdh19</i> -HET = 10.64 ± 0.14 % and <i>Pcdh19</i> -KO = 10.7 ± 0.28 %	ANOVA, F (2, 9) =0.024; p=0.976
4	WT = 13.19 ± 0.28 %, <i>Pcdh19</i> -HET = 13.37 ± 0.16 % and <i>Pcdh19</i> -KO = 13.72 ± 0.23 %	ANOVA, F (2, 9) =1.441; p=0.286
5	WT = 9.34 ± 0.37 %, <i>Pcdh19</i> -HET = 9.16 ± 0.13 % and <i>Pcdh19</i> -KO = 8.98 ± 0.23 %	ANOVA, F (2, 9) =0.478; p=0.635
6	WT = 8.77 ± 0.18 %, <i>Pcdh19</i> -HET = 8.61 ± 0.08 % and <i>Pcdh19</i> -KO = 8.71 ± 0.13 %	ANOVA, F (2, 9) =0.348; p=0.715
7	WT = 9.99 ± 0.3 %, <i>Pcdh19</i> -HET = 10.16 ± 0.11 % and <i>Pcdh19</i> -KO = 9.78 ± 0.09 %	Independent-samples Kruskal-Wallis test, p = 0.167
8	WT = 10.5 ± 0.26 %, <i>Pcdh19</i> -HET = 10.5 ± 0.27 % and <i>Pcdh19</i> -KO = 10.26 ± 0.26 %	ANOVA, F (2, 9) =0.268; p=0.771
9	WT = 9.75 ± 0.34 %, <i>Pcdh19</i> -HET = 9.54 ± 0.22 % and <i>Pcdh19</i> -KO = 9.47 ± 0.31 %	ANOVA, F (2, 9) =0.249; p=0.785
10	WT = 10.64 ± 0.15 %, <i>Pcdh19</i> -HET = 10.36 ± 0.16 % and <i>Pcdh19</i> -KO = 10.21 ± 0.56 %	ANOVA, F (2, 9) =0.39; p=0.688

Table A. 16. Details of the statistical analysis of DAPI distribution in P20 animals.

P20 PV

BIN	QUANTIFICATION	STATISTICAL ANALYSIS
1	WT = 1.49 ± 0.35 %, <i>Pcdh19</i> -HET = 1.21 ± 0.18 % and <i>Pcdh19</i> -KO = 1.39 ± 0.46 %	ANOVA, F (2, 9) =0.158; p=0.856
2	WT = 9.69 ± 3.73 %, <i>Pcdh19</i> -HET = 9.97 ± 0.71 % and <i>Pcdh19</i> -KO = 11.26 ± 1.24 %	ANOVA, F (2, 9) =0.131; p=0.879
3	WT = 10.49 ± 1.55 %, <i>Pcdh19</i> -HET = 8.49 ± 0.57 % and <i>Pcdh19</i> -KO = 9.27 ± 1.18 %	ANOVA, F (2, 9) =0.739; p=0.504
4	WT = 16.92 ± 1.98 %, <i>Pcdh19</i> -HET = 16.98 ± 1.86 % and <i>Pcdh19</i> -KO = 15.96 ± 1.89 %	ANOVA, F (2, 9) =0.09; p=0.914
5	WT = 17.27 ± 1.67 %, <i>Pcdh19</i> -HET = 19.96 ± 2.91 % and <i>Pcdh19</i> -KO = 17.72 ± 0.87 %	ANOVA, F (2, 9) =0.523; p=0.61
6	WT = 17.02 ± 1.65 %, <i>Pcdh19</i> -HET = 18.18 ± 1.43 % and <i>Pcdh19</i> -KO = 17.42 ± 1.69 %	ANOVA, F (2, 9) =0.139; p=0.872
7	WT = 14.62 ± 3.47 %, <i>Pcdh19</i> -HET = 14.43 ± 1.2 % and <i>Pcdh19</i> -KO = 16.36 ± 1.02 %	ANOVA, F (2, 9) =0.231; p=0.798
8	WT = 8.03 ± 1.82 %, <i>Pcdh19</i> -HET = 8.61 ± 0.44 % and <i>Pcdh19</i> -KO = 7.59 ± 2.02 %	ANOVA, F (2, 9) =0.104; p=0.902
9	WT = 2.3 ± 0.73 %, <i>Pcdh19</i> -HET = 1.81 ± 0.44 % and <i>Pcdh19</i> -KO = 2.91 ± 0.59 %	ANOVA, F (2, 9) =0.857; p=0.456
10	WT = 2.18 ± 1.24 %, <i>Pcdh19</i> -HET = 0.34 ± 0.22 % and <i>Pcdh19</i> -KO = 0.13 ± 0.13 %	Independent-samples Kruskal-Wallis test, p = 0.336

Table A. 17. Details of the statistical analysis of PV distribution in P20 animals.

P20 CR SSC

BIN	QUANTIFICATION	STATISTICAL ANALYSIS
1	WT = 5.64 ± 2.35 %, <i>Pcdh19</i> -HET = 7.13 ± 1.16 % and <i>Pcdh19</i> -KO = 5.54 ± 1.73 %	ANOVA, F (2, 9) =0.241; p=0.791
2	WT = 22.41 ± 2.56 %, <i>Pcdh19</i> -HET = 21.45 ± 0.52 % and <i>Pcdh19</i> -KO = 24.54 ± 1.84 %	ANOVA, F (2, 9) =0.733; p=0.507
3	WT = 21.52 ± 3.73 %, <i>Pcdh19</i> -HET = 17.65 ± 2.15 % and <i>Pcdh19</i> -KO = 23.79 ± 2.14 %	ANOVA, F (2, 9) =1.248; p=0.332
4	WT = 9.89 ± 2.13 %, <i>Pcdh19</i> -HET = 10.39 ± 1.17 % and <i>Pcdh19</i> -KO = 9.23 ± 1.07 %	ANOVA, F (2, 9) =0.145; p=0.867
5	WT = 11.33 ± 1.87 %, <i>Pcdh19</i> -HET = 12.98 ± 1.88 % and <i>Pcdh19</i> -KO = 15.22 ± 4.47 %	ANOVA, F (2, 9), F=0.423; p=0.667
6	WT = 7.18 ± 1.85 %, <i>Pcdh19</i> -HET = 9.63 ± 1.61 % and <i>Pcdh19</i> -KO = 5.59 ± 1.64 %	ANOVA, F (2, 9) =1.424; p=0.29
7	WT = 6.94 ± 2.99 %, <i>Pcdh19</i> -HET = 3.73 ± 0.44 % and <i>Pcdh19</i> -KO = 4.27 ± 0.46 %	ANOVA, F (2, 9) =0.947; p=0.423
8	WT = 6.57 ± 1.35 %, <i>Pcdh19</i> -HET = 5.68 ± 1.43 % and <i>Pcdh19</i> -KO = 4.06 ± 1.05 %	ANOVA, F (2, 9) =0.976; p=0.414
9	WT = 5.83 ± 1.66 %, <i>Pcdh19</i> -HET = 9.84 ± 1.78 % and <i>Pcdh19</i> -KO = 5.34 ± 0.8 %	Independent-samples Kruskal-Wallis test, p = 0.087
10	WT = 2.68 ± 0.9 %, <i>Pcdh19</i> -HET = 1.51 ± 0.71 % and <i>Pcdh19</i> -KO = 2.41 ± 0.9 %	Independent-samples Kruskal-Wallis test, p = 0.526

P20 CR SSC and MC

LAYER	QUANTIFICATION	STATISTICAL ANALYSIS
I	WT = 2.55 ± 0.88 %, <i>Pcdh19</i> -HET = 2.86 ± 0.54 % and <i>Pcdh19</i> -KO = 1.45 ± 0.44 %	ANOVA, F (2, 9) =1.297; p=0.32
II/III	WT = 52.36 ± 3.66 %, <i>Pcdh19</i> -HET = 50.01 ± 4.49 % and <i>Pcdh19</i> -KO = 52.7 ± 1.56 %	Independent-samples Kruskal-Wallis test, p = 0.779
IV	WT = 12.76 ± 1.32 %, <i>Pcdh19</i> -HET = 19.72 ± 1.62 % and <i>Pcdh19</i> -KO = 16.67 ± 2.17 %	ANOVA, F (2, 9) =1.282; p=0.324
V	WT = 20.35 ± 1.7 %, <i>Pcdh19</i> -HET = 19.72 ± 1.57 % and <i>Pcdh19</i> -KO = 19.87 ± 1.84 %	ANOVA, F (2, 9) =0.038; p=0.963
VI	WT = 11.98 ± 0.68 %, <i>Pcdh19</i> -HET = 12.36 ± 1.79 % and <i>Pcdh19</i> -KO = 9.31 ± 1.14 %	ANOVA, F (2, 9) =1.67; p=0.242

Table A. 18. Details of the statistical analysis of CR distribution in P20 animals.

P20 CB

BIN	QUANTIFICATION	STATISTICAL ANALYSIS
1	WT = 4.32 ± 2.03 %, <i>Pcdh19</i> -HET = 3.38 ± 1.78 % and <i>Pcdh19</i> -KO = 3.94 ± 0.31 %	ANOVA, F (2, 9) =0.092; p=0.913
2	WT = 21.8 ± 1.23 %, <i>Pcdh19</i> -HET = 23.69 ± 0.93 % and <i>Pcdh19</i> -KO = 24.19 ± 1.68 %	ANOVA, F (2, 9) =0.912; p=0.436
3	WT = 24.4 ± 0.67 %, <i>Pcdh19</i> -HET = 25.71 ± 2.42 % and <i>Pcdh19</i> -KO = 23.96 ± 0.92 %	Independent-samples Kruskal-Wallis test, p = 0.735
4	WT = 30.85 ± 1.05 %, <i>Pcdh19</i> -HET = 28.69 ± 1.3 % and <i>Pcdh19</i> -KO = 30.01 ± 0.78 %	ANOVA, F (2, 9) =1.039; p=0.393
5	WT = 10.87 ± 3.81 %, <i>Pcdh19</i> -HET = 9.98 ± 0.98 % and <i>Pcdh19</i> -KO = 9.83 ± 2.08 %	ANOVA, F (2, 9) =0.047; p=0.954
6	WT = 2.51 ± 0.38 %, <i>Pcdh19</i> -HET = 2.73 ± 0.1 % and <i>Pcdh19</i> -KO = 2.91 ± 0.43 %	ANOVA, F (2, 9) =0.35; p=0.714
7	WT = 2.17 ± 0.17 %, <i>Pcdh19</i> -HET = 2.96 ± 0.26 % and <i>Pcdh19</i> -KO = 1.98 ± 0.25 %	ANOVA, F (2, 9) =5.023; p=0.034 Post-hoc test Tukey HSD, WT vs <i>Pcdh19</i> -HET, p=0.089; WT vs <i>Pcdh19</i> -KO, p=0.841; <i>Pcdh19</i> -HET vs. <i>Pcdh19</i> -KO, p=0.037
8	WT = 1.9 ± 0.2 %, <i>Pcdh19</i> -HET = 1.83 ± 0.3 % and <i>Pcdh19</i> -KO = 1.92 ± 0.21 %	ANOVA, F (2, 9) =0.039; p=0.962
9	WT = 0.92 ± 0.2 %, <i>Pcdh19</i> -HET = 0.87 ± 0.35 % and <i>Pcdh19</i> -KO = 1.12 ± 0.23 %	Independent-samples Kruskal-Wallis test, p = 0.511
10	WT = 0.26 ± 0.12 %, <i>Pcdh19</i> -HET = 0.15 ± 0.07 % and <i>Pcdh19</i> -KO = 0.14 ± 0.07 %	ANOVA, F (2, 9) =0.571; p=0.584

P20 CB DL

BIN	QUANTIFICATION	STATISTICAL ANALYSIS
6	WT = 32.14 ± 2 %, <i>Pcdh19</i> -HET = 32.98 ± 2.29 % and <i>Pcdh19</i> -KO = 36.77 ± 2.57 %	ANOVA, F (2, 9) =0.215; p=0.811
7	WT = 28.56 ± 1.45 %, <i>Pcdh19</i> -HET = 35.07 ± 1.39 % and <i>Pcdh19</i> -KO = 23.27 ± 2.43 %	ANOVA, F (2, 9) =10.634; p=0.004 Post-hoc test Tukey HSD, WT vs <i>Pcdh19</i> -HET, p=0.073; WT vs <i>Pcdh19</i> -KO, p=0.154; <i>Pcdh19</i> -HET vs. <i>Pcdh19</i> -KO, p=0.003
8	WT = 24.33 ± 0.52 %, <i>Pcdh19</i> -HET = 20.66 ± 2.58 % and <i>Pcdh19</i> -KO = 24.19 ± 4.35 %	Independent-samples Kruskal-Wallis test, p = 0.39
9	WT = 11.83 ± 1.44 %, <i>Pcdh19</i> -HET = 9.63 ± 2.81 % and <i>Pcdh19</i> -KO = 13.69 ± 1.62 %	ANOVA, F (2, 9) =0.931; p=0.429
10	WT = 3.14 ± 1.48 %, <i>Pcdh19</i> -HET = 1.67 ± 0.71 % and <i>Pcdh19</i> -KO = 2.07 ± 1.12 %	ANOVA, F (2, 9) =0.437; p=0.659

Table A. 19. Details of the statistical analysis of CB distribution in P20 animals.

P20 SST SSC

BIN	QUANTIFICATION	STATISTICAL ANALYSIS
1	WT = 3.58 ± 2.16 %, <i>Pcdh19</i> -HET = 3.79 ± 0.84 % and <i>Pcdh19</i> -KO = 4.15 ± 1.25 %	ANOVA, F (2, 9) =0.036; p=0.964
2	WT = 7.84 ± 0.57 %, <i>Pcdh19</i> -HET = 11.56 ± 2.96 % and <i>Pcdh19</i> -KO = 5.31 ± 1.2 %	ANOVA, F (2, 9) =2.811; p=0.113
3	WT = 4.57 ± 0.67 %, <i>Pcdh19</i> -HET = 9.66 ± 1.38 % and <i>Pcdh19</i> -KO = 6.04 ± 2.31 %	ANOVA, F (2, 9) =2.678; p=0.122
4	WT = 6.11 ± 1.73 %, <i>Pcdh19</i> -HET = 4.11 ± 0.29 % and <i>Pcdh19</i> -KO = 6.14 ± 2.19 %	ANOVA, F (2, 9) =0.513; p=0.615
5	WT = 11.21 ± 1.34 %, <i>Pcdh19</i> -HET = 10.58 ± 1.62 % and <i>Pcdh19</i> -KO = 17.71 ± 2.21 %	ANOVA, F (2, 9) =5.257; p=0.031 Post-hoc test Tukey HSD, WT vs <i>Pcdh19</i> -HET, p=0.964; WT vs <i>Pcdh19</i> -KO, p=0.06; <i>Pcdh19</i> -HET vs. <i>Pcdh19</i> -KO, p=0.04
6	WT = 12.55 ± 3.48 %, <i>Pcdh19</i> -HET = 8.09 ± 2.3 % and <i>Pcdh19</i> -KO = 8.13 ± 3.16 %	ANOVA, F (2, 9) =0.72; p=0.513
7	WT = 11.56 ± 1.31 %, <i>Pcdh19</i> -HET = 10.65 ± 1.18 % and <i>Pcdh19</i> -KO = 10.91 ± 1.85 %	ANOVA, F (2, 9) =0.103; p=0.904
8	WT = 12.4 ± 0.53 %, <i>Pcdh19</i> -HET = 15.79 ± 0.4 % and <i>Pcdh19</i> -KO = 15.81 ± 4.34 %	ANOVA, F (2, 9) =0.602; p=0.568
9	WT = 19.15 ± 3.3 %, <i>Pcdh19</i> -HET = 20.42 ± 3.21 % and <i>Pcdh19</i> -KO = 14.82 ± 2.72 %	ANOVA, F (2, 9) =0.905; p=0.439
10	WT = 11.02 ± 2.53 %, <i>Pcdh19</i> -HET = 5.35 ± 2.61 % and <i>Pcdh19</i> -KO = 10.98 ± 3 %	ANOVA, F (2, 9) =1.435; p=0.288

P20 SST SSC and MC

LAYER	QUANTIFICATION	STATISTICAL ANALYSIS
I	WT = 2.04 ± 0.47 %, <i>Pcdh19</i> -HET = 1.89 ± 0.22 % and <i>Pcdh19</i> -KO = 2.06 ± 0.81 %	Independent-samples Kruskal-Wallis test, p = 0.794
II/III	WT = 24.63 ± 3.36 %, <i>Pcdh19</i> -HET = 23.32 ± 2.14 % and <i>Pcdh19</i> -KO = 19.85 ± 1.56 %	ANOVA, F (2, 9) =0.999; p=0.406
IV	WT = 15.57 ± 0.74 %, <i>Pcdh19</i> -HET = 11.43 ± 1.46 % and <i>Pcdh19</i> -KO = 12.99 ± 2.12 %	ANOVA, F (2, 9) =1.825; p=0.216
V	WT = 31.18 ± 3.36 %, <i>Pcdh19</i> -HET = 38.51 ± 3.43 % and <i>Pcdh19</i> -KO = 32.29 ± 3.4 %	ANOVA, F (2, 9) =1.354; p=0.306
VI	WT = 26.58 ± 4.51 %, <i>Pcdh19</i> -HET = 24.85 ± 2.03 % and <i>Pcdh19</i> -KO = 32.82 ± 3.34 %	ANOVA, F (2, 9) =1.483; p=0.278

Table A. 20. Details of the statistical analysis of SST distribution in P20 animals.

OPEN FIELD MALES

Trial 2

P21

TIME (min)	QUANTIFICATION	STATISTICAL ANALYSIS
5	WT SGH = 585.9 ± 39.31 cm, WT MGH = 996.73 ± 136.47 cm and KO MGH = 722.14 ± 76.94 cm	ANOVA, F (2, 41) = 6.607; p=0.003 Post-hoc test Tukey HSD, WT SGH vs WT MGH, p=0.002 ; WT SGH vs KO MGH, p=0.406; WT MGH vs KO MGH, p=0.07
10	WT SGH = 692.84 ± 61.22 cm, WT MGH = 929.38 ± 118.05 cm and KO MGH = 806.51 ± 67.58 cm	Independent-samples Kruskal-Wallis test, p = 0.274
15	WT SGH = 810.48 ± 63.26 cm, WT MGH = 860.55 ± 77.13 cm and KO MGH = 831.95 ± 60.75 cm	ANOVA, F (2, 41) = 0.134; p=0.875
20	WT SGH = 759.74 ± 53.7 cm, WT MGH = 890.8 ± 106.27 cm and KO MGH = 814.17 ± 63.84 cm	ANOVA, F (2, 41) = 0.829; p=0.444

P60

TIME (min)	QUANTIFICATION	STATISTICAL ANALYSIS
5	WT SGH = 1290.46 ± 74.43 cm, WT MGH = 1230.58 ± 89.57 cm and KO MGH = 1383.32 ± 71.29 cm	ANOVA, F (2, 38) = 0.861; p=0.431
10	WT SGH = 1121.99 ± 67.98 cm, WT MGH = 1150.98 ± 68.13 cm and KO MGH = 1042.61 ± 55.2 cm	Independent-samples Kruskal-Wallis test, p = 0.274
15	WT SGH = 1081.52 ± 78.31 cm, WT MGH = 1054.52 ± 54.57 cm and KO MGH = 1044.68 ± 60.62 cm	Independent-samples Kruskal-Wallis test, p = 0.985
20	WT SGH = 975.61 ± 60.61 cm, WT MGH = 950.92 ± 108.13 cm and KO MGH = 866.27 ± 64.75 cm	ANOVA, F (2, 38) = 0.596; p=0.556

Table A. 21. Details of the statistical analysis of open field behaviour in male mice.

OPEN FIELD FEMALES

Trial 2

P21

TIME (min)	QUANTIFICATION	STATISTICAL ANALYSIS
5	WT SGH = 441.46 ± 47.42 cm, WT MGH= 867.31 ± 89.87 cm and HET MGH = 1121.25 ± 99.45 cm	ANOVA, F (2, 40) =21.772; p=0 Post-hoc test Tukey HSD, WT SGH vs WT MGH, p=0.001 ; WT SGH vs HET MGH, p=0 ; WT MGH vs HET MGH, p=0.079
10	WT SGH = 740.27 ± 63.61 cm, WT MGH= 908.23 ± 82.32 cm and HET MGH = 963.56 ± 48.81 cm	ANOVA, F (2, 40) =3.181; p=0.052
15	WT SGH = 637.38 ± 71.41 cm, WT MGH= 817.2 ± 76.45 cm and HET MGH = 863.62 ± 66.06 cm	ANOVA, F (2, 40) =2.893; p=0.067
20	WT SGH = 668.47 ± 70.05 cm, WT MGH= 776.04 ± 60.16 cm and HET MGH = 745.33 ± 63.28 cm	Independent-samples Kruskal-Wallis test, p = 0.546

P60

TIME (min)	QUANTIFICATION	STATISTICAL ANALYSIS
5	WT SGH = 882.14 ± 63.85 cm, WT MGH= 1331.95 ± 88.07 cm and HET MGH = 1273.9 ± 68.51 cm	ANOVA, F (2, 40) =12.246; p=0 Post-hoc test Tukey HSD, WT SGH vs WT MGH, p=0 ; WT SGH vs HET MGH, p=0.001 ; WT MGH vs HET MGH, p=1
10	WT SGH = 972.25 ± 64.09 cm, WT MGH= 1031.21 ± 80.82 cm and HET MGH = 989.47 ± 59.63 cm	Independent-samples Kruskal-Wallis test, p = 0.886
15	WT SGH = 904.1 ± 70.92 cm, WT MGH= 914.24 ± 59.6 cm and HET MGH = 1019.99 ± 90.9 cm	ANOVA, F (2, 40) =0.682; p=0.511
20	WT SGH = 902.79 ± 75.44 cm, WT MGH= 934.21 ± 84.72 cm and HET MGH = 979.53 ± 78.62 cm	Independent-samples Kruskal-Wallis test, p = 0.423

Table A. 22. Details of the statistical analysis of open field behaviour in female mice.